High-resolution reconstruction of atmospheric CO_2 concentrations during the last interglacial based on the EDC ice core

Inaugural Dissertation

of the Faculty of Science,
University of Bern

presented by

Lucas Silva

from Portugal

Supervisor of the doctoral thesis:

Prof. Dr. Thomas F. Stocker

Prof. Dr. Hubertus Fischer

Climate and Environmental Physics
Physics Institute of the University of Bern

High-resolution reconstruction of atmospheric CO_2 concentrations during the last interglacial based on the EDC ice core

Inaugural Dissertation

of the Faculty of Science,
University Bern

presented by

Lucas Silva

from Portugal

Supervisor of the doctoral thesis:

Prof. Dr. Thomas F. Stocker

Prof. Dr. Hubertus Fischer

Climate and Environmental Physics
Physics Institute of the University of Bern

Accepted by the Faculty of Science.

Bern, 29. April 2022

The Dean:
Prof. Dr. Zoltan Balogh

To my loving wife,
Inês,
and the wonderful sons she gave me,
Raul and Artur.

Summary

The successful reconstruction of past atmospheric CO_2 concentrations from Antarctic ice cores started in the early 1980s. Each newly published record is the product of painstaking discrete measurements of hand-sized samples from ice cores that can reach more than 3 kilometers of depth. Hence, high-resolution reconstructions of CO_2 are usually limited to a specific window of time of the last 800 thousand years (800 ka). Using the EDC ice core, we reconstructed atmospheric CO_2 concentrations during Marine Isotope Stage 5 (MIS 5; 135–106 ka). The new dataset covers the penultimate deglaciation, the last interglacial, and the last glacial inception in unprecedented centennial resolution. Our new record shows remarkably stable CO_2 concentrations for ten thousand years during MIS 5e. Simultaneously, a series of worldwide climatic changes took place, such as falling temperatures in the oceans and over the poles, growing ice sheets, generalized climate instability in the Northern Hemisphere, and changes in the Earth's orbital parameters. The lack of marked variability in the CO_2 record during this period can be explained by an unusual combination of dynamic carbon fluxes and the lack of a suitable deep ocean storage reservoir. As enigmatic as the plateau is the last glacial inception when CO_2 suddenly drops from interglacial levels and resumes its coupling with Antarctic temperature. We propose that a Northern Hemisphere trigger sourced this threshold-like behavior.

Despite the centennial-scale resolution achieved with the MIS 5 record, we only tentatively interpret submillennial CO_2 features. While building the dataset, we realized that CO_2 showed sharp oscillations between neighboring data points, too fast to be fingerprinted by true atmospheric variability. Much of the ensuing work tackled the understanding of CO_2 fluctuations at the centimeter scale and how they affected our record. We concluded that while the high resolution allowed the establishment of precisely timed slope changes, individual fluctuations at the centennial scale were likely the result of fractionation effects during the bubble enclosure process in the ice core.

The measurement device used to reconstruct CO_2 at the University of Bern is the end product of decades of accumulated knowledge on how to measure CO_2 from ancient air bubbles trapped in polar ice. The centrifugal ice microtome (CIM), continuously developed and improved since 2008, is a dry-extraction technique with state-of-the-art precision and high sample throughput. During this Ph.D., the implemented improvements regarding the CIM related to statistical analysis of different potential sources of error. These finesses allowed for a deeper understanding of the system's intricacies and increased confidence when interpreting its output concentrations.

List of abbreviations

aU	Authigenic Uranium
AABW	Antarctic bottom water
AAIW	Antarctic intermediate water
ACP	Air cooled multi-stage roots pump
AICC12	Antartic Ice Core Chronology
AIM	Antarctic isotope maxima
AMOC	Atlantic meridional overturning circulation
AR6	Sixth Assessment Report
B/A	Bølling/Allerød
BAS	British Antarctic Survey
BB	Bernhard Bereiter
BCTZ	Bubble to clathrate transition zone
BE-OI	Beyond EPICA - Oldest Ice
BIA	Blue ice area
CDJ	Carbon dioxide jump
CE	Common Era
CF	ConFlat®
CIM	Centrifugal ice microtome
CNA	Christoph Nehrbass-Ahles
COLDEX	Centre for OLDest Ice EXploration
D-O	Dansgaard-Oeschger
DIC	Dissolved inorganic carbon
EAIS	East Antarctic ice sheet
EDC	EPICA Dome Concordia
EDML	EPICA Dronning Maud Land
EK	*Einkristall* - gas free ice
EPICA	European Project for Ice Coring in Antarctica
EQS	Equilibrium climate sensitivity
GAD	Gas-age distribution
GHG	Greenhouse gas
GOC	Global Overturning Circulation
HS	Heinrich Stadial
IGE	Institut des Géosciences de l'Environnement

IR	Infrared
IRD	Ice-rafted debris
IRLSM	Infrared laser spectrometer
IPCC	Intergovernmental Panel on Climate Change
IPICS	International Partnership for Ice Core Sciences
IQR	Interquartile range
ITCZ	Intertropical Convergence Zone
KUP	Climate and Environmental Physics, University of Bern
LDC	Little Dome C
LGI	Last glacial inception
LGM	Last glacial maximum
LIG	Last interglacial
LN_2	Liquid nitrogen
LOESS	Locally estimated scatterplot smoothing
LS	Lucas Silva
MBE	Mid-Brunhes event
MIS	Marine Isotope Stage
MOT	Mean ocean temperature
MPT	Mid-Pleistocene Transition
MWP	Meltwater Pulse
NA	North Atlantic
NAC	North Atlantic Current
NADW	North Atlantic deep water
NDC	Nationally determined contribution
NDIR	Non-dispersive infrared
NGRIP	North Greenland Ice Core Project
NH	Northern Hemisphere
NHSI	Northern Hemisphere Summer Insolation
PCTFE	Polychlorotrifluoroethylene
PETM	Paleocene-Eocene thermal maximum
PMIP	Paleoclimate Modelling Intercomparison Project
QCLAS	Quantum Cascade Laser Absorption Spectrometer
SA	South Atlantic
SAZ	Subantarctic Zone
SC	Steering Committee
SEM	Standard error of the mean
SH	Southern Hemisphere
SHW	Southern Hemisphere Westerlies
SIO	Scripps Institution of Oceanography

SO	Southern Ocean
SPG	Subpolar gyre
SSP	Shared Socioeconomic Pathway
SST	Sea surface temperature
STP	Standard temperature and pressure
T-x	Termination x
TAC	Total air content
TMP	Turbomolecular pump
UNFCCC	United Nations Framework Convention on Climate Change
UPS	Uninterruptible power supply
VCR	Vacuum coupling radiation
VOICE	Vostok Oldest Ice Challenge
WAIS	West Antarctica ice sheet
WD	WAIS Divide
XPS	Extruded polystyrene
YD	Younger Dryas

Contents

Chapter 1

Introduction

1.1 The CO_2 record through time

Direct measurements of carbon dioxide (CO_2) concentrations in the atmosphere were first performed in 1958, at the Mauna Loa Observatory, in Hawaii (Tans and Keeling, 2017). Today, almost one hundred observatory sites worldwide measure atmospheric concentrations of CO_2 monthly, and they all unequivocally show the same overall rising trend (see Figure 1.1).

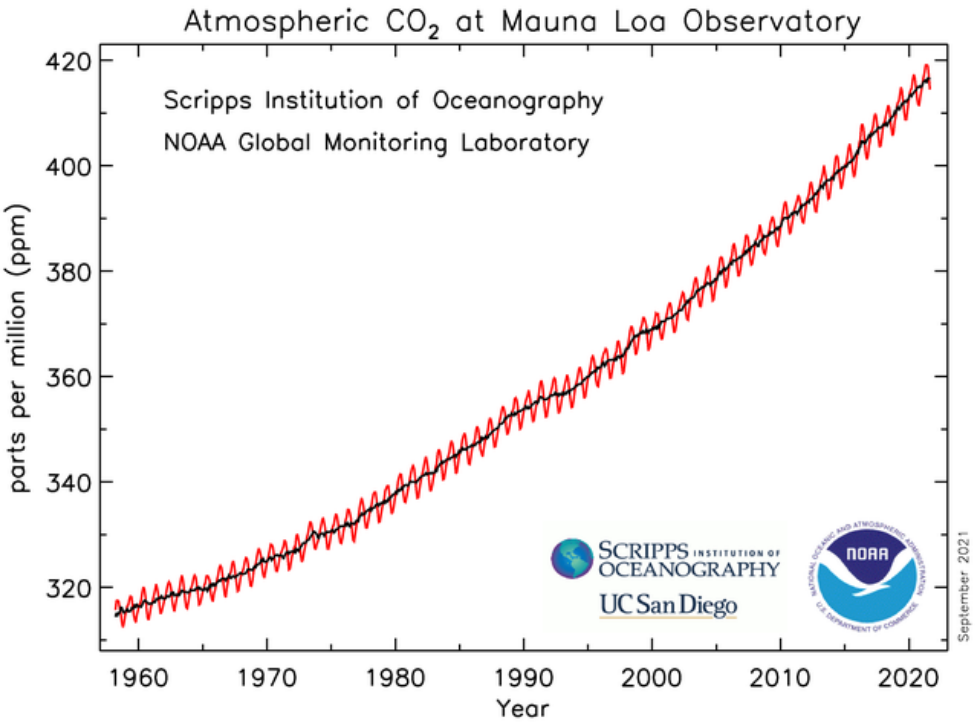

Figure 1.1: Historical evolution of atmospheric CO_2 concentrations since 1958 from the Mauna Loa Observatory, Hawaii. The red line represents the evolution of monthly mean values and evidences a seasonal signal. The black line represents the same mean monthly values, but detrended from the seasonal signal by applying a running average. Carbon dioxide concentrations are reported here as dry air mole fractions and expressed in parts per million (ppm). Source: Dr. Pieter Tans, NOAA/GML (gml.noaa.gov/ccgg/trends/) and Dr. Ralph Keeling, Scripps Institution of Oceanography (scrippsco2.ucsd.edu/).

In 60 years, the atmospheric CO_2 concentration rose by approximately 100 ppm, corresponding to an increase of 30%. At face value these numbers are impressive, but it is impossible to interpret this change without knowing the natural variability of CO_2 in the atmosphere, both in terms of amplitude and rate of change. The knowledge on natural CO_2 variability only came in the 1980s, when we had a first glimpse on how CO_2 levels are different between glacial and interglacial periods, based on Antarctic ice cores. Delmas et al. (1980) showed that the last glacial transition entailed a 100 ppm rise as well (from approximately 200 to 300 ppm) but this time over the course of five millennia (see Figure 1.2). Furthermore, their study suggested that atmospheric CO_2 remained relatively constant throughout the past 10 thousand years (10 ka; 1 ka =1 kiloannum = 1000 years before present, where present is defined as the year 1950 of the Common Era (CE)). Neftel et al. (1985) further supported this scenario, showing that the unusual rise during the 20^{th} century in fact started around 1800, after which the CO_2 concentration suddenly deviated away from the observed boundaries of the Holocene epoch.

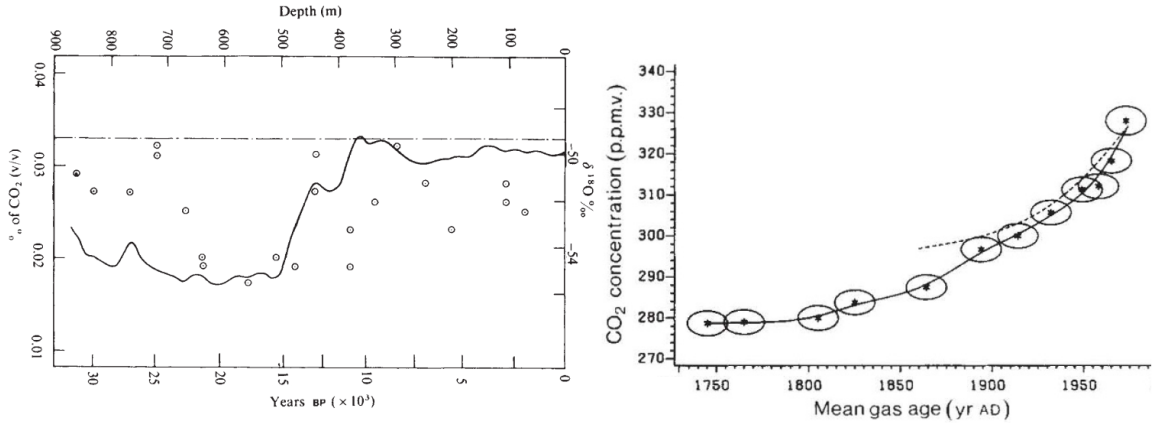

Figure 1.2: Early CO_2 reconstructions from Antarctic ice cores. Left: first record of the evolution of atmospheric CO_2 across the last deglaciation (black line) from Dome C. The dotted line was the CO_2 concentration at the time of publication. Right: CO_2 rise since 1750, from Siple Dome. Notice the good agreement with Figure 1.1 for 1950 onward. Figures taken and adapted from Delmas et al. (1980) and Neftel et al. (1985).

At the end of the 20^{th} century a major breakthrough finally settled the unusualness of the present CO_2 rise. In 1999, J. Petit and colleagues publish the results of a 3.6-kilometer deep ice core from Vostok station, in Antarctica. It gives us a clear and continuous climate history of the past 400 ka that no other environmental proxy can. The record covers four glacial cycles, and the evidence is clear: the 20^{th}-century rise of atmospheric CO_2 is without precedents. Importantly, the record shows carbon dioxide and Antarctic temperature co-varying very closely through cold and warm times. This data-based evidence was the nail in the coffin reinforcing previously raised concerns already in the 1970s (Broecker, 1975; Siegenthaler and Oeschger, 1978): what consequences on global temperatures will the current anthropogenic CO_2 rise have?

Another twenty years have passed since the Petit et al. (1999) paper, and yet many

questions still lay wide open. It is well established that CO_2 is a powerful greenhouse gas and that it plays a central role in the climate system through multiple and complex feedback mechanisms with other climate drivers (Arrhenius, 1896). Still, determining the exact interplay of these intricate connections under different boundary conditions is still subject to debate.

Amidst the scientific discussion, having a set of comprehensive and reliable data allows one to argue on more solid grounds. In this respect, our knowledge about past CO_2 levels has grown considerably in the last 20 years, although there is still much left to explore. It is exciting to see existing datasets improving precision and resolution, and to witness the development of novel measurement techniques. As we feed more reliable data into climate models, we are moving closer toward comprehensively understanding how the climate system operates; and in these stirred times of climate change, never were high-quality measurements so urgently needed.

1.1.1 A deep-past perspective

With the mindset of understanding current global warming by studying past climate change, much effort has been invested into achieving a clear picture of how atmospheric CO_2 varied throughout the planetary evolution of the Earth. The latest deep-past compilation guides us as far back as 420 million years ago (420 Ma), to the beginning of the Devonian Period, a time when the tectonic plates were still merging to create the Pangaea supercontinent (Foster et al., 2017). Ever since then, the Earth has seen very drastic swings both in the concentration of atmospheric CO_2 and climate as a whole (Figure 1.3). This long-term variability naturally shaped the necessary boundaries for life to bloom. For example, during the 60 million years that span the Devonian Period (ca. 419–359 Ma), atmospheric CO_2 concentrations progressively declined from 2000 parts per million (2000 ppm) to 400 ppm, with an accompanying global transformation from very warm to cold conditions, punctuated even by glaciation events (Foster et al., 2017).

Given the present challenge of climate change, with CO_2 concentrations around 415 ppm[i], it is perhaps surprising to learn that the initial high levels of CO_2 during the Devonian did not prevent a series of decisive evolutionary breakthroughs. This seemingly inhospitable super greenhouse climate favored the development of land vascular plants and the continental expansion of the first forests (Brugger et al., 2019). Progressive greening fueled the uptake and subsequent burial of carbon from the atmosphere into deep sedimentary layers. The expansion of forests also strengthened silicate weathering rates that further sequestered CO_2. The result was the development of a substantial continental carbon reservoir and the progressive lowering of atmospheric CO_2 levels. Life during the Devonian experienced an immense diversification of fish species and, as new coastal land opportunities became available, also witnessed the first vertebrates leaving the ocean to colonize the land. Para-

[i] As of June 2021, NOAA/GML (gml.noaa.gov/ccgg/trends/)

doxically, the modern-like CO_2 concentrations encountered by the end of the Devonian also set the stage for the Late Devonian Extinction, a series of episodes mainly affecting marine life that collectively stands as one of the five largest extinction events in the history of the Earth (Bambach, 2006). Gradual cooling and retreating sea levels may have particularly impacted prevailing shallow warm-water marine communities (Brugger et al., 2019). Many hypotheses have been put forward regarding the specific causes, but there is consensus that this mass extinction was not a stand-alone discernible peak in proxy records. Instead, it encompasses up to seven smaller events spread over 25 million years.

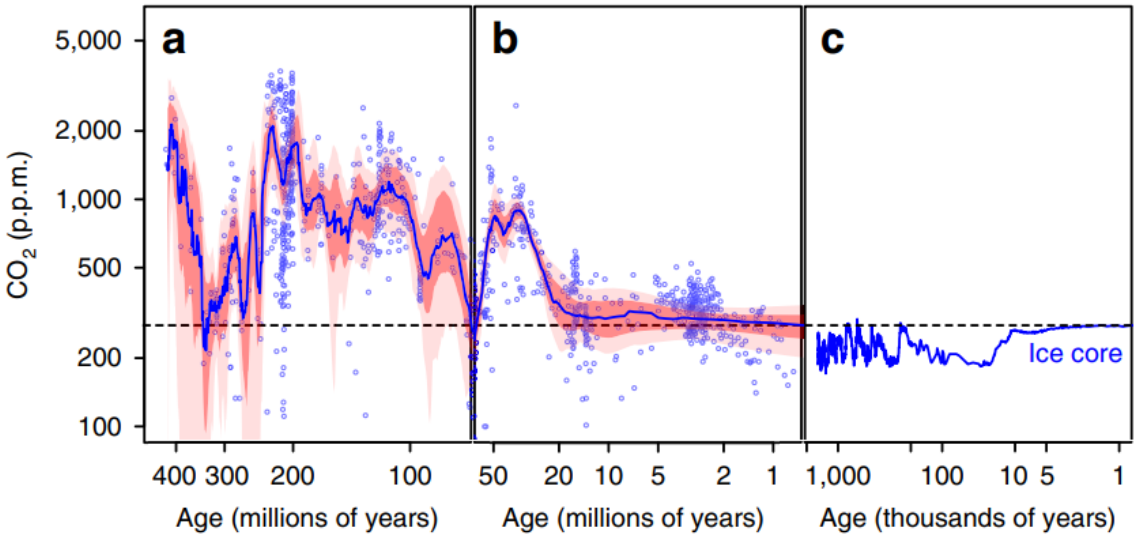

Figure 1.3: A compilation of available CO_2 reconstructions since the Devonian Period, ca. 420 Ma. Panels a) and b) show proxy-based CO_2, mostly from paleosols, with a best locally estimated scatterplot smoothing (LOESS) fit and associated uncertainty envelope. The uncertainty of ice core data in panel c) is too small to be shown at this scale (σ ∼1–3 ppm for individual records. See Bereiter et al. (2015) for a compilation). Adapted with permission from Foster et al. (2017).

While climate change during the Devonian was significant and left an indelible biospheric fingerprint, it was also slow-paced in nature. In these multi-million-year time scales, long-term mechanisms such as silicate weathering and the rearrangement of tectonic plates are some of the dominant factors behind environmental change. In contrast, CO_2 paleo records also evidence periods of fast climate change caused by different drivers. One example is the Paleocene-Eocene Thermal Maximum (PETM) which took place ca. 56 Ma. Figure 1.4 evidences the PETM as an outstanding event superimposed on a longer multi-million year warming trend. Constraints on the exact atmospheric concentration change of CO_2 are poor, but the change is bound to have encompassed several hundred ppm (Rae et al., 2021). The PETM is also characterized by a large negative carbon isotope excursion, between -4 to -6‰(permil). To put this number into context, the transition between the last ice age into the currently warm Holocene epoch entailed a fluctuation of -0.4‰(Schmitt et al., 2012). It evidences that the huge release of carbon came from ^{13}C-depleted sources (either CO_2 or

CH_4). Since it is unlikely that such an amount of carbon could easily be discharged into the atmosphere from any available CO_2 reservoir at the time, the leading hypothesis explaining the transient nature of the event are either a sudden prodigious release of methane from deep ocean hydrates, or volcanic emissions (Gehler et al., 2016; Haynes and Hönisch, 2020). Within a time frame of 3–20 thousand years, a total of 2300 to 12 000 petagrams of carbon (Pg C) may have been released to the atmosphere, according to a recent review (Gingerich, 2019). Global average temperatures then spiked by 5–8 °C and severe ocean acidification followed, with massive extinction of 35–50% of benthic foraminifera, among other deep-sea species (Kennett and Stott, 1991).

Interestingly, the wake of such drastic changes brought renewed opportunities for some species. The post PETM period saw increased diversity and speciation of some communities, with new mammalian orders appearing and spreading worldwide (Woodburne et al., 2009; Upham et al., 2021). Primates, in specific, likely first appeared during the mid-Cretaceous Period, around 90 Ma (Tavaré et al., 2002). It was, however, only following the PETM that they started to thrive. They benefited from the extinction of other terrestrial mammals during the PETM, warm Eocene climates, and a surge in plant diversification, which together created new favorable habitats.

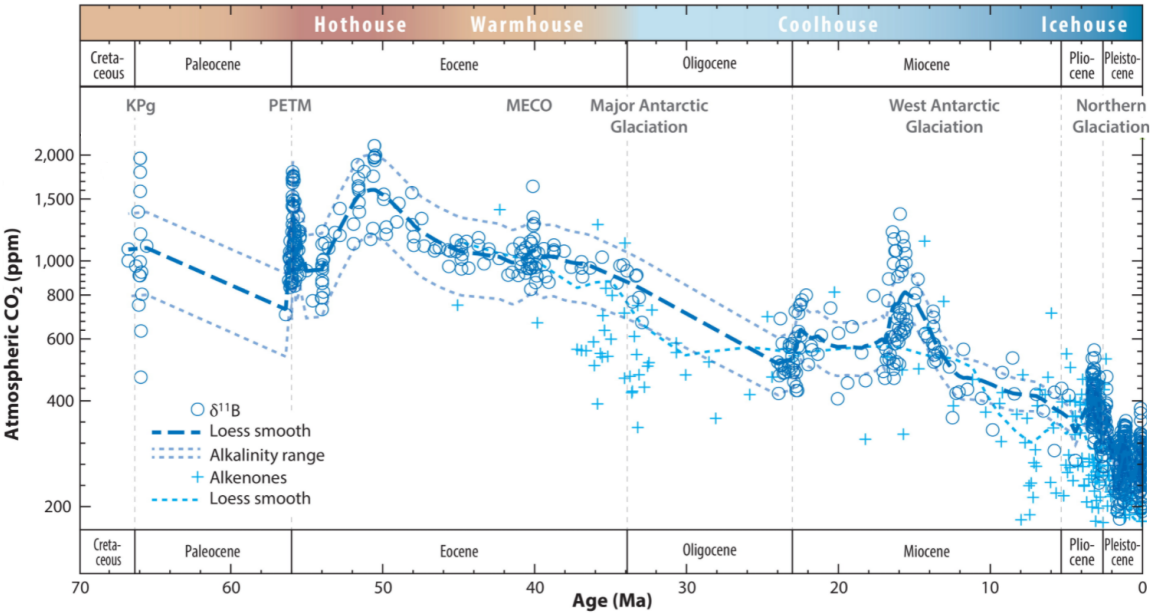

Figure 1.4: A compilation of proxy-based CO_2 reconstructions for the past 70 Ma from boron isotopes in planktic foraminifera and carbon isotopes in alkenones. Adapted with permission from Rae et al. (2021).

Carbon dioxide plays an indisputable, albeit complex, role in the climate of the Earth. Studying the deep past shows that throughout times of either slow or fast atmospheric CO_2 variability, life, holistically, did not necessarily fade nor flourish; instead, it transformed and adapted to new environmental conditions. Where one species saw misfortune, another one

experienced radiation. It remains unknown how the human race will live through ongoing climate change and the overall extent of the damage. What is certain, however, is that the challenge ahead is of gargantuan proportions, if we wish to maintain our societies and lifestyle that we hold presently (see Subsection 1.1.3). The PETM was the most abrupt event regarding carbon emissions available in the geological record, with estimates ranging from 0.3–1.5 $\mathrm{Pg\,C\,yr^{-1}}$ (Gingerich, 2019). By comparison, the decade 2010–19 had a mean emission rate of $9.6 \pm 0.5\,\mathrm{Pg\,C\,yr^{-1}}$, about ten times more than the PETM (Friedlingstein et al., 2020).

1.1.2 The last 800 ka

If the last 450 Ma saw wild fluctuations of CO_2 on geological time scales, a closer look at the past 800 ka reveals a somewhat more predictive behavior. In particular, the last 800 ka hold a special meaning for ice core climate scientists as it corresponds to the age of the oldest continuous ice core so far retrieved (EPICA Community Members, 2004). It was drilled in the early 2000s within the European Project for Ice Coring in Antarctica (EPICA) at Dome Concordia (EDC). The EDC ice core covers eight glacial cycles in unmatched resolution, offering a unique opportunity to study paleoclimate and carbon cycle changes in great detail. Figure 1.5 displays some of the most important records that have been derived from the EDC ice core and that have comprehensively been measured for the whole 800 ka. The covariation between temperature and CO_2 is striking and it evidences the 100 ka cyclicity of glacial/interglacial periods, as it was seen first in the Vostok ice core. The high-resolution allows studying the interplay of these parameters and the feedbacks that led to the particular response of our planet through time, going beyond the general orbital imprint that had long been shown (Hays et al., 1976). The discovery that orbital variations are not enough to cause the recorded amplitudes on temperature fueled research on feedback processes that could be amplifying the orbital insolation forcing (Wunsch, 2004). Greenhouse gases are naturally the foremost candidate, and climate simulations on the last deglaciation usually require a 30%–60% CO_2 increase relative to the glacial level to reproduce the observed temperature increase (Weaver et al., 1998; Schneider von Deimling et al., 2006).

Irrespective of possible leads and lags between Antarctic temperature and CO_2 (Shakun et al., 2012; Parrenin et al., 2013; Chowdhry Beeman et al., 2019), the 800 ka record shows the natural boundaries of both parameters during glacial and interglacial times absent of anthropogenic interference. Armed with this background information, it is now clear that our present atmosphere contains at least 100 ppm more of CO_2 with respect to past interglacials. It remains to be quantified what will the impact on future climate be, given the unexpected extra CO_2. While the implications for the near-future will affect biodiversity (see Subsection 1.1.3), sustained abnormally high CO_2 concentrations will likely interfere with the natural glacial/interglacial cycles that used to be orbital-paced. Two major studies suggested that combining the weak orbital forcing of the Holocene with the long lifetime of anthropogenic

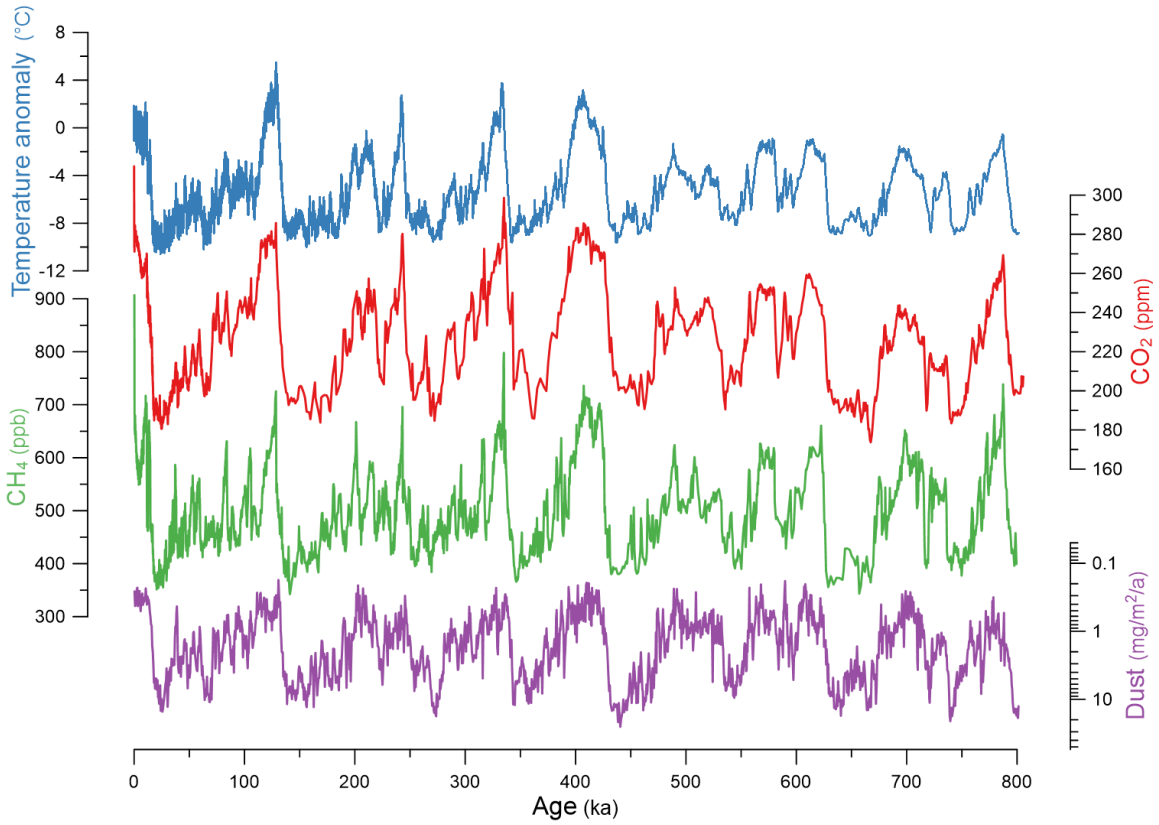

Figure 1.5: Paleoclimatic record of the last eight glacial cycles seen from the EDC ice core. From top to bottom: deuterium water isotope (blue; Jouzel et al. (2007)), CO_2 (red; Lüthi et al. (2008)), CH_4 (green; Loulergue et al. (2008)) and dust (purple; Lambert et al. (2008)).

CO_2 in the atmosphere may result in the current interglacial lasting another 100 000 to 500 000 years (Archer and Ganopolski, 2005; Ganopolski et al., 2016). In comparison, the interglacials of the past 800 ka lasted approximately 10 000 years, but the Holocene might be an exceptional period in this respect (Berger and Loutre, 2002). In 1972, eminent paleoclimate scientists gathered in a conference entitled "The Present Interglacial, How and When Will it End?" (Kukla and Matthews, 1972). Drawing knowledge from previous interglacials, they concluded that

> "(...) if nature were allowed to run its course unaltered by man, events similar to those which ended the last interglacial should be expected to occur perhaps as soon as the next few centuries."

The development of more sophisticated models and the retrieval of late Quaternary high-resolution datasets have recently cast some doubt on this statement. Two recent studies, based on insolation-CO_2 thresholds for glacial inceptions, found that around 1750 CE our planet narrowly missed a critical tipping point that would have led to a descent into a glacial period. Having missed it, they predict the planet to stay under interglacial conditions

for another 50 000 years. This extended period results from weak summer insolation in the boreal latitudes that will prevent the formation of large ice sheets in the Northern Hemisphere (NH) (Ganopolski et al., 2016; Talento and Ganopolski, 2021).

The EDC record has had a profound impact on our understanding of the glacial cycles of the late Pleistocene. It also has given a paleo perspective on the anthropogenic fingerprint and how unprecedented it is. Whether to understand the past or predict future pathways for our planet (Tzedakis et al., 2012), paleoclimate data have introduced important constraints on climate simulations and will remain a practical testbed for the accuracy of the models.

1.1.3 Future projections

The year 2021 saw the release of the first installment of the Sixth Assessment Report (AR6) by the Intergovernmental Panel on Climate Change (IPCC). The contribution by Working Group 1 is a mammoth undertaking by more than two hundred scientists worldwide to convey in a single volume the most up-to-date assessment of the physical science basis of the climate system. Current projections of climate change for the upcoming decades and centuries are as worrisome as ever (IPCC, 2021a). Figure 1.6 appears in the Technical Summary of AR6 as the first figure and puts the latest projections in perspective with deep paleo reconstructions. The three specific Shared Socioeconomic Pathways (SSP) represent three possible courses of action of human society in the coming centuries. In particular, each one represents a combination of a particular narrative of human development and an associated set of climate policies.

- **SSP1: Sustainability – Taking the Green Road**

  The optimistic SSP1 assumes high investment in education and health, with economic growth rooted in environmentally sustainable practices. It sees the world gradually shifting towards green policies and cutting CO_2 emissions drastically, with a peak in atmospheric CO_2 emissions and global surface temperatures by 2040. In the long-term, atmospheric CO_2 concentrations will remain outside the boundaries of the last 800 ka, but the associated warming of ($<$1.5 °C) implies overall low adaptation and mitigation efforts.

- **SSP2: Middle of the Road**

  Scenario SSP2 foresees a continuation of historical patterns of development well into the following centuries. Societal inequalities remain worldwide, with the environment deteriorating while more sustainable policies are slowly and asymmetrically put into motion. Rising temperatures lead us to warming levels last recorded during the mid-Pliocene, about 3-4 Ma.

- **SSP5: Fossil-fueled Development – Taking the Highway**

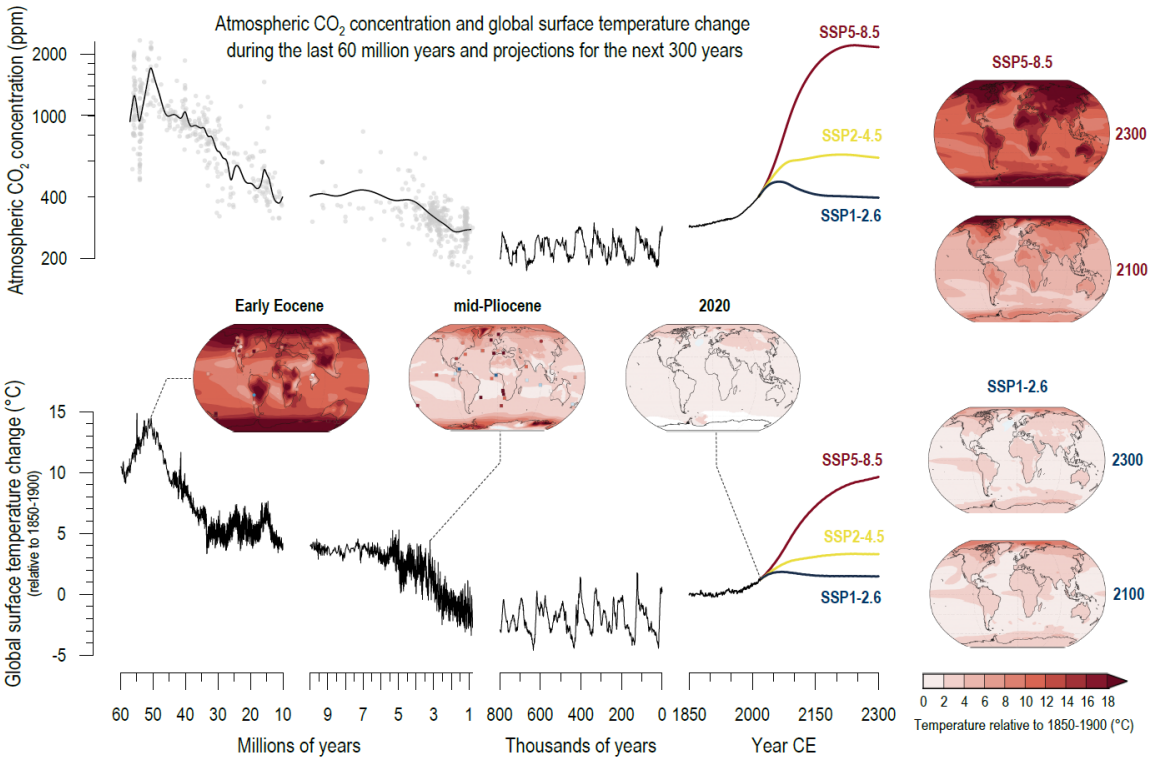

Figure 1.6: Long-term perspective on the progression of CO_2 and global surface temperature for the past 60 Ma from a compilation of multiple environmental paleoproxies. Projections until 2300 from different SSP scenarios. Taken from the Technical Summary of the WG I contribution to IPCC AR6 (Arias et al., 2021).

> This path embodies fast technological progress at the expense of fossil-fuel combustion. Like in SSP1, human development is prioritized, with investments in education, health, and a growing economy. Widespread energy-intensive lifestyles lay enormous stress on the environment, with a general trust that geo-engineering will reverse it. By 2300, the particular “worst-case" scenario SSP5-8.5 pathway takes us as far back as the early Eocene, the warmest period of the last 60 Ma, with global surface temperature changes of more than 13 °C relative to pre-industrial times.

The global stocktake on the implementation of the Paris Agreement goals is underway until 2023. Meanwhile, a report from the United Nations Framework Convention on Climate Change (UNFCCC) already projects failure in meeting the 1.5 °C target (see Figure 1.7). The latest data on nationally determined contributions (NDCs) project a global cut of 16% of emissions by 2030 relative to 2010, much less than the 45% required to stay below 1.5 °C. As it is, we are therefore on our way to track scenario SSP2-4.5, with an expected warming of 2.7 °C by 2100. This pathway implies a continuous rise of greenhouse gas concentrations well into the next century. In my view, it would yield more public action if we stopped promoting the already missed SSP1-2.6 scenario and the worst-case SSP5-8.5 as realistic pathways. As it stands, the “Middle of the Road" nomenclature gives the false impression

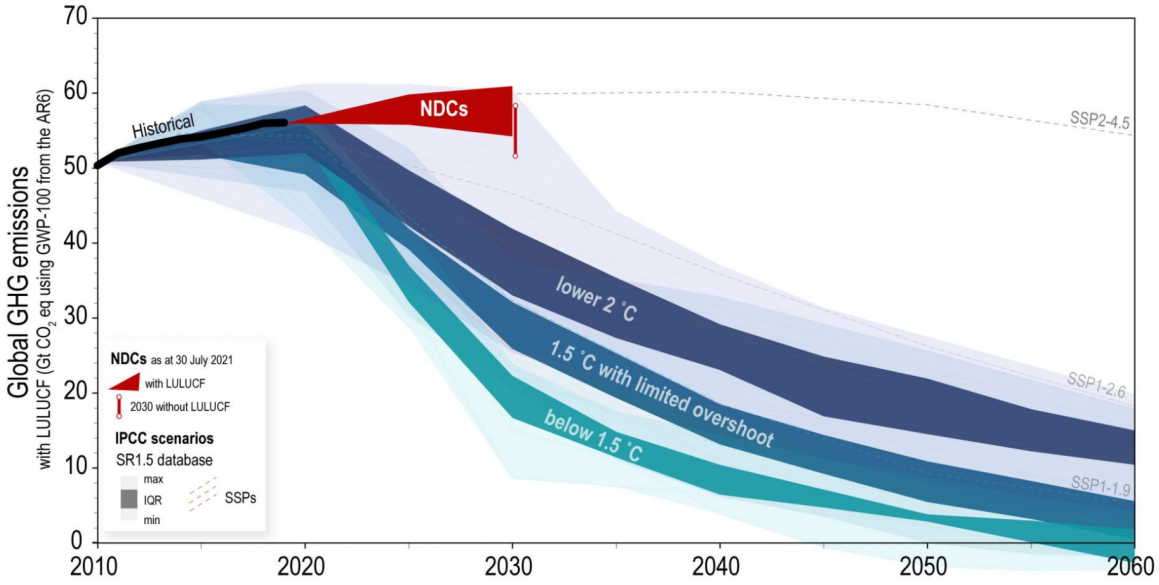

Figure 1.7: Future pathways for the evolution of global greenhouse gas (GHG) emissions, with current projections for 2030 from available NDCs. The depicted scenarios are from IPCC SR1.5 (2018). Taken from UNFCCC. Secretariat (2021).

that we are actually not doing that bad — when sadly we are still dangerously interfering with the climate system, in blatant contrast to Article 2 of the UNFCCC (United Nations and Canada, 1992):

> "The ultimate objective of this Convention and any related legal instruments that the Conference of the Parties may adopt is to achieve, in accordance with the relevant provisions of the Convention, stabilization of greenhouse gas concentrations in the atmosphere at a level that would prevent dangerous anthropogenic interference with the climate system. Such a level should be achieved within a time-frame sufficient to allow ecosystems to adapt naturally to climate change, to ensure that food production is not threatened and to enable economic development to proceed in a sustainable manner."

To this date, 137 countries have officially pledged to carbon neutrality, mostly centered around 2050. However, neither pledges nor NDCs are legally binding unless the country transforms it as an official policy or enshrines it in law. Indeed, 99 out of 137 countries still have their pledges purely under discussion, inhibiting proper legal action as there is no defined official standing.

1.2 Reconstructing past CO_2

1.2.1 Rationale

Taken as a black body, the Earth has an emission temperature of −18 °C, following an application of the Stefan-Boltzmann black body law [ii]. The fact that global average surface temperatures are much higher (14.88 °C in 2020, NOAA (2021)) is due to the presence of greenhouse gases in the lowermost layer of the atmosphere. These gases partly absorb the black body radiation of the Earth in the near infrared. Following absorption, the greenhouse gas molecules experience an increase in temperature and subsequently reemit heat in all directions, with half of it radiating downwards and the other half radiating upwards. Heat that is radiated upwards will continue to encounter other greenhouse molecules in a cascading effect until the greenhouse gas concentration is so small that upward radiated heat goes directly into space. On the other hand, heat that is radiated downwards will eventually reach the surface and be absorbed. The net effect of this process is an added warming of the surface of the Earth, and the specific concentration of greenhouse gases in the atmosphere dictates how much warming we experience. In this respect, water vapor is by far the dominant greenhouse gas in the atmosphere, but its concentration is strongly temperature-regulated. Following a positive feedback loop, increasing temperature leads to more water vapor in the atmosphere, which through its greenhouse effect raises temperature further. Therefore, water vapor is an amplifier of any thermal fluctuation, be it positive or negative. The greenhouse effect by water vapor thus plays an important role in anthropogenic climate change, as it amplifies any increase or decrease of temperature caused by other drivers. Among them, the relative abundance and strength of CO_2 gives it the largest positive radiative forcing as a climate change driver (see Figure 1.8).

Following this rationale, it is inevitable that changes in the concentration of atmospheric CO_2 will lead to a change in the total radiative forcing, which will cascade into a change in global temperature. The degree to which a change in radiative forcing affects global temperature is encapsulated in the equilibrium climate sensitivity (EQS) parameter. As of today, best estimates indicate an extra 3 °C of warming for every doubling of the radiative forcing (IPCC, 2021b). However, the *very likely* range stands between 2 and 5 °C — an uncertainty that somehow evidences how much we still do not know about the consequences of radically raising the concentration of greenhouse gases in the atmosphere. Irrespective of this knowledge gap, the fact that we have 95% confidence that the EQS is >2 °C is reason enough to worry, as the world is already experiencing losses and extreme events due to climate change with warming currently at >1.1 °C (WMO, 2021).

In order to improve our estimates, we need climate models that better capture the physical mechanisms behind climate change and draw a more realistic picture of what is to come. While we try to convey our current understanding of how the climate operates

[ii] This estimate belongs in any high-school physics textbook

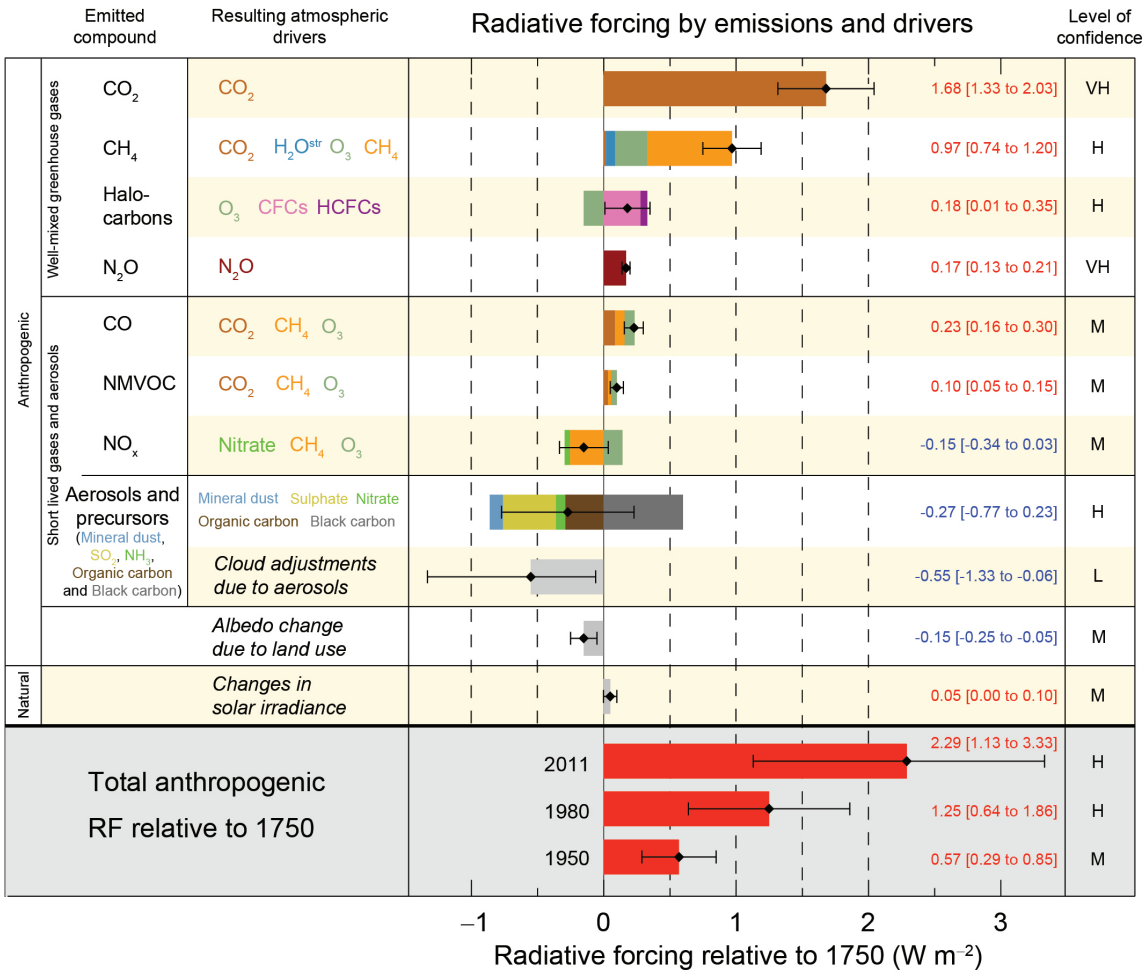

Figure 1.8: Radiative forcing for the main drivers of climate change in 2011 relative to 1750. Taken from IPCC (2013)

through climate models, their accuracy needs to be validated by satisfactorily simulating well-documented past climate change. From there, the knowledge leap by correctly modeling paleo data is hopefully translated into more comprehensive and better climate models and hence, better projections. Granted, no climate model is perfect — but they all benefit from having better paleo datasets to constrain their results with.

1.2.2 Ice cores

But how can we open a window to look into the past and attain paleoclimate data? How does one reconstruct essential climate parameters such as global average temperature, mean sea level, or the concentration of greenhouse gases in the atmosphere? The answer lies in the interpretation of environmental proxies, a set of natural recorders in the environment that preserve information about past climate variability. Tree rings, pollen, ice cores, ocean sediments, and corals are some of the most frequent tools in paleoclimatology, allowing us

to quantify past climate change. In the case of past atmospheric CO_2, Antarctic ice cores are the only direct atmospheric paleo archive covering the last 800 ka (EPICA Community Members, 2004).

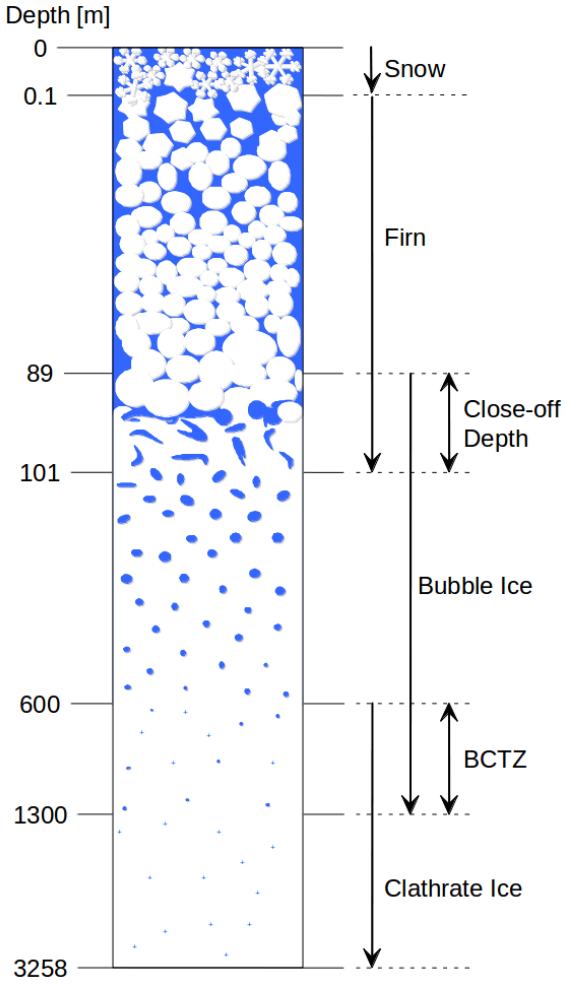

Figure 1.9: Vertical profile of a typical ice core with specific transition depths from the EDC ice core, as an example. Adapted from Schwander (1996) and Bereiter (2012).

Ice cores provide a wealth of paleoclimate data. They can be deciphered by analyzing either its ice or gas phase (see Figure 1.9). As snow fall events accumulate at the surface, individual layers shift downwards due to gravitational settling and glacier flow while density increases. The crystalline structure experiences mounting hydrostatic pressure with increasing depth, and snow crystals gradually become ice crystals through sintering. This process happens in the firn column, a porous zone with a mixture of snow and ice, typically at 50–100 m below the surface, depending on local accumulation rates and temperature (Neff, 2014). The firn column exchanges air with the atmosphere through an irregular network of ducts and interstitial air pockets that eventually connect to the surface (Schwander and Stauffer, 1984). The tight spacing prevents bulk airflow, and instead, transport occurs through slow molecular diffusion, leading to fractionation. As the firn column deepens,

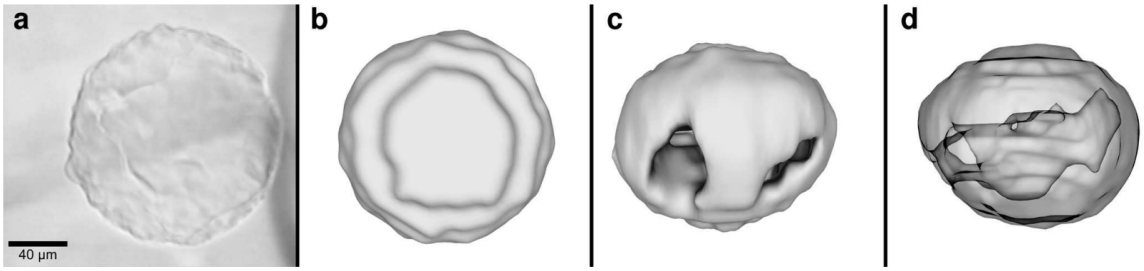

Figure 1.10: Raman tomography of a typical clathrate in an ice core. Sample taken from the EPICA Dronning Maud Land (EDML) ice core in the BCTZ at 1005 m depth; a) microscopic image; b) 3D reconstruction; c) side view, showing holes d) semi-transparent side view, with visible ice intrusion. Adapted from Weikusat et al. (2015) with permission.

growing hydrostatic pressure forces the crystals to pack and reorganize, assuming different configurations. Therefore, they grow and reorient themselves progressively until becoming a continuous mass. The arrival at the close-off depth marks the definite trapping of air occlusions through the closure of exchange channels by the surrounding ice matrix.

Beyond the close-off depth, bubbly ice undergoes further deformation as it moves deeper into the ice and the overlying hydrostatic pressure intensifies. When the inner gas pressure surpasses the dissociation pressure of the N_2 and the O_2 inside the bubble, the latter collapses and may form an air hydrate (clathrate) instead (see Figure 1.10). In this process, the hosting ice lattice rearranges its crystallographic shape to accommodate the guest molecules of low molecular weight (e.g., N_2, O_2, CO_2). These often result in cubic or hexagonal lattices, each one caging one to two individual gas molecules [iii]. In this purely physical phase change, no chemical reaction occurs, leaving the preserved atmospheric constituents individually intact. The transition from air bubbles to clathrates can take place over hundreds of meters, in a zone called the bubble to clathrate transition zone (BCTZ), as the hydrates slowly nucleate (Uchida et al., 2014). Below the BCTZ, only clathrates exist.

Although bubbles and clathrates in an ice core contain direct atmospheric samples of past times, there are still challenges when measuring the contents of the gas phase and the interpretation is not entirely straightforward. For example, the dynamic air exchange between the bottom of the firn and the air at the surface across the porous system of the firn is a complex matter (Schwander and Stauffer, 1984; Fourteau et al., 2017). Fractionation processes also happen even after the bubble enclosure process is completed, with an increase in overloading pressure leading to preferential diffusion of lighter molecules (e.g. O_2, Ar) from the bubble to the ice matrix (Kobashi et al., 2015). Further down, differences in permeation coefficients lead to enrichment in relative concentrations between bubbles and clathrates during the clathratization process in and below the BCTZ (Lüthi et al., 2010; Shackleton et al., 2019; Haeberli et al., 2021). And yet, despite having to account for these

[iii] Ball-like structures are also possible, such as a pentagonal dodecahedron, hexagonal truncated trapezohedron, or hexadecahedron

effects, the clear advantage of analyzing CO_2 on ice cores over other environmental proxies is the non-need of transfer functions. The purpose of these functions is to translate the measured parameter into the inferred physical quantity. They necessarily include certain assumptions about the acting mechanisms and, to a certain degree, a grain of faith as well. Bypassing these functions by directly measuring a sample of the atmosphere grants the analysis of ice cores a much bigger chance at correctly representing past absolute levels of atmospheric CO_2.

Time-wise, the oldest continuous ice core spans the last eight glacial-interglacial cycles, when our planet oscillated between cold (glacial) and warm (interglacial) periods[iv]. This relatively recent time window includes many time scales of climate change, ranging from slow, orbital-induced variations to decade-long abrupt events. It offers opportunities to precisely reconstruct the planet's climate under many different boundary conditions and is a precious testbed for climate simulations (e.g., the Paleoclimate Modelling Intercomparison Project (PMIP)- Phase 4; (Otto-Bliesner et al., 2017; Kageyama et al., 2021).

As it is the case with all other environmental archives, ice cores impose a trade-off between age span and resolution. Greenland ice cores currently do not extend beyond the last interglacial (LIG), ca. 129–116 ka, but in return can offer yearly resolution from present until 60 ka, allowing the study of seasonal signals (Svensson et al., 2008). On the other hand, ice cores from the East Antarctic Plateau result from desert-like precipitation conditions, with low accumulation rates of only a few centimeters of ice-equivalent per year. Such ice cores, stretching currently between 400–800 ka, can hardly offer sub-centennial resolution for CO_2 reconstructions since their gas-age distribution (GAD) has a large width. In other words, the low accumulation characteristics force a slow bubble enclosure process, whereby at the moment of closure the bubble air content is best described by a gaussian distribution over time with a long tail toward the past (Spahni et al., 2003). It should be noted that this gas-age distribution does not apply for ice phase archive, which is formed by the progressive layering and sintering of snow events. This leads to an important feature of ice cores, in which the air content of a bubble at any given depth is always younger than than the ice surrounding it. Furthermore, in the deepest parts of the ice core, the hydrostatic pressure at 2–3 km of depth induces severe thinning, and dominant smoothing processes erase high-frequency variability (Petit et al., 1999; Lüthi et al., 2008; Motoyama, 2007). Despite these shortcomings, the resolution and accuracy of low-accumulation ice cores are still markedly superior to other proxies covering the same period, as evidenced in panel c) of Figure 1.3.

1.2.3 Proxies of paleo CO_2

Carbon dioxide is a well-mixed greenhouse gas. When trapped in polar ice, the recorded atmospheric concentration closely reflects a global mean, with local conditions not playing

[iv] Snapshots of two-million-year-old ice have been retrieved from the Allan Hills blue ice area, but not a continuous record (Yan et al., 2019)

a significant role. This feature leads to a relatively straightforward interpretation without having to disentangle multiple source regions and local noise effects. It also allows for comparison between ice cores from different locations, although offsets exist that are not yet well understood (Nehrbass-Ahles, 2017). The implicit trade-off in directly obtaining a global CO_2 mean from ice cores is the loss of information about the processes that lead to the release or capture of CO_2. In this respect, environmental proxies of CO_2 that possess a local imprint also carry information about site characteristics. If correctly decoupled, they thus theoretically may offer more information. More importantly, the ice core record is relatively short-lived compared to geological time scales. It is then very convenient that many different paleo proxies of CO_2 have been developed over the years, as they tend to extend a lot deeper in time. Without them, we would have access to only a tiny window of the Earth's evolution (see Subsection 1.1.1).

Boron isotopes of foraminifera

Extracting pCO_2 from the isotopic composition of boron in foraminifera is currently one of the best options to reconstruct past CO_2 on time scales of millions of years. It has the advantage of providing an almost continuous record since 55 Ma, but these reconstructions require certain critical assumptions that tend to be more fragile as we go further back in time at the million-year scale.

Analyzing the boron isotopic composition of foraminifera is foremost a means to calculate the pH of seawater. The isotopic ratio ($^{11}B/^{10}B$) of borate ion ($B(OH)_4{}^-$) in seawater increases with higher pH. With the incorporation of borate in the skeletons and shells of planktic species, this pH information is locked and eventually stored in ocean sediments as the organisms fossilize. From here, pH is translated to pCO_2 through the knowledge that a higher level of atmospheric CO_2 leads to ocean acidification by increasing the amount of dissolved inorganic carbon (DIC). Alas, this transfer function needs several other constraints, such as pressure, temperature, and salinity. Moreover, it requires assumptions about the specific boron isotopic composition of seawater, past ocean alkanility, air-sea gas exchange characteristics, and particular physiological features of the foraminifera species that regulate the incorporation of the borate ion (Hönisch et al., 2019).

Figure 1.11 shows a fair agreement between boron-derived pCO_2 and ice core CO_2 records for the last 800 ka. Despite the relatively large error bars, both datasets seem to agree very well in terms of absolute concentrations, lending support to reconstructions of pCO_2 with boron isotopes in time windows when ice cores are not available. Recently, Rae et al. (2018) showed a pronounced contribution of the Southern Ocean (SO) to the CO_2 rise during the last deglaciation, through boron isotope analysis of corals. This result underlines that boron isotopes can be an important extra source of paleoclimatic information, even at low resolution and within the time scales of ice cores.

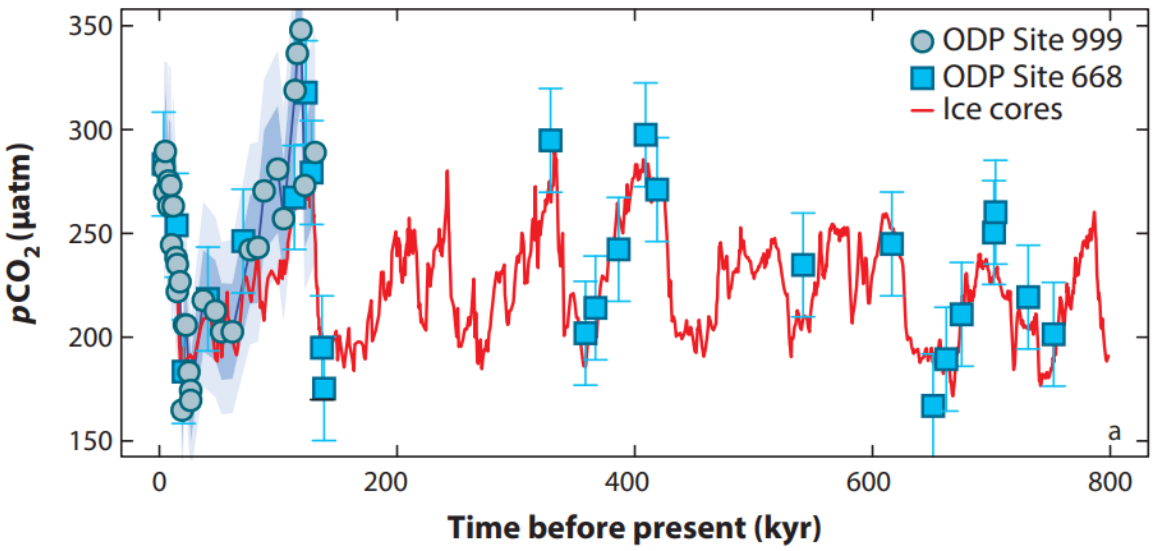

Figure 1.11: Compilation of pCO_2 derived from Boron isotopes for the past 800 ka. Light blue squares from Hönisch et al. (2009); Grey circles from Foster (2008) and recalculated by Martínez-Botí et al. (2015); red line from a CO_2 compilation by Bereiter et al. (2015). Adapted from Foster and Rae (2016) with permission.

Marine phytoplankton $\delta^{13}C$

Much like continental plants, marine phytoplankton also preferentially assimilate isotopically light CO_2 during photosynthesis. The result is a fractionation ε between δ^{13}C of seawater and δ^{13}C of the algae organic composition. This parameter ε can be determined by analyzing δ^{13}C of foraminifera and organic matter from the same ocean sediment core. Since ε is further regulated by the availability of CO_2 in seawater (less CO_2 meaning less isotopic discrimination), a relationship can be established between $CO_{2(aq)}$ and ε (Pagani, 2013).

Of all the organic compounds that have been investigated as candidates for this proxy, alkenones are by far the most widely used. Alkenone-based reconstructions span the last 50 Ma and, for compilation purposes, fill an important gap during the Oligocene epoch (ca. 33–25 Ma) where boron-derived pCO_2 datasets are not available. For reconstructions older than 100 Ma, a strong contender is phytane. Being a sidechain of chlorophyll-a, it benefits from its extreme longevity and pervasiveness throughout the geological record. The oldest CO_2 proxy to date is based on phytanes and reaches back to 455 Ma (Witkowski et al., 2018).

Perhaps the biggest hurdle to δ^{13}C-based reconstructions is the need to accurately know past local sea surface temperatures (SSTs), which has led to underestimations of pCO_2 in the literature (Pagani et al., 2010; Super et al., 2018). Incidentally, alkenones themselves also provide a way for SST estimates via the analysis of its unsaturation ratio $U^{k'}_{37}$ (Sikes and Volkman, 1993).

Other proxies

Boron isotope-derived and alkenone-derived pCO_2 records provide together a general framework for the evolution of CO_2 for the past 65 Ma (Foster and Rae, 2016). In this time scale, the study of specific shorter periods may benefit from looking at supplementary reconstructions from other CO_2 proxies, such as paleosols (Tabor and Myers, 2015) or fossilized leaves (e.g., stomatal frequencies, leaf gas exchange proxies, and leaf $\delta^{13}C$). The interpretation of such records needs to be careful since existing overlaps with the ice core record can show local disagreements of up to 100 ppm; instead, applying a LOESS fit can return average concentrations that are broadly in line with ice cores (Cui et al., 2020). In particular, over-interpretation of records from stomatal frequency has led to unsubstantiated claims of fast CO_2 excursions during the last deglaciation (Steinthorsdottir et al., 2013; Köhler et al., 2015) and early Holocene (Wagner et al., 1999; Indermühle et al., 1999; Wagner et al., 2002). Contrastingly, on much longer time-scales of millions of years, leaf-based reconstructions have been very useful in constraining past CO_2 variability, and reinforce CO_2 as a primary climate driver throughout the Phanerozoic Eon (540 Ma – Present; Royer et al. (2001, 2004)).

1.3 Latest CO_2 reconstructions from ice cores

The last decade has seen a substantial leap forward in the field of paleo reconstructions of atmospheric CO_2 concentrations. New ice core sites, upgraded extraction systems, and combined international efforts have helped to significantly improve the 800 ka atmospheric CO_2 record. Indeed, many new datasets are now available that should belong in a novel compilation, updating the commonly cited revision by Bereiter et al. (2015). Here we review the most relevant updates on CO_2 records to have appeared since 2015.

1.3.1 Bridging the gaps

The Vostok ice core was until 2020 the only ice core providing a record of CO_2 data for the time window of Marine Isotope Stage (MIS) 6–11, ca. 150–400 ka (Petit et al., 1999). While remaining a landmark in itself, the Vostok record is nowadays subpar to other records, both in accuracy and precision. High sample throughput of current dry-extraction systems (Bereiter et al., 2013) would also allow for gains in resolution over the average 1500 years of the Vostok ice core. Committed to improving the CO_2 record during this period, the Climate and Environmental Physics division of the University of Bern (Switzerland) and the Institut des Géosciences de l'Environnement (IGE) of the University of Grenoble Alpes (France) have thus established in 2014 a joint plan of measurements using the EDC ice core. Efforts have recently led to new records for MIS 5 (Silva et al. (2022), see also Chapter 4), MIS 6 (Shin et al. (2020), see also Chapter 5.2) and MIS 9-11 (Nehrbass-Ahles et al. (2020),

[iv] See `https://paleo-co2.org/` for more information on non-ice core CO_2 proxies

see also chapter 5.1). Ongoing campaigns will deliver the remaining MIS 7 (Grenoble) and MIS 8 (Bern) CO_2 records in 2022, thus closing the so-called Vostok gap.

1.3.2 Abrupt events

The traditional view on millennial-scale variability of atmospheric CO_2 has the Southern Ocean (SO) as its leading source and sink. If the SO is in a highly stratified state, such as during the last glaciation, added warming or increased wind stress at the surface can stimulate slow outgassing of CO_2 stored in the intermediate and deep ocean layers as a result of latitudinal shifts of the Intertropical Convergence Zone (ITCZ) (Skinner et al., 2010; Menviel et al., 2018). This release mechanism can describe the linear increase and decrease of CO_2 during Carbon Dioxide Maxima (CDM) events in the last glaciation, with rising rates in the order of 5–7 ppm ka^{-1} (Bereiter et al., 2012). Coincidentally, Antarctic temperature also exhibits the same triangular pattern, in the shape of Antarctic Isotope Maxima (AIM) events. This co-variation between CDM and AIM events during the last glaciation suggests a close link between CO_2 and Antarctic temperature (see Figure 1.12), and has been recorded in several Antarctic ice cores: Byrd (Ahn and Brook, 2007; Ahn et al., 2012), Talos Dome (Ahn and Brook, 2008; Bereiter et al., 2012), Siple Dome (Ahn et al., 2012; Ahn and Brook, 2014), EDML (Bereiter et al., 2012) and West Antarctic Ice Sheet (WAIS) Divide (WD; Bauska et al. (2018, 2021)).

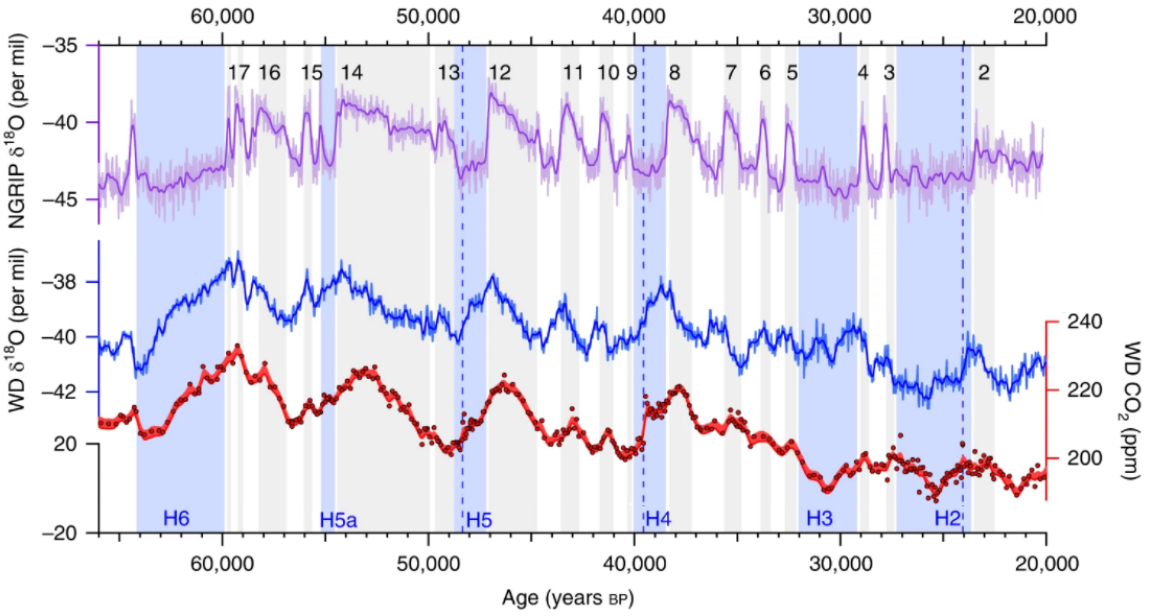

Figure 1.12: The last glaciation recorded in the Northern and Southern Hemisphere through ice cores. Purple: $\delta^{18}O$ water isotope record as a Greenlandic temperature proxy from the North Greenland Ice Core Project (NGRIP), with D-O events numbered 2–17. Blue: $\delta^{18}O$ water isotope record as an Antarctic temperature record from the WAIS Divide (WD) ice core. Red: Atmospheric CO_2 concentrations from the WD ice core. H2–6 and accompanying blue-shaded columns represent Heinrich stadials (Rhodes et al., 2015). Adapted from Bauska et al. (2021).

In contrast to the millennial-scale pace of CO_2 and Antarctic temperature, the NH can experience much faster climate variability. During periods when the Atlantic Meridional Overturning Circulation (AMOC) is switched off (i.e., the equatorial heat exchange between the North and South Atlantic is small), there is a buildup of heat in the Southern Hemisphere (SH), with an accompanying rise in CO_2. This relatively slow rise eventually ends with an abrupt recovery of the AMOC and a subsequent massive transport of heat to the North Atlantic (NA). These sharp increases in temperature in the Northern Hemisphere are dubbed Dansgaard-Oeschger (D-O) events and are present in all Greenlandic deep ice cores that span the last glaciation (e.g., Greenland Ice-core Project (GRIP) Members (1993); Grootes et al. (1993); North Greenland Ice Core Project members (2004); NEEM Community Members (2013)). The concept of a thermal bipolar seesaw has been proposed (Stocker and Johnsen, 2003) and refined (Pedro et al., 2018) to explain this mechanism, in which the key ingredient in this interplay between the NH and the SH is a large heat reservoir in the SH. Figure 1.13 shows one plausible schematic to explain the interhemispheric dynamics during glaciations, with CO_2 acting as one possible control on AMOC changes (Banderas et al., 2015; Zhang et al., 2017). Nonetheless, this is a debated topic and other scenarios could cause the AMOC variations, such as NH freshwater input (Vellinga and Wood, 2002; Cael and Jansen, 2020), atmospheric teleconnections (Hogg et al., 2016; Thomas et al., 2009) or salinity-based changes (Peltier and Vettoretti, 2014).

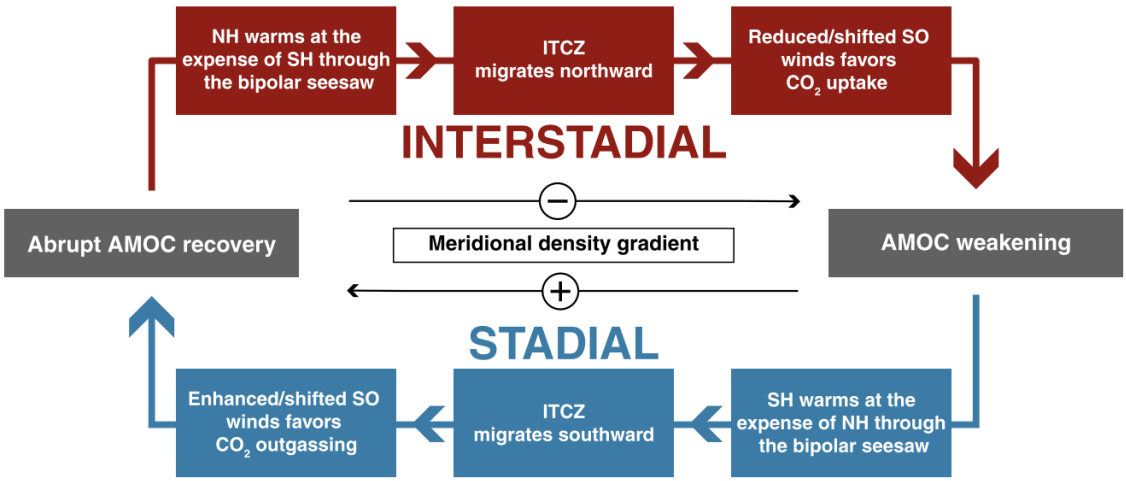

Figure 1.13: Schematic of interhemispheric variability during glacial periods through coupled dynamics between CO_2 and AMOC strength. Taken from Banderas et al. (2015) with permission.

Regardless of the precise mechanisms at play, the scientific community until recently assumed that even during exceptionally disrupting occasions such as D-O events, CO_2 progressed at the millennial-scale, but not abruptly[v]. Other instances of dramatic NH climate

[v] A clear exception to this are glacial terminations, but these are exceptional in so many levels that they form a particular case by themselves.

change, such as the 8.2 ka event or the series of cold events during the LIG, also did not leave an imprint on global CO_2 (Ahn et al., 2014; Tzedakis et al., 2018). Therefore, it came as a significant surprise to discover that atmospheric CO_2 can also sharply increase at the centennial-scale, during both glacial and interglacial periods (Nehrbass-Ahles et al., 2020; Bauska et al., 2021). New high-resolution ice cores and improved dry-extraction methods made it possible to unlock the previously hidden CO_2 spikes and jumps co-occurring with the switching on of the AMOC, hinting that these abrupt events may be an overall pervasive feature throughout the 800 ka record.

The last deglaciation

Researchers from Oregon State University have recently published CO_2 data from the WD ice core, covering the past 66 ka (Marcott et al., 2014; Bauska et al., 2016, 2018, 2021). These studies bring new insights into abrupt CO_2 variability during the last glacial cycle, previously hampered by low resolution. The WD ice core benefits from a very high present-day accumulation rate of $22\,\mathrm{cm\,yr^{-1}}$ of ice equivalent (ie), and an average temperature of $-30\,^{\circ}\mathrm{C}$ (WAIS Divide Project Members, 2013). This contrasts sharply with ice cores from the East Antarctic Plateau, where accumulation rates can be 10-fold smaller (EDC: $2.7\,\mathrm{cm\,yr^{-1}}$ ie (EPICA Community Members, 2004); Vostok: $2.2\,\mathrm{cm\,yr^{-1}}$ ie (Petit et al., 1999)). Such difference means that the WD ice core possesses a much narrower GAD, allowing to record decadal variability of atmospheric CO_2 concentrations.

Marcott et al. (2014) showed that during the last deglaciation (23–9 ka) the rise of CO_2 was punctuated by three distinct and sudden carbon releases at 16.3, 14.8 and 11.7 ka (see Figure 1.14). While the last deglaciation saw an average rise of CO_2 of $10\,\mathrm{ppm\,ka^{-1}}$ (a typical feature of all glacial terminations of the past 800 ka), the three events saw 10–15 ppm increases in just 100 to 200 years. These step-wise rises preceded plateau periods, each lasting 1000 to 1500 years when CO_2 concentrations remained stable. Overall, this step-wise picture is a confirmation of a previous effort from Monnin et al. (2001) with the EDC ice core, which due to higher firn diffusion and much wider GAD characteristics of the EDC site was not able to capture the fine structure that the WD ice core offers.

It is challenging to explain such fast CO_2 variability under the usual framework of slow carbon release from the SO, especially since CO_2 seems to decouple from Antarctic temperature during these steps. In specific, the 14.8 ka event is coeval with the onset of the Bølling-Allerød (B/A) interstadial, while the 11.7 ka event is concomitant with the end of the Younger Dryas (YD) period. These two transitions are marked by reorganizations of the AMOC and ice-rafted debris (IRD) events in the NA, which led Marcott et al. to tentatively state that the AMOC must play a critical role in the CO_2 profile during the deglaciation. Nevertheless, the B/A and YD periods are themselves peculiar, since counterparts in other deglaciations for the past 800 ka do not exist. Lacking a concrete explanation, one could thus eventually dismiss these CO_2 excursions as simply part of an overall more complex and

not well-understood particular mechanism of climate variability. Unfortunately, the same reasoning cannot be applied to the earlier 16.3 ka CO_2 step which, while being similar to the other two later events at 14.8 and 11.7 ka, did not leave an imprint in any other major paleomarker. The only apparent culprit to the 16.3 ka jump is a recorded Heinrich event around the same time (Stern and Lisiecki, 2013). The ice discharge may have temporarily shifted the ITCZ southward through cooling in the NA, and therefore intensified and pushed the southern westerlies poleward, leading to increased coastal upwelling and outgassing of CO_2 (Anderson et al., 2009). On the other hand, the penultimate deglaciation also saw a very long and intense Heinrich event, itself containing at least three intense separate subevents (Tzedakis et al., 2018); yet, there is no evidence of significant CO_2 excursions during the penultimate deglaciation that match the magnitude of the steps recorded in the last deglaciation (Landais et al., 2013; Silva et al., 2022). It remains thus elusive if these centennial excursions of CO_2 are just a particular case of the last deglaciation or if they are an overall feature of past deglaciations that is currently not well-resolved in the ice core record.

The last glacial period

Very recently, abrupt CO_2 variability has also been found at different instances before the last deglaciation. Bauska et al. (2021, 2018) confirmed a sudden release of CO_2 during the onset of Heinrich stadial 4 (HS-4; 39.5 ka; previously reported in Ahn et al. (2012)) and revealed a similar abrupt excursion for the onset of HS-5 (48.4 ka). These events happened under significantly different boundary conditions than the events reported by Marcott et al. (2014): the onsets of HS-4 and HS-5 occurred under full glacial boundary conditions, while the events during the last deglaciation happened in an already warmer state, with increased concentration of greenhouse gases, decreased sea ice extension, higher sea level, and poleward-shifted polar fronts, to name just a few parameters. Using a carbon cycle box-model, Marcott et al. (2014) simulated the contributions from both NH and SH processes to the evolution of CO_2 during the last glacial period. The results attribute millennial-scale variability to SH processes (as expected) and a superimposed contribution from NH processes at the centennial scale, specifically during interstadials. The simulations fail, nevertheless, to capture the centennial pulses of CO_2 at the onset of HS-4 and HS-5, leaving a question mark as to the source of these events.

Marine Isotope Stage 9–11

The interglacial that occurred during Marine Isotope Stage 11 is one of the best analogues to the Holocene epoch in terms of insolation patterns, making this interglacial an advantageous case study to understand the ongoing climate change under similar climate boundary conditions (Loutre and Berger, 2003). The record by Nehrbass-Ahles et al. (2020) confirmed previous evidence of an exceptionally long interglacial with a stable baseline of CO_2 (Petit

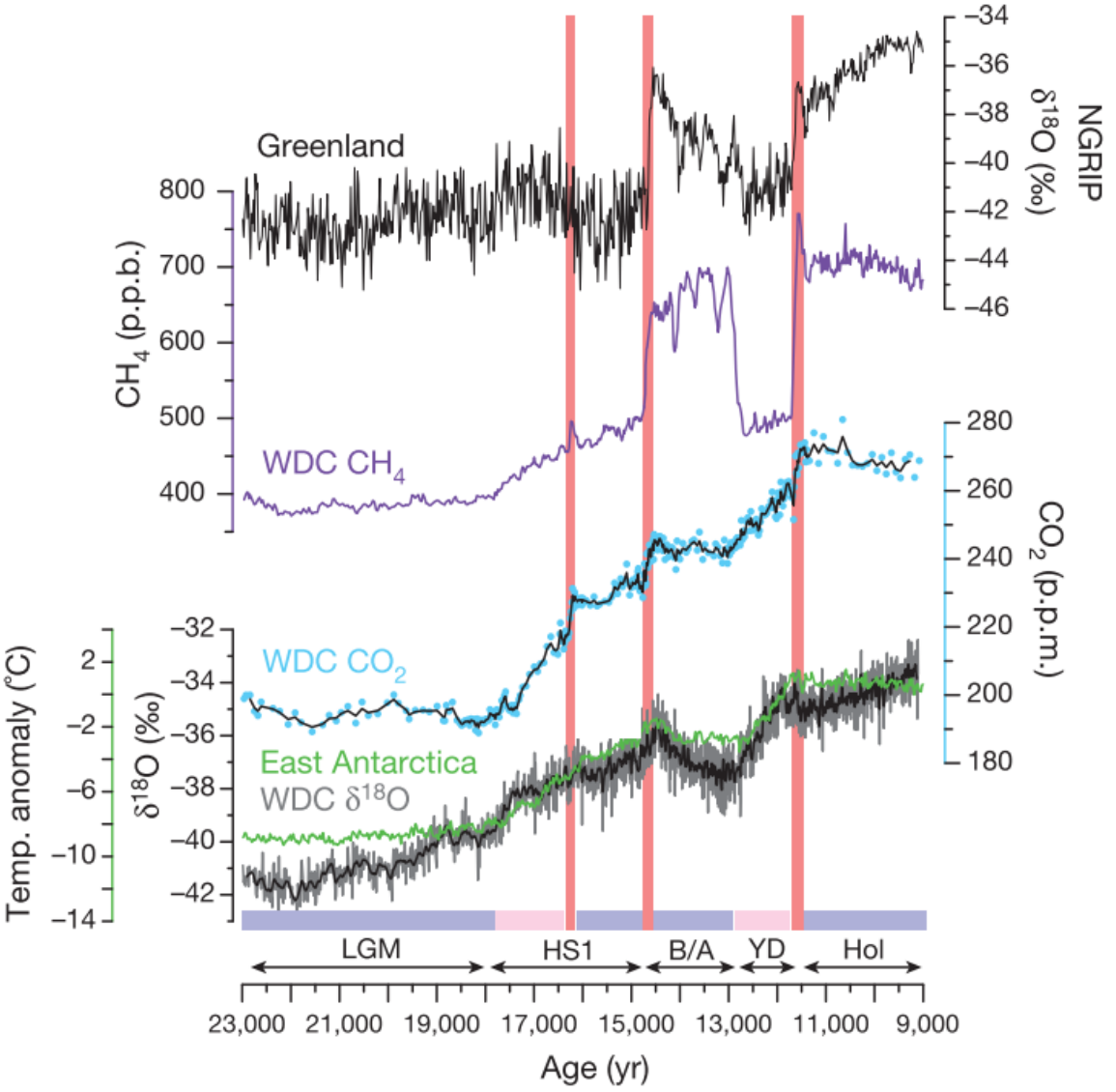

Figure 1.14: Step-wise profile of CO_2 during the last deglaciation. Red bands indicate three abrupt events, decoupled from Antarctic temperature as seen through the $\delta^{18}O$ water isotope record. Black: Greenland $\delta^{18}O$ from NGRIP (North Greenland Ice Core Project members, 2004). Purple: Methane record from the WD ice core (WAIS Divide Project Members, 2013; Marcott et al., 2014). Blue: Discrete CO_2 measurements from WD, with a 5-point running weighted average (black). Green: Antarctic temperature stack (Parrenin et al., 2013). Black: $\delta^{18}O$ water isotope record from the WD ice core (WAIS Divide Project Members, 2013). LGM – Last Glacial Maximum; HS1 – Heinrich Stadial 1; B/A – Bølling-Allerød; YD – Younger Dryas; Hol – Holocene. Adapted from Marcott et al. (2014).

et al., 1999), covering the substages MIS 11c to 11e, from 427 to 393 ka. The highlight is the unveiling of a series of carbon dioxide jumps (CDJs), fast releases of CO_2 superimposed on millennial-scale variability (see Section 5.1). Particularly, the most unexpected feature is CDJ$^-$ 11c (ca. 415 ka), a sudden CO_2 excursion already well into established interglacial conditions, when CO_2 spiked by 13 ppm in less than 200 years, an amount not accounting for signal attenuation due to bubble enclosure processes (Nehrbass-Ahles et al., 2020). While the amplitude and duration of this singular event are similar to what had already been re-

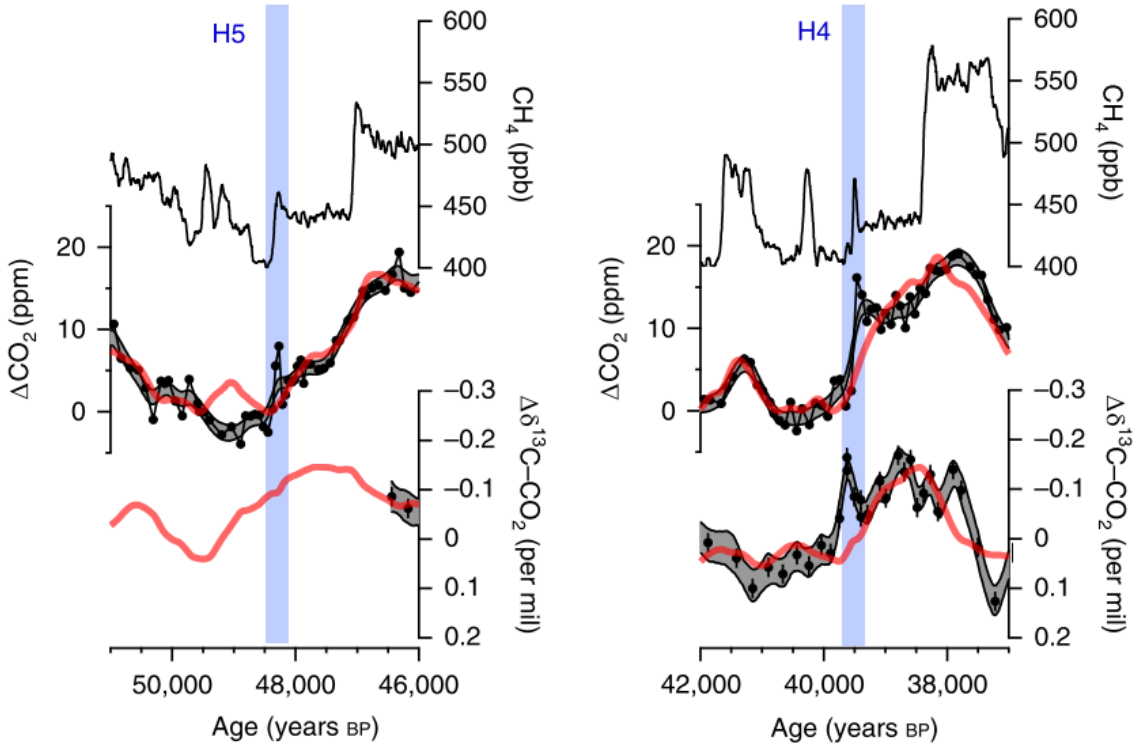

Figure 1.15: Evolving atmospheric CO_2 concentrations during Heinrich stadials 4 and 5. Red line represents the best-fit model solution of CO_2 and $\delta^{13}CO_2$. Blue bands highlight the CO_2 abrupt excursions, coeval with CH_4 peaks. From top to bottom: WD CH_4 (Rhodes et al., 2015); WD CO_2 (Bauska et al., 2021); WD $\delta^{13}CO_2$ (Bauska et al., 2016, 2018). Adapted from Bauska et al. (2021).

ported in Marcott et al. (2014) during deglacial times, it was the first time that such a quick release was seen during a warm interglacial period. Nehrbass-Ahles et al. (2020) associate CDJ$^-$ 11c with a possible perturbation of the AMOC induced by large freshwater forcing. The lack of a clear and coeval CH_4 response puts this pulse in the same category as the ones found during HS-4 (Bauska et al., 2021) and HS-1 (Marcott et al., 2014). However, the lack of other well-dated and well-resolved proxy data for the MIS 11 stage makes it unclear whether this AMOC change was a strengthening or a weakening.

The last interglacial

Assuming that freshwater discharge in the NA from the remnants of the NH ice cap is a necessary ingredient for the particular CO_2 pulse during MIS 11, it makes thus sense that we do not observe any further significant centennial-scale variability for the rest of the interglacial, as the NH ice sheet had by then retreated significantly. Such reasoning is also consistent with the CO_2 record for the LIG (see Chapter 4), where no major centennial-scale changes were found for most of the MIS 5e plateau. It is therefore remarkable that the MIS 5 record also shows a sudden CO_2 excursion during interglacial conditions at 127.5 ka, this time immediately after the overshoot that marks the end of the penultimate deglaciation

(see Figure 1.16).

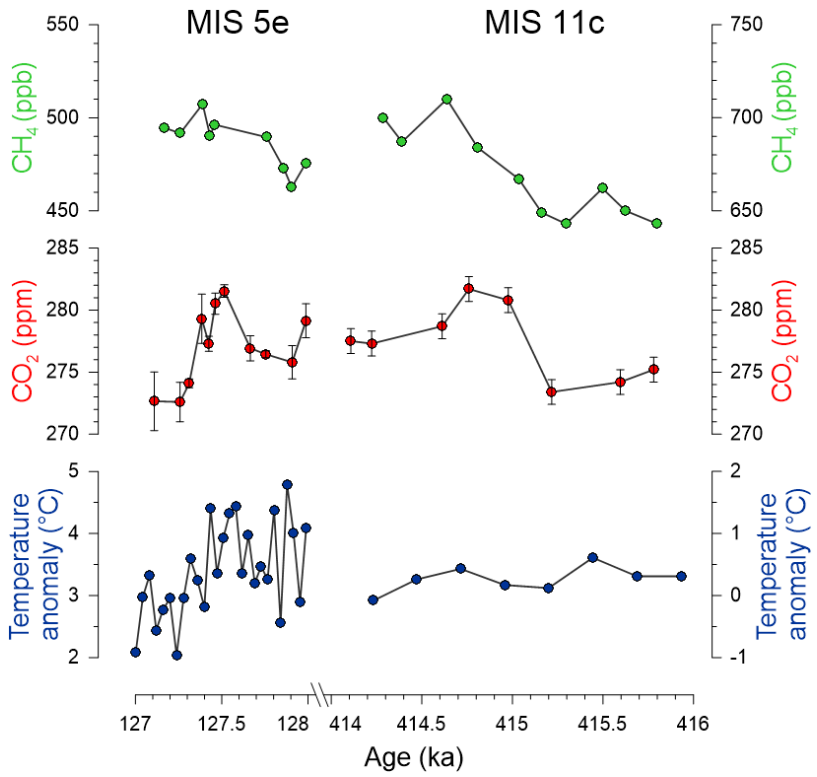

Figure 1.16: Comparison between interglacial CO_2 jumps from MIS 5e and MIS 11c. From top to bottom: CH_4 (Loulergue et al., 2008; Schmidely et al., 2021; Nehrbass-Ahles et al., 2020); CO_2 (Chapter 4; Nehrbass-Ahles et al. (2020)); Antarctic temperature anomaly derived from a deuterium record (Jouzel et al., 2007)).

While taking place under different orbital configurations (Yin and Berger, 2012), this CDJ in the MIS 5e record shares some similarities with the interglacial pulse that Nehrbass-Ahles et al. (2020) found: no marked CH_4 change (Schmidely et al., 2021; Loulergue et al., 2008), rising sea levels (Grant et al., 2014; Rohling et al., 2019) and warm conditions both in the NH and the SH (Barker et al., 2011; NEEM Community Members, 2013). Regarding the AMOC, the MIS 5e pulse is coeval with increased North Atlantic deep water (NADW) formation and an associated invigoration of the AMOC (Galaasen et al., 2014), while for CDJ$^-$ 11c the status of the AMOC is unclear. Applying the definition by Nehrbass-Ahles et al. (2020), the MIS 5 pulse would also be a CDJ$^-$, where the minus sign represents the lack of a coeval CH_4 response. However, there is a marked imprint in Antarctic temperature for the MIS 5 pulse (see also Chapter 4) that we do not observe for MIS 11 and that we cannot ascribe to a lack of resolution in MIS 11 (Pol et al., 2011, 2014). Therefore, it seems incoherent to label both pulses under the same category. One possibility is that the MIS 5 excursion is the result of freshwater discharge in the SO from the Antarctic ice sheet (Hayes et al., 2014). The cold event caused a reduction in Antarctic bottom water (AABW), creating an interhemispheric density gradient that fueled an increase in NADW formation (Broecker, 1998). This scenario would have created the necessary conditions for

an AMOC perturbation and subsequent changes in CO_2, e.g., through changes in the wind belts (Buizert et al., 2018). The same mechanism is unlikely to have occurred for CDJ$^-$ 11c, since Antarctic temperatures were at that time still far from peak values, making coastal freshening due to Antarctic ice sheet mass loss less likely.

1.3.3 Early Holocene

The recent study by Shin et al. (2021) has increased the available ensemble of CO_2 reconstructions for the early Holocene (11.7–7 ka). This time window is particularly exciting for the paleo and climate modeling community as a possible template for past warm climates, with the added advantage that its relatively young age places it within the reach of many different environmental proxies. Figure 1.17 shows an ensemble of available reconstructions of atmospheric CO_2 for the early Holocene from multiple Antarctic ice cores. The new record from Siple Dome (blue) is a major contribution to this period that, notwithstanding its importance, is lacking such a high-resolution record. It appears to smoothly extend the previous Siple Dome record and broadly accompanies the WD record until 11.7 ka. However, two caveats are worth noting. Firstly, there is no overlap with the previous Siple Dome record by Ahn and Brook (2014), which does not completely exclude an offset between the two records. Secondly, the high scatter observed in the WD ice core is likely a product of bubble enclosure effects below the BCTZ that lead to non-climatic centimeter-scale variability of CO_2, which hampers the search for a common cyclicity signal (Shackleton et al. (2019); see also Section 3.3). On the other hand, all the other records were obtained measuring depths that only contained bubbly ice.

The high-resolution characteristic of the new Siple Dome record gives rise to an apparent fast variability at the centennial scale. Despite the scatter, submillennial climatic features may be present in the new record, which could be revealed with the right statistical tools and comparison with other proxies. It is also possible that this variability is a product of centimeter-scale processes in the ice core record itself that alter the CO_2 concentrations at specific depths (see Chapter 4).

It is also important to stress that Figure 1.17 does not picture all the available datasets for this period, likely because they do not add particular value to the analysis of high-frequency signals in the Siple Dome ice core. Nevertheless, they would add important information on how different locations in Antarctica record the atmospheric CO_2 signal for this period. In particular:

- Lourantou et al. (2010) provide more measurements on the EDC ice core with a dry extraction device that would increase resolution on the 11.7–9 ka window.
- The Taylor Dome record by Indermühle et al. (1999) was further extended by Smith et al. (1999) and Fischer et al. (1999) with good agreement on baseline values.
- The low-resolution Vostok record is missing (Petit et al., 1999).

- There are low resolution data available from Dome F, resorting to both wet extraction (Kawamura et al., 2003) and dry extraction devices (Kawamura et al., 2007). They agree amongst each other, and also follow the same baseline as the EDC compilation and Vostok.

Most importantly, there is a notorious disagreement in terms of absolute values between the records in Figure 1.17. In-situ production of CO_2 on certain drilling sites is a possibility, as well as analytical offsets stemming from different extraction devices (Indermühle et al., 1999; Ahn et al., 2009). Not mentioned by the authors, however, is a possible connection between accumulation rates and total offsets. Low accumulation sites such as EDC, Vostok (not plotted), and Dome Fuji (not plotted) follow the same low baseline with a CO_2 optimum in the range of 265–270 ppm, while higher accumulation sites such as Siple Dome and WD belong to a higher baseline, with a maximum of CO_2 in between 270–275 ppm. Conversely, unpublished data from Talos Dome (Nehrbass-Ahles, 2017) also show atmospheric CO_2 concentrations following the high baseline from Siple Dome and WD, even if Talos Dome shows an accumulation rate of $8.5\,\mathrm{cm\,yr^{-1}}$ ie (Stenni et al., 2002). However, the relationship between accumulation rate and offset, if existent, needs not to be linear but could follow a threshold instead. The accumulation rate at Talos Dome is still on average 3–4 times higher than the accumulation rate on other sites on the East Antarctic Ice Sheet (EAIS) and could be above a hypothetical threshold value that allows the recording of the true atmospheric signal and related centennial-scale variability. This would mean that not only do the low accumulation sites smooth the signal but also somehow deplete the CO_2 concentration through a not yet known process. An alternative hypothesis is that the low accumulation sites prevent *in situ* production of CO_2 due to their extremely low temperatures and low concentration of potential organic precursors; conversely, coastal sites (such as Talos or Siple Dome) are subject to a small *in situ* production of CO_2 that introduces a positive bias.

While important in itself, a coherent reconstruction of the early Holocene will lay the foundations to understand the uncharacteristic rise of CO_2 that is found in the last 7 ka, a feature not observed in the same way in any other interglacial of the past 800 ka (Lüthi et al., 2008). An early anthropogenic interference due to agricultural developments by ancient civilizations, dubbed the "Ruddiman hypothesis" (Ruddiman, 2003, 2007), was initially proposed. Isotope analysis and simulations from carbon cycle models strongly counter this hypothesis (Joos et al., 2004; Elsig et al., 2009).

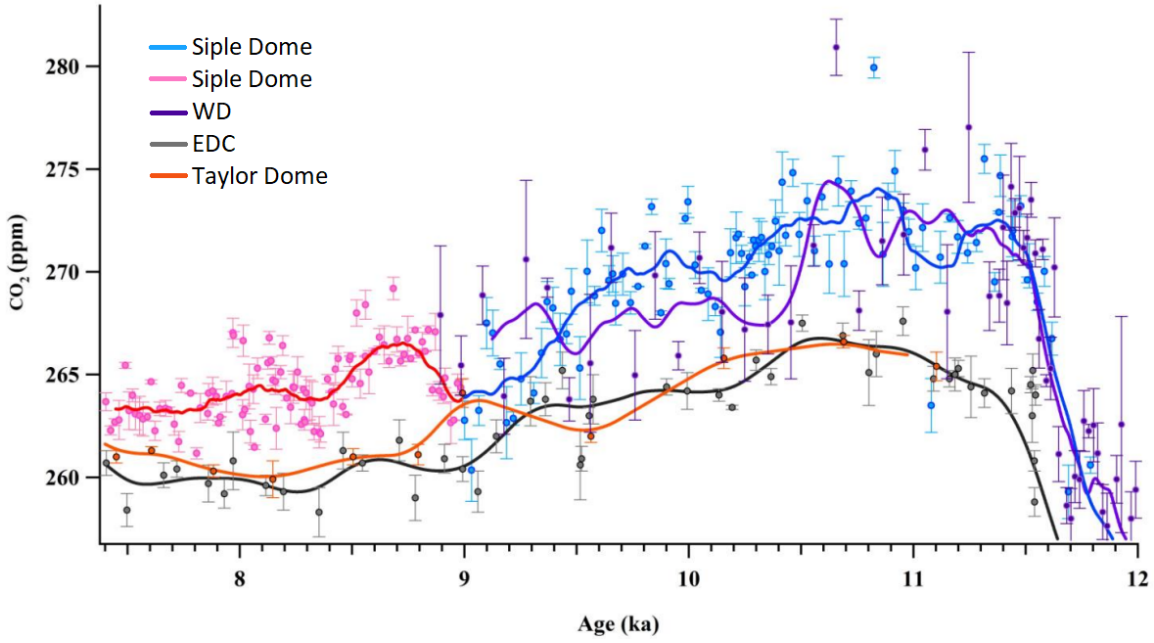

Figure 1.17: Ensemble of Antarctic ice core CO_2 records for the early Holocene, with 250-year running means. Plotted records stem from Siple Dome (blue: Ahn and Brook (2014); pink: Shin et al. (2021)), WD (purple: Marcott et al. (2014)), EDC (grey: Monnin et al. (2001); Flückiger et al. (2002); Monnin et al. (2004)) and Taylor Dome (orange: (Indermühle et al., 1999)). Adapted from Shin et al. (2021).

1.4 The search for the oldest ice

1.4.1 Motivation

The International Partnership for Ice Core Sciences (IPICS) regards the recovery of a continuous and stratigraphically undisturbed million-year-old ice core as one of the greatest challenges in ice core science in the coming years (Wolff et al., 2020). After the EDC ice core broke the record as the oldest ice core available in the early 2000s, scientists worldwide turned their attention to locations in Antarctica that could contain even older ice. Since then, several international teams have formed in the quest for this ice, and the first drilling activity is expected to start already in the austral summer of 2021/22.

The overarching motivation, however, goes far beyond the challenge of breaking the record. Retrieving a continuous 1.5 million-year ice core would cover the Mid-Pleistocene Transition (MPT), a period that is one of the most enigmatic problems for paleoclimatologists. Marine sediments show that before 1.2 Ma our planet oscillated between glacial and interglacial states in cycles lasting approximately 41 thousand years (Lisiecki and Raymo (2005); see Figure 1.18). Ice core records, however, evidence much longer cycles of about 100 thousand years over the last 800 ka. This change in pace happened sometime during the period 1.2–0.7 Ma (Clark et al., 2006; Elderfield et al., 2012; Yehudai et al., 2021) and the reasons behind it are still elusive. Many hypotheses have surfaced (Chalk et al., 2017;

Berends et al., 2021), but only a set of continuous and high-resolution climate data can comprehensively evaluate them.

In this sense, it is essential to prioritize measurements of paleo parameters that likely played the biggest roles during the MPT, as the amount of ice available in the deepest parts will be scarce due to extreme thinning. For example, one latest modelling effort indicates a depth-age scale of 19 ka m^{-1} near the basal unit where 1.5 Ma ice should exist (Lilien et al., 2021). In this scenario, it follows that attaining a resolution that allows to satisfactorily resolve the 41 ka cycles will necessarily force the individual samples to be small and to sample multiple times on a single ice core bag. A compromise is then inevitable, where some traditional ice core measurements will not take place, even with prospects of replicate coring. Capturing the variability of greenhouse gases in order to reconstruct the radiative forcing will be a top priority. Special focus will likely be put on measuring CO_2, as understanding changes in the carbon cycle through the MPT is one of the key pieces to understand the fundamental reasons behind the transition.

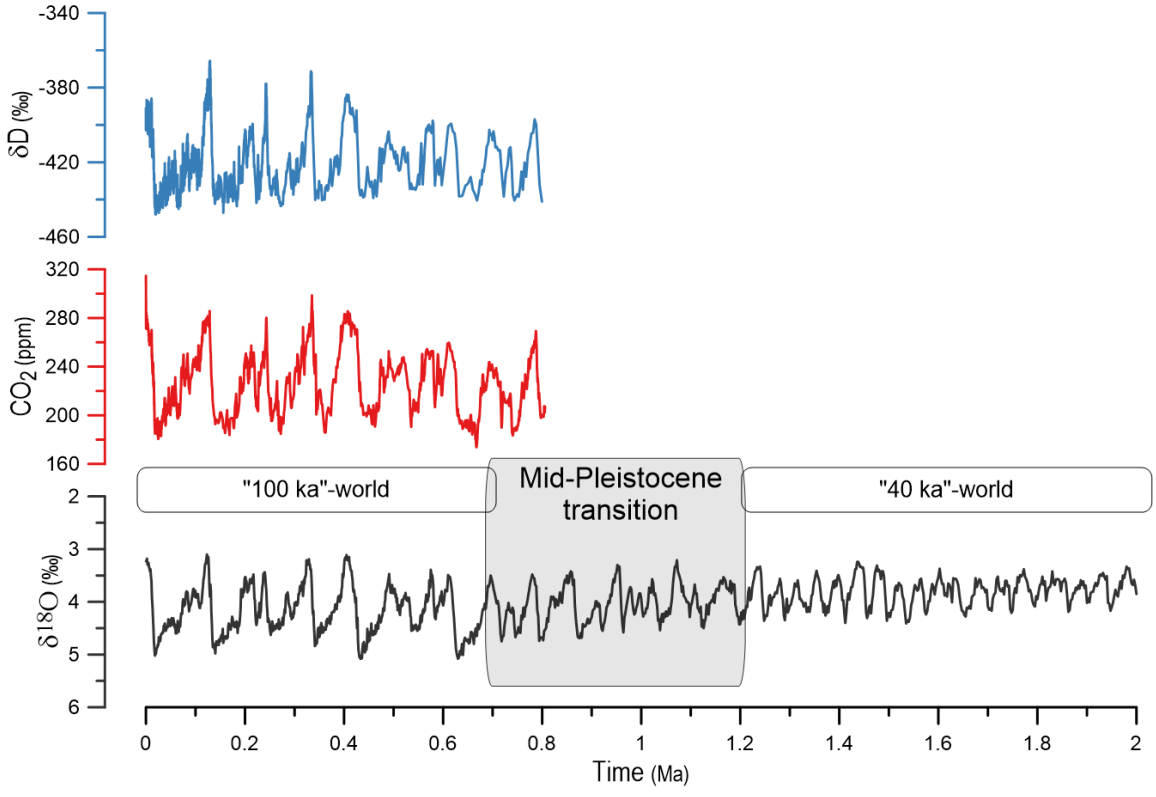

Figure 1.18: The mid-Pleistocene transition seen from a stack of benthic records. Evident is the change in pace from a dominant 41 ka ciclycity to a slower 41 ka pace. While CO_2 (red; Lüthi et al. (2008)) and Antarctic temperature (blue; Jouzel et al. (2007)) from ice core records broadly correlate with marine benthic $\delta^{18}O$ (black; Lisiecki and Raymo (2005)) for the past 800 ka, it is uncertain that this relationship also held during the MPT.

On a side note, it is pertinent to note that political interests may add an extra layer of complexity in the quest for the oldest ice. As per the Antarctic Treaty (active since 1961),

all nations may establish stations in Antarctica under the exclusive umbrella of scientific research. At the time, the treaty suspended existing territorial claims and enforced a policy of non-militarization. In 1998, the Protocol on Environmental Protection came into effect, further banning any set of profitable activities, such as mining. So far, the Antarctic Treaty has been a successful case of international collaboration and environmental protection, but this may change in the medium term. The Protocol on Environmental Protection will go through a revision in 2048, and with it, there could be a challenge of anti-mining regulations. Pressing needs for mining and fishing resources, growing tourism opportunities, and the strategic importance of an Antarctic foothold may all play a role in the future of Antarctica. It is not implausible to think that under a scientific flag lies a long-term political agenda. An array of established and successful research stations in Antarctica with proven results could very well support further political claims if the Antarctic Treaty becomes too fragile. It is thus important that the quest for the oldest ice does not become a race, but rather the result of international cooperation. With the endorsement of IPICS, studies like Fischer et al. (2013) are a prime example of an internationally inclusive scientific approach.

1.4.2 The challenge

If the EDC ice core timeline of 800 ka was already an outstanding accomplishment, pushing the record beyond 1 million years requires a much more thorough study of local conditions. The presence of such old ice is a tricky combination of favorable topography, accumulation rate, ice flow, and, perhaps most importantly, basal melting due to geothermal heat flux (Fischer et al. (2013); see also Figure 1.19). The past years have seen a great effort in reconstructing maps of geothermal heat flux in the East Antarctic Plateau, where minima could indicate less melting near the bedrock and higher chances for oldest ice. Nevertheless, individual heat flux reconstructions still differ largely both in absolute value, spatial distribution and resolution (Sutter et al., 2019). Airborne and ground-based radar observations coupled with ice-flow models have helped to pre-select promising sites.

Current efforts stem from different countries/consortia, each one attempting to retrieve the oldest ice from a different location. Figure 1.20 shows tentative drilling areas, together with support research stations for each project. In this section, I briefly compile the latest efforts from each country/consortia.

Little Dome C (Europe)

The Beyond EPICA - Oldest Ice (BE-OI) project[vi] is a European effort of 14 different institutions from 10 nations and funding under the European Union Horizon 2020 programme, with a total budget of about €30M. National contributions to the project may come in kind, or through coverage of the costly logistics. The project aims to retrieve a continuous 1.5

[vi] See https://www.beyondepica.eu/ for further information

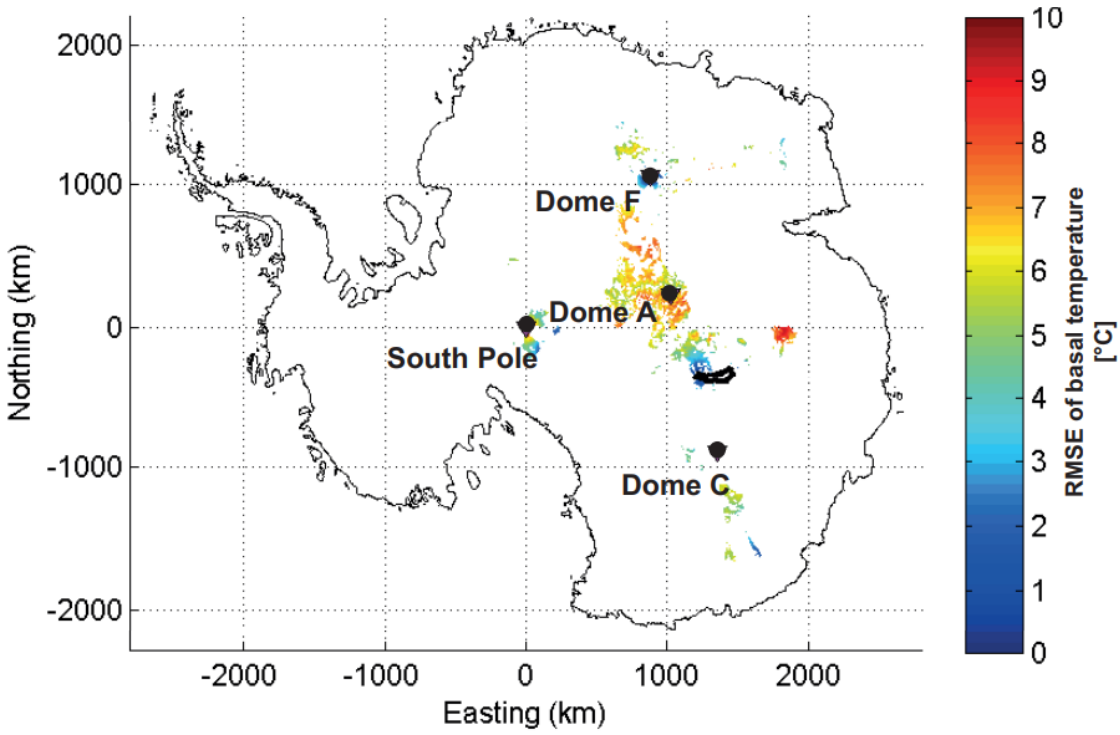

Figure 1.19: Potential locations of oldest ice according to an early study in 2013. It laid the foundations for more precise pinpointing of the most promising sites that will be drilled in the coming years. Adapted from (Fischer et al., 2013).

million-year-old ice core from the East Antarctic plateau. The Patch B site, at Little Dome C (LDC; 75.2992 S, 122.4451 E), was finally selected in 2019 and is situated within about 40 km of Concordia Station where the previous EPICA Dome C ice core was drilled (see Figure 1.21). Very recent work has offered further support to the existence of ice at least 1.5 million years old in the bottom-most 10% of the ice (Cavitte et al., 2020). That should still be enough ice to resolve the 41-thousand year cycles, as the 1.5 Ma target is expected to be found approximately 65 m above a basal (likely stagnant) ice unit, with a low risk of disturbance (Lilien et al., 2021). The oldest ice will be extremely thinned, with about 15 thousand years of climatic information per each meter of ice core (see Figure 1.22).

Given the massive undertaking of deep drilling in the EAIS, rapid drilling techniques have been championed to quickly check whether the site indeed possesses the oldest ice (Fischer et al., 2013). For the BE-OI project, several instruments were developed, such as the Swiss RADIX drill (Rapid Access Drilling and Ice eXtraction; Schwander et al. (2014)), the UK's RAID (Rapid Access Isotope Drill, Rix et al. (2019)) and the French SUBGLACIOR probe (in-SitU proBing of GLACier Ice for a better understanding of the Orbital Response of climate; (Alemany et al., 2014)). RADIX has been successfully tested in Greenland, while RAID has been deployed in Antarctica ((Mulvaney et al., 2021)). The SUBGLACIOR probe, which also provides on-board tracer analytics is still under development (Alemany et al.,

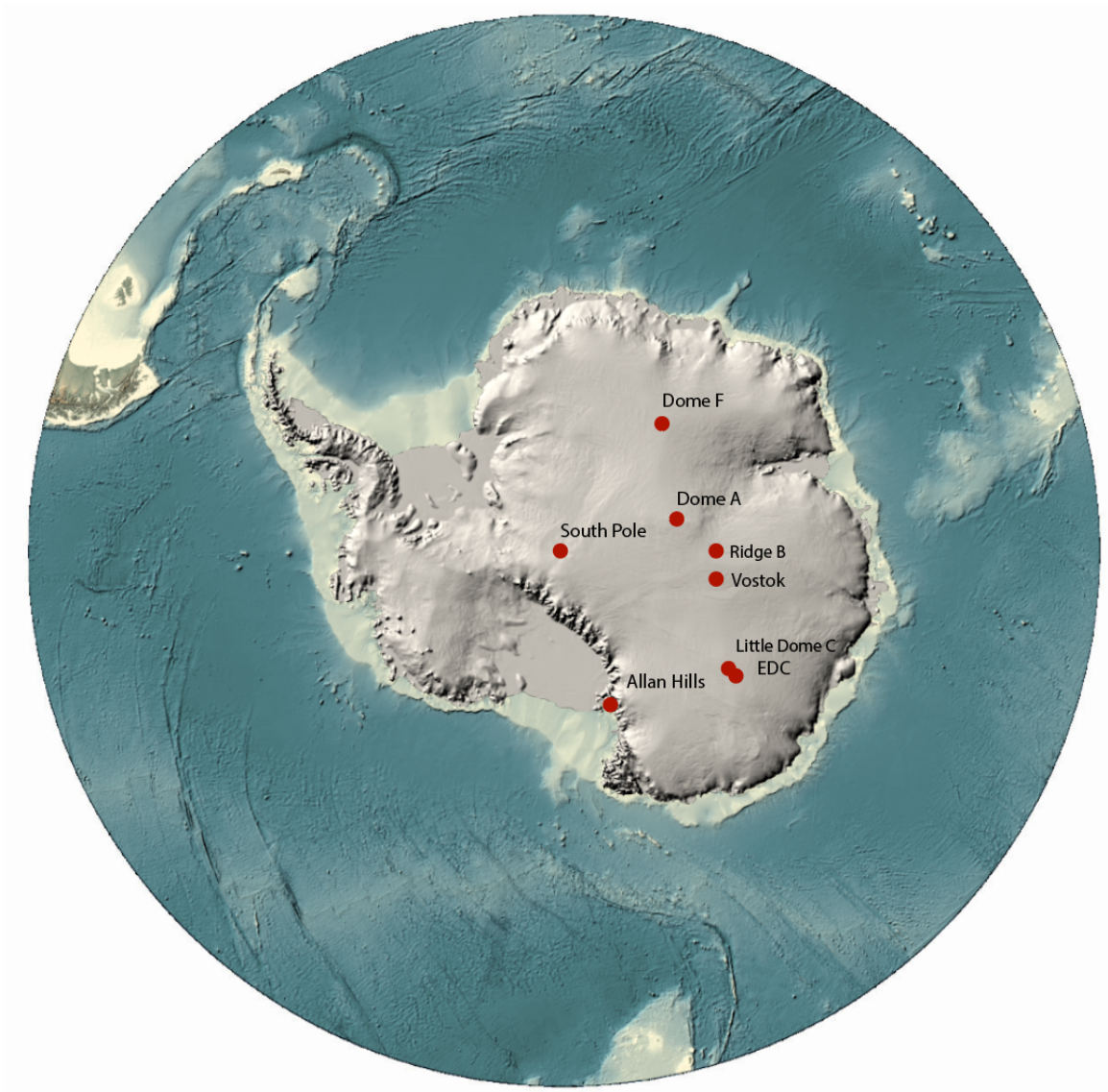

Figure 1.20: Current deep drilling sites and promising locations for oldest ice drilling in Antarctica. Map generated using the Antarctic Digital Elevation Model from the ArcGIS Online tool, Earthstar Geographics.

2020).

The first season in 2019/20 established camp and set up the drill tent. Drilling of the pilot hole is scheduled to start in 2021/22, accompanied by nearby drilling with the RADIX drill. Bedrock is expected to be reached in 2024/25, with replicate coring of the oldest ice either in the same or the following season. Traverses from LDC to the Dumont d'Urville French Station will transport the oldest ice, with special care for the transport to Europe to be carried out at −50 °C. Several consortia have been already formed and a cutting plan is currently established (IPICS, 2020).

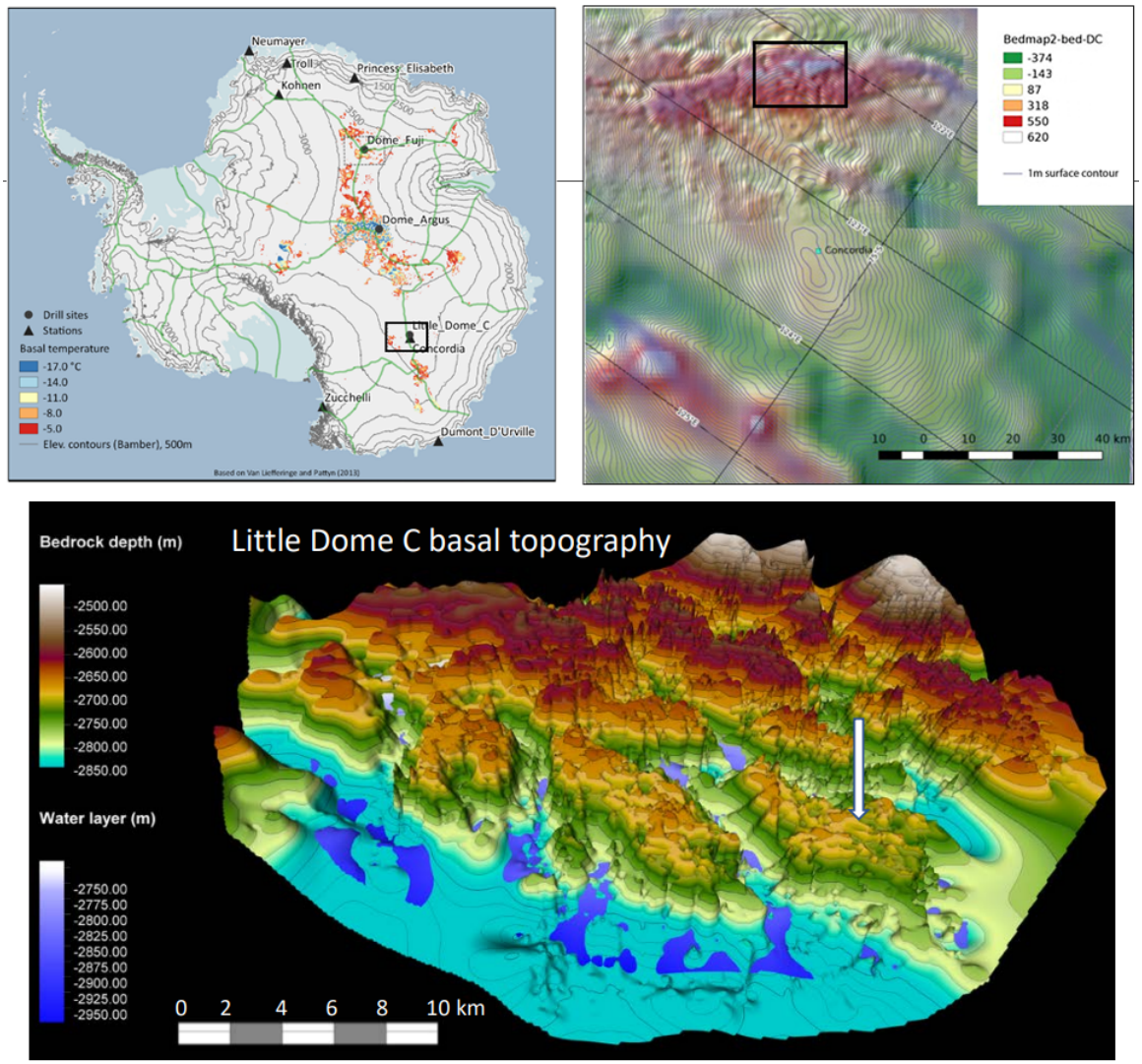

Figure 1.21: LDC location and basal topography. Top-left: basal temperature map for the most promising sites on the EAIS with main drill sites and stations (adapted from Van Liefferinge and Pattyn (2013)). Top-right: Bedrock topography of LDC and Dome C. Bottom: LDC basal topography, with the arrow indicating the drill site (updated on October 2021). Source: Robert Mulvaney (British Antarctic Survey). Reprinted with permission.

Allan Hills / South Pole (U.S.A.)

The Allan Hills blue ice area (BIA), about 200 km from the U.S.-operated McMurdo station on Ross Island, is known to have very old ice, albeit not continuous. The ice that outcrops in this region has been dated as old as 2.7 Ma, but other unexplored ice patches could be even older (Yan et al., 2019). As for a continuous record, some nearby areas could feasibly contain ice stretching back to 1 Ma (Kehrl et al., 2018), but it is for the moment unclear if the site has the potential to store ice encompassing the whole MPT. One of the great benefits of a BIA is that the old ice is found relatively near the surface (at around 200 m in case of the study of Yan et al. (2019)) and not near bedrock, which would ease and quicken

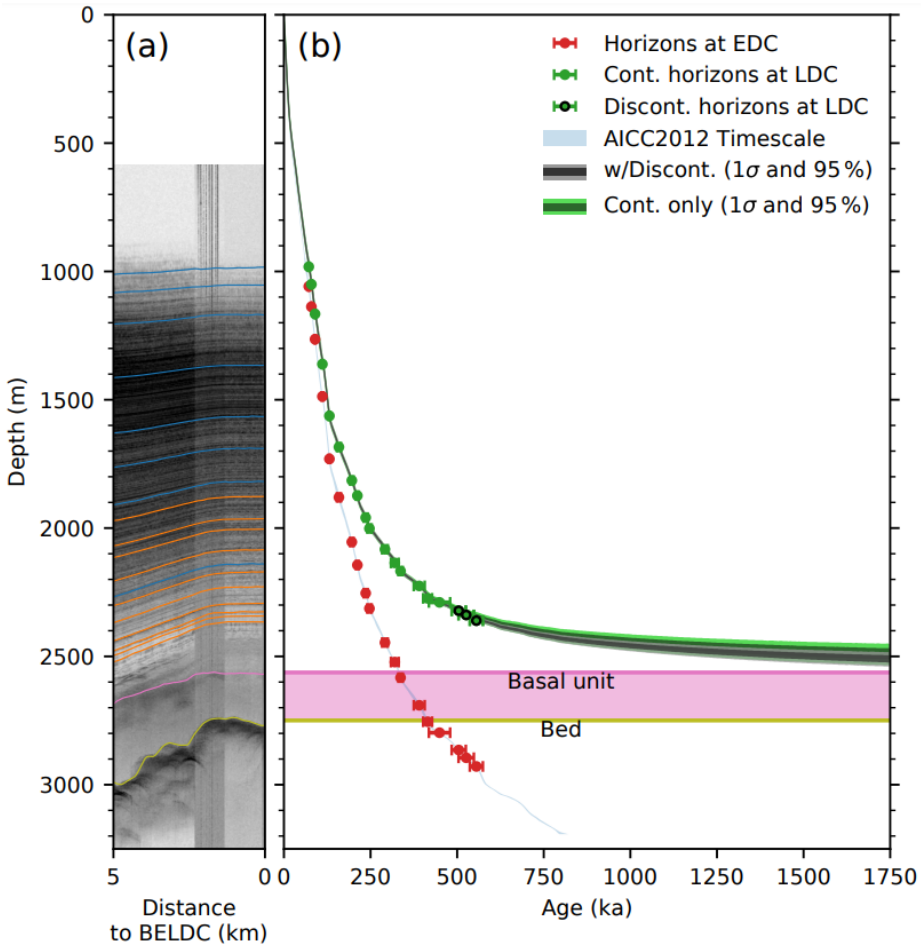

Figure 1.22: Estimate of age-depth scale at LDC. a) Radargram with colored isochrones showed traceable stratigraphy up to 500 ka. b) Model results (green) indicate the presence of at least 1.5 million-year old ice above the basal unit. Taken from Lilien et al. (2021) and reprinted with permission.

the drilling process, making it very cost-effective.

The USA has not exactly narrowed down their search for continuous oldest ice in a specific location, but they do intend to focus on the area between the South Pole and Dome A (IPICS, 2020; Texas Geosciences, 2021). Public statements by some researchers also seem to point to further exploratory work near Allan Hills and other BIAs for discontinuous ice in 2023/24 and beyond (Ice Core Working Group (2020); Ed Brook, pers. comm.). In addition, more drilling is expected at Allan Hills in the season 2022/23 (Ed Brook, pers. comm.). One published study indicates reconnaissance work around Titan Dome, ca. 200 km away from the South Pole, and concludes it not to be a candidate for oldest ice drilling, although other regions around the South Pole could still feature such old ice (Beem et al., 2021).

To identify the exact drilling site, US scientists rely on two quick melting probes: RAID[vii] and the "Ice Diver". The former is also capable to sample ice and even core the bedrock below, while the latter has been announced in press releases to be still under development

[vii] https://www.rapidaccessicedrill.org/

(Oregon State University, 2021). The underlying operating mode in both devices is through optically detecting and logging dust content as the probe penetrates the ice. From the logged dust records one can then roughly estimate an ice age equivalent by identifying glacial/interglacial periods of high/low dust concentrations, respectively. The RAID probe was successfully tested in 2019/20 at Minna Bluffs, Victoria Land, reaching bedrock in 2 days (Goodge et al., 2021).

In September 2021, the US Centre for OLDest Ice EXploration (COLDEX) received confirmation of $25M funding for 5 years (typically renewed for another 5 years) to pursue the search for the oldest ice (NSF, 2021).

The first phase of the project (COLDEX Phase 1) is expected to last between 2021–26 and will comprise drilling in blue ice areas, educational opportunities, and outreach. Drilling and analysis of a deep ice core reaching 1.5 Ma (COLDEX Phase 2) are planned to take place in the years 2026–31 (Ice Core Working Group, 2021).

Ridge B (Russia)

Under the Vostok Oldest Ice Challenge (VOICE; Lipenkov and Raynaud (2015)) Russia plans to search for the oldest ice near Ridge B (79.02°S, 93.69°E), located near Dome B and about 291 km from the Vostok station (78.4645°S, 106.8339°E). New ice dating tools have revealed meteoric ice as old as 1.2 Ma near at the bottom section of the Vostok core (3500–3538 m) (Lipenkov et al., 2019). This implies that if we follow that ice flow line upstream, in an area around Dome B, we may potentially find even older ice, and stratigraphically undisturbed. Preliminary results in that region have shown that Dome B has been relatively stable in the past 1 Ma, with less than 50% probability that the pressure melting point has been reached at the basal ice layer (Skakun et al., 2019). The first prospective visit to the site happened in January 2021 (Ekaykin et al., 2021) and further developments are to be expected.

The assembly and building of a new Vostok station are underway and should be finished by 2023. The new infrastructure will logistically reinforce the VOICE project, with drilling starting in 2024 in the best scenarios (IPICS, 2020). In the meantime, the drilling and study of old meteoric ice continue at Vostok station, with replicate cores being collected via sidetracking (Turkeev et al., 2021).

Dome Fuji (Japan)

Dome Fuji (or Dome F) currently has the second oldest ice core reaching 720 ka back in time (Motoyama, 2007). The area received scouting attention from several teams as a candidate for oldest ice (Rodriguez-Morales et al., 2020; Karlsson et al., 2018; Tsutaki et al., 2021) and recent modelling efforts do consider Dome F to be a good candidate (Fischer et al., 2013; Karlsson et al., 2018; Van Liefferinge et al., 2018). The latest compilation of local subglacial topography studies indicates a complex array of subglacial lakes and

valleys, setting important final constraints when narrowing down the exact drilling site. This selection should soon be finished, with a particular candidate located ca. 70 km from Dome F being the most promising contender. According to the latest IPICS Oldest Ice Meeting, a new deep drill has been developed by the Japanese team and has already undergone first tests (IPICS, 2020). Tentative schedules have camp being set in 2023 and deep drilling in the years 2024–26.

Dome Argus (China)

Dome Argus (or Dome A) is the highest plateau in Antarctica, with an altitude over 4000 m and winter temperatures dipping below −90 °C. Such inhospitable conditions made it one of the most secluded places on Earth until 2009 when China inaugurated its third research station. Very sparse scientific output is published about deep coring at Kunlun station. Drilling conditions at core DK-1 seem to be particularly harsh, with very slow progress in the past decade (Zhang et al., 2014; Hu et al., 2021).

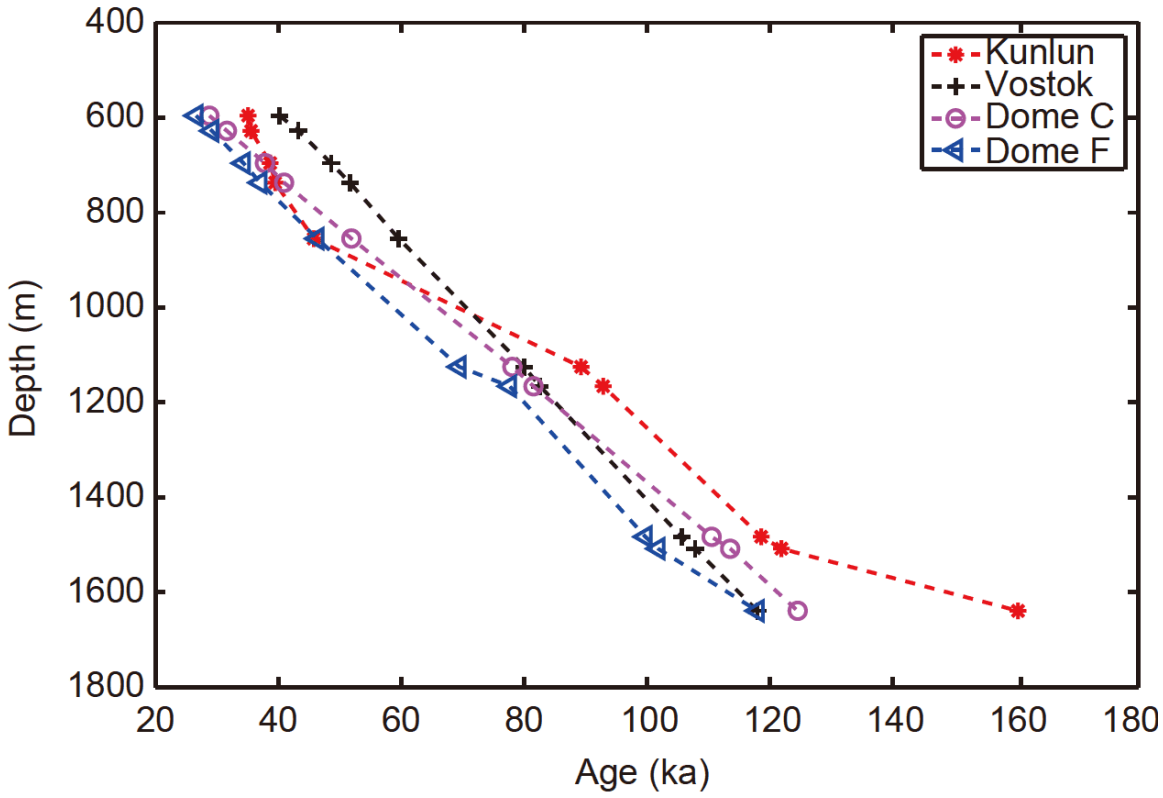

Figure 1.23: Hint for Dome A potential as an oldest ice location. From Tang et al. (2019).

There are nevertheless a series of studies indicating that Dome A could hold ice older than 1 Ma under the surface (Xiao et al., 2008; Fischer et al., 2013; Zhao et al., 2018). In particular, preliminary dating up to 160 ka seems to reveal that below one-third of its thickness Dome A is older than Vostok, Dome F, or Dome C (see Figure 1.23). It remains to

be seen if the very difficult accessibility and extreme weather conditions of Dome Argus can be overcome. Poor visibility conditions often exclude flight access, making the long traverse (1258 km) from the coastal station Zhongshan the only alternative (Ma et al., 2010; Minghu et al., 2011). The new ice breaker MV Xue Long 2 (2019) and a fifth Antarctic station to be opened in 2022 are likely to help in this quest.

Little Dome C (Australia)

Under the *Million Year Ice Project*, Australia aims to find the oldest ice also at Little Dome C. Following joint efforts in Texas radar surveying around Dome C (Young et al., 2017), Australia will drill in an area dubbed Patch A, only a few kilometers from Patch B, where the European consortium has already set up its drill camp. If both projects succeed, this will mean a virtually duplicate core, fulfilling thus one of the IPICS goals, as replication is required to exclude any stratigraphic disturbances in the record.

Initial camp setup and drilling of the access hole is scheduled to take place this season in 2021/22 with air support. In 2022/23, a 1300 km traverse from Casey research station will deliver most of a mobile station and camp infrastructure. The best scenario predicts 4–5 drilling seasons needed to reach the oldest ice.

The search for the oldest ice is part of a 20-year-long action plan and has a budget of AU$36M (Commonwealth of Australia, 2016). The arrival of the new ice breaker RSV Nuyina and the successful completion of a 10-meter drill represent important steps for the Australian team[viii].

Dome C (South Korea)

As per the last IPICS oldest ice meeting in 2020 (IPICS, 2020), South Korea also intends to search for the oldest ice in the EAIS. This ambition fits into an overarching logic of expansion of Antarctic studies and strengthening of foreign partnerships through international collaboration, which started in 2014 with the opening of Jang Bogo research station, in Terra Nova Bay, along the coast of Victoria Land.

Having located a potential site ca. 200 km east of Dome C, shallow drilling and radar investigations are planned to take place in 2023–26, with deep drilling initiating afterwards in 2027. For this purpose the Antarctic Korean Route Expedition (or K-route) is being established (KOPRI, 2020) — a 3000 km inland journey starting from Jang Bogo, passing through Concordia station and finishing at South Pole (see Figure 1.24). The traverses will help scout exact areas around Dome C for the deep drilling site. Currently, parallel work on the oldest ice from BIAs such as Larsen Glacier or the Elephant Moraine is also underway (Lee et al., 2021; Jang et al., 2017).

[viii] www.antarctica.gov.au/news/2021/australian-antarctic-division-drills-into-ambitious-new-season/

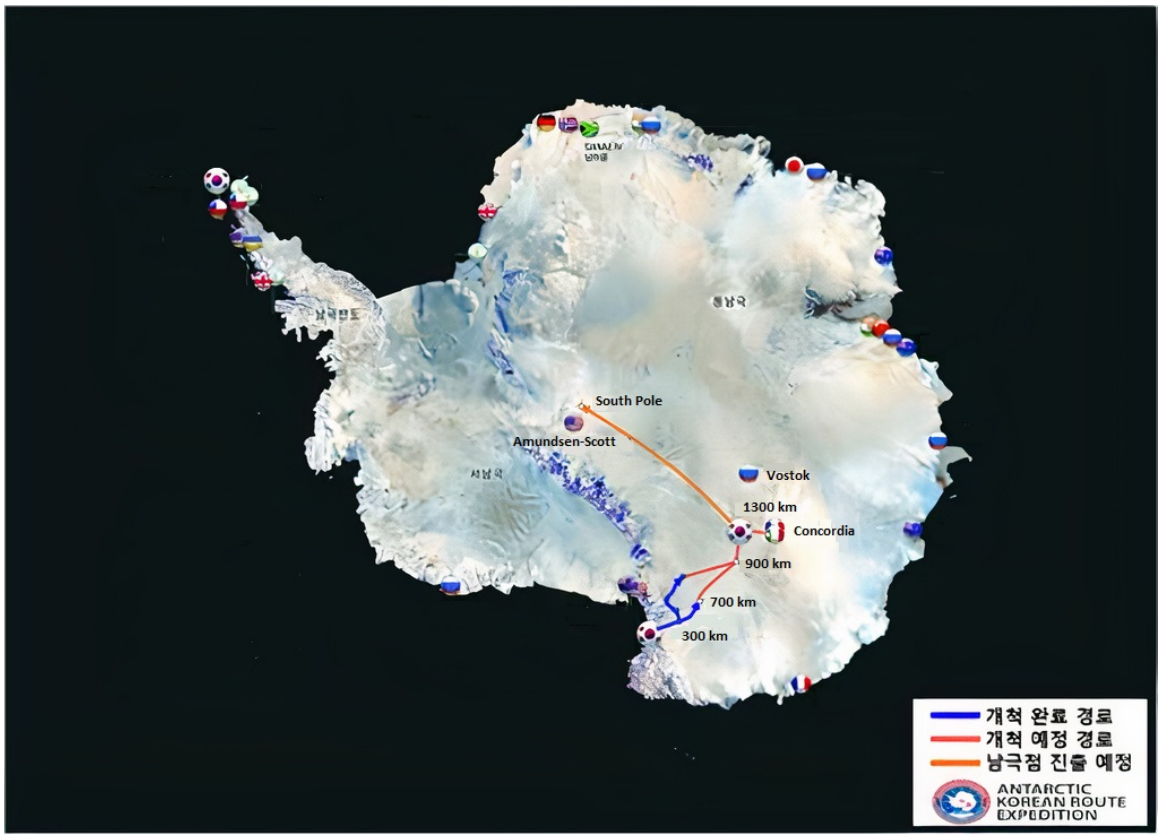

Figure 1.24: Progress and plans for the K-route, departing from Jang Bogo. Blue: route successfully established, since 2017; red: route expected to be claimed in the next seasons; orange: expected path toward the South Pole. Source: Korean Polar Research Institute (adapted).

1.5 Thesis objectives

The experimental nature of this Ph.D. kept me focused on working in the laboratory, between measuring ice core samples and running optimization experiments. Having inherited a fully functioning extraction system, I was entrusted to produce high-quality data with a sub-millennial resolution, benefiting from the system's very high sample throughput (Chapter 2). While attaining such a record for the LIG, an unexpected signal variability fostered a series of investigations and experiments at the centimeter scale (Chapter 3). Only after this learning process did we manage to extract a meaningful climatic signal and offer an interpretation of the record (Chapter 4). Chapter 5 follows the planned measurement campaign, with a preliminary dataset and analysis (see also Subsection 1.3.1).

Throughout the Ph.D., there were also punctual opportunities to collaborate with measurements and discussions for other manuscripts. The results are presented in Chapter 5. Other parallel work involved contributing to the Sixth Assessment Report of the IPCC, which is briefly reviewed in the Appendix A.1. The thesis is completed by the outlook (Chapter 6), where I suggest a possible path for the next eventual Ph.D. student, including

ice to be measured and ways to improve the current extraction system.

This thesis aims:

- To improve existing atmospheric CO_2 records from Antarctic ice cores, through an increase in resolution and precision.
- To report important modifications in the measurement protocol.
- To document experiments related to optimization of the extraction device, processes in the ice at the centimeter-scale, and what we have learned from them.
- To comprehensively describe the main components of the CIM, creating a reference unit from where future systems can be devised.

The first point stems from the competitive characteristic of the CIM with respect to other extraction systems worldwide. The other three points are especially important to keep the know-how of the CIM updated. With the ever-growing pile of lab books, notes, and not-so-well-documented little experiments, I hope to create a go-to document that will not only ease the accessing of information but also avoid reinventing the wheel in some topics.

References

Ahn, J. and Brook, E. J. (2007). Atmospheric CO_2 and climate from 65 to 30 ka B.P. *Geophysical Research Letters*, 34(10).

Ahn, J. and Brook, E. J. (2008). Atmospheric CO_2 and climate on millennial time scales during the last glacial period. *Science*, 322(5898):83–85.

Ahn, J. and Brook, E. J. (2014). Siple Dome ice reveals two modes of millennial CO_2 change during the last ice age. *Nature Communications*, 5(1):3723.

Ahn, J., Brook, E. J., and Buizert, C. (2014). Response of atmospheric CO_2 to the abrupt cooling event 8200 years ago. *Geophysical Research Letters*, 41(2):604–609.

Ahn, J., Brook, E. J., and Howell, K. (2009). A high-precision method for measurement of paleoatmospheric CO_2 in small polar ice samples. *Journal of Glaciology*, 55(191):499–506.

Ahn, J., Brook, E. J., Schmittner, A., and Kreutz, K. (2012). Abrupt change in atmospheric CO_2 during the last ice age. *Geophysical Research Letters*, 39(18).

Alemany, O., Chappellaz, J., Triest, J., Calzas, M., Cattani, O., Chemin, J., Desbois, Q., Desbois, T., Duphil, R., Falourd, S., Grilli, R., Guillerme, C., Kerstel, E., Laurent, B., Lefebvre, E., Marrocco, N., Pascual, O., Piard, L., Possenti, P., Romanini, O., Thiebaut, V., and Yamani, R. (2014). The SUBGLACIOR drilling probe: concept and design. *Annals of Glaciology*, 55(68):233–242.

Alemany, O., Talalay, P., Boissonneau, P., Chappellaz, J., Chemin, J. F., Duphil, R., Lefebvre, E., Piard, L., Possenti, P., and Triest, J. (2020). The SUBGLACIOR drilling probe: hydraulic considerations. *Annals of Glaciology*, 62(84):131–142.

Anderson, R. F., Ali, S., Bradtmiller, L. I., Nielsen, S. H. H., Fleisher, M. Q., Anderson, B. E., and Burckle, L. H. (2009). Wind-driven upwelling in the southern ocean and the deglacial rise in atmospheric co_2. *Science*, 323(5920):1443–1448.

Archer, D. and Ganopolski, A. (2005). A movable trigger: Fossil fuel CO_2 and the onset of the next glaciation. *Geochemistry, Geophysics, Geosystems*, 6(5).

Arias, P. A., Bellouin, N., Coppola, E., Jones, R. G., Krinner, G., Marotzke, J., Naik, V., Palmer, M. D., Plattner, G. K., Rogelj, J., Rojas, M., Sillmann, J., Storelvmo, T., Thorne, P. W., Trewin, B., Achuta Rao, K., Adhikary, B., Allan, R. P., Armour, K., Bala, G., Barimalala, R., Berger, S., Canadell, J. G., Cassou, C., Cherchi, A., Collins, W., Collins, W. D., Connors, S. L., Corti, S., Cruz, F., Dentener, F., Dereczynski, C., Di Luca, A., Diongue Niang, A., Doblas-Reyes, F., Dosio, A., Douville, H., Engelbrecht, F., Eyring, V., Fischer, E., Forster, P., Fox-Kemper, B., Fuglestvedt, J., Fyfe, J., Gillett, N., Goldfarb, L., Gorodetskaya, I., Gutierrez, J., Hamdi, R., Hawkins, E., Hewitt, H., Hope, P., Islam, A., Jones, C., Kaufman, D., Kopp, R., Kosaka, Y., Kossin, J., Krakovska, S., Lee, J. Y., Li, J., Mauritsen, T., Maycock, T. K., Meinshausen, M., Min, S. K., Monteiro, P., Ngo-Duc, T., Otto, F., Pinto, I., Pirani, A., Raghavan, K., Ranasinghe, R., Ruane, A. C., Ruiz, L., Sallée, J. B., Samset, B. H., Sathyendranath, S., Seneviratne, S., Sörensson, A., Szopa, S., Takayabu, I., Tréguier, A. M., van den Hurk, B., Vautard, R., von Schuckmann, K., Zaehle, S., Zhang, X., and Zickfeld, K. (2021). Technical Summary. *Cambridge University Press. In Press.* In Climate Change 2021: The Physical Science Basis. Contribution of Working Group I to the Sixth Assessment Report of the Intergovernmental Panel on Climate Change [Masson-Delmotte, V., P. Zhai, A. Pirani, S.L. Connors, C. Péan, S. Berger, N. Caud, Y. Chen, L. Goldfarb, M.I. Gomis, M. Huang, K. Leitzell, E. Lonnoy, J.B.R. Matthews, T.K. Maycock, T. Waterfield, O. Yelekçi, R. Yu, and B. Zhou (eds.)].

Arrhenius, S. (1896). On the Influence of Carbonic Acid in the Air upon the Temperature of the Ground. *Philosophical Magazine and Journal of Science*, 41(5):237–276.

Bambach, R. K. (2006). Phanerozoic biodiversity mass extinctions. *Annual Review of Earth and Planetary Sciences*, 34(1):127–155.

Banderas, R., Alvarez-Solas, J., Robinson, A., and Montoya, M. (2015). An interhemispheric mechanism for glacial abrupt climate change. *Climate Dynamics*, 44(9):2897–2908.

Barker, S., Knorr, G., Edwards, R. L., Parrenin, F., Putnam, A. E., Skinner, L. C., Wolff, E. W., and Ziegler, M. (2011). 800,000 years of abrupt climate variability. *Science*, 334(6054):347–351.

Bauska, T. K., Baggenstos, D., Brook, E. J., Mix, A. C., Marcott, S. A., Petrenko, V. V., Schaefer, H., Severinghaus, J. P., and Lee, J. E. (2016). Carbon isotopes characterize rapid changes in atmospheric carbon dioxide during the last deglaciation. *Proceedings of the National Academy of Sciences*, 113(13):3465–3470.

Bauska, T. K., Brook, E. J., Marcott, S. A., Baggenstos, D., Shackleton, S., Severinghaus, J. P., and Petrenko, V. V. (2018). Controls on millennial-scale atmospheric CO_2 variability during the last glacial period. *Geophysical Research Letters*, 45(15):7731–7740.

Bauska, T. K., Marcott, S. A., and Brook, E. J. (2021). Abrupt changes in the global carbon cycle during the last glacial period. *Nature Geoscience*, 14(2):91–96.

Beem, L. H., Young, D. A., Greenbaum, J. S., Blankenship, D. D., Cavitte, M. G. P., Guo, J., and Bo, S. (2021). Aerogeophysical characterization of Titan Dome, East Antarctica, and potential as an ice core target. *The Cryosphere*, 15(4):1719–1730.

Bereiter, B. (2012). *Atmospheric CO_2 reconstruction using polar ice cores: Development of a new dry extraction device and insights from highly resolved records.* PhD thesis, University of Bern.

Bereiter, B., Eggleston, S., Schmitt, J., Nehrbass-Ahles, C., Stocker, T. F., Fischer, H., Kipfstuhl, S., and Chappellaz, J. (2015). Revision of the EPICA Dome C CO_2 record from 800 to 600 kyr before present. *Geophysical Research Letters*, 42(2):542–549.

Bereiter, B., Lüthi, D., Siegrist, M., Schüpbach, S., Stocker, T. F., and Fischer, H. (2012). Mode change of millennial CO_2 variability during the last glacial cycle associated with a bipolar marine carbon seesaw. *Proceedings of the National Academy of Sciences*, 109(25):9755–9760.

Bereiter, B., Stocker, T. F., and Fischer, H. (2013). A centrifugal ice microtome for measurements of atmospheric CO_2 on air trapped in polar ice cores. *Atmospheric Measurement Techniques*, 6(2):251–262.

Berends, C. J., Köhler, P., Lourens, L. J., and van de Wal, R. S. W. (2021). On the cause of the Mid-Pleistocene Transition. *Reviews of Geophysics*, 59(2):e2020RG000727.

Berger, A. and Loutre, M. F. (2002). An exceptionally long interglacial ahead? *Science*, 297(5585):1287–1288.

Broecker, W. S. (1975). Climatic Change: Are We on the Brink of a Pronounced Global Warming? *Science*, 189(4201):460–463.

Broecker, W. S. (1998). Paleocean circulation during the Last Deglaciation: A bipolar seesaw? *Paleoceanography*, 13(2):119–121.

Brugger, J., Hofmann, M., Petri, S., and Feulner, G. (2019). On the sensitivity of the Devonian climate to continental configuration, vegetation cover, orbital configuration, CO_2 concentration, and insolation. *Paleoceanography and Paleoclimatology*, 34(8):1375–1398.

Buizert, C., Sigl, M., Severi, M., Markle, B. R., Wettstein, J. J., McConnell, J. R., Pedro, J. B., Sodemann, H., Goto-Azuma, K., Kawamura, K., Fujita, S., Motoyama, H., Hirabayashi, M., Uemura, R., Stenni, B., Parrenin, F., He, F., Fudge, T. J., and Steig, E. J. (2018). Abrupt ice-age shifts in southern westerly winds and Antarctic climate forced from the north. *Nature*, 563(7733):681–685.

Cael, B. B. and Jansen, M. F. (2020). On freshwater fluxes and the Atlantic meridional overturning circulation. *Limnology and Oceanography Letters*, 5(2):185–192.

Cavitte, M. G. P., Young, D. A., Mulvaney, R., Ritz, C., Greenbaum, J. S., Ng, G., Kempf, S. D., Quartini, E., Muldoon, G. R., Paden, J., Frezzotti, M., Roberts, J. L., Tozer, C. R., Schroeder, D. M., and Blankenship, D. D. (2020). A detailed radiostratigraphic data set for the central East Antarctic Plateau spanning the last half million years. *Earth System Science Data Discussions*, pages 1–27.

Chalk, T. B., Hain, M. P., Foster, G. L., Rohling, E. J., Sexton, P. F., Badger, M. P. S., Cherry, S. G., Hasenfratz, A. P., Haug, G. H., Jaccard, S. L., Martínez-García, A., Pälike, H., Pancost, R. D., and Wilson, P. A. (2017). Causes of ice age intensification across the Mid-Pleistocene Transition. *Proceedings of the National Academy of Sciences*, 114(50):13114–13119.

Chowdhry Beeman, J., Gest, L., Parrenin, F., Raynaud, D., Fudge, T. J., Buizert, C., and Brook, E. J. (2019). Antarctic temperature and CO_2: near-synchrony yet variable phasing during the last deglaciation. *Climate of the Past*, 15(3):913–926.

Clark, P. U., Archer, D., Pollard, D., Blum, J. D., Rial, J. A., Brovkin, V., Mix, A. C., Pisias, N. G., and Roy, M. (2006). The middle Pleistocene transition: characteristics, mechanisms, and implications for long-term changes in atmospheric pco_2. *Quaternary Science Reviews*, 25(23):3150–3184. Critical Quaternary Stratigraphy.

Commonwealth of Australia (2016). Australian Antarctic Strategy and 20 Year Action Plan. Technical report.

Cui, Y., Schubert, B. A., and Jahren, A. H. (2020). A 23 m.y. record of low atmospheric CO_2. *Geology*, 48(9):888–892.

Delmas, R. J., Ascencio, J. M., and Legrand, M. (1980). Polar ice evidence that atmospheric CO_2 20,000 yr BP was 50% of present. *Nature*, 284.

Ekaykin, A. A., Bolshunov, A. V., Lipenkov, V. Y., Scheinert, M., Eberlein, L., Brovkov, E., Popov, S. V., and Turkeev, A. V. (2021). First glaciological investigations at Ridge B, central East Antarctica. *Antarctic Science*, 33(4):418–427.

Elderfield, H., Ferretti, P., Greaves, M., Crowhurst, S., McCave, I. N., Hodell, D., and Piotrowski, A. M. (2012). Evolution of Ocean Temperature and Ice Volume Through the Mid-Pleistocene Climate Transition. *Science*, 337(6095):704–709.

Elsig, J., Schmitt, J., Leuenberger, D., Schneider, R., Eyer, M., Leuenberger, M., Joos, F., Fischer, H., and Stocker, T. F. (2009). Stable isotope constraints on holocene carbon cycle changes from an antarctic ice core. *Nature*, 461(7263):507–510.

EPICA Community Members (2004). Eight glacial cycles from an Antarctic ice core. *Nature*, 429(6992):623–628.

Fischer, H., Severinghaus, J., Brook, E., Wolff, E., Albert, M., Alemany, O., Arthern, R., Bentley, C., Blankenship, D., Chappellaz, J., Creyts, T., Dahl-Jensen, D., Dinn, M., Frezzotti, M., Fujita, S., Gallee, H., Hindmarsh, R., Hudspeth, D., Jugie, G., Kawamura, K., Lipenkov, V., Miller, H., Mulvaney, R., Parrenin, F., Pattyn, F., Ritz, C., Schwander, J., Steinhage, D., van Ommen, T., and Wilhelms, F. (2013). Where to find 1.5 million yr old ice for the IPICS "Oldest-Ice" ice core. *Climate of the Past*, 9(6):2489–2505.

Fischer, H., Wahlen, M., Smith, J., Mastroianni, D., and Deck, B. (1999). Ice core records of atmospheric CO_2 around the last three glacial terminations. *Science*, 283(5408):1712–1714.

Flückiger, J., Monnin, E., Stauffer, B., Schwander, J., Stocker, T. F., Chappellaz, J., Raynaud, D., and Barnola, J.-M. (2002). High-resolution Holocene N_2O ice core record and its relationship with CH_4 and CO_2. *Global Biogeochemical Cycles*, 16(1):10–1–10–8.

Foster, G. L. (2008). Seawater pH, pCO2 and [CO2-3] variations in the caribbean sea over the last 130 kyr: A boron isotope and B/Ca study of planktic foraminifera. *Earth and Planetary Science Letters*, 271(1-4):254–266.

Foster, G. L. and Rae, J. W. (2016). Reconstructing ocean pH with boron isotopes in foraminifera. *Annual Review of Earth and Planetary Sciences*, 44(1):207–237.

Foster, G. L., Royer, D. L., and Lunt, D. J. (2017). Future climate forcing potentially without precedent in the last 420 million years. *Nature Communications*, 8(1):14845.

Fourteau, K., Faïn, X., Martinerie, P., Landais, A., Ekaykin, A. A., Lipenkov, V. Y., and Chappellaz, J. (2017). Analytical constraints on layered gas trapping and smoothing of atmospheric variability in ice under low-accumulation conditions. *Climate of the Past*, 13(12):1815.

Friedlingstein, P., O'Sullivan, M., Jones, M. W., Andrew, R. M., Hauck, J., Olsen, A., Peters, G. P., Peters, W., Pongratz, J., Sitch, S., Le Quéré, C., Canadell, J. G., Ciais, P., Jackson, R. B., Alin, S., Aragão, L. E. O. C., Arneth, A., Arora, V., Bates, N. R., Becker, M., Benoit-Cattin, A., Bittig, H. C., Bopp, L., Bultan, S., Chandra, N., Chevallier, F., Chini, L. P., Evans, W., Florentie, L., Forster, P. M., Gasser, T., Gehlen, M., Gilfillan, D., Gkritzalis, T., Gregor, L., Gruber, N., Harris, I., Hartung, K., Haverd, V., Houghton, R. A., Ilyina, T., Jain, A. K., Joetzjer, E., Kadono, K., Kato, E., Kitidis, V., Korsbakken, J. I., Landschützer, P., Lefèvre, N., Lenton, A., Lienert, S., Liu, Z., Lombardozzi, D., Marland, G., Metzl, N., Munro, D. R., Nabel, J. E. M. S., Nakaoka, S.-I., Niwa, Y., O'Brien, K., Ono, T., Palmer, P. I., Pierrot, D., Poulter, B., Resplandy, L., Robertson, E., Rödenbeck, C., Schwinger, J., Séférian, R., Skjelvan, I., Smith, A. J. P., Sutton, A. J., Tanhua, T., Tans, P. P., Tian, H., Tilbrook, B., van der Werf, G., Vuichard, N., Walker, A. P., Wanninkhof, R., Watson, A. J., Willis, D., Wiltshire, A. J., Yuan, W., Yue, X., and Zaehle, S. (2020). Global carbon budget 2020. *Earth System Science Data*, 12(4):3269–3340.

Galaasen, E. V., Ninnemann, U. S., Irvalı, N., Kleiven, H. K. F., Rosenthal, Y., Kissel, C., and Hodell, D. A. (2014). Rapid reductions in North Atlantic deep water during the peak of the last interglacial period. *Science*, 343(6175):1129–1132.

Ganopolski, A., Schellnhuber, H. J., and Winkelmann, R. (2016). Critical insolation–CO_2 relation for diagnosing past and future glacial inception. *Nature*, 529(7585):200–203.

Gehler, A., Gingerich, P. D., and Pack, A. (2016). Temperature and atmospheric CO_2 concentration estimates through the PETM using triple oxygen isotope analysis of mammalian bioapatite. *Proceedings of the National Academy of Sciences*, 113(28):7739–7744.

Gingerich, P. D. (2019). Temporal scaling of carbon emission and accumulation rates: Modern anthropogenic emissions compared to estimates of PETM onset accumulation. *Paleoceanography and Paleoclimatology*, 34(3):329–335.

Goodge, J. W., Severinghaus, J. P., Johnson, J., Tosi, D., and Bay, R. (2021). Deep ice drilling, bedrock coring and dust logging with the Rapid Access Ice Drill (RAID) at Minna Bluff, Antarctica. *Annals of Glaciology*, pages 1–16.

Grant, K. M., Rohling, E. J., Ramsey, C. B., Cheng, H., Edwards, R. L., Florindo, F., Heslop, D., Marra, F., Roberts, A. P., Tamisiea, M. E., and Williams, F. (2014). Sea-level variability over five glacial cycles. *Nature Communications*, 5(1):5076.

Greenland Ice-core Project (GRIP) Members (1993). Climate instability during the last interglacial period recorded in the GRIP ice core. *Nature*, 364(6434):203–207.

Grootes, P. M., Stuiver, M., White, J. W. C., Johnsen, S., and Jouzel, J. (1993). Comparison of oxygen isotope records from the GISP2 and GRIP Greenland ice cores. *Nature*, 366(6455):552–554.

Haeberli, M., Baggenstos, D., Schmitt, J., Grimmer, M., Michel, A., Kellerhals, T., and Fischer, H. (2021). Snapshots of mean ocean temperature over the last 700,000 years using noble gases in the epica dome c ice core. *Climate of the Past*, 17(2):843–867.

Hayes, C. T., Martínez-García, A., Hasenfratz, A. P., Jaccard, S. L., Hodell, D. A., Sigman, D. M., Haug, G. H., and Anderson, R. F. (2014). A stagnation event in the deep South Atlantic during the last interglacial period. *Science*, 346(6216):1514–1517.

Haynes, L. L. and Hönisch, B. (2020). The seawater carbon inventory at the Paleocene-Eocene Thermal Maximum. *Proceedings of the National Academy of Sciences*, 117(39):24088–24095.

Hays, J. D., Imbrie, J., and Shackleton, N. J. (1976). Variations in the Earth's Orbit: Pacemaker of the Ice Ages. *Science*, 194(4270):1121–1132.

Hogg, A., Southon, J., Turney, C., Palmer, J., Bronk Ramsey, C., Fenwick, P., Boswijk, G., Friedrich, M., Helle, G., Hughen, K., Jones, R., Kromer, B., Noronha, A., Reynard, L., Staff, R., and Wacker, L. (2016). Punctuated Shutdown of Atlantic Meridional Overturning Circulation during Greenland Stadial 1. *Scientific Reports*, 6(1):25902.

Hönisch, B., Hemming, N. G., Archer, D., Siddall, M., and McManus, J. F. (2009). Atmospheric carbon dioxide concentration across the Mid-Pleistocene Transition. *Science*, 324(5934):1551–1554.

Hu, Z., Shi, G., Talalay, P., Li, Y., Fan, X., An, C., Zhang, N., Li, C., Liu, K., Yu, J., Yang, C., Li, B., Liu, B., and Ma, T. (2021). Deep ice-core drilling to 800 m at Dome A in East Antarctica. *Annals of Glaciology*, pages 1–12.

Hönisch, B., Eggins, S., Haynes, L., Allen, K., Holland, K., and Lorbacher, K. (2019). *Boron proxies in Paleoceanography and Paleoclimatology*. John Wiley & Sons, Ltd.

Ice Core Working Group (2020). Presentations: 2020 Ice Core Working Group Meeting. *Ice Drilling Program Ice Core Working Group Meeting*. Presentation by E. Brook.

Ice Core Working Group (2021). Presentations: 2021 Ice Core Working Group Meeting. *Ice Drilling Program Ice Core Working Group Meeting*. Presentation by E. Brook.

Indermühle, A., Stocker, T. F., Joos, F., Fischer, H., Smith, H. J., Wahlen, M., Deck, B., Mastroianni, D., Tschumi, J., Blunier, T., Meyer, R., and Stauffer, B. (1999). Holocene carbon-cycle dynamics based on co_2 trapped in ice at Taylor Dome, Antarctica. *Nature*, 398(6723):121–126.

Indermühle, A., Stauffer, B., Stocker, T. F., Raynaud, D., and Barnola, J.-M. (1999). Early Holocene Atmospheric CO_2 Concentrations. *Science*, 286(5446):1815.

IPCC (2013). IPCC, 2013: Summary for Policymakers. In: Climate Change 2013: The Physical Science Basis. Contribution of Working Group I to the Fifth Assessment Report of the Intergovernmental Panel on Climate Change. *Cambridge University Press*. Stocker, T.F. and Qin, D. and Plattner, G.-K. and Tignor, M. and Allen, S.K. and Boschung, J. and Nauels, A. and Xia, Y. and Bex, V. and Midgley, P.M. (eds.).

IPCC (2021a). IPCC, 2021: Climate Change 2021: The Physical Science Basis. Contribution of Working Group I to the Sixth Assessment Report of the Intergovernmental Panel on Climate Change. *Cambridge University Press*. Masson-Delmotte, V. and Zhai, P. and Pirani, A. and Connors, S.L. and Péan, C. and Berger, S. and Caud, N. and Chen, Y. and Goldfarb, L. and Gomis, M.I. and Huang, M. and Leitzell, K. and Lonnoy, E. and Matthews, J.B.R. and Maycock, T.K. and Waterfield, T. and Yelekçi, O. and Yu, R. and Zhou, B. (eds.) In press.

IPCC (2021b). IPCC, 2021: Summary for Policymakers. In: Climate Change 2021: The Physical Science Basis. Contribution of Working Group I to the Sixth Assessment Report of the Intergovernmental Panel on Climate Change. *Cambridge University Press*. Masson-Delmotte, V. and Zhai, P. and Pirani, A. and Connors, S.L. and Péan, C. and Berger, S. and Caud, N. and Chen, Y. and Goldfarb, L. and Gomis, M.I. and Huang, M. and Leitzell, K. and Lonnoy, E. and Matthews, J.B.R. and Maycock, T.K. and Waterfield, T. and Yelekçi, O. and Yu, R. and Zhou, B. (eds.). In press.

IPCC SR1.5 (2018). Global warming of 1.5°C. An IPCC Special Report on the impacts of global warming of 1.5°C above pre-industrial levels and related global greenhouse gas emission pathways, in the context of strengthening the global response to the threat of climate change, sustainable development, and efforts to eradicate poverty. *Cambridge University Press*. Masson-Delmotte, V. and Zhai, P. and Pörtner, H. O. and Roberts, D. and Skea, J. and Shukla, P.R. and Pirani, A. and Moufouma-Okia, W. and Péan, C. and Pidcock, R. and Connors, S. and Matthews, J. B. R. and Chen, Y. and Zhou, X. and Gomis, M. I. and Lonnoy, E. and Maycock, T. and Tignor, M. and Waterfield, T. (eds.). In Press.

IPICS (2020). Minutes of meeting: IPICS Oldest Ice virtual meeting 27/10/2020. Technical report.

Jang, Y., Han, Y., Ryu, H., Moon, J., Ju, H.-T., Yang, J.-W., Lee, H.-G., Jun, S. J., Lee, J., Hur, S. D., Lee, J. I., and Ahn, J. (2017). A preliminary study for blue ice in Victoria Land, East Antarctica. *Journal of the geological society of Korea*, 53(4):567–580.

Joos, F., Gerber, S., Prentice, I. C., Otto-Bliesner, B. L., and Valdes, P. J. (2004). Transient simulations of Holocene atmospheric carbon dioxide and terrestrial carbon since the Last Glacial Maximum. *Global Biogeochemical Cycles*, 18(2).

Jouzel, J., Masson-Delmotte, V., Cattani, O., Dreyfus, G., Falourd, S., Hoffmann, G., Minster, B., Nouet, J., Barnola, J.-M., Chappellaz, J., Fischer, H., Gallet, J. C., Johnsen, S., Leuenberger, M., Loulergue, L., Lüthi, D., Oerter, H., Raisbeck, G., Raynaud, D., Schilt, A., Schwander, J., Selmo, E., Souchez, R., Spahni, R., Stauffer, B., Steffensen, J. P., Stenni, B., Stocker, T. F., Tison, J. L., Werner, M., and Wolff, E. W. (2007). Orbital and millennial Antarctic climate variability over the past 800,000 years. *Science*, 317(5839):793–796.

Kageyama, M., Harrison, S. P., Kapsch, M.-L., Lofverstrom, M., Lora, J. M., Mikolajewicz, U., Sherriff-Tadano, S., Vadsaria, T., Abe-Ouchi, A., Bouttes, N., Chandan, D., Gregoire, L. J., Ivanovic, R. F., Izumi, K., LeGrande, A. N., Lhardy, F., Lohmann, G., Morozova, P. A., Ohgaito, R., Paul, A., Peltier, W. R., Poulsen, C. J., Quiquet, A., Roche, D. M., Shi, X., Tierney, J. E., Valdes, P. J., Volodin, E., and Zhu, J. (2021). The pmip4 last glacial maximum experiments: preliminary results and comparison with the pmip3 simulations. *Climate of the Past*, 17(3):1065–1089.

Karlsson, N. B., Binder, T., Eagles, G., Helm, V., Pattyn, F., Van Liefferinge, B., and Eisen, O. (2018). Glaciological characteristics in the Dome Fuji region and new assessment for "Oldest Ice". *The Cryosphere*, 12(7):2413–2424.

Kawamura, K., Nakazawa, T., Aoki, S., Sugawara, S., Fujii, Y., and Watanabe, O. (2003). Atmospheric CO_2 variations over the last three glacial–interglacial climatic cycles deduced from the Dome Fuji deep ice core, Antarctica using a wet extraction technique. *Tellus B: Chemical and Physical Meteorology*, 55(2):126–137.

Kawamura, K., Parrenin, F., Lisiecki, L., Uemura, R., Vimeux, F., Severinghaus, J. P., Hutterli, M. A., Nakazawa, T., Aoki, S., Jouzel, J., Raymo, M. E., Matsumoto, K., Nakata, H., Motoyama, H., Fujita, S., Goto-Azuma, K., Fujii, Y., and Watanabe, O. (2007). Northern Hemisphere forcing of climatic cycles in Antarctica over the past 360,000 years. *Nature*, 448(7156):912–916.

Kehrl, L., Conway, H., Holschuh, N., Campbell, S., Kurbatov, A. V., and Spaulding, N. E. (2018). Evaluating the duration and continuity of potential climate records from the Allan Hills blue ice area, East Antarctica. *Geophysical Research Letters*, 45(9):4096–4104.

Kennett, J. P. and Stott, L. D. (1991). Abrupt deep-sea warming, palaeoceanographic changes and benthic extinctions at the end of the Palaeocene. *Nature*, 353(6341):225–229.

Kobashi, T., Ikeda-Fukazawa, T., Suwa, M., Schwander, J., Kameda, T., Lundin, J., Hori, A., Motoyama, H., Döring, M., and Leuenberger, M. (2015). Post-bubble close-off fractionation of gases in polar firn and ice cores: effects of accumulation rate on permeation through overloading pressure. *Atmospheric Chemistry and Physics*, 15(24):13895–13914.

KOPRI (2020). Annual Report of Korean Polar Research Institute. Technical report.

Kukla, G. J. and Matthews, R. K. (1972). When will the present interglacial end? *Science*, 178(4057):190–191.

Köhler, P., Fischer, H., Schmitt, J., Brook, E. J., and Marcott, S. A. (2015). Comment on "Synchronous records of pCO2 and δ14C suggest rapid, ocean-derived pCO2 fluctuations at the onset of Younger Dryas" by Steinthorsdottir et al. *Science*, 107:267–270.

Lambert, F., Delmonte, B., Petit, J.-R., Bigler, M., Kaufmann, P. R., Hutterli, M. A., Stocker, T. F., Ruth, U., Steffensen, J. P., and Maggi, V. (2008). Dust-climate couplings over the past 800,000 years from the EPICA Dome C ice core. *Nature*, 452(7187):616–619.

Landais, A., Dreyfus, G., Capron, E., Jouzel, J., Masson-Delmotte, V., Roche, D. M., Prié, F., Caillon, N., Chappellaz, J., Leuenberger, M., Lourantou, A., Parrenin, F., Raynaud, D., and Teste, G. (2013). Two-phase change in CO_2, Antarctic temperature and global climate during Termination II. *Nature geoscience*, 6(12):1062–1065.

Lee, G., Ahn, J., Ju, H., Ritterbusch, F., Oyabu, I., Kim, S., Moon, J., Buizert, C., Ghosh, S., Kawamura, K., Lu, Z.-T., Hong, S., Han, C. H., Hur, S. D., Jiang, W., and Yang, G.-M. (2021). Chronostratigraphy of blue ice at the Larsen Glacier in Northern Victoria Land, East Antarctica. *The Cryosphere Discussions*, 2021:1–38.

Lilien, D. A., Steinhage, D., Taylor, D., Parrenin, F., Ritz, C., Mulvaney, R., Martín, C., Yan, J.-B., O'Neill, C., Frezzotti, M., Miller, H., Gogineni, P., Dahl-Jensen, D., and Eisen, O. (2021). Brief communication: New radar constraints support presence of ice older than 1.5 Myr at Little Dome C. *The Cryosphere*, 15(4):1881–1888.

Lipenkov, V. Y. and Raynaud, D. (2015). Climatic change in the middle of the Pleistocene and the problem of studying the most ancient Antarctic ice from Vostok station. *Ice and Snow*, 55(4):95–106.

Lipenkov, V. Y., Salamatin, A. N., Jiang, W., Ritterbusch, F., Bender, M. L., Orsi, A., Landais, A., Uchida, T., Ekaykin, A. A., Raynaud, D., Yang, G.-M., Lu, Z.-T., and Chappellaz, J. (2019). New ice dating tools reveal 1.2 ka old meteoric ice near the base of the Vostok ice core. In *EGU General Assembly*.

Lisiecki, L. E. and Raymo, M. E. (2005). A Pliocene-Pleistocene stack of 57 globally distributed benthic δ^{18}o. *Paleoceanography*, 20(1).

Loulergue, L., Schilt, A., Spahni, R., Masson-Delmotte, V., Blunier, T., Lemieux, B., Barnola, J.-M., Raynaud, D., Stocker, T. F., and Chappellaz, J. (2008). Orbital and millennial-scale features of atmospheric CH_4 over the past 800,000 years. *Nature*, 453(7193):383–386.

Lourantou, A., Lavrič, J. V., Köhler, P., Barnola, J.-M., Paillard, D., Michel, E., Raynaud, D., and Chappellaz, J. (2010). Constraint of the CO_2 rise by new atmospheric carbon isotopic measurements during the last deglaciation. *Global Biogeochemical Cycles*, 24(2).

Loutre, M. and Berger, A. (2003). Marine Isotope Stage 11 as an analogue for the present interglacial. *Global and Planetary Change*, 36(3):209–217.

Lüthi, D., Bereiter, B., Stauffer, B., Winkler, R., Schwander, J., Kindler, P., Leuenberger, M., Kipfstuhl, S., Capron, E., Landais, A., Fischer, H., and Stocker, T. F. (2010). CO_2 and O_2/N_2O variations in and just below the bubble-clathrate transformation zone of Antarctic ice cores. *Earth and Planetary Science Letters*, 297(1-2):226–233.

Lüthi, D., Le Floch, M., Bereiter, B., Blunier, T., Barnola, J.-M., Siegenthaler, U., Raynaud, D., Jouzel, J., Fischer, H., Kawamura, K., and Stocker, T. F. (2008). High-resolution carbon dioxide concentration record 650,000–800,000 years before present. *Nature*, 453(7193):379–382.

Ma, Y., Bian, L., Xiao, C., Allison, I., and Zhou, X. (2010). Near surface climate of the traverse route from Zhongshan Station to Dome A, East Antarctica. *Antarctic Science*, 22(4):443–459.

Marcott, S. A., Bauska, T. K., Buizert, C., Steig, E. J., Rosen, J. L., Cuffey, K. M., Fudge, T. J., Severinghaus, J. P., Ahn, J., Kalk, M. L., McConnel, J. R., Sowers, T., Taylor, K. C., White, J. W. C., and Brook, E. J. (2014). Centennial-scale changes in the global carbon cycle during the last deglaciation. *Nature*, 514(7524):616–619.

Martínez-Botí, M. A., Marino, G., Foster, G. L., Ziveri, P., Henehan, M. J., Rae, J. W. B., Mortyn, P. G., and Vance, D. (2015). Boron isotope evidence for oceanic carbon dioxide leakage during the last deglaciation. *Nature*, 518(7538):219–222.

Menviel, L., Spence, P., Yu, J., Chamberlain, M. A., Matear, R. J., Meissner, K. J., and England, M. H. (2018). Southern Hemisphere westerlies as a driver of the early deglacial atmospheric CO_2 rise. *Nature Communications*, 9(1):2503.

Minghu, D., Cunde, X., Yuansheng, L., Jiawen, R., Shugui, H., Bo, J., and Bo, S. (2011). Spatial variability of surface mass balance along a traverse route from Zhongshan station to Dome A, Antarctica. *Journal of Glaciology*, 57(204):658–666.

Monnin, E., Indermühle, A., Dällenbach, A., Flückiger, J., Stauffer, B., Stocker, T. F., Raynaud, D., and Barnola, J.-M. (2001). Atmospheric CO_2 Concentrations over the Last Glacial Termination. *Science*, 291(5501):112–114.

Monnin, E., Steig, E. J., Siegenthaler, U., Kawamura, K., Schwander, J., Stauffer, B., Stocker, T. F., Morse, D. L., Barnola, J.-M., Bellier, B., Raynaud, D., and Fischer, H. (2004). Evidence for substantial accumulation rate variability in Antarctica during the Holocene, through synchronization of CO_2 in the Taylor Dome, Dome C and DML ice cores. *Earth and Planetary Science Letters*, 224(1):45–54.

Motoyama, H. (2007). The second deep ice coring project at Dome Fuji, Antarctica. *Scientific Drilling*, 5:41–43.

Mulvaney, R., Rix, J., Polfrey, S., Grieman, M., Martìn, C., Nehrbass-Ahles, C., Rowell, I., Tuckwell, R., and Wolff, E. (2021). Ice drilling on Skytrain Ice Rise and Sherman Island, Antarctica. *Annals of Glaciology*, pages 1–13.

National Science Foundation (2021). *New Science and Technology Centers to address vexing societal problems.* `https://www.nsf.gov/news/special_reports/announcements/090921.jsp/` [Accessed: 30.09.2021].

NEEM Community Members (2013). Eemian interglacial reconstructed from a Greenland folded ice core. *Nature*, 493(7433):489–494.

Neff, P. D. (2014). A review of the brittle ice zone in polar ice cores. *Annals of Glaciology*, 55(68):72—82.

Neftel, A., Moor, E., Oeschger, H., and Stauffer, B. (1985). Evidence from polar ice cores for the increase in atmospheric CO_2 in the past two centuries. *Nature*, 315(6014):45–47.

Nehrbass-Ahles, C. (2017). *Millenial-scale atmospheric CO_2 reconstructions using multiple Antarctic ice cores.* PhD thesis, University of Bern.

Nehrbass-Ahles, C., Shin, J., Schmitt, J., Bereiter, B., Joos, F., Schilt, A., Schmidely, L., Silva, L., Teste, G., Grilli, R., Chappellaz, J., Hodell, D., Fischer, H., and Stocker, T. F. (2020). Abrupt CO_2 release to the atmosphere under glacial and early interglacial climate conditions. *Science*, 369(6506):1000–1005.

NOAA (2021). State of the Climate: Global Climate Report for September 2021. Technical report, NOAA National Centers for Environmental Information.

North Greenland Ice Core Project members (2004). High-resolution record of Northern Hemisphere climate extending into the last interglacial period. *Nature*, 431(7005):147–151.

Oregon State University (2021). *Oregon State to lead National Science Foundation-funded Center for Oldest Ice Exploration.* `https://today.oregonstate.edu/news/oregon-state-lead-national-science-foundation-funded-center-oldest-ice-exploration` [Accessed: 30.09.2021].

Otto-Bliesner, B. L., Braconnot, P., Harrison, S. P., Lunt, D. J., Abe-Ouchi, A., Albani, S., Bartlein, P. J., Capron, E., Carlson, A. E., Dutton, A., Fischer, H., Goelzer, H., Govin, A., Haywood, A., Joos, F., LeGrande, A. N., Lipscomb, W. H., Lohmann, G., Mahowald, N., Nehrbass-Ahles, C., Pausata, F. S. R., Peterschmitt, J.-Y., Phipps, S. J., Renssen, H., and Zhang, Q. (2017). The PMIP4 contribution to CMIP6 – Part 2: Two interglacials, scientific objective and experimental design for Holocene and Last Interglacial simulations. *Geoscientific Model Development*, 10.

Pagani, M. (2013). Biomarker-based inferences of past climate: The alkenone pCO_2 proxy. In Turekian, K. and Heinrich, H., editors, *Treatise on Geochemistry: Second Edition*, pages 361–378.

Pagani, M., Liu, Z., LaRiviere, J., and Ravelo, A. C. (2010). High earth-system climate sensitivity determined from pliocene carbon dioxide concentrations. *Nature Geoscience*, 3(1):27–30.

Parrenin, F., Masson-Delmotte, V., Köhler, P., Raynaud, D., Paillard, D., Schwander, J., Barbante, C., Landais, A., Wegner, A., and Jouzel, J. (2013). Synchronous change of atmospheric CO_2 and Antarctic temperature during the last deglacial warming. *Science*, 339(6123):1060–1063.

Pedro, J. B., Jochum, M., Buizert, C., He, F., Barker, S., and Rasmussen, S. O. (2018). Beyond the bipolar seesaw: Toward a process understanding of interhemispheric coupling. *Quaternary Science Reviews*, 192:27–46.

Peltier, W. R. and Vettoretti, G. (2014). Dansgaard-Oeschger oscillations predicted in a comprehensive model of glacial climate: A "kicked" salt oscillator in the Atlantic. *Geophysical Research Letters*, 41(20):7306–7313.

Petit, J.-R., Jouzel, J., Raynaud, D., Barkov, N. I., Barnola, J.-M., Basile, I., Bender, M., Chappellaz, J., Davis, M., Delaygue, G., Delmotte, M., Kotlyakov, V. M., Legrand, M., Lipenkov, V. Y., Lorius, C., Pépin, L., Ritz, C., Saltzman, E., and Stievenard, M. (1999). Climate and atmospheric history of the past 420,000 years from the Vostok ice core, Antarctica. *Nature*, 399(6735):429.

Pol, K., Debret, M., Masson-Delmotte, V., Capron, E., Cattani, O., Dreyfus, G., Falourd, S., Johnsen, S., Jouzel, J., Landais, A., Minster, B., and Stenni, B. (2011). Links between MIS 11 millennial to sub-millennial climate variability and long term trends as revealed by new high resolution EPICA Dome C deuterium data – a comparison with the Holocene. *Climate of the Past*, 7(2):437–450.

Pol, K., Masson-Delmotte, V., Cattani, O., Debret, M., Falourd, S., Jouzel, J., Landais, A., Minster, B., Mudelsee, M., Schulz, M., and Stenni, B. (2014). Climate variability features of the last interglacial in the East Antarctic EPICA Dome C ice core. *Geophysical Research Letters*, 41(11):4004–4012.

Rae, J. W., Zhang, Y. G., Liu, X., Foster, G. L., Stoll, H. M., and Whiteford, R. D. (2021). Atmospheric CO_2 over the past 66 million years from marine archives. *Annual Review of Earth and Planetary Sciences*, 49(1):609–641.

Rae, J. W. B., Burke, A., Robinson, L. F., Adkins, J. F., Chen, T., Cole, C., Greenop, R., Li, T., Littley, E. F. M., Nita, D. C., Stewart, J. A., and Taylor, B. J. (2018). CO_2 storage and release in the deep Southern Ocean on millennial to centennial timescales. *Nature*, 562(7728):569–573.

Rhodes, R. H., Brook, E. J., Chiang, J. C. H., Blunier, T., Maselli, O. J., McConnell, J. R., Romanini, D., and Severinghaus, J. P. (2015). Enhanced tropical methane production in response to iceberg discharge in the North Atlantic. *Science*, 348(6238):1016–1019.

Rix, J., Mulvaney, R., Hong, J., and Ashurst, D. (2019). Development of the British Antarctic Survey Rapid Access Isotope Drill. *Journal of Glaciology*, 65(250):288–298.

Rodriguez-Morales, F., Braaten, D., Trong Mai, H., Paden, J., Gogineni, P., Yan, J.-B., Abe-Ouchi, A., Fujita, S., Kawamura, K., Tsutaki, S., Van Liefferinge, B., Matsuoka, K., and Steinhage, D. (2020). A mobile, multichannel, UWB radar for potential ice core drill site identification in East Antarctica: Development and first results. *IEEE Journal of Selected Topics in Applied Earth Observations and Remote Sensing*, 13:4836–4847.

Rohling, E. J., Hibbert, F. D., Grant, K. M., Galaasen, E. V., Irvalı, N., Kleiven, H. F., Marino, G., Ninnemann, U., Roberts, A. P., Rosenthal, Y., Schulz, H., Williams, F. H., and Yu, J. (2019). Asynchronous Antarctic and Greenland ice-volume contributions to the last interglacial sea-level highstand. *Nature Communications*, 10(1):5040.

Royer, D. L., Berner, R. A., and Beerling, D. J. (2001). Phanerozoic atmospheric CO_2 change: evaluating geochemical and paleobiological approaches. *Earth-Science Reviews*, 54(4):349–392.

Royer, D. L., Berner, R. A., Montañez, I. P., Tabor, N. J., and Beerling, D. J. (2004). CO_2 as a primary driver of Phanerozoic climate. *GSA Today*, 14(3):3–7.

Ruddiman, W. F. (2003). The anthropogenic greenhouse era began thousands of years ago. *Climatic Change*, 61(3):261–293.

Ruddiman, W. F. (2007). The early anthropogenic hypothesis: challenges and responses. *Reviews of Geophysics*, 45(4).

Schmidely, L., Nehrbass-Ahles, C., Schmitt, J., Han, J., Silva, L., Shin, J., Joos, F., Chappellaz, J., Fischer, H., and Stocker, T. F. (2021). CH_4 and N_2O fluctuations during the penultimate deglaciation. *Climate of the Past*, 17(4):1627–1643.

Schmitt, J., Schneider, R., Elsig, J., Leuenberger, D., Lourantou, A., Chappellaz, J., Köhler, P., Joos, F., Stocker, T. F., Leuenberger, M., and Fischer, H. (2012). Carbon isotope constraints on the deglacial co_2 rise from ice cores. *Science*, 336(6082):711–714.

Schneider von Deimling, T., Held, H., Ganopolski, A., and Rahmstorf, S. (2006). Climate sensitivity estimated from ensemble simulations of glacial climate. *Climate Dynamics*, 27(2):149–163.

Schwander, J. (1996). Gas diffusion in firn. In Wolff, E. W. and Bales, R. C., editors, *Chemical Exchange Between the Atmosphere and Polar Snow*, pages 527–540, Berlin, Heidelberg. Springer Berlin Heidelberg.

Schwander, J., Marending, S., Stocker, T., and Fischer, H. (2014). Radix: a minimal-resources rapid-access drilling system. *Annals of Glaciology*, 55(68):34–38.

Schwander, J. and Stauffer, B. (1984). Age difference between polar ice and the air trapped in its bubbles. *Nature*, 311(5981):45–47.

Shackleton, S., Bereiter, B., Baggenstos, D., Bauska, T. K., Brook, E. J., Marcott, S. A., and Severinghaus, J. P. (2019). Is the noble gas-based rate of ocean warming during the Younger Dryas overestimated? *Geophysical Research Letters*, 46(11):5928–5936.

Shakun, J. D., Clark, P. U., He, F., Marcott, S. A., Mix, A. C., Liu, Z., Otto-Bliesner, B., Schmittner, A., and Bard, E. (2012). Global warming preceded by increasing carbon dioxide concentrations during the last deglaciation. *Nature*, 484(7392):49–54.

Shin, J., Ahn, J., Chowdhry Beeman, J., Lee, H.-G., and Brook, E. J. (2021). Millennial variations of atmospheric CO_2 during the early Holocene (11.7–7.4 ka). *Climate of the Past Discussions*, pages 1–22.

Shin, J., Nehrbass-Ahles, C., Grilli, R., Chowdhry Beeman, J., Parrenin, F., Teste, G., Landais, A., Schmidely, L., Silva, L., Schmitt, J., Bereiter, B., Stocker, T. F., Fischer, H., and Chappellaz, J. (2020). Millennial-scale atmospheric CO_2 variations during the Marine Isotope Stage 6 period (190–135 ka). *Climate of the Past*, 16(6):2203–2219.

Siegenthaler, U. and Oeschger, H. (1978). Predicting future atmospheric carbon dioxide levels. *Science*, 199(4327):388–395.

Sikes, E. L. and Volkman, J. K. (1993). Calibration of alkenone unsaturation ratios (Uk'37) for paleotemperature estimation in cold polar waters. *Geochimica et Cosmochimica Acta*, 57(8):1883–1889.

Silva, L., Nehrbass-Ahles, C., Schmidely, L., Schmitt, J., Fischer, H., and Stocker, T. F. (2022). Centennial-scale CO_2 variability in the last interglacial. *In preparation*.

Skakun, A., Lipenkov, V., Parrenin, F., Ritz, C., and Popov, S. (2019). On the availability of old meteoric ice in the vicinity of Dome B, East Antarctica. In *EGU General Assembly*.

Skinner, L. C., Fallon, S., Waelbroeck, C., Michel, E., and Barker, S. (2010). Ventilation of the deep Southern Ocean and deglacial CO_2 rise. *Science*, 328(5982):1147–1151.

Smith, H. J., Fischer, H., Wahlen, M., Mastroianni, D., and Deck, B. (1999). Dual modes of the carbon cycle since the Last Glacial Maximum. *Nature*, 400(6741):248–250.

Spahni, R., Schwander, J., Flückiger, J., Stauffer, B., Chappellaz, J., and Raynaud, D. (2003). The attenuation of fast atmospheric CH_4 variations recorded in polar ice cores. *Geophysical Research Letters*, 30(11).

Steinthorsdottir, M., Wohlfarth, B., Kylander, M. E., Blaauw, M., and Reimer, P. J. (2013). Stomatal proxy record of co_2 concentrations from the last termination suggests an important role for co_2 at climate change transitions. *Quaternary Science Reviews*, 68:43–58.

Stenni, B., Proposito, M., Gragnani, R., Flora, O., Jouzel, J., Falourd, S., and Frezzotti, M. (2002). Eight centuries of volcanic signal and climate change at Talos Dome (East Antarctica). *Journal of Geophysical Research: Atmospheres*, 107(D9):ACL 3–1–ACL 3–13.

Stern, J. V. and Lisiecki, L. E. (2013). North Atlantic circulation and reservoir age changes over the past 41,000 years. *Geophysical Research Letters*, 40(14):3693–3697.

Stocker, T. F. and Johnsen, S. J. (2003). A minimum thermodynamic model for the bipolar seesaw. *Paleoceanography*, 18(4).

Super, J. R., Thomas, E., Pagani, M., Huber, M., O'Brien, C., and Hull, P. M. (2018). North Atlantic temperature and pCO_2 coupling in the early-middle Miocene. *Geology*, 46(6):519–522.

Sutter, J., Fischer, H., Grosfeld, K., Karlsson, N. B., Kleiner, T., Van Liefferinge, B., and Eisen, O. (2019). Modelling the antarctic ice sheet across the mid-pleistocene transition – implications for oldest ice. *The Cryosphere*, 13(7):2023–2041.

Svensson, A., Andersen, K. K., Bigler, M., Clausen, H. B., Dahl-Jensen, D., Davies, S. M., Johnsen, S. J., Muscheler, R., Parrenin, F., Rasmussen, S. O., Röthlisberger, R., Seierstad, I., Steffensen, J. P., and Vinther, B. M. (2008). A 60 000 year Greenland stratigraphic ice core chronology. *Climate of the Past*, 4(1):47–57.

Tabor, N. J. and Myers, T. S. (2015). Paleosols as indicators of paleoenvironment and paleoclimate. *Annual Review of Earth and Planetary Sciences*, 43(1):333–361.

Talento, S. and Ganopolski, A. (2021). Evolution of the climate in the next million years: A reduced-complexity model for glacial cycles and impact of anthropogenic CO_2 emissions. *Earth System Dynamics Discussions*, 2021:1–31.

Tang, X., Sun, B., and Wang, T. (2019). Radar isochronic layer dating for a deep ice core at Kunlun Station. *Science China Earth Sciences*.

Tans, P. and Keeling, C. D. (2017). Atmospheric Monthly In Situ CO_2 Data - Mauna Loa Observatory, Hawaii (Archive 2021-09-07). In Scripps CO2 Program Data. UC San Diego Library Digital Collections.

Tavaré, S., Marshall, C. R., Will, O., Soligo, C., and Martin, R. D. (2002). Using the fossil record to estimate the age of the last common ancestor of extant primates. *Nature*, 416(6882):726–729.

Texas Geosciences (2021). *UT joins NSF-funded Center for Oldest Ice Exploration.* `https://www.jsg.utexas.edu/news/2021/09/ut-joins-nsf-funded-center-for-oldest-ice-exploration/` [Accessed: 30.09.2021].

Thomas, E. R., Wolff, E. W., Mulvaney, R., Johnsen, S. J., Steffensen, J. P., and Arrowsmith, C. (2009). Anatomy of a Dansgaard-Oeschger warming transition: High-resolution analysis of the North Greenland Ice Core Project ice core. *Journal of Geophysical Research: Atmospheres*, 114(D8).

Tsutaki, S., Fujita, S., Kawamura, K., Abe-Ouchi, A., Fukui, K., Motoyama, H., Hoshina, Y., Nakazawa, F., Obase, T., Ohno, H., Oyabu, I., Saito, F., Sugiura, K., and Suzuki, T. (2021). High-resolution subglacial topography around Dome Fuji, Antarctica, based on ground-based radar surveys conducted over 30 years. *The Cryosphere Discussions*, 2021:1–20.

Turkeev, A. V., Vasilev, N. I., Lipenkov, V. Y., Bolshunov, A. V., Ekaykin, A. A., Dmitriev, A. N., and Vasilev, D. A. (2021). Drilling the new 5G-5 branch hole at Vostok Station for collecting a replicate core of old meteoric ice. *Annals of Glaciology*, pages 1–6.

Tzedakis, P. C., Drysdale, R. N., Margari, V., Skinner, L. C., Menviel, L., Rhodes, R. H., Taschetto, A. S., Hodell, D. A., Crowhurst, S. J., Hellstrom, J. C., Fallick, A. E., Grimalt, J. O., McManus, J. F., Martrat, B., Mokeddem, Z., Parrenin, F., Regattieri, E., Roe, K., and Zanchetta, G. (2018). Enhanced climate instability in the North Atlantic and southern Europe during the Last Interglacial. *Nature Communications*, 9(1):4235.

Tzedakis, P. C., Wolff, E. W., Skinner, L. C., Brovkin, V., Hodell, D. A., McManus, J. F., and Raynaud, D. (2012). Can we predict the duration of an interglacial? *Climate of the Past*, 8(5):1473–1485.

Uchida, T., Yasuda, K., Oto, Y., Shen, R., and Ohmura, R. (2014). Natural supersaturation conditions needed for nucleation of air-clathrate hydrates in deep ice sheets. *Journal of Glaciology*, 60(224):1111—-1116.

UNFCCC. Secretariat (2021). Nationally determined contributions under the Paris Agreement. Synthesis report by the secretariat. Technical report, UNFCCC.

United Nations and Canada (1992). United Nations Framework Convention on Climate Change. Technical report, United Nations. New York, General Assembly.

Upham, N. S., Esselstyn, J. A., and Jetz, W. (2021). Molecules and fossils tell distinct yet complementary stories of mammal diversification. *Current Biology*.

Van Liefferinge, B. and Pattyn, F. (2013). Using ice-flow models to evaluate potential sites of million year-old ice in Antarctica. *Climate of the Past*, 9(5):2335–2345.

Van Liefferinge, B., Pattyn, F., Cavitte, M. G. P., Karlsson, N. B., Young, D. A., Sutter, J., and Eisen, O. (2018). Promising Oldest Ice sites in East Antarctica based on thermodynamical modelling. *The Cryosphere*, 12(8):2773–2787.

Vellinga, M. and Wood, R. A. (2002). Global climatic impacts of a collapse of the Atlantic thermohaline circulation. *Climatic Change*, 54(3):251–267.

Wagner, F., Aaby, B., and Visscher, H. (2002). Rapid atmospheric CO_2 changes associated with the 8,200-years-B.P. cooling event. *Proceedings of the National Academy of Sciences*, 99(19):12011–12014.

Wagner, F., Bohncke, S. J. P., Dilcher, D. L., Kürschner, W. M., van Geel, B., and Visscher, H. (1999). Century-scale shifts in early Holocene atmospheric CO_2 concentration. *Science*, 284(5422):1971–1973.

WAIS Divide Project Members (2013). Onset of deglacial warming in West Antarctica driven by local orbital forcing. *Nature*, 500(7463):440–444.

Weaver, A. J., Eby, M., Fanning, A. F., and Wiebe, E. C. (1998). Simulated influence of carbon dioxide, orbital forcing and ice sheets on the climate of the Last Glacial Maximum. *Nature*, 394(6696):847–853.

Weikusat, C., Kipfstuhl, S., and Weikusat, I. (2015). Raman tomography of natural air hydrates. *Journal of Glaciology*, 61(229):923–930.

Witkowski, C. R., Weijers, J. W. H., Blais, B., Schouten, S., and Damsté, J. S. S. (2018). Molecular fossils from phytoplankton reveal secular pCO_2 trend over the Phanerozoic. *Science Advances*, 4(11):eaat4556.

WMO (2021). State of Global Climate 2021: WMO Provisional Report. Technical report, World Meteorological Organization.

Wolff, E., Brook, E., Dahl-Jensen, D., Fujii, Y., Jouzel, J., Lipenkov, V., Severinghaus, J., Fischer, H., van Ommen, T., Bauska, T., and Higgins, J. (2020). White paper: The oldest ice core: A 1.5 million year record of climate and greenhouse gases from Antarctica. Technical report, IPICS. *In update*.

Woodburne, M. O., Gunnell, G. F., and Stucky, R. K. (2009). Climate directly influences Eocene mammal faunal dynamics in North America. *Proceedings of the National Academy of Sciences*, 106(32):13399–13403.

Wunsch, C. (2004). Quantitative estimate of the Milankovitch-forced contribution to observed Quaternary climate change. *Quaternary Science Reviews*, 23(9):1001–1012.

Xiao, C., Li, Y., Hou, S., Allison, I., Bian, L., and Ren, J. (2008). Preliminary evidence indicating Dome A (Antarctica) satisfying preconditions for drilling the oldest ice core. *Chinese Science Bulletin*, 53(1):102–106.

Yan, Y., Bender, M. L., Brook, E. J., Clifford, H. M., Kemeny, P. C., Kurbatov, A. V., Mackay, S., Mayewski, P. A., Ng, J., Severinghaus, J. P., and Higgins, J. A. (2019). Two-million-year-old snapshots of atmospheric gases from Antarctic ice. *Nature*, 574(7780):663–666.

Yehudai, M., Kim, J., Pena, L. D., Jaume-Seguí, M., Knudson, K. P., Bolge, L., Malinverno, A., Bickert, T., and Goldstein, S. L. (2021). Evidence for a northern hemispheric trigger of the 100,000-y glacial cyclicity. *Proceedings of the National Academy of Sciences*, 118(46).

Yin, Q. Z. and Berger, A. (2012). Individual contribution of insolation and CO_2 to the interglacial climates of the past 800,000 years. *Climate Dynamics*, 38(3):709–724.

Young, D. A., Roberts, J. L., Ritz, C., Frezzotti, M., Quartini, E., Cavitte, M. G. P., Tozer, C. R., Steinhage, D., Urbini, S., Corr, H. F. J., van Ommen, T., and Blankenship, D. D. (2017). High-resolution boundary conditions of an old ice target near Dome C, Antarctica. *The Cryosphere*, 11(4):1897–1911.

Zhang, N., An, C., Fan, X., Shi, G., Li, C., Liu, J., Hu, Z., Talalay, P., Sun, Y., and Li, Y. (2014). Chinese first deep ice-core drilling project DK-1 at Dome A, Antarctica (2011-2013): progress and performance. *Annals of Glaciology*, 55(68):88—98.

Zhang, X., Knorr, G., Lohmann, G., and Barker, S. (2017). Abrupt North Atlantic circulation changes in response to gradual CO_2 forcing in a glacial climate state. *Nature Geoscience*, 10(7):518–523.

Zhao, L., Moore, J. C., Sun, B., Tang, X., and Guo, X. (2018). Where is the 1-million-year-old ice at Dome A? *The Cryosphere*, 12(5):1651–1663.

Chapter 2

The Centrifugal Ice Microtome

The centrifugal ice microtome (CIM) is a customized dry-extraction device for CO_2 measurements on ice cores. The design and assembly of its modules took approximately seven years, but the idea behind it was only made possible by the accumulated knowledge of different measurement apparatus at the University of Bern since the 1980s.

While Bereiter et al. (2013) succinctly describe the CIM and Nehrbass-Ahles (2017) reports a series of improvements, a part-by-part description is lacking. Understanding the purpose and limitations of each element is key if one wishes to improve the system and not carry over some of the shortcomings. In this chapter I try to convey the most relevant information about the CIM in a quick-guide format.

2.1 A timeline of developments

The first dry-extraction device for CO_2 reconstructions at the University of Bern was developed in the early 1980s (Zumbrunn et al., 1982). The so-called Needle Cracker relied on movable steel needles to crush 1 cm^3 ice samples under vacuum at $-22\,°C$. The released air was then analysed with an infrared laser spectrometer (IRLSM). The device was successfully operated for 30 years and its data output was the basis of a series of landmark articles in ice core science (Neftel et al., 1982, 1988; Indermühle et al., 1999; Monnin et al., 2001; Siegenthaler et al., 2005; Lüthi et al., 2008; Bereiter et al., 2012). Throughout the years the Needle Cracker underwent incremental improvements, although the basic principles remained the same (see Bereiter (2012) for an historic overview). By the late 2000s, work was underway at the University of Bern to design a novel dry-extraction system. The goal was to circumvent well-known shortcomings of the Needle Cracker, for instance:

- Different extraction efficiencies for bubbly (70%) and clathrated ice (55%) (Lüthi, 2006)
- Contamination of ambient air CO_2 while loading samples (Zumbrunn et al., 1982)
- CO_2 enrichment from mechanical friction of metal parts
- Gas fractionation while measuring standard gases (Monnin, 2000)

- Lack of automated routines
- Operator bias (Bereiter, 2012)
- Gas analytical module approaching the end of its lifetime (Bereiter, 2012; Gay, 2012)

In 2005, Dieter Lüthi (MSc) reports on developments on a new device called the Ice Mill. It had much higher extraction efficiency than the Needle Cracker, but the complex design led to leak issues that could not be solved (Lüthi, 2006). The project was abandoned definitively in 2007 (Bereiter, 2007).

In 2007, Bernhard Bereiter (MSc) starts developing a new gas analytical system, as it was becoming increasingly hard to work with the IRLSM at the end of its lifetime, when manufacturer support was no longer available (Bereiter, 2007). He settles for adapting a commercial gas analyzer that is relatively inexpensive, easy to work with and overall less complex, albeit less accurate, than the IRLSM. The chosen gas analyzer is the LI-7000 from LI-COR Biosciences, hereafter only referred to as LI-COR (see Section 2.3.3). The LI-COR was designed for both CO_2 and H_2O atmospheric measurements at room pressure in the lab or for field work. It was therefore necessary to adapt it to the low sample pressures (0–10 mbar) achieved with ice core samples and recalibrate it for the wide range of CO_2 concentrations in the paleo record (180–300 ppm). The LI-COR is successfully tested in a separate test-rig, but not yet coupled to neither the Needle Cracker nor the Ice Mill (Bereiter, 2007).

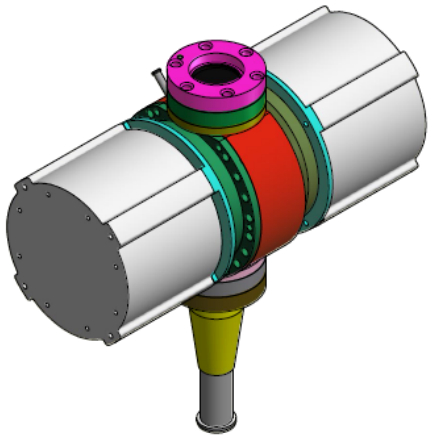

Figure 2.1: 3D view of the CIM. Note the magnetic bearings (grey) that are fastened to the mantle (red). Also visible is the top CF flange from where the sample is loaded (magenta) and the funnel in the bottom where the ice leftovers are collected (yellow).

In 2009, Renato Winkler (MSc) introduces the bellow, a movable volume that allows precise control on the gas pressure inside the measurement cell (Winkler (2009); see also Section 2.3.2). This eliminates known gas fractionation issues that were associated with the handling of manual full-metal valves (Monnin, 2000). The bellow is controlled by an in-house developed LabVIEW VI, which paves the way towards automation.

In 2011, Michael Siegrist (MSc) brings together the LI-COR, the bellow and the standard tanks and starts to work toward a fully automated gas analysis system (Siegrist, 2011). The measurement routines become faster and the operator bias is eliminated. Several issues are found and corrected, mostly related to the customised settings of the LI-COR for ice core research.

In parallel to these developments, Bernhard Bereiter (PhD; 2008–12) is focusing on the development of a novel extraction system (see Section 2.3.1). The goal was to avoid the

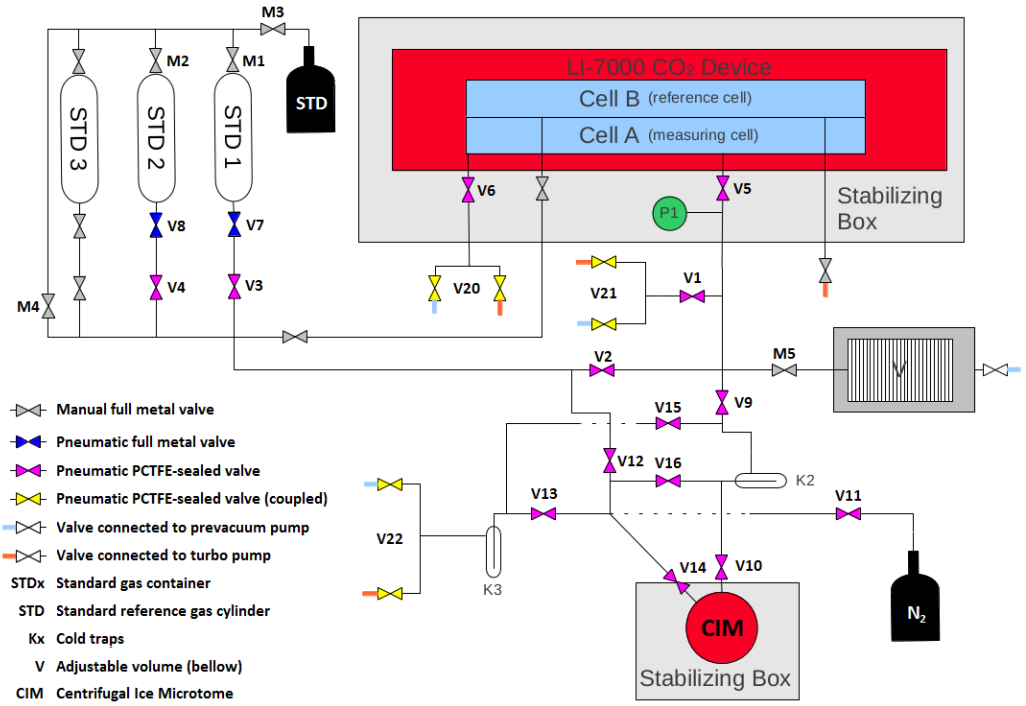

Figure 2.2: Schematic of the CIM. Taken from Nehrbass-Ahles (2017).

known ambient air contamination that occurred with the Needle Cracker and eliminate metal-on-metal frictional movements that released CO_2 and contaminated the gas sample. The chosen design is based on a magnetic bearingless technology for lubricant-free, high-purity pumping systems from Levitronix®. The centrifugal ice microtome (CIM) is developed step by step, undergoing many shapes and tests (see Figure 2.1). After proof of concept is reached, the CIM is coupled to the LI-COR, bellow and standard gas unit to form a unified system. The LabVIEW code for the measurement routine is progressively built and at its final stage the only remaining non-automated tasks are the sample loading and the subsequent removal of the ice remnants. By 2012 the first successful measurements are carried out, with the CIM outperforming the Needle Cracker in accuracy (offset of 2.0 vs 4.9 ppm), precision (1σ reproducibility of 1.1 vs 2.7 ppm), extraction efficiency (overall >90% for the CIM vs 70% (bubbly ice) and 55% (clathrated ice) for the Needle Cracker) and sample throughput (maximum of 20 instead of 6 samples per day) (Bereiter et al., 2013).

In his PhD work (2013–17), Christoph Nehrbass-Ahles (CNA) successfully undertakes several measurement campaigns with the CIM using different ice cores (EDC, Talos Dome, WAIS, Taylor Glacier). The extensive measurements lead to the establishment of standard operational procedures and to further refinements in temperature stabilization and leak tightness. The result is a substantial improvement in measurement reproducibility and long-term reliability of the device (Nehrbass-Ahles, 2017). The current measurement apparatus of the CIM is shown in Figure 2.2.

The work during this PhD (2017–22) involved the measurement and analysis of fast CO_2 variability in highly-resolved ice core datasets. To determine to what extent the signals were ice-core-related or a product of experimental error, several investigations were pursued to better understand some of the limitations of the system (see Chapter 3). The resulting statistical analysis provides a better understanding of which parameters should be prioritized when measuring with the CIM. A few new corrections have also been implemented that improve reproducibility and help to identify outliers.

In 2018 the Needle Cracker was disassembled and transferred to the Museum of Natural History in Neuchâtel. There it was displayed for a full year as part of the exhibition *"Poles, feu la glace"*, in the context of scientific research in Antarctica and climate change[i].

In 2019, the CO_2 lab underwent renovations. The CIM is currently no longer standing in a hallway, but instead it had been accommodated inside a dedicated laboratory with temperature control. A gas cabinet was added with an easy to work supply line of N_2. The configuration of the CIM remained essentially the same, but it benefited from the removal of a few dead volumes, easier access for maintenance actions and overall space gains that made the measurement routine a little easier.

2.2 The measurement routine

The measurement routine of the CIM works in a loop, with processes running in parallel to save time. Each cycle lasts 15 minutes, from which 5 minutes require active input from the operator. Its steps were concisely summarized by my predecessor in his thesis; for a more detailed explanation see Section A.2.3. The following list describing the measurement cycle was taken *verbatim* from Nehrbass-Ahles (2017):

1. Loading of the new sample into the CIM and evacuation of the extraction chamber
2. Sample extraction (shaving of the ice followed by an optional waiting time)
3. Expansion (and drying) of the extracted air towards the LI-7000
4. Pushing the dry sample air into the LI-7000 and starting the measurement
5. Evacuation of the LI-7000 measurement cell
6. Expansion of the calibration gas in the LI-7000 and adjustment of the pressure level to that of the previous sample and starting the calibration measurement
7. Evacuation of the LI-7000 measurement cell
8. Starting of a zero measurement for signal baseline determination

[i] https://www.museum-neuchatel.ch/expositions/poles-poles-feu-la-glace/ (visited on 31/12/2021)

An important aspect of the measurement routine of the CIM is the fact that the current and the previous sample are being processed simultaneously, albeit at early and late stages, respectively. As soon as one sample is extracted from the CIM and sent to the gas analyzer, the operator can immediately load another sample. The extraction of this new sample will therefore take place while the previous one is being analysed in the LI-COR.

This feature saves time and increases sample throughput. On a typical measurement day, 16 ice core samples can be measured in approximately 8 hours, already including the time needed for sample preparation, shutting on/off routines and the measurement of 5–7 gas free ice samples. If need be, the CIM can process up to a maximum of 24 samples per day, but this is not sustainable for consecutive days of measurements as the CIM needs enough time over night to remove the built up ice.

The downside of processing samples in parallel is that problems arising with one particular sample may have a negative cascading effect in the upcoming sample. For instance, a late closure of the system after reloading will reduce the final vacuum quality of that loaded sample and may alter the temperature of the other sample that is waiting inside the LI-COR to be measured (see Sections 3.1.2 and 3.1.3).

2.3 The CIM piece by piece

2.3.1 The extraction head

An extensive, though perhaps nowadays incomplete, review of different gas extraction methods is presented in Bereiter (2012). In comparison to other dry-extraction devices available worldwide, the CIM is, as of today, the only one relying on magnetic levitation. This feature brings several notable advantages, for example:

- Most techniques involve large metal surfaces relative to the ice sample size that crush/mill/grate the ice in order to release the trapped air ((Delmas et al., 1980; Neftel et al., 1982; Etheridge et al., 1988)). In contrast, the CIM knife is only 3.7 cm wide and stays passively fixed, while the magnetically operated rotor pushes the sample against and past the knife.

- Vacuum quality stays unperturbed during extraction because the magnetic field that drives the shaving acts remotely. Contrastingly, mechanical movements such as the crushing of needles will involve other metal elements (such as shafts, bearings or bellows) that present opportunities for leaks.

- The remote control of the movement of the rotor means that the operator only needs an opening big enough to load the sample. This prevents contamination from room atmosphere more effectively and enhances the purge power of the N_2 outward flow while loading a sample.

- The high rotational speed up to 1700 RPM produces much finer ice powder, with no discernible difference in extraction efficiency between bubbly and clathrated ice.

A schematic cross-section view shows the shaving mechanism of the CIM (see Figure 2.3). An ice sample (A) is placed in the recess of the sample holder (B) via the loading cap (F). After closure and evacuation, the sample holder levitates concentrically with respect to the mantle (C) through the application of a magnetic field. That same magnetic field induces the rotor to spin at speeds up to 1700 RPM. This accelerates the ice sample centripetally, radially pushing it against the mantle as it spins with the rotor. At every revolution, the ice sample is shaved when pressed against a knife (D) placed at the lower end of the CIM. Ice powder is collected at the funnel (E) and removed after each extraction through the cleaning cap opening (G).

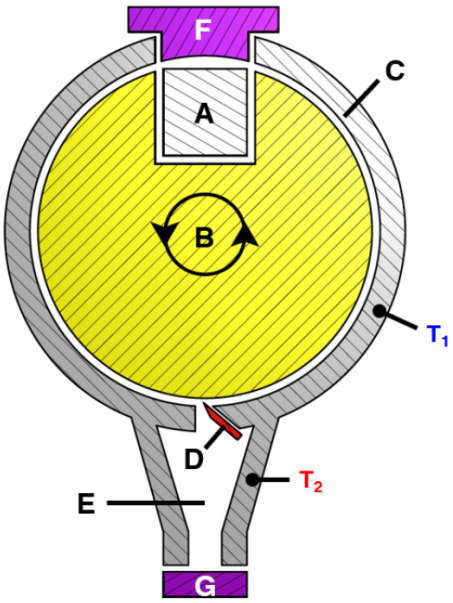

Figure 2.3: Cross-section of the CIM displaying the shaving process (simplified). A) Ice sample; B) Rotor; C) Mantle; D) Knife; E) Funnel; F) Top opening; G) Bottom opening; T1/T2) Temperature sensors.

The radical transition from the established Needle Cracker to such a novel concept meant of course many challenges due to the many new parts. In the following I list the most relevant elements that compose the extraction head and their main features.

2.3.1.1 The rotor

The rotor is a custom-built stainless steel sample holder for the CIM. It consists of one main cylinder with a recess (see Figure 2.3). Welded to the bases of the main cylinder are two other concentric cylinder arms that encase the Levitronix magnets at their extremities. In order for the center of mass to be coincident with the geometric center of the rotor, the main cylinder was machined in its interior, making it hollow (see Figure 2.4). This air pocket in turn made the welding phase of the arms very difficult. Therefore, a small hole was made in one of the bases of the arms, in order for the warm air to evacuate during the welding. This small hole was then welded with a special laser welding technique. The weld was thoroughly tested, but a very small virtual leak cannot be excluded.

2.3.1.2 The magnetic bearings

The magnetic bearings technology used by the CIM is part of the core business of Levitronix®, a company specialized in providing pump systems and mixers. The contactless concept allows fluid pumping in high purity applications where progressive wear and the usage of

lubricants is an issue, such as the medical industry. It was not designed to work under vacuum or sub-zero temperatures. The customised adaptation of the magnetic levitating system meant thus a huge undertaking by Bernhard Bereiter in close collaboration with engineers at Levitronix®. Special firmware was developed and many non-intended destructive tests were performed before reaching success.

The magnetic field created by the bearings is either on or off. This feature means that upon activation the rotor levitates immediately, and when shut down the rotor free falls from a height of 1–2 millimeters. This hard touchdown is unfortunately inevitable (Antony Sibilia, Levitronix, *pers. comm.*, September 2020). Over time, as the rotor lands on the inner copper rings it is possible that residual copper flakes are scrapped off.

The measurement routine has the bearings applying a magnetic field that forces the rotor to spin with a two-step velocity profile. First, at 1400 RPM for 15 s and afterward at 1700 RPM for 70 s. These two speeds were chosen via trial-and-error, with speeds below 1400 RPM not successfully shaving the ice and speeds above 1700 RPM leading to too much rotation instability and generation of excess heat. CNA suggested experimenting with a ramp-up velocity profile instead of the two-step procedure (see Nehrbass-Ahles (2017)), but the risks of accidentally destroying the CIM do not compensate any eventual gain in the shaving procedure. It cannot be stressed enough that the settings of the Levitronix® software that control the magnetic bearings should not be changed without a very good reason.

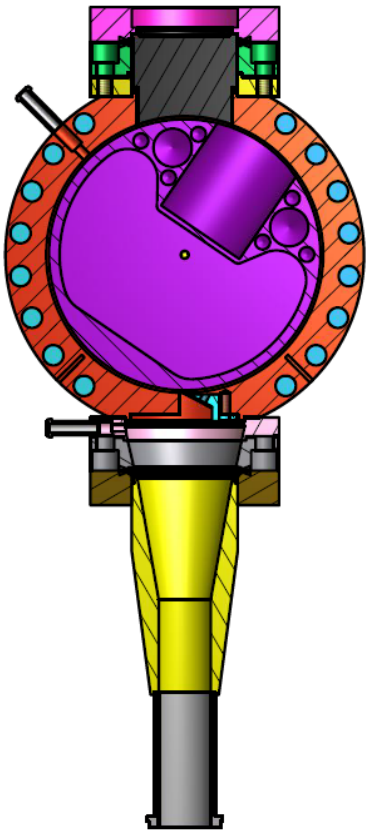

Figure 2.4: Cross-sectional view of the CIM showing the rotor and its hollow design (purple). Notice also the inlet and outlet (grey;left), the mantle (orange), the knife holder (light blue) and the funnel (yellow).

2.3.1.3 The knife

The knife is one of the most critical elements inside the CIM. It plays a role in the extraction efficiency and final ice grain size, but also in contamination issues as a likely candidate for CO_2 adsorption/desorption effects (Zumbrunn et al., 1982). Its position deep inside the CIM lowers the risk of exposure from the surrounding room atmosphere. Nevertheless, the ice cleaning procedure after every measurement (when brushes are introduced in its vicinity) could still theoretically provide the necessary pathway for contamination, even with an active N_2 purge.

The knife is made of titanium grade 5 alloy, which grants it more corrosion resistance over stainless steel while still possessing a comparable tensile strength. It also avoids the carbon content of the stainless version, a cause for possible CO_2 release (Bereiter et al., 2013). The downside of using titanium is an increased difficulty in achieving and maintaining the sharpness of the edge.

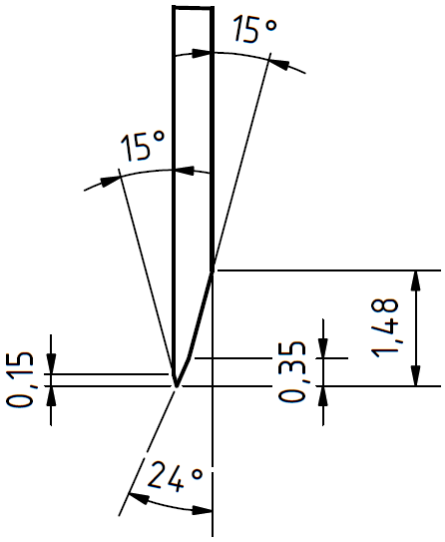

Figure 2.5: Partial blueprint of the CIM knife geometry. Note the two cutting angles at 15° and 24°.

Sharpening the knife is an overall painstaking and delicate procedure that should be performed only when strictly necessary. The main difficulty is the assembly of the knife after sharpening due to the limited available space for maneuvering. This step is usually achieved after three to four tries (see Section A.3.3). The whole operation is user-sensitive and often leads to failed shavings and subsequent wasting of samples. To counter this issue, I have developed a new sharpening routine that attempts to achieve a more long-lasting and consistent final sharpness of the knife. Still, I recommend sharpening the knife only prior to a measurement campaign or when the ice powder looks unreasonably coarse.

Previously, a small whetstone of unknown grit was used, and the user would sharpen the blade much like a kitchen knife, trying to preserve the 15° and 24° angles by hand, until it was considered that the blade was sharp enough (see Figure 2.5). The process was not standardized and certainly did not grant the knife the same level of sharpness in-between procedures.

After some initial manual attempts with different whetstones and shaving kits, the team of mechanics at KUP ingeniously developed a knife holder that simplifies the sharpening task (see Figure 2.6). The holder now allows for a large whetstone to be fixed while the user can perform shaving laps. They consist of moving the blade both in the parallel and perpendicular directions, all the while respecting the blade angles.

Subsequent tests revealed a much finer ice powder, i.e., a sign of increased sharpness and increased extraction efficiency. However, this change also brought unexpected hurdles. The finer powder tends to stick more to the inner surfaces of the CIM, demanding a more thorough cleaning procedure. The user now needs to brush 2–3 times more with both the coarser and the finer brush in order to clean the funnel after each measurement. The earlier than usual occurrence of "knocking sounds"[ii] during measurement days seems to indicate that the fine ice powder is now more likely to be blown towards the surroundings of the

[ii]Sounds associated with the unintentional hitting of the rotor against the inner copper rings during the extraction phase.

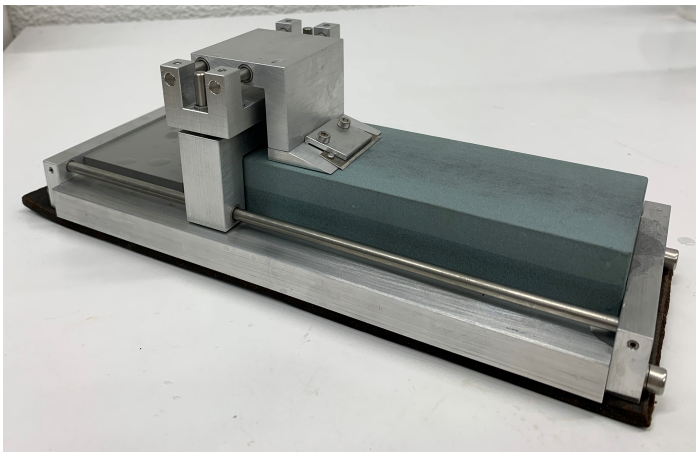

Figure 2.6: The new knife sharpening setup developed by the workshop.

rotor instead of going directly into the funnel. Surprisingly, the finer powder also brought a very high occurrence of measurements with unsuccessful shaving (5–6 per day). The samples either got radially stuck inside the recess or did not shave completely, leaving small debris behind. It is possible that the fine ice powder is sticking to the knife itself, blocking the escape path to the funnel and/or inhibiting the shaving. It is hard to pinpoint this as the only culprit, as previously the N_2 purge pressure had been lowered from 2 to 1 bar (over pressure). The lower purge pressure was tried in order to improve vacuum conditions and avoid N_2 dilution of the ice sample, but could have worsened the blow-out of the ice powder (see also Section 3.1.2). Moreover, the recent change from "cubic" to "cheese-like" samples, which significantly changed the shape of the sample, also seems to play a role, since only cheese-like ice core samples get stuck, but never gas-free EK samples (see Section 3.2.2).

The most likely scenario behind the stuck samples is that the previously blunt knife was "coarsely" crushing all samples regardless of shape. A very sharp knife, however, now slowly shaves the ice layer by layer until the sample gradually reaches a length that equals the diameter of the recess, and gets therefore horizontally stuck, hanging just above the knife at every rotation.

After much head scratching followed by trial and error I arrived at the following configuration:

- **Maintain N_2 purge set at 2 bar overpressure.** At first, lowering this pressure seemed to be a good compromise between having enough pressure to blow out the ice powder and at the same time achieving good vacuum. As it turns out, some samples were contaminated with abnormally high CO_2, which likely came from a too gentle purge.

- **Shaving time increased to 25 seconds at 1400 RPM followed by 100 seconds at 1700 RPM.** The usual 15 s + 70 s were no longer enough because the sharp blade now actually shaves the sample, which takes longer than the previous blunt knife that

broke away small chunks of ice. The new settings were chosen in a purely empirical way.

- **Position sample with the edge facing the knife.** This positioning of the sample allows for the knife to attack the edge of the sample from the start and seems to result in significantly less events of non-shaving.

- **Keep samples below 9 grams**. This will roughly keep the maximum inner length of the sample below 34 mm, which is the radius of the recess, and thus avoiding the samples being stuck.

This configuration seems to minimize the issues mentioned above. The tests were performed after sharpening the blade with a 400 and 1000 grit whetstone. The recently acquired 3000 and 8000 grit finer whetstones have yet to be tested. It could be that they offer a sharper and more long-lasting edge, but it could also be that the Titanium knife will not allow any further sharpening.

2.3.1.4 The glass encasements

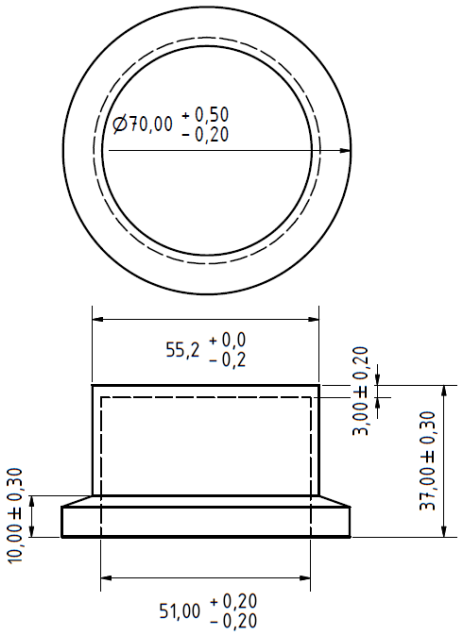

Figure 2.7: Blueprint of a glass encasement for the CIM.

The glass encasements are the most sensitive element of the CIM. They are positioned concentrically with the two extremities of the rotor where the magnets stand (see Figures 2.7 and 2.9). Placed immediately above them are the magnetic bearings, whose magnetic field actuates on the magnets and makes the rotor rotate. The glass encasements also act as seals between the inside of the CIM at very low pressure and the outer room atmosphere. Glass was chosen as it met the need for a non-ferromagnetic material that could also act as a seal and be physically and chemically inert. However, shaping glass to meet tolerances in the sub-millimeter range is a very difficult task for glassblowers[iii]. On average, only one out three of the ordered glass encasements met the tight tolerances required to fit correctly inside the CIM. Due to the proximity to the rotor, imbalances during the rotation of the rotor at high speed have led to the destruction of the glass encasements. This is one of worst scenarios for the CIM, involving near total disassembly in order to remove all glass shards.

[iii]Intelligent Quartz Solutions - https://www.iqs.glass/

2.3.1.5 The funnel

The funnel is the collecting vessel for shaved ice during the extraction phase. It requires cleaning at the end of each measurement cycle with a coarse and a fine brush, while being blown by a 2 bar overpressure flow of N_2. Access to the funnel is made by manually unscrewing the VCR connecting plug with a pair of spanners. The funnel itself is detached from the CIM in case of maintenance of the knife or retightening of the copper or gold gaskets immediately above it.

The funnel structure is a custom-made invention that requires time and patience to assemble by the workshop. An open-ended, funnel-shape stainless steel structure is welded to a ConFlat® (CF) flange at the large end (see Figure 2.8). At the short end, a VCR gland is welded that will permit the closure of the funnel with a female nut and a male blind plug. The female nut is silver plated, which eases the tightening procedure. Progressive wear of the silver plating will lead to difficulties in closing the system and eventually leaks. At this point the replacement of the female nut unfortunately requires disassembling the funnel, followed by cutting and rewelding of the CF weld. This operation is delicate and the new weld points need to be thoroughly leak-tested. For this reason, it is wise to try to extend the lifetime of the female nut by replacing the male plug once every 1–2 weeks of measurements or as soon as it is damaged. Frequent cleaning of the thread during measurements avoids buildup of ice in its grooves and reduces stress.

Figure 2.8: The CIM funnel, sitting upside-down with respect to its position in the CIM.

2.3.1.6 The outer mantle

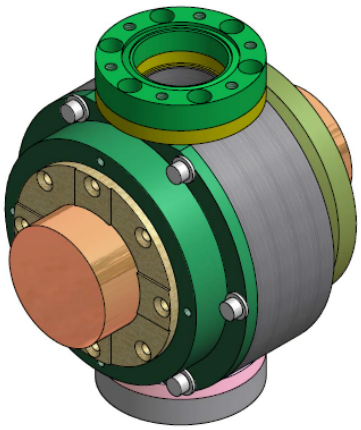

Figure 2.9: 3D view of the CIM mantle (dark grey). Notice the small M5 screws (light grey) fastening the lateral opening and the glass encasements (orange) at both ends.

The outer mantle of the CIM was machined from a single block of stainless steel (see Figure 2.9). The major access to the interior of the CIM is done via a lateral opening, dividing the CIM into one smaller and one bigger hemisphere. Space constraints dictated that the two parts have to be assembled with M5 screws, which are not as ideally big and sturdy as the preferred M6 screws for this particular case. This feature has resulted into this junction being susceptible to leaks, and the user should inspect this area carefully when leak-testing the CIM. When retightening, it should be kept in mind that these screws are more prone to damage via overtightening.

The inlets that have been welded to the mantle are also particularly fragile (see Figure 2.4). The lower one allows for flushing when opening the top CF flange, while the upper one helps to blow out shaved ice when cleaning the funnel.

2.3.1.7 The seals

The CIM uses several types of sealing materials in different places and for different functions:

- **Copper gaskets**
  Copper gaskets are used in the upper and lower CF flanges. They are single-use and allow for very good vacuum for our purposes. The sexless CF flanges have a knife edge where the gasket sits. Upon compression, the hard stainless steel knife edge indents the relatively softer copper gasket creating a groove and sealing the two ends. Theoretically, if the groove is not deep enough, the same gasket could be used again by applying more pressure and deepening the groove. For practical purposes, we nevertheless employ the gaskets as single-use.

- **VCR gaskets**
  The gasket used in the VCR connection in the funnel is a silver-plated nickel gasket. The seal is achieved by putting the gasket between the gland and the male blind plug. The round edge of the gland presses slightly on the gasket, creating a groove. Given the softness of the gasket, the area of contact is relatively large while the groove is not very deep. This means that the gasket can be used multiple times. While CNA used one gasket every 7 measurements, I use one gasket every 3–4 measurements. I have noticed it is quite difficult to maintain reproducibility in vacuum quality as the gasket undergoes more and more utilization.

- **Gold seals**
  The CIM possesses three high-purity gold seals. They are located between the main body and the upper/lower CF flanges, and in the main body opening that splits the CIM inside in two parts. The seal is obtained by looping gold wire in the respective groove and tightening afterwards. Gold is very ductile and partially elastic, which helps to fill small gaps in the inevitably uneven and imperfect tightening procedure. The gold seals under the CF flanges lose tightness over time, which is more likely a fault from the screw rather than from the gold. Nevertheless, after much thermal cycling this is a spot where leaks typically occur. I recommend to tighten these M6 screws with 8 N m.

- **Indium seals**
  Following the replacement of some indium seals with gold seals (see Nehrbass-Ahles (2017)), the CIM is currently left with only two indium seals. They are placed at each glass encasement seat, as the fragility of these elements requires a very malleable and adaptive seal. Screwing the indium seals is particularly challenging and requires special care. Given the softness of the indium seal, the screws will never offer great resistance while being fastened, giving the impression that they are permanently loose. Therefore there is the danger of suddenly applying too much tension in the glass encasements and breaking them.

2.3.2 The bellow

The bellow (*Faltenbalg*) is a movable volume that regulates the pressure of the sample gas that is sent to the LI-COR (see Figure 2.10). It was introduced by Renato Winkler in order to eliminate the most sensitive and tricky measurement step with the Needle Cracker (Winkler, 2009). After an ice core sample had been measured, a standard gas measurement followed to calibrate it. The operator had then to very gently open a manual valve and let standard gas flow to the measurement cell. The goal was to replicate the pressure previously attained by the ice core sample, which proved very difficult. The task required experience and even then reproducibility was poor. Critically, there was evidence that the partial and slow opening of the manual valve led to strong gas fractionation issues (see Monnin (2000), Section 5.7). Therefore, with the introduction of the bellow came the first steps towards automation, as the bellow was controlled by a LabVIEW VI (*Steuerung*[iv]). At the time, the bellow was coupled to the Needle Cracker and to the Ice Mill (Lüthi, 2006). Later, given its success, Bereiter et al. (2013) coupled it to the CIM.

The bellow is enclosed in a tight Plexiglas casing that is kept under vacuum by the magnetic coupled oil pump (see Section 2.3.6.3). This allows it to be at near-equilibrium with the vacuum on its inside during measurements. The small tolerance for pressure gradients

[iv] German word that can be loosely translated as "control interface"

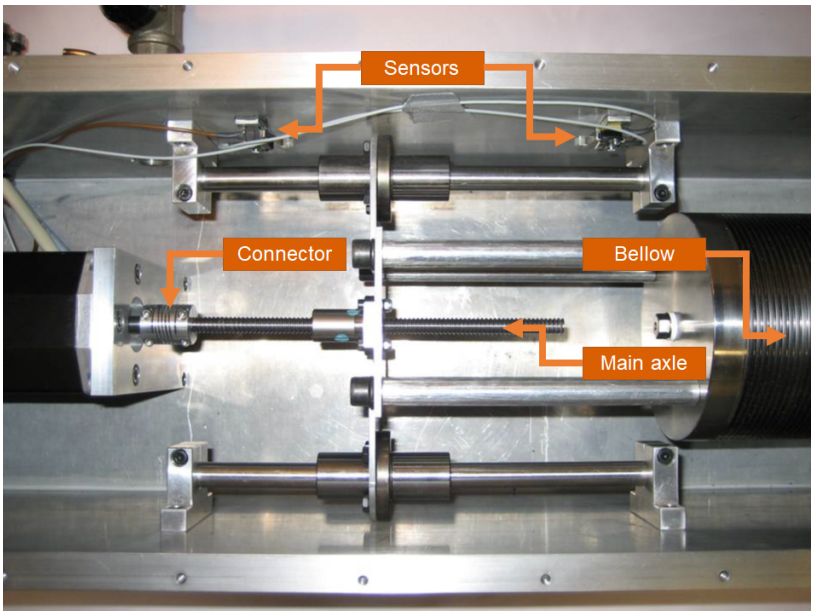

Figure 2.10: Overview of the bellow. Adapted from Winkler (2009).

between the inside and outside of the bellow implies a complicated procedure of quasi-static pressure adjustment every time the bellow is brought from vacuum to atmospheric pressure or vice-versa (see Section A.4.2). In case of a sudden high pressure gradient (e.g., loss of vacuum inside the Plexiglas during a power outage or exposure to a high pressure (>1 bar) N_2 flushing flow), the bellow will immediately deflate/inflate, leading to rupture of either the bellow itself or the delicate connector that couples the motor and the main rotating axle (spindle). While the connector has a spring-like design that gives it elastic memory to sustain the constant cycles of compression and extension, it cannot respond to such a sudden stretching force. Replacing the connector is a painstaking task that should be avoided at all costs (see Section A.4.3).

2.3.3 The LI-COR

The LI-7000 is a differential, non-dispersive infrared (NDIR) gas analyzer. It shares most of its features with other commercially available NDIR sensors. It was first tested as a less complex alternative to the aging infrared laser spectrometer (IRLSM) from the Needle Cracker, if only a little less accurate. Its original apparatus works as follows (see Figure 2.11):

1. A vacuum-sealed tungsten filament acts as an infrared (IR) source.

2. IR radiation is modulated with a chopping shutter toward two individually sealed measurement cells. At both ends of the measurement cells are sapphire windows that allow high power transmission in the near infrared.

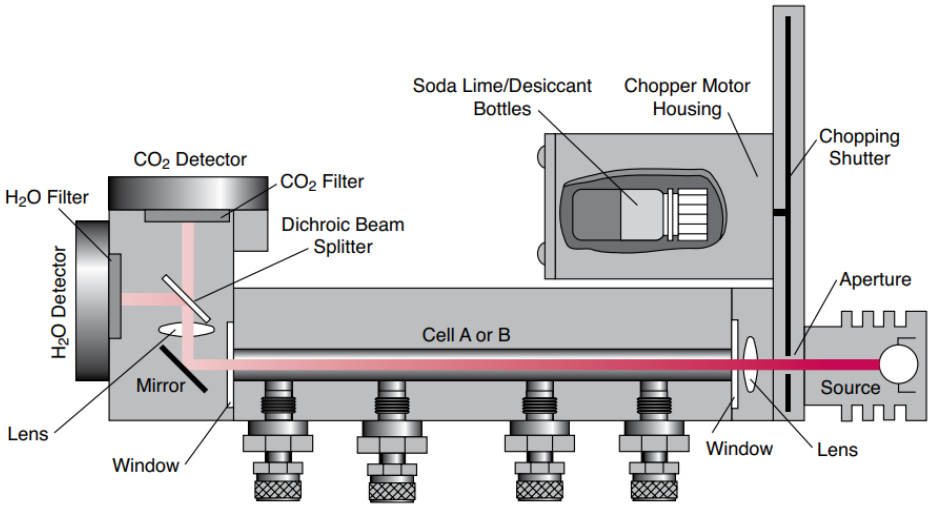

Figure 2.11: Schematic of the LI-7000. Taken from LI-COR Biosciences (2007).

3. CO_2 molecules inside the measurement cell absorb very specific bands of the IR light, while letting the remaining wavelengths pass through.

4. Light reaches a CO_2 optical filter that blocks all wavelengths except the thin CO_2 absorption band centered around 4.255 µm.

5. A solid state CO_2 detector reads the amount of light received. The difference between the initial IR light radiated from the source and the amount detected is proportional to the number of CO_2 molecules in the cell.

6. The simultaneous measurement of a standard gas with a well-known CO_2 concentration in one cell and a sample gas in the other cell allows for the calculation of the absolute CO_2 concentration of the sample gas.

The LI-COR mostly targets atmospheric measurements, and not very low pressure situations such as the extraction of small amounts of gas from ice core samples. Therefore, instead of its original setup as a differential analyzer, one of the measurement cells is now constantly pumped to be kept at vacuum. Measurements in this cell are referred to as “zero measurements", as their only purpose is to assess the background signal. The second cell is where all gas measurements take place, sequentially hosting the sample gas followed by the calibration gas. From this it follows that a single measurement of an ice core sample in fact encompasses four individual measurements with the LI-COR:

1. Zero measurement

2. Sample gas measurement

3. Calibration gas measurement

4. Zero measurement

The “zero" background signal is in fact an interpolation between steps 1 and 4, as the baseline of the LI-COR slowly drifts throughout a day. The last “zero measurement" serves as the first “zero measurement" for the next sample. Having the calibration gas measured after the sample gas allows for the bellow to adjust the pressure of calibration gas as closely as possible to the previously logged pressure of the sample gas. A mathematical treatment of how the CO_2 raw concentration is calculated can be found in Siegrist (2011).

The compact design of the LI-COR was also a very welcomed plus, as the CIM was initially designed to be assembled for field measurements. While the latter never materialized, it helped to reduce the overall apparatus size in the lab.

Another helpful feature of the LI-COR is its easy maintenance without requiring factory recalibration. The nickel-plated optical cells can be removed and cleaned simply with compressed air, while the desiccant bottles can be readily exchanged by the user. In 2016 the tungsten filament was replaced and it should last 5–10 years according to the manufacturer.

Temperature fluctuations are the main responsible for fast oscillations of the background signal. To circumvent this issue, the LI-COR is located inside an insulating boxed and maintained at 26.5 °C with a Peltier thermoelectric sensor and a JUMO cTRON controller. After opening the box, reaching stable temperature conditions ($\pm$ 0.05 °C) takes at least two days. Stabilization of the LI-COR background signal after turning it on takes 1–2 weeks. This should be taken into account when planning measurement campaigns.

2.3.4 The standard gas unit

The CIM has three standard gas tanks (see Figure 2.2). Tank I is usually reserved for standard gas with a concentration of 254.50 ppm (SIO254), tank II for standard gas with a CO_2 concentration of 285.02 ppm (SIO285) and tank III is currently not in use. The tanks are made of uncoated stainless steel.

The standard procedure for refilling the tanks was implemented by CNA and suggests refilling with a final pressure of 1.0–1.1 bar. This setting usually allows an EK sample to return a pressure in the bellow ($p@Vmax$) in the range 0.9–1.0 mbar, which is close to what is released from an 8 g ice core sample. In this way, there is increased confidence that the EK sample is replicating the ice core sample extraction process to the best of our abilities. However, refilling the standard tanks with just 1.0–1.1 bar means that after 5–7 measurement days the tanks need to be refilled again. This is a time-consuming procedure that lasts 24h. Preliminary tests were carried out comparing the results of EK samples from high-pressurized (>2 bar) and low-pressurized tanks (<0.5 bar), with unclear results. These

tests were done separately by CNA and me, had different system conditions and both lacked a large enough number of EK samples. This experiment should definitely be repeated in the future, perhaps expanding the refill pressure range to 3–4 bar. If a conclusion is reached that the refill pressure has no impact on CO_2 offsets, this would mean a significant decrease in this maintenance procedure and much less waste of standard gas.

2.3.5 The tubing network

The CIM uses 1/4 inch stainless steel tubing for most of its network. Most fittings and other elements follow the Imperial System, but some specific applications are in the Metric System. It is thus necessary to identify the difference correctly and use the appropriate tools.

As the CIM was developed module by module (see Section 2.1), some dead volumes could be avoided if the whole system had to be rebuilt from scratch. Obviously this a major undertaking for a minimal gain, and under the motto *"Never change a running system"* only small changes have been implemented in 2019, while renovating the lab.

It is important to note that the tubing length as shown in Figure 2.2 does not match its true size. Pumping efficiencies can thus be very different from the expectations of the operator according to different chosen pathways.

2.3.6 The vacuum units

2.3.6.1 The turbomolecular pumps

Turbomolecular pumps (TMP) are used in the CIM to achieve high vacuum conditions. The CIM uses two TMPs: one for the LI-COR and another for the CIM extraction head. The TMPs used are combined pumping stations that include both a diaphragm backing pump and the TMP itself (HiCube 80 Classic, Pfeiffer Vacuum®). The only difference between the CIM TMP (PM S22 250 00) and the LI-COR TMP (PM S22 310 00) is that the latter has an additional fore-vacuum safety valve that prevents back-flushing in case of a power outage. Both have a final vacuum pressure of $<1 \times 10^{-8}$ mbar.

The semi-automatic characteristic of the measurement routine prevents the operator from erroneously exposing the TMPs to high pressures. However, during non-measurement tasks when the valve control is fully manual there is the risk of flooding the TMPs. The most common mistake is to expose the TMPs to high pressure N_2, instead of first achieving a fore vacuum with the roughing ACP pump. These events cause an immediate shutdown of the TMP and decrease their lifetime. Under dry conditions, the ACP is capable to pump an atmosphere of N_2 at 2 bar (overpressure) inside the CIM and reach pressures in the order of 1×10^{-5} mbar in approximately 30–60 s. Only then can the switch to the TMP take place safely. As an upper limit, one should avoid pumping with the TMP on pressures higher than 1×10^{-4} mbar, switching to the ACP instead.

The pressure gauge used for the LI-COR TMP is a cold-cathode transmitter (IKR 251, PTR25500, Pfeiffer Vacuum®), capable of reading pressures down to 2×10^{-8} mbar. The pressure gauge for the CIM is a more sophisticated dual Pirani/cold cathode (PKR 251, PTR26001, Pfeiffer Vacuum®) that has a minimum range of 5×10^{-9} mbar. Both gauges have the benefit of easy maintenance which is characteristic of cold-cathode transmitters. Every other year the gauges should be cleaned, which involves gently scrubbing the inner walls of the gauge.

Even though the gauges are full-range (i.e. they are suitable for pressures ranging from vacuum to atmosphere) and corrosion resistant, it is good practice to shut them off before bringing them to atmosphere. Likewise, they should be only turned on after reaching a vacuum range of at least 1×10^{-3} mbar.

I recommend staying with the standard mode of operation of the TMPs (1500 Hz) and referring to the manual in case of doubt. It should be nonetheless mentioned that the standby mode (1000 Hz) can also be used when no measurements are taking place but it is inconvenient to shut down the system entirely, such as during holidays. This helps to extend the lifetime of the device and save energy.

2.3.6.2 The ACP roughing pump

The air cooled multi-stage roots pump (ACP; model ACP 15 from Pfeiffer Vacuum®) is a roughing pump that does not have any oil and thus offers a much smaller degree of contamination. It also has virtually no maintenance, although care must be taken with respect to water vapor. The pump is meant to work under dry conditions, but the nature of the CIM means that inevitably some water will be taken up by the ACP as the cold traps in the CIM are not 100% efficient. Special care must be taken to avoid the ACP to pump on the nearby cold trap at the end of a measurement day (see also Section 2.3.7.2). This occurs when the cold trap loses its cooling liquid nitrogen (LN_2). If it is suspected that the ACP pumped an unusually high amount of water vapor, then the gas ballast must be opened for 10 minutes while in running mode to remove the water.

2.3.6.3 The magnetic coupled oil pump

The magnetic coupled oil pump (Duo 10 M, Pfeiffer Vacuum®) is a roughing pump used to create vacuum inside the Plexiglas box where the bellow is placed. Without the vacuum the bellow cannot be used for measurements. This pump has minimal maintenance and replaces the previous oil pump that did not work reliably. The magnetic coupling feature of the pumps axes avoids oil leakage and frequent malfunctioning issues. The operator only needs to check the oil level regularly.

When shutting down the system, it is wise to avoid back-flushing from the pump towards the bellow. For that matter, the pump must be opened very briefly at its inlet and only afterwards shut down. This manual operation needs to be quick (less than a second, ideally),

to avoid the pump being exposed to room atmosphere for too long. Note also that the outlet of the pump is connected to an outgoing fume line, as the exhaust gases can be toxic.

In case of a power outage, an electro-pneumatic angle valve (AVC 016 PA, Pfeiffer Vacuum®) prevents the flushing of the bellow and keeps the current vacuum level. Leakage through the Plexiglas casing will nevertheless cause the vacuum to be lost and inflict permanent damage to the bellow connector. The pump must therefore be running at all times, except if the bellow is safely brought to room pressure on both sides (see Section A.4.2). Moreover, an overcurrent circuit breaker has been installed that blocks feeding currents over 5 A from reaching the pump. In the past, some pumps failed to restart when power was turned back on after a power outage. This led to an initial very high current that caused the pumps to ignite and cause severe fire damage.

2.3.7 The cooling system

The cooling system of the CIM has significant room for improvement when designing a new extraction system. The ethanol tubing network that cools the CIM overnight to −23 °C is not uniformly distributed, nor is the disposition of the liquid nitrogen (LN_2) spitters that cool the system during measurements (see Section 2.3.7.3). Both lead to temperature gradients that could be slightly biasing the measured CO_2 concentrations (see Section 3.1.3).

2.3.7.1 The LAUDA thermostat

The LAUDA (Proline 845) is the main thermostat of the CIM, allowing the extraction head to be cooled down to −23 °C. It uses a mixture of ethanol (94%) and isopropanol (5%) as the cooling agent, in an 8 liter bath. It can cool from room temperature to −23 °C in just 20 minutes and can achieve a minimum temperature of −45 °C. While it is convenient that the LAUDA can cool so quickly, there is an inevitable gain of heat by the cooling agent while traversing the pipeline connecting the LAUDA and the CIM. This makes the applicable cooling rates for the CIM much more gentle. For example, while in measurement mode, the LAUDA is usually set to −34 °C in order for the CIM to reach −23 °C, which is a very significant gradient. A traditional setting is to set the LAUDA to cool down from room temperature to −34 °C from 5:00 PM the day before until 03:00 AM of the following day, and then stay at −34 °C. This setting allows the CIM to gently cool and reach −23 °C by 08:00 AM, with a cooling rate of $\sim 3\,^{\circ}\mathrm{C\,h^{-1}}$. It is very important that one applies the slowest possible cooling/warming rates to the CIM. Failure to do so in the past has led to full breakdown of the magnetic bearings. Huge thermal stress can lead to structural micro cracks, which eventually grow. It can also lead to small displacements of the copper coils in the magnetic bearings. If this happens, the generated magnetic field will change, causing the rotor to rotate around a modified center of mass and eventually crashing against the glass encasements. This is an error that has happened in the past and must be carefully avoided.

The LAUDA circulates the cold ethanol in a closed pipeline circuit that enters the CIM through the right side. From here, the tubing goes to the front side where it twists and turns on a single plane before returning to the LAUDA. This cooling distribution is far from optimal. Ideally, the cooling of the cubic box should happen homogeneously on all surfaces, with the tubing being distributed in the front, back, top, bottom, left and right sides. If practical constrains allow only one surface to be covered by the tubing, then this should be the top surface, from where the cooling is more effective. It would be unpractical to reshape the CIM cooling tubing at this point, especially since temperature-related effects seem to be small (see Section 3.1.3). Nevertheless, this should be kept in mind when designing a new system.

2.3.7.2 The cold traps

The CIM as a whole has three cold traps which freeze water vapor from the moist air from the extraction (see Figure 2.2). The first and most important cold trap is K2, placed immediately at the outlet of the CIM after valve V10 and set to −85 °C. Its main function is to dry the sample gas, while its positioning ensures that the extracted gas travels the least distance possible with the presence of water. This is a critical aspect because water vapor favors the transport of CO_2, which fractionates the gas with length (Stauffer and Oeschger, 1985; Bereiter et al., 2013). The second cold trap (K3) is placed between the pumps and the CIM and acts as a shield, in order for water not to be discharged into the sensitive pumps. A third cold trap (not shown) is placed immediately next to the ACP. It is immersed in a very large LN_2 dewar, to guarantee that the system can be safely pumped overnight and be ready for measurements in the next day

2.3.7.3 The LN_2 spitters

The spitters are flexible PE tubes that allow liquid nitrogen to be sprinkled inside the CIM insulating box in order to keep the CIM cold. The idea and the design are described in Schmitt (2006) and Schmitt et al. (2011). The spitters feed on an LN_2-filled dewar and their spitting ends are distributed inside the box. Once the atmospheric temperature inside the box goes above −27 °C, a small current passes through a resistor dipped in the LN. The current makes the resistor warm and heat the nearby LN_2, which expands through the tubes. Given the non-centered placement of the dewar and overall space constraints, it is very difficult to maintain a homogeneous distribution of the spitters. In addition, every time the CIM is opened and the dewar removed, the positioning of the spitters needs to be reset, with inevitable non-reproducibility.

2.3.7.4 The insulating box

The insulating box around the CIM extraction head is made of connecting boards of extruded polystyrene (XPS). The multiple inlets and outlets required multiple opening cuts and the adding of many sealing strips. Some heat leak points are inevitable, with the ones near the bottom of the box being the most significant for thermal control. There is definitively room for improvement regarding the unnecessarily big air gap between the funnel and the XPS lower panel, although a design improvement has not been pursued so far, mostly because the impact of temperature fluctuations had not yet been assessed (see Section 3.1.3).

To ensure reproducible conditions attention must be paid to the way the box is assembled prior to any day of measurements. Usual mistakes include uneven screwing of the front and upper panel, non-tight attachment of the upper and lower lid and forgetting to turn on the fans.

2.3.8 The LabVIEW program

The LabVIEW code that supports the CIM was an incremental effort from two Master students, one PhD student and one experienced technician. As it was not built all at once with a clear plan, the code has a series of imperfections, leading to routines that do not always run at the same expected time, or to sudden mysterious errors that make the measurement loop inexplicably crash. I recommend against changes to any VI unless the operator is very comfortable with LabVIEW.

2.3.8.1 Steuerung2.vi

Steuerung2.vi is the main interface for routine measurements with the CIM (see Figure 2.12). While the measurement routine is described step-by-step in Section A.2.3, here I review some of the most important controllers and indicators in the VI.

- **Super Early Hobeln / Early Hobeln / Late Hobeln**
  The “Super Early Hobeln" is the default measurement mode of the CIM. Only measurements performed this way are comparable with each other and overall valid. Experimenting with the other modes should not be attempted without first reading the documentation in Nehrbass-Ahles (2017).

  The difference between the three cases of shaving (*Hobeln*) is the inclusion of a waiting time after the extraction takes place. While bubbles burst immediately during the shaving process, smaller clathrates among the shaved ice will relax and open after a few minutes. This effect was noticed first with the Needle Cracker by Anklin (1994) and a waiting routine was introduced later on by (Siegenthaler, 2006). As for the CIM, the Super Early Hobeln allocates 5 minutes of waiting time, the Early Hobeln waits only 1 minute and the Late Hobeln does not include a waiting time at all. The inclusion

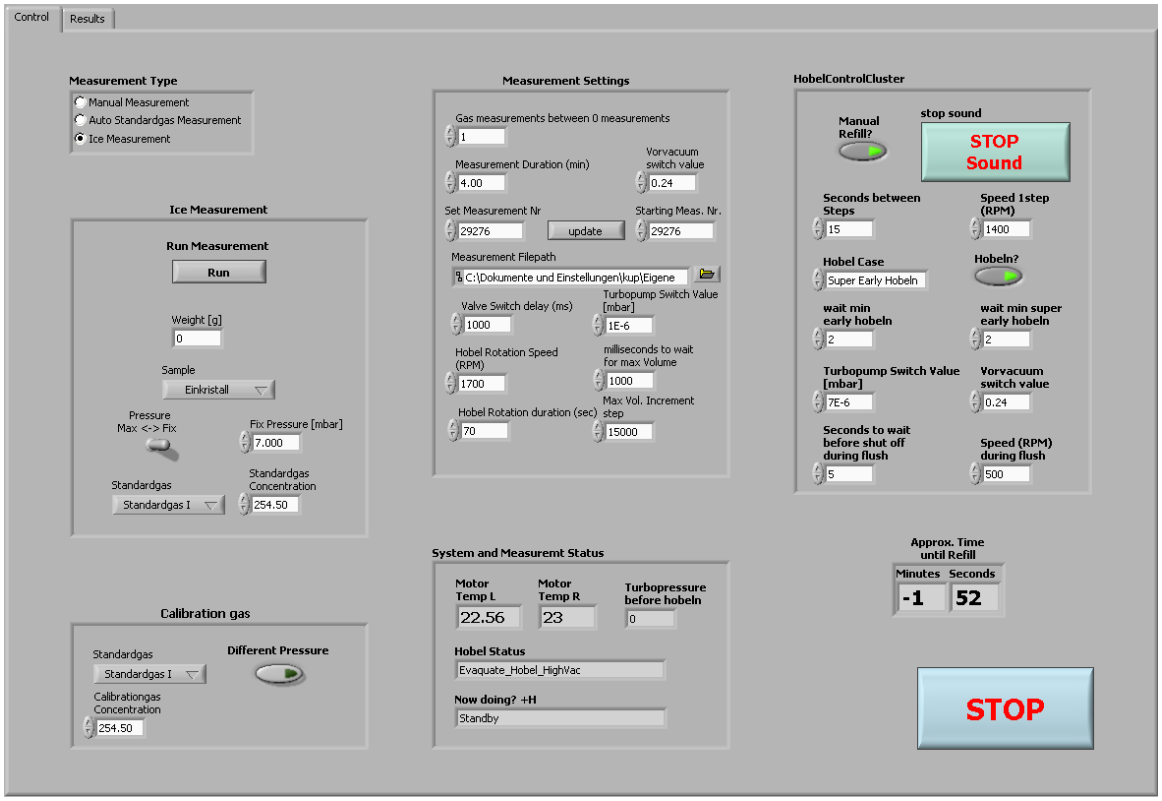

Figure 2.12: User interface of Steuerung2.vi.

of the waiting time makes the vacuum pumping time shorter, but still sufficient (see Section 3.1.2).

- **Measurement time**
  The parameter "measurement time" refers to the integration time of the LI-COR and is set to four minutes, following the recommendation on Siegrist (2011). The four minutes represent a compromise between allowing the gas analyzer to reach a precision of less than 1 ppm while leaving enough time for evacuation of the supply tubing. Experimenting with this setting needs to be carefully done, as it will change the sensitivity of the CO_2 measurement. It may also influence the timing of other processes running in parallel.

- ***Vorvacuum* switch value**
  This sets the pressure threshold at which the system stops pumping with the ACP roughing pump and starts pumping with the TMP. At the start of a measurement day, the baseline level of the ACP can oscillate in the range 0.20–0.30 mbar. Historically, CNA would adjust the *Vorvacuum* parameter just a little higher than the observed baseline (e.g., 0.25 *Vorvacuum* for a baseline of 0.21 mbar). If the *Vorvacuum* pressure value is not eventually reached when pumping with the ACP, then the switch to the TMP will not happen. Samples have been wasted due to this reason, mostly because the default value of 0.24 mbar was not updated at the beginning of the day. It may also happen that the lack of LN_2 in one of the cold traps leads to a water vapor flow that inhibits the ACP reaching the desired *Vorvacuum* pressure. I decided to set the *Vorvacuum* at 0.30 mbar and had no problems ever since.

- **Magnetic bearing temperature (left/right)**
  Both temperatures should stabilize around -22 or $-23\,^{\circ}C$ by the middle of a measurement day. However, if they start drifting too much and/or a gradient of more than $2\,^{\circ}C$ develops between the left and right bearing, this could be a sign of poor distribution of the LN spitters, lack of LN_2 inside the CIM dewar or some issue with the Jumo thermostat that controls the temperature threshold for the LN_2 spitters.

- **Set measurement number + Update**
  The starting measurement number should be set to the next following integer before starting the measurements. This prevents the system from using the last zero value as a reference, and instead calibrates the measurement according to the new zero measurement.

  The option “Set measurement number" and the “Update" button allow the user to see the corresponding range of measurements in the "Results" tab. However, for unknown reasons this sometimes disturbs the measurement loop. Strange errors have occurred toward the end of the day when this option was used. I recommend only updating

the values after the measurements have stopped, but while the Steuerung2.vi is still running.

2.3.8.2 ManualValveControl.vi

This subVI allows the user to actuate valves using the LabVIEW interface. A mechanical switch must be turned on in the back of the main valve board in order for the subVI to work. This same switch disables the manual handling of the valves, meaning that at any time the valves are controlled either manually or through the VI, but never simultaneously.

A recurrent mistake is to try to activate the valves in the mechanical board while the subVI is running. It will not produce any result as the valves will not respond. However, as soon as the switch is triggered back, the valves will assume any configuration that the user may have naïvely changed, which may lead to disaster. Therefore, it is important to keep in mind the configuration of the board at all times and always act carefully.

2.3.8.3 Pressure log

The pressure log allows the monitoring of pressure at four pressure gauges: TMP LICOR (CH1), ACP (CH2), Bellow (CH3) and TMP CIM (CH4). In 2020, I rediscovered this subVI which conveniently lets the user log the vacuum pumping phase as felt near the CIM TMP. The simultaneous pressure in the CIM was found to be approximately 3–4 orders of magnitude higher, in the order of 10^{-4} to 10^{-3} mbar, under dry conditions (Nehrbass-Ahles (2017), Chapter 2, pp.26–27). More importantly, the pressure logged immediately upstream of the CIM TMP is proportional to the pressure inside the CIM during the pumping phase.

Observing the rate of pressure drop now allows to assess whether a leak is currently hampering the final vacuum *(pBeforeHobeln)*, or if degassing events are taking place (see Section 3.1.2). It also lets one more accurately determine long-term evolution of vacuum conditions over night (between measurement days), or for several days under dry conditions.

2.3.8.4 FaltenbalgManualMove.vi

The FaltenbalgManualMove.vi is a useful tool for manipulating the bellow. In some complicated procedures, such as exchanging the connector, this subVI can help to test the correct functioning of the bellow. It can also help to assess if a connector has sustained damage by rapidly testing it.

2.4 Auxiliary equipment

2.4.1 The N_2 line

A gas cabinet is now available in the new CO_2 lab. It can store up to four 50 liter gas flasks, with two of them connected simultaneously to the N_2 line. It allows for the reserve flask to

automatically feed the N_2 line when the active flask is depleted, maintaining a steady gas flow. This is a significant improvement over the single standing N_2 flask that was used until recently. Having a single flask meant replacing it in-between measurements as soon as its levels became low. This procedure was not only a safety hazard but also prone to induce mistakes while measuring. It also meant a waste of leftover gas in the bottle that is now avoidable. The gas cabinet is sealed and has an exhaust system that vents any potentially harmful leak. It is also rated for fire protection up to 90 minutes.

Changing the gas cylinders in the cabinet can now be done safely while not measuring. The procedure can be found in a protocol near the gas cabinet. Special attention must be paid to open all necessary valves to the maximum, regardless on whether the green stripe is already visible. Failure to do so has led to poor N_2 flow and failed measurements.

From the point of view of measurement quality, the new N_2 line is an important asset as it maintains the pressure of the purge gas constant. Previously, the progressive drawdown of N_2 from the main flask meant that the preset 2 bar (overpressure) would slowly drift to lower values, forcing the operator to constantly reset the regulator back to 2 bar, with the associated uncertainty that comes with a manual single-step regulator and an analog reading. The purge gas pressure has an influence on the vacuum quality and residual N_2 impacts CO_2 offsets through sample dilution (see Section 3.1.2). In hindsight, introducing a two-step regulator[v] in the N_2 flask would have eliminated the drifting 2 bar issue, but objectively these fluctuations are not likely to have impacted the quality of measurements in a detectable way.

2.4.2 The valves

Previously used dry-extraction devices at KUP relied on manual bellow-sealed valves exclusively. Though reliable, manually operating the many valves while measuring with the Needle Cracker, for instance, was not only exhausting but also prone to mistakes and user bias. In an effort to automate the system, Bereiter (2012) introduced pneumatic-actuated diaphragm-sealed valves as an alternative (6LVV-DPS6M, Swagelok®). These are considerably less expensive than the pneumatic-actuated version of the previous manual valves, while also needing less space. Rather than a full-metal connection, the diaphragm-sealed valves use a polychlorotrifluoroethylene (PCTFE) gasket. PCTFE is an inert polymer, but given the CO_2 adsorption/desorption effects on stainless steel surfaces reported by Zumbrunn et al. (1982), it was critical to know if these phenomena would also apply to this new material. Tests performed at the time indicated no influence of these valves on CO_2 concentrations, but it is important to stress that they were done with the Needle Cracker, as the CIM had not yet been developed fully (see Bereiter (2012), Annex). Extensive usage of the CIM until the present day seems nonetheless to agree that the valves are harmless,

[v] A two-step regulator keeps a constant outgoing pressure at the outlet regardless of the absolute pressure inside the flask. They are also significantly more expensive than single-step regulators.

but it cannot be excluded that an effect is happening below the detection limit.

Despite the 20 PCTFE valves distributed in the CIM, there are still some manual bellow-sealed valves for non-routine procedures (SS-6H-MM, Swagelok®). The CIM also has two special pneumatic-actuated bellow-sealed valves which seal the gas standard tanks I and II (MS-4B-5C, Swagelok®). The full-metal contact is made of alloy 400 instead of stainless steel, which increases corrosion resistance. The very robust actuators also offer increased lifetime.

All valves are prone to failure, but special attention should be paid to the outgoing valves from the CIM (V10 and V14) which are heavily used and subject to the biggest air flows. Other critical valves include the trio V20/21/22 which switch between the roughing ACP pump and the high vacuum TMP pump. These are also heavily used and likely undergo the biggest pressure gradients. When malfunctioning, small back-flushing peaks can be seen in the monitored pressure when the valves are actuated.

As important as the main valves themselves are the FESTO® solenoid valves that actuate the main valves with air pressure. These are warranted by FESTO® for one year only, which is a very short time. Most controllers end up lasting several years, but nevertheless they require a frequent weekly check. As they age, controllers become leaky and the valves may not be receiving the necessary air pressure to be opened. Note that the electronic valve board will still light up when the controller is activated even if there is a malfunction, which can lead to mistakes.

2.4.3 The UPS

An uninterruptible power supply (UPS) is a device that offers protection against power surges and power outages. The UPS is plugged to the power outlet, while the devices that require protection are connected to the UPS. During a power surge, a higher than expected voltage is inflicted to any device plugged to the power outlet, potentially damaging them. The UPS blocks any fluctuations in the nominal voltage and maintains a steady supply of power. During a power outage, the battery in the UPS can provide power for approximately ten minutes at maximum capacity. Fortunately, most non-planned power outages experienced at KUP are very short-lived.

The CIM uses two UPS (APC Smart-UPS RT, 2000W). The first supports the PC and the magnetic bearings while the second is connected to everything else except the vacuum pumps. This setting keeps both UPS with a low load, meaning that they can provide power for much longer than the rated 10 minutes in case of a power outage. While theoretically the UPS could also power the magnetic coupled oil pump, the high power consumption of the latter (0.45 kW) would diminish the battery time of the UPS in detriment of all other components of the CIM.

The problem with a power outage is therefore failure of the vacuum pumps. The TMPs will slowly bring back the CIM to atmospheric pressure which, albeit inconvenient, is in itself

not harmful. In any case, it is possible to conserve some degree of vacuum and avoid complete contamination by quickly closing all valves at the main air pressure supply. The main issue if power fails is the immediate shutdown of the magnetic coupled oil pump that keeps the bellow at vacuum (see Section 2.3.6.3). In this case the vacuum will be progressively lost, compressing the bellow and irreversibly damaging the connector (see Section 2.3.2). It is unknown how much time needs to elapse before the connector undergoes permanent damage, but I estimate that one has at least a 15 minutes time window to turn on again the vacuum pump after a power outage. This time is imposed by the leak rate through the Plexiglas casing, which has never been quantified.

2.4.4 The computer

The CIM computer is an outdated equipment more than ten years old, still running Windows XP. The LabVIEW cards that control the CIM are just as old and very difficult to replace in case of failure. One major hurdle in developing a novel extraction system will be in salvaging and transferring the existing LabVIEW VIs to work on more recent equipment. The computer is connected to the KUP network but it is not connected to the internet, as updates to the operating system have been feared as potentially harmful to the CIM. Throughout this PhD there were plans to transfer everything to a new PC, but after realizing the size of the task and the forthcoming development of a new extraction system it was deemed not worth the time investment. Due to the potentially unexpected failure of the hard drive of the PC, frequent data backups are strongly recommended.

References

Anklin, M. (1994). *Kohlenstoffdioxid Bestimmungen in Luftproben aus einem neuen Tiefbohrkern von Summit (Grönland).* PhD thesis, University of Bern.

Bereiter, B. (2007). Test und Adaption eines kommerziellen IR-Absorptionsanalysegerätes für CO_2-Messungen an polaren Eisbohrkernen. Master's thesis, University of Bern.

Bereiter, B. (2012). *Atmospheric CO_2 reconstruction using polar ice cores: Development of a new dry extraction device and insights from highly resolved records.* PhD thesis, University of Bern.

Bereiter, B., Lüthi, D., Siegrist, M., Schüpbach, S., Stocker, T. F., and Fischer, H. (2012). Mode change of millennial CO_2 variability during the last glacial cycle associated with a bipolar marine carbon seesaw. *Proceedings of the National Academy of Sciences*, 109(25):9755–9760.

Bereiter, B., Stocker, T. F., and Fischer, H. (2013). A centrifugal ice microtome for measurements of atmospheric CO_2 on air trapped in polar ice cores. *Atmospheric Measurement Techniques*, 6(2):251–262.

Delmas, R. J., Ascencio, J. M., and Legrand, M. (1980). Polar ice evidence that atmospheric CO_2 20,000 yr BP was 50% of present. *Nature*, 284.

Etheridge, D. M., Pearman, G. I., and de Silva, F. (1988). Atmospheric trace-gas variations as revealed by air trapped in an ice core from Law Dome, Antarctica. *Annals of Glaciology*, 10:28–33.

Gay, A. (2012). Trace gases in ice cores : Diffusion model for noble gases and methane and CO2 measurements on Antarctic ice. Master's thesis, University of Bern.

Indermühle, A., Stocker, T. F., Joos, F., Fischer, H., Smith, H. J., Wahlen, M., Deck, B., Mastroianni, D., Tschumi, J., Blunier, T., Meyer, R., and Stauffer, B. (1999). Holocene carbon-cycle dynamics based on co$_2$ trapped in ice at Taylor Dome, Antarctica. *Nature*, 398(6723):121–126.

LI-COR Biosciences (2007). LI-7000 CO_2/H_2O Analyzer Instruction Manual. Technical report.

Lüthi, D., Le Floch, M., Bereiter, B., Blunier, T., Barnola, J.-M., Siegenthaler, U., Raynaud, D., Jouzel, J., Fischer, H., Kawamura, K., and Stocker, T. F. (2008). High-resolution carbon dioxide concentration record 650,000–800,000 years before present. *Nature*, 453(7193):379–382.

Lüthi, D. (2006). Entwicklung einer neuen Extraktionsmethode und CO_2-Konzentrationsmessungen an polaren Eisbohrkernen. Master's thesis, University of Bern.

Monnin, E. (2000). CO_2 Konzentrationsmessungen an polaren Eisbohrkernen, insbesondere Dome Concordia, Antarktis. Master's thesis, University of Bern.

Monnin, E., Indermühle, A., Dällenbach, A., Flückiger, J., Stauffer, B., Stocker, T. F., Raynaud, D., and Barnola, J.-M. (2001). Atmospheric CO_2 Concentrations over the Last Glacial Termination. *Science*, 291(5501):112–114.

Neftel, A., Oeschger, H., Schwander, J., Stauffer, B., and Zumbrunn, R. (1982). Ice core sample measurements give atmospheric CO_2 content during the past 40,000 yr. *Nature*, 295(5846):220–223.

Neftel, A., Oeschger, H., Staffelbach, T., and Stauffer, B. (1988). CO_2 record in the Byrd ice core 50,000–5,000 years BP. *Nature*, 331(6157):609–611.

Nehrbass-Ahles, C. (2017). *Millenial-scale atmospheric CO_2 reconstructions using multiple Antarctic ice cores*. PhD thesis, University of Bern.

Schmitt, J. (2006). *A sublimation technique for high-precision $\delta^{13}C$ on CO_2 and CO_2 mixing ratio from air trapped in deep ice cores*. PhD thesis, University of Bremen.

Schmitt, J., Schneider, R., and Fischer, H. (2011). A sublimation technique for high-precision measurements of δ^{13}co$_2$ and mixing ratios of co$_2$ and n$_2$o from air trapped in ice cores. *Atmospheric Measurement Techniques*, 4(7):1445–1461.

Siegenthaler, U. (2006). *Atmosphärische CO_2-Konzentration der letzten 650'000 Jahre anhand von Messungen an Antarktischen Eisbohrkernen*. PhD thesis, University of Bern.

Siegenthaler, U., Stocker, T. F., Monnin, E., Lüthi, D., Schwander, J., Stauffer, B., Raynaud, D., Barnola, J., Fischer, H., Masson-Delmotte, V., and Jouzel, J. (2005). Stable carbon cycle - climate relationship during the late Pleistocene. *Science*, 310(5752):1313–1317.

Siegrist, M. (2011). Entwicklung einer automatisierten Messanlage für CO_2 Messungen an polaren Eisbohrkernen. Master's thesis, University of Bern.

Stauffer, B. and Oeschger, H. (1985). Gaseous components in the atmosphere and the historic record revealed by ice cores. *Annals of Glaciology*, 7:54–59.

Winkler, R. (2009). Entwicklung eines Standardgas-Dosiersystems zur teilweisen Automatisierung des CO_2-Messverfahrens an antarktischen Eisbohrkernen. Master's thesis, University of Bern.

Zumbrunn, R., Neftel, A., and Oeschger, H. (1982). CO_2 measurements on 1-cm^3 ice samples with an IR laserspectrometer (IRLS) combined with a new dry extraction device. *Earth and Planetary Science Letters*, 60(2):318–324.

Chapter 3

New measurement techniques & experiments

3.1 Exploring sources of error

In the course of a measurement day there are many issues that can occur unexpectedly. Some of them interfere with the quality of the measurements, others represent logistical hurdles and a few have not yet been fully understood to assess their impact. In this section, I compile a series of experiments that were designed to better understand processes that could induce error in the CO_2 measurements. The experiments reflect my gradual understanding of the limitations of the CIM and the search for improved experimental setups and methods.

3.1.1 Role of the surface roughness

- The role of sample surface roughness on possible measurement offsets was studied.
- Two sets of gas-free ice samples were separately prepared with different surface roughness: one set was cut with a saw-blade, while the other was fashioned by hand with a shaving blade.
- Results were statistically inconclusive due to the small sample number and the experiment needs to be repeated.

During sample preparation, it is customary to hold the sample with the gloves as little time as possible in order not to heat it. This means that the procedure focuses on a quick shave of the initial 10–12 g sample until reaching about 8 g, while fashioning a spherical shape as much as possible. In this process, not all of the initial cubic surfaces are necessarily shaved, with some maintaining the sub-millimeter raw roughness imprinted previously by the saw-blade, while others have the smoother roughness from the final manual shaving.

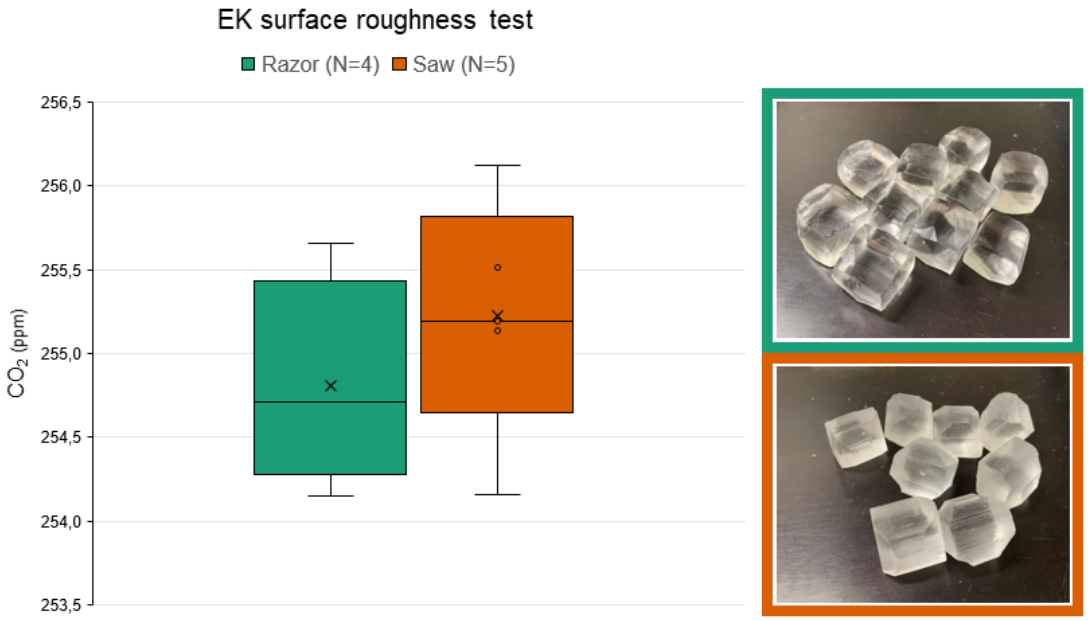

Figure 3.1: Effect of surface roughness on EK samples. Left: Box and whiskers plots of CO_2 concentrations of EK samples mixed with standard gas SIO254 (with a CO_2 concentration of 254.5 ppm) for two sets of EK samples with different surface roughness. Samples for the EK roughness test. Top-right: samples cut with a band saw and afterwards hand shaved with a shaving blade (smooth). Bottom-right: samples cut with a band saw only (rough).

It has been shown that CO_2 adsorbs to amorphous ice surfaces with efficient trapping in the temperature range 100–160 K, while the same effect does not apply for crystalline ice (Andersson et al., 2004). Based on this information, the adsorption of ambient air to freshly cut samples during the time between their preparation and their measurement should not play an important role in terms of contamination. Furthermore, increasing temperature lowers the activation energy required in the adsorption/desorption process, making it even less likely that at 250 K there could be CO_2 adsorbed to the sample surface. Even if there are contaminants adsorbed to the sample surface, they are likely to be pumped away during the evacuation stage, as the ice surface sublimates.

Despite all this, I designed a small experiment with gas-free ice (*Einkristall* – EK) samples of varying roughness to investigate the impact of sample surface roughness in the sub-millimeter range during the preparation stage (see the right side of Figure 3.1). In a first set of samples only a band saw was used, giving the samples the shape of a truncated cube. In a second set, the samples were first cut with a band saw and afterwards shaved by hand with a shaving blade on all surfaces, giving them a more spherical-like shape. Due to technical difficulties only nine out of twenty samples could be measured with sufficient quality. The results in Figure 3.1 (left) do not allow for a definitive conclusion and it would be interesting to repeat the experiment in the future.

Each sample is subject to a 2 bar flow of N_2 just before being loaded in the CIM. This flushing prevents ambient air to breach the CIM and helps to clean the sample before it is placed in the sample holder. Given this added precaution, I would not expect surface

roughness to offset the measurement by a discernible amount. If, however, there is such an effect, then I would expect the rougher band saw cut to provide more contact points which CO_2 molecules can adsorb to, and thus provoke more contamination. A rougher surface will also make it harder for any adsorbed gas to be pumped away during vacuum pumping given the higher surface-energy bonding.

3.1.2 Vacuum quality before extraction and leak tightness

- Efforts to better tighten the CIM have led to an increase of vacuum pumping efficiency in dry conditions (half-life $\tau_{1/2}$ from 20 to 10 days in the pressure range 10^{-6}–10^{-8} mbar, measured directly upstream of the TMP).
- Logging of pressure during the evacuation stage now allows to understand different sources affecting the vacuum quality before extraction, namely leaks, degassing events, total evacuation time and the presence of leftover N_2.
- A significant link between vacuum quality before extraction and CO_2 offsets has been found, but the overall spread is too high to risk introducing a correction function.

At first instance, it is the overall tightness of the CIM that constrains the vacuum conditions in measurement mode. The tightness of the system is best assessed by logging the pressure at room temperature and under dry conditions for several weeks. Left alone, the turbomolecular pump (TMP) will gradually impose a better vacuum through an exponential decay of the pressure inside the CIM. Figure 3.2 shows various recorded runs in chronological order throughout the duration of the PhD. The logged pressure immediately upstream from the TMP is proportional to the pressure inside the CIM. My ability to properly tighten the CIM increased over time, with vacuum “half-life" decreasing roughly by 50%, from 20 to 10 days. This applies only when the molecular flow regime is reached and the pressure logged upstream of the TMP enters the range 10^{-6}–10^{-8} mbar. The improvement came from a growing knowledge regarding where leaks typically develop and which screws to preferentially tighten. Specifically, I discovered that the M6 screws that compress the upper and lower gold CF seals tend to get loose over time, likely due to long-term relaxation from thermal cycles. Before any measurement campaign it is best practice to tighten these screws with 8 N m of torque and perform a comprehensive leak test.

Figure 3.2 does not show the system achieving a steady state pressure even after two months of pumping. This means that leaks cannot be the only source of gas molecules and that likely the there is a continuous desorption from the inner stainless steel walls that simply takes very long to get rid of.

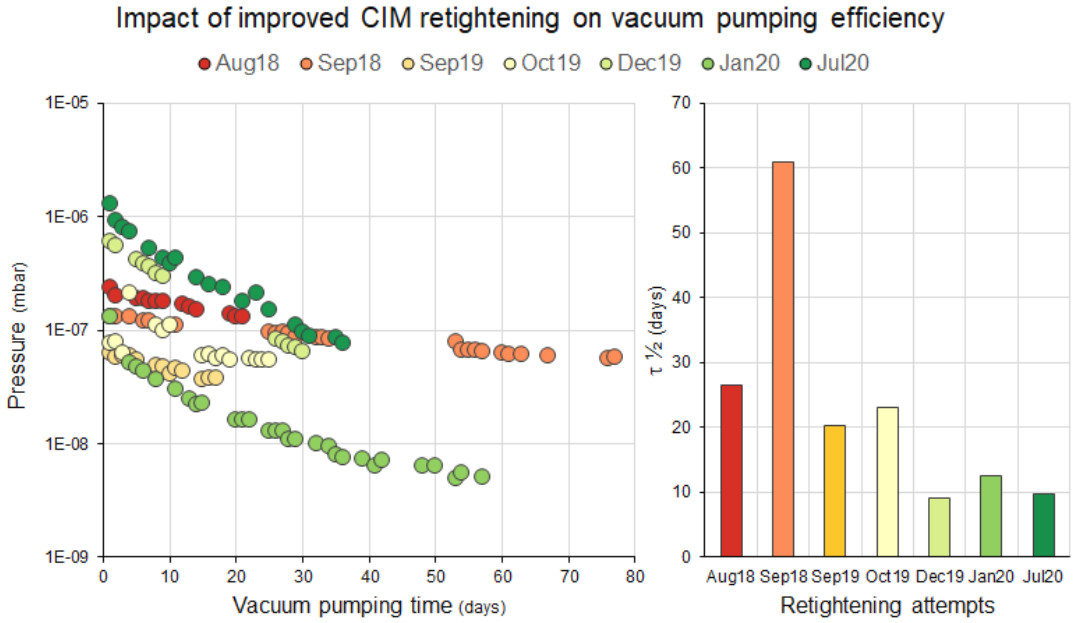

Figure 3.2: Evolution of CIM tightness in the period 2018–20. Left: logged pressure directly upstream of the TMP as a proportional indicator of vacuum conditions inside the CIM. Right: Estimated half-life of vacuum pressure for various runs. Notice the left-right chronological order and the red-green coloring to indicate a positive evolution in tightening.

Keeping track of the evolution of the pressure *pBeforeHobeln* of different samples is a quick way to evaluate the quality of vacuum conditions throughout a measurement day. This pressure reading is taken at the end of the evacuation phase and immediately before the extraction phase. The pressure is logged in flow mode directly upstream of the TMP and is proportional to the vacuum level inside the CIM. It can thus be viewed as an indicator of vacuum quality. As a rule of thumb, EK measurements are expected to have a *pBeforeHobeln* in the range of $1\text{–}4 \times 10^{-7}$ mbar and real ice core samples should belong to the range of $3\text{–}6 \times 10^{-7}$ mbar. Measurements falling outside these ranges need to be carefully considered on an individual basis. As a definite cutoff, all measurements with *pBeforeHobeln* higher than 1×10^{-6} mbar should be excluded. However, it is important to keep in mind that vacuum conditions tend to worsen throughout a day and also throughout consecutive days of measurements, as there is an inevitable buildup of ice within the CIM that is not easily evacuated over night. In this sense, it is wise to evaluate individually odd *pBeforeHobeln* values with respect to daily averages, or with respect to replicates, if available.

Apart from daily or weekly trends, an unexpectedly high value of *pBeforeHobeln* for a single measurement can be a symptom of many different problems. In the following subsections I review the different processes leading to a high *pBeforeHobeln* and how to interpret it.

High pBeforeHobeln as a major leak indicator

Careless tightening of the lower VCR gasket can lead to a significant leak from ambient air into the CIM and an abnormally elevated CO_2 content. These offsets can be in the order of tens of ppm and are usually easy to distinguish and label as a mistake. A severe leak can disturb the vacuum level to the extent of preventing the switch from the ACP roughing pump to the TMP, leading to an interruption of the measurement loop. Major leaks are rare and often result from a moment of distraction.

High pBeforeHobeln as the result of degassing

Small releases of air occur for real ice samples during the evacuation stage. These are manifested through small reversals in vacuum quality, corresponding to the degassing of air inclusions due to progressive sublimation of the outer ice layers and the opening of the enclosed air bubbles (see Figure 3.3). This process is so far the only explanation to the different final vacuum levels between real ice core samples and EK samples. I thus introduced the habit of logging for each sample the whole evacuation stage by using the forgotten auxiliary tool *Pressurechangerate.vi*, developed by Bernhard Bereiter (BB). This allows to subsequently evaluate if a high level of *pBeforeHobeln* was eventually due to heavy degassing, which is in itself harmless, or something else. If happening at an early stage, the extra air from the degassing event is quickly evacuated and does not have time to adsorb to the inner surfaces of the CIM. This means that the pressure curve usually has time to revert to its baseline after the excursion. If happening at a later stage, the event will lead to a high *pBeforeHobeln* that does not at all reflect the expected vacuum conditions for that particular sample.

High pBeforeHobeln as the result of short evacuation time

The sample reloading routine is a multi-stage process with little margin for error. Through repetition an operator can be trained and develop the necessary muscle memory so that the procedure can be executed with little to no conscious effort (see Subsection A.2.3). The total reloading time needs to fall within a narrow window, so as to not interfere with the measurement loop of the current and of the upcoming sample. A steady yet unhurried pace from an experienced operator leads to a reloading time between 2 min 30 s and 2 min 45 s [i].

Unfortunately, even for an experienced operator, there are a myriad of mistakes that can occur during the reloading routine as energy and patience are slowly drained throughout long measurement days. Often, small cascading mistakes are hard to avoid and the sample reloading takes longer than expected. Due to design constraints of the LabVIEW interface, a longer reloading time forcefully leaves less time for the subsequent vacuum pumping and

[i] This is the equivalent of a time of closure between 00:12:00 and 00:11:45 as per the LabVIEW virtual instrument internal countdown clock

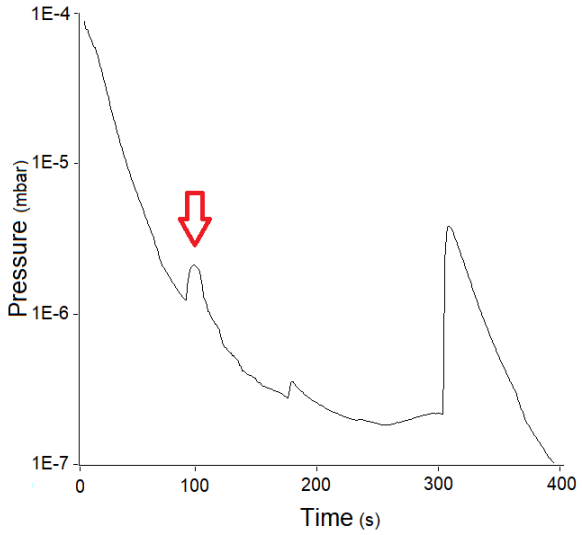

Figure 3.3: Profile of the evacuation step for an EDC ice core sample (2406.84 m depth, ca. 276.2 ka, fully clathrated, measurement number #28488), as seen from the pressure gauge immediately upstream from the TMP. The red arrow indicates a degassing event. Being an early event, the drawdown profile still managed to go back to the baseline decay level, showing that the degassing event was merely a superimposed incident on an exponential decay. The big excursion at ∼300 s indicates the end of the evacuation step and the subsequent beginning of the shaving. Note that the logged pressure is only proportional to the higher pressure inside the CIM and does not reflect real extraction vacuum conditions.

thus to a higher pressure before extraction (*pBeforeHobeln*). Therefore, after acquiring some skill as an operator I decided to enforce a reloading time of exactly 2 min 45 s in an effort to standardize conditions as much as possible. Figure 3.4 shows the influence of different reloading times on *pBeforeHobeln*. Only EK samples were considered, as ice core samples are prone to degassing. As expected, slower reloading routines lead to worse vacuum conditions. What is perhaps a bit surprising is the big scatter obtained even when strictly closing the system after 2 min 45 s, which evidences that there are other factors also contributing to the final *pBeforeHobeln*.

Enforcing a determined closure time came with some difficulties as well. It meant that for most samples I would load the sample with 5–10 seconds to spare, and wait for the remaining time to pass. However, when problems arose, I would have to increase the pace in order to make it in time. Not only this made it more likely for mistakes to occur, but also made the task a lot more stressful. By chance, enforcing this procedure led me to discover that the moment of closure does not necessarily precede immediately the vacuum pumping. This extra waiting time is unpredictable and stems from the complex way the LabVIEW VI is built, with processes running in parallel that sometimes have to wait for one another. During one particularly difficult measurement day (09/02/2021), there was an average waiting time of 30s between system closure and the moment the N_2 purge gas started to be evacuated from the CIM. The waiting time seems to gets larger for very fast closure procedures (2 min 15 s or less, i.e., finishing before 00:12:15), which therefore reduces the gain of hurrying the process. In the end, I eventually reverted my decision of forcing a

Figure 3.4: Effect of reloading time on pBeforeHobeln for EK samples. The green circumferences (<2 min 45 s) represent reloading routines when everything went very smoothly and I managed to be particularly efficient. Orange and purple circles represent the vast majority of measurements, where only light additional tasks were eventually performed, such as extra cleaning efforts, replacing screws or repositioning the sample. The pink circumferences represent less fortunate routines that involved major losses of time, usually related to buildup of ice in the thread, deep cleaning, tightening issues in the lower VCR or sample mispositioning.

certain closure time. I decided instead to keep on employing the same principle as Christoph Nehrbass-Ahles (CNA) did and close the system as soon as possible.

Regarding total evacuation time, it is also worthy of note that EK samples and real ice core samples have different pumping times. EK samples have a reset timer that gives them, on average, an extra one minute of pumping in comparison with real ice core samples. For some unknown reason, this effect also applies to the real ice core sample that usually comes right after the EK measurement, but not to the remaining samples. This unfortunate feature of the LabVIEW Vi adds another element impacting *pBeforeHobeln* and should be rooted out when developing a novel extraction system. It is clear that the LabVIEW routines have great potential to be improved, although this was not the focus of this PhD.

High pBeforeHobeln from leftover N_2

A slightly imperfect tightening of the lower VCR gasket can lead to small leaks. A small leak would not contaminate the sample with outside air, but it would prevent attaining reasonable vacuum, leaving behind N2 that will dilute the gas sample. From experience, these are the most common leaks and they occur more often toward the end of measurement days. The inability to maintain steady torque levels comes from the progressive tiredness of

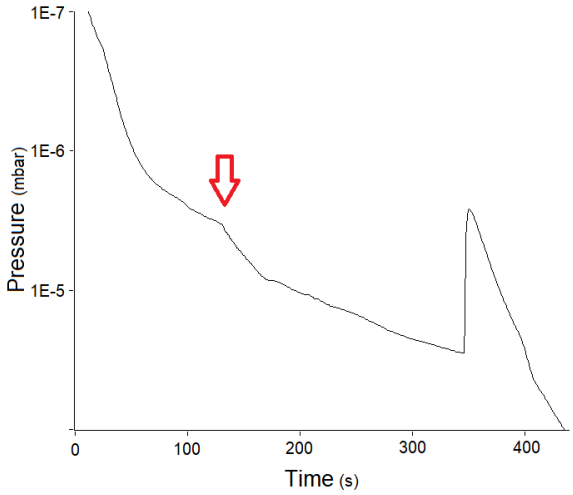

Figure 3.5: Vacuum pumping before extraction for an EDC ice core measurement (#28549). The insufficiently steep slope at t∼120 s was the visual cue that there was a small leak and that the VCR gasket needed to be retightened. Indeed, retightening (red arrow) led to an immediate steepening of the slope. Final vacuum quality was logged at t∼350 s, with the subsequent sharp increase indicating the beginning of the extraction phase.

the operator and a buildup of leftover ice in the tightening nut and thread.

Replacing the VCR gasket more often would address this issue. Although VCR gaskets are intended for single use, reuse is possible if the gasket is not yet fully indented. The gasket gets harder to indent with each use, and thus the operator needs to adequately increase the applied torque in order to maintain the same tightness. A more frequent replacement of the gasket demands less effort of torque adjustment from the operator, and thus diminishes the risk of a leak. CNA replaced the gasket every 7^{th} measurement, while I've instituted a replacement every 3–4 measurements. At ∼12 CHF per gasket, this is a significant increase in measurement costs, but I believe it is worthwhile.

There is also the possibility to monitor the vacuum pumping phase by using the auxiliary tool *Pressurechangerate.vi*, developed by BB. A well-trained eye can evaluate whether the VCR gasket needs to be retightened just by assessing the rate of pressure decay (see Figure 3.5). Unnecessary retightening can lead to an overtightened VCR that likely will need to be replaced in the next sample loading. The inevitable removal of the XPS insulating material in order to gain access to the VCR gasket also leads to an undesirable increase in the temperature of the CIM (see Section 2.3.7.4). I suspect, however, that it is far worse if a sample is lost due to bad vacuum conditions than the effects just mentioned. Therefore, when in doubt, I recommend to retighten. It is also important to interpret samples that have been retightened carefully. In case of an initial severe leak that is fixed with retightening, it is possible that the sample has been hopelessly contaminated even though the final *pBeforeHobeln* is within an unsuspicious range.

The high amount of EK measurements during the past few years allows us to investigate the impact of variability of *pBeforeHobeln* on possible CO_2 offsets. With respect to the standard gas SIO254, with a concentration of 254.50 ppm, one traditionally expects a positive

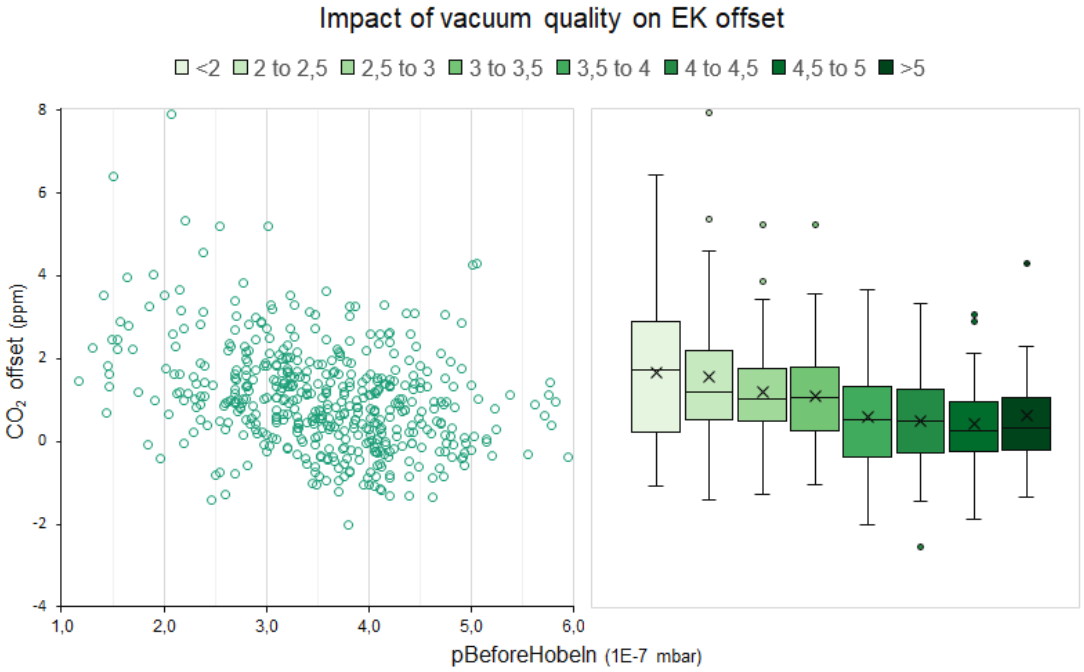

Figure 3.6: CO_2 offset as a function of vacuum quality for EK samples. Left: CO_2 offset for $N = 380$ EK samples, with respect to the standard SIO254, since 2018. Right: The same dataset as on the left side, but in the format of binned box and whiskers plots to reveal the linear drop of CO_2 offset with increasing *pBeforeHobeln*.

CO_2 offset fluctuating around 1 ppm, mostly thought to come from the extraction itself (see Subsection 3.1.6 for further details). However, a deeper statistical treatment has been missing. Figure 3.6 shows the CO_2 offset as a function of *pBeforeHobeln* for a total of 484 EK measurements since 2018. Despite the high scatter, there is a noticeable inverse proportionality for $pBeforeHobeln < 5 \times 10^{-7}$ mbar, evidenced more clearly when binning the data set in box and whiskers plots. Many measurements in the range $pBeforeHobeln > 5 \times 10^{-7}$ mbar were discarded as they were not considered to be representative of satisfactory EK measurements, leading to a selective bias in the plotted data. This is also the reason why scatter seems to increase with decreasing *pBeforeHobeln*, as I never discarded any EK measurements due to very low *pBeforeHobeln* (i.e., very good vacuum).

Performing a linear regression of CO_2 as a function of *pBeforeHobeln* returns a slope of 0.6 ± 0.1 ppm $(10^{-7}\,\text{mbar})^{-1}$, excluding data points with $pBeforeHobeln > 5 \times 10^{-7}$ mbar. Such a steep slope was a little unexpected and has relevant implications for potential correction purposes. It means that two ice core replicates with their respective *pBeforeHobeln* typically differing by 1.1×10^{-7} mbar (average value for the MIS 5 dataset, for $N = 230$ true pairs of replicates) are expected to present a mismatch in their CO_2 concentrations of $\sim$0.7 ppm. This value is in the same order of the pooled standard deviation of CO_2 for MIS 5 of 1.1 ppm and is thus likely to be one of the main components of the variability between true replicates. Unfortunately, the high level of scatter inhibits applying an offset correction as it would unrealistically distort the dataset. On the other hand, this result underlines the

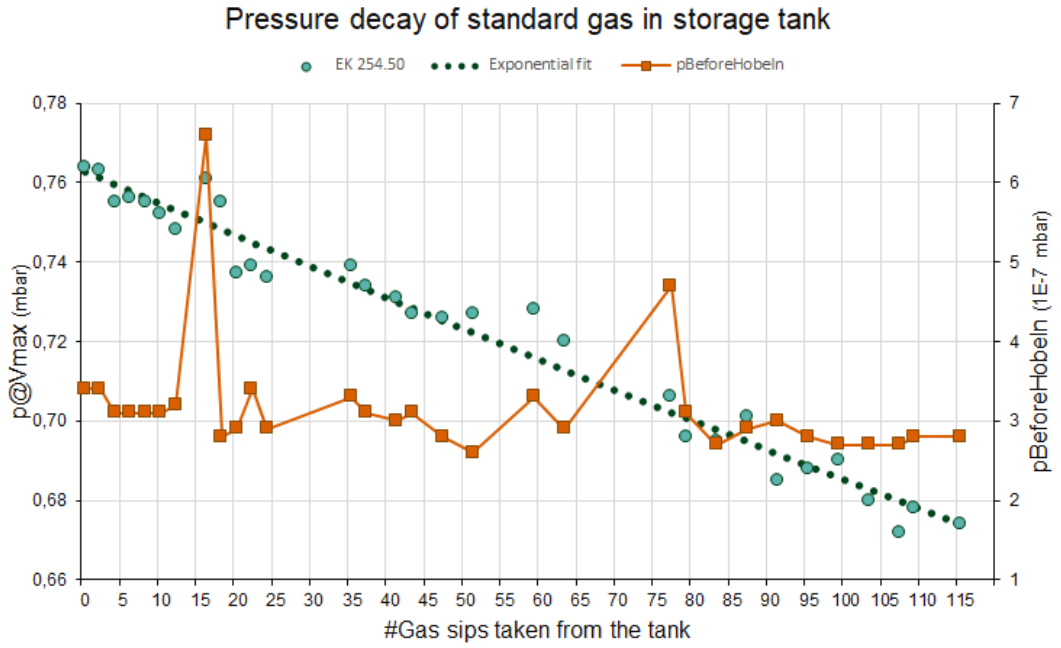

Figure 3.7: Pressure logged inside the bellow at maximum volume (*p@Vmax*) for a series of EK measurements, in the frame of the "Alternating EK / No EK" experiment (see Section 3.1.4). The decay of the parameter *p@Vmax* (green circles) is directly proportional to the available quantity of leftover standard gas in the storage tanks. Gaps between EK samples are due to calibration measurements in the LI-COR or standard gas measurements. The orange line and the square markers display the *pBeforeHobeln* for each measurement. Vacuum quality was generally very good, fluctuating around 3×10^{-7} mbar, except for two abrupt excursions, namely after aliquot #16 and #77.

importance of maintaining similar vacuum conditions from sample to sample.

One possible explanation for the negative linear relationship between *pBeforeHobeln* and CO_2 offset is the dilution of the CO_2 content of the sample in leftover N_2 from an ineffective (or too short) vacuum pumping phase. To test this hypothesis I checked whether the apparent TAC value for an EK sample is higher when the vacuum is poorer, indicating the presence of leftover N_2. However, this is not a straightforward test because the amount of injected standard gas into the CIM during EK measurements is not constant. Instead, the injected amount is dictated by the exponential decay of the pressure inside the standard tanks, where the standard is stored. Figure 3.7 indirectly shows this typical decay, in terms of the logged pressure when the bellow is in its maximum volume (*p@Vmax*), together with information about vacuum quality (*pBeforeHobeln*). This data set is particularly trustworthy as it stems from three days that consisted of EK measurements only, when I managed to keep exact track of the number of aliquots withdrawn from the standard tanks [ii]. The plot shows excursions of *p@Vmax* with respect to the exponential fit curve, which was expected. However, while the peak in *pBeforeHobeln* after 16 aliquots is very likely suggesting leftover N_2 and inducing a higher *p@Vmax*, the small changes in *pBeforeHobeln* elsewhere cannot explain the variability in *p@Vmax*. In fact, *pBeforeHobeln* was consistently around $\sim 3 \times 10^{-7}$ mbar, reflecting very stable vacuum conditions that hardly could have been improved.

The big surprise came when analysing the correlation between the residuals of *p@Vmax* and the CO_2 offset for the same data set. Figure 3.8 shows a negative correlation with a Pearson coefficient of -0.4 ($N = 31$), indicating an association of medium strength between the two parameters. The linear fit indicates that a residual *p@Vmax* of 0.01 mbar should lead to a negative offset of 0.5 ppm. However, if that same residual of 0.01 mbar were to be of pure N_2, this would correspond to a relative volume enrichment of 1–1.5%. Such an amount of N_2 would therefore correspond to a depletion of 2.5–3.5 ppm, given the standard gas of 254.50 ppm that we used in the experiment. Leftover N_2, by itself, is therefore insufficient to explain the dilution. One possibility is that the leak that induces the inefficient pumping of N_2 is also introducing ambient air CO_2, counteracting the N_2 dilution. This is hard to inspect, as the compensation would be dependent on the severity of the leak, which is unknown.

From this experiment I conclude that large swings of *pBeforeHobeln* definitely play a role in CO_2 offsets, but there are also other controls on *p@Vmax* that also affect it by the same magnitude. This is treated in the next section.

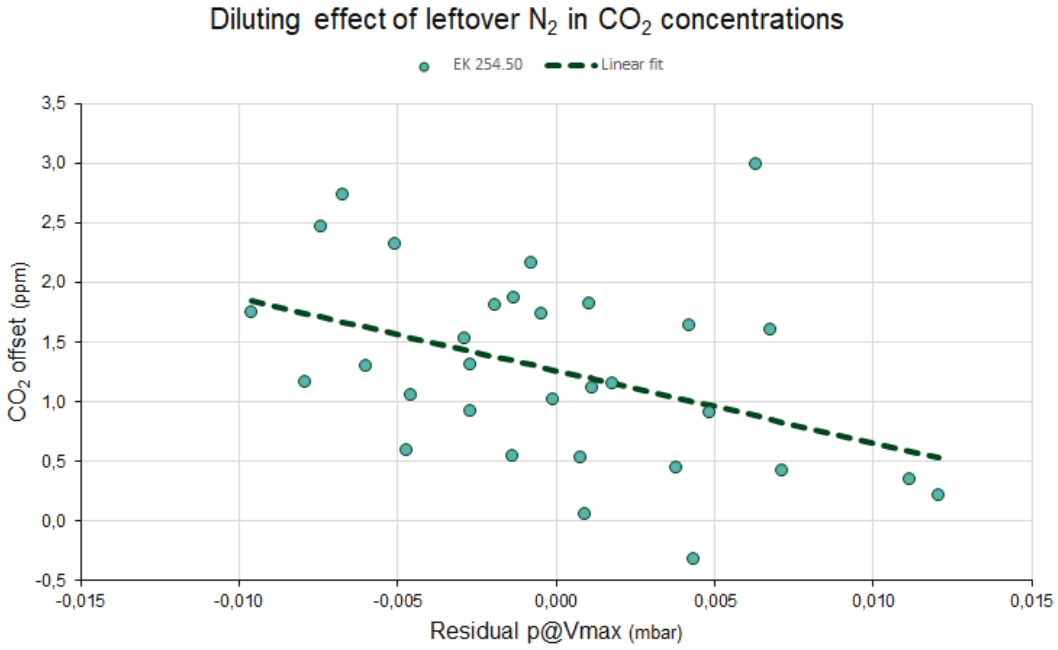

Figure 3.8: CO_2 offset as a function of the residuals of *p@Vmax*. The data set used is the same as the one used for Figure 3.7. The residuals were calculated from the exponential decay best fit and are interpreted as leftover N_2 from inefficient pumping that dilute the CO_2 concentrations.

[ii] This data set forms the basis for the EK/NoEK experiment (see Section 3.1.4)

3.1.3 Influence of temperature

- Neither CO_2 offsets nor fluctuations on *p@Vmax* seem to be dependent on temperature fluctuations inside the CIM extraction chamber.
- This does not exclude, however, that temperature changes felt by the sample gas afterwards inside the bellow are playing a role.
- If the gas temperature inside the bellow does change, it is predicted that an increase temperature will lead to an underestimation of CO_2 concentrations.
- The temperature of the funnel could be playing a role in final vacuum quality (and indirectly on CO_2 offsets) as this part of the CIM is particularly vulnerable to temperature swings.

Apart from TAC and leftover N_2, only a heat flux can theoretically impact *p@Vmax*. In an isochoric process, such as the heating of the sample gas while inside the bellow at fixed volume, added heat will increase both gas temperature and pressure. The largest heat source in our case is the lab atmosphere, as the CIM extraction head gets partially exposed for 2–3 minutes at every sample loading when the thermal insulation panels need to be removed. Slight temporal changes in lab air temperature during a measurement day can also play a role, directly heating or cooling the bellow casing. Regardless of where the heating takes place, what is key is that when expanding a warmer than usual gas into the LI-COR the bellow will need to push less air into the measurement cell in order to achieve the pre-requested pressure of 7 mbar. Subsequently, fewer CO_2 molecules will be available for absorption inside the measurement cell, leading to a misevaluation of an apparent smaller CO_2 concentration. It is important to note that the very next standard gas measurement that will be used as a reference is unlikely to be influenced by temperature offsets between the CIM and the bellow, since the standard gas travels from the storage tanks at room temperature directly to the LI-COR, bypassing the CIM altogether.

In practice, the CIM extraction head indeed has frequent observable fluctuations of 1 °C in its averaged temperature per measurement that, applying the ideal gas law $pV = nRT$, should lead to an accompanying change in pressure of 0.01 mbar. This is roughly the same amplitude of the superimposed variability with respect to the exponential fit line that we see in *p@Vmax* on Figure 3.7. We need therefore to test the hypothesis of temperature-driven *p@Vmax* residuals, as seen in Figure 3.8. In this case, changes in *p@Vmax* that are caused by temperature variations in the CIM should not lead to CO_2 offsets, but simply reflect a higher or smaller efficiency in transferring air from the CIM into the bellow. A colder CIM will retain more air while a warmer CIM will lead to more air making it into the bellow.

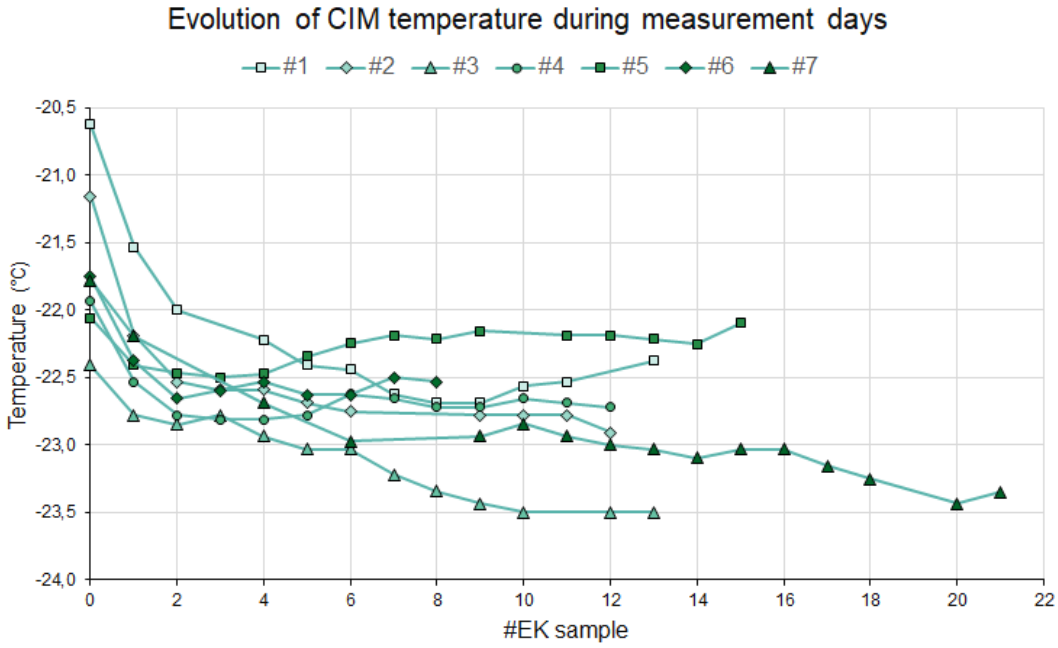

Figure 3.9: Temperature profile for 7 distinct measurement days where only EK samples were measured, in ascending chronology. Temperature is displayed as the average between the left and the right bearing temperatures. Gaps result from excluded measurements.

Measurements obtained during "EK days"[iii] are handy for investigating this temperature dependence further, as they are characterized by more stable vacuum conditions and possess generally less experimental mistakes that tend to add noise. Figure 3.9 shows the CIM temperature evolution for seven different "EK days". Note the initial decay until reaching stable conditions as a result of the turning on of the liquid nitrogen spitters at the beginning of each measurement day. While theoretically one could exclude the starting measurements from this transient period and adapt the measurement routine, it would mean a waste of time and EK samples that I do not think it is fully justified, especially since a temperature correction function could eventually be implemented. Also, experimenting fully with the LAUDA cooler settings has not yet received enough attention and could help eliminate the initial temperature decay. Note also the different absolute temperature plateaus for different days, likely due to particular lab room temperatures on those days. Such offsets are likely to be less pronounced in the future given that now the lab is equipped with better thermal control and isolation.

As seen before, given that different measurement days have their average temperature stabilizing at different plateaus, and given that specific daily vacuum quality can offset CO_2 concentrations, I have decided to use relative offsets with respect to the daily average for both temperature and CO_2. The left and middle panels of Figure 3.10 depict the same

[iii] An "EK day" is a day devoted exclusively to measuring EK samples in order to establish the current system offset with greater confidence. It is usually done before starting a measurement campaign or when there reasons to suspect that the CIM may have been contaminated.

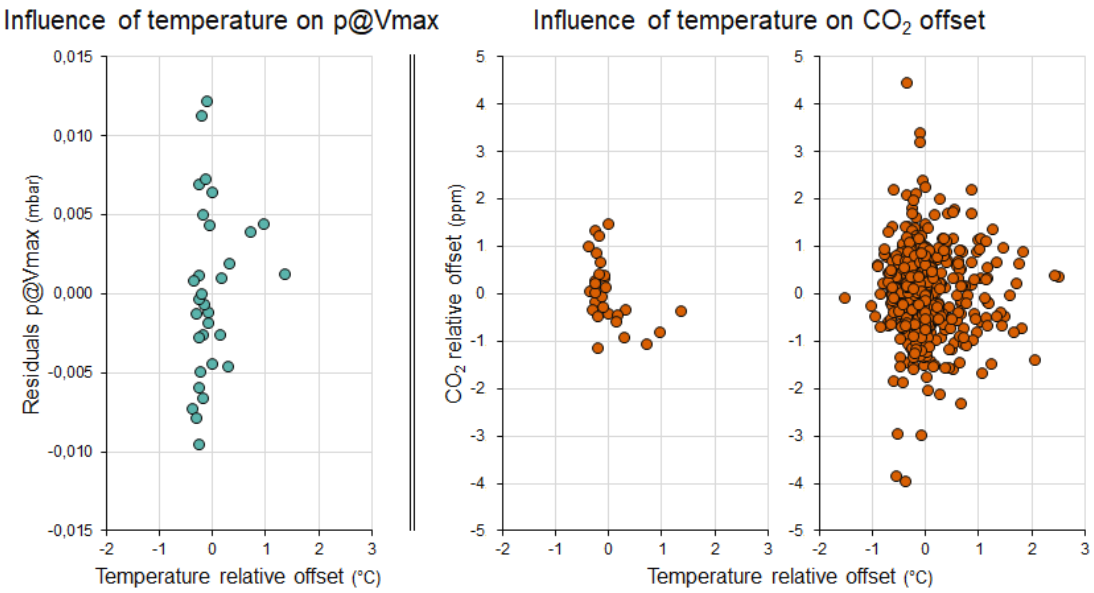

Figure 3.10: Effect of CIM temperature fluctuations on $p@Vmax$ and CO_2. The CIM temperature was calculated as the average between the left and the right bearing temperatures. Left: Residuals of the expected $p@Vmax$ as a function of temperature offsets to the daily temperature average, for the same dataset as in Figure 3.8. Middle: Same as left, but using the CO_2 relative offset to the daily average. Right: Same as middle, but expanding the results to all EK measurements since 2018.

dataset from Figure 3.8. Despite the expectations of a temperature dependence on $p@Vmax$ and, indirectly, on CO_2 concentrations, no obvious correlation between these parameters seems to exist. Extending the dataset to include all EK measurements since 2018 seems to confirm CIM extraction temperature as not being a primary driver of CO_2 offsets.

Since the CIM definitely has temperature swings and since temperature has to play a role in $p@Vmax$, I have come to believe that the CIM temperature plotted in Figures 3.9–3.10 is only a first order estimate of the gas temperature when it reaches the LI-COR. The temperature parameter that really plays a role in $p@Vmax$ is the temperature of the gas when it is logged inside the bellow — which, unfortunately, is an unknown. It could be the case that temperature fluctuations experienced by the gas while inside the CIM are in the end buffered while the gas is expanding toward the bellow. This effect would render temperature gradients in the CIM not relevant for $p@Vmax$ changes. For TAC estimates we assume that the gas reaches ambient temperature during the process of being transferred from the CIM to the bellow. The fact that we are able to satisfactory reproduce other TAC records under this assumption lends credit to this temperature stabilization assumption (see Section 3.4).

Another unexplored possibility is that the cold trap that is placed between the CIM and the bellow is playing a bigger role than extraction temperature fluctuations. As the cold trap gets progressively full throughout a measurement day and as ice builds up inside the CIM, it is possible that the cold trap lets water vapor psdd in a non-linear way from measurement

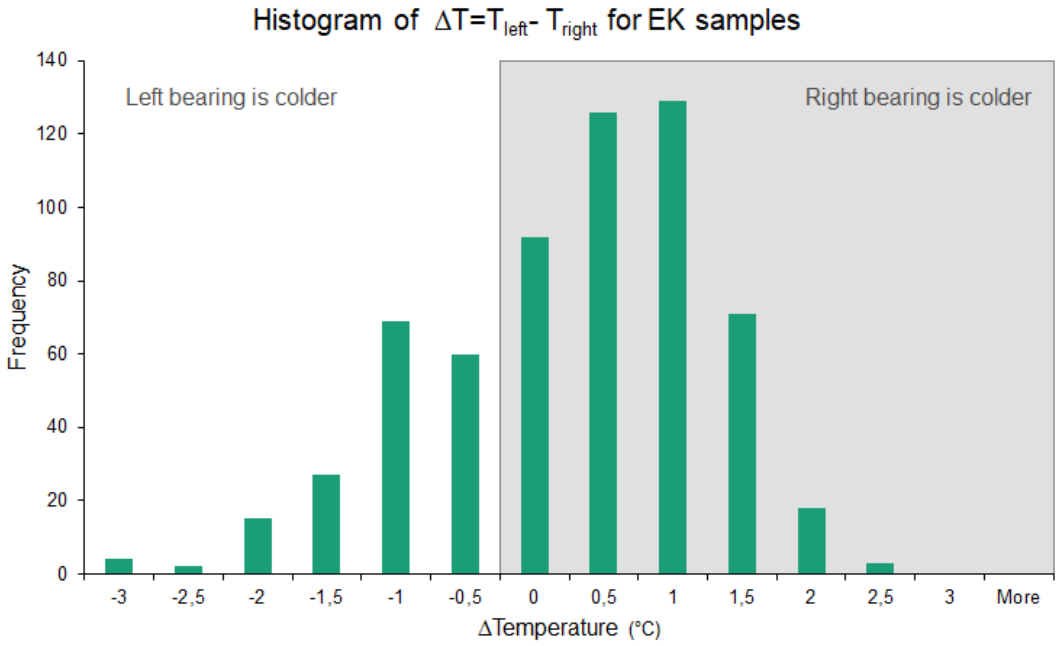

Figure 3.11: Histogram of ΔT between the left and right bearings for a total of N=616 EK measurements since 2018. Labels on the x-axis represent the lower limit of the bin.

to measurement. In order to test this, one would have to filter measurements done only in the early runs of a measurement day, and only for the first of a series of measurement days, to ensure similar conditions for the cold trap. Not only id this logistically hard, it would also likely lead to a very small sample size.

Left/right bearing temperature

The temperature of the CIM is logged separately on the right and left magnetic bearings. There is a spatial temperature gradient that comes from an inevitably non-homogeneous distribution of the cooling LN spitters. I have settled on a certain disposition of the LN spitters that is slightly different than the one employed by CNA and that, I believe, improves the homogeneity of cooling. Nevertheless, it is still imperfect, and as a result the right bearing is subject to a more direct cooling with LN than the left bearing, which leads often to an average temperature difference of 0.5–1 °C after the temperature has stabilized during a measurement day (see Figure 3.11).

CNA reported a correlation of $r^2 = 0.27$ between the left bearing absolute temperature and CO_2 offsets, but no correlation for the right bearing (Nehrbass-Ahles (2017), p.53). More recently, the compilation of more than 600 EK measurements since 2018 do not show any correlation between temperature and CO_2 offsets for either of the bearings (see Table 3.1). The different disposition of the LN spitters may be partially causing the different values found by me and CNA, but it is also possible that different methods and filtering

Table 3.1: Squared Pearson correlation coefficients (r^2) between bearing temperatures and CO_2 offsets for EK samples obtained by different operators, and possibly with different cooling schemes. CNA – Christoph Nehrbass-Ahles; LS – Lucas Silva)

Correlation r^2		
Operator	Left bearing	Right bearing
CNA	0.27	0.03
LS	0.0004	0.007

have been used to calculate r^2. In any case, if indeed there was at some point a correlation between left bearing temperature and CO_2 offset, it is reassuring to know that it was a negative correlation. This would fit the scenario of a low temperature gas being carried into the bellow and misleading the LI-COR by achieving the threshold pressure but sending too much air into the LI-COR, as explained in beginning of this section. CNA reports the negative correlation as being counter-intuitive, based on an argument that an increase of temperature leads to an increase of the water vapor pressure, which in turn favors desorption of accumulated CO_2 from the stainless steel inner walls of the CIM. Personally, I am inclined to believe that desorption effects should be small since after every sample loop the CIM walls are flushed with 2 bar of N_2 and contamination by outside atmospheric CO_2 is negligible.

Funnel temperature

The funnel is the CIM part that is most vulnerable to temperature swings. Due to its exposed position, its temperature oscillates 3–4 °C every sample iteration during the cleaning routine. Readings of the funnel temperature have always been interpreted just qualitatively as an indicator of eventual troubles during cleaning. Keeping the funnel temperature stable implicitly prevents large swings of the CIM temperature, which is regarded as the extraction temperature. In a few measurements, the lower lid has accidentally fallen off during the measurement cycle, leaving the system exposed and leading to a higher *pBeforeHobeln* of about $2–3 \times 10^{-7}$ mbar. I speculate that the warmth may be inducing higher local desorption of gas from the inner stainless steel walls of the CIM nearby the funnel, but the results are too few to quantify the effect. This is nevertheless yet another reminder of how important it is to maintain temperature control throughout a measurement day, including during the seamlessly harmless cleaning routine.

3.1.4 Extraction-related offsets

- An experiment involving EK samples quantified a total extraction-related offset of 2.0 ± 0.6 ppm. The result is statistically significant ($p \ll 0.05$) and holds for two different standard gases used.
- The same experiment revealed a depletion of CO_2 of about 0.6–0.9 ppm relative to the referenced value when no sample was present. The cause is so far unknown, but N_2 dilution is probably the main justification .
- As a by-product, it was possible to study the impact of sample volume in the reading of *p@Vmax*. Although the effect is definitely present, differences in sample weight and volume when fashioning ice core samples should only play a minor and undistinguishable role in *p@Vmax*, ultimately not being a reason for concern.

Alternating EK/No EK experiment

The purpose of measuring an EK is to calculate the experimental CO_2 offset of the extraction process. By mixing an EK sample with standard air with a known concentration, we are trying to mimic the process of real ice core samples in order to quantify all possible processes that can offset absolute concentrations. The exact steps behind measuring real ice core samples or EK samples are however not entirely equal. A few important caveats need to be taken into account:

- Real ice core samples degas during the vacuum pumping phase, while EK samples do not. This is the main reason why *pBeforeHobeln* is always lower for an EK sample than for a real ice core sample on any given measurement day.
- The standard gas travels along different routes when measuring EK or when being used for calibration, and thus could be subject to different degrees of fractionation. The different routes also imply different temperature gradients.
- The amount of standard gas that is injected in each EK measurement follows the exponential decay of the pressure inside the standard tanks. Therefore, it is not constant (see Figure 3.7). Nehrbass-Ahles reports a maximum difference of 2 ppm between EK samples that were measured when the tanks were at high pressure (∼2 bar) or at very low pressure (∼0.5 bar), but no comprehensive statistical analysis is available (Nehrbass-Ahles (2017), p.46). It would be a good idea to repeat this experiment to properly assess this potential effect. During my PhD I did use a larger range of

pressures from the standard tanks, but I never noticed an effect on EK CO_2 concentrations.

- Fashioning an EK sample is a straightforward task and it is therefore easy to maintain reproducibility in terms of shape, roughness and total handling time. On the other hand, real ice core samples require a customized approach in order to avoid contamination. Final shape can be more or less elongated, and while minimum roughness can be enforced, this may imply extended handling time (see also Section 3.2). It cannot be ruled out that these differences when fashioning samples are not having an effect during the extraction phase.

- The differences in shape alone can promote more or less degassing during vacuum pumping, but it can also be the case that certain shapes are more favorable in terms of shaving, i.e., require less revolutions and contact with the knife, which could have an impact on the final offset.

An experiment dubbed “Alternating EK / No EK" was carried out that consisted in a series of EK measurements where I alternated between loading or not actually loading an EK sample. The idea was to investigate how much of the CO_2 offset can be attributed to the shaving mechanism and to check whether other mechanisms could be at play. The alternating characteristic allows for the fake EK measurement (without an actual EK) to be performed while the CIM is wet. The software of course does not know if an actual sample has been loaded or not, and therefore proceeds with everything as if it were a normal EK measurement, i.e., adding of the standard gas, shaving, waiting time and gas expansion. For a more robust result, I decided to run this experiment twice in order to use the two main standard gases that we have available, namely SIO254 and SIO285. I also performed routine standard gas measurements just to verify that the gases indeed were close to their referenced value. In these routine measurements, the standard gases are directly fed into the LI-COR and bypass the CIM altogether.

The results are displayed in Figures 3.12 (top) and 3.13 (top), and summarized in Table 3.2. They show that the presence of the EK sample introduces a positive CO_2 offset for both standard gases, with EK measurements being on average 2 ppm higher than the runs without any EK sample. Taken at face value, this quantity could be seen as the total extraction offset. However, "No EK" results also show depleted CO_2 concentrations with respect to the standard gas measurements, which was a little unexpected. A CO_2 depletion could be coming from N_2 dilution, as discussed in Section 3.1.2. This is not worrisome, as the same effect is affecting real ice core samples. Unfortunately, it could also be that the depletion is caused by the transport of standard gas between the standard tanks and the CIM extraction unit, meaning that the gas is already in CO_2-depleted state before the extraction takes place, which is not the case for ice core samples. Such an effect could be due to fractionation by preferential adsorption of CO_2 to the stainless inner tubing that connects the standard tanks

Table 3.2: Results from the "Alternating EK / No EK" experiment. *Nominal reference* – absolute concentration expected to be found withing the standard gas flask, as per external calibration. *Standard measurement* – results from measuring the standard gas by injecting them directly into the LI-COR and bypassing the CIM. Done under dry conditions. *EK* – measurements with gas free ice that mimic the extraction procedure for real ice core samples. Done under wet conditions. *No EK* – same as EK, but without a sample being loaded. Done under wet conditions. The p value for both standards refers to the probability that the datasets "EK" and "No EK" originate from the same distribution.

Alternating EK / No EK experiment				
Type of measurement	SIO254	N	SIO285	N
Nominal reference	254.50 ± 0.02		285.02 ± 0.03	
Standard measurement	255.1 ± 0.6	4	284.8 ± 0.6	24
EK	255.6 ± 0.9	19	286.3 ± 0.4	10
No EK	253.6 ± 0.7	16	284.2 ± 0.4	8
CO_2 offset (EK - No EK)	2.0 ± 1.1		2.1 ± 0.6	
p	2×10^{-8}		7×10^{-9}	

to the CIM. If this is the case, then one should positively offset all ice core measurements by the average depleted amount with respect to the reference value, i.e., ∼1 ppm. One future experiment should be designed where routine standard gas measurements (from standard tanks directly into the LI-COR) are alternated with measurements where the standard gas is forced to go through the CIM instead of going directly into the CIM, all at room temperature. This would clarify if the CO_2 depletion has to do with the chosen path or if it is purely a feature of extraction dynamics.

Role of sample volume

As a by-product, the "Alternating EK / No EK" experiment unexpectedly revealed sample weight as another factor impacting the reading of *p@Vmax*. Figures 3.12 (bottom) and 3.13 (bottom) show the expected decay of *p@Vmax* with increasing number of measurements. The data sets composed by EK or No EK data points follow exponential decays offset to one another, signaling that the presence of the extra volume from the EK sample leads to a higher pressure reading of *p@Vmax* than the cases without a sample. In short, this implies that uneven EK weights throughout a measurement day could induce a misinterpretation of the fluctuations of *p@Vmax* as being leaks, for example.

For real ice core measurements, it is logical that more sample weight will mean more pressure in the bellow, as there are more bubbles available. But in the case of EK samples, it is not at all straightforward to reason that the adding of a sample should also lead to higher *p@Vmax*. A smaller sample (or no sample at all) allows for more standard gas to be injected into the CIM. On the other hand, regarding the next step, a smaller sample means that less air will transition from the CIM into the bellow. In the end, it is the ratio of volumes that dictates the final pressure. In this case, the CIM has a volume that is in the same order of magnitude as the volume of the bellow, but at the same time it is much larger than the volume of the piping from where the gas comes from. Given these constraints, being able

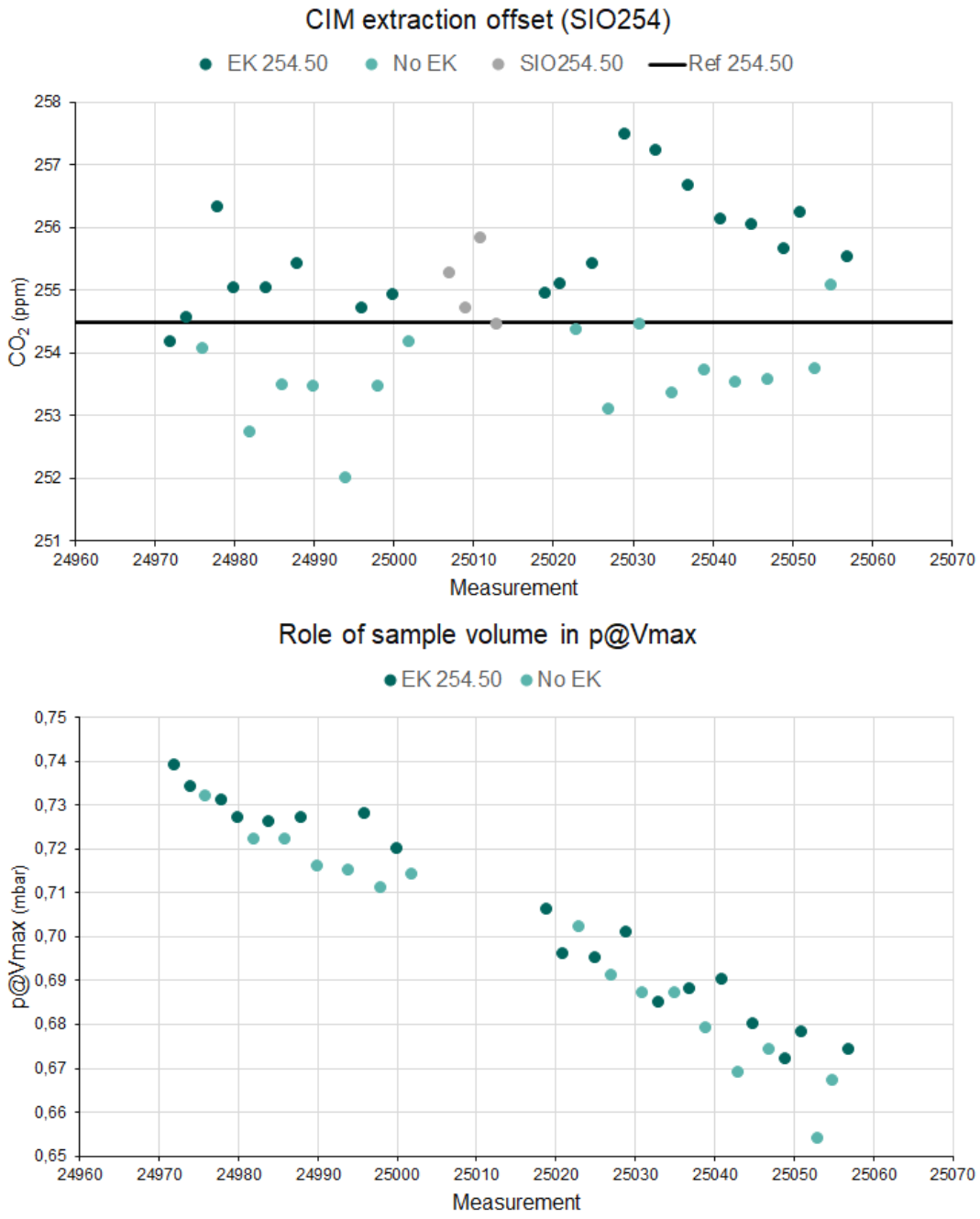

Figure 3.12: Results from the alternating EK/No EK experiment using the standard gas SIO254. Top: CO_2 extraction offsets while using EK samples (teal), or no samples at all (light blue). For comparison, direct standard gas measurements were also performed, without going through the CIM at all (grey). The black line represents the calibrated CO_2 concentration of the standard gas flask at 254.50 ppm. Bottom: pressure readings after extraction when the bellow is at its maximum volume ($p@Vmax$)

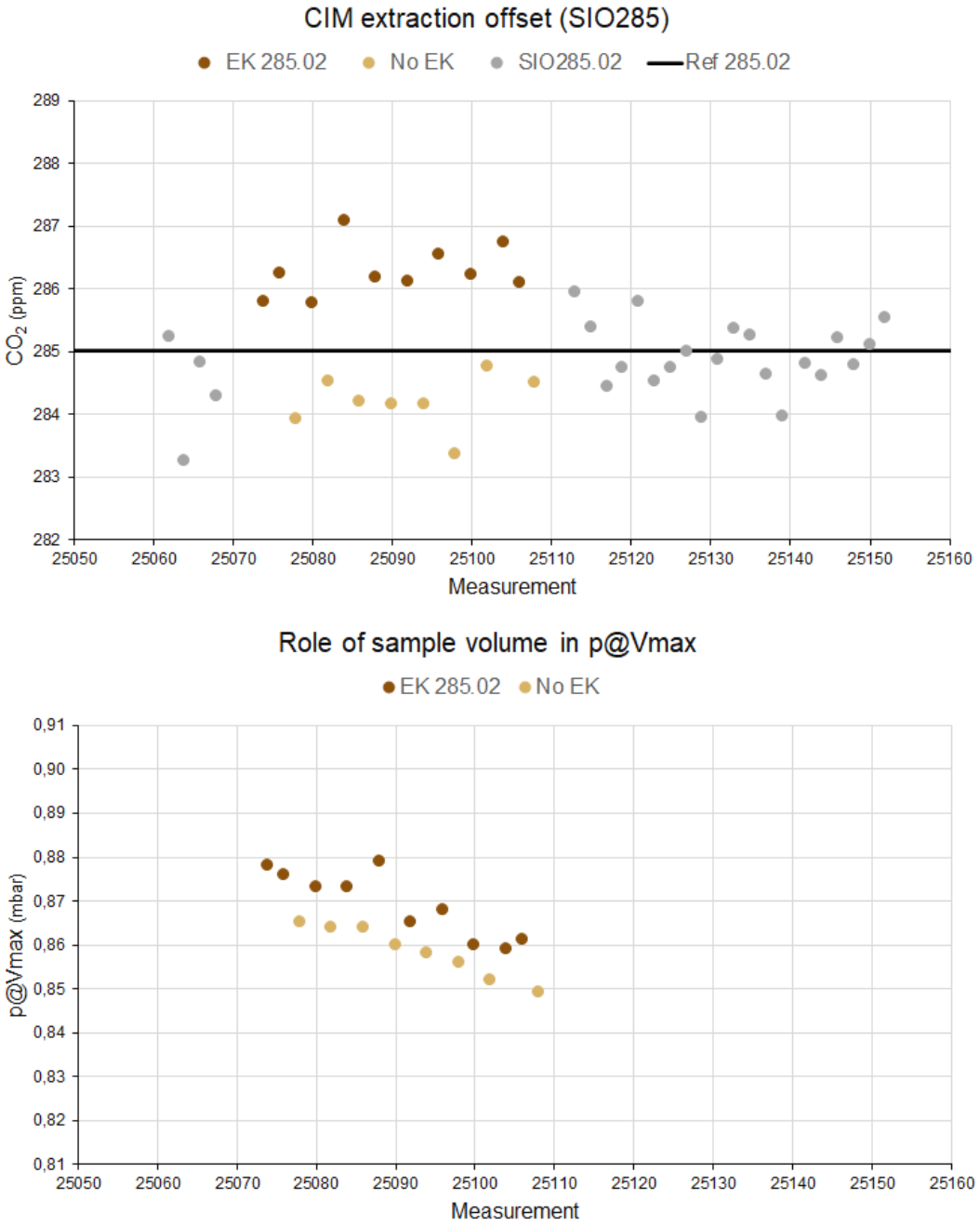

Figure 3.13: Results from the alternating EK/No EK experiment using the standard gas SIO285. Top: CO_2 extraction offsets while using EK samples (brown), or no samples at all (light brown). For comparison, direct standard gas measurements were also performed, without going through the CIM at all (grey). The black line represents the calibrated CO_2 concentration of the standard gas flask at 285.02 ppm. Bottom: pressure readings after extraction when the bellow is at its maximum volume ($p@Vmax$)

to push more air into the bellow by adding a sample ends up being much more important than allowing extra air to transition from the piping into the CIM in the previous step.

Luckily, the impact of sample weight in the final *p@Vmax* should not be a major concern. Figure 3.13 shows an average offset of about 0.01 mbar for a total weight change of 8 g (indicating presence or absence of an EK sample, typically with 8 g. Even if weight differences among EK samples amount to 10–20%, which probably could result from careless sample preparation, this would mean an offset in *p@Vmax* in the range of 0.001–0.002 mbar. Not only are these values too small to be discernible from background noise, they would also only imply a CO_2 offset of 0.05–0.1 ppm, according to the linear fit on Figure 3.8.

Sources of offsets

Nehrbass-Ahles (2017) wrote extensively about potential sources of offsets in CO_2 reconstructions, ranging from processes happening in the ice sheet, in the ice core during storage and analytic effects. Here we focus briefly and exclusively on offsets that stem from the extraction phase within the CIM.

Offsets in dry-extraction devices that rely on mechanical crushing of ice samples are thought to stem mostly from friction between metal surfaces and from incomplete extraction efficiencies (see Bereiter et al. (2012), Supporting Information). Regarding friction-related offsets, EK measurements serve the purpose of correcting for this nuisance, but it is of interest to understand why the offset happens in the first place. The CIM keeps friction to a minimum thanks to magnetic levitation, but the unavoidable presence of the titanium knife makes it a source of potential CO_2 artifacts. The knife is subject to collisions with ice samples at 1700 RPM and becomes progressively dull. The pins and the screw that keep the holder and the knife in place also undergo these vibrations and become a tiny CO_2 source themselves. Maintaining the knife sharp in principle helps to attenuate this effect. However, the lack of any obvious change in EK measurements after resharpening procedures, both by me and my predecessors, shows that, although not completely excluded, the knife is likely not an important driver of CO_2 offsets (see Nehrbass-Ahles (2017), Figure 2.19).

Upon maintenance of the CIM, fine copper particles were found inside the CIM, close to the copper rings that hold the glass encasements. These were likely a result of prolonged scratching from the rotor, through imbalanced dynamics that sometimes happens during measurements, friendly dubbed "knocking sounds". Knocking sounds can actually be very severe and tend to happen towards the end of the day when there is a buildup of ice that disturbs the regular revolutions of the rotor. The issue with the copper flakes is that CO_2 is favorably adsorbed on copper oxide under standard conditions (Isahak et al., 2013). During maintenance operations, the CIM extraction unit is sometimes mistakenly exposed to ambient air (2–3 times per year) and the recurrent knocking sounds are unavoidable, paving the way to conditions that could be altering CO_2 concentrations. Unfortunately, regular cleaning procedures of the CIM inner parts are far too dangerous to consider, and

thus we have to tolerate such circumstances.

There is likely a dynamic equilibrium between mechanisms slightly enriching (CO_2 release from the knife; contamination from outside air) or depleting (preferential CO_2 adsorption to metal surfaces; N_2 dilution) CO_2 concentrations during the extraction phase. This is supported by the small 1 ppm positive offset that we find for EK measurements. Such an offset has been present since the CIM is fully operational and is not problematic as long as it stays relatively constant (see Section 3.1.6 for more details). Furthermore, there are other parameters whose potential impacts have not yet been fully understood and/or quantified (temperature of extraction (Section 3.1.3); exact extraction efficiency). In light of the recent high-resolution studies that have been produced with the CIM and their good agreement with previously published records, there is good reason to believe that, as a whole, extraction-related offsets are not a major source of concern (Nehrbass-Ahles et al., 2020; Silva et al., 2022).

3.1.5 Calibration efforts

- In February, 2019, the two main standards were calibrated against 4 other standards.
- There is an offset of 0.15 ppm, which is negligible for us.

In February, 2019, the two standard gas flasks used for CO_2 measurements were controlled by Peter Nyfeler to assess their absolute concentrations. The calibration was achieved with respect to six other standards (see Table 3.3), and the results reveal that over time the two flasks have developed an offset to their referenced concentrations that is negligible for the purpose of CO_2 measurements (see Table 3.4). Given that both standard flasks are still above 100 bar, there is no need to worry at the moment about gradual fractionation. These should only be relevant when the flask pressure drops below ∼20 bar (Leuenberger et al., 2015). For the time being I have decided not to apply any correction as the offset to the nominal reference is so small.

Table 3.3: Standard gas cylinders used for the new calibration. All results can be checked at `https://gml.noaa.gov/ccl/refgas.html`. All concentrations are on the WMO X2007 scale.

Cylinder	mole fraction (ppm)
CA04556	192.44
CA04568	258.86
CA04561	294.95
CA03901	363.08
CA07066	400.81
CA06929	490.40

Table 3.4: New calibration results performed by Peter Nyfeler at KUP. The average offset of 0.15 ppm with respect to their nominal reference is not a reason to worry. Calibration results can be checked at `https://gml.noaa.gov/ccl/refgas.html`. All concentrations are on the WMO X2007 scale.

Type of measurement	SIO254 (CB10164)	SIO285 (CB10177)
Nominal reference	254.50 ± 0.02	285.02 ± 0.03
New calibration	254.65 ± 0.02	284.18 ± 0.02

3.1.6 Long-term evolution of SIO285, vacuum quality and EK measurements

- SIO285 measurements have been stable, reflecting good quality of the standards and reliable performance of the LI-COR throughout the years.
- Vacuum conditions can vary sharply in both short and long term. These shifts are mostly related to interfering with the leak tightness status of the system through maintenance procedures, or to intense measuring and its associated small recovering time between measurement days.
- EK measurements show marked variability. Abrupt fluctuations are linked to vacuum quality (*pBeforeHobeln)*, but long term trends are still not well understood. Thorough maintenance operations at once (cleaning inside of CIM; leak-testing; resharpening the blade) seems to reset the system to a CO_2 offset average of +1 ppm.

Maintaining EK samples within a small and steady range of variability lends extra trust to the accompanying measurements. This task is hard, because the CIM as a whole is continuously undergoing small changes. In the long term (∼years), ageing and wear leads to progressive failure of components such as valves, oxidized inner copper rings, or the quality of the funnel thread. In the medium term (∼months), maintaining leak tightness is difficult as the CIM is exposed to thermal amplitudes of ∼50 °C. In the short term (∼weeks), degrading knife sharpness and the constant need to refill the standard gas tanks require maintenance procedures that may induce offsets or change shaving characteristics. All these reasons support the idea of conducting measurement campaigns instead of isolated measurements. In these campaigns, full day measurements are performed 3–4 times a week, with the operator in an immersive measurement mode [iv]. The focus is on getting the measurements as quickly as reasonably possible while making little to no changes to the system. This methodology ensures similar conditions for all samples and makes it easier to spot mistakes. In practice, however, it is difficult to enforce long measurement campaigns due to the unavoidable presence of tough measurement days, operator mistakes and sometimes

[iv] Ideally, no other side tasks such as teaching assisting duties are present

part breakdowns that together lead to maintenance hiatuses. A successful example of this is the MIS 5 gap filling campaign, comprising 21 days of measurements spread over 70 days, without any major hurdles. Conversely, the set of experiments around centimeter-scale CO_2 variability dragged on for more than five months and were full of difficulties (see Figure 3.14). In hindsight, these could have been partly avoided by planning a more compact schedule before the start.

Figure 3.14 shows the evolution of standard gas measurements, vacuum conditions (*pBeforeHobeln*) and EK measurements over the course of this PhD. Note that the x-axis is in units of measurement number. It roughly reflects a time evolution, but it does not linearly scale with it. The small variability around the reference value showed by the SIO285 measurements confirms that both standards gas and the LI-COR are reliable over several years. For future calibration purposes of the LI-COR, SIO285 measurements are performed within the range 4–9 mbar. In days where a low pressure was chosen (4 or 5 mbar) there is a noticeable increase in the spread as the relative error increases. This is surely contributing, at least partially, to the observed small-scale variability. It should also be noted that the SIO285 data plotted in Figure 3.14 are not used to calibrate or correct any ice core measurements. Instead, an average of five SIO285 measurements are usually just performed prior to starting a measurement day in order to double-check that both the standards and the LI-COR are performing as expected. In this process, SIO285 is measured as an unknown gas against SIO254, the latter acting as the calibration gas. This is not the same procedure as the calibration of ice core samples, where one measurement of SIO254 is carried out for each ice core sample (see the measurement routine in Section 2.2).

Contrastingly, vacuum quality, as indirectly portrayed by *pBeforeHobeln*, is a much more sensitive parameter that can abruptly change if the system undergoes maintenance, likely due to exposure to ambient air and/or tightening issues. When looking at short periods, consecutive days of intense measuring (>20 samples/day[v]) will also imprint an increasing trend in *pBeforeHobeln* as the system cannot fully dry overnight.

EK measurements seem to oscillate smoothly as a whole, but they are also prone to trends, jumps and sudden changes of slope. In particular, during the MIS 5 gapfilling campaign, very good and stable vacuum conditions (*pBeforeHobeln*) did not prevent a marked valley-like progression of EK measurements. This shows that there are other long-term drivers affecting how the EK CO_2 offset evolves, even though *pBeforeHobeln* can definitely influence the CO_2 offset of individual EK samples. It is unknown what causes the slow drift of EK measurements. As mentioned, the valley-like progression of EK measurements during the MIS 5 campaign led to CO_2 concentrations going below the reference value of 254.50 ppm for the first time ever. Whatever mysterious process that was depleting the CO_2 concentrations was reset after the CIM maintenance event, which involved disassembling

[v]The number refers to the amount of ice core samples per day. On average, there are also 5–7 EK measurements that need to be performed in order to calculate the extraction-related offset for that particular day.

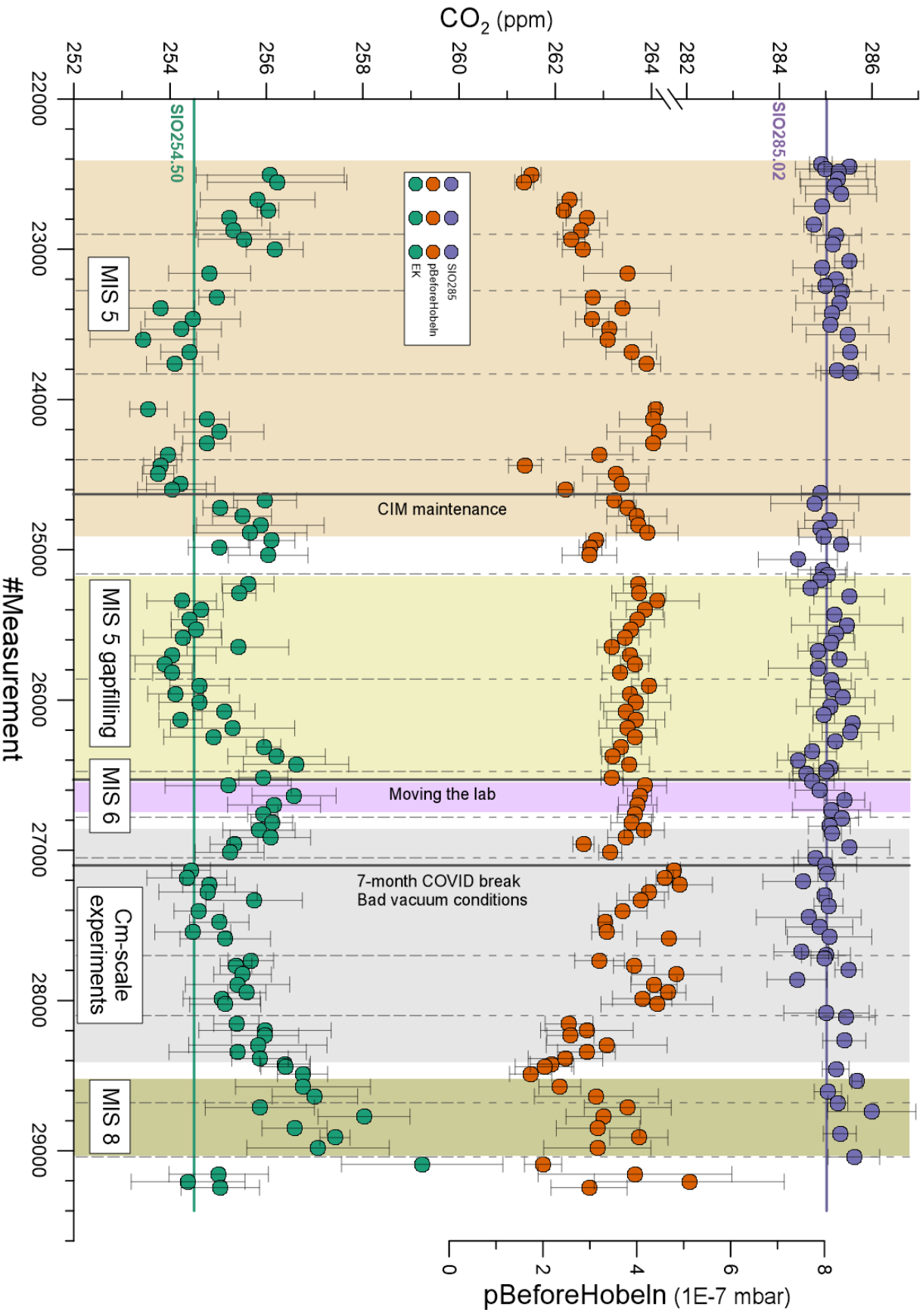

Figure 3.14: Collection of measurements for SIO285, *pBeforeHobeln* and EK samples. Data points represent a daily average with an error bar of 1σ. Vertical solid lines indicate particular events. Vertical dotted lines indicate a refill of the standard gases. Vertical colored bands indicate different measurement campaigns. Purple: Daily average of SIO285 standard gas measurements. No measurements were taken between 23800–24600 simply in the interest of time. On average, 6 measurements were done per data point. Red: Daily average of *pBeforeHobeln* of the corresponding EK measurements in green. Abrupt jumps indicate sudden changes in vacuum quality/leak tightness. Green: EK measurements as part of regular measurement days or as part of "Ek Days". On average, 6 measurements were done per data point.

and cleaning the system completely.

3.2 Shape-related effects

3.2.1 Round- *vs* cubic-shaped samples

- A systematic difference in CO_2 concentrations was found between pairs of true ice replicates.
- The outer and more elongated replicate yielded on average a CO_2 concentration that is 0.3 ppm higher than the inner cubical replicate.
- The source of the extra CO_2 is likely a combination of larger surface-to-area ratio and its location within the core which is more prone to contamination.
- This prompted the introduction of a shape correction parameter in the calculations and the design of a new and more robust cutting scheme.

Assessing the impact of the current cutting-scheme

The small sample size required by the CIM typically enables more than one ice replicate per depth level on an ice core. In the case of the EDC ice core, CNA adopted the following cutting scheme for the A-cut, which is the cut generally available for gas measurements (see Figure 3.15). The rationale behind this cutting scheme lies on previous experiments by BB with different sample sizes and shapes. They ultimately led to the conclusion that cubic samples with roughly 8 g should yield the best results. This was based on the following:

- Cubic samples with 8 cm^3 met the criteria of not having any inner diagonal with more than 34 mm, in which case it would not fit with the inner diameter of the sample holder.
- In contrast with other elongated samples, the cubic ones did not lead to sample wedging in the CIM sample recess and experienced smooth shaving instead.
- They were straightforward and fast to prepare with the ice saw without the need of any special equipment.

In accordance to these results, the cutting scheme in Figure 3.15 then sensibly allows for one inner ideal cubic sample (1), one outer sample with an approximate cubic shape (2), and a third less suitable and very elongated sample that encompasses most of the outer area that had been previously in contact with drilling fluid (3). CNA routinely discarded sample

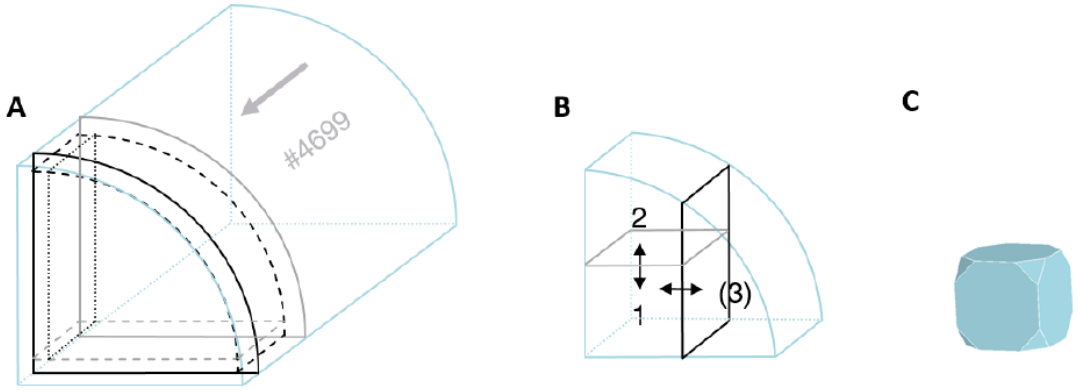

Figure 3.15: Traditional sample cutting scheme for the an EDC A cut piece. A) A 2.5 cm chunk sample is cut from the main A cut, and its edges trimmed. B) Sample 1 (dubbed "cubic") and sample 2 (dubbed "round") are split from the chunk and used as true replicates, each one weighing around 9–11 g at this stage. Sample 3 is usually discarded as it does not possess enough weight and/or has too elongated shape. C) Ideal shape of samples 1 and 2, after being manually trimmed with a shaving blade, weighing approximately 8 g. Focus is on eliminating any sharp edges, especially the vertices. Adapted from Nehrbass-Ahles (2017), p.31.

(3) as he found that it did not improve the record significantly, i.e., it frequently did not agree well with samples (1) and (2). He also felt, in general, that sample (2) yielded slightly higher CO_2 concentrations and was more prone to contamination than sample (1), but he did not have access to any statistics that could confirm this.

Results from a t-test between “round” and “cubic” samples

In order to process CO_2 data generated by the CIM, CNA developed a dedicated excel spreadsheet. While it allows for an overall interpretation of the dataset as a whole, it lacks flexibility to study more in-depth statistics. Following a reorganization of the same excel sheet, it is now possible to compare ice replicates in a more user-friendly and straightforward way. Figure 3.16 shows a comparison between the ice replicates that form the MIS 5 record on Chapter 4. The data points were chosen only pertaining depth levels with exactly two ice replicates and where no evident source of error was to be found (i.e., no samples from Steering Committee (SC) cuts, remeasurement combinations or other potentially suspicious backgrounds). The inner cubic sample was dubbed “cubic” while the outer one was dubbed “round”, given its segment of the outer ice core cut (see also Figure 3.15). The two Gaussian distributions have their means offset of 0.3 ppm relative to each other and were subject to a t-test, in order to verify whether the offset was significant other not. A p-value of p=0.00536 allows us to confidently reject the null-hypothesis (with more than 99.4% certainty) that the two sets of replicates represent the same overall population. Therefore, the systematic 0.3 ppm difference is statistically significant and should be corrected for when calculating CO_2 concentrations per depth level.

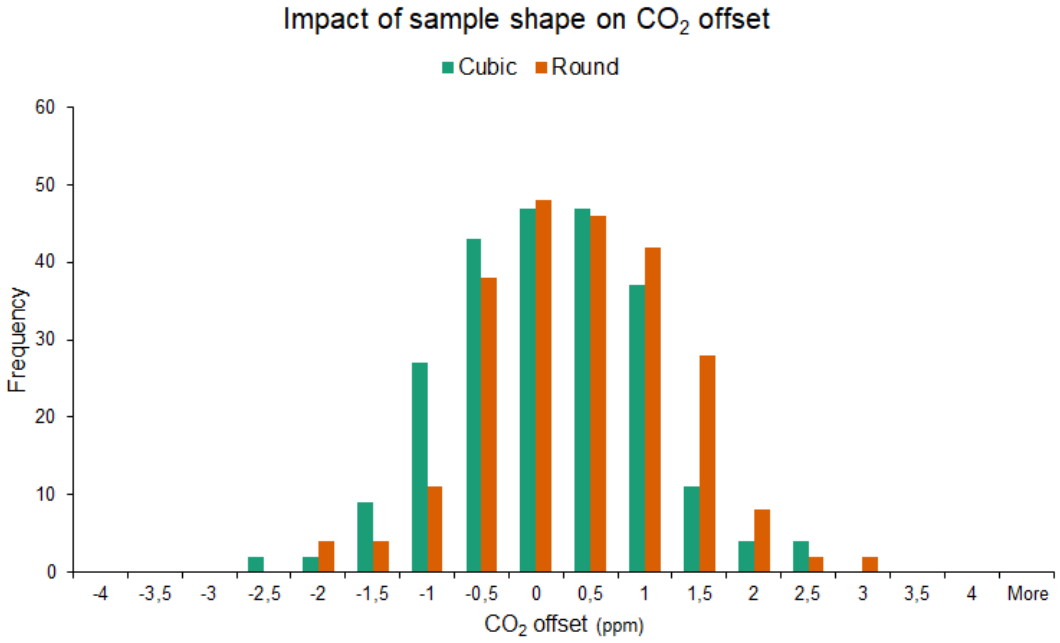

Figure 3.16: Histogram of CO_2 offsets with respect to the average per depth level replicates according to their shape. The data stems from the MIS 5 dataset used in Chapter 4. X-axis labels refer to the minimum limit of each bin, e.g.,"0" means 0–0.5

Justification and correction

Theoretically speaking, it would make just as much sense to search for reasons behind a CO_2 depletion in the "cubic" sample as searching for an explanation as to why is the "round" sample enriched in CO_2. However, the depletion mechanisms that we are aware of (i.e., adsorption of CO_2 to metal walls and N_2 dilution) should not be disturbed by geometric differences of the sample or minute differences in volume (see Section 3.1.4). I therefore hypothesize that the 0.3 ppm offset can be exclusively attributed as extra CO_2 in the "round" sample and that it is the sum of two main sources:

- **Differences in surface-to-volume ratio**
  The elongated shape of the "round" sample gives it a higher surface-to-volume ratio than the "cubic" counterpart. It is also technically more challenging to fashion, with increased chances of a final shape with pointy ends or live edges. Both features facilitate degassing during the evacuation stage in comparison to a spherically-ideal sample. If the vacuum pumping entails fractionation occurring on the outer layers of the sample, then this effect is amplified in "round" samples.

- **Relative location within the ice core**
  The drilling of an ice core requires drilling fluid to act as a lubricant and to prevent closure of the hole. Breaks and stress cracks along the cylindrical surface of the ice core allow this fluid to contaminate the core within a couple of millimeters of depth.

Over time, atmospheric contamination via these same cracks, together with age-related relaxation of the ice leads to a worsening of the original CO_2 content of the outer layers of the core. Due to this, the outer 3–5 millimeters of the core are always trimmed during sample preparation, following the recommendation in Bereiter et al. (2009). It cannot be ruled out, however, that during this manual process some degree of contamination remains, which will have a greater impact on the outer sample ("round"), than on the inner sample ("cubic") on the cutting scheme from Figure 3.15.

This shape correction is objectively small when compared to other error sources such as the LI-COR analytical error or extraction offsets in general. Nevertheless, it improves the standard deviation of each depth level and improves the pooled standard deviation of the record as a whole.

3.2.2 Cheese-shaped samples

- A new sample cutting scheme now allows for 3 replicates per depth level.
- The replicates have equal weight, shape and proportional share of the core.
- Correct positioning of the sample inside the CIM prevents most difficulties related to the new sample shape.
- There is no reason to believe that they perform any worse than the traditionally cut samples.
- The extra replicate increases trust in concentrations per depth level, but also involves a 50% extra work load that needs to be considered.

New cutting scheme and sample holder

Motivated by the discovery of a shape-dependent CO_2 difference, I decided to design a new cutting scheme and sample holder that would grant an equal share of the core among true replicates. This can only be accomplished by radially splitting the EDC A cut and taking it as an approximation of a circular section. Depending on the observer, the replicates now assume the form of slices from of a wide range of cylindrically-shaped edibles. Pie, cake and cheese came to mind, but being in Switzerland, the choice was rather obvious.

Figure 3.17 shows the cutting sequence for cheese-shaped samples using an EK slab as an example. Regarding sample preparation, the new sample holder significantly speeds up the cutting process. The hands of the operator are also kept a bit further away from the saw, which is a security improvement in an overall delicate procedure.

Cheese-shaped samples come with a series of advantages:

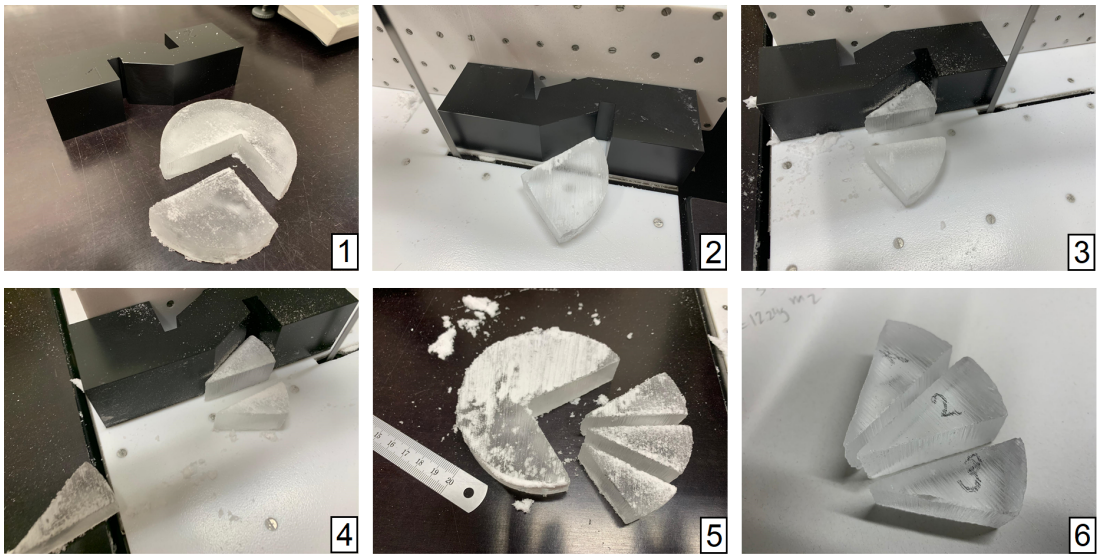

Figure 3.17: Cutting sequence using the new sample holder. 1) An EDC A cut is mimicked from a slab of an EK stick. 2–3) The first sample is positioned and cut with the long edge pressing against the holder. 4) The holder is rotated 180° and the second and third samples can be cut in similar fashion. 5–6) The cheese-shaped samples are ready.

- Three replicates per depth level, instead of just two, leading to more trustworthy averages per depth level and less waste of ice.
- Equal shape for all replicates.
- No compromise on sample weight ($\sim 8\,\mathrm{g}$ for each of the three replicates).
- Equal radial share of ice and bubble content, i.e., no more inner/outer samples.

Naturally, the new shape comes with disadvantages as well. The choice of shape initially fell on cubical samples because they are the closest to the ideal spherical case, when the ice is microtomed evenly and the sphere radius homogeneously decreases after every revolution. Elongated samples were associated to more wedging and knocking sounds as a consequence of a less gentle shaving process. All the experiments so far with cheese-shaped samples have not revealed any significant increase in the occurrence of knocking sounds, but there are occasional issues with the orientation of the sample inside the recess. For instance, placing the sample lying on one of its parallel surfaces leads often to either incomplete shavings or to the sample being radially stuck. Loading the sample edge-first also seems to lead to incomplete shavings. Conversely, the best results have been attained by placing the sample sitting on its round surface, with the edge facing the knife first, likely because it is easier for the knife to start shaving the sample from this aggressive stance. In general, if a too large surface is centripetally pushed against the knife, there is a chance that the shaving will not occur. Since the knife is peaking inward merely 0.26 mm it has happened that the sample essentially jumps over the knife at every rotation and barely any shaving takes place.

The new cutting scheme does not necessarily substitute the old one, but merely offers the added option of having an extra true horizontal replicate. Nehrbass-Ahles et al. (2020)

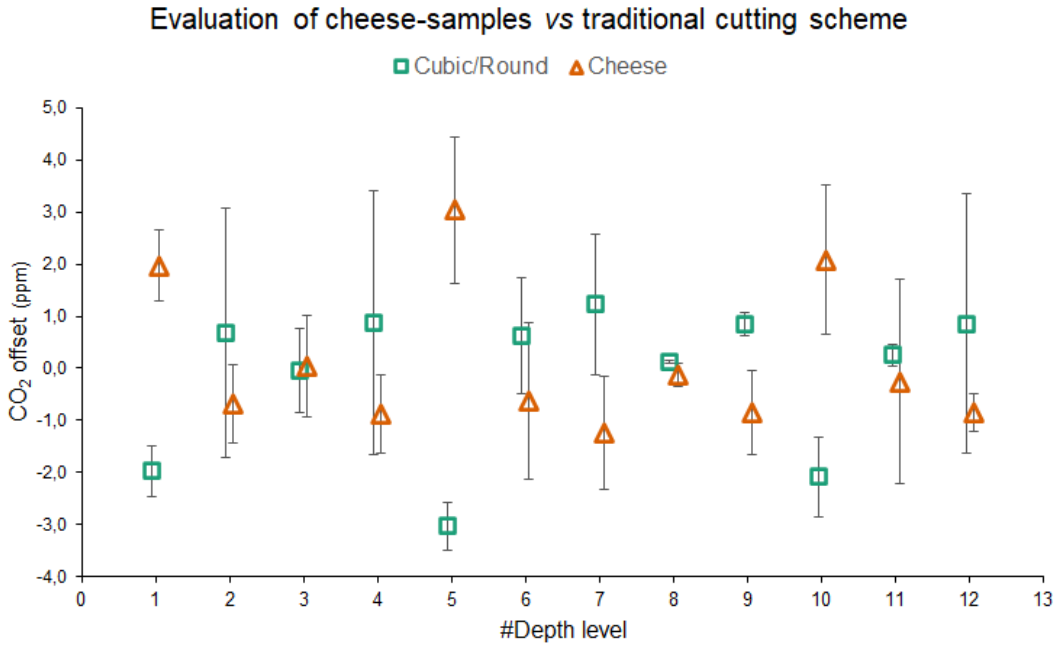

Figure 3.18: Comparison of CO_2 measurements using cubic/round samples (teal) and cheese-shaped samples (orange) for 12 depth levels between Offsets were calculated with respect to the average of the cubic/round and cheese-shaped samples taken together for each depth level. Error bars represent the standard error of the mean (SEM), calculated as SEM $= \sigma/\sqrt{N}$

used only 2 replicates per depth level to attain a very coherent and smooth record, mainly because the 2 replicates agreed well with each other. In this case, adding another replicate would likely not have improved the overall record substantially. It would, however, have led to an extra 50% of measurements, which is a very significant undertaking that needs to be pondered over. I believe cheese-shaped samples should be employed when there is either no prior knowledge about what is being measured, or when centimeter-scale variability is suspected to be present (see also the following Section 3.3).

Evaluating cheese-shaped samples *vs* traditional cutting scheme

The performance of cheese-shaped samples was tested using remaining samples from the MIS 5 campaign. Each remaining piece had an immediate vertical neighbor where two replicates had been previously measured with the traditional cutting scheme, i.e., with one "round" and one "cubic" sample [vi]. Figure 3.18 shows the comparison between cheese-shaped samples and cubic/round samples for 12 distinct depth levels, evenly distributed across the MIS 5 time window (104–130 ka). There is no statistical evidence that the two data sets differ from one another ($p = 0.63$, N=12, single sample t-test for the offset between the two datasets), but there is reason to believe that centimeter-scale variability is inflicting unusually high differences in some cases (see also Section 3.3). In particular, depth levels 1, 5 and 10 show offsets 4–5 times bigger than the spread between replicates, a feature

that cannot be attributed to measurement errors nor to statistical chance. Interestingly, neglecting these 3 particular depth levels leads to a scenario where cubic/round samples are significantly enriched in CO_2 with respect to cheese-shaped samples, by an average of 1.2 ± 0.8 ppm (p = 0.001, N=9, single sample t-test for the offset between the two datasets). Since the usual offset culprits can be excluded in this case (poor vacuum quality, N_2 dilution, different EK baselines, temperature) only shape-related divergences can be invoked to explain the offset, if it really exists. By simplicity, the set of geometrically similar cheese-shaped replicates has to been interpreted as the more likely to be correct.

3.3 Centimeter-scale CO_2 variability

- Unusually abrupt CO_2 variability found during the MIS 5e plateau prompted research on centimeter-scale fluctuations.
- Full bag experiments revealed up to 20 ppm excursions at depths 300-500 m below the end of the BCTZ on EDC ice. Results are consistent with a previous study on EDML ice.
- The effect is likely due to fractionation during the transformation of bubbles into clathrates, enriching the CO_2 concentration of some centimeter-scale layers that are early formed at the expense of its neighboring layers that are formed later on.
- Measurements on ice at much deeper depths in the range 2650–2750 m showed that long-term diffusion-induced smoothing erases the centimeter-scale variability.

3.3.1 Motivation

The motivation to study centimeter-scale CO_2 variability on ice cores came from the analysis of the MIS 5e substage interglacial using EDC ice (see Chapter 4). In comparison with the other interglacials after the Mid-Brunhes Event (i.e., MIS 1, MIS 7 and MIS 11), the MIS 5e plateau was remarkably stable, averaging 275.4 ppm during 12 ka (115–127 ka). Nevertheless, fast excursions up to 5 ppm are apparent at the centennial scale that are superimposed on the millennial-scale variability (see Figure 3.19). Several reasons can be invoked to discard these fluctuations as being atmospheric in nature. Firstly, given the gas-age distribution

[vi] When requesting EDC ice for CO_2 measurements with the CIM it is customary to ask for 5 cm long ice pieces from “A" cuts. Each piece is split into two 2.5 cm vertically neighboring smaller pieces, each one in turn allowing for two or three true horizontal replicates depending on sample-cutting scheme.

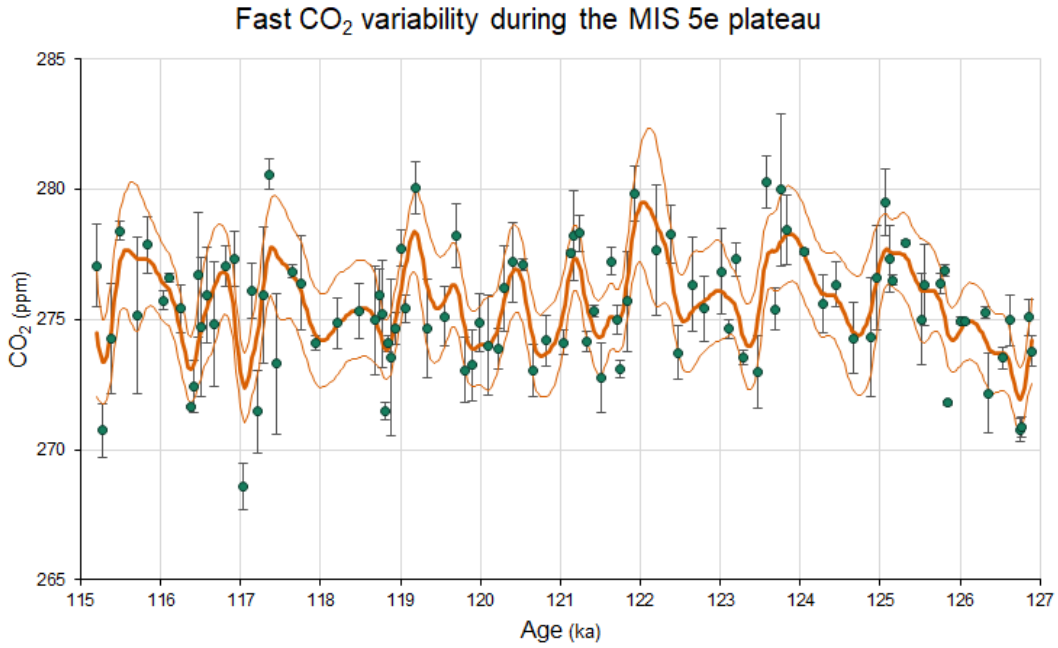

Figure 3.19: CO_2 variability recorded on EDC for the MIS 5 acme. Green data points indicate the average per depth level, mostly with two replicates each. The average resolution for this period is 120 years. The orange spline was obtained with a Monte Carlo method with 10000 runs and a cutoff period of 500 years. The upper and lower limit indicate 2σ bands.

(GAD) of the EDC record during MIS 5e, it is expected that two ice core samples 100 years old apart share 50% of their atmospheric content (Spahni et al., 2003). It was in fact this particular feature that inhibited us from setting an even more ambitious resolution goal when planning the measurement campaign. Given this limitation, any sudden concentration jump between two neighboring data points would mean a much bigger atmospheric signal, which makes this scenario even more unlikely from the point of view of an otherwise stable interglacial.

Secondly,an abrupt CO_2 excursion would leave a multi-century lasting imprint on CO_2 concentrations. This is supported by the CO_2 ice core paleo record, which evidences that while sudden releases of CO_2 can be as fast as 13 ppm per century (Marcott et al., 2014), the following transient drawdowns never exceeded the rate of 2 ppm per century[vii]. These can be found for instance after the overshoots of Terminations II–IV (see Chapter 4, Petit et al. (1999) and Nehrbass-Ahles et al. (2020)).

Finally, the fact that many peaks are created by single data points hints at noise-like sources being more likely the reason for the variability than the presence of atmospheric fine structures. On the other hand, the few short-lived CO_2 excursions that have been documented so far usually start with a sharp release and a subsequent slower drawdown to equilibrium, which does not apply to what we observe in the MIS 5 plateau. For instance,

[vii]Rates recorded in the EDC ice core. The true atmospheric signal rates are necessarily steeper, as the bubble enclosure characteristics damp the signal.

the CDJ$^-$ 11c during MIS 11 shows well this pattern (Nehrbass-Ahles et al., 2020). For the last deglaciation, the small plateaus that follow the step-wise CO_2 behavior can be seen as slow drawdowns superimposed on the rising trend of the deglaciation (Marcott et al., 2014).

3.3.2 Full bag experiments

With the purpose of clarifying the nature of the variability during MIS 5, I performed a series of centimeter-scale measurements at two different time points within the MIS 5e plateau. The lengthy measurements, as a whole dubbed “Full bag experiments", involved measuring entire 55 cm EDC ice core bags, sampled at every 2.5 cm. At first only two replicates were available per depth level, but with the development of the cheese-shaped sample scheme, I eventually retrieved three replicates per depth level. Bag #3081 was the first one to be measured from ice that was already stored in Bern, but unfortunately only less than 30 cm of ice were left for this experiment.

The “Full bag experiment" followed a similar investigation performed by Lüthi et al. (2010). In that study, the authors found large variability of up to 25 ppm at the centimeter scale in the EDML ice core, at depths just below the BCTZ. They attributed the effect to centimeter-scale layering of clathrates within the BCTZ, instead of a linear increase of the clathrate to bubble ratio with depth. Borrowing knowledge from known fractionation mechanisms in O_2/N_2 ratios in the BCTZ, CO_2 could be preferentially taken up in early-formed clathrates leading to enriched layers at the expense of its neighboring CO_2 depleted and later-formed clathrates. It is feasible that these particular enclosure and layering features that are characteristic of EDML ice at those depths are also to be found in the EDC ice core.

The chosen EDC bags were bags #2884 and #3081, at depths ∼1586 m and ∼1694 m, corresponding to late and early plateau conditions during MIS 5e substage, respectively. At these depths the ice was fully clathrated in the ice core, and the bags are significantly deeper in the ice than the BCTZ, which for the EDC ice core is estimated to lie in the range 600–1200 m[viii]. Care was taken to pick time windows when no particular fast variability was expected, as it avoids the known staggered layering effect, although this is more prone to happen during deglaciations or other extended periods of abrupt change (Fourteau et al., 2017, 2020).

Figure 3.20 depicts the results for these two bags, where the most prominent feature is the 15 ppm spike within 10 cm for the late interglacial (top). In both bags, oscillations of 4–5 ppm within a few centimeters are present. For comparison, both the absolute accuracy of the LI-COR and the observed reproducibility with EK samples are below 1 ppm. Moreover, the main peak appears to have formed at the expense of the depletion of neighboring depths. Since CO_2 is a relatively big and heavy molecule among the most common air constituents,

[viii] The ice was fully clathrated while inside the ice core, but twenty years of storage have made them relax into plate-like inclusions that are visible to the naked eye

the apparent CO_2 enrichment during the peak likely indicates the escape of lighter and more strongly permeating gases such as O_2 to adjacent depth levels. This is consistent with Lüthi et al. (2010), where $\delta O_2/N_2$ follows well the CO_2 variability found in the region below the BCTZ in the EDML ice core. The variations are explained with fractionation during the transformation process of bubbles into clathrates. At that stage, some gas species are preferentially taken up in the clathrate phase, ultimately leading to changes in relative concentrations. As clathrates slowly form at different layers, early and late clathrates will possess different gas content, as the state of their surroundings is different. Given this framework, the depth levels that show enriched CO_2 content in Figure 3.20 should correspond to layers where clathrates formed earlier than their neighbors. With increasing depth, slow diffusion of gases through the ice lattice gradually counterbalances this effect, smoothing out centimeter-scale differences (Bereiter et al., 2009).

Apart from the peak, it is also noteworthy that in both bags the average spread between true replicates of the same depth level is much smaller than the total variability of the bag taken as a whole. In other words, the horizontal spread ($1\sigma_{horizontal}$) of the ice core is smaller than the vertical spread ($1\sigma_{vertical}$; see also Table 3.5). This suggests different physical mechanisms acting on the z-axis and on the plane normal to it, and it contrasts with the assumption of Lüthi et al. (2010) that horizontal spread can be representative of vertical spread as well (see Figure 3 of Lüthi et al. (2010)). From the point of view of the formation of clathrates, it makes sense that certain layers can facilitate the nucleation process according to their dust content (Ohno et al., 2010). With dust content changing at the centimeter-scale as snow gets deposited, it is expected that clathrates will be formed unevenly throughout the BCTZ, instead of the idealized linear transition from bubbles to clathrates with increasing depth and hydrostatic pressure.

The results from bag #2884 support the claim that the fast variability during the MIS 5e plateau is not atmospheric. The fluctuations found inside a single bag is at odds with the width of the GAD which requires all samples in one bag to essentially have the same CO_2 mixing ratio. The desired high-resolution will inevitably lead to sometimes sampling a bag at depths showing an artificial peak, explaining the observed random fluctuations. It is difficult nevertheless to exclude individual peaks based on this argument, as it would require measuring many more direct neighboring samples to get a glimpse of the true average of that particular bag is behaving.

The next step was to extend the full bag measurements to sections deeper along the core so as to study how centimeter-scale variability acts further away from the BCTZ. Benefiting from the existing measurements during MIS 9–11 we chose bags #4824 (MIS 10; glacial conditions) and #4974 (MIS 11; interglacial conditions). The results in Figure 3.21 correspond to the expected diminished variability in terms of both the vertical and horizontal spread as diffusion has had enough time to erase the sharp centimeter scale variability (Lüthi et al. (2010); see also Table 3.5). It also helps to explain why Nehrbass-Ahles et al. (2020)

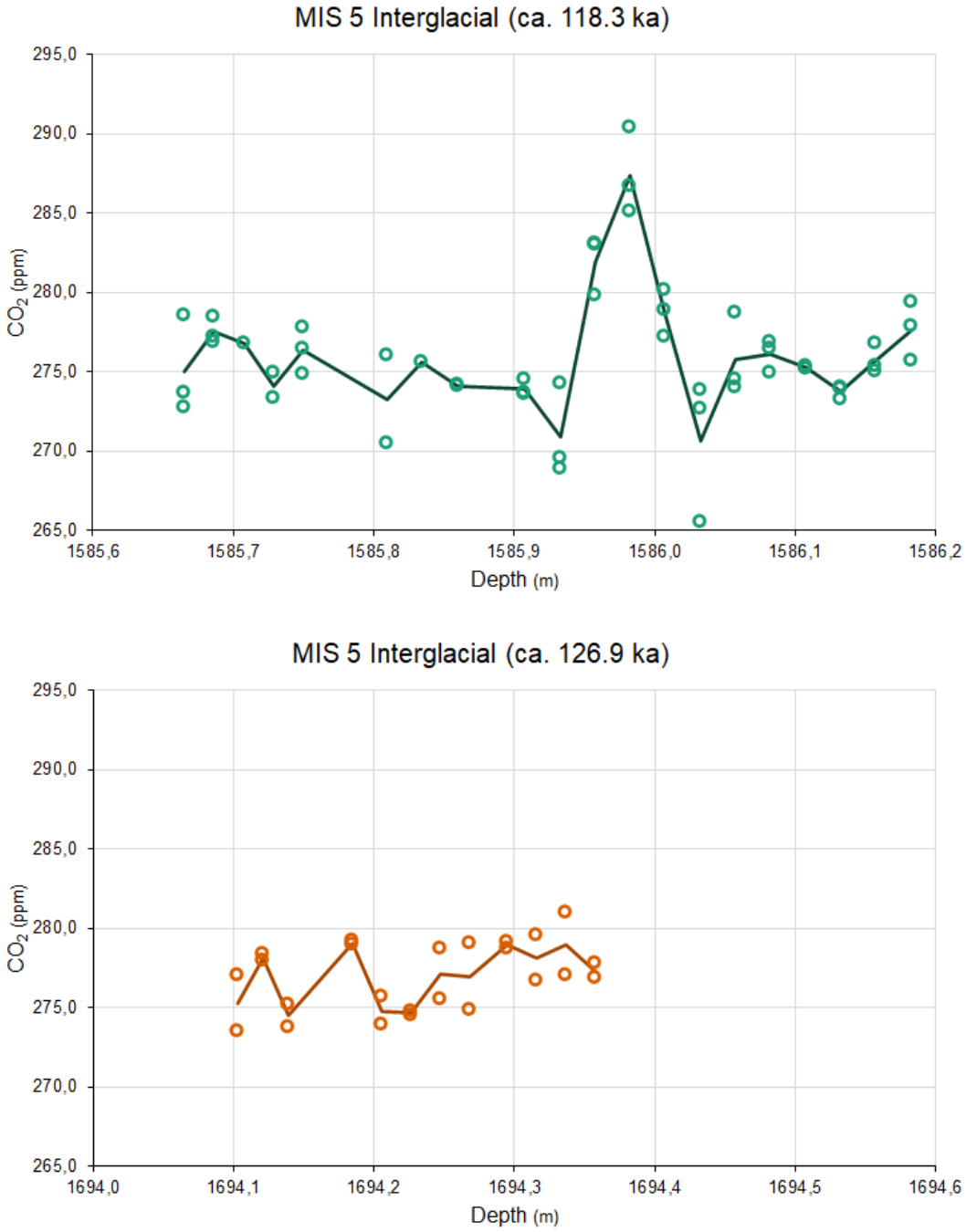

Figure 3.20: Full bag experiment for bags #2884 (top) and #3081 (bottom), both belonging to the MIS 5e plateau. The uncertainty associated with each individual data point is 1 ppm. Note that less than 30 cm were available for Bag #3081, and at that point the cheese-shaped sample cutting scheme had not yet been developed.

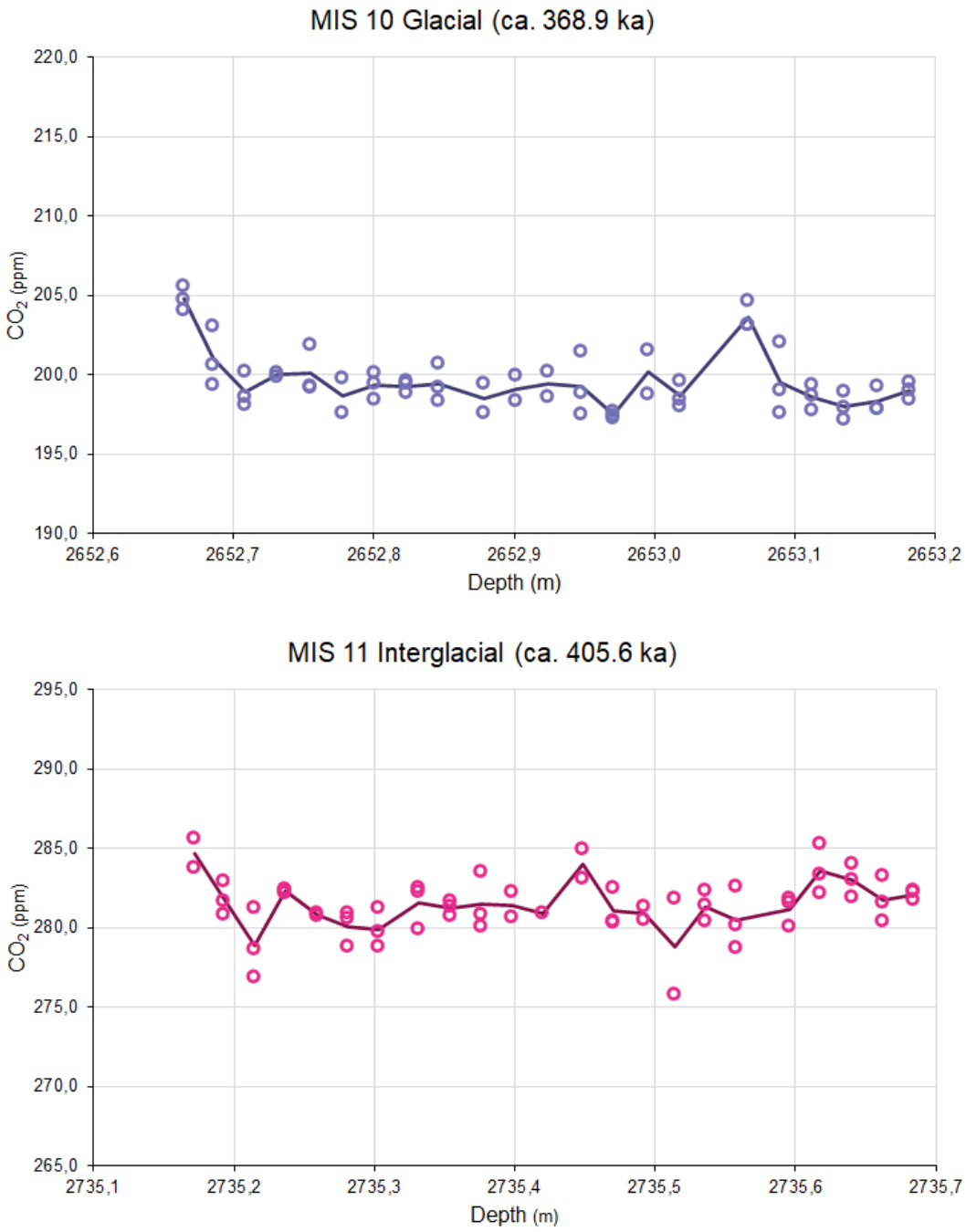

Figure 3.21: Full bag experiment for bags #4824 (top) and #4974 (bottom). The uncertainty associated with each individual data point is 1 ppm.

Table 3.5: Results from the "Full bag" experiment. Age calculated using the AICC12 age scale (Bazin et al., 2013; Veres et al., 2013). CO_2 is the average of all depth levels within the bag. $1\sigma_{horizontal}$ is the average of all individual standard deviations between replicates of a single depth level. $1\sigma_{vertical}$ is the standard deviation considering the average CO_2 of each depth level.

Full bag experiment				
#EDC bag	#2884	#3081	#4824	#4974
$\text{Depth}_{initial}$ (m)	1585.67	1694.10	2652.66	2735.17
Depth_{final} (m)	1586.18	1694.36	2653.18	2735.68
$\text{Age}_{initial}$ (ka)	118.32	126.89	367.80	405.53
Age_{final} (ka)	118.37	126.90	368.06	405.70
δ_{age} (ka)	0.05	0.01	0.24	0.17
$\overline{CO_2}$ (ppm)	276.0	277.0	199.6	281.4
$1\sigma_{horizontal}$ (ppm)	1.7	1.4	1.1	1.3
$1\sigma_{vertical}$ (ppm)	3.7	1.8	1.7	1.4

obtained a smooth CO_2 record during MIS 9–11, while the MIS 5 exhibits greater variability, even though the extraction system was the same. No striking difference is apparent between measurements in glacial or interglacial ice, apart from the expected lower CO_2 concentrations and TAC values (not shown) for the glacial data set. This is important because it suggests that gradients in accumulation rates are not a driving factor behind the variability. The results also replicate well what had already been found by Nehrbass-Ahles et al. (2020).

Figure 3.22 summarizes in a jitter plot the spread of the various bags measured, together with the standard deviation of standard gas and EK measurements. The latter two represent the reproducibility of the LI-COR and the CIM, respectively, apart from fluctuations of the gases or shape-related issues with the EK samples. MIS 5 bags scatter significantly more than MIS 10/11 bags, although admittedly the comparison could improve with a larger sample number.

Despite the conclusion that the overall variability during MIS 5e does not reflect a true atmospheric signal, this does not rule out that the interglacial acme was void of any climatic events or trends. Marked atmospheric CO_2 changes have been seen during other interglacial periods, namely the Holocene and MIS 11. Specifically, at around the turn of 17^{th} century, during the period commonly labeled as the "Little Ice Age", atmospheric CO_2 concentrations dropped 7–10 ppm in 20–50 years, as recorded in the Law Dome and WAIS records (Etheridge et al., 1996; MacFarling Meure et al., 2006; Ahn et al., 2012). Other records from Dronning Maud Land ice cores also show a decreasing trend which has been smoothed out according to lower accumulation rates (Siegenthaler et al., 2005; Rubino et al., 2016). It cannot thus be excluded that similar events also took place during MIS 5e. In the case of our record, the atmospheric imprint is either mixed among the centimeter-scale variability or it was not captured at all due to the wide GAD of the EDC ice core.

Going back earlier in the Holocene, a high-resolution record from Siple Dome was obtained with the intent to investigate whether the 8.2 ka event had an accompanying imprint in atmospheric CO_2 (Ahn et al., 2014). Siple Dome is a high accumulation site (12.4 cm yr^{-1}

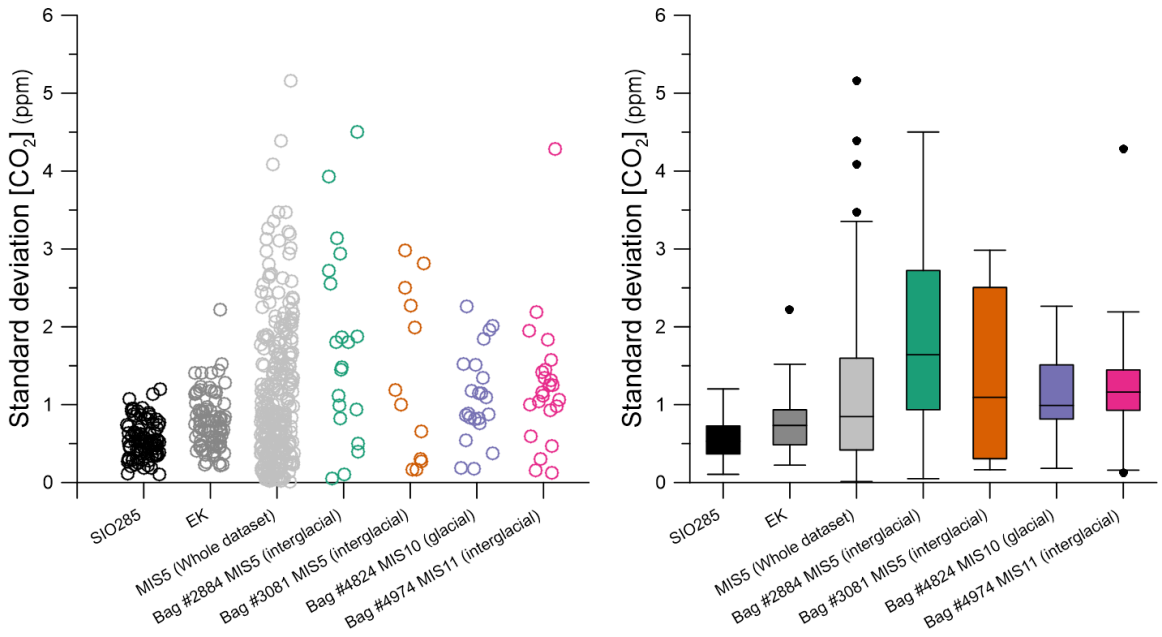

Figure 3.22: Left: Jitter plot for different datasets acquired with the CIM, in order to study the reproducibility of the system and the horizontal spread of true replicates on an ice core. For SIO285 (standard gas; N=87) and EK (gas free ice; N=83) each circumference represents the standard deviation of an ensemble of 5–7 daily measurements. For all other datasets, each circumference represents the standard deviation between replicates (2–3) of a single depth level. "MIS 5 (Whole dataset)" encompasses N=283 depth levels, 104–135 ka. Right: Same as left, but displayed in box plots. Box boundaries represent the interquartile range (IQR) with the horizontal bar as the median. Whiskers display the extreme values as $1.5 \times IQR$ and Black dots are outliers. See Table 3.5 for more details.

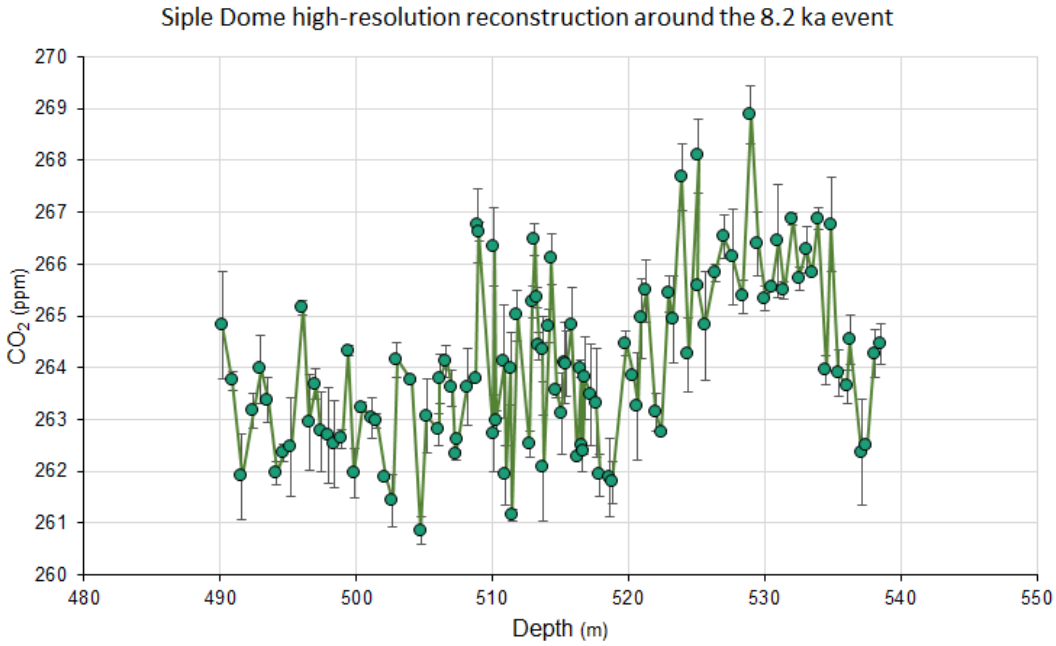

Figure 3.23: High-resolution reconstruction of atmospheric CO_2 concentrations across the 8.2 ka event from the Siple Dome ice core (Ahn et al., 2014).

of water equivalent), roughly five times higher than what is found at the EDC site (Brook et al., 2005). This feature, together with the relatively low ice thinning for this time period, allowed for an average resolution below 16 years, while sampling approximately every 45 cm (see Figure 3.23). Ahn et al. (2014) inferred the presence of fast decadal variations of 3–4 ppm by applying a Gaussian filter. No detailed explanation was given pertaining the origin of the abrupt variability other than being a background oscillation. However, the presence of the filter may suggest that the authors did not interpret the raw data as portraying the true atmospheric signal, even though the oscillations were 3–4 times bigger than the reported error. If they were a true climatic signal, then events similar in magnitude such as the Little Ice Age would have to have been a very pervasive feature of the Holocene climate. A simpler explanation is that the observed variability is also a product of CO_2 artefacts being provoked by occlusion processes (Lüthi et al., 2010). They are enhanced by the fact that, being a relatively young record at 500 m depth, smoothing processes due to neither diffusion nor thinning cannot be playing a big role at this point. Furthermore, the mean sampled depth of 7 cm, although bigger than for the MIS 5 record, is likely not enough to average out any sudden spikes in the CO_2 record.

3.3.3 Results from other ice cores

Other centimeter-scale studies have been conducted on other Antarctic ice cores, which generally also show significant non-climatic fluctuations of CO_2 concentrations. In the 1980s, a laboratory intercomparison project took place between the University of Bern and the

University of Grenoble, the two leading institutions performing measurements of CO_2 on ice cores. The results revealed large fluctuations up to 25 ppm within a few centimeters in two Antarctic cores (Barnola et al., 1983). Figure 3.24 shows the results for ice cores from Byrd (A) and Dome Concordia (B). Already then the authors noted heterogeneities during the occlusion process as a plausible explanation. At that time, the different extraction methods were neither as accurate nor as precise as today, but it is important to note that imbalanced extraction efficiencies for bubbles and clathrates did not play a role in the results, as the ice cores that were analysed were not deep enough to contain clathrates, but had only bubbles instead. This is especially interesting as it rules out the fractionation-induced variability invoked for the below BCTZ effect (Lüthi et al., 2010).

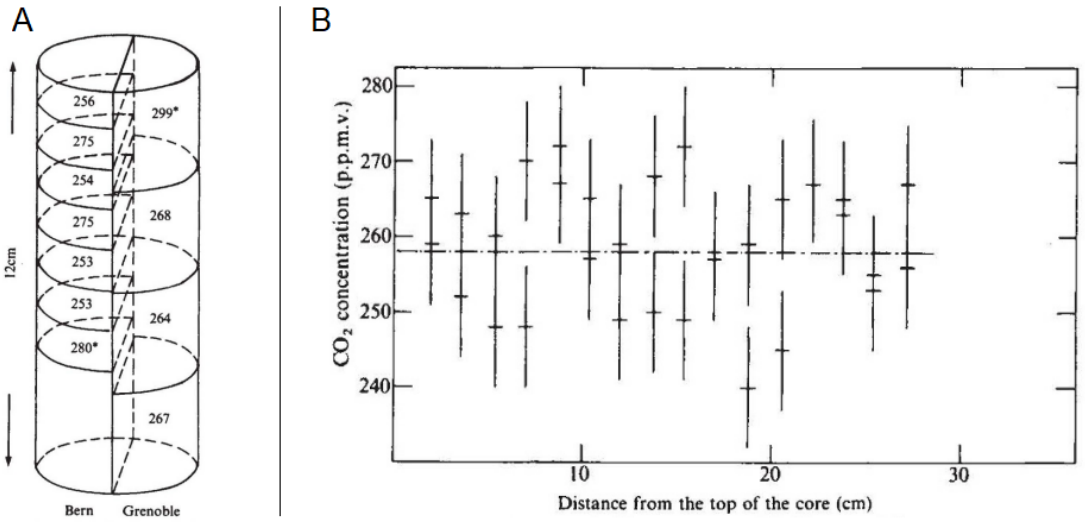

Figure 3.24: Study of centimeter-scale CO_2 variability as part of a laboratory intercomparison project between the University of Bern and the University of Grenoble. A) Results from a split Byrd core, at 401.5 m. The asterisks indicate the presence of cracks. B) CO_2 concentrations for an ice core from Dome C at 132.9 m, with measurements every 1.5 cm obtained at the University of Bern with an early version of a Needle Cracker extraction system. Adapted from Barnola et al. (1983)

In another intercomparison project, this time between the University of Bern and the Oregon State University, ice from Taylor Glacier was used to investigate eventual differences between the dry-extraction devices of the two institutes. The glacier is flowing horizontally, which means that the ice core should follow a particular isochrone as it is being drilled, which makes it a perfect candidate for an intercomparison project. Age is defined according to the direction of flow, but for the purpose of investigating centimeter-scale variations this is not so relevant.

Figure 3.25 shows the results of two cores drilled at different locations, representing Holocene and LGM conditions, although the exact age is unknown. The variability is not so dramatic in this case, but it still is puzzling to explain it. The CIM was performing particularly well at the time of these measurements, so it is hard to attribute the oscillations to experimental conditions. Unfortunately, the intercomparison project came to a halt and

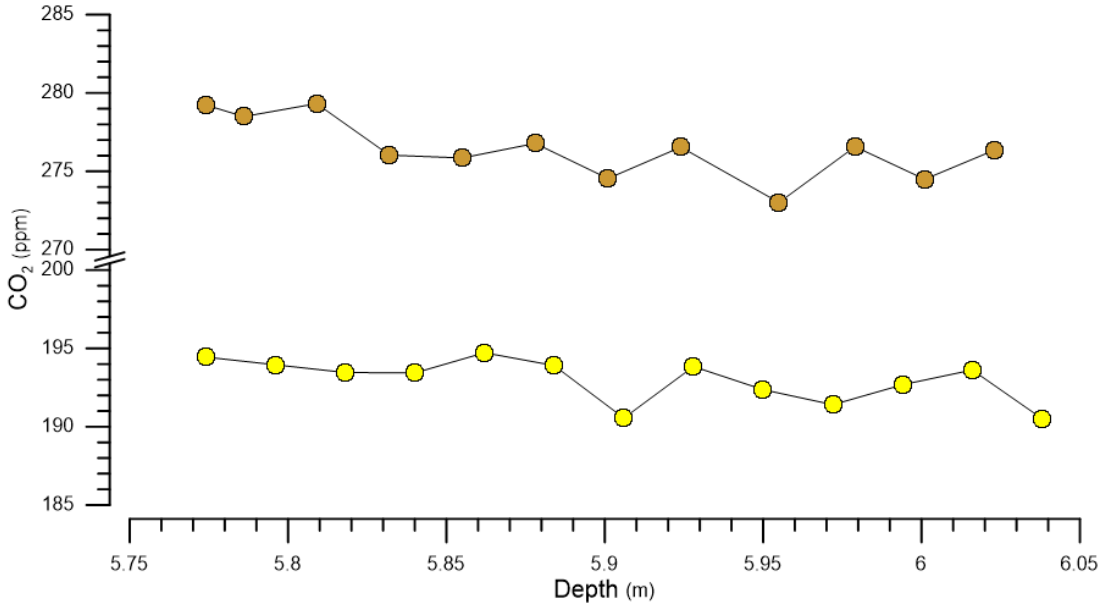

Figure 3.25: Measurements from two cores from Taylor glacier at around 6 m depth. Orange: Holocene. Yellow: LGM. Each datapoint represents a single measurement per depth level. Measurements performed by CNA. See Nehrbass-Ahles (2017).

the results from the Oregon State University are not yet available.

3.4 Retrieving a TAC record

- Tentative TAC records can now be retrieved with the CIM as an accompanying dataset of the CO_2 measurements.
- Retro-calculated records for MIS 5 and MIS 11 are in good agreement with existing records.
- While absolute TAC values are only to be taken at face-value, the typical high-resolution records allow for interpretations in terms of relative changes.

While the CIM was not specifically designed to perform TAC measurements, it came as a pleasant surprise that reasonable TAC records could be derived as a byproduct of pressure readings in the bellow right after extraction. For MIS 5 and MIS 9–11, the obtained results reproduce well the existing datasets, allowing further climatic interpretations. On the plus side, the high resolution helps to overcome the high scatter, and thus millennial-scale trends can be clearly identified. Nevertheless, some assumptions about unknowns in the calculations hinder absolute TAC measurements. It follows then that comparisons with the existing records can only be done after applying a parameterized scaling factor, and

interpretations can only follow if considering relative changes.

TAC is usually expressed in units of $\mathrm{ml\,kg^{-1}}$ at standard temperature and pressure (STP). Hence, using the ideal gas law one can write

$$TAC = \frac{V_0}{m} = \frac{n \cdot R \cdot T_0}{m \cdot p_0} \tag{3.1}$$

where T_0 and p_0 are the standard temperature (273.15 K) and pressure (1.013×10^5 Pa). The volume of the bellow is by far the greatest volume when compared to the CIM and the connecting tubing. This means that when the gas expands from the CIM to the bellow the majority of the gas molecules will be transferred to the bellow. More importantly, the proportion of the molecules reaching the bellow (n_b) with respect to the initial about that is extracted (n) must remain constant, since the expansion procedure does not change from sample to sample. For the purpose of an initial TAC estimate, to first order we can approximate that all the gas is sent into the bellow after extraction and write

$$n \simeq n_b = \frac{p_b \cdot V_b}{R \cdot T_b} \tag{3.2}$$

where the subscript b denotes the bellow. Substituting in Equation 3.1 we get

$$TAC = \frac{p_b}{m} \cdot \frac{V_b}{p_0} \cdot \frac{T_0}{T_b} \tag{3.3}$$

Both p_b and m are determined experimentally, and V_b/p_0 is a constant. The temperature of the sample gas T_b when inside the bellow is unfortunately unknown. The bellow has a large inner surface-to-volume ratio and the metal walls are at room temperature, which facilitates heat exchange. Given the low heat capacity of the small amount of gas present inside the bellow, and given that the expansion still takes 10–20 s, it is reasonable to assume that the gas reaches room temperature until the logging of the pressure at maximum volume ($p@Vmax$). Following a similar argument as above, what is most of all important is that the parameter T_b stays stable across all measurements, since the temperature of the CIM is also relatively stable and because the timings of expansion of the gases are always the same.

Given the uncertainties in the TAC record, Christoph Nehrbass-Ahles at the British Antarctic Survey (BAS) measured a total of 15 samples throughout MIS 5 that were meant to serve as a calibration baseline. Though already producing reliable measurements, the TAC measurement device at BAS is still under final development and no published methods article is available yet. It is important to note that all the TAC measurements performed at BAS were done with ice samples that were immediate neighbors of the CO_2 / TAC samples measured with the CIM, with their average depth levels being 2.5 cm apart. These samples were carefully chosen, and the main priority was that their neighboring samples had had good indications of having been correctly measured in terms of CO_2 and TAC. This means good reproducibility, good vacuum conditions, and good agreement with nearby data points

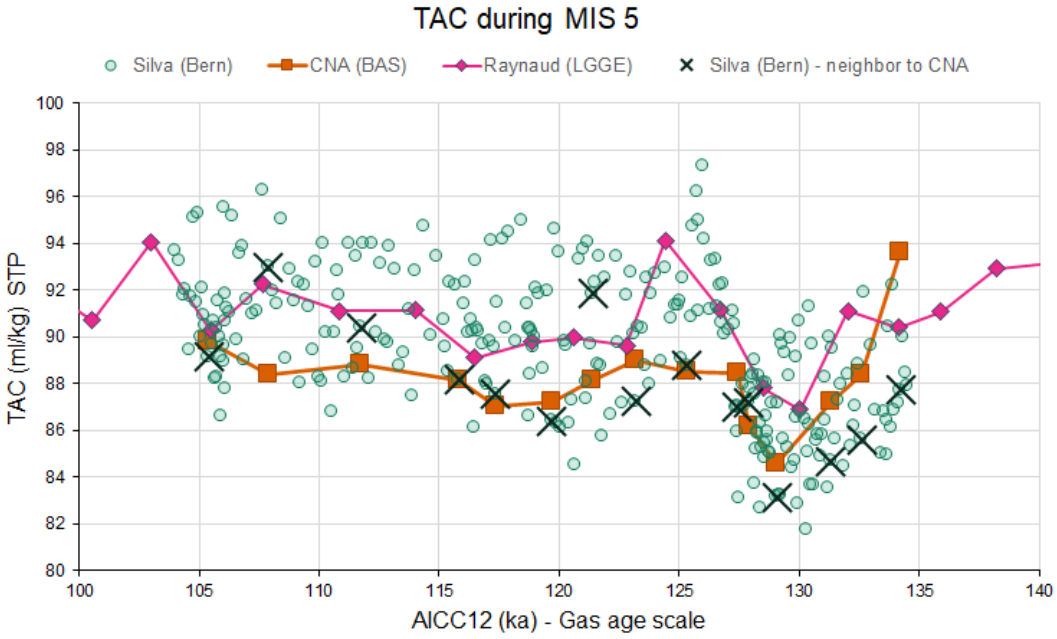

Figure 3.26: TAC datasets for MIS 5. Green circles: extracted with the CIM at the University of Bern (see also Chapter 4. Orange squares: calibration samples extracted at BAS with a dedicated TAC system. They serve as reference for the TAC values from the CIM. Magenta diamonds: extracted at LGGE (Raynaud et al., 2007).

(i.e., no signs of sharp centimeter-scale fluctuations). TAC values for the MIS 5 record were then obtained by calculating a scaling parameter K from the dataset from CNA, so that

$$TAC_{CIM} = K \cdot \frac{p_b}{m} \tag{3.4}$$

where the K parameter minimizes the residuals between the Bernese and the British dataset. The residuals were calculated taking only into consideration the Bernese samples that were direct neighbors to the British samples.

Figure 3.26 depicts the TAC record for MIS 5, together with the record from (Raynaud et al., 2007) and the calibration measurements by CNA. Despite the high level of scatter, the high-resolution CIM TAC record reveals an abrupt shift in the range 129–126 ka that had not been sufficiently resolved by the other reconstructions.

It also stands out that the chosen samples to be measured at BAS generally seem to be at the lower limit of the CIM record, together with their vertical neighbors. This suggests that the spread seen in the CIM TAC record is not the product of random fluctuations around the true average value. Instead, it is likely that the correct baseline for TAC is near the lower limit of the CIM TAC record, with all the other positively offset data points having been artificially enriched in TAC through poor vacuum conditions. This conclusion is only possible because I selected samples for BAS that I knew were in good conditions and whose neighboring ice pieces had been measured for CO_2 concentrations successfully. This makes it very unlikely, statistically speaking, that they would all belong to the lower bound of the

data set. It is worthy of note that the two TAC data points measured with the CIM in Bern that are clearly above the lower bound (at ca. 107 and 121 ka; black crosses) do not show any significant deviations in their respective CO_2 concentrations with respect to other neighboring data points.

The uncertainty of the weight of the sample contributes to the same order of magnitude as the uncertainty of the bellow temperature towards the final TAC uncertainty ($\sim \pm 4\,\mathrm{ml\,kg^{-1}}$). The lack of precision while weighing the sample in the cold room can definitely be improved with a more suitable scale and a more careful procedure. This effect of sample mass adds random scatter as there is no positive or negative bias in the weight measurement. The sublimation and accompanying degassing events that take place during the evacuation phase, however, are leading to a negative bias in the TAC calculation. On top of this, the CIM has a 90–100% extraction efficiency for clathrated ice, likely varying with the level of sharpness of the shaving knife. This incomplete extraction efficiency has been reported in measured samples from the BCTZ from Talos Dome (Bereiter et al., 2012). In that study, the authors found systematically too low CO_2 concentrations as the result of the preferential opening of bubbles over clathrates, and the known CO_2 enrichment of clathrated iced over bubbly ice.

References

Ahn, J., Brook, E. J., and Buizert, C. (2014). Response of atmospheric CO_2 to the abrupt cooling event 8200 years ago. *Geophysical Research Letters*, 41(2):604–609.

Ahn, J., Brook, E. J., Mitchell, L., Rosen, J., McConnell, J. R., Taylor, K., Etheridge, D., and Rubino, M. (2012). Atmospheric CO_2 over the last 1000 years: A high-resolution record from the West Antarctic Ice Sheet (WAIS) Divide ice core. *Global Biogeochemical Cycles*, 26(2).

Andersson, P. U., Någård, M. B., Witt, G., and Pettersson, J. B. C. (2004). Carbon dioxide interactions with crystalline and amorphous ice surfaces. *The Journal of Physical Chemistry A*, 108(21):4627–4631.

Barnola, J. M., Raynaud, D., Neftel, A., and Oeschger, H. (1983). Comparison of CO_2 measurements by two laboratories on air from bubbles in polar ice. *Nature*, 303(5916):410–413.

Bazin, L., Landais, A., Lemieux-Dudon, B., Kele, H. T. M., Veres, D., Parrenin, F., Martinerie, P., Ritz, C., Capron, E., and Lipenkov, V. Y. (2013). An optimized multi-proxy, multi-site Antarctic ice and gas orbital chronology (AICC2012): 120-800 ka. *Climate of the Past*, 9:1715–1731.

Bereiter, B., Lüthi, D., Siegrist, M., Schüpbach, S., Stocker, T. F., and Fischer, H. (2012). Mode change of millennial CO_2 variability during the last glacial cycle associated with a bipolar marine carbon seesaw. *Proceedings of the National Academy of Sciences*, 109(25):9755–9760.

Bereiter, B., Schwander, J., Lüthi, D., and Stocker, T. F. (2009). Change in CO_2 concentration and O_2/N_2 ratio in ice cores due to molecular diffusion. *Geophysical Research Letters*, 36(5).

Brook, E. J., White, J. W., Schilla, A. S., Bender, M. L., Barnett, B., Severinghaus, J. P., Taylor, K. C., Alley, R. B., and Steig, E. J. (2005). Timing of millennial-scale climate change at Siple Dome, West Antarctica, during the last glacial period. *Quaternary Science Reviews*, 24(12):1333–1343.

Etheridge, D. M., Steele, L. P., Langenfelds, R. L., Francey, R. J., Barnola, J.-M., and Morgan, V. I. (1996). Natural and anthropogenic changes in atmospheric CO_2 over the last 1000 years from air in Antarctic ice and firn. *Journal of Geophysical Research: Atmospheres*, 101(D2):4115–4128.

Fourteau, K., Faïn, X., Martinerie, P., Landais, A., Ekaykin, A. A., Lipenkov, V. Y., and Chappellaz, J. (2017). Analytical constraints on layered gas trapping and smoothing of atmospheric variability in ice under low-accumulation conditions. *Climate of the Past*, 13(12):1815.

Fourteau, K., Martinerie, P., Faïn, X., Ekaykin, A. A., Chappellaz, J., and Lipenkov, V. (2020). Estimation of gas record alteration in very low-accumulation ice cores. *Climate of the Past*, 16(2):503–522.

Isahak, W. N. R. W., Ramli, Z. A. C., Ismail, M. W., Ismail, K., Yusop, R. M., Hisham, M. W. M., and Yarmo, M. A. (2013). Adsorption–desorption of CO_2 on different type of copper oxides surfaces: Physical and chemical attractions studies. *Journal of CO_2 Utilization*, 2:8–15.

Leuenberger, M. C., Schibig, M. F., and Nyfeler, P. (2015). Gas adsorption and desorption effects on cylinders and their importance for long-term gas records. *Atmospheric Measurement Techniques*, 8(12):5289–5299.

Lüthi, D., Bereiter, B., Stauffer, B., Winkler, R., Schwander, J., Kindler, P., Leuenberger, M., Kipfstuhl, S., Capron, E., Landais, A., Fischer, H., and Stocker, T. F. (2010). CO_2 and O_2/N_2O variations in and just below the bubble-clathrate transformation zone of Antarctic ice cores. *Earth and Planetary Science Letters*, 297(1-2):226–233.

MacFarling Meure, C., Etheridge, D., Trudinger, C., Steele, P., Langenfelds, R., van Ommen, T., Smith, A., and Elkins, J. (2006). Law Dome CO_2, CH_4 and N_2O ice core records extended to 2000 years BP. *Geophysical Research Letters*, 33(14).

Marcott, S. A., Bauska, T. K., Buizert, C., Steig, E. J., Rosen, J. L., Cuffey, K. M., Fudge, T. J., Severinghaus, J. P., Ahn, J., Kalk, M. L., McConnel, J. R., Sowers, T., Taylor, K. C., White, J. W. C., and Brook, E. J. (2014). Centennial-scale changes in the global carbon cycle during the last deglaciation. *Nature*, 514(7524):616–619.

Nehrbass-Ahles, C. (2017). *Millenial-scale atmospheric CO_2 reconstructions using multiple Antarctic ice cores*. PhD thesis, University of Bern.

Nehrbass-Ahles, C., Shin, J., Schmitt, J., Bereiter, B., Joos, F., Schilt, A., Schmidely, L., Silva, L., Teste, G., Grilli, R., Chappellaz, J., Hodell, D., Fischer, H., and Stocker, T. F. (2020). Abrupt CO_2 release to the atmosphere under glacial and early interglacial climate conditions. *Science*, 369(6506):1000–1005.

Ohno, H., Lipenkov, V. Y., and Hondoh, T. (2010). Formation of air clathrate hydrates in polar ice sheets: heterogeneous nucleation induced by micro-inclusions. *Journal of Glaciology*, 56(199):917—-921.

Petit, J.-R., Jouzel, J., Raynaud, D., Barkov, N. I., Barnola, J.-M., Basile, I., Bender, M., Chappellaz, J., Davis, M., Delaygue, G., Delmotte, M., Kotlyakov, V. M., Legrand, M., Lipenkov, V. Y., Lorius, C., Pépin, L., Ritz, C., Saltzman, E., and Stievenard, M. (1999). Climate and atmospheric history of the past 420,000 years from the Vostok ice core, Antarctica. *Nature*, 399(6735):429.

Raynaud, D., Lipenkov, V., Lemieux-Dudon, B., Duval, P., Loutre, M.-F., and Lhomme, N. (2007). The local insolation signature of air content in antarctic ice. a new step toward an absolute dating of ice records. *Earth and Planetary Science Letters*, 261(3):337–349.

Rubino, M., Etheridge, D. M., Trudinger, C. M., Allison, C. E., Rayner, P. J., Enting, I., Mulvaney, R., Steele, L. P., Langenfelds, R. L., Sturges, W. T., Curran, M. A. J., and Smith, A. M. (2016). Low atmospheric CO_2 levels during the Little Ice Age due to cooling-induced terrestrial uptake. *Nature Geoscience*, 9(9):691–694.

Siegenthaler, U., Monnin, E., Kawamura, K., Spahni, R., Schwander, J., Stauffer, B., Stocker, T. F., Barnola, J.-M., and Fischer, H. (2005). Supporting evidence from the EPICA Dronning Maud Land ice core for atmospheric CO2 changes during the past millennium. *Tellus B: Chemical and Physical Meteorology*, 57(1):51–57.

Silva, L., Nehrbass-Ahles, C., Schmidely, L., Schmitt, J., Fischer, H., and Stocker, T. F. (2022). Centennial-scale CO_2 variability in the last interglacial. *In preparation*.

Spahni, R., Schwander, J., Flückiger, J., Stauffer, B., Chappellaz, J., and Raynaud, D. (2003). The attenuation of fast atmospheric CH_4 variations recorded in polar ice cores. *Geophysical Research Letters*, 30(11).

Veres, D., Bazin, L., Landais, A., Toyé Mahamadou Kele, H., Lemieux-Dudon, B., Parrenin, F., Martinerie, P., Blayo, E., Blunier, T., Capron, E., Chappellaz, J., Rasmussen, S. O., Severi, M., Svensson, A. M., Vinther, B. M., and Wolff, E. W. (2013). The Antarctic ice core chronology (AICC2012): an optimized multi-parameter and multi-site dating approach for the last 120 thousand years. *Climate of the Past*, 9(4):1733–1748.

Chapter 4

Assessing atmospheric CO_2 variability during Marine Isotope Stage 5 based on the EDC ice core

Lucas Silva[1,2], Christoph Nehrbass-Ahles[1,2,3], Loïc Schmidely[1,2], Jochen Schmitt[1,2], Hubertus Fischer[1,2], and Thomas F. Stocker[1,2]

[1]Climate and Environmental Physics, Physics Institute, University of Bern, Switzerland

[2]Oeschger Centre for Climate Change Research, University of Bern, Switzerland

[3]Godwin Laboratory for Palaeoclimate Research, Department of Earth Sciences, University of Cambridge, UK

Manuscript in preparation

Abstract

Ice core records of atmospheric carbon dioxide (CO_2) have shown past CO_2 concentrations playing a key role in glacial-interglacial transitions. Yet, the precise mechanisms behind millennial- and centennial-scale CO_2 variability are still being debated. While glacial terminations have been widely studied, glacial inceptions have received relatively little attention. The last glacial inception offers the best opportunity to do so, as it is still within the reach of high-resolution paleo reconstructions. Here we present an ice core CO_2 dataset covering Marine Isotope Stage 5 (MIS 5; 135–106 ka) with centennial resolution. Our results show stable CO_2 concentrations during MIS 5e for ten thousand years amidst changes in insolation, declining Antarctic temperatures, and climate instability in the Northern Hemisphere. Glacial inception in CO_2 takes place several thousand years after the cooling onset in both poles and already in the presence of extensive ice sheets. While inception was fundamentally driven by an obliquity-based trigger, we propose that late MIS 5e warmth in the Northern Hemi-

sphere also played a key role by critically maintaining global overturning circulation and inhibiting the AMOC from switching to a glacial mode. Only when the northern ice sheets and associated cold hydrographic boundaries reached enough far south to perturb NADW formation did the warm period in the NH end. With it, an AMOC switch to glacial mode allowed deep ocean storage of CO_2 and provoked the late CO_2 drawdown.

4.1 Introduction

Ice cores enable paleo reconstructions of key climate parameters of the Earth (Jouzel et al., 2007; Loulergue et al., 2008; Lüthi et al., 2008). Specifically, air bubbles trapped in Antarctic ice cores contain direct samples of the past atmosphere and allow the reconstruction of carbon dioxide concentrations (CO_2). Antarctic temperature reconstructions using water isotopes show that Antartic temperature and CO_2 covaried strongly across glacial-interglacial cycles (EPICA Community Members, 2004). However, the mechanisms behind the exact interplay and timing of carbon fluxes between multiple reservoirs during glacial-interglacial transitions are yet to be pinned down (Sigman et al., 2021).

While high-resolution ice core studies cover a few key periods of the last 800 ka (Bauska et al., 2021; Marcott et al., 2014; Nehrbass-Ahles et al., 2020; Shin et al., 2020), many gaps remain to be filled. Past interglacials are particularly interesting as they can be used as testbeds to conduct experiments to model future climate (Past Interglacials Working Group of PAGES, 2016). In this regard, Marine Isotope Stage 5 (MIS 5e; 129–116 ka) offers a somewhat warmer-than-today scenario and a multitude of available paleoenvironmental datasets to help constrain boundary conditions (Otto-Bliesner et al., 2017, 2013; Hoffman et al., 2017). Here, we present a record of CO_2 from the EPICA Dome C (EDC) ice core from Marine Isotope Stage (MIS) 5, encompassing termination II (T-II; 135–129 ka), MIS 5e (129–116 ka) and the last glacial inception (116–106 ka). The dataset was obtained with a dry-extraction technique (Bereiter et al., 2013) (Methods). It spans the period 135–106 ka with an average resolution of 110 years, in good agreement with previous ice core datasets of coarser resolution and improving on precision of the data (Bereiter et al., 2012; Landais et al., 2013; Lourantou et al., 2010; Schneider et al., 2013; Petit et al., 1999). According to the EDC gas age distribution (GAD), a resolution of ∼100 years means that two neighboring datapoints in our record share approximately 50% of their gas content (Spahni et al., 2003). This characteristic is a product of firn processes and bubble enclosure characteristics of the EDC ice core, and sets a limit for the detection of sub-centennial climate variability.

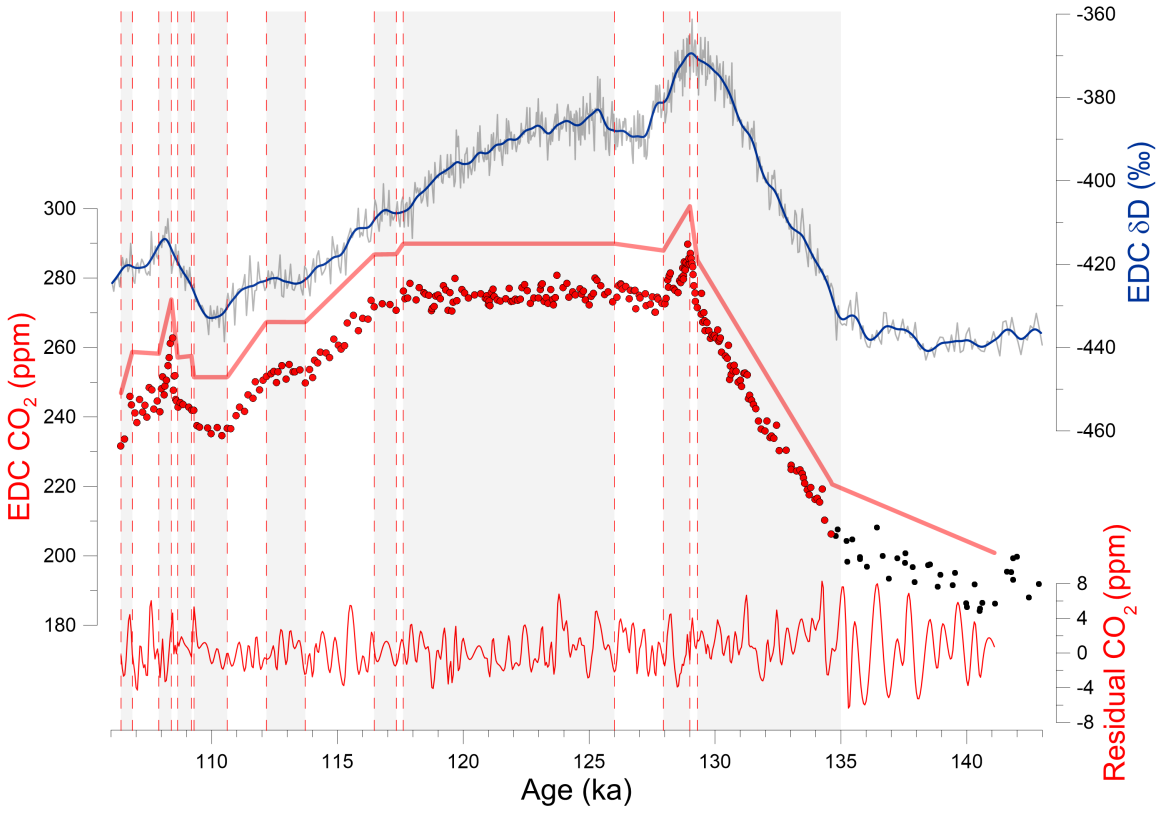

Figure 4.1: CO_2 and δD during MIS 5. From top to bottom: EDC δD (grey; Jouzel et al. (2007)) with a Monte Carlo spline (blue; 1000 year cut off period); EDC CO_2 from this study (red dots) and from a compilation by Shin et al. (2020) (black dots), with a piecewise linear fit (thick red line; shifted by +15 ppm for clarity) and respective residuals (red line; see Methods). Age scale from Extier et al. (2018). Vertical red lines and shaded bars indicate changes in the piecewise linear fit.

Our record highlights the millennial-scale variability of CO_2 as being well approximated by a piecewise linear function (Fig. 4.1). The high resolution allows precise timing of the transitions between these intervals that were not resolved in previous records (Fig. S4.10). On the other hand, we interpret the superimposed CO_2 variability on centennial scales only tentatively, assigning possible climatic fingerprints on an individual basis. In this regard, only some of the centennial-scale features in the CO_2 can be linked to counterparts in the δD record (Fig. 4.2b). This is either caused by a decoupling between the two parameters or due to the CO_2 features not reflecting climate variations. This cautious approach is motivated by a series of experiments that revealed fast CO_2 variability at the centimeter scale within the ice core and not related to the analytical uncertainty (see Section 3.3.2). We propose that this effect originates from fractionating processes during clathrate formation, similar to what happens below the bubble to clathrate transition zone (BCTZ) of the EDML ice core (Lüthi et al., 2010).

4.2 T-II

CO_2 rose linearly with three well-defined rates during T-II (Fig. 4.1). Around 135 ka, the CO_2 rate increased more than threefold, from 3.0 ± 0.3 ppm/ka (141–135 ka; R^2=0.77) to 10.5 ± 0.2 ppm/ka (135–129 ka; R^2=0.99). This transition was coeval with the onset of both Heinrich Stadial 11 (HS 11; 135–130 ka; Fig. 4.2a) and meltwater pulse (MWP) 2B (Fig. 4.2h) (Marino et al., 2015). It has been suggested that the specific orbital configuration of T-II resulted in very strong insolation forcing in the Northern Hemisphere (NH), driving the long HS 11 event and continuous melting of the NH ice sheets (Carlson, 2008). The ensuing freshwater discharge from HS 11 in the NA triggered a shutdown of the Atlantic Meridional Overturning Circulation (AMOC) (Böhm et al., 2015) with the consequent activation of the bipolar seesaw (Stocker and Johnsen, 2003). Accordingly, the gradual warming of the SO and intensified upwelling promoted CO_2 degassing, entailing a positive feedback on atmospheric temperatures (Denton et al., 2010).

Superimposed on the steady linear increase of CO_2 between 135–129 ka, our record suggests three centennial-scale events that may reflect atmospheric variability (Fig. 4.2c, vertical yellow bars). In general, these events can be regarded as small jumps on top of a baseline of increasing CO_2 that are followed by small plateaus. For simplicity, we label them as events #1 (133.6–133.2 ka), #2 (131.25–131.0 ka) and #3 (130.0–129.5 ka). Counterparts of these events are noticeable in the deuterium record (Fig. 4.2b) and have been previously identified (Pol et al., 2014). The co-occurrence of events in CO_2 and Antarctic temperature suggests the existence of another possible CO_2 event at around 132.3 ka, although not sufficiently resolved in our record. It is difficult to pinpoint the specific causes behind each of these short-lived events given the paucity of proxy data for T-II with sub-millennial resolution. However, instead of looking for individual mechanisms and evidence in other proxy records to link them with, it could be framed that the CO_2 T-II record is in itself the result of a sequence of intermittent releases of CO_2 that are followed by relaxation periods. In this way, the idea of a baseline linear increase under equilibrium is removed. As a consequence, the apparent jumps can no longer be perceived as abnormal rates of CO_2 emissions on top of a “natural" trend. In this framework, the plateaus need not necessarily be regarded as relaxation periods but rather as perturbations that decelerated the CO_2 rise. Sustained warming of Antarctica by a weak AMOC would have facilitated episodes of meltwater discharge in the SO from decaying Antarctic ice sheets (Weber et al., 2014; Zhuravleva et al., 2017). The subsequent cooling could have reduced gas exchange due to surface water stratification, acting as a temporary lid to the bottom waters below rich in dissolved inorganic carbon (François et al.,

1997). We hypothesize that such a mechanism of CO_2 slowdown was the underlying cause for the plateaus seen during events #2 and #3. It has been shown that the long HS 11 event contained internal variability, translated into three separate periods of varying discharge (Tzedakis et al., 2018). It cannot be excluded that this did not have an impact on the status of the AMOC, which may thus have briefly left its off mode during HS 11 and modulated specific rates of CO_2 emission (Banderas et al., 2015); available $^{231}Pa/^{230}Th$ records, a proxy for AMOC strength, are nevertheless too coarse to confirm or disproof such short-lived changes (Böhm et al., 2015).

The plateau during event #3 deserves nevertheless more attention. It was previously reported as a decoupling period between CO_2 and Antarctic temperature (Landais et al., 2013). However, a more recent and better resolved deuterium record also reveals a coeval plateau, allowing us to dismiss this hypothesis (Pol et al., 2014). In contrast with the previous two plateaus, it was simultaneous with reduced sea surface temperatures (SSTs) in the Atlantic sector of the Subantarctic Zone (SAZ) (Fig. 4.2g), subdued Mediterranean SSTs (Fig. 4.2f), constant nitrous oxide (N_2O) emissions (Fig. 4.2e), and the end of HS 11 in the North Atlantic (NA) (Fig. 4.2a). We suggest that the likelihood of a meltwater discharge episode in the SO was increased at this time with respect to the previous events #2 and #3, as Antarctica approached peak MIS 5e warmth. It has also been suggested that the sea level rise following MWP-2B (and hence HS 11) was driven mostly by Antarctic ice reduction, as the bulk of the NH ice sheets collapsed earlier in T-II (Marino et al., 2015).

Collectively, the CO_2 plateaus during T-II were likely driven by intrinsically different causes than those found during T-I. Indeed, the plateaus in T-I were much longer, lasting one to two thousand years, and can only exclusively be found after abrupt CO_2 releases, which do not have counterparts in T-II (Marcott et al., 2014). Furthermore, the CO_2 jumps at 14.8 ka and 11.7 ka are directly connected to the onset of the Bølling-Allerød period and the end of the Younger Dryas. These transitions involved major reorganizations of the AMOC, which in the case of T-II only happened at a later stage of the termination. It is remarkable that a third CO_2 jump occurring at 16.3 ka could not be resolved in an earlier reconstruction using the EDC ice core (Monnin et al., 2001). It cannot be excluded that our record failed to resolve very abrupt events due to the relatively wide gas-age distribution (GAD) of the EDC ice core. Nevertheless, all three abrupt events during T-I and associated plateaus showed a concomitant release of CH_4. The absence of such CH_4 releases during T-II (Fig. 4.2d) leads us to suggest that the centennial-scale CO_2 variability found during terminations I and II had fundamentally different causes.

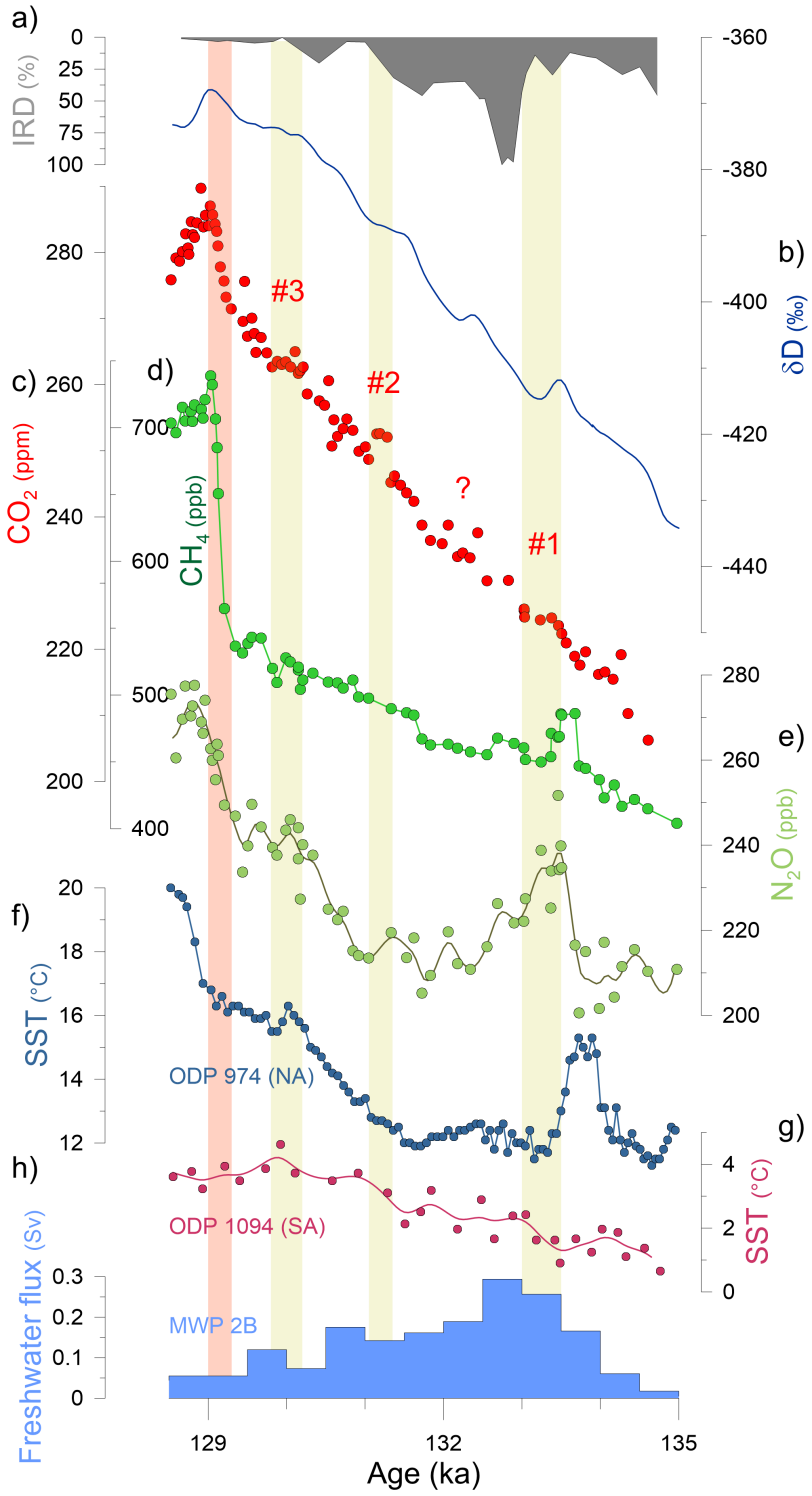

Figure 4.2: Compilation of ice core and marine records during T-II. a) IRD (%) at site ODP984 (NA; Bjorn drift, south of Iceland; Mokeddem et al. (2014)); b) EDC δD (Monte Carlo spline with 1000 year cut off period; Pol et al. (2014)); c) EDC CO_2 from this study (red dots) #1–3 and "?" indicate sub-millennial events. d) EDC CH_4 (Schmidely et al., 2021; Loulergue et al., 2008); e) EDC N_2O (Monte Carlo spline with 1000 year cut off period; Schmidely et al. (2021)); f) SST from site ODP974 on a radiometrically constrained age-scale (Mediterranean; Alboran Sea; Martrat et al. (2014); Marino et al. (2015); g) SST from site ODP1094 (SA; Hodell et al. (2003)); h) freshwater flux (Marino et al., 2015). All ice core records transferred to the age scale from Extier et al. (2018).

4.3 Overshoot

The end of T-II saw a 15 ppm increase of CO_2 in less than 350 years (Fig. 4.3e; vertical red bar). The rate of increase, 50 ± 4 ppm/ka (R^2=0.97), represents nearly a fivefold increase with respect to the rise rate of CO_2 throughout the rest of T-II. While this transition between different rates is very abrupt, it is worth mentioning that changes in accumulation rate may have also shaped the CO_2 evolving slopes. As Antarctic temperature rose, higher accumulation rates accelerated the bubble enclosure process, diminishing the effect of smoothing processes and enabling the gas phase of the ice core archive capable of recording a signal closer to the prevailing atmospheric content at that time.

A sharp rise of CH_4 took place simultaneously with the CO_2 increase (Fig. 4.3f), following the pattern of abrupt CH_4 increases observed at the end of all terminations of the past 800 ka (Loulergue et al., 2008). The appearance of northern-sourced waters at ODP983 (NE Atlantic) and ODP1063 (NW Atlantic) at that time is suggested by a positive shift in benthic foraminiferal $\delta^{13}C$ on both sites at the end of T-II (Fig. S4.11) (Deaney et al., 2017; Barker et al., 2015; Channell et al., 1997). A shift towards less radiogenic values in records of the neodymium isotopic composition (ε_{Nd}) in the same period (Böhm et al., 2015) supports the claim of an AMOC resumption through renewed North Atlantic Deep Water (NADW) formation (Fig. S4.11). The timing of this reinvigoration is coeval with the CO_2 and CH_4 overshoots in our records, following an overall mechanism similar to the CO_2 jumps at 14.8 ka and 11.7 ka during T-I (Marcott et al., 2014) and the rise associated with Dansgaard-Oeschger (D-O) event 8 during the last glacial period (Bauska et al., 2018). Moreover, all events also saw rising N_2O, no distinguishable fingerprint in $\delta^{13}C_{atm}$, either stable or continued warming in Antarctica and greater NADW formation (Schneider et al., 2013; Bauska et al., 2018; Schilt et al., 2010; Schmitt et al., 2012; Bauska et al., 2016). The CO_2 jumps have been linked in the literature to various factors including changes in solubility with enhanced NADW (Menviel et al., 2015), fast releases from the deep Southern Ocean (SO) under transient conditions (Rae et al., 2018) or displacements of the Southern Hemisphere (SH) Westerlies (SHW) (Toggweiler et al., 2006). Other terminations in the past 800 ka also exhibit an overshoot of CO_2 and CH_4, but marine records are too scarce and poorly resolved to infer AMOC changes at those times.

Antarctic temperature, as seen in the deuterium record proxy, increased only slightly during the 15 ppm CO_2 overshoot of MIS 5e (Fig. 4.3d), which contrasts with the apparent link discussed before between subevents in both deuterium and CO_2. Despite the possible causal link between CO_2 and Antarctic temperature during the subevents, it is nonetheless important to note that the increments in CO_2 (<5 ppm)

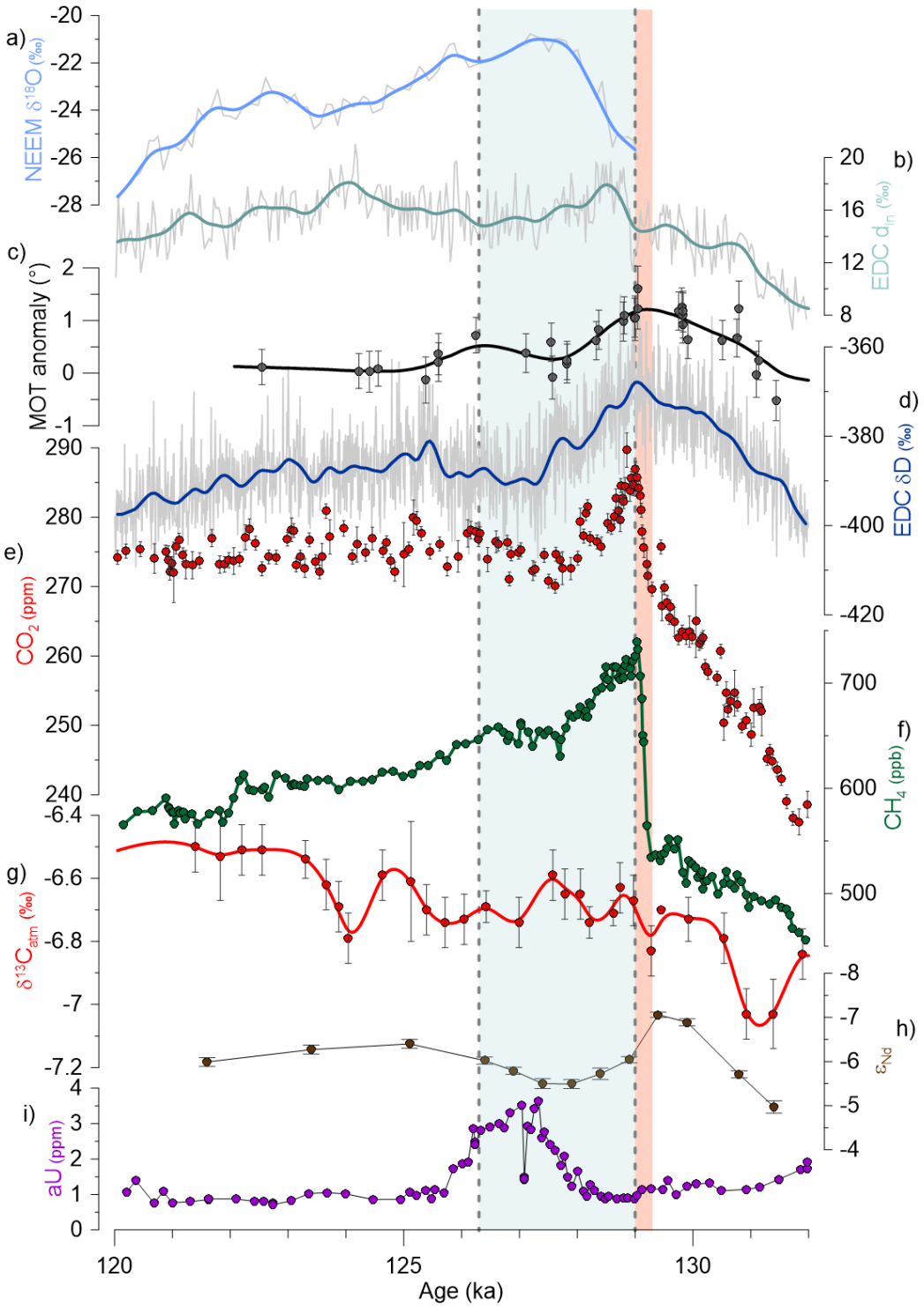

Figure 4.3: Compilation of ice core and marine records for early MIS 5e. a) NEEM $\delta^{18}O$ NEEM Community Members (2013); b) EDC deuterium excess (d_{ln}; Landais et al. (2021)); c) MOT anomaly and original spline (Shackleton et al., 2020); d) EDC deuterium (Pol et al., 2014)); b) EDC δD (Monte Carlo spline with 1000 year cut off period; Pol et al. (2014)); e) EDC CO_2 (this study); f) EDC CH_4 (Schmidely et al., 2021; Loulergue et al., 2008); g) EDC atmospheric $\delta^{13}C$ (Schneider et al., 2013); h) ε_{Nd} from site PS1768-8 (SO, Atlantic sector, Weddell Sea, Huang et al. (2020)); authigenic Uranium from site ODP1094 (SO, Atlantic sector, Hayes et al. (2014)). Vertical red bar indicates the sharp transition to the CO_2 overshoot. Vertical blue bar indicates the period of CO_2 drawdown and slight undershoot. All splines obtained with a Monte Carlo method and a cut off period of 1000 years. All ice core records transferred to the age scale from Extier et al. (2018). Marine records in their original age scale.

could not have been enough to drive temperature upwards through a small increase in radiative forcing. Instead, the coupling between CO_2 and deuterium during the subevents is perhaps signaling that the SO, a moisture source for the EDC site, was regulating both CO_2 and local Antarctic temperature at the same time. In this regard, the moment of the CO_2 overshoot seems to mark a decoupling between the SO and CO_2. This may be interpreted in different ways: either the deuterium record became limited as a proxy for Antarctic temperature, or the CO_2 source for the overshoot was external to SO processes, or both. Changes in the SO moisture source could have affected the isotopic composition of the advected moisture, imprinting on the deuterium signal. However, the deuterium excess record shows no change during the overshoot (Fig. 4.3b). Moreover, a recent record of mean ocean temperature (MOT) also does not show an overshoot (Fig. 4.3c) (Shackleton et al., 2020). It is important to state that lead-lag relationships between CO_2 and Antarctic temperature are very hard to establish, due to the gas age - ice age difference (Δage) that exists in ice cores. Even during peak warmth conditions such as ca. 128 ka, when accumulation rates are at a maximum, the EDC site has a Δage in the order of 1.5-2 ka (Bazin et al., 2013).

The lack of a clear change in $\delta^{13}C_{atm}$ (Fig. 4.3g) constrains possible CO_2 sources. For instance, ventilation of old carbon-enriched layers from glacial times could explain the CO_2 rise, but would simultaneously deplete $\delta^{13}C_{atm}$. Borrowing studies from the similar CO_2 abrupt rise at the Bølling onset (e.g. 12 ppm rise, coeval AMOC invigoration, sharp CH_4 peak, no major change in $\delta^{13}C_{atm}$), two explanations can be proposed. One modelling study found rapid AMOC invigoration to induce abrupt increases in CO_2 and CH_4, invoking changes in land carbon storage (Köhler et al., 2005). Very recently, a fast northward expansion of Antarctic intermediate water (AAIW) coeval with the CO_2 rise has been demonstrated from an Atlantic core with high sedimentation rate during T-I (Yu et al., 2022). This fast moving water mass is suggested to have been responsible from 4–8 ppm of the total change, inducing outgassing through its particularly inefficient carbon sequestering characteristics. Both mechanisms could be linked to the CO_2 overshoot at the end of T-II, although differences in the initial climatic conditions at the onset of the abrupt rise might play an additional role (Köhler et al., 2005).

The CO_2 overshoot was followed by a slight reduction of CO_2 relative to the long-term mean of the CO_2 plateau. An authigenic uranium (aU) record from the SA, a proxy for bottom water oxygenation, shows a surprising peak well into the interglacial, centered around 127 ± 1 ka, indicating a period of poor oxygen supply during the CO_2 reduction, i.e. an AABW reduction event (Fig. 4.3i) (Hayes et al., 2014). Another recent aU record from the Indian SAZ also posits an AABW reduction event during the MIS 5e plateau, albeit less well-resolved (Amsler et al., 2021). An effort

to extend the aU record until 470 ka did not find equivalent AABW reductions after the MIS 7e or the MIS 9e interglacial overshoots, suggesting that the MIS case may be a singular event (Glasscock et al., 2020). The onset of the AABW reduction event matches a deuterium excess fast transition, indicating a shift in moisture sources from the Indian sector of the SO (Fig. 4.3b) (Landais et al., 2021). One possible sequence of events could start with rising Antarctic temperatures at the end of T-II that progressively lead to more Antarctic ice sheet melting. At a critical threshold (peak temperature), massive freshwater discharge would spill into the SO. Open ocean conditions with largely absent seasonal sea ice (Guarino et al., 2020; Chadwick et al., 2020; Yan et al., 2021) could have facilitated the spread of fresh water in the upper layers, establishing a density gradient that effectively trapped CO_2 through reduced vertical mixing, decreasing atmospheric CO_2. The freshwater event leads to a reorganization of the SHW, hinted at by the shift in deuterium excess (d_{excess}). An equatorward push of the SHW would move the westerlies away from of the Antarctic Circumpolar Current and its carbon-rich mid-depth waters, decreasing CO_2 through reduced SO leakage (Anderson et al., 2009). Attributing the CO_2 uptake to increased marine storage is also coherent with a -0.1‰/-0.2‰ drop in $\delta^{13}C_{atm}$ (128–125 ka), a change that is even more pronounced considering the overall rising trend in the period 130–120 ka (Fig. 4.3g) (Schneider et al., 2013). Finally, a recent reconstruction from the Weddell Sea shows a period with less negative ε_{Nd}, supporting the hypothesis of AABW reduction (Fig. 4.3h) (Huang et al., 2020). The large duration of this reduction (ca. 2.5 thousand years) led to a 5–10 ppm undershoot of CO_2 with respect to the 127–117 ka baseline. This is conceptually interesting, as it evidences a mechanism able to pull CO_2 from transiently abnormal high concentrations to below equilibrium concentrations under the boundary conditions of an interglacial period. In this light, it is possible that the AABW reduction even helped to partially shape the peak of the CO_2 overshoot, although this cannot be confirmed due to age scale uncertainties. Moreover, if the AABW reduction drove CO_2 uptake and, indirectly, Antarctic cooling, then it might further explain the known interhemispheric delay in peak warmth conditions between the Northern and Southern hemispheres (Fig. 4.3a and 4.3d) (NEEM Community Members, 2013; Govin et al., 2012; Capron et al., 2014).

A peculiarity of our CO_2 data is the presence of a peak immediately after the overshoot, ca. 127 ka. While taking place under different orbital configurations (Yin and Berger, 2012), this peak during MIS 5e shares some similarities with the only other interglacial CO_2 peak ever found, during MIS 11c (ca. 415 ka) (Nehrbass-Ahles et al., 2020). Namely, no marked CH_4 changes (Fig. 3f), rising sea levels (Grant et al., 2014) and warm conditions both in the NH and the SH (see also Section 1.3.2).

Regarding the AMOC, the MIS 5e peak is coeval with increased NADW formation and an associated invigoration of the AMOC (Galaasen et al., 2014), while for the MIS 11c peak the status of the AMOC is unclear. One possibility is that the MIS 5e peak is linked to the sharp reversal seen in the aU record at around 127 ka. Assuming AABW reduction as the cause for the broad peak in aU, the contrasting reversal event suggests a mechanism of a different nature. Changing wind belts could enhance deep ventilation and promote upwelling, explaining both signals in CO_2 and aU, but there is no evidence of such changes. Records of SO productivity could help constrain hypotheses, but very high-resolution would be required in this particular time period (Jaccard et al., 2013; Studer et al., 2015).

4.4 Plateau and inception

4.4.1 Orbital forcing

Our results confirm a decoupling between CO_2 and Antarctic temperature at the end of the MIS 5e plateau, previously reported in other studies (Fischer et al., 1999; Hodell et al., 2001; Schneider et al., 2013). It is important to stress that Antarctic temperature does not necessarily reflect global average temperature, to which CO_2 is directly coupled through radiative forcing. Furthermore, Antarctic temperature is derived from the deuterium proxy, which has some limitations (Buizert et al., 2021). Nevertheless, understanding the origin of this lag is central to understanding the glacial inception that followed thereafter.

Cooling in Antarctica toward glacial inception began at 122.6 ± 0.4 ka, while CO_2 started declining at 117.6 ± 0.4 ka, leading to a delay of 5.0 ± 0.6 ka[i]. Similar lags between CO_2 and Antarctic temperature are a pervasive characteristic of glacial inceptions of the past 800 ka, although with varying amplitudes. From an orbital standpoint, glacial inceptions of the past 800 ka exclusively occur when obliquity is declining and never after its minimum (Tzedakis et al., 2012b). However, no obvious threshold exists between obliquity and glacial inception as seen in the δD record (Figs. 4.4a and 4.4b). Meanwhile, the CO_2 decreases that are counterparts to the Antarctic cooling at glacial inception occur under different configurations of precession-driven Northern Hemisphere Summer Insolation (NHSI) (Figs. 4.4c and 4.4d). For instance, during MIS 13 and MIS 17 the decrease in Antarctic temperature takes place near a maximum of NHSI, while for all other interglacials it happens near a minimum. For both MIS 13 and MIS 17 it is only after reaching the ensuing minima in NHSI that CO_2 proceeds to decrease to glacial levels. These two CO_2 transitions happen several thousand years after the initial Antarctic cooling, although corresponding oscillations

[i]Thresholds calculated using the Rampfit software (Mudelsee, 2000). See also Figure 4.1

in δD can still be found at already close to glacial levels. In the case of MIS 13 and MIS 17, the Antarctic cooling that leads to glacial inception is coeval with peak warmth conditions in Antarctica. Interestingly, evaluating the orbital configurations for peak warmth during interglacials instead of the glacial inception point reveals an apparent threshold for obliquity of $23.7 \pm 0.1°$ (Figs. 4.5a and 4.5b). Such a threshold would then dictate the moment cooling starts in Antarctica during an interglacial, with initial conditions such as elevation of the ice sheet, location and moisture source settings adding variability.

Due to their transient nature, the overshoots that follow some deglaciations were not considered when selecting peak warmth periods to determine the obliquity threshold. The only exception is MIS 7e, which has the overshoot as its only peak. If there is indeed an obliquity threshold that initiates cooling in Antarctica, then it may help justify both the very sharp profile of the MIS 7e overshoot and the absence of an interglacial plateau immediately afterwards. Noticeably, this orbital threshold also seems to induce cooling during glacial periods, provided that full glacial conditions are not yet present, such as during MIS 5a, MIS 7a and MIS 18d.

The time delay between initial cooling in Antarctica and the definitive drop of CO_2 to glacial levels can thus be quantified to first order by the time delay between the orbital threshold of 23.68° during decreasing obliquity and the ensuing minimum in NHSI (Fig. 4.6). Following this rationale, it is noteworthy that the present MIS 1 interglacial has already crossed the lower boundary of the obliquity range of $23.7 \pm 0.1°$ around one thousand years ago, being presently at approximately 23.4°. Furthermore, the last minimum in NHSI (462 W/m^2) happened around 800 CE, while CO_2 started to fall toward glacial levels on average ca. 1.3 ± 1.6 ka after the NHSI minimum during the past glacial inceptions of the last 800 ka. However, none of them took place under such high insolation minima as the recent one (462 W/m^2) (Laskar et al., 2004). It has been suggested that a precessional beat during MIS 1 has been skipped, resembling the weak precessional cycle during MIS 11 that also did not induce glacial inception (Masson-Delmotte et al., 2006). The very low eccentricity shared by both MIS 1 and MIS 11 dampened the precessional oscillations, preventing NHSI to fall significantly and in turn inhibiting the sustained growth of the northern hemisphere ice sheets. This agrees with the widespread view that the length of MIS 1 will be much larger than the average duration of previous interglacials, even if not accounting for anthropogenic interference (Berger and Loutre, 2002; Tzedakis et al., 2012a; Ganopolski et al., 2016).

This perspective with orbital triggers establishes the MIS 5e CO_2–Antarctic temperature lag as a recurrent feature at the end of interglacials, and not something that needs to be justified *per se*. From here, the next step is to investigate what particular

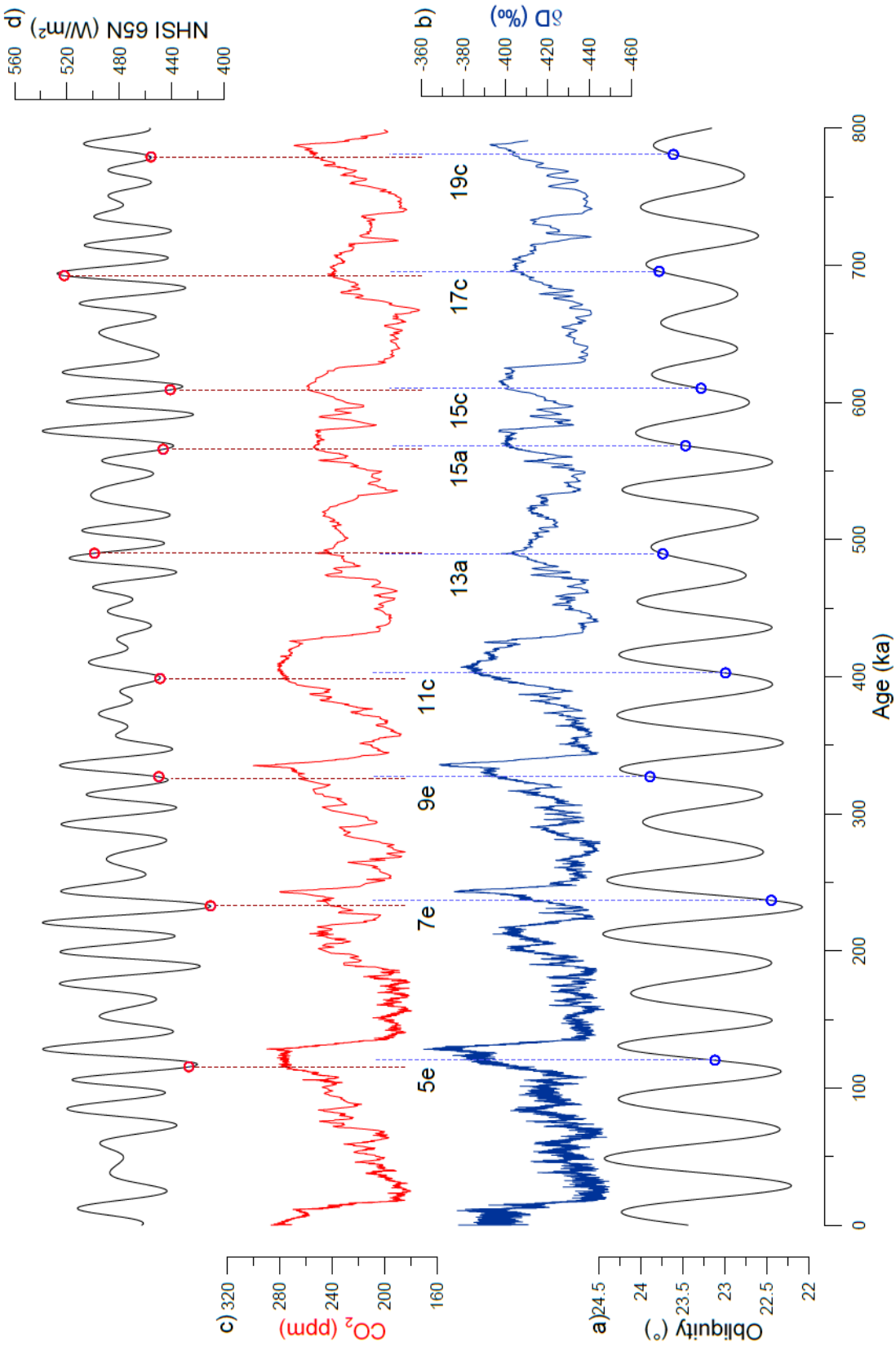

Figure 4.4: Timing of glacial inceptions of the past 800 ka. a) Obliquity (Laskar et al., 2004); b) EDC deuterium (Jouzel et al., 2007); c) EDC CO_2 compilation (this study; Bereiter et al. (2015) and references therein; Nehrbass-Ahles et al. (2020); Shin et al. (2020)); d) NHSI at 65N June (Laskar et al., 2004). Blue vertical lines and circles indicate the timing of glacial inception for Antarctic temperature and the respective obliquity value. Red vertical lines and circles represent CO_2 transitions that are the counterpart events of the glacial inception points in Antarctic temperature, and their respective NHSI values. The spacing between the blue and the red dashed lines indicates the lag between CO2 and Antarctic temperature during glacial inception. Labels indicate the respective MIS substages.

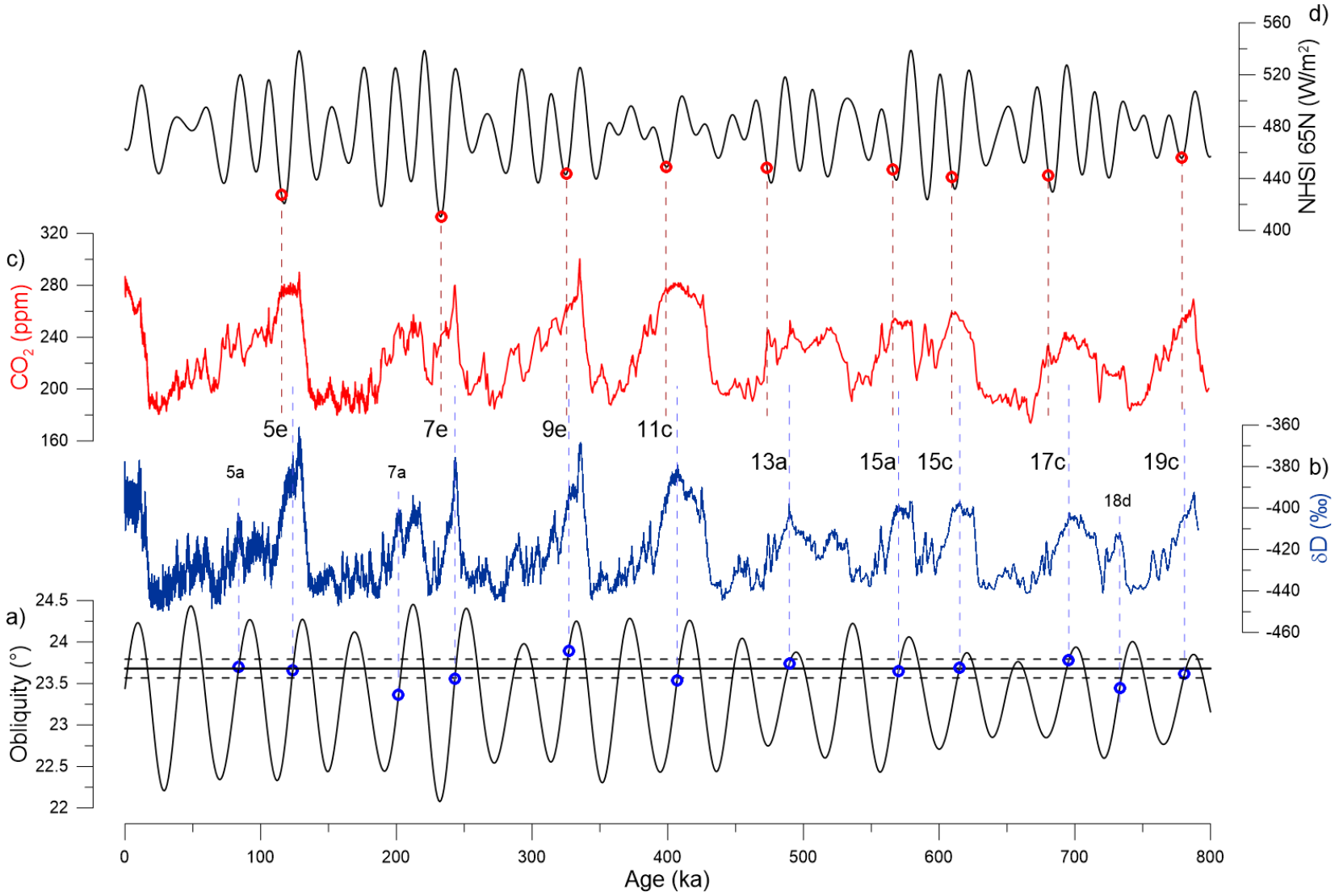

Figure 4.5: Same as Figure 4.4, but with different timings for Antarctic temperature and atmospheric CO_2. Blue lines indicate the beginning of cooling in Antarctica during interglacials, with overshoots after the terminations not being considered (except MIS 7e). Red lines indicate glacial inception as seen from the CO_2 record. The horizontal black solid line shows the average obliquity threshold value for cooling in Antarctica with $\pm 1\sigma$ black dashed lines.

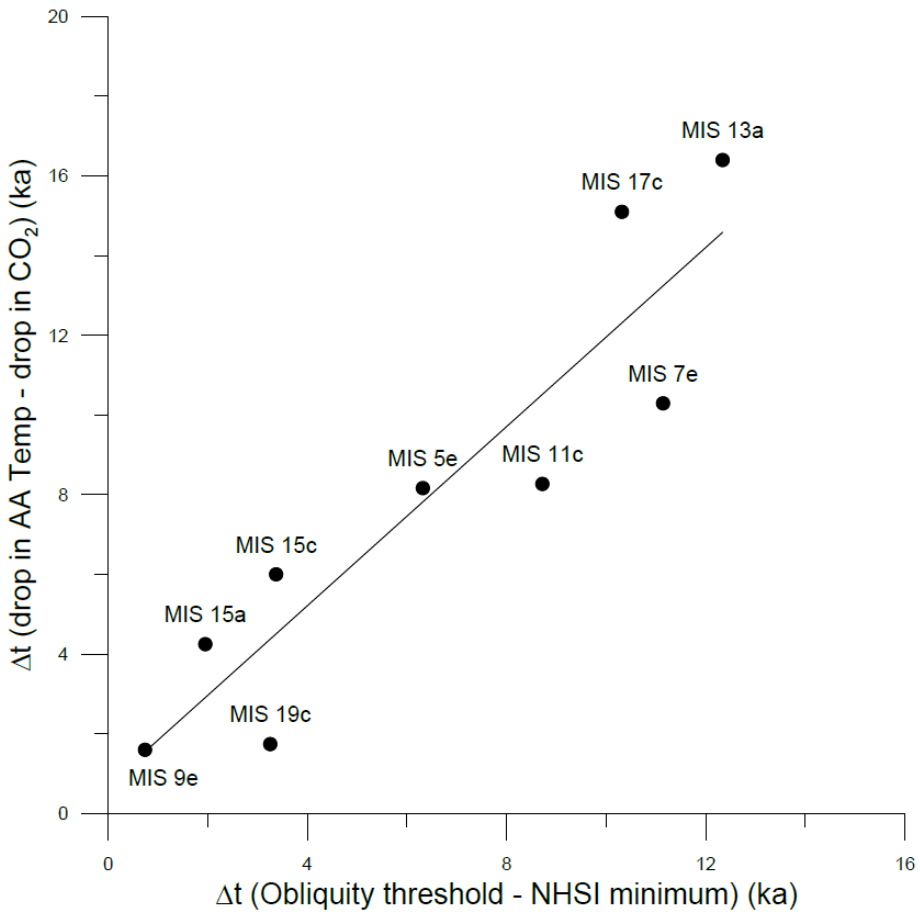

Figure 4.6: Obliquity and NHSI as orbital drivers of initial cooling in Antarctica and glacial inception of CO_2, respectively. X-axis: time delay between the obliquity threshold 23.7° and the next minimum in NHSI. Y-axis: time delay between beginning of cooling in Antarctica and the glacial inception as seen in atmospheric CO_2.

effects it had on the sequence of events that led to glacial inception.

4.4.2 A Northern Hemisphere trigger

The period 125–117 ka saw stable CO_2 concentrations (275.0 ± 2.2 ppm) (Fig. 4.7e) despite paleo data indicating enhanced climate variability in the NH (Pol et al., 2014; Tzedakis et al., 2018; Wilcox et al., 2020). Indeed, reconstructions from NA marine sediments reveal a series of cold events throughout the same period (Fig. 4.7, vertical blue bars) (McManus et al., 1994; Oppo et al., 2006; Tzedakis et al., 2018), with the marine climate optimum lasting only 2–3 ka (Oppo et al., 2006). The lack of fingerprints in the CO_2 record during 125–117 ka suggests spatially contained events, not disrupting the formation of NADW and thus not disturbing the ventilation settings in the SO (Böhm et al., 2015). Nevertheless, the concomitant rearrangements of the NA currents significantly shaped the later stages of the MIS 5e in the NH (Galaasen et al., 2014; Irvalı et al., 2016; Barker et al., 2015; Mokeddem et al., 2014). Notably, a

weakened subpolar gyre in the period 119–115 ka, possibly due to enhanced Arctic sea ice export with declining insolation (Born et al., 2010), paved the way for a warmer and saltier North Atlantic Current to flow into the Nordic Seas (Irvalı et al., 2016; Mokeddem et al., 2014; Born et al., 2010). The added moisture and heat prolonged the warm interglacial conditions in Scandinavia while supporting local fast ice sheet growth well after the minimum in NH Summer Insolation (Fig. 4.7b) (Born et al., 2010; Risebrobakken et al., 2007; Ruddiman and McIntyre, 1979). Moreover, the increase in salinity through freshwater sequestration by the ice sheets fuelled a reinvigoration of the thermohaline circulation through northward density-driven buoyancy fluxes (McManus et al., 2002). The compensating advection from thermocline waters would have helped sustain a warm northward-limb of the AMOC (Risebrobakken et al., 2007; Gordon, 1986). By 116 ka, sufficiently large NH ice sheets would facilitate cold event 25 (C25), a widespread cold event in the NH, with ice-rafted debris (IRD) at multiple locations (Fig. 4.7l) (Galaasen et al., 2014; Tzedakis et al., 2018; McManus et al., 1994; Oppo et al., 2006; Mokeddem et al., 2014), cooling of the deep ocean (Fig. 4.7f), falling SSTs (Oppo et al., 2006; Risebrobakken et al., 2005) and tree line retreats in Europe (Sánchez Goñi et al., 2005). Changes in vegetation may have been particularly important, as the replacement of forests by tundra significantly increased the albedo. This positive feedback would have accelerated rapid ice sheet expansion (Gallimore and Kutzbach, 1996), with a recent study suggesting closure of the Davis and the Denmark Strait at around 114 ka (Bahadory et al., 2021). This would have impacted ocean circulation in the NA, namely nearby NADW formation. Taken together, the aftermath of C25 would have implied reduced NADW formation and a shallower AMOC, which is in line with evidence of prior northward expansion of AABW (Govin et al., 2009).

Paleotracers of AMOC strength ($^{231}Pa/^{230}Th$) do not agree on whether the AMOC was left unchanged (Böhm et al., 2015) or even enhanced (Guihou et al., 2011) during inception. On the other hand, a recent record of ε_{Nd} suggests reduced influence of NADW in the Indian sector of the SO, coeval with the CO_2 decrease (Williams et al., 2021). In addition, a recent box model combined with multiple proxy data attributes the 40 ppm drop across the MIS 5e/5d transition mostly to a weakening of the global overturning circulation (GOC) (O'Neill et al., 2021). Interestingly, that study excluded sea ice as a key to explain the CO_2 reduction, avoiding a much debated mechanism that currently lacks unambiguous proxy evidence (Ai et al., 2020; Kohfeld and Chase, 2017; Williams et al., 2021; Yin et al., 2021). Instead, the substitution of NADW in the abyssal ocean by denser AABW during periods of weakened GOC has been shown to increase CO_2 deep storage (Brovkin et al., 2012). This scenario supports an increase in the $\delta^{13}C_{DIC}$ gradient between deep and abyssal depths, for

the Atlantic, Pacific and Indian oceans during the same time period (Oliver et al., 2010; O'Neill et al., 2021).

In comparison to other contemporary proxy data, the marked inflection point in our CO_2 data at 117 ka after a long period of stable concentrations hints at a trigger-based mechanism. The millennial-scale variability of $\delta^{13}C_{atm}$ (Fig. 4.7h) during 125–117 shows that different carbon fluxes were at play in that time period, combining to produce a stable CO_2 progression. At 117 ka one or more processes suddenly become dominant, leading to the CO_2 decrease. We suggest that the sustained entrainment of a warm and salty AMOC branch in the NH high latitudes during the late MIS 5e indirectly maintained stable CO_2 concentrations in the period 122–117 ka by preventing deep carbon sequestration in the SO through active NADW formation. As the NH ice sheets coalesced, the warm AMOC's northward access was cut off, halting NADW formation. There followed the expansion of Antarctic-sourced waters in the deep ocean, leading to increased CO_2 storage capacity and more efficient trapping in a layered ocean in glacial mode (Govin et al., 2009). We propose that this shift was the necessary trigger to the CO_2 drawdown at 117 ka, after which CO_2 and temperature gradually became coupled again at 110 ka during MIS 5d (Fig. 4.7d). The extension of mild interglacial conditions in the NH at a time when both poles were already in a cooling phase (Fig. 4.7c and 4.7d) helps thus to explain the 5 ka lag between CO_2 and δD during inception. Other studies have proposed different causes for the same lag (Schneider et al., 2013; Ai et al., 2020; Kohfeld and Chase, 2017; Williams et al., 2021; Fischer et al., 1999; Uemura et al., 2018). Arguments based on obliquity-induced temperature gradients attribute strengthened SHW as the basis of prolonged CO_2 stability (Ai et al., 2020; Uemura et al., 2018). While changes in SHW have been shown to feature near obliquity minima (Fig. 4.7a) (Timmermann et al., 2014), it is nevertheless not very likely that strengthened upwelling would exactly compensate for the solubility-driven CO_2 uptake and maintain the same rates seen in the period 127–122 ka. Sea ice-related barrier mechanisms have been proposed to increase stratification in the SO, with the lag mirroring the time needed for shifts in deep-water circulation (Kohfeld and Chase, 2017; Williams et al., 2021). Nevertheless, diatom sea ice proxies do not show a coherent progression around 117 ka that would explain the CO_2 drawdown (Hartman et al., 2021; Jones et al., 2021). According to our sequence of events, since the cascading mechanisms that led to the CO_2-temperature lag were initiated by a weakened subpolar gyre through increased Arctic sea ice export during periods of decreasing NHSI, it is plausible to assume that a similar sequence of events took place during other interglacials. Indeed, the interglacial during MIS 15a also evidences a lag between CO_2 and temperature (Jouzel et al., 2007; Lüthi et al., 2008), while also sharing a similar orbital configuration with MIS 5 (Fig.S 4.12) (Yin

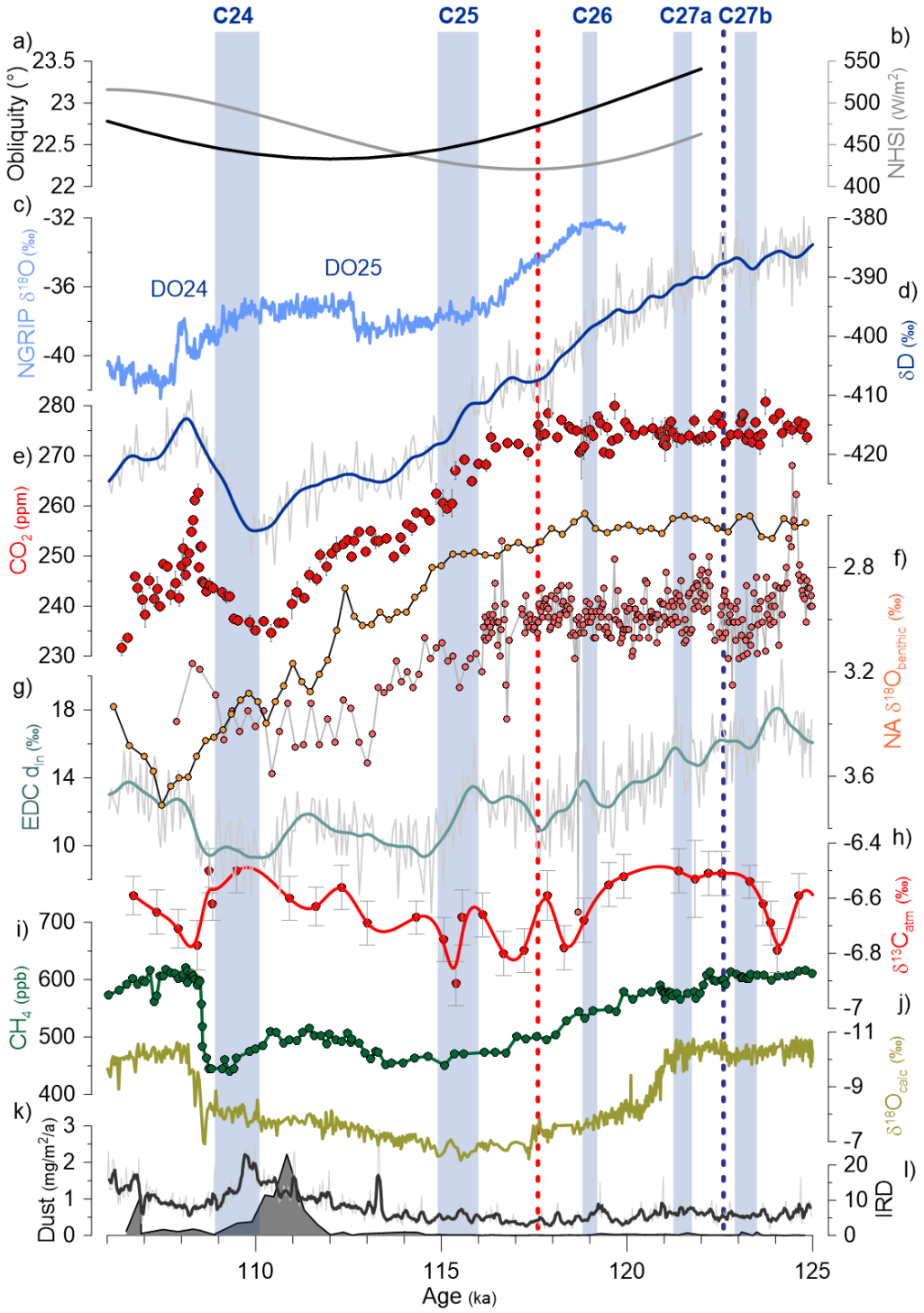

Figure 4.7: MIS 5e plateau and glacial inception. a) Obliquity (Laskar et al., 2004); b) NGRIP $\delta^{18}O$ (North Greenland Ice Core Project members, 2004); c) NHSI at 65N June (Laskar et al., 2004); d) EDC δD (Jouzel et al., 2007)); e) EDC CO_2 (this study); f) NA benthic $\delta^{18}O$ (light orange: NEAP-18K Chapman and Shackleton (1999); dark orange: MD03-2664 (Galaasen et al., 2014)); g) EDC d_{ln} (Landais et al., 2021); h) EDC δ^{13}C (Schneider et al., 2013); i) EDC CH_4 (Schmidely et al., 2021; Loulergue et al., 2008); j) calcite $\delta^{18}O$ from asian speleothems (Cheng et al., 2016); k) EDC dust with a 5-point running average (Lambert et al., 2008); l) NA IRD stack (Lisiecki and Stern, 2016). Vertical red and blue dashed lines indicate inception transitions for CO_2 and δD, respectively. Vertical blue bars indicate cold events in the NH, transferred to a radiometrically dated age scale (Tzedakis et al., 2018). All splines obtained with a Monte Carlo method and a cut off period of 1000 years. All ice core records transferred to the age scale from Extier et al. (2018). Marine records in their original age scale.

and Berger, 2012).

Our CO_2 data reveal a plateau during inception at around 114–112 ka, possibly related to D-O 25 (Capron et al., 2012; North Greenland Ice Core Project members, 2004). Closure of the Bering Strait could be linked to this pause in the CO_2 drawdown via a temporary strengthening of the AMOC, but more data is needed to verify this hypothesis (Hu et al., 2015). The millennia-scale variability evidenced in CO_2, δD and CH_4 during 114–111 ka can be regarded as smoothed triangular peaks superimposed on a decaying baseline. While this view would fit with the triangular-shaped progressions for CO_2 and δD seen later during the glacial period, the CH_4 evolution is rather mysterious. Incidentally, D-O 25 was the first D-O event of the last glacial cycle. It happened under relatively warm conditions and its small magnitude makes it hardly discernible in most paleo records covering inception. It has been reported that D-O 25 and the subsequent interstadial were thus very peculiar, representing regional features more than sharing characteristics with other D-O events (Capron et al., 2012).

4.4.3 CO_2 and Antarctic temperature coupling/decoupling

A closer look at CO_2 and Antarctic temperature during inception reveals a strong covariance from 117 ka onward, i.e. from the moment CO_2 starts to decrease (Fig. 4.8). This is further evidenced by the ramp-like shape of both profiles, indicating little to no lag between the two of them. Contrastingly, that coupling does not seem to have been active during the plateau. Looking at δD as a proxy that is controlled partly by processes in the SO, we can again argue that perhaps the true coupling/decoupling mechanism that is at stake during inception is the one between CO_2 and the SO. To some extent, this follows the same coupling/decoupling feature that is present at the end of T-II. With this reasoning, it could be hypothesized that the CO_2-δD coupling was interrupted at the end of T-II and only resumed during inception. Supporting this idea is the hysteresis plot in Figure 4.9. At equilibrium, it is expected that an increase in CO_2 leads to an increase in global temperature (and by extension in Antarctic temperature) and vice-versa. This is evidenced in the positive slopes during T-II and inception. However, it is remarkable that the slope of CO_2 drawdown during the inception is different than the slope of CO_2 rise during T-II, in terms of ppm/degree (or ppm/‰) by almost 50%. The different slopes suggests that at least one (but maybe both) of either T-II or inception happened with CO_2 and Antarctic temperature out of equilibrium. In this framework, it is more likely that the abrupt termination had an out of equilibrium relationship rather than the more slow-paced inception. If CO_2 was therefore tracking temperature throughout T-II, it is almost paradoxical that the overshoot (i.e., the decoupling event) actually allowed CO_2 to

eventually catch up. Likewise, this conceptual framing also allows for the apparent lag between CO_2 and Antarctic temperature during inception to have led to the subsequent fast CO_2 uptake per unit of temperature. It is nevertheless also possible that the equilibrium relationship between CO_2 and temperature varied according to the departing state (cold or warm period), explaining the different rates. In order to proceed this discussion further, a similar treatment would have to be applied to other glacial-interglacial cycles, but unfortunately high-resolution CO_2 records are lacking in this respect.

Understanding the sequence of events around glacial inception requires constraining the carbon budget and quantifying carbon fluxes between reservoirs. Such information could, for example, shed light on how different fluxes interacted during the MIS 5e plateau to result in very stable CO_2 concentrations in the period 127–117 ka. In this sense, a record of $\delta^{13}C_{atm}$ can help disentangle the contributions from different reservoirs as their isotopic signatures differ. Using CO_2 and $\delta^{13}C_{atm}$ ice core records, deconvolution methods, based on the Bern carbon cycle model (Joos et al., 1996), have been previously applied to the Holocene (Indermühle et al., 1999; Elsig et al., 2009). Departing from multiple hypothesis of mechanisms of change, Indermühle et al. (1999) were able to pin down changes in SSTs and in the terrestrial biomass as the main drivers of CO_2 and $\delta^{13}C_{atm}$ for the past 11 ka. A similar study on the Holocene, but using a $\delta^{13}C_{atm}$ record of much higher resolution, refined the previous findings by (Indermühle et al., 1999) and attributed the 20 ppm increase in CO_2 and the slight -0.5± decrease in $\delta^{13}C_{atm}$ during the early Holocene to carbonate compensation effects (Elsig et al., 2009). This illustrates the ability of the model in differentiating different sources and highlights the needed constraints from highly-resolved datasets of CO_2 and $\delta^{13}C_{atm}$. Obtaining a similar type of information for MIS 5 would certainly help in understanding the coupling/decoupling of CO_2 and Antarctic temperature during T-II and glacial inception. Moreover, given that such a feature appears to have occurred in previous interglacials, it could represent an important step in our understanding of the fundamental mechanisms behind glacial-interglacial climate variability.

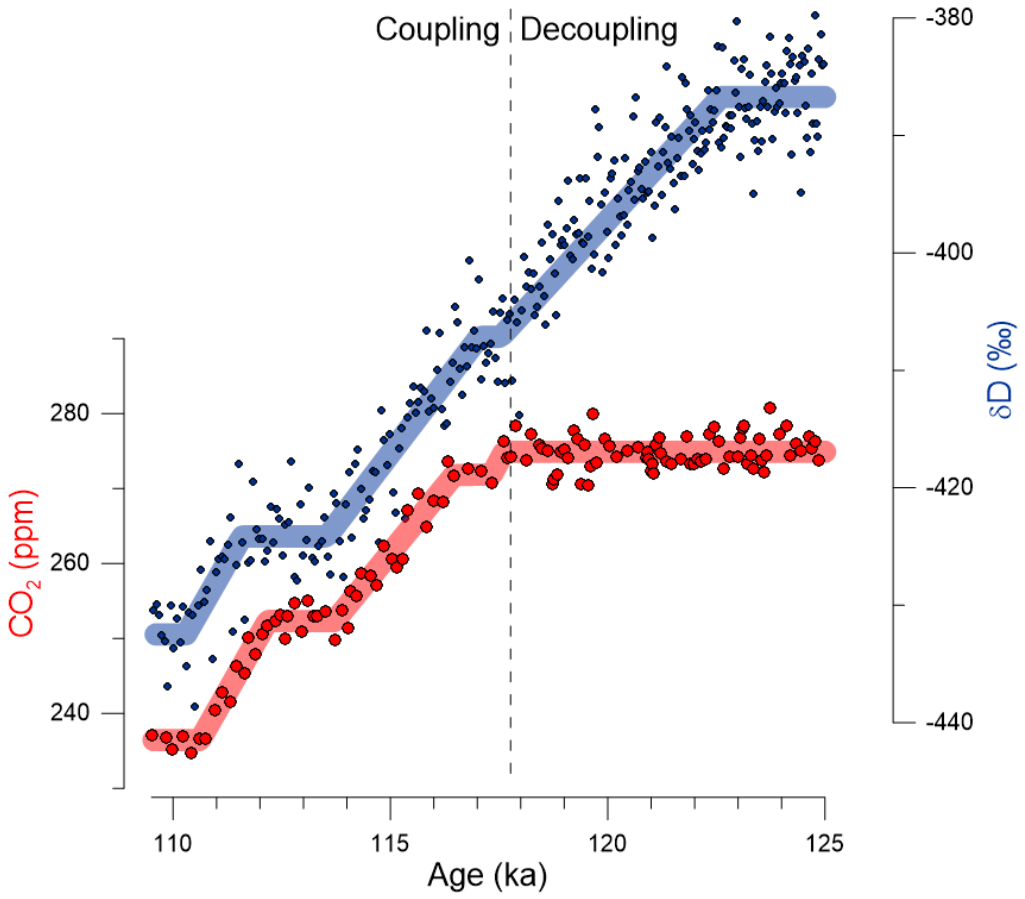

Figure 4.8: CO_2 and deuterium evolution during inception. Red: CO_2 (this study); blue: δD (Jouzel et al., 2007). Age scale by (Extier et al., 2018). Ramp fitting done with the Rampfit software (Mudelsee, 2000).

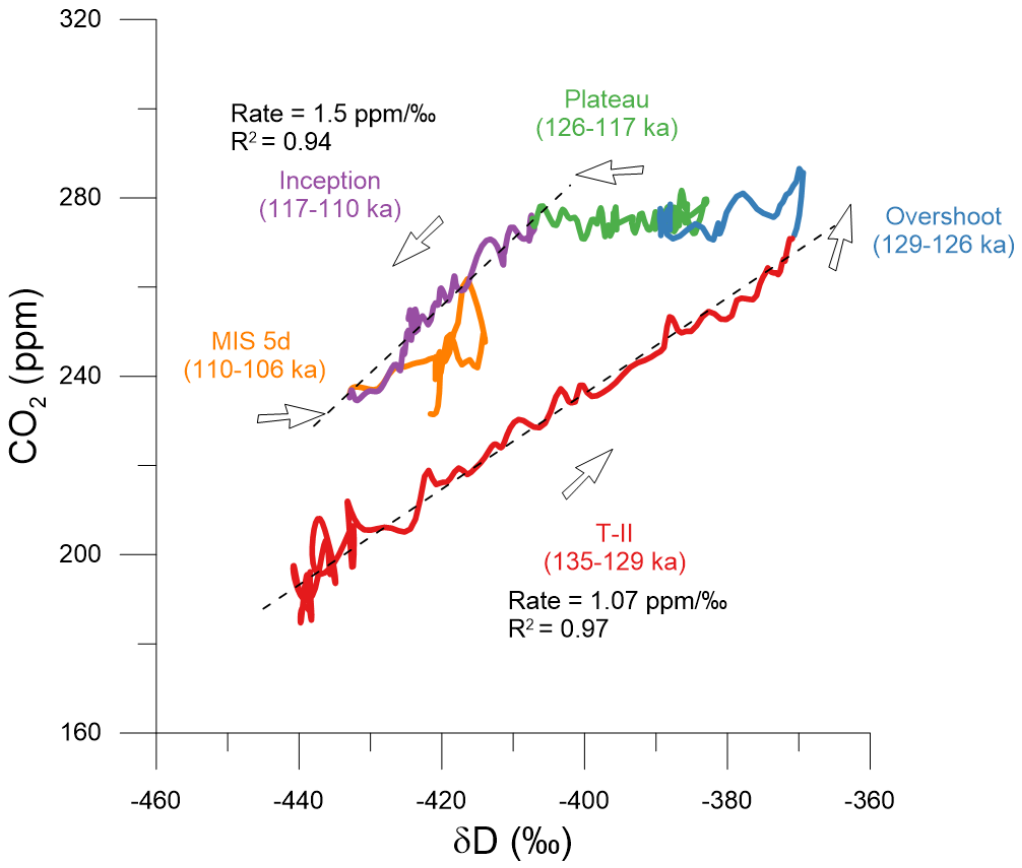

Figure 4.9: CO_2 and Antarctic temperature hysteresis plot for MIS 5e. The multi-colored line represents a one-to-one assignment between CO_2 and deuterium splines obtained with a Monte Carlo method using a 1000 year cut off period. Dashed lines indicate linear fits for T-II and inception. Arrows indicate the sequence of periods from past to present.

4.5 Supplementary materials

Materials and methods

For the period 135–104 ka we performed a total of 674 single measurements, producing 282 individual datapoints, each one typically an average of 2 horizontal replicates from the same depth level. All samples were taken from the EDC ice core from depths in the range 1452–1784 meters, and measured at the University of Bern with the centrifugal ice microtome (Bereiter et al., 2013). The average sampling resolution for this period is 100 years with a pooled standard deviation of replicate samples of 1 ppm.

We extended our record in the range 145–135 ka in lower resolution in order to overlap with the MIS 6 record by Shin et al. (2020). No significant offsets were found, and thus both records can be spliced continuously.

The splines used throughout this Chapter are based on a Monte Carlo method that builds on the concept on Enting splines (Enting, 1987). They are able to handle time series with uneven time steps, and varying individual error bars. A cut off period can be defined, allowing to filter a certain range of frequencies. These splines have been applied successfully in the paleoclimate literature (Schmitt et al., 2012; Schneider et al., 2013).

Age scale

A novel age scale for the period 650–100 ka has been published (Extier et al., 2018). It improves the AICC12 age scale (Bazin et al., 2013; Veres et al., 2013) particularly during the period 120–100 ka, by using a novel $\delta^{18}O_{atm}$ record aligned to new speleothem datasets. Importantly, Extier et al. (2018) also provide a new age scale for the NGRIP ice core, bringing a more coherent sequence of events around D-O events 24 and 25. Given our discussion revolving glacial inception mechanisms, we decided to adopt the new age scale instead of AICC12. One major implication of the new age scale is that theglacial inception as seen in the CO_2 record has been shifted from 115.5 ka to 117.6 ka. However, Δage has not changed significantly between AICC12 and the new age scale, amounting to a maximum of 200 years (Thomas Extier, pers. comm.). Thus, the relative timing between CO_2 and δD remains essentially unchanged.

Piecewise linear fitting

The piecewise linear fit of our CO_2 record (Fig. 4.1) was obtained by a combination of ramp fitting (Mudelsee, 2000) and the detection of abrupt changes with the MATLAB routine $findchangepts$ from the Signal Processing Toolbox. The list of obtained break

points were then fed to a piecewise linear least square fit MATLAB routine (Guido Albertin, 2022). The residuals in Figure 4.1 were obtained by first calculating a Monte Carlo spline with a 200 year cut off period and then subtracting the piecewise linear fit.

Supplementary figures

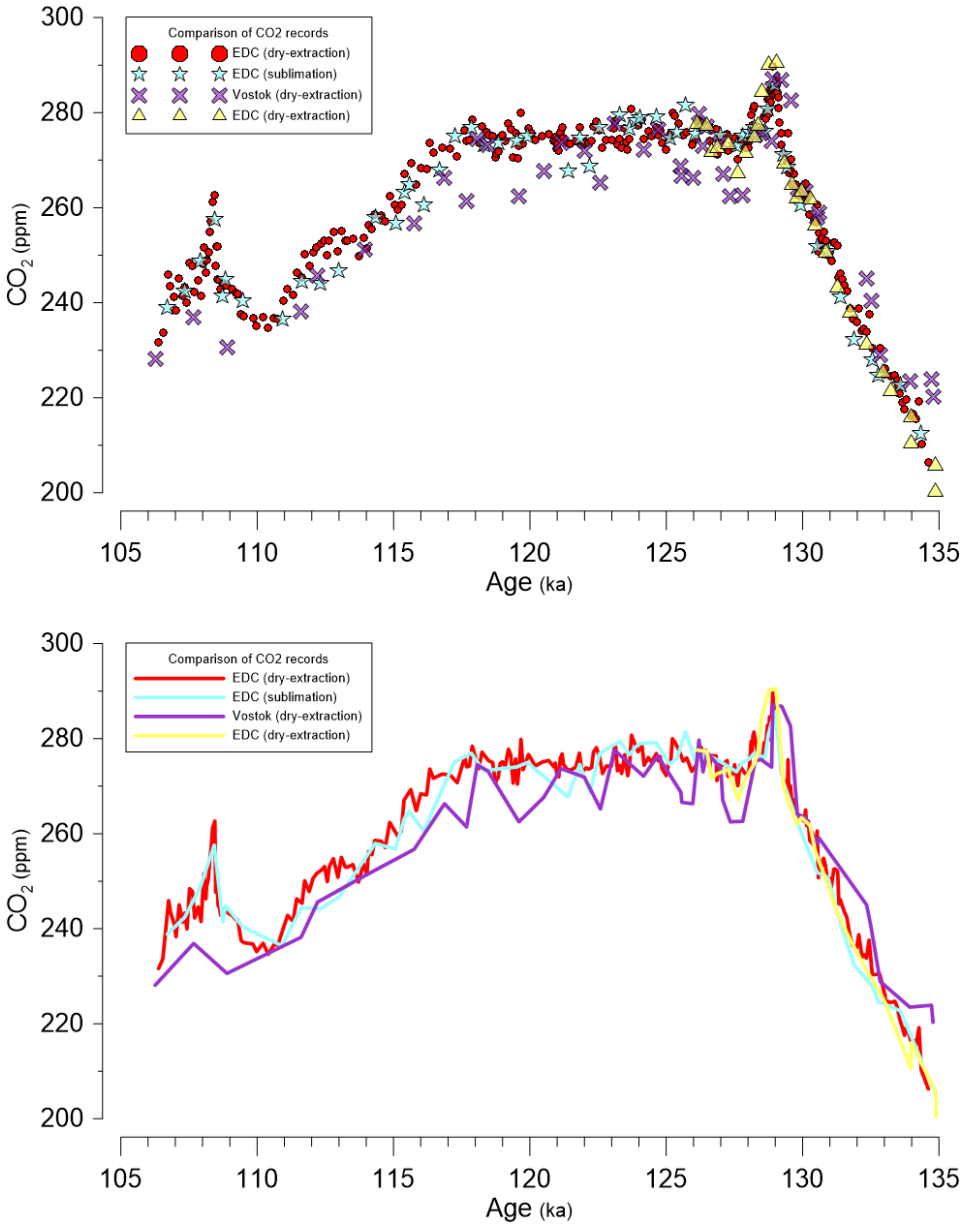

Figure 4.10: Comparison of CO_2 records (a selection). Red: this study; blue (Schneider et al., 2013); yellow (a compilation from Landais et al. (2013) and Lourantou et al. (2010)); purple (Petit et al., 1999). All records on the age scale by Extier et al. (2018).

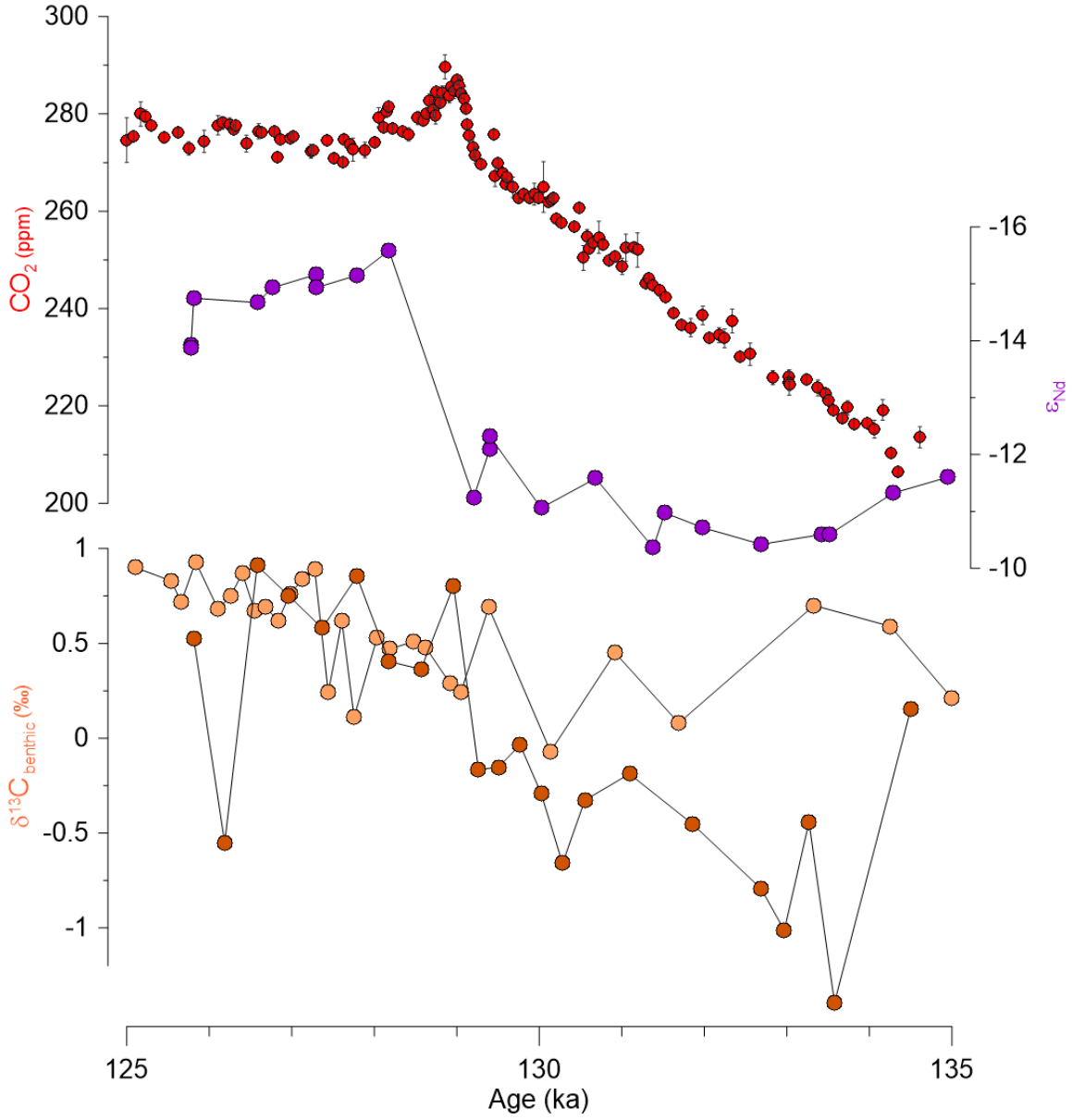

Figure 4.11: Evidence for AMOC invigoration at the end of T-II. Red: EDC CO_2 (this study); purple: ε_{Nd} from site ODP1063 (NA; Bermuda rise; Böhm et al. (2015); Deaney et al. (2017)); orange: benthic $\delta^{13}C$ from site ODP1063 (NW Atlantic; Bermuda rise; Deaney et al. (2017)); brown: benthic $\delta^{13}C$ from site ODP983 (NE Atlantic; Gardar Drift, south of Iceland; Channell et al. (1997)). All records transferred to the age scale by Extier et al. (2018).

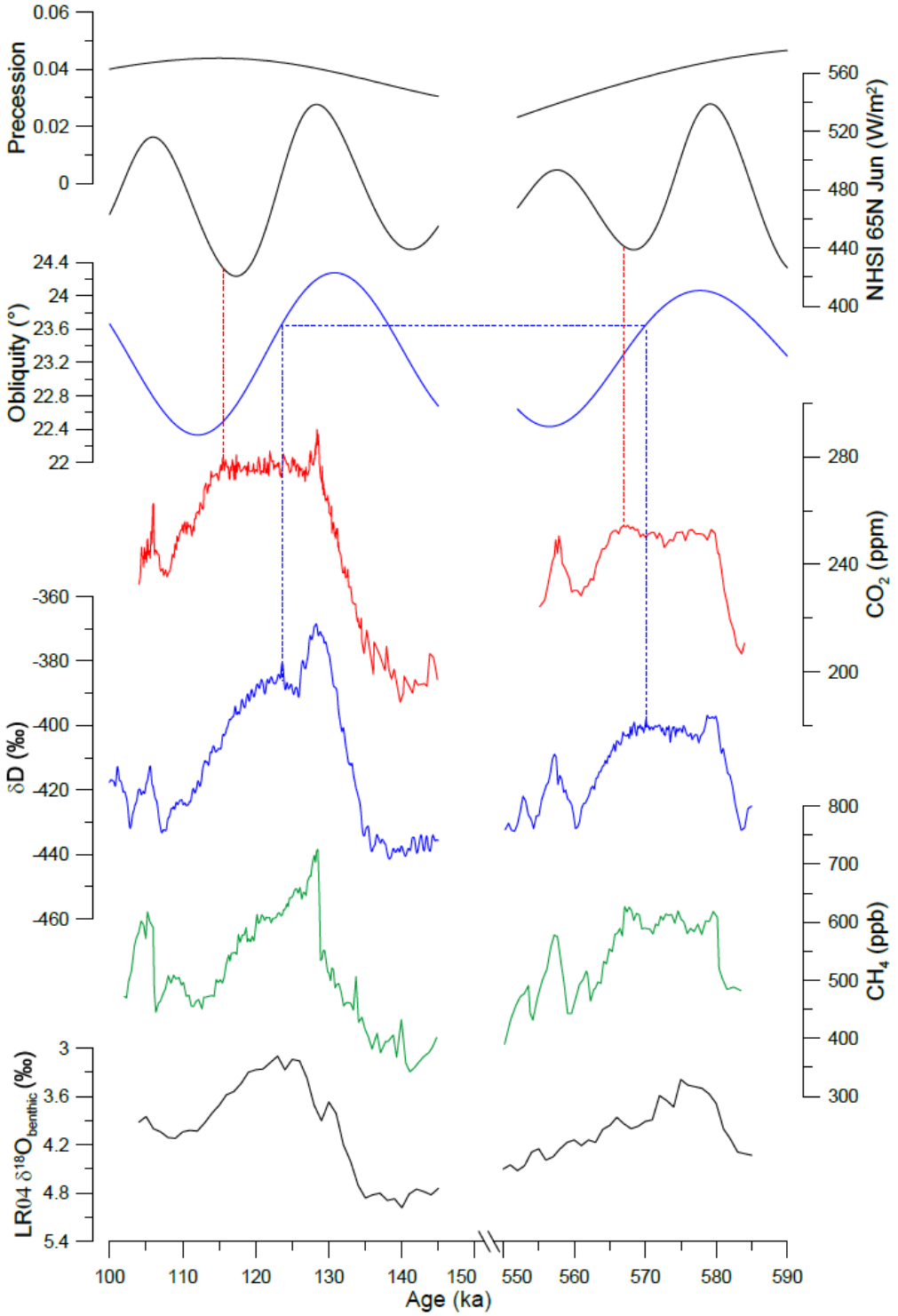

Figure 4.12: Comparison of CO_2-δD inception lags between MIS 5 and MIS 15a. From top to bottom: Orbital parameters from Laskar et al. (2004); EDC CO_2 (this study; Siegenthaler et al. (2005)); EDC deuterium (Jouzel et al., 2007); CH_4 (Loulergue et al., 2008); LR04 benthic $\delta^{18}O$ stack (Lisiecki and Raymo, 2005). Vertical blue lines indicate peak δD during the interglacials and corresponding obliquity. Vertical red lines indicate inception according to the CO_2 records and corresponding NHSI. Ice core records on the AICC12 age scale.

References

Ai, X. E., Studer, A. S., Sigman, D. M., Martínez-García, A., Fripiat, F., Thöle, L. M., Michel, E., Gottschalk, J., Arnold, L., Moretti, S., Schmitt, M., Oleynik, S., Jaccard, S. L., and Haug, G. H. (2020). Southern Ocean upwelling, Earth's obliquity, and glacial-interglacial atmospheric CO $_2$ change. *Science*, 370(6522):1348–1352.

Amsler, H. E., Thöle, L. M., Stimac, I., Geibert, W., Ikehara, M., Kuhn, G., Esper, O., and Jaccard, S. L. (2021). Bottom water oxygenation changes in the Southwestern Indian Ocean as an indicator for enhanced respired carbon storage since the last glacial inception. *Climate of the Past Discussions*. Preprint.

Anderson, R. F., Ali, S., Bradtmiller, L. I., Nielsen, S. H. H., Fleisher, M. Q., Anderson, B. E., and Burckle, L. H. (2009). Wind-driven upwelling in the southern ocean and the deglacial rise in atmospheric co_2. *Science*, 323(5920):1443–1448.

Bahadory, T., Tarasov, L., and Andres, H. (2021). Last glacial inception trajectories for the Northern Hemisphere from coupled ice and climate modelling. *Climate of the Past*, 17(1):397–418.

Banderas, R., Alvarez-Solas, J., Robinson, A., and Montoya, M. (2015). An interhemispheric mechanism for glacial abrupt climate change. *Climate Dynamics*, 44(9):2897–2908.

Barker, S., Chen, J., Gong, X., Jonkers, L., Knorr, G., and Thornalley, D. (2015). Icebergs not the trigger for North Atlantic cold events. *Nature*, 520(7547):333–336.

Bauska, T. K., Baggenstos, D., Brook, E. J., Mix, A. C., Marcott, S. A., Petrenko, V. V., Schaefer, H., Severinghaus, J. P., and Lee, J. E. (2016). Carbon isotopes characterize rapid changes in atmospheric carbon dioxide during the last deglaciation. *Proceedings of the National Academy of Sciences*, 113(13):3465–3470.

Bauska, T. K., Brook, E. J., Marcott, S. A., Baggenstos, D., Shackleton, S., Severinghaus, J. P., and Petrenko, V. V. (2018). Controls on millennial-scale atmospheric CO_2 variability during the last glacial period. *Geophysical Research Letters*, 45(15):7731–7740.

Bauska, T. K., Marcott, S. A., and Brook, E. J. (2021). Abrupt changes in the global carbon cycle during the last glacial period. *Nature Geoscience*, 14(2):91–96.

Bazin, L., Landais, A., Lemieux-Dudon, B., Kele, H. T. M., Veres, D., Parrenin, F., Martinerie, P., Ritz, C., Capron, E., and Lipenkov, V. Y. (2013). An optimized multi-proxy, multi-site Antarctic ice and gas orbital chronology (AICC2012): 120-800 ka. *Climate of the Past*, 9:1715–1731.

Bereiter, B., Eggleston, S., Schmitt, J., Nehrbass-Ahles, C., Stocker, T. F., Fischer, H., Kipfstuhl, S., and Chappellaz, J. (2015). Revision of the EPICA Dome C CO_2 record from 800 to 600 kyr before present. *Geophysical Research Letters*, 42(2):542–549.

Bereiter, B., Lüthi, D., Siegrist, M., Schüpbach, S., Stocker, T. F., and Fischer, H. (2012). Mode change of millennial CO_2 variability during the last glacial cycle associated with a bipolar marine carbon seesaw. *Proceedings of the National Academy of Sciences*, 109(25):9755–9760.

Bereiter, B., Stocker, T. F., and Fischer, H. (2013). A centrifugal ice microtome for measurements of atmospheric CO_2 on air trapped in polar ice cores. *Atmospheric Measurement Techniques*, 6(2):251–262.

Berger, A. and Loutre, M. F. (2002). An exceptionally long interglacial ahead? *Science*, 297(5585):1287–1288.

Böhm, E., Lippold, J., Gutjahr, M., Frank, M., Blaser, P., Antz, B., Fohlmeister, J., Frank, N., Andersen, M. B., and Deininger, M. (2015). Strong and deep atlantic meridional overturning circulation during the last glacial cycle. *Nature*, 517(7532):73–76.

Born, A., Kageyama, M., and Nisancioglu, K. H. (2010). Warm Nordic Seas delayed glacial inception in Scandinavia. *Climate of the Past*, 6(6):817–826.

Brovkin, V., Ganopolski, A., Archer, D., and Munhoven, G. (2012). Glacial CO_2 cycle as a succession of key physical and biogeochemical processes. *Climate of the Past*, 8(1):251–264.

Buizert, C., Fudge, T. J., Roberts, W. H. G., Steig, E. J., Sherriff-Tadano, S., Ritz, C., Lefebvre, E., Edwards, J., Kawamura, K., Oyabu, I., Motoyama, H., Kahle, E. C., Jones, T. R., Abe-Ouchi, A., Obase, T., Martin, C., Corr, H., Severinghaus, J. P., Beaudette, R., Epifanio, J. A., Brook, E. J., Martin, K., Chappellaz, J., Aoki, S., Nakazawa, T., Sowers, T. A., Alley, R. B., Ahn, J., Sigl, M., Severi, M., Dunbar, N. W., Svensson, A., Fegyveresi, J. M., He, C., Liu, Z., Zhu, J., Otto-Bliesner, B. L., Lipenkov, V. Y., Kageyama, M., and Schwander, J. (2021). Antarctic surface temperature and elevation during the Last Glacial Maximum. *Science*, 372(6546):1097–1101.

Capron, E., Govin, A., Stone, E. J., Masson-Delmotte, V., Mulitza, S., Otto-Bliesner, B., Rasmussen, T. L., Sime, L. C., Waelbroeck, C., and Wolff, E. W. (2014). Temporal and spatial structure of multi-millennial temperature changes at high latitudes during the Last Interglacial. *Quaternary Science Reviews*, 103:116–133.

Capron, E., Landais, A., Chappellaz, J., Buiron, D., Fischer, H., Johnsen, S. J., Jouzel, J., Leuenberger, M., Masson-Delmotte, V., and Stocker, T. F. (2012). A global picture of the first abrupt climatic event occurring during the last glacial inception. *Geophysical Research Letters*, 39(15).

Carlson, A. E. (2008). Why there was not a Younger Dryas-like event during the Penultimate Deglaciation. *Quaternary Science Reviews*, 27(9-10):882–887.

Chadwick, M., Allen, C., Sime, L., and Hillenbrand, C.-D. (2020). Analysing the timing of peak warming and minimum winter sea-ice extent in the Southern Ocean during MIS 5e. *Quaternary Science Reviews*, 229:106134.

Channell, J., Hodell, D., and Lehman, B. (1997). Relative geomagnetic paleointensity and $\delta^{18}O$ at ODP Site 983 (Gardar Drift, North Atlantic) since 350 ka. *Earth and Planetary Science Letters*, 153(1):103–118.

Chapman, M. R. and Shackleton, N. J. (1999). Global ice-volume fluctuations, North Atlantic ice-rafting events, and deep-ocean circulation changes between 130 and 70 ka. *Geology*, 27(9):795–798.

Cheng, H., Edwards, R. L., Sinha, A., Spötl, C., Yi, L., Chen, S., Kelly, M., Kathayat, G., Wang, X., Li, X., Kong, X., Wang, Y., Ning, Y., and Zhang, H. (2016). The Asian monsoon over the past 640,000 years and ice age terminations. *Nature*, 534(7609):640–646.

Deaney, E. L., Barker, S., and Van de Flierdt, T. (2017). Timing and nature of AMOC recovery across Termination II and magnitude of deglacial CO_2 change. *Nature communications*, 8(1):1–10.

Denton, G. H., Anderson, R. F., Toggweiler, J. R., Edwards, R. L., Schaefer, J. M., and Putnam, A. E. (2010). The Last Glacial Termination. *Science*, 328(5986):1652–1656.

Elsig, J., Schmitt, J., Leuenberger, D., Schneider, R., Eyer, M., Leuenberger, M., Joos, F., Fischer, H., and Stocker, T. F. (2009). Stable isotope constraints on holocene carbon cycle changes from an antarctic ice core. *Nature*, 461(7263):507–510.

Enting, I. (1987). On the use of smoothing splines to filter CO_2 data. *Journal of Geophysical Research: Atmospheres*, 92(D9):10977–10984.

EPICA Community Members (2004). Eight glacial cycles from an Antarctic ice core. *Nature*, 429(6992):623–628.

Extier, T., Landais, A., Bréant, C., Prié, F., Bazin, L., Dreyfus, G., Roche, D. M., and Leuenberger, M. (2018). On the use of $\delta^{18}O_{atm}$ for ice core dating. *Quaternary Science Reviews*, 185:244–257.

Fischer, H., Wahlen, M., Smith, J., Mastroianni, D., and Deck, B. (1999). Ice Core Records of Atmospheric CO2 Around the Last Three Glacial Terminations. *Science*, 283(5408):1712–1714.

François, R., Altabet, M. A., Yu, E.-F., Sigman, D. M., Bacon, M. P., Frank, M., Bohrmann, G., Bareille, G., and Labeyrie, L. D. (1997). Contribution of Southern Ocean surface-water stratification to low atmospheric CO_2 concentrations during the last glacial period. *Nature*, 389(6654):929–935.

Galaasen, E. V., Ninnemann, U. S., Irvalı, N., Kleiven, H. K. F., Rosenthal, Y., Kissel, C., and Hodell, D. A. (2014). Rapid reductions in North Atlantic deep water during the peak of the last interglacial period. *Science*, 343(6175):1129–1132.

Gallimore, R. G. and Kutzbach, J. E. (1996). Role of orbitally induced changes in tundra area in the onset of glaciation. *Nature*, 381(6582):503–505.

Ganopolski, A., Schellnhuber, H. J., and Winkelmann, R. (2016). Critical insolation–CO_2 relation for diagnosing past and future glacial inception. *Nature*, 529(7585):200–203.

Glasscock, S. K., Hayes, C. T., Redmond, N., and Rohde, E. (2020). Changes in Antarctic Bottom Water Formation During Interglacial Periods. *Paleoceanography and Paleoclimatology*, 35(8).

Gordon, A. L. (1986). Interocean exchange of thermocline water. *Journal of Geophysical Research*, 91(C4):5037.

Govin, A., Braconnot, P., Capron, E., Cortijo, E., Duplessy, J.-C., Jansen, E., Labeyrie, L., Landais, A., Marti, O., Michel, E., Mosquet, E., Risebrobakken, B., Swingedouw, D., and Waelbroeck, C. (2012). Persistent influence of ice sheet melting on high northern latitude climate during the early Last Interglacial. *Climate of the Past*, 8(2):483–507.

Govin, A., Michel, E., Labeyrie, L., Waelbroeck, C., Dewilde, F., and Jansen, E. (2009). Evidence for northward expansion of Antarctic Bottom Water mass in the Southern Ocean during the last glacial inception. *Paleoceanography*, 24(1).

Grant, K. M., Rohling, E. J., Ramsey, C. B., Cheng, H., Edwards, R. L., Florindo, F., Heslop, D., Marra, F., Roberts, A. P., Tamisiea, M. E., and Williams, F. (2014). Sea-level variability over five glacial cycles. *Nature Communications*, 5(1):5076.

Guarino, M.-V., Sime, L. C., Schröeder, D., Malmierca-Vallet, I., Rosenblum, E., Ringer, M., Ridley, J., Feltham, D., Bitz, C., Steig, E. J., Wolff, E., Stroeve, J., and Sellar, A. (2020). Sea-ice-free Arctic during the Last Interglacial supports fast future loss. *Nature Climate Change*, 10(10):928–932.

Guido Albertin (2022). *Piecewise linear least square fit*. `https://www.mathworks.com/matlabcentral/fileexchange/40913-piecewise-linear-least-square-fit` [Accessed: 24.03.2022].

Guihou, A., Pichat, S., Govin, A., Nave, S., Michel, E., Duplessy, J.-C., Telouk, P., and Labeyrie, L. (2011). Enhanced Atlantic Meridional Overturning Circulation supports the Last Glacial Inception. *Quaternary Science Reviews*, 30(13-14):1576–1582.

Hartman, J. D., Sangiorgi, F., Barcena, M., Tateo, F., Giglio, F., Albertazzi, S., Trincardi, F., Bijl, P., Langone, L., and Asioli, A. (2021). Sea-ice, primary productivity and ocean temperatures at the Antarctic marginal zone during late Pleistocene. *Quaternary Science Reviews*, 266:107069.

Hayes, C. T., Martínez-García, A., Hasenfratz, A. P., Jaccard, S. L., Hodell, D. A., Sigman, D. M., Haug, G. H., and Anderson, R. F. (2014). A stagnation event in the deep South Atlantic during the last interglacial period. *Science*, 346(6216):1514–1517.

Hodell, D. A., Charles, C. D., and Sierro, F. J. (2001). Late Pleistocene evolution of the ocean's carbonate system. *Earth and Planetary Science Letters*, 192(2):109–124.

Hodell, D. A., Venz, K. A., Charles, C. D., and Ninnemann, U. S. (2003). Pleistocene vertical carbon isotope and carbonate gradients in the south atlantic sector of the southern ocean. *Geochemistry, Geophysics, Geosystems*, 4(1):1–19.

Hoffman, J. S., Clark, P. U., Parnell, A. C., and He, F. (2017). Regional and global sea-surface temperatures during the last interglaciation. *Science*, 355(6322):276–279.

Hu, A., Meehl, G. A., Han, W., Otto-Bliestner, B., Abe-Ouchi, A., and Rosenbloom, N. (2015). Effects of the Bering Strait closure on AMOC and global climate under different background climates. *Progress in Oceanography*, 132:174–196.

Huang, H., Gutjahr, M., Eisenhauer, A., and Kuhn, G. (2020). No detectable Weddell Sea Antarctic Bottom Water export during the Last and Penultimate Glacial Maximum. *Nature Communications*, 11(1):424.

Indermühle, A., Stocker, T. F., Joos, F., Fischer, H., Smith, H. J., Wahlen, M., Deck, B., Mastroianni, D., Tschumi, J., Blunier, T., Meyer, R., and Stauffer, B. (1999). Holocene carbon-cycle dynamics based on co_2 trapped in ice at Taylor Dome, Antarctica. *Nature*, 398(6723):121–126.

Irvalı, N., Ninnemann, U. S., Kleiven, H. K. F., Galaasen, E. V., Morley, A., and Rosenthal, Y. (2016). Evidence for regional cooling, frontal advances, and East Greenland Ice Sheet changes during the demise of the last interglacial. *Quaternary Science Reviews*, 150:184–199.

Jaccard, S. L., Hayes, C. T., Martinez-Garcia, A., Hodell, D. A., Anderson, R. F., Sigman, D. M., and Haug, G. H. (2013). Two Modes of Change in Southern Ocean Productivity Over the Past Million Years. *Science*, 339(6126):1419–1423.

Jones, J., Kohfeld, K., Bostock, H., Crosta, X., Liston, M., Dunbar, G., Chase, Z., Leventer, A., Anderson, H., and Jacobsen, G. (2021). Sea Ice Changes in the Southwest Pacific Sector of the Southern Ocean During the Last 140,000 Years. *Climate of the Past Discussions*. Preprint.

Joos, F., Bruno, M., Fink, R., Siegenthaler, U., Stocker, T. F., Quéré, C. L., and Sarmiento, J. L. (1996). An efficient and accurate representation of complex oceanic and biospheric models of anthropogenic carbon uptake. *Tellus B: Chemical and Physical Meteorology*, 48(3):394–417.

Jouzel, J., Masson-Delmotte, V., Cattani, O., Dreyfus, G., Falourd, S., Hoffmann, G., Minster, B., Nouet, J., Barnola, J.-M., Chappellaz, J., Fischer, H., Gallet, J. C., Johnsen, S., Leuenberger, M., Loulergue, L., Lüthi, D., Oerter, H., Raisbeck, G., Raynaud, D., Schilt, A., Schwander, J., Selmo, E., Souchez, R., Spahni, R., Stauffer, B., Steffensen, J. P., Stenni, B., Stocker, T. F., Tison, J. L., Werner, M., and Wolff, E. W. (2007). Orbital and millennial Antarctic climate variability over the past 800,000 years. *Science*, 317(5839):793–796.

Kohfeld, K. E. and Chase, Z. (2017). Temporal evolution of mechanisms controlling ocean carbon uptake during the last glacial cycle. *Earth and Planetary Science Letters*, 472:206–215.

Köhler, P., Joos, F., Gerber, S., and Knutti, R. (2005). Simulated changes in vegetation distribution, land carbon storage, and atmospheric CO_2 in response to a collapse of the North Atlantic thermohaline circulation. *Climate Dynamics*, 25(7):689.

Lambert, F., Delmonte, B., Petit, J.-R., Bigler, M., Kaufmann, P. R., Hutterli, M. A., Stocker, T. F., Ruth, U., Steffensen, J. P., and Maggi, V. (2008). Dust-climate couplings over the past 800,000 years from the EPICA Dome C ice core. *Nature*, 452(7187):616–619.

Landais, A., Dreyfus, G., Capron, E., Jouzel, J., Masson-Delmotte, V., Roche, D. M., Prié, F., Caillon, N., Chappellaz, J., Leuenberger, M., Lourantou, A., Parrenin, F., Raynaud, D., and Teste, G. (2013). Two-phase change in CO_2, Antarctic temperature and global climate during Termination II. *Nature geoscience*, 6(12):1062–1065.

Landais, A., Stenni, B., Masson-Delmotte, V., Jouzel, J., Cauquoin, A., Fourré, E., Minster, B., Selmo, E., Extier, T., Werner, M., Vimeux, F., Uemura, R., Crotti, I., and Grisart, A. (2021). Interglacial Antarctic–Southern Ocean climate decoupling due to moisture source area shifts. *Nature Geoscience*, 14(12):918–923.

Laskar, J., Robutel, P., Joutel, F., Gastineau, M., Correia, A. C. M., and Levrard, B. (2004). A long-term numerical solution for the insolation quantities of the Earth. *Astronomy & Astrophysics*, 428(1):261–285.

Lisiecki, L. E. and Raymo, M. E. (2005). A Pliocene-Pleistocene stack of 57 globally distributed benthic δ^{18}o. *Paleoceanography*, 20(1).

Lisiecki, L. E. and Stern, J. V. (2016). Regional and global benthic δ^{18}o stacks for the last glacial cycle. *Paleoceanography*, 31(10):1368–1394.

Loulergue, L., Schilt, A., Spahni, R., Masson-Delmotte, V., Blunier, T., Lemieux, B., Barnola, J.-M., Raynaud, D., Stocker, T. F., and Chappellaz, J. (2008). Orbital and millennial-scale features of atmospheric CH_4 over the past 800,000 years. *Nature*, 453(7193):383–386.

Lourantou, A., Lavrič, J. V., Köhler, P., Barnola, J.-M., Paillard, D., Michel, E., Raynaud, D., and Chappellaz, J. (2010). Constraint of the CO_2 rise by new atmospheric carbon isotopic measurements during the last deglaciation. *Global Biogeochemical Cycles*, 24(2).

Lüthi, D., Bereiter, B., Stauffer, B., Winkler, R., Schwander, J., Kindler, P., Leuenberger, M., Kipfstuhl, S., Capron, E., Landais, A., Fischer, H., and Stocker, T. F. (2010). CO_2 and O_2/N_2O variations in and just below the bubble-clathrate transformation zone of Antarctic ice cores. *Earth and Planetary Science Letters*, 297(1-2):226–233.

Lüthi, D., Le Floch, M., Bereiter, B., Blunier, T., Barnola, J.-M., Siegenthaler, U., Raynaud, D., Jouzel, J., Fischer, H., Kawamura, K., and Stocker, T. F. (2008). High-resolution carbon dioxide concentration record 650,000–800,000 years before present. *Nature*, 453(7193):379–382.

Marcott, S. A., Bauska, T. K., Buizert, C., Steig, E. J., Rosen, J. L., Cuffey, K. M., Fudge, T. J., Severinghaus, J. P., Ahn, J., Kalk, M. L., McConnel, J. R., Sowers, T., Taylor, K. C., White, J. W. C., and Brook, E. J. (2014). Centennial-scale changes in the global carbon cycle during the last deglaciation. *Nature*, 514(7524):616–619.

Marino, G., Rohling, E. J., Rodríguez-Sanz, L., Grant, K. M., Heslop, D., Roberts, A. P., Stanford, J. D., and Yu, J. (2015). Bipolar seesaw control on last interglacial sea level. *Nature*, 522(7555):197–201.

Martrat, B., Jimenez-Amat, P., Zahn, R., and Grimalt, J. O. (2014). Similarities and dissimilarities between the last two deglaciations and interglaciations in the North Atlantic region. *Quaternary Science Reviews*, 99:122–134.

Masson-Delmotte, V., Dreyfus, G., Braconnot, P., Johnsen, S., Jouzel, J., Kageyama, M., Landais, A., Loutre, M.-F., Nouet, J., Parrenin, F., Raynaud, D., Stenni, B., and Tuenter, E. (2006). Past temperature reconstructions from deep ice cores: relevance for future climate change. *Climate of the Past*, 2(2):145–165.

McManus, J. F., Bond, G. C., Broecker, W. S., Johnsen, S., Labeyrie, L., and Higgins, S. (1994). High-resolution climate records from the North Atlantic during the last interglacial. *Nature*, 371(6495):326–329.

McManus, J. F., Oppo, D. W., Keigwin, L. D., Cullen, J. L., and Bond, G. C. (2002). Thermohaline Circulation and Prolonged Interglacial Warmth in the North Atlantic. *Quaternary Research*, 58(1):17–21.

Menviel, L., Spence, P., and England, M. (2015). Contribution of enhanced Antarctic Bottom Water formation to Antarctic warm events and millennial-scale atmospheric CO2 increase. *Earth and Planetary Science Letters*, 413:37–50.

Mokeddem, Z., McManus, J. F., and Oppo, D. W. (2014). Oceanographic dynamics and the end of the last interglacial in the subpolar North Atlantic. *Proceedings of the National Academy of Sciences*, 111(31):11263–11268.

Monnin, E., Indermühle, A., Dällenbach, A., Flückiger, J., Stauffer, B., Stocker, T. F., Raynaud, D., and Barnola, J.-M. (2001). Atmospheric CO_2 Concentrations over the Last Glacial Termination. *Science*, 291(5501):112–114.

Mudelsee, M. (2000). Ramp function regression: a tool for quantifying climate transitions. *Computers & Geosciences*, 26(3):293–307.

NEEM Community Members (2013). Eemian interglacial reconstructed from a Greenland folded ice core. *Nature*, 493(7433):489–494.

Nehrbass-Ahles, C., Shin, J., Schmitt, J., Bereiter, B., Joos, F., Schilt, A., Schmidely, L., Silva, L., Teste, G., Grilli, R., Chappellaz, J., Hodell, D., Fischer, H., and Stocker, T. F. (2020). Abrupt CO_2 release to the atmosphere under glacial and early interglacial climate conditions. *Science*, 369(6506):1000–1005.

North Greenland Ice Core Project members (2004). High-resolution record of Northern Hemisphere climate extending into the last interglacial period. *Nature*, 431(7005):147–151.

Oliver, K. I. C., Hoogakker, B. A. A., Crowhurst, S., Henderson, G. M., Rickaby, R. E. M., Edwards, N. R., and Elderfield, H. (2010). A synthesis of marine sediment core δ^{13}C data over the last 150 000 years. *Climate of the Past*, 6(5):645–673.

O'Neill, C. M., Hogg, A. M., Ellwood, M. J., Opdyke, B. N., and Eggins, S. M. (2021). Sequential changes in ocean circulation and biological export productivity during the last glacial–interglacial cycle: a model–data study. *Climate of the Past*, 17(1):171–201.

Oppo, D. W., McManus, J. F., and Cullen, J. L. (2006). Evolution and demise of the Last Interglacial warmth in the subpolar North Atlantic. *Quaternary Science Reviews*, 25(23-24):3268–3277.

Otto-Bliesner, B. L., Braconnot, P., Harrison, S. P., Lunt, D. J., Abe-Ouchi, A., Albani, S., Bartlein, P. J., Capron, E., Carlson, A. E., Dutton, A., Fischer, H., Goelzer, H., Govin, A., Haywood, A., Joos, F., LeGrande, A. N., Lipscomb, W. H., Lohmann, G., Mahowald, N., Nehrbass-Ahles, C., Pausata, F. S. R.,

Peterschmitt, J.-Y., Phipps, S. J., Renssen, H., and Zhang, Q. (2017). The PMIP4 contribution to CMIP6 – Part 2: Two interglacials, scientific objective and experimental design for Holocene and Last Interglacial simulations. *Geoscientific Model Development*, 10.

Otto-Bliesner, B. L., Rosenbloom, N., Stone, E. J., McKay, N. P., Lunt, D. J., and andJ. T. Overpeck, E. C. B. (2013). How warm was the last interglacial? new model-data comparisons. *Philosophical Transactions of the Royal Society A: Mathematical, Physical and Engineering Sciences*, 371(2001):276–279.

Past Interglacials Working Group of PAGES (2016). Interglacials of the last 800,000 years. *Reviews of Geophysics*, 54(1):162–219.

Petit, J.-R., Jouzel, J., Raynaud, D., Barkov, N. I., Barnola, J.-M., Basile, I., Bender, M., Chappellaz, J., Davis, M., Delaygue, G., Delmotte, M., Kotlyakov, V. M., Legrand, M., Lipenkov, V. Y., Lorius, C., Pépin, L., Ritz, C., Saltzman, E., and Stievenard, M. (1999). Climate and atmospheric history of the past 420,000 years from the Vostok ice core, Antarctica. *Nature*, 399(6735):429.

Pol, K., Masson-Delmotte, V., Cattani, O., Debret, M., Falourd, S., Jouzel, J., Landais, A., Minster, B., Mudelsee, M., Schulz, M., and Stenni, B. (2014). Climate variability features of the last interglacial in the East Antarctic EPICA Dome C ice core. *Geophysical Research Letters*, 41(11):4004–4012.

Rae, J. W. B., Burke, A., Robinson, L. F., Adkins, J. F., Chen, T., Cole, C., Greenop, R., Li, T., Littley, E. F. M., Nita, D. C., Stewart, J. A., and Taylor, B. J. (2018). CO_2 storage and release in the deep Southern Ocean on millennial to centennial timescales. *Nature*, 562(7728):569–573.

Risebrobakken, B., Dokken, T., and Jansen, E. (2005). Extent and variability of the meridional Atlantic circulation in the eastern Nordic seas during Marine Isotope Stage 5 and its influence on the inception of the last glacial. In Drange, H., Dokken, T., Furevik, T., Gerdes, R., and Berger, W., editors, *Geophysical Monograph Series*, volume 158, pages 323–339. American Geophysical Union.

Risebrobakken, B., Dokken, T., Otterå, O. H., Jansen, E., Gao, Y., and Drange, H. (2007). Inception of the Northern European ice sheet due to contrasting ocean and insolation forcing. *Quaternary Research*, 67(1):128–135.

Ruddiman, W. F. and McIntyre, A. (1979). Warmth of the Subpolar North Atlantic Ocean During Northern Hemisphere Ice-Sheet Growth. *Science*, 204(4389):173–175.

Schilt, A., Baumgartner, M., Schwander, J., Buiron, D., Capron, E., Chappellaz, J., Loulergue, L., Schüpbach, S., Spahni, R., Fischer, H., and Stocker, T. F. (2010). Atmospheric nitrous oxide during the last 140,000 years. *Earth and Planetary Science Letters*, 300(1-2):33–43.

Schmidely, L., Nehrbass-Ahles, C., Schmitt, J., Han, J., Silva, L., Shin, J., Joos, F., Chappellaz, J., Fischer, H., and Stocker, T. F. (2021). CH_4 and N_2O fluctuations during the penultimate deglaciation. *Climate of the Past*, 17(4):1627–1643.

Schmitt, J., Schneider, R., Elsig, J., Leuenberger, D., Lourantou, A., Chappellaz, J., Köhler, P., Joos, F., Stocker, T. F., Leuenberger, M., and Fischer, H. (2012). Carbon isotope constraints on the deglacial co_2 rise from ice cores. *Science*, 336(6082):711–714.

Schneider, R., Schmitt, J., Köhler, P., Joos, F., and Fischer, H. (2013). A reconstruction of atmospheric carbon dioxide and its stable carbon isotopic composition from the penultimate glacial maximum to the last glacial inception. *Climate of the Past*, 9(6).

Shackleton, S., Baggenstos, D., Menking, J. A., Dyonisius, M. N., Bereiter, B., Bauska, T. K., Rhodes, R. H., Brook, E. J., Petrenko, V. V., McConnell, J. R., Kellerhals, T., Häberli, M., Schmitt, J., Fischer, H., and Severinghaus, J. P. (2020). Global ocean heat content in the Last Interglacial. *Nature Geoscience*, 13(1):77–81.

Shin, J., Nehrbass-Ahles, C., Grilli, R., Chowdhry Beeman, J., Parrenin, F., Teste, G., Landais, A., Schmidely, L., Silva, L., Schmitt, J., Bereiter, B., Stocker, T. F., Fischer, H., and Chappellaz, J. (2020). Millennial-scale atmospheric CO_2 variations during the Marine Isotope Stage 6 period (190–135 ka). *Climate of the Past*, 16(6):2203–2219.

Siegenthaler, U., Monnin, E., Kawamura, K., Spahni, R., Schwander, J., Stauffer, B., Stocker, T. F., Barnola, J.-M., and Fischer, H. (2005). Supporting evidence from the EPICA Dronning Maud Land ice core for atmospheric CO2 changes during the past millennium. *Tellus B: Chemical and Physical Meteorology*, 57(1):51–57.

Sigman, D. M., Fripiat, F., Studer, A. S., Kemeny, P. C., Martínez-García, A., Hain, M. P., Ai, X., Wang, X., Ren, H., and Haug, G. H. (2021). The southern ocean during the ice ages: A review of the antarctic surface isolation hypothesis, with comparison to the north pacific. *Quaternary Science Reviews*, 254:106732.

Spahni, R., Schwander, J., Flückiger, J., Stauffer, B., Chappellaz, J., and Raynaud, D. (2003). The attenuation of fast atmospheric CH_4 variations recorded in polar ice cores. *Geophysical Research Letters*, 30(11).

Stocker, T. F. and Johnsen, S. J. (2003). A minimum thermodynamic model for the bipolar seesaw. *Paleoceanography*, 18(4).

Studer, A. S., Sigman, D. M., Martínez-García, A., Benz, V., Winckler, G., Kuhn, G., Esper, O., Lamy, F., Jaccard, S. L., Wacker, L., Oleynik, S., Gersonde, R., and Haug, G. H. (2015). Antarctic Zone nutrient conditions during the last two glacial cycles: ANTARCTIC ZONE NUTRIENT CONDITIONS. *Paleoceanography*, 30(7):845–862.

Sánchez Goñi, M., Loutre, M., Crucifix, M., Peyron, O., Santos, L., Duprat, J., Malaizé, B., Turon, J.-L., and Peypouquet, J.-P. (2005). Increasing vegetation and climate gradient in Western Europe over the Last Glacial Inception (122–110 ka): data-model comparison. *Earth and Planetary Science Letters*, 231(1-2):111–130.

Timmermann, A., Friedrich, T., Timm, O. E., Chikamoto, M. O., Abe-Ouchi, A., and Ganopolski, A. (2014). Modeling Obliquity and CO2 Effects on Southern Hemisphere Climate during the Past 408 ka. *Journal of Climate*, 27(5):1863–1875.

Toggweiler, J. R., Russell, J. L., and Carson, S. R. (2006). Midlatitude westerlies, atmospheric CO_2, and climate change during the ice ages. *Paleoceanography*, 21(2).

Tzedakis, P. C., Channell, J. E. T., Hodell, D. A., Kleiven, H. F., and Skinner, L. C. (2012a). Determining the natural length of the current interglacial. *Nature Geoscience*, 5(2):138–141.

Tzedakis, P. C., Drysdale, R. N., Margari, V., Skinner, L. C., Menviel, L., Rhodes, R. H., Taschetto, A. S., Hodell, D. A., Crowhurst, S. J., Hellstrom, J. C., Fallick, A. E., Grimalt, J. O., McManus, J. F., Martrat, B., Mokeddem, Z., Parrenin, F., Regattieri, E., Roe, K., and Zanchetta, G. (2018). Enhanced climate instability in the North Atlantic and southern Europe during the Last Interglacial. *Nature Communications*, 9(1):4235.

Tzedakis, P. C., Wolff, E. W., Skinner, L. C., Brovkin, V., Hodell, D. A., McManus, J. F., and Raynaud, D. (2012b). Can we predict the duration of an interglacial? *Climate of the Past*, 8(5):1473–1485.

Uemura, R., Motoyama, H., Masson-Delmotte, V., Jouzel, J., Kawamura, K., Goto-Azuma, K., Fujita, S., Kuramoto, T., Hirabayashi, M., Miyake, T., Ohno, H., Fujita, K., Abe-Ouchi, A., Iizuka, Y., Horikawa, S., Igarashi, M., Suzuki, K., Suzuki, T., and Fujii, Y. (2018). Asynchrony between Antarctic temperature and CO2 associated with obliquity over the past 720,000 years. *Nature Communications*, 9(1):961.

Veres, D., Bazin, L., Landais, A., Toyé Mahamadou Kele, H., Lemieux-Dudon, B., Parrenin, F., Martinerie, P., Blayo, E., Blunier, T., Capron, E., Chappellaz, J., Rasmussen, S. O., Severi, M., Svensson, A. M., Vinther, B. M., and Wolff, E. W. (2013). The Antarctic ice core chronology (AICC2012): an optimized multi-parameter and multi-site dating approach for the last 120 thousand years. *Climate of the Past*, 9(4):1733–1748.

Weber, M. E., Clark, P. U., Kuhn, G., Timmermann, A., Sprenk, D., Gladstone, R., Zhang, X., Lohmann, G., Menviel, L., Chikamoto, M. O., Friedrich, T., and Ohlwein, C. (2014). Millennial-scale variability in Antarctic ice-sheet discharge during the last deglaciation. *Nature*, 510(7503):134–138.

Wilcox, P. S., Honiat, C., Trüssel, M., Edwards, R. L., and Spötl, C. (2020). Exceptional warmth and climate instability occurred in the European Alps during the Last Interglacial period. *Communications Earth & Environment*, 1(1):57.

Williams, T. J., Martin, E. E., Sikes, E., Starr, A., Umling, N. E., and Glaubke, R. (2021). Neodymium isotope evidence for coupled Southern Ocean circulation and Antarctic climate throughout the last 118,000 years. *Quaternary Science Reviews*, 260:106915.

Yan, Y., Spaulding, N. E., Bender, M. L., Brook, E. J., Higgins, J. A., Kurbatov, A. V., and Mayewski, P. A. (2021). Enhanced moisture delivery into Victoria Land, East Antarctica, during the early Last Interglacial: implications for West Antarctic Ice Sheet stability. *Climate of the Past*, 17(5):1841–1855.

Yin, Q. Z. and Berger, A. (2012). Individual contribution of insolation and CO_2 to the interglacial climates of the past 800,000 years. *Climate Dynamics*, 38(3):709–724.

Yin, Q. Z., Wu, Z. P., Berger, A., Goosse, H., and Hodell, D. (2021). Insolation triggered abrupt weakening of Atlantic circulation at the end of interglacials. *Science*, 373(6558):1035–1040.

Yu, J., Oppo, D. W., Jin, Z., Lacerra, M., Ji, X., Umling, N. E., Lund, D. C., McCave, N., Menviel, L., Shao, J., and Xu, C. (2022). Millennial and centennial CO_2 release from the Southern Ocean during the last deglaciation. *Nature Geoscience*.

Zhuravleva, A., Bauch, H. A., and Van Nieuwenhove, N. (2017). Last Interglacial (MIS5e) hydrographic shifts linked to meltwater discharges from the East Greenland margin. *Quaternary Science Reviews*, 164:95–109.

Chapter 5

Co-authored research

5.1 Abrupt CO_2 release to the atmosphere under glacial and early interglacial climate conditions

Christoph Nehrbass-Ahles, Jinhwa Shin, Jochen Schmitt, Bernhard Bereiter, Fortunat Joos, Adrian Schilt, Loïc Schmidely, **Lucas Silva**, Gregory Teste, Jérôme Chappellaz, David Hodell, Hubertus Fischer and Thomas F. Stocker

Published in *Science*, 369, 1000-1005 (2020) (doi: 10.1126/science.aay8178)

Abstract Pulse-like carbon dioxide release to the atmosphere on centennial time scales has only been identified for the most recent glacial and deglacial periods and is thought to be absent during warmer climate conditions. Here, we present a high-resolution carbon dioxide record from 330,000 to 450,000 years before present, revealing pronounced carbon dioxide jumps (CDJ) under cold and warm climate conditions. CDJ come in two varieties that we attribute to invigoration or weakening of the Atlantic meridional overturning circulation (AMOC) and associated northward and southward shifts of the intertropical convergence zone, respectively. We find that CDJ are pervasive features of the carbon cycle that can occur during interglacial climate conditions if land ice masses are sufficiently extended to be able to disturb the AMOC by freshwater input.

Title: Abrupt CO_2 release to the atmosphere under glacial and early interglacial climate conditions

Authors: C. Nehrbass-Ahles[1,2,3*], J. Shin[4], J. Schmitt[1,2], B. Bereiter[1,2,5], F. Joos[1,2], A. Schilt[1,2], L. Schmidely[1,2], L. Silva[1,2], G. Teste[4], R. Grilli[4], J. Chappellaz[4], D. Hodell[3], H. Fischer[1,2], and T. F. Stocker[1,2].

Affiliations:

[1]Climate and Environmental Physics, Physics Institute, University of Bern, Switzerland

[2]Oeschger Centre for Climate Change Research, University of Bern, Switzerland

[3]Godwin Laboratory for Palaeoclimate Research, Department of Earth Sciences, University of Cambridge, UK

[4]IGE, Grenoble INP, IRD, CNRS, Univ. Grenoble Alpes, France

[5]Laboratory for Air Pollution / Environmental Technology, Empa, Dübendorf, Switzerland

*Correspondence to: cn425@cam.ac.uk

Abstract: Pulse-like CO_2 release to the atmosphere on centennial timescales has only been identified for the most recent glacial and deglacial periods and is thought to be absent during warmer climate conditions. Here, we present a high-resolution CO_2 record from 330,000 to 450,000 years before present, revealing pronounced Carbon Dioxide Jumps (CDJ) under cold and warm climate conditions. CDJ come in two varieties that we attribute to invigoration or weakening of the Atlantic Meridional Overturning Circulation and associated northward and southward shifts of the Intertropical Convergence Zone, respectively. We find that CDJ are pervasive features of the carbon cycle that can occur during interglacial climate conditions if land ice masses are sufficiently extended to be able to disturb the Atlantic Meridional Overturning Circulation by freshwater input.

One Sentence Summary: Ice core record reveals centennial-scale CO_2 releases to the atmosphere under past cold and warm climate states.

Main Text: Analyses of Antarctic ice cores have demonstrated that atmospheric CO_2 has been a major driver of Earth's climate on orbital to millennial time scales (*1-3*). However, evidence of sub-millennial scale CO_2 variability is only available for the last ~60 thousand years (ka), i.e., not beyond the last glacial period (e.g., *4-6*). Climate-carbon cycle perturbations during previous interglacial periods serve as first-order templates for the natural response of Earth's climate system to warmer climatic background conditions (*7*), but so far the use of CO_2 records to decipher sub-millennial scale variations has been hampered by insufficient temporal resolution of existing ice core records.

Previous research identified two principal modes of CO_2 variability on millennial to centennial time scales: (i) millennial-scale Carbon Dioxide Maxima (CDM) frequently occurring during the last glacial period (*4, 5, 8*) and (ii) centennial-scale Carbon Dioxide Jumps (CDJ) caused by pulse-like CO_2 releases to the atmosphere, most prominently occurring during the last deglaciation (*6, 9*).

CDM are characterized by a triangular shape of evolving CO_2 changes. They closely covary with Antarctic temperature proxy records on millennial timescales as evidenced by the Antarctic Isotope Maxima (*4, 8, 10*). During cold periods (stadials) in the Northern Hemisphere (NH), CO_2 is observed to increase gradually and in parallel to the bipolar seesaw response in Antarctic temperature (*11*) at typical rates of ~1 ppm per century (*4, 8*). CDM reach amplitudes of up to 30 ppm before their trends are reversed connected with a sudden strengthening of the Atlantic Meridional Overturning Circulation (AMOC) linking the onset of Dansgaard-Oeschger (DO) events (i.e., abrupt warming over Greenland) and the start of slow cooling in the Southern Ocean (SO) region (*4, 8, 11*).

In contrast, abrupt CDJ do not directly correspond to variations in Antarctic temperature but are associated with either DO events or Heinrich Stadials (HS) in the NH (*6, 12, 13*). The latter are characterized by extended cold periods in the NH associated with a

weakened AMOC (*14-16*). The few CDJ identified so far are superimposed on gradually increasing millennial CO_2 trends connected to CDM or glacial terminations and lead to a sudden 10 to 15 ppm CO_2 rise within less than ~250 years at rates of ~10 ppm per century, about ten times faster than CDM. As of yet, CDJ have only been identified during the last deglaciation (Termination I) (*6, 9*) and for HS 4 (*12, 13*), occurring at 39.5 ka BP (thousand years before present, defined as 1950 CE). CDJ are synchronous with either major methane (CH_4) rises linked to DO events or small CH_4 peaks associated with HS, suggesting a link with sudden AMOC changes and poleward shifts of the Intertropical Convergence Zone (ITCZ) (*6, 17, 18*). Here we address whether CDJ also occur during glacial growth phases and interglacial climate conditions and therefore whether they are a pervasive feature of the past carbon cycle.

Centennial to millennial-scale CO_2 variability between ~150 and 400 ka BP could not be explored because of insufficient measurement precision and low temporal resolution of the existing CO_2 record available for this period (*1*). Here we investigate the older part of this interval by presenting a high-resolution record of CO_2 mole fractions covering a full glacial-interglacial cycle from 330 to 450 ka BP [i.e., Marine Isotope Stage (MIS) 9e - 12a (*19*)], measured on samples from the EPICA Dome C (EDC) ice core using an improved dry-extraction technique (*20*). In comparison to earlier data (*1, 2*), we enhance the precision by a factor of three (now ~1 ppm) and increase temporal resolution four to six times (now ~300 years on average).

Together with CO_2 we improve the resolution of the existing EDC CH_4 record (*21*) to an average of ~250 years at periods of abrupt changes (*20*). This permits a direct comparison of the CH_4 imprint of fast climate changes in the NH with the Southern Hemisphere bipolar seesaw response in Antarctic temperature and atmospheric CO_2 (*4, 8*). We combine our ice core data with new records of benthic $\delta^{13}C$ and $\delta^{18}O$ of *C. wuellerstorfi* (*22*) and planktic

$\delta^{18}O$ of *G. bulloides* (*23*). These stable isotope data are measured on marine sediment core samples from the International Ocean Discovery Program (IODP) Site U1385 located on the Iberian Margin off the coast of Portugal in a water depth of ~2600 m below sea level (*20*). A temporal resolution of ~150 years on average enables us to directly compare our ice core data to this independent paleoclimatic archive of hydrological change in the North Atlantic (NA).

On orbital timescales, the new CO_2 record reveals generally high CO_2 levels persisting above 260 ppm (*24*) over ~35 ka during the exceptionally long interglacial period MIS 11c - e from 427 to 393 ka BP (Fig. 1B) extending over more than one precessional cycle (*25*). The minimum CO_2 value of 187.6±1.0 ppm is reached at 358 ka BP coinciding with the lowest sea surface temperature (SST) [Fig. 2D, 2G, and 2H, (*26*)]. However, the onset of the deglacial CO_2 rise towards MIS 9e (Termination IV), only takes place ~13.5 ka later at 344.5 ka BP. The end of this deglacial CO_2 increase (~335 ka BP) is marked by a peak CO_2 value of 300.4±1.0 ppm, representing the highest natural CO_2 mole fraction derived from Antarctic ice cores over the past 800 ka. Superimposed on this orbital trend we identify different types of millennial to centennial-scale CO_2 variability, occurring most frequently during, but not limited to, the glacial growth phase.

On millennial timescales, the CO_2 record mirrors the variability in the EDC temperature proxy [Fig. 1A, 2A, (*10*)] and dust flux records [Fig. 2B, (*27*)], a feature previously observed over the last 800 ka in lower resolution CO_2 data (*2, 3*). Our new benthic $\delta^{18}O$ record from the IODP Site U1385 follows the same pattern (Fig. 2C) indicating the influence of southern-sourced deep-water as first noted for the last glacial period (MIS 3) (*28*). Our results demonstrate that this correlation also applies to MIS 10a - 11a, thereby emphasizing the key role of SO processes in the bipolar seesaw (*4, 11*) and associated global-scale climate regime shifts in shaping atmospheric CO_2 on millennial timescales. We identify in total seven CDM events (Fig. 1B). The two youngest events (CDM 9e and 10b) were

identified previously (*1*), but not the oldest five (CDM 11a.1 to 11e). Furthermore, our record shows that the covariation of CO_2 and the Antarctic temperature proxy (*10*) holds also for the extended interglacial period MIS 11c (Fig. 1A, 1B), where both Antarctic temperatures and CO_2 gradually increase along with the summer insolation at 65°N (*25*). The time where CO_2 and Antarctic temperature cease to covary in our record is at the end of MIS 11c, when Antarctic temperature leads the CO_2 decrease by several thousand years, similar to what is observed for the glacial inception after the penultimate interglacial (*29*).

On the centennial timescale, we detect eight CDJ occurring under very different climate boundary conditions (Fig. 1B). They are marked by centennial-scale peaks in the rate of change of CO_2 exceeding a threshold of 1.5 ppm per century in the ice core record [Fig. 1D, (*20*)]. The close correlation of millennial-scale CO_2 variability with Antarctic temperature (Fig. 1A) does not hold for CDJ (Fig. 3A, S1A). While all CDJ lead to an abrupt ~10 ppm rise in CO_2 (Table S1), their underlying causes may be different (*13, 30*). We distinguish two varieties of CDJ based on the presence (or absence) of a major simultaneous CH_4 rise at the same depth level of the ice core (*20*).

The first variety of CDJ is synchronous with rapid rises in the CH_4 record greater than 50 ppb (Fig. 1C, 3C) and growth rates exceeding 20 ppb per century as recorded in the EDC ice core (Fig. 1E, 3E). We dub these pulse-like CO_2 release events CDJ+. Following this definition, we identify five new CDJ+ (9e, 11a.2 - 4, and 11e; Fig. 1B). The major CH_4 rises associated with CDJ+ indicate abrupt DO-like warming in the NH directly linked to AMOC invigorations (*6, 17*). Direct evidence for such AMOC strengthening comes from associated abrupt rises in SST in the NH (Fig. 2F - H) and increases of benthic $\delta^{13}C$ values (Fig. 2I), indicative of the inflow of NA deep-water masses at IODP Site U1385. These findings are consistent with the two previously identified CDJ+ events during the last deglaciation at the onsets of the Bølling-Allerød and Preboral periods (*6, 9*).

5.1. Abrupt CO_2 release to the atmosphere under glacial and early interglacial climate conditions

The most pronounced CDJ+ (CDJ+ 9e) takes place during early interglacial conditions when CO_2 values are already above 285 ppm, a level that is higher than typical peak CO_2 mole fractions during interglacial conditions over the past 800 ka (*3*). The time resolution for CDJ+ 9e is better than 90 years and shows an exceptionally fast CO_2 increase of ~10 ppm per century, as preserved in the ice archive. Accounting for the smoothing of atmospheric signals by the bubble enclosure process, we estimate an original rate of atmospheric CO_2 increase of 26.2±17.6 ppm per century [Fig. 3B, Table S1, (*20*)]. This provides a benchmark of the possible range and speed of positive carbon cycle feedbacks connected to AMOC variations during the deglaciation. This rate exceeds previous estimates of maximum pre-industrial atmospheric increase rates (*31*) by a factor of seven, but this is still a factor of nine lower than recent anthropogenic growth rates over the past decade (*32*). The CO_2 decrease after CDJ+ 9e shows that natural processes during interglacial conditions allowed for a sustained CO_2 removal from the atmosphere estimated at ~2 ppm per century for about 2 ka (Fig. 1B, 3B).

The second variety of CDJ occurs independently from major responses in the EDC CH_4 record (Fig. 1E, 3C, 3E, see supplementary text) and is dubbed CDJ−. We identify two CDJ− (10a and 11a.2), which share similar characteristics with the two CDJ− events associated with HS 1 during the last deglaciation (~16 ka BP) and HS 4 (*6, 12, 13*). We speculate that CDJ− can be attributed to carbon cycle processes caused by AMOC weakening. Although direct AMOC records do not yet exist for MIS 9e - 12a, abrupt decreases of benthic $\delta^{13}C$ indicate intrusions of Antarctic Bottom Water masses at IODP Site U1385 (Fig. 2I) likely due to AMOC weakening, similar to that which happened during HS in the last glacial period (*14, 15*). Note that major HS (HS 10.1 and HS 10.2) are identified in Fig. 2 by the drop in $U^{k'}_{37}$-based sea surface temperature (Fig. 2G) and the decrease in benthic $\delta^{13}C$ (Fig. 2I) indicative of a reduced state of the AMOC. While CDJ− 10a is likely

related to carbon cycle responses to an AMOC slow-down caused by massive ice discharge during HS 10.1 (Fig. 2I), there exists only ambiguous evidence for CDJ− 11a.2 being associated with freshwater forcing. Low CH_4 levels (Fig. 2E) and cold SST in the NA (Fig. 2F) indicate stadial conditions in the NH associated with CDJ− 11a.2. Given the relative age uncertainties between our ice core and independently dated records (*33, 34*), the $\delta^{18}O$ calcite record from Sanbao Cave [Fig. 2J, (*35*)] indicates a major shift of the ITCZ that may be associated with CDJ− 11a.2 (*18, 36*).

Most notably, the new CO_2 record reveals the clearly distinguishable CDJ 11c (12.9±2.7 ppm increase within 191±123 years, Fig. 3B, Table S1) at 415 ka BP, occurring ~10 ka into interglacial temperature conditions at Dome C, but still at a time of considerable sea level rise [Fig. 2K, (*37*)]. A hiatus in the section older than 407 ka BP at IODP Site U1385 obscures potential signals related to this event (*20*). A distinct peak found in a proxy for SST conditions at 412 ka BP [Fig. 2F, (*38*)] is indicative of hydrographic disturbance in the NA. A possible perturbation of the AMOC at the same time (*39*) may be connected to this event, both of which may be attributed to a major freshwater forcing at the time of near deglaciation of the southern Greenland Ice Sheet in the early part of MIS 11c (*40*). Another recent study suggests a major ice-sheet discharge event into the SO that might also coincide with this CDJ at 415 ka BP (*41*), but dating uncertainties do not permit an unambiguous attribution. While there is limited evidence supporting an AMOC perturbation around 415 ka BP, it remains unclear whether CDJ 11c is associated with an AMOC weakening or strengthening. Given the lack of a major CH_4 rise in our record (Fig. 3C, 3E) we classify this event as a CDJ− (CDJ− 11c); however, it could mechanistically also be a CDJ+, with an atypical CH_4 response caused by already warm climate conditions in the NH.

Invigorations of the AMOC during DO events lead to abrupt increases in cross-equatorial heat transport to the NH (*15, 42*), which may be a necessary (yet not a sufficient)

condition for the occurrence of CDJ+ events (*6, 43*). As a direct consequence of this energy imbalance the ITCZ shifts northward and promotes a poleward shift and intensification of westerlies in the NH (*18, 42*). Driven by this shift in the ITCZ, new tropical wetlands are formed in the NH, which leads to an extended increase in CH_4 production (*17, 18*).

Conversely, we presume that CDJ− are associated with a weakening of the AMOC causing a southward shift of the ITCZ which is promoting the formation of wetlands in the SH. The latter results in an initial overshoot in the CH_4 production that coincides with CDJ− during HS 1 and HS 4 (*18*). These small, short-lived CH_4 peaks of amplitudes smaller than ~50 ppb are distinct from major CH_4 rises associated with CDJ+; however, both CH_4 responses proceed at comparable growth rates. The absence of any short-lived CH_4 peaks related to CDJ– in our record (Fig. 3C, S1C) – similar to those found for HS 1 and HS 4 (*18*) – can be explained by a combination of relatively low sample resolution and the bubble enclosure process that smooths the EDC gas record. The latter results in the obliteration of any potential CH_4 peaks smaller than ~50 ppb lasting for less than 200 years (see supplementary text). Accordingly, we use the absence of a major CH_4 rise as a criterion to distinguish a CDJ– from a CDJ+. Whereas the climate conditions for CDJ+ are characteristic for DO events in the NH, CDJ− appear to be connected with major freshwater forcing and stadial conditions in the NH (*6, 13, 18*).

The strong correspondence of the CO_2 record with Antarctic temperature and benthic $\delta^{18}O$ at the Iberian Margin on the millennial time scale (Fig. 2A, 2C, 2D) suggests a causal link of CDM formation with SO processes (*8*). Proposed CDM generating mechanisms include perturbations in the carbon cycle owing to changes in deep SO ventilation related to changes in stratification, buoyancy forcing, and Southern Hemisphere westerlies (e.g., *44, 45*), variations of the southern sea ice edge (e.g., *46*), efficiency of the biological pump

caused by changes in either the magnitude of dust-induced iron fertilization (e.g., *44*), or mode changes in the AMOC (e.g., *47*).

On the contrary, the underlying CO_2 release mechanisms for the CDJ are poorly understood. Suggested marine mechanisms include outgassing due to increasing SST (*30*), rapid ventilation of accumulated respired carbon from intermediate-depth Atlantic (*43, 48*), or SO deep-water masses (*49, 50*). Despite the coherence of CDJ with AMOC changes, and associated deep-water reorganizations in the NA [Fig. 2I, (*6, 43*)], the carbon source for CDJ may not necessarily originate from the ocean. Proposed terrestrial sources include permafrost thawing in the NH (*51*), drought-induced biomass decomposition (*6, 30*), and changes in precipitation and vegetation distribution connected to ITCZ shifts (*18, 36*). To explain a 10 ppm CDJ in the atmosphere caused by carbon release from the land biosphere, ~80 Pg of carbon are needed (*52*). For most of these processes, a shift of the position of the ITCZ and resulting changes in the mid to high-latitude westerly winds (*53*) are necessary to couple the cross-equatorial heat transport in the NA to the global carbon cycle (*11, 42*).

In summary, our CO_2 record from the EDC ice core provides evidence for centennial-scale CDJ during glacial, deglacial and early interglacial conditions. These suggest fast, pulse-like CO_2 releases to the atmosphere during MIS 9e - 12a that are likely related to abrupt changes in AMOC (Fig. 2I) and shifts in the position of the ITCZ (Fig. 2E). Our data imply that CDJ are a pervasive feature of the natural carbon cycle that may go undetected in CO_2 records of insufficient temporal resolution and precision. We stress that such CDJ also occur during interglacial temperature conditions, as long as fresh-water discharge from remnant ice sheets persists and is able to disturb ocean circulation. Anthropogenic warming and the committed ice sheet melting and associated sea level rise over the coming millennia (*54*) constitute new drivers that might trigger ocean circulation changes, and hence, pulse-like CO_2

releases such as those detected in our record during an earlier interglacial period when AMOC was perturbed.

References and Notes:

1. J. R. Petit *et al.*, Climate and atmospheric history of the past 420,000 years from the Vostok ice core, Antarctica. *Nature* **399**, 429-436 (1999).
2. U. Siegenthaler *et al.*, Stable carbon cycle-climate relationship during the late Pleistocene. *Science* **310**, 1313-1317 (2005).
3. D. Lüthi *et al.*, High-resolution carbon dioxide concentration record 650,000-800,000 years before present. *Nature* **453**, 379-382 (2008).
4. B. Bereiter *et al.*, Mode change of millennial CO_2 variability during the last glacial cycle associated with a bipolar marine carbon seesaw. *Proc. Natl. Acad. Sci. U.S.A.* **109**, 9755-9760 (2012).
5. J. Ahn, E. J. Brook, Siple Dome ice reveals two modes of millennial CO_2 change during the last ice age. *Nat. Commun.* **5**, 3723 (2014).
6. S. A. Marcott *et al.*, Centennial-scale changes in the global carbon cycle during the last deglaciation. *Nature* **514**, 616-619 (2014).
7. H. Fischer *et al.*, Palaeoclimate constraints on the impact of 2°C anthropogenic warming and beyond. *Nat. Geosci.* **11**, 474-485 (2018).
8. J. Ahn, E. J. Brook, Atmospheric CO_2 and climate on millennial time scales during the last glacial period. *Science* **322**, 83-85 (2008).
9. E. Monnin *et al.*, Atmospheric CO_2 concentrations over the last glacial termination. *Science* **291**, 112-114 (2001).
10. J. Jouzel *et al.*, Orbital and millennial Antarctic climate variability over the past 800,000 years. *Science* **317**, 793-796 (2007).

11. T. F. Stocker, S. J. Johnsen, A minimum thermodynamic model for the bipolar seesaw. *Paleoceanography* **18**, 1087 (2003).

12. J. Ahn, E. J. Brook, A. Schmittner, K. Kreutz, Abrupt change in atmospheric CO_2 during the last ice age. *Geophysical Research Letters* **39**, 5 (2012).

13. T. K. Bauska *et al.*, Controls on millennial-scale atmospheric CO_2 variability during the last glacial period. *Geophys. Res.* **45**, 7731-7740 (2018).

14. S. R. Hemming, Heinrich events: Massive late Pleistocene detritus layers of the North Atlantic and their global climate imprint. *Rev. Geophys.* **42**, RG1005 (2004).

15. L. G. Henry *et al.*, North Atlantic ocean circulation and abrupt climate change during the last glaciation. *Science* **353**, 470-474 (2016).

16. Heinrich Stadials are directly linked to massive glacial ice and meltwater discharges from Hudson Strait known as Heinrich events.

17. M. Baumgartner *et al.*, NGRIP CH4 concentration from 120 to 10 kyr before present and its relation to a $\delta^{15}N$ temperature reconstruction from the same ice core. *Clim. Past* **10**, 903-920 (2014).

18. R. H. Rhodes *et al.*, Enhanced tropical methane production in response to iceberg discharge in the North Atlantic. *Science* **348**, 1016-1019 (2015).

19. L. B. Railsback, P. L. Gibbard, M. J. Head, N. R. G. Voarintsoa, S. Toucanne, An optimized scheme of lettered marine isotope substages for the last 1.0 million years, and the climatostratigraphic nature of isotope stages and substages. *Quat. Sci. Rev.* **111**, 94-106 (2015).

20. Materials and methods are available as supplementary materials at the Science website.

21. L. Loulergue *et al.*, Orbital and millennial-scale features of atmospheric CH_4 over the past 800,000 years. *Nature* **453**, 383-386 (2008).

22. Benthic $\delta^{13}C$ of *C. wuellerstorfi* reflects changes in deep-water ventilation related to reorganization of deep-ocean circulation and remineralization of organic carbon. The $\delta^{18}O$ signal of the same species indicates variations in deep-water temperatures.

23. Millennial-scale changes in the planktic $\delta^{18}O$ record of *G. bulloides* follow changes in the sea surface temperature in the North Atlantic.

24. P. C. Tzedakis *et al.*, Interglacial diversity. *Nat. Geosci.* **2**, 751-755 (2009).

25. P. C. Tzedakis *et al.*, Can we predict the duration of an interglacial? *Clim. Past* **8**, 1473-1485 (2012).

26. T. Rodrigues *et al.*, A 1-Ma record of sea surface temperature and extreme cooling events in the North Atlantic: A perspective from the Iberian Margin. *Quat. Sci. Rev.* **172**, 118-130 (2017).

27. F. Lambert, M. Bigler, J. P. Steffensen, M. Hutterli, H. Fischer, Centennial mineral dust variability in high-resolution ice core data from Dome C, Antarctica. *Clim. Past* **8**, 609-623 (2012).

28. N. J. Shackleton, M. A. Hall, E. Vincent, Phase relationships between millennial-scale events 64,000–24,000 years ago. *Paleoceanography* **15**, 565-569 (2000).

29. R. Schneider, J. Schmitt, P. Köhler, F. Joos, H. Fischer, A reconstruction of atmospheric carbon dioxide and its stable carbon isotopic composition from the penultimate glacial maximum to the last glacial inception. *Clim. Past* **9**, 2507-2523 (2013).

30. T. K. Bauska *et al.*, Carbon isotopes characterize rapid changes in atmospheric carbon dioxide during the last deglaciation. *Proc. Natl. Acad. Sci. U. S. A.* **113**, 3465-3470 (2016).

31. F. Joos, R. Spahni, Rates of change in natural and anthropogenic radiative forcing over the past 20,000 years. *Proc. Natl. Acad. Sci. U. S. A.* **105**, 1425-1430 (2008).

32. P. Tans, R. Keeling, "Annual mean CO_2 growth rate for Mauna Loa, Hawaii" (NOAA/ESRL and Scripps Institution of Oceanography, 2020; https://www.esrl.noaa.gov/gmd/ccgg/trends/gr.html). [the easiest access to this source is via the URL]

33. T. Extier *et al.*, On the use of $\delta^{18}O_{atm}$ for ice core dating. *Quat. Sci. Rev.* **185**, 244-257 (2018).

34. L. Bazin *et al.*, An optimized multi-proxy, multi-site Antarctic ice and gas orbital chronology (AICC2012): 120-800 ka. *Clim. Past* **9**, 1715-1731 (2013).

35. H. Cheng *et al.*, The Asian monsoon over the past 640,000 years and ice age terminations. *Nature* **534**, 640-646 (2016).

36. A. Bozbiyik, M. Steinacher, F. Joos, T. F. Stocker, L. Menviel, Fingerprints of changes in the terrestrial carbon cycle in response to large reorganizations in ocean circulation. *Clim. Past* **7**, 319-338 (2011).

37. R. M. Spratt, L. E. Lisiecki, A Late Pleistocene sea level stack. *Clim. Past* **12**, 1079-1092 (2016).

38. S. Barker *et al.*, Icebergs not the trigger for North Atlantic cold events. *Nature* **520**, 333-336 (2015).

39. A. J. Dickson *et al.*, Oceanic forcing of the Marine Isotope Stage 11 interglacial. *Nat. Geosci.* **2**, 428-433 (2009).

40. R. G. Hatfield *et al.*, Interglacial responses of the southern Greenland ice sheet over the last 430,000 years determined using particle-size specific magnetic and isotopic tracers. *Earth Planet. Sci. Lett.* **454**, 225-236 (2016).

41. D. J. Wilson *et al.*, Ice loss from the East Antarctic ice sheet during late Pleistocene interglacials. *Nature* **561**, 383-386 (2018).

42. J. B. Pedro *et al.*, Beyond the bipolar seesaw: Toward a process understanding of interhemispheric coupling. *Quat. Sci. Rev.* **192**, 27-46 (2018).

43. T. Chen *et al.*, Synchronous centennial abrupt events in the ocean and atmosphere during the last deglaciation. *Science* **349**, 1537-1541 (2015).

44. S. L. Jaccard, E. D. Galbraith, A. Martinez-Garcia, R. F. Anderson, Covariation of deep Southern Ocean oxygenation and atmospheric CO_2 through the last ice age. *Nature* **530**, 207-210 (2016).

45. C. Basak *et al.*, Breakup of last glacial deep stratification in the South Pacific. *Science* **359**, 900 (2018).

46. B. B. Stephens, R. F. Keeling, The influence of Antarctic sea ice on glacial–interglacial CO_2 variations. *Nature* **404**, 171-174 (2000).

47. A. Schmittner, E. D. Galbraith, Glacial greenhouse-gas fluctuations controlled by ocean circulation changes. *Nature* **456**, 373-376 (2008).

48. M. Lacerra, D. Lund, J. Yu, A. Schmittner, Carbon storage in the mid-depth Atlantic during millennial-scale climate events. *Paleoceanography* **32**, 780-795 (2017).

49. L. Menviel *et al.*, Southern Hemisphere westerlies as a driver of the early deglacial atmospheric CO_2 rise. *Nat. Commun.* **9**, 2503 (2018).

50. J. W. B. Rae *et al.*, CO_2 storage and release in the deep Southern Ocean on millennial to centennial timescales. *Nature* **562**, 569-573 (2018).

51. P. Köhler, G. Knorr, E. Bard, Permafrost thawing as a possible source of abrupt carbon release at the onset of the Bølling/Allerød. *Nat. Commun.* **5**, 5520 (2014).

52. A. Jeltsch-Thömmes, F. Joos, Modeling the evolution of pulse-like perturbations in atmospheric carbon and carbon isotopes: the role of weathering–sedimentation imbalances. *Clim. Past* **16**, 423-451 (2020).

53. C. Buizert *et al.*, Abrupt ice-age shifts in southern westerly winds and Antarctic climate forced from the north. *Nature* **563**, 681-685 (2018).

54. P. U. Clark *et al.*, Consequences of twenty-first-century policy for multi-millennial climate and sea-level change. *Nat Clim Change* **6**, 360-369 (2016).

55. B. Bereiter, T. F. Stocker, H. Fischer, A centrifugal ice microtome for measurements of atmospheric CO_2 on air trapped in polar ice cores. *Atmos. Meas. Tech.* **6**, 251-262 (2013).

56. P. P. Tans, A. M. Crotwell, K. W. Thoning, Abundances of isotopologues and calibration of CO_2 greenhouse gas measurements. *Atmos. Meas. Tech.* **10**, 2669-2685 (2017).

57. H. Schaefer *et al.*, On the suitability of partially clathrated ice for analysis of concentration and $\delta^{13}C$ of palaeo-atmospheric CO_2. *Earth Planet. Sci. Lett.* **307**, 334-340 (2011).

58. A. Schilt *et al.*, Glacial–interglacial and millennial-scale variations in the atmospheric nitrous oxide concentration during the last 800,000 years. *Quat. Sci. Rev.* **29**, 182-192 (2010).

59. R. Spahni *et al.*, Atmospheric methane and nitrous oxide of the late Pleistocene from Antarctic ice cores. *Science* **310**, 1317-1321 (2005).

60. M. Bock *et al.*, Glacial/interglacial wetland, biomass burning, and geologic methane emissions constrained by dual stable isotopic CH_4 ice core records. *Proc. Natl. Acad. Sci. U.S.A.* **114**, E5778-E5786 (2017).

61. D. Hodell *et al.*, A reference time scale for Site U1385 (Shackleton Site) on the SW Iberian Margin. *Glob. Planet Change* **133**, 49-64 (2015).

62. N. J. Shackleton, R. G. Fairbanks, T.-C. Chiu, F. Parrenin, Absolute calibration of the Greenland time scale: implications for Antarctic time scales and for $\Delta^{14}C$. *Quat. Sci. Rev.* **23**, 1513-1522 (2004).

63. B. Martrat *et al.*, Four climate cycles of recurring deep and surface water destabilizations on the Iberian Margin. *Science* **317**, 502-507 (2007).

64. L. C. Skinner, H. Elderfield, Rapid fluctuations in the deep North Atlantic heat budget during the last glacial period. *Paleoceanography* **22**, PA1205 (2007).

65. P. C. Tzedakis, K. H. Roucoux, L. de Abreu, N. J. Shackleton, The duration of forest stages in southern Europe and interglacial climate variability. *Science* **306**, 2231-2235 (2004).

66. S. Barker *et al.*, 800,000 years of abrupt climate variability. *Science* **334**, 347-351 (2011).

67. H. Craig, Y. Horibe, T. Sowers, Gravitational separation of gases and isotopes in polar ice caps. *Science* **242**, 1675-1678 (1988).

68. T. Sowers, M. Bender, D. Raynaud, Elemental and isotopic composition of occluded O_2 and N_2 in polar ice. *J. Geophys. Res.* **94**, 5137-5150 (1989).

69. D. M. Etheridge *et al.*, Natural and anthropogenic changes in atmospheric CO_2 over the last 1000 years from air in Antarctic ice and firn. *J. Geophys. Res.-Atmos.* **101**, 4115-4128 (1996).

70. S. Eggleston, J. Schmitt, B. Bereiter, R. Schneider, H. Fischer, Evolution of the stable carbon isotope composition of atmospheric CO_2 over the last glacial cycle. *Paleoceanography* **31**, 434-452 (2016).

71. G. B. Dreyfus *et al.*, Firn processes and $\delta^{15}N$: potential for a gas-phase climate proxy. *Quat. Sci. Rev.* **29**, 28-42 (2010).

72. M. L. Bender, Orbital tuning chronology for the Vostok climate record supported by trapped gas composition. *Earth Planet. Sci. Lett.* **204**, 275-289 (2002).

73. B. Bereiter *et al.*, Revision of the EPICA Dome C CO_2 record from 800 to 600kyr before present. *Geophys. Res.* **42**, 542-549 (2015).

74. P. Köhler, C. Nehrbass-Ahles, J. Schmitt, T. F. Stocker, H. Fischer, A 156 kyr smoothed history of the atmospheric greenhouse gases CO_2, CH_4, and N_2O and their radiative forcing. *Earth Syst. Sci. Data* **9**, 363-387 (2017).

75. I. G. Enting, On the use of smoothing splines to filter CO_2 data. *J. Geophys. Res.-Atmos.* **92**, 10977-10984 (1987).

76. J. Schwander, B. Stauffer, Age difference between polar ice and the air trapped in its bubbles. *Nature* **311**, 45 (1984).

77. R. Spahni *et al.*, The attenuation of fast atmospheric CH_4 variations recorded in polar ice cores. *Geophys. Res.* **30**, 1571 (2003).

78. C. Buizert *et al.*, Gas transport in firn: multiple-tracer characterisation and model intercomparison for NEEM, Northern Greenland. *Atmos. Chem. Phys.* **12**, 4259-4277 (2012).

79. P. Köhler, G. Knorr, D. Buiron, A. Lourantou, J. Chappellaz, Abrupt rise in atmospheric CO_2 at the onset of the Bølling/Allerød: in-situ ice core data versus true atmospheric signals. *Clim. Past* **7**, 473-486 (2011).

80. K. Fourteau *et al.*, Analytical constraints on layered gas trapping and smoothing of atmospheric variability in ice under low-accumulation conditions. *Clim. Past* **13**, 1815-1830 (2017).

81. R. H. Rhodes *et al.*, Local artifacts in ice core methane records caused by layered bubble trapping and in situ production: a multi-site investigation. *Clim. Past* **12**, 1061-1077 (2016).

82. S. Bihorel, M. Baudin, "R Port of the 'Scilab' Neldermead Module" (Version 1.0-11, 2018; https://cran.r-project.org/web/packages/neldermead/neldermead.pdf). [the easiest access to this source is via the URL]

83. F. Parrenin *et al.*, Synchronous change of atmospheric CO_2 and Antarctic temperature during the last deglacial warming. *Science* **339**, 1060-1063 (2013).

84. C. Buizert *et al.*, The WAIS Divide deep ice core WD2014 chronology - Part 1: Methane synchronization (68-31 kaBP) and the gas age-ice age difference. *Clim. Past* **11**, 153-173 (2015).

85. D. York, Least-squares fitting of a straight line. *Can. J. Phys.* **44**, 1079-1086 (1966).

86. D. Lüthi *et al.*, CO_2 and O_2/N_2 variations in and just below the bubble–clathrate transformation zone of Antarctic ice cores. *Earth Planet. Sci. Lett.* **297**, 226-233 (2010).

Acknowledgments: The authors thank M. Häberli, O. Eicher, S. Eggleston, C. Bréant, J. Beck, and B. Seth for assistance with sample acquisition. We acknowledge the support of G. Aufresne who conducted additional CH_4 measurements at IGE. Samples from Site U1385 were provided by the International Ocean Discovery Program (IODP). J. Booth, S. Crowhurst, J. Nicolson, J. Rolfe, and M. Mleneck-Vautravers are thanked for laboratory support. Thanks to R. Walther, S. Marending, K. Grossenbacher, H.P. Moret, and R. Bleisch for technical assistance and E. Brook for helpful comments on an earlier version of the manuscript. **Funding:** This work is a contribution to the "European Project for Ice Coring in Antarctica" (EPICA), a joint European Science Foundation/European Commission scientific program, funded by the European Union and by national contributions from Belgium, Denmark, France, Germany, Italy, The Netherlands, Norway, Sweden, Switzerland, and the United Kingdom. The main logistic support was provided by IPEV and PNRA. This is

EPICA publication no. ###. C.N., J. Schmitt, B.B., F.J., A.S., L. Schmidely, L.Silva, H.F., and T.F.S. acknowledge long-term financial support by the Swiss National Science Foundation (SNF project numbers #200020_159563, #200020_172745, #200020_172506, #200020_172476, and #20FI21_189533). This project is TiPES contribution ###: This project has received funding from the European Union's Horizon 2020 research and innovation program under grant agreement #820970. **Author contributions:** C.N., J. Schmitt, B.B., J.C., D.H., H.F., and T.F.S. designed the research. C.N. performed the measurements with contributions from J. Shin, A.S., G.T, and R.G.. Data analyses were led by C.N. with contributions from J. Schmitt, B.B., F.J., L. Schmidely, L. Silva, D.H., H.F., and T.F.S.. C.N. and T.F.S. led the writing of the manuscript with inputs from all authors. **Competing interests:** The authors declare no competing interests. **Data and materials availability:** All data are available online in the supplementary materials and through the PANGAEA data depository (https://doi.org/10.1594/PANGAEA.915146).

Supplementary Materials:

Materials and Methods
Supplementary text
Figures S1-S9
Table S1
References (*55-86*)
Data S1-S2

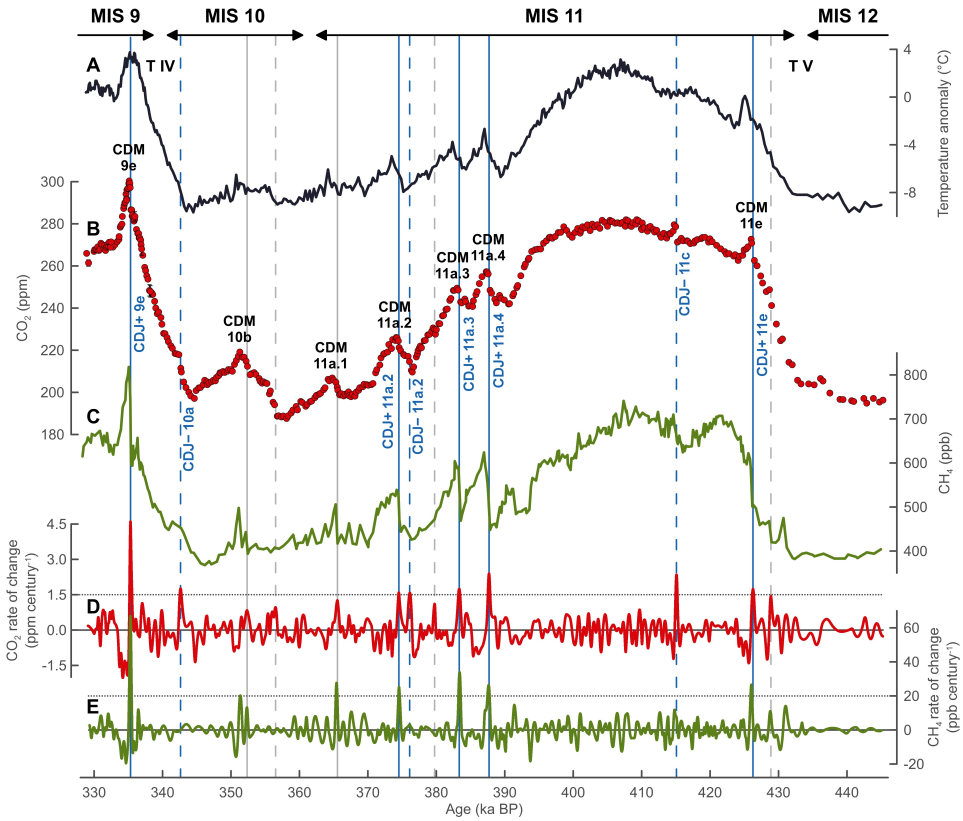

Fig. 1. High-resolution CO_2 and improved CH_4 records compared to Antarctic temperature during MIS 9e - 12a. (**A**) Antarctic temperature anomalies (*10*). (**B**) CO_2 record (this study). (**C**) CH_4 compilation [this study, (*20*)]. (**D**) Rate of change of CO_2 in the ice core record derived from (B) (*20*). (**E**) Rate of change of CH_4 in the ice core record derived from (C) (*20*). All data are based on measurements of EDC ice core samples and are plotted on the AICC2012 age scale (*34*). Identified CDM and CDJ are labelled according to the MIS assignment by Ref. (*19*). Distinct CDJ in the CO_2 record are highlighted by blue vertical lines, positioned at the peaks in (D) exceeding a threshold value of 1.5 ppm per century (*20*). CDJ+ (solid lines) coincide with major CH_4 rises greater 50 ppb at growth rates greater than 20 ppb per century (E), while CDJ− (dashed lines) do not. Further potential events with positive rates below 1.5 ppm per century (D) are not labelled but marked by grey vertical lines.

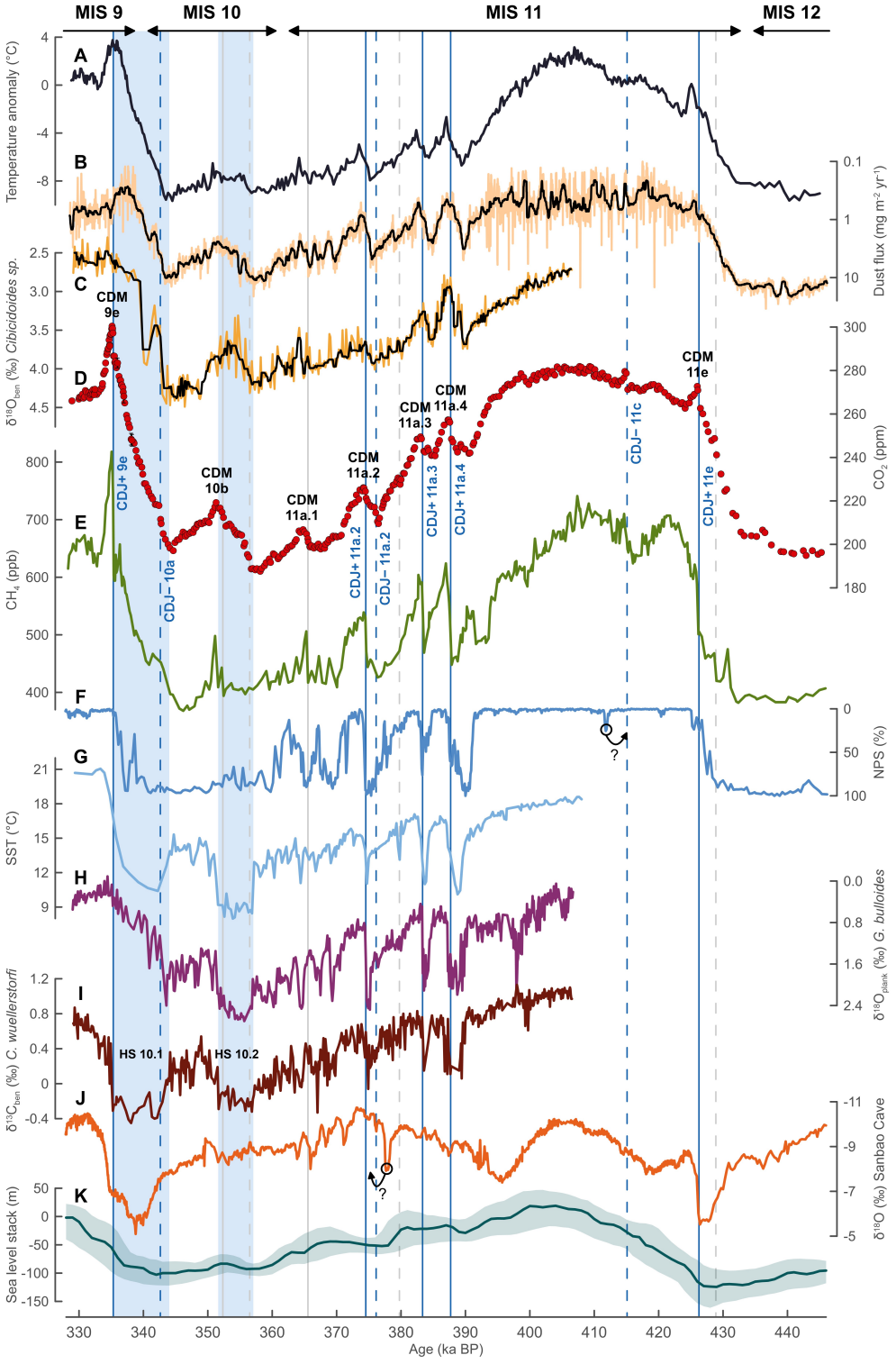
MIS 9
MIS 10
MIS 11
MIS 12
A
B
C
D
E
F
G
H
I
J
K
Temperature anomaly (°C)
Dust flux (mg m⁻² yr⁻¹)
δ18Obsn (‰) Cibicidoides sp.
CO2 (ppm)
CH4 (ppb)
NPS (%)
SST (°C)
δ18Oplank (‰) G. bulloides
δ13Cbsn (‰) C. wuellerstorfi
δ18O (‰) Sanbao Cave
Sea level stack (m)
CDM 9e
CDM 10b
CDM 11a.1
CDM 11a.2
CDM 11a.3
CDM 11a.4
CDM 11e
CDJ+ 9e
CDJ− 10a
CDJ+ 11a.2
CDJ− 11a.2
CDJ+ 11a.3
CDJ+ 11a.4
CDJ− 11c
CDJ+ 11e
HS 10.1
HS 10.2
Age (ka BP)

Fig. 2. Comparison of high-resolution CO_2 and improved CH_4 records with marine sediment and speleothem data covering MIS 9e - 12a. (**A**) EDC temperature anomalies (*10*). (**B**) EDC dust flux (*27*), including a ~500 year running median. (**C**) Benthic $\delta^{18}O$ *C. wuellerstorfi* from IODP Site U1385 on the Iberian Margin (this study), including a ~500 year running median. (**D**) EDC CO_2 record (this study). (**E**) EDC CH_4 compilation [this study, (*20*)]. (**F**) Relative proportion of the polar planktic foraminifera *N. pachyderma* from ODP Site 983 (*38*). (**G**) $U^{k'}_{37}$ based SST from IODP Site U1385 (*26*). (**H**) Planktic $\delta^{18}O$ *G. bulloides* from IODP Site U1385 (this study). (**I**) Benthic $\delta^{13}C$ *C. wuellerstorfi* from IODP Site U1385 (this study). (**J**) $\delta^{18}O$ Sanbao Cave record in Hubei, China (*35*). (**K**) Global sea level stack (probability maximum) including 95% probability intervals (*37*). All records are given on the AICC2012 age scale (*34*) or are transferred to AICC2012 (*20*), with the exception of (J) and (K). Arrows in (F) and (J) highlight potential age scale inconsistencies. Labelling and vertical lines are identical to Fig. 1. Blue bands indicate HS 10.1 and HS 10.2 (see text for details).

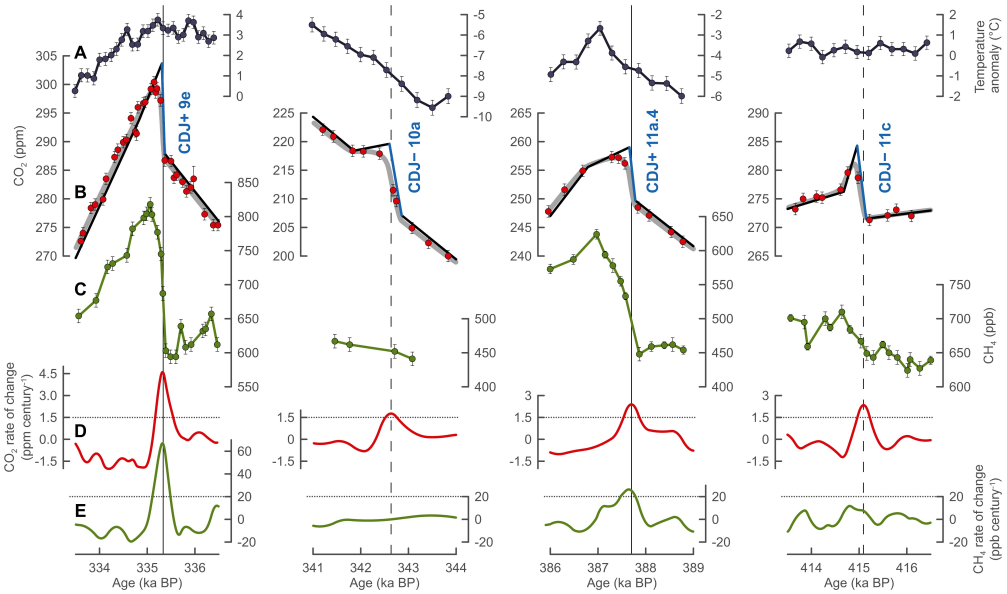

Fig. 3. Detailed view of the two varieties of CDJ. (**A-E**) Identical to Fig. 1. The black linear segments in (B) indicate first-order approximations of the atmospheric CO_2 evolution. The blue segment highlights the actual CDJ event. These approximations for the atmospheric trajectories are optimized, so that the CO_2 curve after smoothing by the bubble enclosure process (grey lines) fit the ice core data (red dots) best. The firn smoothing is realized applying new gas enclosure characteristics for the EDC ice core (*20*). See Table S1 for details. All remaining CDJ are shown in Fig. S1.

Science AAAS

Supplementary Materials for

Abrupt CO_2 Release to the Atmosphere under Glacial and Early Interglacial Climate Conditions

C. Nehrbass-Ahles, J. Shin, J. Schmitt, B. Bereiter, F. Joos, A. Schilt, L. Schmidely, L. Silva, G. Teste, R. Grilli, J. Chappellaz, D. Hodell, H. Fischer, and T. F. Stocker.

correspondence to: cn425@cam.ac.uk

This PDF file includes:

Other Supplementary Materials for this manuscript includes the following:

Data S1 to S2

Materials and Methods

EPICA Dome C CO_2 measurements

The majority of CO_2 measurements on the EPICA Dome C (EDC) ice core were performed at Climate and Environmental Physics (CEP), Physics Institute, University of Bern, Switzerland. The data were measured using the recently developed dry-extraction system, the Centrifugal Ice Microtome (CIM), described in detail in Ref. (*55*). With this friction-free extraction system, we performed a total of 1161 single measurements with a polar ice sample throughput of up to 24 samples per day. On average, individual ice samples weighed 7.3±0.8 g after approximately 5 mm was trimmed from the outer surfaces. Additionally, we performed 463 control measurements throughout the measurement campaign to correct offsets related to the extraction process and to monitor potential system drifts. These measurements involve expanding a standard gas over a gas-free ice sample that is treated identically to a polar ice sample, and is measured against the same calibration gas (*55*). Typically, we made one control measurement for every four polar ice samples amounting to five to seven control measurements per measurement day. Over the course of the measurement campaign, which was approximately one year, the mean control measurement was 2.31±1.21 ppm higher than the calibrated value of the reference gas that has been mixed over the gas-free ice. All polar ice measurements have been corrected using the daily average of these control measurements.

All individual depth levels were measured at least in duplicate. For approximately 50% of all samples, a set of vertically contiguous (i.e., directly neighboring) replicate measurements were performed on a different day, leading to a mean sample replication of three samples per final data point. All CIM measurements were grouped (i.e., averaged) to depth sections of usually ~5 cm (in rare cases up to 12 cm) in the vertical direction, thereby integrating the signal on average over 23±7 years until 425 ka BP (thousand years before present, where present is defined as 1950 CE), and 60±16 years beyond. In total we provide 387 new data points between 330 and 450 ka BP [i.e., Marine Isotope Stage (MIS) 9e - 12a]. The pooled standard deviation for all replicate samples is 1.0 ppm, which is used as an error estimate for all CIM measurements. All CIM CO_2 measurements are referenced to the WMOX2007 mole fraction scale (*56*) using four different primary dry air standards calibrated at the NOAA Earth System Research Laboratory, Boulder, USA ranging between 192.44±0.11 and 363.08±0.06 ppm CO_2.

An additional 33 measurements between 297 and 353 ka BP were performed at the Institut des Géosciences de l'Environnement (IGE), Univ. Grenoble Alpes, France using the Ball Mill extraction technique described in detail in Ref. (*57*). Here, larger samples of 42.5±2.5 g were used. The extracted air of each sample is analyzed five consecutive times (i.e., in total five sample injections into the gas analyzer). The precision of the system amounts to an average of ~1.7 ppm and is based on the standard deviation of these five injections, thus does not include the additional extraction variability of replicate samples. The CO_2 measurements are calibrated using a working standard (233.7±0.4 ppm CO_2, synthetic dry air provided by Air Liquide, Grenoble, France), which has been referenced to two primary dry air standards with calibrated CO_2 mole fractions of 238.34±0.04 ppm and 260.26±0.20 ppm, provided by the NOAA Earth System Research Laboratory, Boulder, USA and the Commonwealth Scientific and Industrial Research Organisation (CSIRO), Australia, respectively.

Gas ages for all CO_2 measurements produced by the CIM and Ball Mill were calculated using the average depth levels of each depth section using the AICC2012 chronology (*34*). We do not find any significant inter-laboratory offset; however, this comparison is only based on 11 directly neighboring samples. Note that due to their lower temporal resolution, the Ball Mill data younger than 328 ka BP are not shown in Fig. 1B and Fig. 2D. All CO_2 data are available in Data S1.

EPICA Dome C CH_4 measurements and compilation of CH_4 data

The existing CH_4 record for MIS 9e - 12a consists of measurements from two experimental setups, one employed at CEP, the other at IGE (*21*). Here we improve the temporal resolution using the same experimental setups. A total of 92 unpublished CH_4 data points had been produced in 2008 using the CEP setup, within the scope of the work by Ref. (*58*), but remained unpublished. The method used for these samples is identical to that described in Ref. (*21*). Secondly, we performed 41 new measurements at IGE at time periods of abrupt climate change connected to Carbon Dioxide Jump (CDJ) events in the CO_2 record. In previous publications, an offset correction between the IGE and CEP setups involved adding 6 ppb to the IGE data (*59*). This correction is obsolete for the new IGE data as an improved contamination correction has been introduced, removing the interlaboratory offset. Lastly, we complement the above described data with 54 published data points by Ref. (*60*), that have been measured at CEP; however, with an independent setup. A visual overview of this data can be found in Fig. S2. All CH_4 data are available in Data S1.

The majority of the 92 CH_4 data points produced by Ref. (*58*) are vertically contiguous (i.e., directly neighboring) to those published by Ref. (*21*) and should be considered replicate measurements. In our CH_4 compilation (Data S1), we combine two individual measurements to one data point in cases where the vertical depth difference between two neighboring CH_4 data points is smaller than 10 cm (typically less than 5 cm). This entails a CH_4 signal integration over 28±14 years on average, which is less than the smoothing resulting from the firn column (see below). The uncertainty of these averaged values is calculated using Gaussian error propagation. We use this CH_4 compilation in all figures showing EDC CH_4 data in MIS 9e - 12a, with the exception of Fig. S2B where the full data set is shown.

Ocean sediment data from IODP Site U1385 (Shackleton site, Iberian Margin)

Isotope data from the International Ocean Discovery Program (IODP) Site U1385 between 329 and 407 ka BP were measured on the planktic foraminifera *G. bulloides* (Fig. 2H) and epibenthic species belonging to the genus *Cibicidoides* (Fig. 2C, 2I). A condensed section or hiatus in the sedimentation rate in older sections covering MIS 11c - e prevents us from reconstructing hydrographic changes on centennial time scales (*61*). Most analyses were made on *C. wuellerstorfi* but when this species was rare, other species were used for benthic $\delta^{18}O$ (i.e., *C. mundulus*, *C. robertsonianus*) (Fig. 2C). Only *C. wuellerstorfi* data are presented for benthic $\delta^{13}C$ (Fig. 2I) because other species may live infaunally and therefore do not record the $\delta^{13}C$ signal of the bottom water. All measurements were made at the Godwin Laboratory of Palaeoclimate Research, University of Cambridge, UK using the same methods as those described in Ref. (*61*). All marine sediment data are available in Data S2.

Piston cores from the Iberian Margin off Portugal contain clear signals of millennial variability of both surface and deep-water masses (*28, 62*). Variations in planktic $\delta^{18}O$ and alkenone saturation index ($U^{k'}_{37}$) reflect the temperature variations in Greenland over the last glacial cycle (*63*). In the same sediment core, the benthic $\delta^{18}O$ signal resembles the δD record in Antarctica ice cores (*28, 62*) capturing each of the Antarctic Isotope Maxima events during the last glaciation (*10*). Millennial variations in benthic $\delta^{18}O$ are affected by changes in deep-water temperature and water mass hydrography, and are assumed to be a signal that originates from the Southern Ocean (SO) (*28, 64*). We synchronized IODP Site U1385 with EDC on the AICC2012 age scale (*34*) by correlating the benthic $\delta^{18}O$ and δD records (Fig. 2C, 2A) (cf. *65, 66*). This correlation results in agreement between the planktic $\delta^{18}O$ record and the CH_4 compilation (Fig. 2H, 2E). The observed phasing of the planktic and benthic $\delta^{18}O$ signals at IODP Site U1385 is consistent with the relative changes in temperature between Antarctica and Greenland deduced from CH_4 synchronization.

Gravitational correction of the CO_2 and CH_4 data

Before small samples of the atmosphere become trapped in the ice, the air first needs to diffuse through the firn column of a polar ice sheet. Under the influence of the Earth's gravitational field heavier molecules become enriched compared to the air that entered the firn at the surface of the ice sheet (*67*), while lighter molecules become depleted. This process is commonly referred to as gravitational settling. The magnitude of this effect is dependent on the thickness of the diffusive firn column and therefore varies with changing temperature and accumulation rates. Atmospheric $\delta^{15}N_2$ (the isotopic signal of N_2) can be safely assumed to be constant over orbital time scales, which makes the $\delta^{15}N_2$ of the air trapped in the ice an ideal tracer of gravitational effects and can also be used to correct for other gas species that are subject to change in the atmosphere, such as CO_2 and CH_4 (*68, 69*).

With approximately 44 g mol^{-1} CO_2 is heavier than the mean molar weight of air, which amounts to 29 g mol^{-1} causing slightly higher CO_2 mole fractions where bubble formation takes place. With 16 g mol^{-1} CH_4 is lighter than air leading to slightly lower CH_4 mole fractions at bubble close off. While the correction of such effects is vital for reconstructions of stable isotopic ratios (e.g., *29*), it was not systematically corrected for in previous studies solely focusing on mole fractions, as the effect is only on the order of 1% of the measured value.

Although this systematic bias is well known, many authors refrained from applying this correction, possibly due to the lack of $\delta^{15}N_2$ data (or similar proxies) or the generally small magnitude of the correction which often was smaller than the measurement precision. However, with steadily increasing technical capabilities and a growing body of $\delta^{15}N_2$ data the above raised arguments are obsolete. In particular, with respect to the accumulating evidence for systematic non-trivial offsets between different CO_2 reconstructions this correction is necessary (*4, 70*).

To estimate the gravitational correction for EDC data, we use $\delta^{15}N_2$ measurements published by Ref. (*71*). For each of our data points, we find the corresponding EDC δD value by linear approximation of the δD data set published by Ref. (*10*). Subsequently, we make use of the linear relationship between δD and $\delta^{15}N_2$ to approximate our $\delta^{15}N_2$ as previously proposed by Ref. (*29*). The Vostok data shown in Fig. S2A are corrected using a linear regression between δD (*10*) and $\delta^{15}N_2$ (*72*). The additional error introduced by this correction is negligible compared to the experimental errors of the CO_2 mole fractions. The gravitational correction for our measurements involves reducing the uncorrected CO_2 data by 1.1 to 2.5 ppm and adding between 2 and 6 ppb to the CH_4 data.

Note that all CO_2 and CH_4 values shown in Fig. 1, 2, 3, S1, and S2 are corrected for gravitational effects. In order to provide CO_2 mole fractions that are consistent with previously published CO_2 compilations where gravitational corrections have not been consistently applied (*73, 74*), we also provide uncorrected CO_2 and CH_4 data in Data S1.

Calculating the rate of CO_2 and CH_4 change in the ice core record

To calculate rate of change in CO_2 (Fig. 1D) on centennial to millennial timescales, superimposed orbital trends have to be removed from the data set first (cf. *66*). This is achieved by subtracting a smoothing spline from the data set (*75*), with cut-off periods (i.e., degrees of smoothing) ranging from 6 to 14 ka (Fig. S3A). Subsequently, we use a second set of smoothing splines with cut-off periods ranging from 0.4 to 1.2 ka to interpolate these detrended data to obtain annually resolved equidistant records (Fig. S3B - F). These interpolated data are used to calculate central finite differences to approximate the first derivative of these CO_2 records (Fig. S3G - K). For the removal of orbital scale variability, we choose the 10 ka cut-off period smoothing function, which is a compromise between preserving sub-millennial scale variability while removing the orbital-scale glacial-interglacial trends. The interpolation of the detrended data is done using a 0.8 ka cut-off period smoothing function, which is a compromise

between the amplification of high-frequency noise and loss of signal amplitude of potential CDJ events (cf. *66*). The same methodology is used for calculating the rate of change in the CH_4 record (Fig. 1E).

Estimating realistic Gas Age Distributions for the EDC ice core

The air trapped at a particular depth of the ice core is a mixture over decades to millennia depending on accumulation rate and site temperature (*76*). The atmospheric air diffuses through the firn column and mixes with older air masses before it gets trapped in the ice. Most importantly, bubbles in the firn-ice transition (lock-in) zone close off slowly and not at the same time which leads to an attenuation or low-pass filtering of the atmospheric signal (*77, 78*). This process scales with the time it takes a single layer of firn/ice to pass through the lock-in zone. The age difference (delta age) between the ice and the mean age of the gas trapped within the ice is a first-order indicator of average accumulation rates over the entire firn column. With decreasing accumulation these effects become more pronounced, leading to a particularly strong signal attenuation and multi-millennial delta ages in the Vostok and EDC ice core that are from low-accumulation sites located on the Antarctic Plateau. The age of the enclosed air after this firn column-induced smoothing is described by a probability density function. It is often referred to as the Gas Age Distribution (GAD), and its width is different for each depth section depending on past accumulation rates and temperatures. Figure S4 shows three typical shapes (blue lines) of commonly used GAD for the EDC ice core (*77, 79*), two of which are representative for warm interglacial (pre-industrial) and cold glacial conditions (Last Glacial Maximum), respectively.

Recently, Ref. (*80*) described an empirical method to estimate GAD for the Vostok ice core based on the direct comparison between continuously measured CH_4 records. This method involves finding a generic GAD that convolves the high-frequency CH_4 signal captured by the West Antarctic Ice Sheet Divide (WD) ice core (*18*) at points of fast CH_4 transitions (in their case DO 17 at ~59 ka BP) to match the smoothed version of the identical atmospheric signal in the Vostok ice core. The assumption is made that the continuous WD CH_4 record provides an insignificantly smoothed version of the atmospheric signal (*6*). Ref. (*80*) raised concern that commonly used modelled estimates of GAD for low-accumulation sites during glacial conditions may be systematically too wide. Consequently, such GAD would lead to a systematic overestimation of the firn column-induced smoothing effect. However, it is yet unknown whether this finding is unique to the Vostok ice core under glacial conditions or whether interglacial GAD estimates are affected in a similar way. Moreover, it is not clear – although likely – whether this applies to other ice cores with similar temperature and accumulation regimes, such as the EDC ice core.

Indirect evidence that commonly used GAD for the EDC ice core (*77*) are too wide comes from a study by Ref. (*79*). They estimated the atmospheric CO_2 rise rates for the CDJ+ found at the onset of the Bølling-Allerød (BA) period (*9*) using a GAD similar to that predicted by Ref. (*77*) (Fig. S4). By comparison with the WD CO_2 record, their estimations were later shown to be clear overestimations of the atmospheric rise rates (*6*), which can be explained by the usage of a too wide GAD in the study by Ref. (*79*).

Following the techniques described in Ref. (*80*), it is possible to test the commonly used modelled GAD (*77*) in the case of the EDC ice core. The WD CH_4 record is available at decadal resolution for the period between 10 and 67 ka BP (*18*), where only discretely measured data are available from the EDC ice core (*21*). In comparison to a continuous record, this record is much lower in resolution (approx. 160 years between 10 and 67 ka BP on average) and suffers from staggered layering artefacts (centimeter-scale age scale reversions) that cannot be unambiguously identified in a non-continuous record (*80, 81*). Furthermore, all measurements

over MIS 3 predating ~30 ka BP are located in the brittle ice zone of the EDC ice core, which is prone to sample contamination by drilling fluid and modern air.

Nevertheless, the discrete EDC CH_4 data are sufficient to construct a first-order approximation of a more realistic GAD. Here, we focus on the onsets of three key periods that are associated with fast atmospheric CH_4 rises, namely the Preboral (PB), Younger Dryas (YD), and the BA. In addition, we also include Dansgaard-Oeschger (DO) events 6 - 8 between 33 and 39 ka BP (Fig. S5) associated with a major CH_4 rise for each DO event. Together with the data available for the last deglaciation (10 to 22 ka BP), this interval has the highest temporal resolution (~100 years) in the 10 to 67 ka BP interval where continuous WD CH_4 data are available (*18*). We assume that the GAD can be approximated by log-normal distributions (*79, 80*) and that a single GAD is representative for the enclosure characteristics for these events. Log-normal functions are described by two free parameters: the mean (μ) and standard deviation (σ) of the logarithm. For the sake of simplicity, we fix the standard deviation at a value of σ=1.5 (*80*) and vary only the mean to change the shape of our GAD. We also report the arithmetic mean of the log-normal function [referred to as expected mean in Ref. (*79*)] representing the width of the GAD, given in years (Table S1). The arithmetic mean of a log-normal distribution is given by

$$GAD_{mean} = e^{\mu+0.5\sigma^2}. \quad \text{Eq. S1}$$

We use the *fminbnd* function of the 'neldermead' package in R (*82*) to optimize the EDC bubble enclosure characteristics by smoothing the WD CH_4 data (*18*) to fit the EDC data (*21*). The optimal GAD is determined by minimizing the root-mean-square error (RMSE) between the convoluted WD CH_4 signal and the discrete EDC data, spanning a 2 ka time window centered around the inflection point of the abrupt CH_4 rise in the EDC record (Fig. S5). We allow for linear adjustments of the discrete EDC data relative to the continuous WD CH_4 data to compensate for the temporal shift induced by the convolution of the WD CH_4 signal (*79*), as well as general age scale and standardization inconsistencies. To acknowledge the dependency on the absolute value of individual data points we apply a Monte Carlo type approach and vary the discrete CH_4 data within their uncertainty boundaries (±10 ppb) in a random manner. We use the average of 500 iterations to determine the most suitable GAD width for each event. In this context the choice of age scale is critical, as it has a strong influence on the duration of an event. Therefore, we use the age scale as published by Ref. (*83*) that has been specifically optimized for the deglaciation period and includes the PB, YD, and BA events. Note that for all other purposes the AICC2012 age scale is used (*34*). For the glacial GAD – as represented by DO 6 - 8 between 33 and 39 ka BP – a longer time window is chosen for the optimization to compensate for the influence of age scale inconsistencies between the AICC2012 (discrete EDC CH_4 data) (*34*) and the WD2014 age scale (continuous WD CH_4 data) (*84*) and minimize the influence of potential staggered layering artefacts (*18, 80*) in this section (Fig. S5).

The smoothed versions of the WD CH_4 record match the discrete EDC CH_4 data well for all three events during the deglaciation (Fig. S5). In the case of DO 6 - 8 the size of each event in the discrete EDC data is well captured by the smoothed version of the WD CH_4 record, despite obvious age scales issues, indicated by relative shifts between the discrete and smoothed continuous records. The results of this optimization (Fig. S4, S5) point towards a substantial overestimation of the smoothing produced by commonly used modelled EDC enclosure characteristics (*77*), in line with Ref. (*80*).

Since these four time periods are only representative for a given firn column condition, we strive to find a simple model that allows to estimate the GAD width (Eq. S1) for other firn column conditions at Dome C, as approximated by the delta age. Therefore, we plot the arithmetic means of the GAD found for the PB, YD, BA, and DO 6 - 8 against their respective

delta age to the nearest 0.1 ka (Fig. S6). Delta ages are derived from the AICC2012 age scale (*34*) by subtracting the assigned gas age from the respective ice age for each depth interval. We use a 2 ka time window centered around the inflection point of each event to find the corresponding average delta age given on the ice age scale. Subsequently, a linear regression model incorporating the uncertainties for both variables (*85*) is utilized to obtain the following empirical relationship:

$$GAD_{mean} = 0.048(\pm 0.025) \times delta\ age\ (in\ years) + 17(\pm 67)\ years. \quad \text{Eq. S2}$$

This linear function serves as a first-order approximation of more realistic GAD for the EDC ice core, assuming a linear scaling of the GAD width with delta age.

We stress that these GAD estimates are limited in several aspects. Most importantly, these estimates are highly dependent on the used age scale, as the duration of fast CH_4 transitions and the delta age estimate may vary considerably. Also the choice of the GAD template (here a log-normal distribution) might have an influence on the quantitative outcome of this analysis. However, the good correspondence of the WD record smoothed by a log-normal GAD with the measured EDC record strongly suggests that such an influence does not affect the overall conclusions of our study. We recommend that this case study is repeated when higher resolution data from the EDC ice core for selected time periods of fast atmospheric CH_4 change and improved empiric GAD information become available.

Inversed convolution of Carbon Dioxide Jumps

The rates of CO_2 increase archived in the ice core record during CDJ can only be interpreted as lower limits for the unfiltered atmospheric rates. Independent of the original atmospheric trajectory, the growth rates in atmospheric CO_2 must have been higher than recorded in the smoothed ice core record. It is therefore important to consider the air enclosure characteristics of the EDC ice core when attempting to deconvolute the ice core signal and estimate potential atmospheric rates.

Using our GAD estimates for the EDC ice core derived as described above, we provide first-order estimates of atmospheric duration, magnitude of the CO_2 rise, and growth rates for each event identified here. To achieve this, we assume that the centennial to millennial-scale atmospheric trajectories can be approximated by a simple set of linear functions. Our atmospheric rates are estimated following these steps: (i) Find the delta age for the CDJ using the AICC2012 age scale (*34*); (ii) determine a suitable GAD using the linear relationship described above; (iii) guess a simple atmospheric trajectory, smooth this guess using the GAD, calculate RMSE between smoothed guess and the actual CO_2 data, and optimize this atmospheric guess using the Nelder-Mead algorithm; (iv) repeat step (iii) 200 times with randomly modified CO_2 record within the measurement uncertainty (±1 ppm); (v) calculate the median values for the duration, magnitude of the CO_2 rise, and growth rates for each CDJ of these 200 iterations, as indicated by blue segments in Fig. 3B and S1B. The results are shown in Table S1, where the interquartile range of these 200 iterations is used as an error estimate.

Supplementary Text

Comparison of the new CO_2 data set with previously published records

Our new EDC CO_2 data overall agree with the published Vostok 5G measurements [Fig. S2A, (*1*)]. Differences in the two records can be explained by age scale uncertainties beyond 355 ka BP due to the lack of stratigraphic tie points in the Vostok record, leading to inconsistencies of up to ~10 ka (*33, 34*). During MIS 11c - e (~390 to 430 ka BP) our data agree well with the data published by Ref. (*2*) measured on the same ice core. No difference in average mole fractions is found; however, the precision of our new data has been increased

substantially. Towards MIS 12a our new data develops an offset with respect to the data published by Ref. (*2*). Based on the time interval between 438 and 446 ka BP, where CO_2 appears to be stable at a level of 196.2±0.7 ppm (CIM measurements), we determine an offset of 3.5±1.4 ppm between the record published by Ref. (*2*) and our new CIM data, with our data showing lower mole fractions. Such offsets between different Antarctic records are well known, but still lack a coherent explanation and responsible mechanisms are hard to distinguish from each other (*4, 70*). However, the majority of mechanisms cause the CO_2 mole fractions to increase over time, for example due to preferential loss of oxygen during storage of the samples (*4, 70*). The only known effects that lead to lower CO_2 measurements are related to the combination of measurement setups with low extraction efficiencies and ice from either the so called Bubble to Clathrate Transition Zone (*57, 86*) or from depth sections in EDC deeper than 3000 m (*73*). Both mechanisms can be excluded here. Instead, we speculate that the offset is an issue related to standardization methods. While the new data were calibrated using standard reference gases ranging between 192 and 363 ppm (see Materials and Methods), Ref. (*2*) used air standards only ranging between 252 and 342 ppm (cf. *9*), i.e., the lowest concentration standard was still about 50 ppm higher than the lowest measured ice core mole fraction during MIS 12a. In any case, this small glacial offset between the new and older EDC data from this time interval does not affect any of the conclusions drawn in our study.

Estimating the detection limit for CDJ during MIS 9e - 12a in the EPICA Dome C ice core

The absence of CDJ (according to our CDJ definition in the main text) between MIS 10a and late MIS 11a (~345 to 370 ka BP) as well as between early MIS 11e and MIS 12a (~430 to 445 ka BP) raises the question of whether no CDJ events occurred during these periods or if we are only unable to detect them.

It is possible that we do not detect potential CDJ that are smaller than a certain threshold due to the firn column-induced attenuation of the original atmospheric signal. This smoothing effect is strongest for the glacial maxima when temperatures and accumulation rates are at their lowest. Besides the amount of firn smoothing, the detection limit for CDJ in our CO_2 record also depends on the original atmospheric rates and durations of carbon releases to the atmosphere.

We simulate the resulting rate of change of CO_2 as it would be recorded in the EDC ice core (cf. Fig. 1D, 3D, S1D) by smoothing generic CDJ (i.e., simple step functions) and subsequently calculating their rate of change using the same methodology as described above (Fig. S7). We use the maximum firn column-induced smoothing in the MIS 9e - 12a interval, which is found for the glacial maximum during MIS 12a when the delta age reaches its maximum at 4.5±0.3 ka (*34*) resulting in an arithmetic mean of 233±132 years (Eq. S2) for the GAD used here.

Figure S8 demonstrates the influence of both the simulated magnitude of the CO_2 rise (rows) and event duration (columns) in the atmosphere on the estimated growth rates of a CDJ event as it would be recorded by ice core record, whereas Fig. S7 visualizes the impact of different magnitudes of the CO_2 rise at a fixed CDJ duration (Fig. S7A - C) and *vice versa* (Fig. S7D - F).

Other factors – such as sample availability – may also influence the theoretical detection limit, which can lead to the overestimation of the estimated CDJ duration and underestimation of the determined atmospheric CO_2 rise and growth rate. This may be the case for CDJ– 11a.2, CDJ+ 11a.3, and CDJ+ 11e (Fig. S1). In case of CDJ+ 11e – where we exploited all available ice in this depth section – the CH_4 data suggest a later onset of the CDJ by ~100 years (i.e., a shorter duration) than we estimate based on the inverse convolution of the ice core signal (Table S1). The low ice availability is a result of earlier sampling (e.g., *2, 21, 60*) and generally lower ice availability due to low-accumulation rates during the MIS 12a - 11e transition

(Termination V) in the EDC ice core. While the majority of our CO_2 dataset is only marginally affected by limited sample availability, we cannot exclude that potential CDJ with CO_2 rises greater than ~5 ppm remain undetected during the MIS 12a - 11e transition.

In summary, based on the above theoretical considerations we should be able to detect CDJ with an atmospheric CO_2 rises greater than ~5 ppm and a duration of less than ~250 years throughout MIS 9e - 11e, i.e., the majority of our record. The finding is supported by the identification of the third largest CDJ of all eight CDJ identified in this study (CDJ– 10.a; Table S1), which takes place among the coldest conditions during the entire MIS 10a - 11a glacial period. Consequently, CDJ– 10a is associated with more pronounced firn column-induced smoothing of the atmospheric signal as compared to the preceding MIS 10b to late MIS 11a interval (i.e., ~345 to 370 ka BP) where no CDJ are found (Fig. 1), confirming that we do capture major CDJ even when the firn column-induced signal attenuation is relatively strong.

We speculate that CDJ+ become less likely with decreasing temperatures during a glacial period based on previously published lower precision CO_2 data. We assume that at least four CDJ+ occurred during MIS 5a - c associated with DO 19 - 21 and DO 24 based on apparent jumps in the CO_2 trajectories at the time of sharp CH_4 rises (*4, 8*), but no robust conclusion can be drawn from these data. With advancing glacial conditions (i.e., decreasing temperatures and lower sea levels) towards MIS 3 the climatic conditions seem to no longer permit the formation of major CDJ+ (*4, 5, 8*). A single CDJ– associated with Heinrich Stadial (HS) 4 (*12, 13*) is the only CDJ identified for the MIS 3 interval so far, with no indications of CDJ+ associated with major Carbon Dioxide Maxima (CDM) 4, 8, 12, 14, and 17 (numbering refers to the associated DO event) (*4, 8*). With the onset of the last deglaciation connected with rising temperatures and sea level, both types of CDJ seem to become more likely again (*6, 30*). It is thus conceivable that the climatic boundary conditions found during the early glacial growth phases (e.g., MIS 11a, MIS 5a - c) are favorable conditions for the formation of CDJ+ events, that seem to cease towards the coldest conditions reached during the glacial maxima of each glacial cycle (e.g., MIS 10, MIS 3). CDJ–, on the other hand, seem to depend on specific conditions potentially triggered by major freshwater forcing.

CH_4 excursions during Heinrich Stadials in the EPICA Dome C ice core

By comparison with the CDJ− found for HS1 (*6*) and HS4 (*12*), we would expect to find simultaneous short-lived overshoots in the CH_4 record, with amplitudes of less than ~50 ppb (*18*). However, the CDJ− identified here (i.e., CDJ− 10a, 11a2, 11c) show no indication of such signals in the CH_4 data.

We argue that such events cannot be resolved with currently available discrete EDC CH_4 data. This statement is based on considerations for the known events for HS1 and HS4 (*18*), that are smoothed using our linear model for delta age dependent GAD (Fig. S9). In both cases the short-lived CH_4 overshoot is attenuated to a level that cannot be detected in the EDC ice core, at least by using the discrete CH_4 data from Ref. (*21*), due to insufficient temporal resolution and measurement precision. This is in line with Ref. (*80*), who showed that comparable sub-centennial-scale CH_4 variations around DO 17 in the WD CH_4 record are smoothed out in the Vostok ice core.

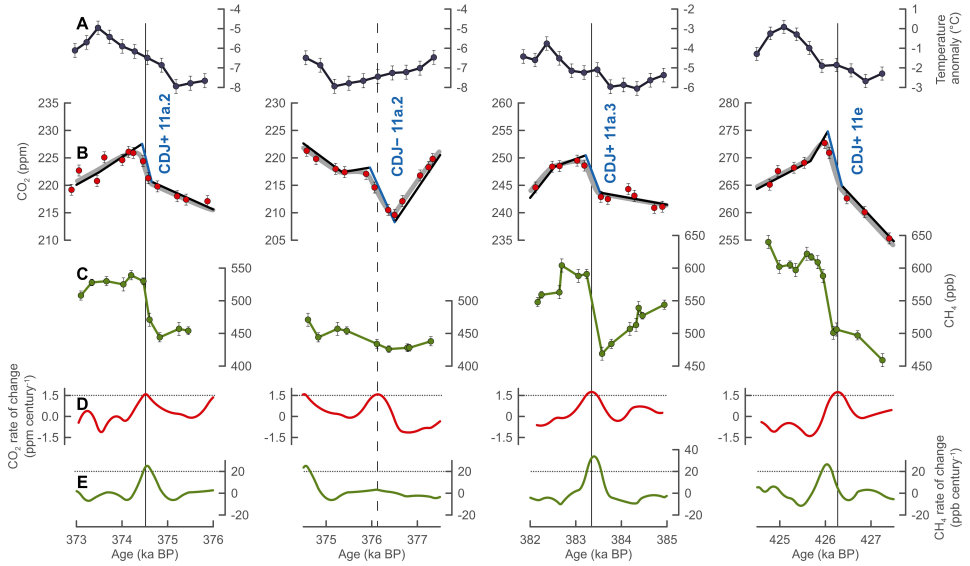

Fig. S1. Extension of Fig. 3. Detailed view of the two varieties of Carbon Dioxide Jumps (CDJ) in the EPICA Dome C (EDC) ice core. (**A**) EDC temperature anomalies (*11*) (**B**) CO_2 data (this study). (**C**) CH_4 compilation (this study, see materials and methods for details). (**D**) Rate of change in CO_2 (cf. Fig. 1D). (**E**) Rate of change in CH_4 (cf. Fig. 1E). CDJ+ are coeval with DO-like CH_4 rises greater 50 ppb at growth rates greater than 20 ppb per century (D), whereas CDJ− are not. The black linear segments in (B) indicate first-order approximations of the atmospheric CO_2 evolution. The blue segment highlights the actual CDJ event. These approximations for the atmospheric trajectories are optimized so that the CO_2 curve after smoothing by the bubble enclosure process (grey lines) fit the ice core data (red points) best. The firn smoothing is realized by applying new gas enclosure characteristics for the EDC ice core (Fig. S4 - S6). See Table S1 for details. All remaining CDJ are shown in Fig. 3.

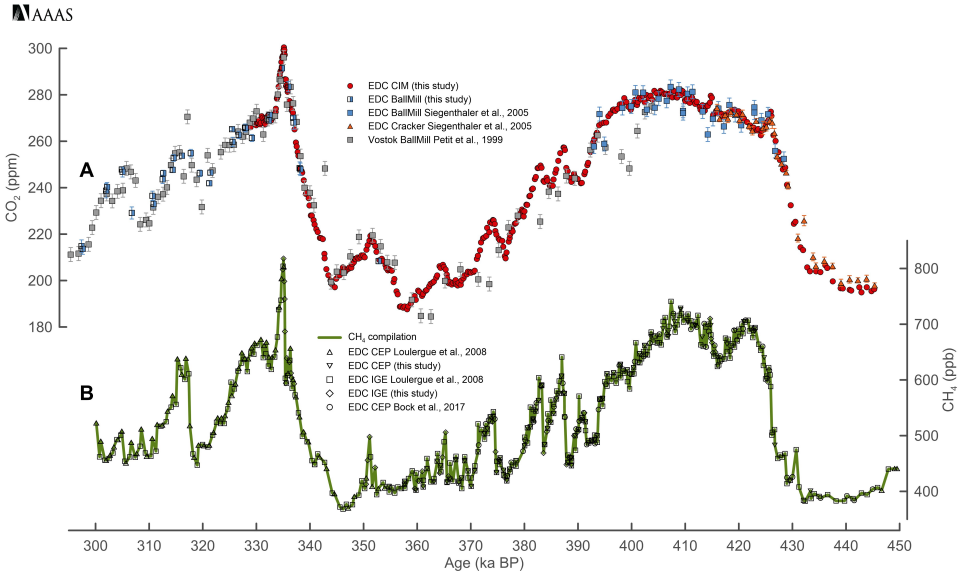

Fig. S2. Comparison between our CO_2 and CH_4 data from the EPICA Dome C (EDC) ice core with previously published data. (**A**) The new EDC CO_2 record overlaps with CO_2 data from the Vostok 5G ice core during 300 to 400 ka BP (*1*) and with previously published data from EDC during 390 to 450 ka BP (*2*). Note that the CO_2 data sets shown here were measured using three different dry extraction devices, namely the Centrifugal Ice Microtome (CIM) (*55*) and the Needle Cracker (*2*) employed at Climate and Environmental Physics (CEP), Physics Institute, University of Bern and the Ball Mill (*1, 2*) employed at the Institut des Géosciences de l'Environnement (IGE), Univ. Grenoble Alpes. (**B**) EDC CH_4 data, mainly based on data published by Ref. (*19*), complemented with new measurements (this study) and previously published data (*60*), all measured at CEP and IGE. Error bars for CH_4 are omitted for clarity. See legends for details.

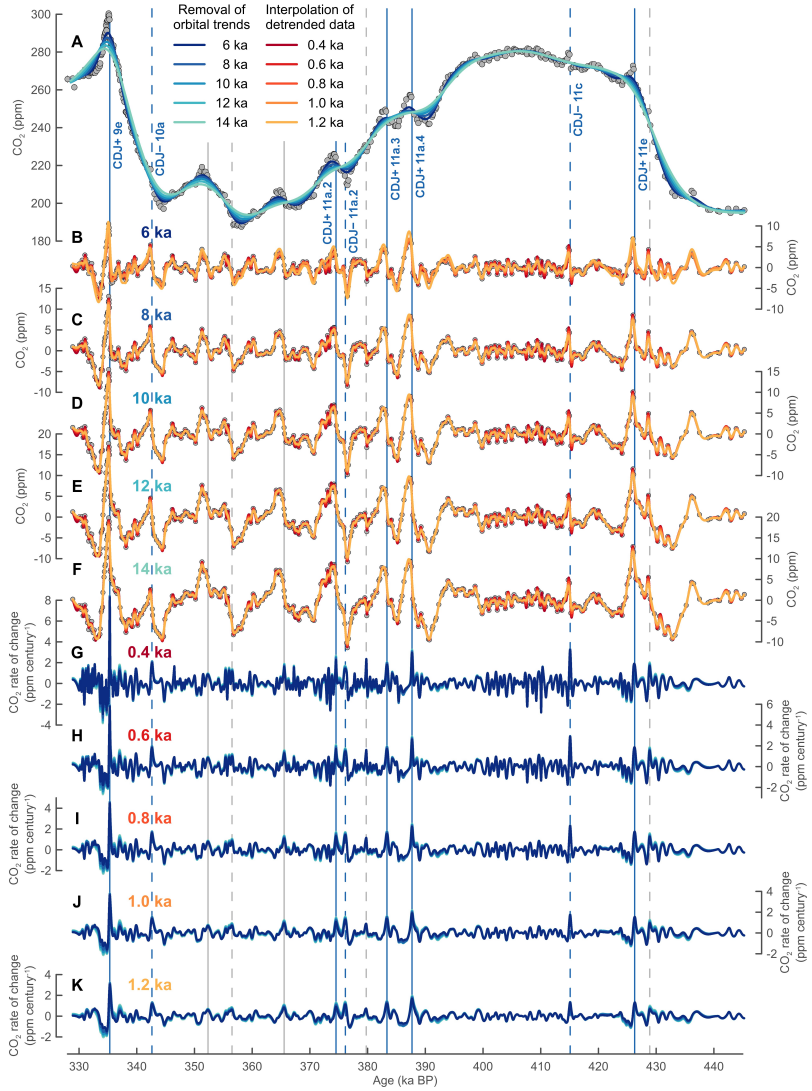

Fig. S3. Calculating the rate of change for our CO_2 record from the EPICA Dome C (EDC) ice core. (**A**) Removal of orbital to multi-millennial trends from the EDC CO_2 record (grey dots, this study) using five different smoothing splines (*75*) with cut-off periods (i.e., degrees of smoothing) ranging from 6 to 14 ka. (**B-F**) Detrended EDC CO_2 record after subtraction of splines shown in (A). A second set of five smoothing splines with cut-off periods ranging from 0.4 to 1.2 ka is applied onto the different detrended data sets, resulting in five times five annually resolved equidistant records containing only the centennial-scale variability. (**G-K**) Resulting rates of change of the detrended and interpolated CO_2 data from (B-F), grouped by their variant of spline interpolation. See legends for color-coding. Labelling and vertical lines are identical to Fig. 1.

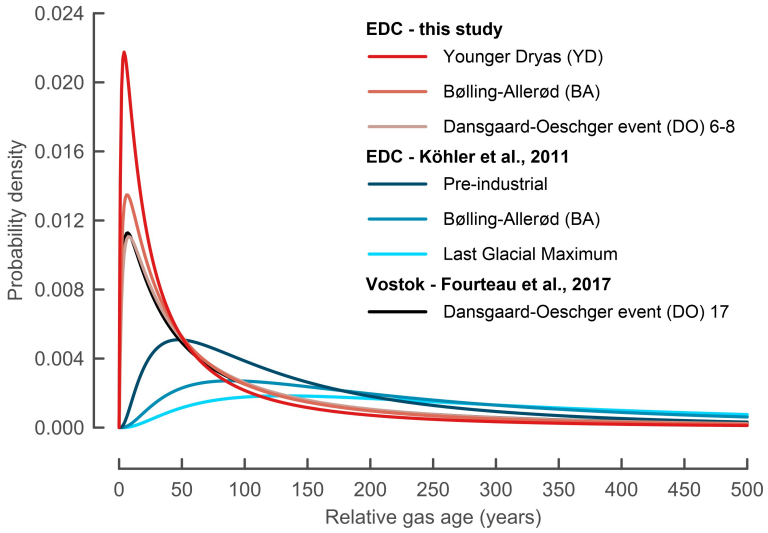

Fig. S4. Gas Age Distributions (GAD) for the low-accumulation sites EPICA Dome C (EDC) and Vostok for different climatic boundary conditions. All GAD shown here are represented by log-normal functions. The scenarios by Ref. (*79*) are approximations for the firn model outputs by Ref. (*77*), while our estimates are based on empirical smoothing of the West Antarctic Ice Sheet Divide (WD) CH_4 record to resemble the effective EDC CH_4 measurements (cf. Fig. S5, S6). The estimated GAD for the Preboreal (PB) is nearly congruent with the GAD for the Younger Dryas (YD) event and is omitted for clarity.

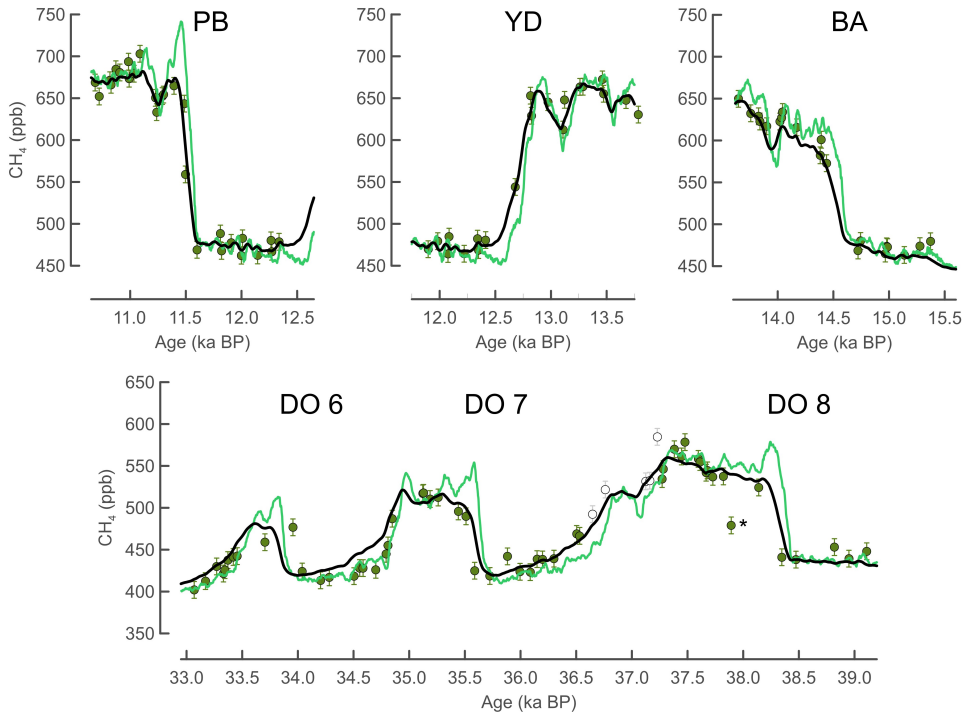

Fig. S5. Abrupt CH_4 transitions at the onsets of four different climatic periods during the last deglaciation and glacial period used for determining Gas Age Distributions (GAD) for the EPICA Dome C (EDC) ice core. These events include the onsets of the Preboral (PB), Younger Dryas (YD), and Bølling-Allerød (BA) during the last deglaciation (*21, 83*) and Dansgaard-Oeschger events (DO) 6 - 8 (*21, 34*) representative for firn column conditions during the colder glacial period. The black lines represent smoothed versions of the continuous West Antarctic Ice Sheet Divide (WD) ice core CH_4 data (light green lines) (*18*). The smoothed signals shown here (black lines) are produced using the mean values from 500 optimization iterations with the discrete EDC CH_4 data (green dots) varied within their uncertainty boundaries. White points in the lower panel lie outside the 2 ka optimization windows centered around the inflection points of the sharp CH_4 rises. The outlier (*) in the discrete EDC CH_4 data at 37.9 ka BP may be an artefact explained by staggered layering and has been excluded from the optimization runs (*80, 81*). See materials and methods for details.

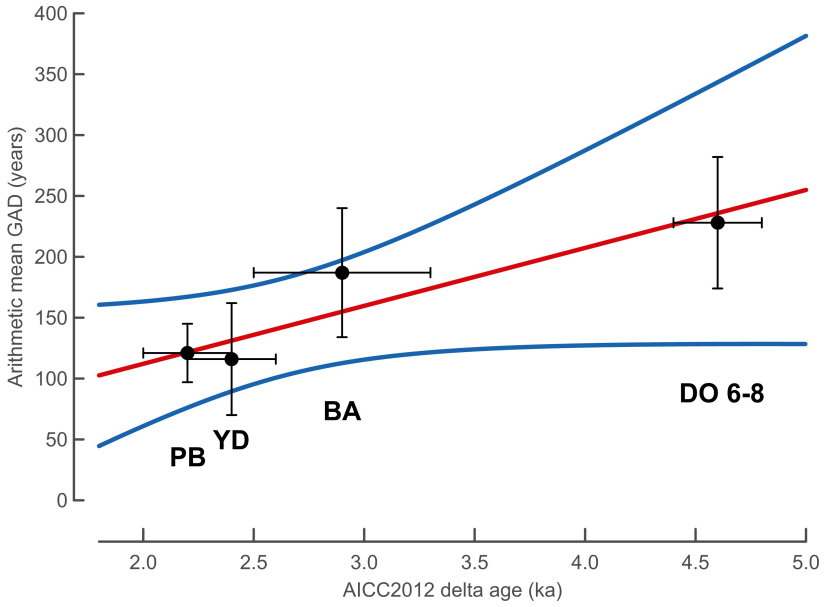

Fig. S6. Linear fit of optimized arithmetic mean values of estimated Gas Age Distributions (GAD) for the EPICA Dome C (EDC) ice core. The arithmetic means are based on a direct comparison between smoothed versions of the continuous CH_4 data from the West Antarctic Ice Sheet Divide (WD) ice core (*18*) and discrete data from EDC ice core (*21, 83*) (Fig. S5). The gas-ice difference (delta age) was determined using the AICC2012 age scale (*34*). Here we focus on the onsets of three key periods, including the Preboral (PB), Younger Dryas (YD), and Bølling-Allerød (BA) periods all characterized by abrupt CH_4 rises. In addition, we also include Dansgaard-Oeschger events (DO) 6 - 8 representative for firn column conditions during the colder glacial period. The used linear regression model (red line, R^2=0.85), including the 95% confidence intervals (blue lines), takes both variable uncertainties (±2 sigma) into account (*85*). All GAD are approximated by log-normal functions. See Fig. S5, Eq. S2, and materials and methods for details.

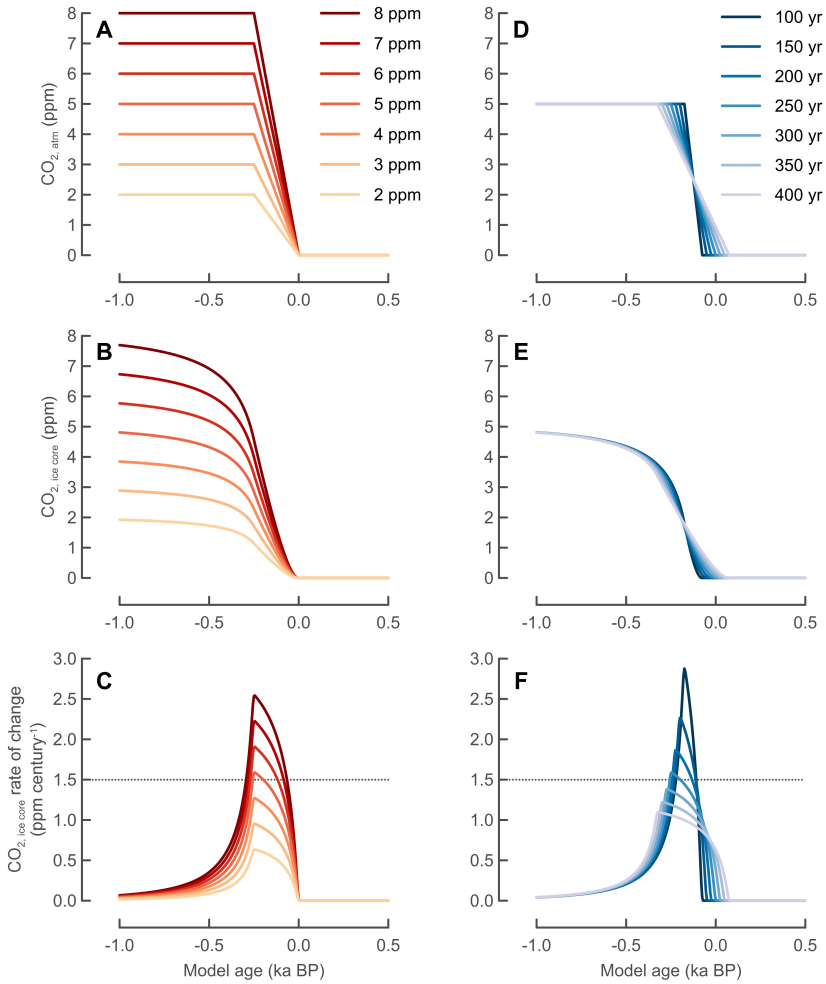

Fig. S7. Detection limit for Carbon Dioxide Jumps (CDJ). (**A**) Generic CDJ events (i.e., simple step functions) with atmospheric CO_2 rises ranging from 2 to 8 ppm and constant durations of 250 years. (**B**) Firn column smoothed version of (A) mimicking signals as they would be recorded by the EPICA Dome C ice core during the MIS 12a glacial maximum. MIS 12a represents the coldest interval associated with the strongest firn column-induced smoothing during MIS 9e - 12a. We estimate an arithmetic mean of 233±132 years for the Gas Age Distribution (GAD) at MIS 12a (Eq. S2) based on an estimated delta age of 4.5±0.3 ka (*34*) (see materials and methods for details). (**C**) Resulting rate of change of (B), comparable to what would be expected to be found in our ice core record (cf. Fig. S3). (**D-F**) Same as (A-C) but fixed 5 ppm CO_2 rises and changing durations (100 to 400 years). The dotted lines in (C) and (F) indicate the chosen threshold of 1.5 ppm per century in our CO_2 ice core record analyses (Fig. 1) used to identify CDJ events. See Fig. S8 for a comprehensive matrix of varying combinations of atmospheric CO_2 rises and durations. See supplementary text for details.

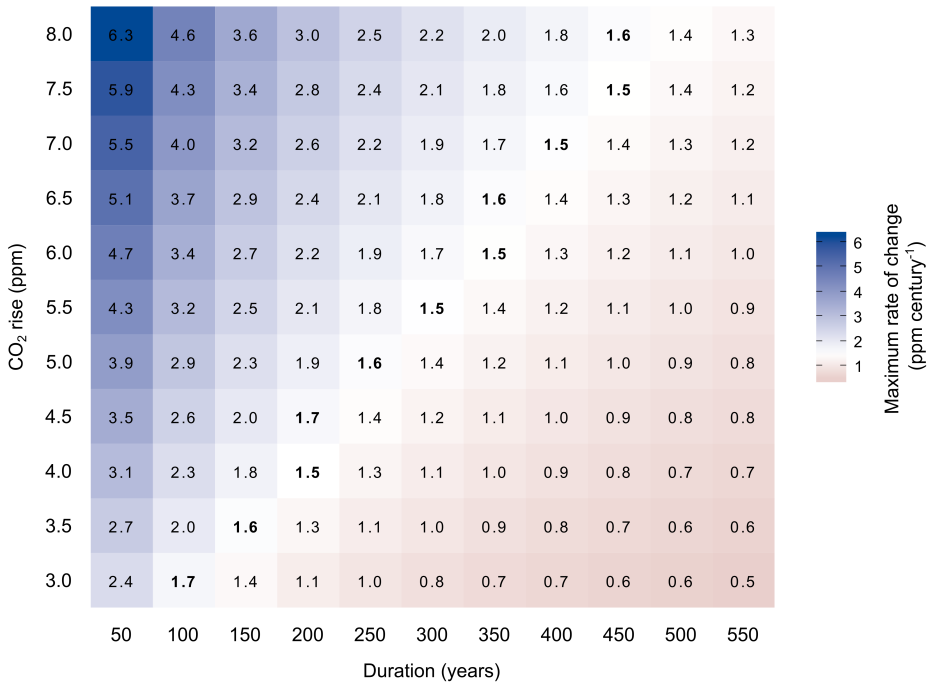

Fig. S8. Heat map of maximum amplitudes in the rates of change of generic Carbon Dioxide Jumps (CDJ) with varying atmospheric CO_2 rises and durations. Generic CDJ with CO_2 rises ranging from 3 to 8 ppm and durations ranging from 50 to 550 years in the atmosphere are smoothed to simulate a signal as it would be archived in the EPICA Dome C (EDC) ice core. Tiles represent peak values of the calculated rate of change of the simulated ice core signal. Identical methodologies to Fig. S7 are used (see supplementary text for details). All combinations of atmospheric CO_2 rises and durations exceeding the threshold value of 1.5 ppm per century in the ice core record would be identified as a CDJ in our EDC CO_2 record. For each magnitude of CO_2 rise (rows) the highest permissible duration that would just allow for CDJ detection is highlighted in bold.

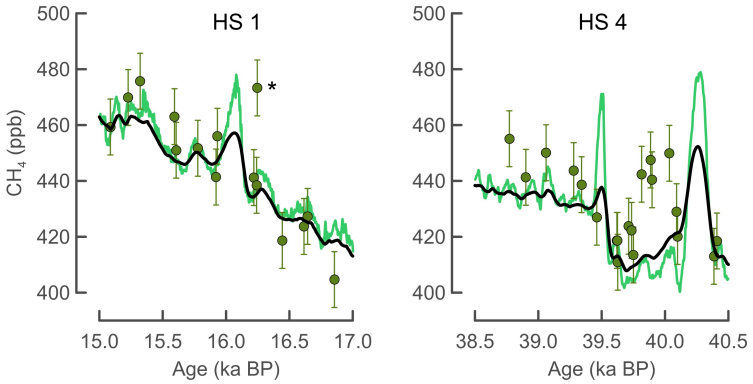

Fig. S9. Smoothing of short-lived overshoots in the CH_4 record in case of the EPICA Dome C (EDC) ice core. An estimation of the EDC firn column-induced smoothing (black line) of short-lived, small amplitude CH_4 overshoots (centered peaks) found in the continuous West Antarctic Ice Sheet Divide (WD) CH_4 record (light green line) for Heinrich Stadials (HS)1 and HS4 (*18*) during the last glacial period. The WD CH_4 record is smoothed using the linear relationship for EDC gas enclosure characteristics established in Fig. S6 (Eq. S2), assuming a gas-ice age difference (delta age) of 3.1±0.3 ka and 4.1±0.3 ka (*34*), resulting in GADs with arithmetic means of 166±103 years (HS1) and 214±123 years (HS4), respectively. Discrete EDC CH_4 data are shown as green dots. Note that mismatches in both records can be explained by age scale inconsistencies. The outlier in the EDC CH_4 record in close proximity to the HS1 WD CH_4 event (*) can likely be explained by staggered layering effects (*80, 81*) and should not be interpreted as an indicator for reduced smoothing of the EDC ice core.

Event	Duration (years)	CO_2 rise (ppm)	Growth rate (ppm century^{-1})	Delta age (ka)	GAD_{mean} (years)
CDJ+ 9e	59±35	15.8±1.1	26.2±17.6	1.8±0.3	103±82
CDJ− 10a	257±81	12.3±1.9	4.9±1.7	3.3±0.3	175±107
CDJ+ 11a.2	203±160	6.8±1.5	3.4±2.6	2.9±0.3	156±100
CDJ− 11a.2	540±170	10.0±1.8	1.9±0.5	3.0±0.3	161±102
CDJ+ 11a.3	225±176	6.7±1.3	3.0±2.1	2.9±0.3	156±100
CDJ+ 11a.4	140±110	9.3±1.2	6.9±6.7	2.9±0.3	156±100
CDJ− 11c	191±123	12.9±2.7	6.9±5.3	2.1±0.3	118±86
CDJ+ 11e	312±103	9.9±1.7	3.2±1.0	2.2±0.3	123±88

Table S1. Estimated atmospheric characteristics for identified Carbon Dioxide Jumps (CDJ). Estimates are based on empirically-derived gas enclosure (firn smoothing) characteristics for the EPICA Dome C (EDC) ice core, commonly referred to as Gas Age Distributions (GAD). The widths of the GAD (GAD_{mean}) are determined based on the ice-gas age difference (delta age) as derived from the AICC2012 age scale (*34*). See materials and methods, Fig. 3B, S1B, S6, and Eq. S2 for details. Note that in the case of CDJ+ 11e the duration is likely overestimated whereas the rate of change is likely underestimated. See supplementary text and Fig. S1 for details.

Data S1 (separate file). Antarctic ice core derived CO_2 and CH_4 data from the EPICA Dome C (EDC) ice core covering Marine Isotope Stage 9e - 12a. An additional compilation of the CH_4 data is provided in a separate worksheet. See materials and methods in the supplementary materials for details.

Data S2 (separate file). Marine sediment core derived planktic $\delta^{18}O$ *G. bulloides* and benthic $\delta^{18}O$ and $\delta^{13}C$ *C. wuellerstorfi* from the International Ocean Discovery Program (IODP) Site U1385 covering Marine Isotope Stage 9e - 12a. See materials and methods in the supplementary materials for details.

5.2 Millennial-scale atmospheric CO_2 variations during the Marine Isotope Stage 6 period (190–135 ka)

Jinhwa Shin, Christoph Nehrbass-Ahles, Roberto Grilli, Jai Chowdhry Beeman, Frédéric Parrenin, Grégory Teste, Amaelle Landais, Loïc Schmidely, **Lucas Silva**, Jochen Schmitt, Bernhard Bereiter, Thomas F. Stocker, Hubertus Fischer and Jérôme Chappellaz

Published in *Climate of the Past*, 16, 2203-2219 (2020) (doi: 10.5194/cp-16-2203-2020)

Abstract Using new and previously published CO_2 data from the EPICA Dome C ice core (EDC), we reconstruct a new high-resolution record of atmospheric CO_2 during Marine Isotope Stage (MIS) 6 (190 to 135 ka) the penultimate glacial period. Similar to the last glacial cycle, where high-resolution data already exists, our record shows that during longer North Atlantic (NA) stadials, millennial CO_2 variations during MIS 6 are clearly coincident with the bipolar seesaw signal in the Antarctic temperature record. However, during one short stadial in the NA, atmospheric CO_2 variation is small (∼5 ppm) and the relationship between temperature variations in EDC and atmospheric CO_2 is unclear. The magnitude of CO_2 increase during Carbon Dioxide Maxima (CDM) is closely related to the NA stadial duration in both MIS 6 and MIS 3 (60—27 ka). This observation implies that during the last two glacials the overall bipolar seesaw coupling of climate and atmospheric CO_2 operated similarly. In addition, similar to the last glacial period, CDM during the earliest MIS 6 show different lags with respect to the corresponding abrupt CH_4 rises, the latter reflecting rapid warming in the Northern Hemisphere (NH). During MIS 6i at around 181.5±0.3 ka, CDM 6i lags the abrupt warming in the NH by only 240±320 years. However, during CDM 6iv (171.1±0.2 ka) and CDM 6iii (175.4±0.4 ka) the lag is much longer: 1290±540 years on average. We speculate that the size of this lag may be related to a larger expansion of carbon-rich, southern-sourced waters into the Northern Hemisphere in MIS 6, providing a larger carbon reservoir that requires more time to be depleted.

Clim. Past, 16, 2203–2219, 2020
https://doi.org/10.5194/cp-16-2203-2020

Climate of the Past
Open Access
EGU

Millennial-scale atmospheric CO_2 variations during the Marine Isotope Stage 6 period (190–135 ka)

Jinhwa Shin[1,a], Christoph Nehrbass-Ahles[2,3], Roberto Grilli[1], Jai Chowdhry Beeman[1], Frédéric Parrenin[1], Grégory Teste[1], Amaelle Landais[4], Loïc Schmidely[2], Lucas Silva[2], Jochen Schmitt[2], Bernhard Bereiter[2,5,b], Thomas F. Stocker[2], Hubertus Fischer[2], and Jérôme Chappellaz[1]

[1]CNRS, Univ. Grenoble-Alpes, Institut des Géosciences de l'Environnement (IGE), Grenoble, France
[2]Climate and Environmental Physics, Physics Institute, and Oeschger Centre for Climate Change Research, University of Bern, Bern, Switzerland
[3]Department of Earth Sciences, University of Cambridge, Cambridge, UK
[4]Laboratoire des Sciences du Climat et de l'Environnement, LSCE/IPSL, CEA-CNRS-UVSQ, Université Paris-Saclay, Gif-sur-Yvette, France
[5]Laboratory for Air Pollution/Environmental Technology, Empa, Dübendorf, Switzerland
[a]current address: Department of Earth and Atmospheric Sciences, University of Alberta, Edmonton, AB, T6G 2E3, Canada
[b]current address: Bruker BioSpin AG, Fällanden, Switzerland

Correspondence: Jérôme Chappellaz (jerome.chappellaz@univ-grenoble-alpes.fr)

Received: 24 November 2020 – Discussion started: 13 December 2019
Revised: 20 July 2020 – Accepted: 25 August 2020 – Published: 14 November 2020

Abstract. Using new and previously published CO_2 data from the EPICA Dome C ice core (EDC), we reconstruct a new high-resolution record of atmospheric CO_2 during Marine Isotope Stage (MIS) 6 (190 to 135 ka) the penultimate glacial period. Similar to the last glacial cycle, where high-resolution data already exists, our record shows that during longer North Atlantic (NA) stadials, millennial CO_2 variations during MIS 6 are clearly coincident with the bipolar seesaw signal in the Antarctic temperature record. However, during one short stadial in the NA, atmospheric CO_2 variation is small ($\sim$ 5 ppm) and the relationship between temperature variations in EDC and atmospheric CO_2 is unclear. The magnitude of CO_2 increase during Carbon Dioxide Maxima (CDM) is closely related to the NA stadial duration in both MIS 6 and MIS 3 (60–27 ka). This observation implies that during the last two glacials the overall bipolar seesaw coupling of climate and atmospheric CO_2 operated similarly. In addition, similar to the last glacial period, CDM during the earliest MIS 6 show different lags with respect to the corresponding abrupt CH_4 rises, the latter reflecting rapid warming in the Northern Hemisphere (NH). During MIS 6i at around 181.5±0.3 ka, CDM 6i lags the abrupt warming in the NH by only 240±320 years. However, during CDM 6iv (171.1±0.2 ka) and CDM 6iii (175.4±0.4 ka) the lag is much longer: 1290±540 years on average. We speculate that the size of this lag may be related to a larger expansion of carbon-rich, southern-sourced waters into the Northern Hemisphere in MIS 6, providing a larger carbon reservoir that requires more time to be depleted.

1 Introduction

Ice core studies allow us to considerably extend our knowledge about natural climate–carbon cycle feedbacks by directly reconstructing atmospheric CO_2 from gas preserved in Antarctic ice sheets (Lüthi et al., 2008; Petit et al., 1999). Comparing atmospheric CO_2 records from Antarctic ice cores with proxies of paleoclimate helps us to understand how atmospheric CO_2 was controlled by carbon exchange with the ocean and land reservoirs on orbital to centennial timescales (Ahn and Brook, 2008, 2014; Bereiter et al., 2012; Higgins et al., 2015; Lüthi et al., 2008; Marcott et al., 2014; Petit et al., 1999).

Previous work on polar ice core records revealed that temperature variations in Greenland and Antarctica on millennial timescales appear to be a pervasive feature during the last glacial period. While Antarctic temperature varied gradually, Greenland temperature changes occurred abruptly. A phase difference can be observed between millennial-scale variations of temperature in the NH and SH (Northern Hemisphere and Southern Hemisphere, respectively), which is referred to as the bipolar seesaw phenomenon (Blunier and Brook, 2001; Pedro et al., 2018; Stocker and Johnsen, 2003). Potential triggers for this climatic variability on the millennial scale are fresh water perturbation in the North Atlantic (NA) or alterations of sea ice extent, surface temperature and salinity in the NA (Bond et al., 1992; Broecker et al., 1992; Heinrich, 1988; McManus et al., 1998), which may reduce the strength of the Atlantic Meridional Overturning Circulation (AMOC). This would cause a reduction in heat transport from the SH to the NH, which leads to an abrupt cooling in the NA region and a gradual warming in the SH (Stocker and Johnsen, 2003) and the opposite behavior when AMOC is strengthened.

Existing CO_2 records show the presence of millennial-scale oscillations on the order of 20 ppm over the last glacial period (Ahn and Brook, 2008, 2014; Bereiter et al., 2012), which generally co-vary with the major water isotope (δD) variations in Antarctic ice cores reflecting Antarctic temperature variations (Ahn and Brook, 2008; Bereiter et al., 2012) (Fig. 1). During cold periods in the NA, referred to as NA stadials, atmospheric CO_2 increased continuously and in parallel to Antarctic temperature increase. Again, at the onset of warming in Greenland, atmospheric CO_2 started to decrease (Ahn and Brook, 2008; Bereiter et al., 2012), generally in line with a co-occurring, slow Antarctic cooling. However, the CO_2 decrease did not always start at exactly the same time as the onset of the abrupt warming in the NA, and the lag itself varied. For example, during Marine Isotope Stage (MIS) 3, Carbon Dioxide Maxima (CDM) lagged behind abrupt temperature change in Greenland by 870±90 years. During MIS 5, the lag of CDM with respect to abrupt temperature warming in the NH was only about 250±190 years (Bereiter et al., 2012). Atmospheric CO_2 variations on millennial scales are thought to be related to the role of the Southern Ocean in carbon uptake and deep-ocean ventilation on millennial timescales (Fischer et al., 2010; Marcott et al., 2014; Schmitt et al., 2012; Sigman and Boyle, 2000; Toggweiler et al., 2006). In addition, atmospheric CO_2 can be affected by changes in the AMOC, which affects the ventilation of carbon from the deep ocean (Denton et al., 2010; Sigman et al., 2007). However, the mechanisms responsible for these oscillations are still a matter of debate (Bouttes et al., 2012; Bozbiyik et al., 2011; Gottschalk et al., 2019; Menviel et al., 2014).

Comparing CO_2 changes on millennial timescales during the past two glacial periods, MIS 3 (60–27 ka) and early MIS 6 (185–160 ka), can provide us with a better understanding of the carbon cycle, due to the similarities but also differences of climate conditions and events during the last two glacial periods (Fig. 1). Proxy evidence indicates that the states of several important components of the climate–carbon cycle were not the same between MIS 3 and MIS 6. Sea ice cover in the South Atlantic was more extensive in MIS 6, and sea surface temperature in the South Atlantic is thought to have been lower (Gottschalk et al., 2020). The bipolar seesaw phenomenon has also been observed during the early MIS 6 period (Cheng et al., 2016; Jouzel et al., 2007; Margari et al., 2010). However, the bipolar seesaw events during MIS 6 are longer than those found during MIS 3. Events of massive iceberg discharge into the NA, which are thought to have driven millennial-scale changes in the meridional overturning circulation during MIS 3 (de Abreu et al., 2003; McManus et al., 1999), appear to be much more frequent during MIS 3 than during MIS 6. During the early MIS 6, iceberg discharge was muted, and during the time period around 175 ka summer insolation levels in the NH approached interglacial values (Berger, 1978). Due to the stronger NH summer insolation, the Intertropical Convergence Zone (ITCZ) had shifted to the north, which intensified monsoon systems in low-latitude regions, such as in Asia, the Apennine Peninsula and the Levant (Ayalon et al., 2002; Bard et al., 2002; Cheng et al., 2016). This may have led to a weaker overturning circulation due to the reduction of the density of the North Atlantic surface water, making the AMOC cell shallower during MIS 6 than during MIS 3 (Gottschalk et al., 2020; Margari et al., 2010).

In order to investigate whether the different climate conditions between MIS 6 and MIS 3 could have impacted the relationship between atmospheric CO_2 and climate, we measured 177 new data points of atmospheric CO_2 concentrations from the EPICA Dome C (EDC) ice core (75°06′ S, 123°24′ E) spanning MIS 6 (190 to 135 ka). This new CO_2 data measured within the scope of this study is complemented with two published datasets (Lourantou et al., 2010; Schneider et al., 2013) and one unpublished CO_2 dataset measured in 2003. We use all of the available data from the EDC ice core to compile a composite dataset of atmospheric CO_2 covering MIS 6. In this work, we significantly improve existing records previously obtained from the Vostok ice core (Petit et al., 1999). The new composite dataset from the EDC core provides a temporal resolution of ∼ 230 years during MIS 6, as compared to 1000 years in the Vostok record. We also improved the relative age uncertainties between ice and gas in the EDC core using δ^{15}N-based estimates of firn column thickness to better constrain leads and lags between peaks in δD (Antarctic Isotope Maxima, or AIM) in the EDC ice core and atmospheric CO_2 concentrations during the early MIS 6, thus establishing a new chronology using new δ^{15}N data during the early MIS 6 in this study and published data from Landais et al. (2013). Finally, we improve the temporal resolution of existing CH_4 data from EDC (Loulergue et al., 2008) from 600 to ∼ 350 years to be

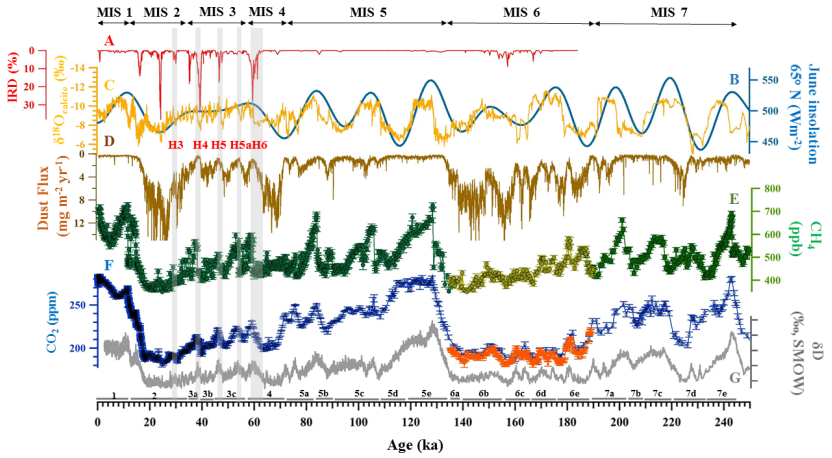

Figure 1. Proxy data over the last 250 ka. **(a)** Ice-rafted debris (IRD) input in the Iberian Margin core MD95-2040 (de Abreu et al., 2003). **(b)** The 21 June insolation for 65° N (Berger, 1978). **(c)** The $\delta^{18}O_{calcite}$ from Sanbao cave, indicative of the strength of the East Asian monsoon (Cheng et al., 2016). **(d)** Dust flux in the EDC ice core (Lambert et al., 2012). **(e)** Published atmospheric CH_4 in EDC (dark green dots) (Loulergue et al., 2008) and a composite atmospheric CH_4 record from EDC derived in this study (light yellow dots). **(f)** Composite CO_2 record from the EDC ice core derived in this study (orange dots) and a published composite CO_2 record from Antarctic ice cores (dark blue dots) (Bereiter et al., 2015). **(g)** The δD in the EDC ice core, Antarctica (Jouzel et al., 2007). Vertical grey bars indicate the timing of Heinrich events during the last glacial period. The event numbers are indicated at the bottom. The marine isotope substage numbers are written at the bottom (Railsback et al., 2015).

able to more precisely calculate the shift of CDM relative to the rapid climate change in the NH. To avoid the age uncertainties between proxy data and atmospheric CO_2 data, CH_4 measurements are used as a time marker of rapid warming in the NH, as over the last glacial period CH_4 and Greenland temperatures are assumed to be synchronous, with a lag of CH_4 of less than $\sim$ 50 years on average (Baumgartner et al., 2014; Rosen et al., 2014).

2 Methods

2.1 CO_2 measurements

In this study, we measured atmospheric CO_2 from 177 depth intervals of the EDC ice core at the Institut des Géosciences de l'Environnement (IGE), France and Climate and Environmental Physics (CEP), Physics Institute, University of Bern, Switzerland. The majority of all atmospheric CO_2 samples (i.e. 150) were measured using the ball mill dry-extraction system coupled to a gas chromatograph at IGE (Schaefer et al., 2011). Each ball mill data point presented in this study corresponds to a single 40 g ice sample, which was measured five times by gas chromatography (five consecutive injections of the same extracted gas). Approximately 5 mm of ice was trimmed from the ice core surfaces before extraction in order to remove the external part that could be potentially contaminated with drilling fluid or might have been subject to gas loss during storage in the freezer (Bereiter et al., 2009). The CO_2 measurements were referenced to a secondary gas standard (synthetic air from Air Liquide, Alphagaz 28416000) containing 233.7 ± 0.4 ppm of CO_2 in dry air, which was referenced to two primary standards (238.34±0.04 from NOAA, CB09707, and 260.26±0.2 from CSIRO, CSIRO1677).

Blank tests using 40 g of artificial bubble-free ice were conducted every 10 measurements to quantify the precision of the system and to correct for the CO_2 contamination caused by the crushing process. Blank tests were conducted in two steps: first, to validate the baseline of the system, a gas standard with 233.7 ± 0.4 ppm was injected over the bubble-free ice in the cell. The gas was then left to equilibrate in the cell for 10 min. The gas was analyzed twice by successive injections into the extraction line and sample loop. Afterwards, the bubble-free ice was crushed and the gas was analyzed five more times. The difference between the results before and after crushing was considered the contamination effect caused by the crushing process. These values were used to estimate the precision of the system. Measured CO_2 should be corrected for contamination caused by the analytical procedure by comparing measured CO_2 of the blank tests with the standard gas value. However, it is not feasible to correct CO_2 concentrations directly. The CO_2 mole fraction is calculated as the ratio between partial pressure of CO_2 and total pressure in the measurement line, which is a relative value. Thus, CO_2 concentration and the concentration of CO_2 con-

tamination are dependent on the total pressure. To avoid this dependence, we corrected the absolute value (partial pressure) of CO_2 in the air by the expected partial pressure of CO_2 contamination, as estimated from the blank tests.

For this study, we used four different extraction chambers to hold the ice core samples during crushing and measurement. Each chamber showed different contamination levels. Therefore, blank tests were conducted on each chamber. The data were corrected by the average of each chamber. For these measurements, the precision of the system was estimated to be ~ 1 ppm on average. On average, the extraction effect correction corresponds to a reduction of the measured CO_2 concentration by 1.7 ± 1.0 ppm (1σ).

Additionally, we measured 65 samples from 27 depth intervals using the Centrifugal Ice Microtome (CIM) (Bereiter et al., 2013) at CEP. At each depth interval replicates were made and analyzed (2.4 on average). Approximately 5 mm of the ice surface were trimmed, and ~ 8 g of samples was analyzed on average. The pooled standard deviation of replicates was ~ 1 ppm. The WMOX2007 mole fraction scale (Tans et al., 2017) was used as a reference for the CO_2 measurements, via four different primary dry air standards for atmospheric CO_2, which were calibrated at the NOAA Earth System Research Laboratory. The standard sample concentrations varied between 192.44 and 363.08 ppm (Nehrbass-Ahles et al., 2020).

Each CO_2 record was corrected for gravitational fractionation, using the $\delta^{15}N$ isotope ratio (Craig et al., 1988). To this end, 88 new data points together with existing δ^{15} (Landais et al., 2013) covering the late MIS 6 (156.4–139.2 ka) were used. $\delta^{15}N$ data were linearly interpolated in age to each corresponding CO_2 data point. On average, the correction corresponds to removing 1.2 ± 0.1 ppm from the measured CO_2. In total, 177 individual ice samples were measured for CO_2 in the depth range from 2036.7 to 1787.5 m along the EDC ice core, corresponding to the time period from 189.4 to 135.4 ka (Bazin et al., 2013).

2.2 CH_4 measurements

We measured the atmospheric CH_4 content of 63 ice core samples, using the wet extraction method at IGE as described in detail in Spahni et al. (2005). This allowed us to improve the temporal resolution of existing CH_4 data (Loulergue et al., 2008) from ~ 600 to 360 years on the AICC2012 chronology (see Fig. S1 in the Supplement). The precision of the system is ~ 11 ppb on average, which was estimated by blank tests.

The previous CH_4 dataset (Loulergue et al., 2008) from EDC has been produced at both IGE and CEP. CH_4 measured at CEP used to be systematically higher than CH_4 measured at IGE by 6 ppb (Loulergue et al., 2008). The offsets are due to differences in corrections for contamination caused by the analytical procedure between the datasets. Previously, 6 ppb had been added to the data obtained at IGE (Loulergue et al., 2008).

In this study, a new data correction was applied to data measured at IGE, and it is no longer necessary to add 6 ppb to the new data. The systematic offset between the new data and the previously published data points (Loulergue et al., 2008) is only 1.7 ± 2.4 ppb ($n = 63$, the standard error of the mean) during MIS 6, (the datasets agree with each other within the measurement uncertainty).

2.3 Nitrogen isotopes

Isotopes of molecular nitrogen in air bubbles were measured by a melting technique at the Laboratoire des Sciences du Climat et de l'Environnement (LSCE), France. The gas was extracted from the ice by a wet extraction technique, and the released air was analyzed by a dual-inlet mass spectrometer (Delta V Plus; Thermo Scientific). The analytical method and data correction are described in detail in Bréant et al. (2019). In total, 151 samples from 88 depth intervals (63 duplicates) between the depths of 2124.7 and 1875.0 m below the surface were measured, corresponding to the time interval from 205 to 154 ka (Fig. S2 in the Supplement). The average resolution on the AICC2012 chronology is ~ 580 years.

2.4 Gas age revision by estimating Δdepth from $\delta^{15}N$

The water isotopic signature (δD), is, unlike CO_2, measured on the ice matrix. Air enclosed in an ice core moves through the porous firn layers at the top of the ice sheet by molecular diffusion and becomes gradually trapped in the ice at the so-called Lock-In Depth (LID, around 100 m below the surface in the case of the EDC ice core). An age difference, thus, exists between the ice and the air at a given depth. For the conditions of the EDC ice core, the age difference can reach up to 5 kyr during glacial maxima and is associated with a large uncertainty (several hundred years; Loulergue et al., 2007). The $\delta^{15}N$ of molecular nitrogen in air bubbles can be used to determine the LID and to calculate the depth difference between synchronous events in the ice matrix and air bubbles, called delta depth (Δdepth), thus creating a more precise relative chronology of the gas – with respect to the ice-phase (Parrenin et al., 2013). We use the Δdepth calculation to adjust the gas chronology of EDC, while the ice chronology from AICC2012 remained unchanged.

We calculate the height of the firn column, h, from $\delta^{15}N$ of N_2 measurements (Craig et al., 1988; Dreyfus et al., 2010; Sowers et al., 1989) using the following equation:

$$h = h_{\mathrm{conv}} + (\delta^{15}\mathrm{N} - \Omega(T)\Delta T_{\mathrm{diff}})\left(\frac{\Delta m \cdot g \cdot 1000}{RT}\right)^{-1}. \quad (1)$$

In this equation, ΔT_{diff} is the temperature difference between the top and the bottom of the diffusive zone as estimated by the Goujon–Arnaud model, where surface temperature

and accumulation are estimated from the stable water isotope record (Loulergue et al., 2007). Ω (T) is the thermal diffusion sensitivity, which has been estimated from laboratory measurements by Grachev and Severinghaus (2003). Δm is the mass difference between ^{14}N and ^{15}N (kg mol^{-1}), g is the gravitational acceleration (9825 m s^{-2} for Antarctica) (Parrenin et al., 2013), and R is the universal gas constant (8314 J mol^{-1}K^{-1}). Finally, h_{conv} is the height of the convective zone at the top of the firn column, which is considered negligible at EDC according to current observations (Landais et al., 2006). The variation of the convective height is related to changes in wind stress. According to Krinner et al. (2000), wind on the East Antarctic plateau varied little during the LGM (Last Glacial Maximum), and we assume that this is also the case for late MIS 6. Moreover, the convective zone was confirmed to be very thin during the last deglaciation by Parrenin et al. (2012). Thus, we assume that h_{conv} is negligible during MIS 6. Δdepth is calculated from the height of the air column using a constant average firn density and a modeled vertical thinning function suggested by Parrenin et al. (2013).

Raw $\delta^{15}N$ data cannot be used directly to calculate Δdepth because bubbles at a given depth in the ice sheet can be trapped at slightly different times, due to small physical variations that affect the gas trapping process. This can lead to age scale inversions on depth intervals up to 1 cm (Etheridge et al., 1992; Fourteau et al., 2017). These layer inversions should not strongly affect our record, as its resolution is larger than the scale of age inversion events (Fourteau et al., 2017). However, the change in Δdepth between two different depths (z) in the ice core, denoted $\partial\Delta\text{depth}/\partial z$, deduced from the raw $\delta^{15}N$ data, shows some values higher than 1, that could correspond to small stratigraphic inversions in the gas phase (Fig. 2). Therefore, a three-point moving average weighted by the time difference between a point and its two neighbors was applied to the $\delta^{15}N$ dataset. The weights for the three points are equal if the time difference is less than or equal to 500 years, which is close to the average sampling resolution of the $\delta^{15}N$ dataset. Otherwise, the neighboring data points are weighted by $500/\Delta T$, where ΔT is the time difference. This avoids assigning too much weight to neighboring points where the resolution in the record is lower, which would lead to local over-smoothing.

Δdepth as estimated using the three-point moving average weighted by the time difference is shown in Fig. 2. The difference of the Lock-In Depth in Ice Equivalent (LIDIE) calculated on the AICC2012 age scale (Bazin et al., 2013) and deduced from $\delta^{15}N$ in this study is 0.5 ± 3.0 m, or 0.7 ± 5.6 % on average (see Fig. S3 in the Supplement). The AICC2012 LIDIE was calculated using a background scenario derived from δD, using a linear relationship between δD and $\delta^{15}N$. Our results show this relationship to be relatively unbiased but not entirely exact (Fig. S3 in the Supplement). The Δdepth values are used to update the EDC gas chronology from the original AICC2012 age scale, while the ice chronology remains unchanged. For MIS 6, this method significantly reduces the relative age uncertainty between air and ice to 900 years on average with respect to the original AICC2012 chronology (see Fig. S4 in the Supplement).

2.5 Age scale of the MD01-2444 marine sediment record

The MD01-2444 marine sediment core from the Iberian Margin (Margari et al., 2010) represents an important archive for the interpretation of our CO_2 record, as it is well resolved during MIS 6, and it provides high-resolution benthic and planktonic foraminiferal records. The original MD01-2444 age scale was built by matching the benthic $\delta^{18}O$ record (Shackleton et al., 2000) to the δD record from EDC on the EDC03 ice age scale (Parrenin et al., 2007) using 11 tie points (Margari et al., 2010). In order to make optimal use of the record, its relative chronology with respect to EDC requires additional improvement using the latest version of the EDC age scale. Thus, in this study, we recalculated the age of the tie points using the AICC2012 chronology (Bazin et al., 2013), and the age of the sediment record was linearly interpolated between the tie points (Table S1 in the Supplement).

2.6 Definition of NA stadial duration

Due to the absence of a Greenland temperature record for MIS 6, the durations of the six NA stadials must be identified using other proxies. Here, we used two methods using both ice core and sediment core proxies. First, we estimated the durations of the six NA stadials using $\delta^{18}O$ of planktonic foraminifera and tree pollen in MD01-2444, which reflect temperature variability in the NH (Margari et al., 2010) (Fig. 3). The midpoint of the stadial transitions in both $\delta^{18}O$ of planktonic foraminifera and tree pollen in MD01-2444 were used to identify the NH stadial transitions. The time interval between two stadial transition points were defined as the NA stadial duration. Using this approach the duration of stadial at 6ii in the NH could not unambiguously be determined due to small variations in the foraminifera and the pollen record. However, the average age difference between the durations identified using the two records is only 205 years, which is less than the sampling resolution of MD01-2444 during MIS 6. The uncertainty of the timing of each stadial transition was estimated as half of the temporal difference between maxima and minima of $\delta^{18}O$ of planktonic foraminifera. The mean values for stadial onsets and terminations are shown as dashed lines in Fig. 3. However, not all of the stadial durations during MIS 6c to 6d are entirely unambiguous using this method.

Second, we recalculated the durations of the six NA stadials during MIS 6 period using a method developed by Margari et al. (2010). Figure 3 also shows a synthetic Greenland $\delta^{18}O_{ice}$ record (Barker et al., 2011) and Antarctic δD

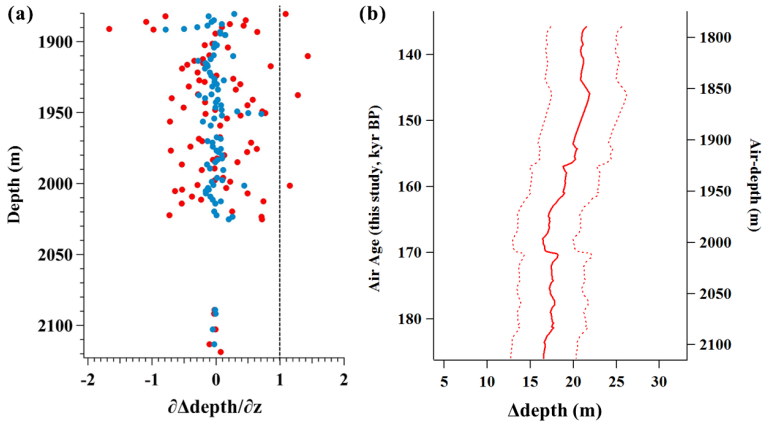

Figure 2. **(a)** $\partial\Delta\text{depth}/\partial z$ as a function of depth. Red dots represent raw δ^{15}N measurements, and blue dots represent a weighted three-point running mean (see text for details). The dashed vertical grey line indicates $\partial\Delta\text{depth}/\partial z = 1$. **(b)** Δdepth (bold line) for the EDC ice core from 1787.5 to 1870.2 m below the surface, deduced from δ^{15}N and the thinning function calculated in this depth range. The two dashed lines correspond to the analytical uncertainties.

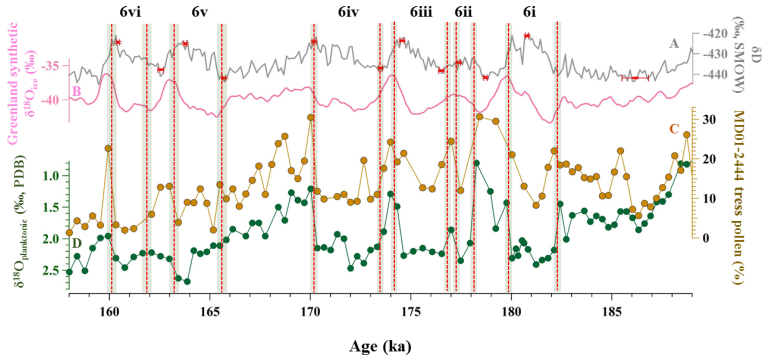

Figure 3. The durations of the six NA stadials during MIS 6: **(a)** δD of the EDC ice core (Jouzel et al., 2007), **(b)** synthetic Greenland $\delta^{18}O_{ice}$ record (Barker et al., 2011), **(c)** tree pollen percentage in the MD01-2444 core (Margari et al., 2010) and **(d)** δ^{18}O of planktonic foraminifera in the MD01-2444 core (Margari et al., 2010). Proxy data shown here are given on the AICC2012 age scale. Red lines indicate the midpoints of the stadial transition of both δ^{18}O of planktonic foraminifera and tree pollen in MD01-2444. Light green bars indicate the uncertainty of the duration of each stadial transition, estimated as half the temporal difference between maxima and minima of δ^{18}O of planktonic foraminifera before and after the transition. Red dots indicate minima and maxima of δD in the EDC ice core as selected in this study. The event numbers are indicated at the top.

variations on the AICC2012 age scale. The interval between the maximum and the preceding minimum of δD in the EDC record can also be used to estimate the duration of the stadial transitions (Gottschalk et al., 2020; Margari et al., 2010). In most cases, the synthetic Greenland $\delta^{18}O_{ice}$ record and the interval between the maximum and the preceding minimum of δD in the EDC record confirm the definition of NA stadials selected by δ^{18}O of planktonic foraminifera and tree pollen in MD01-2444. However, the duration of the NA stadial in MIS 6iii is not clearly confirmed by synthetic Greenland $\delta^{18}O_{ice}$ and δD in the EDC (Fig. 3).

The interval between each maximum and the preceding minimum of δD in the EDC record was calculated to estimate the stadial durations using the second method (Gottschalk et al., 2020; Kawamura et al., 2017; Margari et al., 2010). Maxima and minima in the δD record were selected by finding zero values in the second (Savitzky–Golay filtered) derivative of the data (the same method we used to pick minima and maxima of atmospheric CO_2 and temperature; Figs. S5–S6, Tables S2–S3 in the Supplement). In one case (the minimum before MIS 6i) two potential minima were selected by this method; these values were then averaged.

The red dots and error bars in the EDC δD record in Fig. 3 show the estimated minima and maxima of temperature corresponding to stadial transitions using this method, along with their uncertainties. However, using this tool, durations of MIS 6ii and 6i are apparently overestimated due to ambiguities concerning the definition of the maximum in MIS 6i and minimum in 6ii.

Neither our method nor that of Margari et al. (2010) can be considered absolutely correct. To account for the differences between the two methods, we took the stadial duration to be the mean of the durations estimated by the two methods (Table S4 in the Supplement).

3 Results

3.1 Data compilation

We measured 177 samples of atmospheric CO_2 from EDC during MIS 6 using two extraction systems (the ball mill at IGE and CIM system at CEP). To improve the resolution of our new dataset even further, we made a composite dataset by aligning previous sets of CO_2 measurements made over the MIS 6 period on the EDC ice core to our new data. First, we compared the two existing CO_2 datasets and the new CO_2 dataset from EDC (Fig. 4 and Table S5 in the Supplement). There are two published CO_2 datasets for EDC during MIS6 – the first measured using the ball mill system at IGE (Lourantou et al., 2010) and the second using a sublimation extraction system at CEP (Schneider et al., 2013). We also added unpublished data measured in 2003 using the CEO needle cracker measurement system in 2003 (Monnin et al., 2004; Siegenthaler et al., 2005) (see Supplement for details). All records are on the AICC2012 air age scale (Bazin et al., 2013). All datasets are corrected for the gravitational fractionation effect using the new δ^{15}N data in our study. In total, the datasets contain 237 CO_2 measurement points. Two samples were excluded because of system operator error. Figure 4 shows CO_2 concentrations measured by the ball mill system, sublimation (Schneider et al., 2013), the CIM and the needle cracker. Concentrations from the CIM, sublimation and the needle cracker are systematically higher than CO_2 concentrations measured using the ball mill system (Table S5 in the Supplement).

The offsets between each additional dataset and our data were calculated and corrected using a Monte Carlo procedure to account for uncertainty and a Savitzky–Golay filter used to remove noise from our dataset (Supplement). The offsets between the multiple datasets may be at least in part linked to differences in extraction efficiency between the measurement methods. The sublimation and CIM systems have high extraction efficiency on clathrates and should therefore present more unbiased baseline CO_2 values. However, since these datasets are of much lower resolution, we have aligned all datasets to the baseline value of our ball mill dataset.

Despite the systematic offsets, the other datasets confirm the millennial-scale variations shown in the data from this study (Fig. 4 and Fig. S7 in the Supplement). Although none of the individual additional datasets is of high enough resolution to show millennial-scale variations in detail, when aligned to our data the new data follow the millennial-scale variations with very few outliers. The new composite atmospheric CO_2 record from EDC is shown in Fig. 5.

3.2 Comparison with Vostok CO_2 record for MIS 6

The new composite atmospheric CO_2 record from EDC was compared to the existing CO_2 data from the Vostok ice core, measured using the ball mill system (Fig. S7 in the Supplement), where the CO_2 record from Vostok was aligned to the AICC2012 gas age scale (Bazin et al., 2013). Atmospheric CO_2 data from Vostok are corrected for the gravitational fractionation effect using the existing δ^{15}N data (Bender, 2002).

Atmospheric CO_2 variability in the EDC ice core shows similar general patterns as those retrieved from the Vostok ice core, although previously unidentified features are resolved due to the improved temporal resolution. CO_2 concentrations from Vostok appear systematically higher than those from EDC by 4.6 ± 3.0 ppm on average and the difference increases to more than 10 ppm at the beginning of Termination 2 at around 135 ka.

Three main mechanisms may explain the offsets between the EDC and Vostok measurements: firstly, contamination due to the extraction system was assumed to be negligible at the time of the Vostok sample measurements at IGE (Petit et al., 1999). Based on recent ball mill measurements conducted within the scope of this study, we presume that the neglected correction concerning the data published by Petit et al. (1999) amounts to approximately 1.7 ppm, reducing the average apparent offset to about 3 ppm. Secondly, part of this remaining offset between the new EDC and previously published Vostok record may be related to age scale uncertainties due to a limited number of stratigraphic tie points between the two cores (Bazin et al., 2013). In particular, this effect may explain part of the larger offset during the glacial termination in air younger than 140 ka (Fig. S7 in the Supplement). Thirdly, the ball mill system has a different extraction efficiency depending on the presence of bubbles and/or clathrates in the ice sample, which may affect the accuracy of the reconstructed absolute mean CO_2 level. When the air is extracted from an ice core sample where bubbles and clathrates coexist, different proportions of bubbly and clathrate ice may lead to biased CO_2 concentrations (Lüthi et al., 2010; Schaefer et al., 2011). The Vostok measurements were made on recently drilled ice, in which clathrates had less time to transform into secondary bubbles (Vladimir Lipenkov, 2015 personal communication). Accordingly, at least part of the approximately 3 ppm offset may be due to these systematic extraction differences (see Supplement).

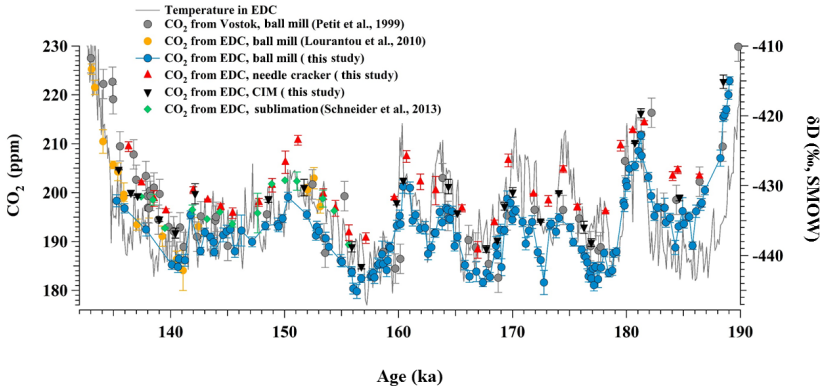

Figure 4. Atmospheric CO_2 from EDC and Vostok ice cores, compared to δD of the ice in the EDC core (temperature proxy) during 190–135 ka. Blue dots represent atmospheric CO_2 from EDC as measured by the ball mill system (this study). The error bars of the new CO_2 data using the ball mill extraction system indicate the standard deviation of five consecutive injections of the gas extracted from each sample into the gas chromatograph added to the precision of the measurement estimated by the reproducibility of the control measurement ($\sim$ 0.8 ppm) using a quadratic sum. Yellow dots represent atmospheric CO_2 from EDC measured using the ball mill system (Lourantou et al., 2010). The error bars indicate the standard deviation of five consecutive injections of the gas extracted from each sample into the gas chromatograph. Red triangles represent atmospheric CO_2 from EDC measured using the needle cracker (this study). The error bars of data points with replicates indicate the standard deviation of the mean of replicates from the same depth interval. Black inverted triangles represent atmospheric CO_2 from EDC measured using the CIM (this study). The error bars of data points with replicates indicate the standard deviation of the mean of replicates from the same depth interval. Green diamonds represent atmospheric CO_2 from EDC measured using sublimation extraction (Schneider et al., 2013). The error bars of data points with replicates indicate the standard deviation of the mean of replicates from the same depth interval (Schneider et al., 2013). Grey dots represent atmospheric CO_2 from the Vostok ice core (Petit et al., 1999). The error bars of the CO_2 data from Vostok (Petit et al., 1999) show the estimated overall accuracy for CO_2 measurements. The grey line represents δD of ice in the EDC core (Jouzel et al., 2007).

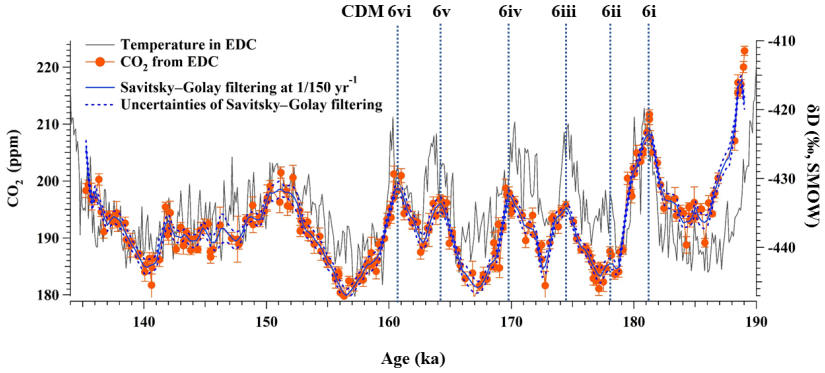

Figure 5. Composite atmospheric CO_2 (left axis) from the EDC ice core (this study) compared to the EDC water isotopic record (right axis) (Jouzel et al., 2007). The blue line indicates a Savitzky–Golay filter using a 150-year cut-off period (dotted blue line). Vertical dotted blue lines indicate the six CDM events that we identify during the early MIS 6. The numbers of the CDM events are indicated at the top of the figure.

In summary, the individual datasets used for our data compilation and the Vostok ice core record all show the same millennial CO_2 variability over MIS 6. Analytical and ice-relaxation-related offsets could be removed to synthesize all records. This allows us to compile a precise and high-resolution record; however, the true absolute mean level of atmospheric CO_2 is only known to be better than 5 ppm, due to this offset correction. However, this has no impact on the conclusions drawn from the millennial CO_2 variability, which is the focus of this study.

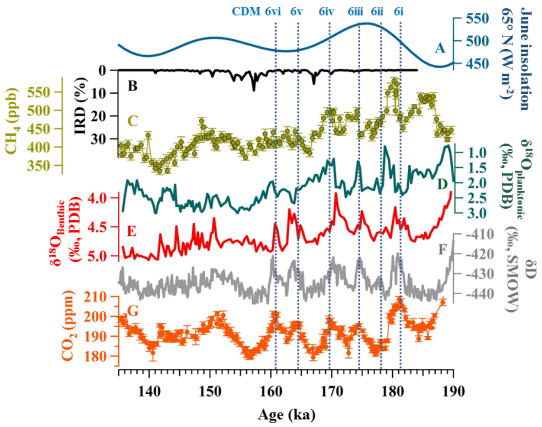

Figure 6. Comparison of climate proxies with atmospheric CO_2 during MIS 6 period. Vertical dotted blue lines indicate the six CDM events during the early MIS 6: **(a)** 21 June insolation at 65° N (Berger, 1978), **(b)** ice-rafted debris (IRD) input in the Iberian Margin core MD95-2040 (de Abreu et al., 2003), **(c)** atmospheric CH_4 in the EDC ice core (Loulergue et al., 2008; this study), **(d)** $\delta^{18}O$ of planktonic foraminifera in the Iberian Margin marine core MD01-2444 (Margari et al., 2010), **(e)** $\delta^{18}O$ of benthic foraminifera in the Iberian Margin marine core MD01-2444 (Margari et al., 2010), **(f)** δD of the EDC ice core (Jouzel et al., 2007) and **(g)** our new composite CO_2 record during the MIS 6 period. The numbers of CDM events are indicated at the top.

3.3 Atmospheric CO_2 variability on millennial timescale

Margari et al. (2010) suggested that MIS 6 can be divided into three sections depending on the degree of climatic variability observed in δD (indicative of Antarctic climate variability) and CH_4 (reflecting NA climate variability) in EDC: early (185.2–157.7 ka), transition (157.7–151 ka) and late MIS 6 (151–135 ka) (Figs. 5 and 6). Climatic oscillations on millennial timescales are pervasive during the early MIS 6 period (185–160 ka) (Barker et al., 2011; Cheng et al., 2016; Jouzel et al., 2007; Margari et al., 2010, 2014), which is similar to MIS 3 (Figs. 1 and 6). However, during the late MIS 6 period, i.e., the Penultimate Glacial Maximum (PGM), millennial variability is subdued and more resembles the climate variability on millennial timescales during MIS 2 (Figs. 1 and 6). During the transitional period from 157 to 151 ka, δD in EDC slowly increased (Jouzel et al., 2007). Like δD in EDC, CO_2 variations on millennial timescales are pervasive during the early MIS 6 period (185–157.7 ka). During the transitional period from 157 to 151 ka, atmospheric CO_2 increased slowly, while during the late MIS 6 period CO_2 variation is subdued (Fig. 5).

While there was an indication of millennial CO_2 variability in the Vostok record, the resolution of that record did not allow us to constrain this variability. We now present clear evidence of millennial variability of CO_2 concentrations during MIS 6 that are associated with Antarctic Isotope Maxima (AIM) events (EPICA Community Members, 2006), thanks to the improved time resolution and precision of the obtained CO_2 data (Fig. 5). To better discuss millennial variability in MIS 6, a Savitzky–Golay filter with a 150-year cut-off period was used to filter out centennial-scale variability and noise (see Fig. 5 and Fig. S5 in the Supplement). Five prominent and one subdued CO_2 variations were detected in atmospheric CO_2 during early MIS 6 (Fig. 5 and Fig. S5 and Table S2 in the Supplement), where we name CDM according to the numbering by Margari et al. (2010) and Gottschalk et al. (2020) (Fig. 5). The five prominent peaks are observed at 160.7 ± 0.3 (CDM 6vi), 164.2 ± 0.3 (CDM 6v), 169.6 ± 0.2 (CDM 6iv), 174.3 ± 0.2 (CDM 6iii) and 181.3 ± 0.1 ka (CDM 6i). Note that the provided uncertainty was calculated with respect to the position of each maximum and does not include the absolute age uncertainty of the ice core (in each case around 3.0 kyr, 1σ) (Bazin et al., 2013). We can also identify one low-amplitude CO_2 peak at around 150 ka, representing another potential candidate for a CDM (Fig. 5). This atmospheric CO_2 variation is of triangular shape and follows the δD pattern. The change of direction is also associated with a CH_4 peak. This variation has analogues in MIS 4 and MIS 10 (Jouzel et al., 2007; Nehrbass-Ahles et al., 2020).

Each CDM is associated with an AIM event. The short AIM 6ii event corresponds to CDM 6ii at around 178 ka. CDM 6ii has an amplitude of only ~ 4 ppm, and the CO_2 variation becomes even less pronounced after filtering. Due to the smoothing of the CO_2 variation at CDM 6ii, atmospheric CO_2 and δD composition in EDC appear decoupled. This observation seems confirmed when considering the relationship between atmospheric CO_2 change and the duration of NA stadials calculated using tree pollen and the $\delta^{18}O$ composition of planktic foraminifera in an Iberian Margin core (Margari et al., 2010) for MIS 6 (Fig. 3 and Table S4 in the Supplement), or using isotopic records from Greenland ice cores (Rasmussen et al., 2014) for MIS 3 as shown in Fig. 7. Here, the magnitude of atmospheric CO_2 change is generally correlated with the NA stadial duration ($r = 0.87$, $n = 6$) during the early MIS 6 period, and CDM 6ii is by far the shortest of all six events detected in MIS6.

We note a similar correlation between the NA stadial duration and atmospheric CO_2 change during MIS 3 ($r = 0.85$, $n = 14$). When the NA stadial duration was shorter than 1500 years, atmospheric CO_2 varied less than 5 ppm (Ahn and Brook, 2014; Bereiter et al., 2012) as is the case for CDM 6ii. Margari et al. (2010) note one exception, AIM 14, during which ice discharge may have led to a stronger perturbation to AMOC.

Both Bereiter et al. (2012) and Ahn and Brook (2014) observed that during short NA stadials which last less than 1300 years, the CO_2 maxima do not appear to have a consistent phase relationship with AIM and CO_2 and δD anomalies are

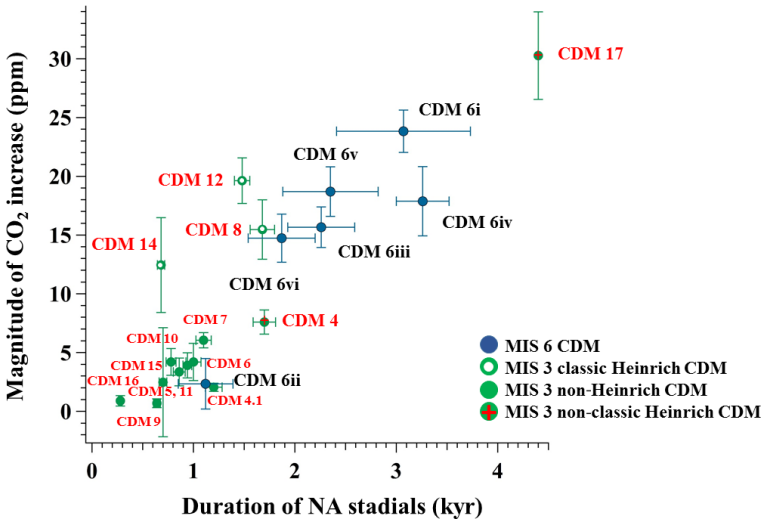

Figure 7. The relationship between NA stadial duration and magnitude of CO_2 increase. Green dots indicate non-Heinrich CDM events during MIS 3, green circles indicate classic Heinrich CDM events during MIS 3 and red-filled green circles indicate non-classic Heinrich CDM events during the MIS 3 period. Blue dots indicate CDM events during MIS 6. Non-classic Heinrich events are defined as ice discharge events with different IRD source signatures from Heinrich events, occurring at transitions in NH ice volume.

not correlated (Ahn and Brook, 2014). We observe the same to be the case when MIS 6 is included ($r = 0.07$, $n = 11$), however, we cannot exclude that the firn column-induced smoothing at EDC obliterated small atmospheric responses with magnitudes smaller than 5 ppm for such short stadials. In both MIS 3 and 6, CO_2 is highly correlated with δD anomalies during the longer stadials ($r = 0.78$, $n = 9$) with a clear increase in CO_2 (Ahn and Brook, 2014; Bereiter et al., 2012).

We observe that during the last two glacial periods, the amplitude of CO_2 is strongly related to the NA stadial duration ($r = 0.88$, $n = 20$). This observation implies that despite the different climate boundary conditions during the last two glacials, the behavior of atmospheric CO_2 was similar (see Fig. 1) and the overall bipolar seesaw coupling of climate and atmospheric CO_2 acted the same way.

3.4 Leads and lags between CO_2 and the abrupt warming in NH

To better understand the link between the bipolar seesaw mechanism and atmospheric CO_2 variability on millennial timescales, we calculated the varying time lag for each CDM following abrupt warming events in the NH (see Figs. S8–S11 in the Supplement) (Bereiter et al., 2012). Due to the lack of an MIS 6 temperature proxy in Greenland, and due to the difficulty of placing marine temperature proxies (Shackleton et al., 2000) on a precise common chronology with the EDC ice core, in this work CH_4 measurements performed on the EDC ice core were used as a time marker of rapid warming in the NH (Baumgartner et al., 2014; Brook et al., 1996; Huber et al., 2006). Because CH_4 and CO_2 signals are both imprinted in the air bubbles, there is no chronological uncertainty when comparing the timing of changes of those two signals. The only remaining uncertainty is related to analytical uncertainties and to the temporal resolution of the two records. We pick intervals when CH_4 increases rapidly by at least 50 ppb over a time period of less than 1 kyr that correspond to AIM (Buizert et al., 2015; Loulergue et al., 2008). The timing of abrupt CH_4 increases was defined as the midpoint between the beginning of the increase of CH_4 and its peak (see Supplement for details). The age uncertainty of the midpoint is defined by half the time difference between the two endpoints.

Figure 8 shows the shifts of CDM with respect to the onset of the abrupt warming in the NH. During the MIS 6 period, three abrupt NH warmings (as inferred from the CH_4 signal) at 181.5 ± 0.3, 175.4 ± 0.40 and 171.1 ± 0.2 ka (2σ) were found. These events correspond to CDM 6i, CDM 6iii and CDM 6iv, respectively. CDM 6vi, CDM 6v and CDM 6ii do not have corresponding rapid changes in the methane record that fulfill our detection criterion of a 50 ppb increase; this may be due to slow gas trapping as compared to interglacial periods, which could smooth out smaller changes. A synthetic Greenland temperature record (Barker et al., 2011) shows abrupt temperature jumps at CDM 6vi, CDM 6v and CDM 6ii as well. However, this record is calculated using EDC δD, and the large relative chronological uncertainty

(∼ 900 years on average) between ice and gas phases does not allow us to make any conclusions about leads and lags using this record. We therefore exclude these events from our lag analysis.

From MIS 6i to MIS 6iv, the lag of CO_2 with respect to abrupt warmings in the NH, which were identified from this chronological comparison between EDC CH_4 and CO_2, becomes significantly larger. During the earliest MIS 6, atmospheric CO_2 increases rapidly (by ∼4.2 ppm in 240 ± 320 years) following the abrupt CH_4 increase at 181.5 ± 0.3 ka. The peak of CDM 6i is nearly synchronous with the onset of the NH abrupt warming (nonsignificant lag of 240 ± 320 years, Fig. 8). During CDM 6iv and 6iii, CO_2 concentrations show a much slower increase over a duration of ∼ 3.3 kyr. Here, the CO_2 maximum lags significantly behind the onset of the NH abrupt warming by 1460 ± 270 years and 1110 ± 460 years, respectively (1290 ± 540 years on average, with the error calculated by propagation of the uncertainties in the individual events). Interestingly, these two CDM events occurred during MIS 6d (Fig. 1), when iceberg discharge was muted and the ITCZ is thought to have shifted northward, intensifying monsoon systems in low-latitude Northern Hemisphere regions, such as in Asia, the Apennine Peninsula and the Levant (Ayalon et al., 2002; Bard et al., 2002; Cheng et al., 2016). This may have led to a weaker overturning circulation due to the reduction of the density of the NA surface water, making the AMOC cell shallower with a smaller threshold in NA during MIS 6 than during MIS 3 (Margari et al., 2010). Therefore, the two different CO_2 lag timescales with respect to abrupt warming in NH during MIS 6 might be explained by this difference in background climate conditions. Indeed, these features during MIS 6 appear fully compatible with those observed during the last glacial period (Bereiter et al., 2012). To compare CO_2 variations with respect to abrupt warming in the NH during the last two glacial periods, in this study we also re-estimated the abrupt CH_4 rise during the last glacial period with the same methodologies. Figure 8 also shows the CO_2 evolution during the onset of abrupt warming in the NH during MIS 3 and MIS 5 (Ahn and Brook, 2014; Bereiter et al., 2012). Atmospheric CO_2 during MIS 3, as shown in Fig. 8, was reconstructed from the Talos Dome ice core (TALDICE). For MIS 5 it was obtained from Byrd and the EPICA Dronning Maud Land (EDML) ice core (Ahn and Brook, 2008; Bereiter et al., 2012). In Bereiter et al. (2012), both TALDICE and EDML records were used during MIS 3 and compared to the onset of abrupt warming in the NH as indicated by the co-occurring CH_4 rise. However, here we only use data from TALDICE, which are more accurate due to the narrower age distribution of the gas trapped in the LID (Bereiter et al., 2012). Using the same method as above, the average value of CDM lag with respect to the abrupt warming in NH was calculated. The average CDM lags with respect to the abrupt warming in the NH for the MIS 3 and 5 periods are 770 ± 180 and 280 ± 240 years. Thus, over the course of the last glaciation, the lag of CO_2 maxima with respect to the abrupt NH warming events significantly increased. We observe the same trend through the millennial events depicted during MIS 6, albeit with different absolute lags.

4 Discussion

4.1 Atmospheric CO_2 variability on millennial timescales

Similar to the AIM amplitude (Capron et al., 2010; EPICA Community Members, 2006), we found that the amplitude of atmospheric CO_2 variations is well correlated to the NA stadial duration during MIS 6 and MIS 3, which implies that the amplitude of CO_2 variations might also be affected by the duration of AMOC disruption during the early MIS 6 period (Margari et al., 2010). This hypothesis is also supported by a recent study using oceanic sediment cores from the Southern Ocean (Gottschalk et al., 2020). The authors report that respired carbon levels in the deep South Atlantic decrease when AMOC is weakened during both glacial periods, and the amount of carbon loss in the deep South Atlantic is highly correlated with the duration of NA stadials.

As mentioned above, atmospheric CO_2 on millennial timescales can be controlled by CO_2 exchange between the ocean and the atmosphere, as well as changes of terrestrial carbon stocks. Coupled climate carbon cycle models reported that the variations of atmospheric CO_2 concentration on millennial timescales are mainly dominated by the deep ocean inventory, requiring a few millennia to re-equilibrate to climate change (Schmittner and Galbraith, 2008). On the other hand, the response of the terrestrial biosphere is usually fast (decadal to centennial timescale) (Bouttes et al., 2012; Menviel et al., 2014; Schmittner and Galbraith, 2008). Although different models differ significantly in the CO_2 response to AMOC changes, the initial CO_2 evolution of the terrestrial biosphere and deep ocean to AMOC perturbations are opposite in model simulations (Gottschalk et al., 2019). Thus, due to the opposite direction of CO_2 change of ocean and terrestrial reservoirs, atmospheric CO_2 variations might be muted if the NH duration is short (Bouttes et al., 2012; Menviel et al., 2014; Schmittner and Galbraith, 2008), while during long stadials the carbon release from the ocean dominates. There is, on the other hand, evidence that not all of the processes of CO_2 exchange follow these general trends. For example, atmospheric CO_2 might be changed on centennial timescales by carbon exchange between the deep and surface ocean (Rae et al., 2018) or atmospheric CO_2 might be influenced slowly by soil decomposition (Köhler et al., 2005), and it is important to note that modeling studies do not agree in the amplitude or even the direction of the modeled net CO_2 exchange.

The more prominent CO_2 changes during stadials involved with the Heinrich events may be related to a stronger reduction of the North Atlantic Deep Water (NADW) forma-

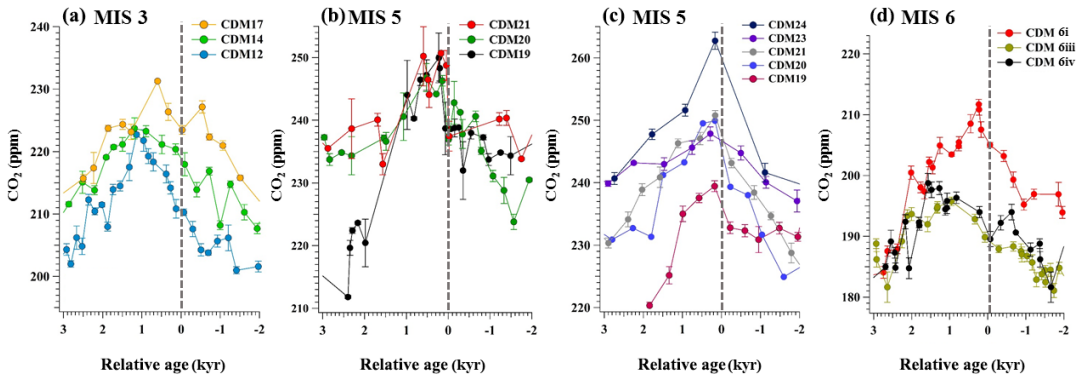

Figure 8. CDM lags relative to abrupt temperature increases in the NH. Dotted grey lines indicate when climate changes abruptly in the NH as indicated by the CH_4 jumps. During the last glacial period, the AIM number corresponds to the DO number for corresponding DO and AIM events, and for MIS6 numbers correspond to event numbers. **(a)** Atmospheric CO_2 as measured using the TALDICE ice core during MIS 3, **(b)** atmospheric CO_2 as measured using the Byrd ice core during MIS 5, **(c)** atmospheric CO_2 as measured using EDML ice core during MIS 5, **(d)** new CO_2 composite as derived in this study for MIS 6. For MIS 6, we selected the 3 CDM that correspond to an abrupt methane increase; the other CDM do not correspond to an abrupt change that fulfill our 50 ppb detection criterion (see main text for details). Note that the scale of the y axis is not the same for the four panels.

tion during Heinrich events (Henry et al., 2016; Margari et al., 2010), which would cause a stronger upwelling of deep water in the Southern Ocean (Menviel et al., 2008; Schmittner et al., 2007). These events may reduce stratification in the Southern Ocean due to an increase in salinity of the surface waters and a relative freshening of the deep water (Schmittner et al., 2007). As a result, atmospheric CO_2 can be increased due to upwelling and outgassing of CO_2 in the Southern Ocean (Schmittner et al., 2007; Schmitt et al., 2012). The co-occurring upwelling in the SO during AIM for the last termination has been examined (Anderson et al., 2009), but due to the lack of proxy data with precise age scale for upwelling in the Southern Ocean, this hypothesis cannot be confirmed during MIS 6.

According to the results of Margari et al. (2010), the six AIM events of MIS 6 were likely affected by AMOC perturbations of similar strength. During these events, there is no clear evidence for freshwater perturbation in the NA (Fig. 1), and the strength of the associated AMOC perturbations is estimated to be similar to that during non Heinrich stadials or non-classic Heinrich (different ice-rafted detritus source signatures from Heinrich events, occurring at transitions in ice volume) AIM events of MIS 3. The durations of NA stadials during early MIS 6 (except for AIM 6ii) appear to be longer than those during non-Heinrich AIM events of MIS 3, which might be caused by the different climate boundary conditions during MIS 3 and the increase of the hydrological cycle during the early MIS 6. A longer duration of the AMOC disruption apparently impacts the amplitude of CO_2 variations (Bouttes et al., 2012; Menviel et al., 2008). Considering that the duration of the AMOC disruption may be related with climate background conditions (Bouttes et al., 2012; Menviel et al., 2008), this observation suggests how different climate background conditions may impact atmospheric CO_2. The strength of AMOC perturbations also appears to be an important factor in determining the amplitude of CO_2 variations. For example, the duration of the Heinrich events in MIS 3 (AIM 8, 12 and 14) is shorter than any of the MIS 6 events except for 6ii, but atmospheric CO_2 varied significantly in all three.

The relationship between the amplitude of atmospheric CO_2 variations and the NA stadial duration is explained by the duration of AMOC disruption during the early MIS 6 period. However, the temporal resolution of $\delta^{18}O$ composition of planktonic foraminifera in MD01-2444 and the precision of the age scale are too low to precisely define the duration of stadials during MIS 6. Additional proxy data providing information about climate change in the NH are needed to confirm the relationship between atmospheric CO_2 variations and the NA stadial duration (Fig. 3). The limited available proxy data permit only to formulate a hypothesis for the mechanisms responsible for CO_2 variability during MIS 6 but not to rigorously test it. To compare the behavior of the bipolar seesaw with atmospheric CO_2 variations, additional investigations about AMOC disturbances and their associated climate responses are needed.

4.2 Why did CO_2 lag the abrupt warming in the NH during MIS 6d?

Two different lags of the CO_2 maxima with respect to NH warming are present in the MIS 6 period (Fig. 8). CDM 6i is nearly synchronous with the abrupt warming in the NH (no

significant lag of 240 ± 320 years), while the lags for CDM 6iii (1110 ± 460 years) and CDM 6iv (1460 ± 270 years) are much longer. Two modes of CO_2 variations are also observed during the last glacial period. As the last glaciation progressed from MIS 5 to MIS 3 (Figs. 1 and 8), the lag of CO_2 maxima with respect to NH millennial-scale warming significantly increased. This observation may be explained by the different AMOC settings in MIS 5 and MIS 3 (Bereiter et al., 2012). We speculate that, as observed during the last glacial period, the configuration of oceanic circulation during MIS 6d might also be the cause of the change in the time lags between NH abrupt warming events and CO_2 variations during the early MIS 6.

Bereiter et al. (2012) explained that during MIS 3 the oceanic circulation in the Atlantic was in a more "glacial" state, with shallower NADW and carbon-rich Antarctic Bottom Water (AABW) extended to the north, while during MIS 5 ocean circulation was similar to the present, in what can be referred to as a "modern-like" state. At the onset of abrupt warming in the NH, AMOC is thought to accelerate rapidly, delivering heat to the north and resuming the formation of NADW. When the NADW cell expands, AABW is withdrawn and the upwelling of carbon-rich deep water in the Southern Ocean is enhanced. Essentially, over the timescale of ocean overturn, part of the previously expanded carbon-rich southern-sourced water is converted to carbon-poor northern-sourced water.

Thus, during MIS 3 CO_2 continues to be released into the atmosphere for another 500 to 1000 years after the NADW resumption (Bereiter et al., 2012). However, during MIS 5 where AABW was not expanded in the NA, less CO_2 can be released from the ocean to the atmosphere after NADW resumption.

The temporal resolution of proxy data related to oceanic circulation during MIS 3 and 5 is unfortunately not sufficient to validate from the marine realm itself whether the two different modes of CO_2 variations reflect the hypothesized mechanism described above. Modeling studies of the carbon stock in AABW and NADW during MIS 5 and 3 have been attempted. However, dependent on the chosen model, the modes of atmospheric CO_2 variation are different (Gottschalk et al., 2019). Some studies (for example, Menviel et al., 2008) mention an atmospheric CO_2 decrease when the AMOC is resumed. Others, for example Bouttes et al. (2012), confirm an atmospheric CO_2 release from the ocean when AMOC resumed.

In spite of the inconclusive modeling studies (Gottschalk et al., 2019), limited proxy evidence does not exclude the possibility that the configuration of AMOC and its changes over MIS 6 may explain the presence of two different CDM lags. We find this hypothesis to be worth at least a speculative discussion. According to the benthic $\delta^{13}C$ record in the MD01-2444 core (Margari et al., 2010), the value of benthic $\delta^{13}C$ during 180–168 ka was lower than during MIS3, which indicates that the NA overturning cell during MIS 6 was likely even shallower than that during MIS 3 (Margari et al., 2010). This implies southern-sourced water masses were more expanded to the north, and the density difference between the northern-sourced water masses and southern-sourced water masses increased. This shallower oceanic circulation during MIS 6 (Margari et al., 2010) could have caused the millennial-scale delays with respect to abrupt NH warming events. It could also explain the longer lag between the abrupt warming in NH and CDM during MIS 6d (1290 ± 540 years on average) when compared to the lags of CDM (770 ± 180 years on average) during MIS 3. However, because of the low accumulation at EDC and its wider age distribution, the estimation of the exact timing of CDM from the EDC ice core might be less accurate compared to that from the TALDICE ice core with a narrower gas age distribution (Bereiter et al., 2012). The remaining uncertainty is related to analytical uncertainties and to the temporal resolution of the two records. To further investigate the exact relationship between CDM and abrupt warming in the NH, additional CO_2 measurements from a higher accumulation site would be helpful.

5 Conclusions

Using new and existing CO_2 data from the EPICA Dome C ice, we reconstruct a high temporal resolution record of atmospheric CO_2 during the MIS 6 period (189–135 ka). In this study, we investigate how different climate background conditions during the last two glacial periods may have impacted atmospheric CO_2. Millennial-scale atmospheric CO_2 changes are revealed during the last two glacial periods, with amplitudes ranging between 15 to 25 ppm, mimicking similar patterns in Antarctic δD variations (Ahn and Brook, 2014; Bereiter et al., 2012). On the other hand, during short NA stadials which last less than 1300 years, atmospheric CO_2 variations are negligible and decoupled from δD in EDC. This finding suggests that during the last two glacial periods the amplitude of millennial CO_2 variations is strongly influenced by the NA stadial duration ($r = 0.88$, $n = 20$).

In the earliest MIS 6 (MIS 6i and 6iv, corresponding to 189 to 169 ka), a change of CO_2 lags with respect to the onset of rapid NH – warming as deduced from atmospheric CH_4 changes – is revealed. CDM 6i (at $\sim$ 182 ka) is nearly synchronous with the abrupt warming in the NH (nonsignificant lag of 240 ± 320 years), while the lags during MIS 6d corresponding to CDM 6iv and 6iii (at $\sim$ 171 and $\sim$ 175 ka, respectively) are much longer, 1290 ± 540 years on average. Similar observations are drawn for the time period covered by our study as for previous studies on MIS 3 and MIS 5 periods, although the lag of CO_2 with respect to NH warming reaches even larger values during MIS 6d. We tentatively attribute this to a generally weaker and shallower AMOC during MIS 6 compared to MIS 3 as suggested by the results from Margari et al. (2010). However, the limited avail-

able proxy data from the marine realm only permits an exploratory discussion of the mechanisms responsible for CO_2 variability during MIS 6. Because the boundary conditions of the last glacial period cannot be applied to MIS 6, additional proxy data and multiple modeling studies conducted during the MIS 6 period are needed.

Data availability. Data available in the Supplement. All data will be available on the NOAA (National Oceanic and Atmospheric Administration) and PANGAEA (Paleoclimatology database websites) shortly.

Supplement. The supplement related to this article is available online at: https://doi.org/10.5194/cp-16-2203-2020-supplement.

Author contributions. The research was designed by JS, RG, FP and JC. The CO_2 measurements were performed by JS with contributions from GT, LS and BB. The data analyses were led by JS with contributions from JCB, RG, FP and JC and HF. The methane data was provided by GT and JC. The nitrogen isotopes data was provided by AL. JS wrote the manuscript with inputs from all authors.

Competing interests. The authors declare that they have no conflict of interest.

Acknowledgements. This work is a contribution to the "European Project for Ice Coring in Antarctica" (EPICA), a joint European Science Foundation/European Commission scientific program, funded by the European Union and by national contributions from Belgium, Denmark, France, Germany, Italy, the Netherlands, Norway, Sweden, Switzerland and the United Kingdom. The main logistical support was provided by IPEV and PNRA. This is EPICA publication no. 316. It also received funding from the European Community's Seventh Framework Programmes ERC-2011-AdG under grant agreement no. 291062 (ERC ICE&LASERS). As it is part of the PhD work of Jinhwa Shin, it was also supported by the LabEX OSUGat2020 project of the Grenoble Observatory of Sciences of the Universe (OSUG). The Swiss authors also acknowledge long-term financial support for ice core research at the University of Bern by the Swiss National Science Foundation under grants 200020_159563, 200020_172745, 200020_172506 and 20FI21_189533. The authors would like to thank Grégoire Aufresne for providing assistance with the additional methane measurements, Xavier Faïn and Kévin Fourteau for their help with the CH_4 analytical system, and Dominique Raynaud for the valuable discussions. We thank Eric Monnin and Urs Siegenthaler for providing additional CO_2 data. We would like to thank Julia Gottschalk for the discussions about CO_2 variability and climate change during the last two glacial periods.

Financial support. This research has been supported by the ERC-2011-AdG (grant no. 291062, ERC ICE&LASERS), the Swiss National Science Foundation (grant no. 200020_159563), the Swiss National Science Foundation (grant no. 200020_172506), the Grenoble Observatory of Sciences of the Universe (LabEX OSUGat2020 project grant), the Swiss National Science Foundation (grant no. 200020_172745), and the Swiss National Science Foundation (grant no. 20FI21_189533).

Review statement. This paper was edited by Denis-Didier Rousseau and reviewed by four anonymous referees.

References

Ahn, J. and Brook, E. J.: Atmospheric CO_2 and climate on millennial time scales during the last glacial period, Science, 322, 83–85, 2008.

Ahn, J. and Brook, E. J.: Siple Dome ice reveals two modes of millennial CO_2 change during the last ice age, Nat. Commun., 5, 3723, https://doi.org/10.1038/ncomms4723, 2014.

Anderson, R., Ali, S., Bradtmiller, L., Nielsen, S., Fleisher, M., Anderson, B., and Burckle, L.: Wind-driven upwelling in the Southern Ocean and the deglacial rise in atmospheric CO_2, Science, 323, 1443–1448, 2009.

Ayalon, A., Bar-Matthews, M., and Kaufman, A.: Climatic conditions during marine oxygen isotope stage 6 in the eastern Mediterranean region from the isotopic composition of speleothems of Soreq Cave, Israel, Geology, 30, 303–306, 2002.

Bard, E., Antonioli, F., and Silenzi, S.: Sea-level during the penultimate interglacial period based on a submerged stalagmite from Argentarola Cave (Italy), Earth Planet. Sci. Lett., 196, 135–146, 2002.

Barker, S., Knorr, G., Edwards, R. L., Parrenin, F., Putnam, A. E., Skinner, L. C., Wolff, E., and Ziegler, M.: 800 000 years of abrupt climate variability, Science, 334, 347–351, 2011.

Baumgartner, M., Kindler, P., Eicher, O., Floch, G., Schilt, A., Schwander, J., Spahni, R., Capron, E., Chappellaz, J., Leuenberger, M., Fischer, H., and Stocker, T. F.: NGRIP CH_4 concentration from 120 to 10 kyr before present and its relation to a $\delta^{15}N$ temperature reconstruction from the same ice core, Clim. Past, 10, 903–920, https://doi.org/10.5194/cp-10-903-2014, 2014.

Bazin, L., Landais, A., Lemieux-Dudon, B., Toyé Mahamadou Kele, H., Veres, D., Parrenin, F., Martinerie, P., Ritz, C., Capron, E., Lipenkov, V., Loutre, M.-F., Raynaud, D., Vinther, B., Svensson, A., Rasmussen, S. O., Severi, M., Blunier, T., Leuenberger, M., Fischer, H., Masson-Delmotte, V., Chappellaz, J., and Wolff, E.: An optimized multi-proxy, multi-site Antarctic ice and gas orbital chronology (AICC2012): 120–800 ka, Clim. Past, 9, 1715–1731, https://doi.org/10.5194/cp-9-1715-2013, 2013.

Bender, M. L.: Orbital tuning chronology for the Vostok climate record supported by trapped gas composition, Earth Planet. Sc. Lett., 204, 275–289, 2002.

Bereiter, B., Eggleston, S., Schmitt, J., Nehrbass-Ahles, C., Stocker, T. F., Fischer, H., Kipfstuhl, S., and Chappellaz, J.: Revision of the EPICA Dome C CO_2 record from 800 to 600 kyr before present, Geophys. Res. Lett., 42, 542–549, 2015.

Bereiter, B., Lüthi, D., Siegrist, M., Schüpbach, S., Stocker, T. F., and Fischer, H.: Mode change of millennial CO_2 variability dur-

ing the last glacial cycle associated with a bipolar marine carbon seesaw, Proc. Natl. Acad. Sci., 109, 9755–9760, 2012.

Bereiter, B., Schwander, J., Lüthi, D., and Stocker, T. F.: Change in CO_2 concentration and O_2/N_2 ratio in ice cores due to molecular diffusion, Geophys. Res. Lett., 36, https://doi.org/10.1029/2008GL036737, 2009.

Bereiter, B., Stocker, T. F., and Fischer, H.: A centrifugal ice microtome for measurements of atmospheric CO_2 on air trapped in polar ice cores, Atmos. Meas. Tech., 6, 251–262, https://doi.org/10.5194/amt-6-251-2013, 2013.

Berger, A. L.: Long-Term Variations of Caloric Insolation Resulting from the Earth's Orbital Elements 1, Quat. Res., 9, 139–167, 1978.

Blunier, T. and Brook, E. J.: Timing of millennial-scale climate change in Antarctica and Greenland during the last glacial period, Science, 291, 109–112, 2001.

Bond, G., Heinrich, H., Broecker, W., Labeyrie, L., McManus, J., Andrews, J., Huon, S., Jantschik, R., Clasen, S., and Simet, C.: Evidence for massive discharges of icebergs into the North Atlantic ocean during the last glacial period, Nature, 360, 245–249, 1992.

Bouttes, N., Roche, D. M., and Paillard, D.: Systematic study of the impact of fresh water fluxes on the glacial carbon cycle, Clim. Past, 8, 589–607, https://doi.org/10.5194/cp-8-589-2012, 2012.

Bozbiyik, A., Steinacher, M., Joos, F., Stocker, T. F., and Menviel, L.: Fingerprints of changes in the terrestrial carbon cycle in response to large reorganizations in ocean circulation, Clim. Past, 7, 319–338, https://doi.org/10.5194/cp-7-319-2011, 2011.

Bréant, C., Landais, A., Orsi, A., Martinerie, P., Extier, T., Prié, F., Stenni, B., Jouzel, J., Masson-Delmotte, V., and Leuenberger, M.: Unveiling the anatomy of Termination 3 using water and air isotopes in the Dome C ice core, East Antarctica, Quaternary Sci. Rev., 211, 156–165, 2019.

Broecker, W., Bond, G., Klas, M., Clark, E., and McManus, J.: Origin of the northern Atlantic's Heinrich events, Clim. Dyn., 6, 265–273, 1992.

Brook, E. J., Sowers, T., and Orchardo, J.: Rapid variations in atmospheric methane concentration during the past 110 000 yrs, Science, 273, 1087–1091, 1996.

Buizert, C., Adrian, B., Ahn, J., Albert, M., Alley, R. B., Baggenstos, D., Bauska, T. K., Bay, R. C., Bencivengo, B. B., Bentley, C. R., Brook, E. J., Chellman, N. J., Clow, G. D., Cole-Dai, J., Conway, H., Cravens, E., Cuffey, K. M., Dunbar, N. W., Edwards, J. S., Fegyveresi, J. M., Ferris, D. G., Fitzpatrick, J. J., Fudge, T. J., Gibson, C. J., Gkinis, V., Goetz, J. J., Gregory, S., Hargreaves, G. M., Iverson, N., Johnson, J. A., Jones, T. R., Kalk, M. L., Kippenhan, M. J., Koffman, B. G., Kreutz, K., Kuhl, T. W., Lebar, D. A., Lee, J. E., Marcott, S. A., Markle, B. R., Maselli, O. J., McConnell, J. R., McGwire, K. C., Mitchell, L. E., Mortensen, N. B., Neff, P. D., Nishiizumi, K., Nunn, R. M., Orsi, A. J., Pasteris, D. R., Pedro, J. B., Pettit, E. C., Price, P. B., Priscu, J. C., Rhodes, R. H., Rosen, J. L., Schauer, A. J., Schoenemann, S. W., Sendelbach, P. J., Severinghaus, J. P., Shturmakov, A. J., Sigl, M., Slawny, K. R., Souney, J. M., Sowers, T. A., Spencer, M. K., Steig, E. J., Taylor, K. C., Twickler, M. S., Vaughn, B. H., Voigt, D. E., Waddington, E. D., Welten, K. C., Wendricks, A. W., White, J. W. C., Winstrup, M., Wong, G. J., and Woodruff, T. E.: Precise interpolar phasing of abrupt climate change during the last ice age, Nature, 520, 661–665, https://doi.org/10.1038/nature14401, 2015.

Capron, E., Landais, A., Lemieux-Dudon, B., Schilt, A., Masson-Delmotte, V., Buiron, D., Chappellaz, J., Dahl-Jensen, D.,Johnsen, S., Leuenberger, M., Loulergue, L., and Oerter, H.: Synchronising EDML and North GRIP ice cores using $\delta^{18}O$ of atmospheric oxygen ($\delta^{18}Oatm$) and CH_4 measurements over MIS5 (80–123 kyr), Quaternary Sci. Rev., 29, 222–234, https://doi.org/10.1016/j.quascirev.2009.07.014, 2010.

Cheng, H., Edwards, R. L., Sinha, A., Spötl, C., Yi, L., Chen, S., Kelly, M., Kathayat, G., Wang, X., and Li, X.: The Asian monsoon over the past 640 000 years and ice age terminations, Nature, 534, 640–646, https://doi.org/10.1038/nature18591, 2016.

Craig, H., Horibe, Y., and Sowers, T.: Gravitational separation of gases and isotopes in polar ice caps, Science, 242, 1675–1678, 1988.

de Abreu, L., Shackleton, N. J., Schönfeld, J., Hall, M., and Chapman, M.: Millennial-scale oceanic climate variability off the Western Iberian margin during the last two glacial periods, Mar. Geol., 196, 1–20, 2003.

Denton, G. H., Anderson, R. F., Toggweiler, J., Edwards, R., Schaefer, J., and Putnam, A.: The last glacial termination, Science, 328, 1652–1656, 2010.

Dreyfus, G. B., Jouzel, J., Bender, M. L., Landais, A., Masson-Delmotte, V., and Leuenberger, M.: Firn processes and $\delta^{15}N$: potential for a gas-phase climate proxy, Quaternary Sci. Rev., 29, 28–42, 2010.

EPICA Community Members: One-to-one coupling of glacial climate variability in Greenland and Antarctica, Nature, 444, 195–198, 2006.

Etheridge, D., Pearman, G., and Fraser, P.: Changes in tropospheric methane between 1841 and 1978 from a high accumulation-rate Antarctic ice core, Tellus B, 44, 282–294, 1992.

Fischer, H., Schmitt, J., Lüthi, D., Stocker, T. F., Tschumi, T.,Parekh, P., Joos, F., Köhler, P., Völker, C., Gersonde, R., Barbante, C., Le Floch, M., Raynaud, D., and Wolff, E.: The role of Southern Ocean processes in orbital and millennial CO_2 variations – A synthesis, Quat. Sci. Rev., 29, 193–205, 2010.

Fourteau, K., Faïn, X., Martinerie, P., Landais, A., Ekaykin, A. A., Lipenkov, V. Ya., and Chappellaz, J.: Analytical constraints on layered gas trapping and smoothing of atmospheric variability in ice under low-accumulation conditions, Clim. Past, 13, 1815–1830, https://doi.org/10.5194/cp-13-1815-2017, 2017.

Gottschalk, J., Battaglia, G., Fischer, H., Frölicher, T. L., Jaccard, S. L., Jeltsch-Thömmes, A., Joos, F., Köhler, P., Meissner, K. J., and Menviel, L., Nehrbass-Ahles, C., Schmitt, J., Schmittner, A., Skinner, L. C., and Stocker, T.: Mechanisms of millennial-scale atmospheric CO_2 change in numerical model simulations, Quaternary Sci. Rev.,220, 30–74, 2019.

Gottschalk, J., Skinner, L. C., Jaccard, S. L., Menviel, L., Nehrbass-Ahles, C., and Waelbroeck, C.: Southern Ocean link between changes in atmospheric CO_2 levels and northern-hemisphere climate anomalies during the last two glacial periods, Quaternary Sci. Rev., 230, 106067, https://doi.org/10.1016/j.quascirev.2019.106067, 2020.

Grachev, A. M. and Severinghaus, J. P.: Laboratory determination of thermal diffusion constants for $^{29}N_2/^{28}N_2$ in air at temperatures from -60 to 0 °C for reconstruction of magnitudes of abrupt

climate changes using the ice core fossil–air paleothermometer, Geochim. Cosmochim. Ac., 67, 345–360, 2003.

Heinrich, H.: Origin and consequences of cyclic ice rafting in the northeast Atlantic Ocean during the past 130 000 years, Quaternary Res., 29, 142–152, 1988.

Henry, L., McManus, J. F., Curry, W. B., Roberts, N. L., Piotrowski, A. M., and Keigwin, L. D.: North Atlantic ocean circulation and abrupt climate change during the last glaciation, Science, 353, 470–474, 2016.

Higgins, J. A., Kurbatov, A. V., Spaulding, N. E., Brook, E., Introne, D. S., Chimiak, L. M., Yan, Y., Mayewski, P. A., and Bender, M. L.: Atmospheric composition 1 million years ago from blue ice in the Allan Hills, Antarctica, Proc. Natl. Acad. Sci., 112, 6887–6891, 201420232, https://doi.org/10.1073/pnas.1420232112, 2015.

Huber, C., Leuenberger, M., Spahni, R., Flückiger, J., Schwander, J., Stocker, T. F., Johnsen, S., Landais, A., and Jouzel, J.: Isotope calibrated Greenland temperature record over Marine Isotope Stage 3 and its relation to CH_4, Earth Planet. Sci. Lett., 243, 504–519, 2006.

Jouzel, J., Masson-Delmotte, V., Cattani, O., Dreyfus, G., Falourd, S., Hoffmann, G., Minster, B., Nouet, J., Barnola, J. M., Chappellaz, J., Fischer, H., Gallet, J. C., Johnsen, S., Leuenberger, M., Loulergue, L., Luethi, D., Oerter, H., Parrenin, F., Raisbeck, G., Raynaud, D., Schilt, A., Schwander, A., Selmo, E., Souchez, R., Spahni, R., Stauffer, B., Steffensen, J. P., Stenni, B., Stocker, T. F., Tison, J. L., Werner, M., and Wolff, E. W.: Orbital and Millennial Antarctic Climate Variability over the Past 800 000 Years, Science 317, 793–796, https://doi.org/10.1126/science.1141038, 2007.

Kawamura, K., Abe-Ouchi, A., Motoyama, H., Ageta, Y., Aoki, S., Azuma, N., Fujii, Y., Fujita, K., Fujita, S., and Fukui, K.: State dependence of climatic instability over the past 720 000 years from Antarctic ice cores and climate modeling, Sci. Adv., 3, e1600446, https://doi.org/10.1126/sciadv.1600446, 2017.

Köhler, P., Joos, F., Gerber, S., and Knutti, R.: Simulated changes in vegetation distribution, land carbon storage, and atmospheric CO_2 in response to a collapse of the North Atlantic thermohaline circulation, Clim. Dyn., 25, 689, https://doi.org/10.1007/s00382-005-0058-8, 2005.

Krinner, G., Raynaud, D., Doutriaux, C., and Dang, H.: Simulations of the Last Glacial Maximum ice sheet surface climate: Implications for the interpretation of ice core air content, J. Geophys. Res., 105, 2059–2070, 2000.

Landais, A., Barnola, J., Kawamura, K., Caillon, N., Delmotte, M., Ommen, T. V., Dreyfus, G., Jouzel, J., Masson-Delmotte, V., Minster, B., Freitag, J., Leuenberger, M., Schwander, J., Huber, C., Etheridge, D., and Morgan, V.: Firn-air $\delta^{15}N$ in modern polar sites and glacial-interglacial ice: a model-data mismatch during glacial periods in Antarctica?, Quaternary Sci. Rev., 25, 49–62, 2006.

Landais, A., Dreyfus, G., Capron, E., Jouzel, J., Masson-Delmotte, V., Roche, D. M., Prié, F., Caillon, N., Chappellaz, J., Leuenberger, M., Lourantou, A., Parrenin, F., Raynaud, D., and Teste, G.: Two-phase change in CO_2, Antarctic temperature and global climate during Termination II, Nat. Geosci., 6, 1062–1065, https://doi.org/10.1038/ngeo1985, 2013.

Loulergue, L., Parrenin, F., Blunier, T., Barnola, J.-M., Spahni, R., Schilt, A., Raisbeck, G., and Chappellaz, J.: New constraints on the gas age-ice age difference along the EPICA ice cores, 0–50 kyr, Clim. Past, 3, 527–540, https://doi.org/10.5194/cp-3-527-2007, 2007.

Loulergue, L., Schilt, A., Spahni, R., Masson-Delmotte, V., Blunier, T., Lemieux, B., Barnola, J.-M., Raynaud, D., Stocker, T. F., and Chappellaz, J.: Orbital and millennial-scale features of atmospheric CH_4 over the past 800 000 years, Nature, 453, 383, https://doi.org/10.1038/nature06950, 2008.

Lourantou, A., Chappellaz, J., Barnola, J.-M., Masson-Delmotte, V., and Raynaud, D.: Changes in atmospheric CO_2 and its carbon isotopic ratio during the penultimate deglaciation, Quaternary Sci. Rev., 29, 1983–1992, 2010.

Lüthi, D., Bereiter, B., Stauffer, B., Winkler, R., Schwander, J., Kindler, P., Leuenberger, M., Kipfstuhl, S., Capron, E., and Landais, A.: CO_2 and O_2/N_2 variations in and just below the bubble-clathrate transformation zone of Antarctic ice cores, Earth Planet. Sci. Lett., 297, 1–2, 226–233, https://doi.org/10.1016/j.epsl.2010.06.023, 2010.

Luthi, D., Le Floch, M., Bereiter, B., Blunier, T., Barnola, J.-M., ¨ Siegenthaler, U., Raynaud, D., Jouzel, J., Fischer, H., Kawamura, K., and Stocker, T. F.: High-resolution carbon dioxide concentration record 650 000–800 000 years before present, Nature, 453, 379–382, https://doi.org/10.1038/nature06949, 2008.

Marcott, S. A., Bauska, T. K., Buizert, C., Steig, E. J., Rosen, J. L., Cuffey, K. M., Fudge, T. J., Severinghaus, J. P., Ahn, J., Kalk, M. L., McConnell, J. R., Sowers, T., Taylor, K. C., White, J. W., and Brook, E. J.: Centennial scale changes in the global carbon cycle during the last deglaciation, Nature, 514, 616–619, https://doi.org/10.1038/nature13799, 2014.

Margari, V., Skinner, L., Tzedakis, P., Ganopolski, A., Vautravers, M., and Shackleton, N.: The nature of millennial-scale climate variability during the past two glacial periods, Nat. Geosci., 3, 127–131, https://doi.org/10.1038/ngeo740, 2010.

McManus, J. F., Anderson, R. F., Broecker, W. S., Fleisher, M. Q., and Higgins, S. M.: Radiometrically determined sedimentary fluxes in the sub-polar North Atlantic during the last 140 000 years, Earth Planet. Sci. Lett., 155, 29–43, 1998.

McManus, J. F., Oppo, D. W., and Cullen, J. L.: A 0.5 million-year record of millennial-scale climate variability in the North Atlantic, Science, 283, 971–975, 1999.

Menviel, L., England, M. H., Meissner, K., Mouchet, A., and Yu, J.: Atlantic-Pacific seesaw and its role in outgassing CO_2 during Heinrich events, Paleoceanography, 29, 58–70, 2014.

Menviel, L., Timmermann, A., Mouchet, A., and Timm, O.: Meridional reorganizations of marine and terrestrial productivity during Heinrich events, Paleoceanography, 23, PA1203, https://doi.org/10.1029/2007PA001445, 2008.

Monnin, E., Steig, E. J., Siegenthaler, U., Kawamura, K., Schwander, J., Stauffer, B., Stocker, T. F., Morse, D. C., Barnola, J.-M., Bellier, B., Raynaud, D., and Fischer, H.: Evidence for substantial accumulation rate variability in Antarctica during the Holocene through synchronization of CO_2 in the Taylor Dome, Dome C and DML ice cores, Earth Planet. Sc. Lett., 224, 45–54, 2004

Nehrbass-Ahles, C., Shin, J., Schmitt, J., Bereiter, B., Joos, F., Schilt, A., Schmidely, L., Silva, L., Teste, G., Grilli, R., Chappellaz, J., Hodell, D., Fischer, H., and Stocker, T. F.: Abrupt CO_2 release to the atmosphere under both glacial and early interglacial conditions, Science, 369, 1000–1005, 2020.

Parrenin, F., Barker, S., Blunier, T., Chappellaz, J., Jouzel, J., Landais, A., Masson-Delmotte, V., Schwander, J., and Veres, D.: On the gas-ice depth difference (δdepth) along the EPICA Dome C ice core, Clim. Past, 8, 1239–1255, https://doi.org/10.5194/cp-8-1239-2012, 2012.

Parrenin, F., Barnola, J.-M., Beer, J., Blunier, T., Castellano, E., Chappellaz, J., Dreyfus, G., Fischer, H., Fujita, S., Jouzel, J., Kawamura, K., Lemieux-Dudon, B., Loulergue, L., Masson-Delmotte, V., Narcisi, B., Petit, J.-R., Raisbeck, G., Raynaud, D., Ruth, U., Schwander, J., Severi, M., Spahni, R., Steffensen, J. P., Svensson, A., Udisti, R., Waelbroeck, C., and Wolff, E.: The EDC3 chronology for the EPICA Dome C ice core, Clim. Past, 3, 485–497, https://doi.org/10.5194/cp-3-485-2007, 2007.

Parrenin, F., Masson-Delmotte, V., Köhler, P., Raynaud, D., Paillard, D., Schwander, J., Barbante, C., Landais, A., Wegner, A., and Jouzel, J.: Synchronous change of atmospheric CO_2 and Antarctic temperature during the last deglacial warming, Science, 339, 1060–1063, 2013.

Pedro, J. B., Jochum, M., Buizert, C., He, F., Barker, S., and Rasmussen, S. O.: Beyond the bipolar seesaw: Toward a process understanding of interhemispheric coupling, Quaternary Sci. Rev., 192, 27–46, 2018.

Petit, J. R., Jouzel, J., Raynaud, D., Barkov, N. I., Barnola, J.-M., Basile, I., Bender, M., Chapellaz, J., Davis, M., Delaygue, G., Delmotte, M., Kotlyakov, V. M., Legrand, M., Lipenkov, V. Y., Lorius, C., Pepin, L., Ritz, C., Saltzmann, E., and Stievenard, M.: Climate and atmospheric history of the past 420 000 years from the Vostok ice core, Antarctica, Nature, 399, 429–436, https://doi.org/10.1038/20859, 1999.

Rae, J. W. B., Burke, A., Robinson, L. F., Adkins, J. F., Chen, T., Cole, C., Greenop, R., Li, T., Littley, E. F. M., Nita, D. C., and Stewart, J. A.: CO_2 storage and release in the deep Southern Ocean on millennial to centennial timescales, Nature, 562, 569–573, 2018.

Railsback, L. B., Gibbard, P. L., Head, M. J., Voarintsoa, N. R. G., and Toucanne, S.: An optimized scheme of lettered marine isotope substages for the last 1.0 million years, and the climatostratigraphic nature of isotope stages and substages, Quaternary Sci. Rev., 111, 94–106, 2015.

Rasmussen, S. O., Bigler, M., Blockley, S. P., Blunier, T., Buchardt, S. L., Clausen, H. B., Cvijanovic, I., Dahl-Jensen, D., Johnsen, S. J., Fischer, H., Gkinis, V., Guillevic, M., Hoek, W. Z., Lowe, J. J., Pedro, J. B., Popp, T., Seierstad, I. K., Steffensen, J. P., Svensson, A. M., Vallelonga, P., Vinther, B. M., Walker, M. J. C., Wheatley, J. J., and Winstrup, M.: A stratigraphic framework for abrupt climatic changes during the Last Glacial period based on three synchronized Greenland ice-core records: refining and extending the INTIMATE event stratigraphy, Quaternary Sci. Rev., 106, 14–28, 2014.

Rosen, J. L., Brook, E. J., Severinghaus, J. P., Blunier, T., Mitchell, L. E., Lee, J. E., Edwards, J. S., and Gkinis, V.: An ice core record of near-synchronous global climate changes at the Bølling transition, Nat. Geosci., 7, 459, https://doi.org/10.1038/ngeo2147, 2014.

Schaefer, H., Lourantou, A., Chappellaz, J., Lüthi, D., Bereiter, B., and Barnola, J.-M.: On the suitability of partially clathrated ice for analysis of concentration and $\delta^{13}C$ of palaeo-atmospheric CO_2, Earth Planet. Sci. Lett., 307, 334–340, 2011.

Schmitt, J., Schneider, R., Elsig, J., Leuenberger, D., Lourantou, A., Chappellaz, J., Köhler, P., Joos, F., Stocker, T. F., and Leuenberger, M.: Carbon isotope constraints on the deglacial CO_2 rise from ice cores, Science, 336, 711–714, 2012.

Schmittner, A., Brook, E. J., and Ahn, J.: Impact of the ocean's overturning circulation on atmospheric CO_2, in: Ocean Circulation: Mechanisms and Impacts, AGU Geophysical Monograph Series, 173, American Geophysical Union, Washington DC, 315–334, 2007.

Schmittner, A. and Galbraith, E. D.: Glacial greenhouse-gas fluctuations controlled by ocean circulation changes, Nature, 456, 373, https://doi.org/10.1038/nature07531, 2008.

Schneider, R., Schmitt, J., Köhler, P., Joos, F., and Fischer, H.: A reconstruction of atmospheric carbon dioxide and its stable carbon isotopic composition from the penultimate glacial maximum to the last glacial inception, Clim. Past, 9, 2507–2523, https://doi.org/10.5194/cp-9-2507-2013, 2013.

Shackleton, N. J., Hall, M. A., and Vincent, E.: Phase relationships between millennial-scale events 64 000–24 000 years ago, Paleoceanography, 15, 565–569, 2000.

Siegenthaler, U., Monnin, E., Kawamura, K., Spahni, R., Schwander, J., Stauffer, B., Stocker, T. F., Barnola, J.-M., and Fischer, H.: Supporting evidence from the EPICA Dronning Maud Land ice core for atmospheric CO_2 changes during the past millennium, Tellus B, 57, 51–57, 2005.

Sigman, D. M. and Boyle, E. A.: Glacial/interglacial variations in atmospheric carbon dioxide, Nature, 407, 859, https://doi.org/10.1038/35038000, 2000.

Sigman, D. M., De Boer, A. M., and Haug, G. H.: Antarctic stratification, atmospheric water vapor, and Heinrich events: A hypothesis for late Pleistocene deglaciations, 173, American Geophysical Union, Washington DC, 315–334, 2007.

Sowers, T., Bender, M., and Raynaud, D.: Elemental and isotopic composition of occluded O_2 and N_2 in polar ice, J. Geophys. Res., 94, 5137–5150, 1989.

Spahni, R., Chappellaz, J., Stocker, T., Loulergue, L., Hausmmann, G., Kawamura, K., Flückiger, J., Schwander, J., Raynaud, D., Masson-Delmotte, V., and Jouzel, J.: Atmospheric Methane and Nitrous Oxide of the Late Pleistocene from Antarctic Ice Cores, Science, 310, 1317–1321, https://doi.org/10.1126/science.1120132, 2005.

Stocker, T. F. and Johnsen, S. J.: A minimum thermodynamic model for the bipolar seesaw, Paleoceanography, 18, PA000920, https://doi.org/10.1029/2003PA000920, 2003.

Tans, P. P., Crotwell, A. M., and Thoning, K. W.: Abundances of isotopologues and calibration of CO_2 greenhouse gas measurements, Atmos. Meas. Tech., 10, 2669–2685, https://doi.org/10.5194/amt-10-2669-2017, 2017.

Toggweiler, J. R., Russell, J. L., and Carson, S. R.: Midlatitude westerlies, atmospheric CO_2, and climate change during the ice ages, Paleoceanography, 21, PA2005, https://doi.org/10.1029/2005PA001154, 2006.

5.3 CH_4 and N_2O fluctuations during the penultimate deglaciation

Loïc Schmidely, Christoph Nehrbass-Ahles, Jochen Schmitt, Juhyeong Han, **Lucas Silva**, Jinhwa Shin, Fortunat Joos, Jérôme Chappellaz, Hubertus Fischer, and Thomas F. Stocker

Published in *Climate of the Past*, 17, 1627-1643 (2021) (doi: 10.5194/cp-17-1627-2021)

Abstract Deglaciations are characterized by the largest natural changes in methane (CH_4) and nitrous oxide (N_2O) concentrations of the past 800 000 years. Reconstructions of millennial- to centennial-scale variability within these periods are mostly restricted to the last deglaciation. In this study, we present composite records of CH_4 and N_2O concentrations from the EPICA Dome C ice core covering the penultimate deglaciation at temporal resolutions of ∼100 years. Our data permit the identification of centennial-scale fluctuations during the transition from glacial to interglacial levels. At ∼134 000 and ∼129 000 years before present (hereafter ka), both CH_4 and N_2O increased on centennial timescales. These abrupt rises are similar to the fluctuations associated with the Dansgaard–Oeschger events identified in the last glacial period. In addition, gradually rising N_2O levels at ∼130 ka resemble a pattern of increasing N_2O concentrations on millennial timescales characterizing the later part of Heinrich stadials. Overall, the events in CH_4 and N_2O during the penultimate deglaciation exhibit modes of variability that are also found during the last deglaciation and glacial cycle, suggesting that the processes leading to changes in emission during the transitions were similar but their timing differed.

Clim. Past, 17, 1627–1643, 2021
https://doi.org/10.5194/cp-17-1627-2021

Climate of the Past
Open Access
EGU

CH_4 and N_2O fluctuations during the penultimate deglaciation

Loïc Schmidely[1], Christoph Nehrbass-Ahles[2], Jochen Schmitt[1], Juhyeong Han[1], Lucas Silva[1], Jinwha Shin[3,a], Fortunat Joos[1], Jérôme Chappellaz[3], Hubertus Fischer[1], and Thomas F. Stocker[1]

[1]Climate and Environmental Physics, Physics Institute and Oeschger Centre for Climate Change Research, University of Bern, Bern 3012, Switzerland
[2]Department of Earth Sciences, University of Cambridge, Cambridge, UK
[3]Institut des Géosciences de l'Environnement (IGE), CNRS, Univ. Grenoble-Alpes, Grenoble, France
[a]present address: Department of Earth and Atmospheric Sciences, University of Alberta, Edmonton, AB, T6G 2E3, Canada

Correspondence: Thomas F. Stocker (thomas.stocker@climate.unibe.ch)

Received: 30 September 2020 – Discussion started: 19 October 2020
Revised: 12 May 2021 – Accepted: 1 July 2021 – Published: 3 August 2021

Abstract. Deglaciations are characterized by the largest natural changes in methane (CH_4) and nitrous oxide (N_2O) concentrations of the past 800 000 years. Reconstructions of millennial- to centennial-scale variability within these periods are mostly restricted to the last deglaciation. In this study, we present composite records of CH_4 and N_2O concentrations from the EPICA Dome C ice core covering the penultimate deglaciation at temporal resolutions of ∼ 100 years. Our data permit the identification of centennial-scale fluctuations during the transition from glacial to interglacial levels. At ∼ 134 000 and ∼ 129 000 years before present (hereafter ka), both CH_4 and N_2O increased on centennial timescales. These abrupt rises are similar to the fluctuations associated with the Dansgaard–Oeschger events identified in the last glacial period. In addition, gradually rising N_2O levels at ∼ 130 ka resemble a pattern of increasing N_2O concentrations on millennial timescales characterizing the later part of Heinrich stadials. Overall, the events in CH_4 and N_2O during the penultimate deglaciation exhibit modes of variability that are also found during the last deglaciation and glacial cycle, suggesting that the processes leading to changes in emission during the transitions were similar but their timing differed.

1 Introduction

Methane (CH_4) and nitrous oxide (N_2O) are currently the second- and third-most potent well-mixed anthropogenic greenhouse gases after carbon dioxide (CO_2) (Myhre et al., 2013). The impact of these trace gases on the Earth's radiative balance in the future depends on the sensitivity of natural sources to anthropogenic warming. Time periods of climate change in the past provide natural templates to study this coupling (Fischer et al., 2018). Reconstructions of greenhouse gas concentrations before the instrumental era are only enabled by analysing the composition of air trapped in tiny bubbles in polar ice cores, reflecting the atmospheric composition at the time the bubbles were formed. Ice core records of CH_4 and N_2O concentrations combined with temperature reconstructions revealed the natural variability of these gases and their coupling to climate change during the glacial cycles of the past 800 000 years. The overall increase in concentrations accompanying deglaciations represents the largest recurring changes (Spahni et al., 2005; Loulergue et al., 2008; Schilt et al., 2010a). Records spanning the last deglaciation (Termination I (TI), 18 000–11 000 years before present (hereafter ka), where present is defined as 1950 Common Era) showed that this overall increase appears as a sequence of millennial and centennial fluctuations superimposed, for CH_4, on longer-term, gradually rising concentrations (Marcott et al., 2014; Rhodes et al., 2015). Records resolving short-term fluctuations within deglaciations are limited to TI, owing to the availability of multiple high-accumulation ice cores.

The aim of this study is to produce a high-resolution deglacial record for the penultimate deglaciation (Termination II (TII), 140–128 ka). We present CH_4 and N_2O composite datasets from the EPICA Dome C (EDC) ice core including 150 new measurements covering the time interval 145–125 ka, combined with the published data of Loulergue et al.

(2008) and Schilt et al. (2010a). We increased the sampling resolution of the aforementioned records by a factor ~ 3.5 and ~ 5 to obtain mean resolutions of 100 and 115 years for CH_4 and N_2O, respectively. These values are on the order of the mean width of the gas age distribution (GAD) for the EDC ice core in the interval 145–125 ka. This width is estimated to range between $\sim$ 110–220 years using the approach of Nehrbass-Ahles et al. (2020), where the width is defined as the arithmetic mean of the distribution, and $\sim$ 50–130 years using the approach of Epifanio et al. (2020), where the width is defined as the spectral width of the distribution. In addition, we also present seven N_2O isotopic measurements ($\delta^{15}N$ (N_2O) and $\delta^{18}O$ (N_2O)), used to assess the integrity of the data with respect to in situ formation of N_2O.

CH_4 and N_2O fluctuations observed during TI belong to recurrent modes of variability. The most studied of these modes characterizes the climate transitions from stadials to interstadials and is most notably exemplified by the transitions associated with the Dansgaard–Oeschger (DO) events of the last glacial period as well as by the transitions to the Bølling–Allerød and the Holocene during TI. This *DO-type* mode of variability is characterized by abrupt increases in CH_4 concentrations ($\sim$ 50–260 ppb in a few centuries), approximately synchronous with the onsets of interstadial Greenland warming by a few decades (Baumgartner et al., 2014; Rosen et al., 2014), while N_2O concentrations exhibit concomitant increases reaching up to $\sim$ 60 ppb, taking more than a century to stabilize because of their longer atmospheric lifetime (Flückiger et al., 2004; Schilt et al., 2010a, 2013). In addition, N_2O concentrations gradually increase in the later part of Heinrich stadials (HSs), extended stadials defined by the occurrence of massive iceberg discharges through the Hudson Strait into the North Atlantic (Hemming, 2004), starting centuries to millennia before interstadial Greenland temperature and CH_4 rises (Schilt et al., 2013). This *late HS-type* mode of N_2O variability characterized the HS during both the last deglaciation (Fischer et al., 2019; Schilt et al., 2014) as well as the last glacial period (Schilt et al., 2013). A second mode of CH_4 variability has been identified during HSs of the last glacial and deglaciation. This *HS-type* mode of CH_4 variability consists of intermittent CH_4 peaks displaying amplitudes of 32–53 ppb and characteristic timescales of 90–190 years, sometimes followed (HS4 and HS5) by elevated background concentrations relative to before the event (Rhodes et al., 2015).

DO-type and HS-type CH_4 fluctuations are likely driven by changes in tropical wetland emissions (Rhodes et al., 2015; Bock et al., 2017), where CH_4 is produced by the decomposition of organic matter under anaerobic conditions. Changes in geologic and pyrogenic emissions as well as changes in the sink strength play only a minor role (Dyonisius et al., 2020; Bock et al., 2010, 2017; Levine et al., 2012; Hopcroft et al., 2017). Wetland emissions are controlled by climate (precipitation, temperature, and atmospheric CO_2 concentration), modulating wetland extent, emission rates, and ecosystem composition (Van Groenigen et al., 2011; Melton et al., 2013; Bloom et al., 2010). Changes in tropical wetland emissions during DO-type fluctuations are linked to the strengthening of monsoonal precipitation in the Northern Hemisphere (NH) tropics, enhancing wetland emission rates (Bock et al., 2017). Increased NH tropical precipitation is associated with northward shifts of the Intertropical Convergence Zone (ITCZ) in response to changes in heat distribution by the Atlantic Meridional Overturning Circulation (AMOC) (Broccoli et al., 2006; Alley, 2007). On the other hand, HS-type CH_4 fluctuations are hypothesized to result from large iceberg discharges, associated with a southward shift of the ITCZ, leading to an intensification of monsoonal precipitation in the Southern Hemisphere (SH) tropics, ultimately producing an increase in wetland emissions (Rhodes et al., 2015).

DO-type N_2O variability is likely driven by changes in emission from the terrestrial and marine biospheres, where N_2O is emitted as a by-product of nitrification and an intermediate product of denitrification (Joos et al., 2019, 2020; Fischer et al., 2019; Schilt et al., 2014). Terrestrial emissions are controlled by climate (precipitation, temperature, and atmospheric CO_2 concentration) and available land area (Joos et al., 2020; Van Groenigen et al., 2011). During TI, the response of terrestrial N_2O emissions for DO-type fluctuations is believed to result from temperature and precipitation changes (Joos et al., 2020) and appeared in phase with Greenland warming with the transition period lasting a maximum of $\sim$ 200 years (Fischer et al., 2019). Marine emissions are linked to the strength of the AMOC, modulating oxygen concentrations in the upper ocean and the amount of available organic matter at depth. For DO-type fluctuations, marine emissions are believed to be stimulated mainly by deoxygenation in the upper ocean as a consequence of the reinvigoration of the AMOC (Joos et al., 2019). Finally, the late HS-type N_2O increase during TI is thought to be driven exclusively by marine emissions (Fischer et al., 2019; Schilt et al., 2014), possibly resulting from a long-term reorganization of the nitrate and oxygen inventories following the preceding AMOC collapse (Schmittner and Galbraith, 2008).

2 Method

The results presented in this study are derived from two different instruments. The $\delta^{15}N$ (N_2O) and $\delta^{18}O$ (N_2O) data were measured with the device described in Schmitt et al. (2014), combining continuous extraction under vacuum with gas chromatography (GC) and isotope ratio mass spectrometry.

CH_4 and N_2O measurements were performed with a completely revised analytical system, firstly employed during this study (comprehensive description in Appendix A). The new apparatus uses continuous extraction under vacuum, comparable to the approach of Schmitt et al. (2014) or

Oyabu et al. (2020), combined with GC techniques to determine CH_4 and N_2O mole fractions in air extracted from small (~ 20 g) ice samples with a sample throughput of five to six samples per day. The instrument is equipped with a thermal conductivity detector, a flame-ionization detector, and an electron-capture detector for the quantification of air, CH_4, and N_2O, respectively. The results are referenced to the World Meteorological Organisation mole fraction scales: the WMOX2004A scale (CH_4) and NOAA-2006A (N_2O) (Dlugokencky et al., 2005; Hall et al., 2007) using three standard gases bracketing the glacial–interglacial range of CH_4 (358.88 ± 0.16 ppb, 838.59 ± 0.28 ppb, and 1729.30 ± 0.34 ppb) and N_2O concentrations (187.10 ± 0.12 ppb, 194.13 ± 0.12 ppb, and 300.20 ± 0.12 ppb). The uncertainty of the measurements derived from the revised instrument amounts to 7 (CH_4) and 6 ppb (N_2O).

3 Results

Our centennial-scale records show the progressions of the overall ~ 390 and ~ 60 ppb increase in CH_4 and N_2O concentration (Fig. 1), respectively, from the end of the Penultimate Glacial Maximum (PGM) to the beginning of the Last Interglacial (LIG). Our CH_4 data identify an outstanding value at ~ 140 ka in the dataset by Loulergue et al. (2008), ~ 80 ppb higher than adjacent samples (Fig. 1). The N_2O data appear substantially more scattered in the early part of the record, especially around the PGM (~ 145–140 ka). This scatter tends to decrease with younger ages. The spikes appear in the interval where the isotopic composition of N_2O becomes enriched in $\delta^{15}N$ (N_2O) (up to 21 ‰) and depleted in $\delta^{18}O$ (N_2O) (down to 41 ‰), compared to the relatively steady values in the ranges ~ 11–14 ‰ and ~ 45–47 ‰, respectively, observed for 125–136 ka (Fig. 1).

Our records display several fluctuations standing out in the overall evolution of the CH_4 and N_2O concentrations. For CH_4, these events are identified based on their high rates of change (> 10 ppb per century, Table 1). CH_4 rises on centennial timescales at ~ 134 and ~ 129 ka. At ~ 134 ka, concentrations increased by ~ 70 ppb in ~ 200 years before declining by ~ 60 ppb in ~ 400 years. The 129 ka event consists of a ~ 200 ppb increase proceeding in ~ 300 years.

The evolution of N_2O concentrations alternates between periods of plateaus and well-marked fluctuations. Similar to CH_4, a feature is resolved at ~ 134 ka where concentrations increased by ~ 30 ppb in ~ 300 years before declining to previous levels in ~ 1000 years. The 129 ka event is also imprinted in our N_2O record and is characterized by a ~ 30 ppb rise in ~ 900 years. In addition, an increase is identified at ~ 130 ka, where concentrations rose by ~ 20 ppb in ~ 700 years. The 130 and 129 ka events are separated by a plateau that lasted ~ 1000 years.

Overall, the improved resolution of our records allowed us to identify features not resolved in the previously published CH_4 and N_2O EDC datasets. In particular, the 134 ka event and the 130 ka event in N_2O are resolved for the first time. Retrieving CH_4 and N_2O concentrations from the same samples enables us to study the relative phasing of both trace gases in the course of these events without age uncertainty. At the onset of the 134 and 129 ka events, the rise in both trace gases occurs simultaneously. In contrast, the 130 ka event in the N_2O record is not accompanied by a concomitant fluctuation in CH_4 concentrations.

4 Discussion

4.1 Non-atmospheric CH_4 and N_2O variability

Interpreting our records in terms of atmospheric variability requires a closer inspection of the extreme values observed in the CH_4 and N_2O records.

The CH_4 data point at ~ 140 ka, previously published by Loulergue et al. (2008), is measured in the section characterized by the widest GAD in our record. For the time interval 141–139 ka, the width of the GAD is on the order of ~ 220 years, using the approach of Nehrbass-Ahles et al. (2020), or ~ 120 years using the approach of Epifanio et al. (2020). At ~ 140 ka, the adjacent data points are ~ 160 years older and ~ 170 years younger than the data point in question. Consequently, it appears unlikely that such an abrupt fluctuation in the ice core record represents an atmospheric signal. Spurious peaks could potentially result from layered bubble trapping (Rhodes et al., 2016; Fourteau et al., 2017, 2020). However, this outlier is measured in a period of otherwise stable CH_4 concentrations, where neither early nor late pore closures are expected to generate an anomaly (Rhodes et al., 2016; Fourteau et al., 2017). Secondly, similarly high concentrations are not observed in our record before the 134 ka event. Such an age anomaly (between the layers enclosing gas of abnormal age and the layers enclosing gas of the expected age) would be unrealistically high compared to the characteristic age anomalies reported by Fourteau et al. (2017) for the Vostok ice core (~ 200 years). Accordingly, we regard this CH_4 data point as an outlier.

The large variability observed in adjacent data points during the early part of the N_2O record (Fig. 1) is unlikely to reflect atmospheric fluctuations given its atmospheric lifetime of 116 ± 9 years (Prather et al., 2015). Elevated concentrations and disproportionately high N_2O variability have been observed in many instances for ice samples rich in mineral dust in both Antarctic and Greenland ice cores and are attributed to in situ production (Flückiger et al., 1999; Sowers, 2001; Flückiger et al., 2004; Spahni et al., 2005; Schilt et al., 2010a, 2013; Fischer et al., 2019). Measurements in the Vostok ice core by Sowers (2001) demonstrated this excess N_2O production to have a strong imprint in both $\delta^{15}N$ (N_2O) and $\delta^{18}O$ (N_2O) records. For some of our EDC samples we ob-

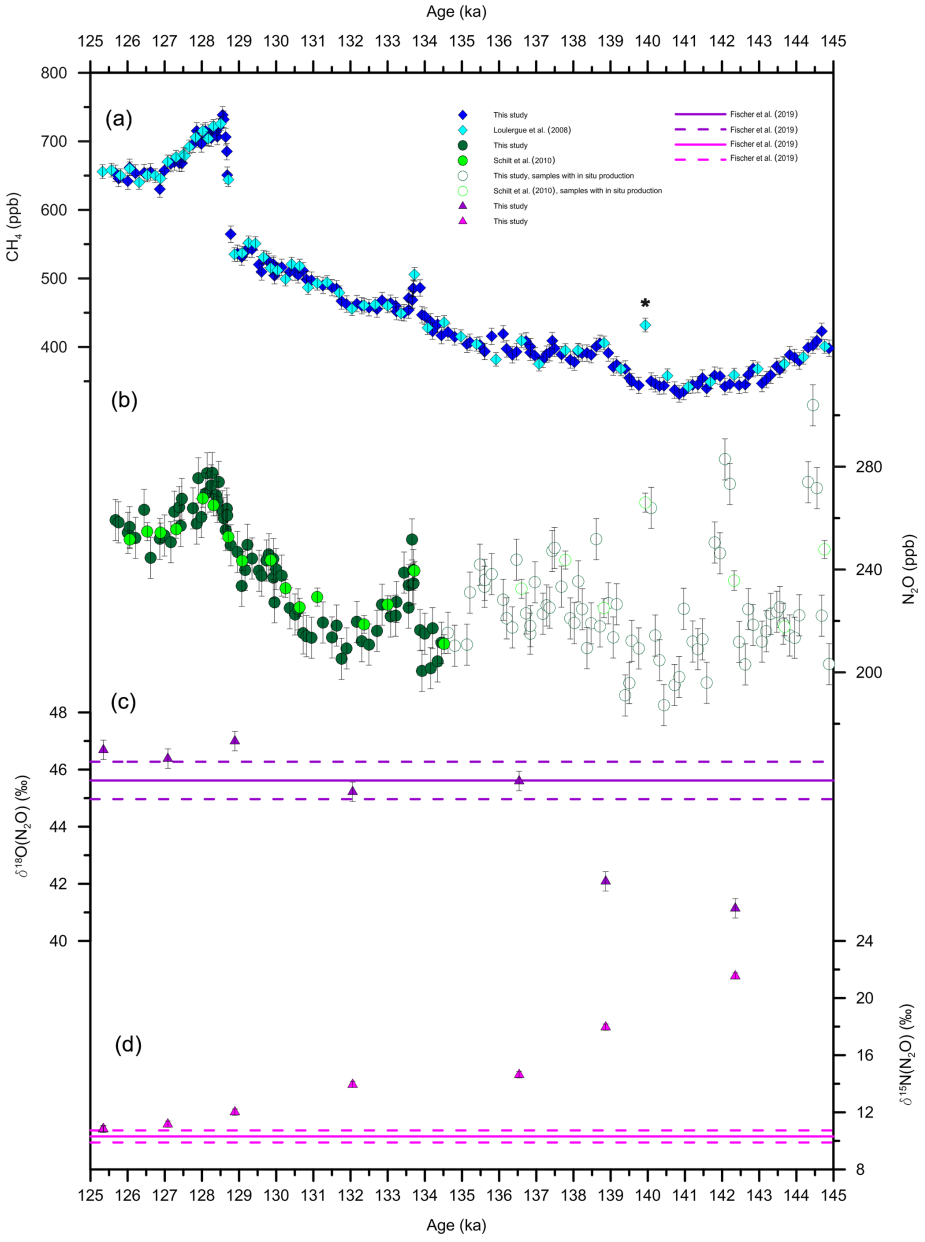

Figure 1. CH_4, N_2O, $\delta^{18}O$ (N_2O), and $\delta^{15}N$ (N_2O) records from the EDC ice core on the AICC2012 timescale (Bazin et al., 2013). The vertical bars represent the uncertainty of the measurements. **(a)** Composite CH_4 record with published data (light blue, Loulergue et al., 2008) and new measurements (this study, dark blue) after offset correction. The asterisk indicates the data point regarded as an outlier. **(b)** Composite N_2O record with published data (light green, Schilt et al., 2010a) and new measurements (this study, dark green) after offset correction. The empty symbols illustrate the data points considered affected by in situ production. **(c)** $\delta^{18}O$ (N_2O) record. For comparison, the average (solid line) and standard deviation (dashed line, 1σ) of $\delta^{18}O$ (N_2O) over TI are included (Fischer et al., 2019). **(d)** $\delta^{15}N$ (N_2O) record. For comparison, the average (solid line) and standard deviation (dashed line, 1σ) of $\delta^{15}N$ (N_2O) over TI are included (Fischer et al., 2019).

Table 1. Characteristics of the events observed at ∼ 134, ∼ 129, and ∼ 130 ka. The indications "up" and "down" in the first column refer to the ascending and descending limbs of the 134 ka event, respectively. The columns "start" and "end" indicate the starting and end points of the events (rounded to the hundred). The columns $C_{initial}$ and C_{final} indicate the concentrations (rounded to the 10) in the years preceding and following the events, respectively. The rates of change are average values over the time period comprised between the start and end points of the events. Rates of change are calculated from spline approximations (cut-off period: 200 years) computed according to Enting (1987) with the same routine as Beck et al. (2018).

Event	Start (ka)	End (ka)	$C_{initial}$ (ppb)	C_{final} (ppb)	Rate of change (ppb per century)
134 (CH_4, up)	134.0	133.8	440	510	35
134 (CH_4, down)	133.8	133.4	510	450	−15
134 (N_2O, up)	133.9	133.6	210	240	10
134 (N_2O, down)	133.6	132.6	240	210	−3
130 (N_2O)	130.7	130	220	240	3
129 (CH_4)	128.9	128.6	530	730	65
129 (N_2O)	129	128.1	240	270	3

serve the same systematic isotopic deviations as for the Vostok samples of that period, with $\delta^{15}N$ (N_2O) and $\delta^{18}O$ (N_2O) values that are more enriched and depleted, respectively, than typical atmospheric values. The coupling with dust is the basis of an empirical artefact detection method applicable to EDC samples. This method considers depth intervals where dust concentrations exceed an arbitrary threshold of 300 µg kg^{-1} as affected by in situ production (Spahni et al., 2005; Schilt et al., 2010a). We follow this approach and define 134.5 ka as the boundary for the section affected by artefacts. This is a slightly younger age than the last value regarded as unbiased by Schilt et al. (2010a). Consequently, we refrain from interpreting N_2O data points older than 134.5 ka as reflecting atmospheric variability.

The younger part of our records are used to study CH_4 and N_2O fluctuations during TII. In particular, we scrutinize our record with respect to the newly resolved variations belonging to the modes of variability presented above. To achieve this, we analyse the characteristics of the individual events as well as the background climate in which they occur.

4.2 The 129 ka event

The 129 ka event refers to the pronounced increase in CH_4 and N_2O concentrations to interglacial levels at the end of TII (Fig. 2). For both gases, this event accounts for about half of the deglacial change in concentrations.

CH_4 and N_2O concentrations rose in parallel with the main resumption of the AMOC, as indicated by the evolution of the isotopic ratio of neodymium 143 and 144 (ε_{Nd}) (Deaney et al., 2017; Böhm et al., 2015). At the same time, the evolution of the isotopic composition of speleothem calcite ($\delta^{18}O$ ($CaCO_3$)) indicates a northward shift of the ITCZ (Cheng et al., 2009, 2016) (Fig. 3). These are fingerprints of DO-type variability. Accordingly, the abrupt CH_4 rise likely reflects the response of terrestrial emissions from NH tropical wetlands. The simultaneous increase in both gases indicates that terrestrial emissions contributed, at least partly, to the N_2O rise at ∼ 129 ka. However, because the deglacial AMOC resumption occurred at this time, it can be assumed that marine sources also played a role. A contribution from both marine and terrestrial emissions is in agreement with the findings of Schilt et al. (2014) and Fischer et al. (2019) for DO-type fluctuations during TI. Higher resolution measurements of the isotopic composition of N_2O combined with a deconvolution, similar to the aforementioned studies, are needed to quantitatively determine the relative contribution of the sources during the 129 ka event.

4.3 The 130 ka event

The 129 ka event is preceded by a phase of rising N_2O concentrations in the interval from 130.7 to 130 ka at the end of HS11 (Fig. 2). This is reminiscent of the pattern of late HS-type increase, where N_2O concentrations rose before the rapid DO-type Greenland temperature and CH_4 increases (Schilt et al., 2013). The timescale of the 130 ka event is in the range of the duration typically observed for these episodes (∼ 0.5–2 millennia) (Schilt et al., 2013), while the N_2O growth rate appears slightly larger (∼ 3 ppb compared to typically ∼ 1 ppb per century). The lack of a concomitant CH_4 fluctuation suggests that only the marine source contributed to the N_2O increase, in agreement with the findings of Schilt et al. (2014) and Fischer et al. (2019) for the late HS1 rise. The change in marine emissions may be linked to a long-term adjustment of the nitrate and oxygen inventories in the upper ocean after a period of AMOC interruption (Schmittner and Galbraith, 2008). Overall, despite the somewhat different rates of change, the 130 ka event likely constitutes an instance of a late-HS N_2O fluctuation during TII. The attribution of the 130 ka feature to the pattern of late HS increase would be strengthened by additional measurements of $\delta^{15}N$ (N_2O) and $\delta^{18}O$ (N_2O), allowing the unambiguous identification of the source contributing to this event.

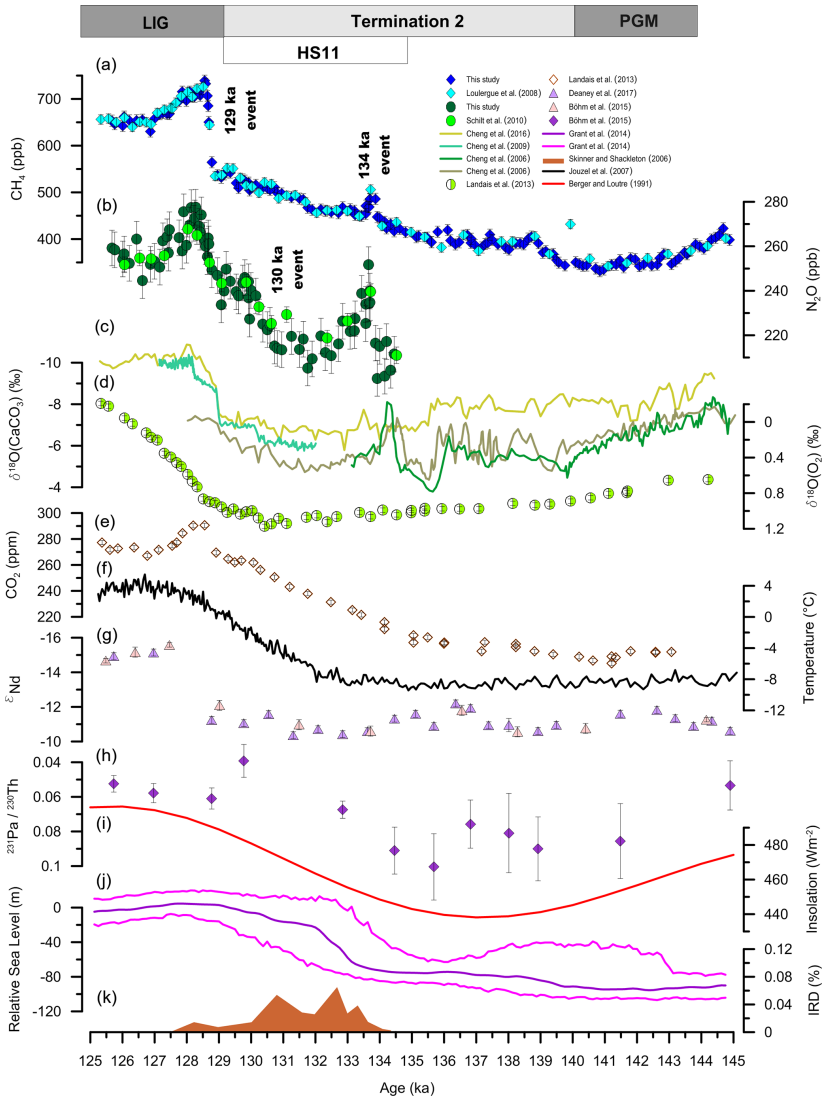

Figure 2. Evolution of the CH_4 and N_2O concentrations combined with complementary climate proxies during TII. The boxes delineate the climate periods mentioned in the text: the Penultimate Glacial Maximum (PGM), Heinrich Stadial 11 (HS11, delineation according to Marino et al., 2015), and the Last Interglacial (LIG). **(a)** Composite CH_4 record. **(b)** Composite N_2O record. **(c)** Speleothem $\delta^{18}O$ ($CaCO_3$) records: Sanbao SB25 (light green) (Cheng et al., 2009), Hulu Cave MSX (khaki) (Cheng et al., 2006), Hulu cave MSP (dark green) (Cheng et al., 2006), and Sanbao–Dongge composite (pale yellow) (Cheng et al., 2016). **(d)** $\delta^{18}O$ (O_2) from EDC on the AICC2012 timescale (Landais et al., 2013). **(e)** CO_2 from EDC on the AICC2012 timescale (Landais et al., 2013). **(f)** Antarctic surface temperature (relative to the last millennium) from EDC on the AICC2012 timescale (Jouzel et al., 2007). **(g)** Composite ε_{Nd} from the sediment core ODP Site 1063 (Deaney et al., 2017), including data points from Böhm et al. (2015) (purple) and new measurements from Deaney et al. (2017) (pale pink), on the timescale of Deaney et al. (2017). **(h)** $^{231}Pa/^{230}Th$ record from the sediment core ODP Site 1063 (Böhm et al., 2015), on the timescale of Deaney et al. (2017). **(i)** Mean summer (June to August) insolation at 40° N (Berger and Loutre, 1991). **(j)** Relative sea level stand from the Red Sea synchronized on a radiometric timescale, including the maximum probability curve (purple) and its 95 % confidence interval (magenta) (Grant et al., 2014). **(k)** Ice-rafted debris (IRD) from Skinner and Shackleton (2006) on the radiometric timescale of Marino et al. (2015).

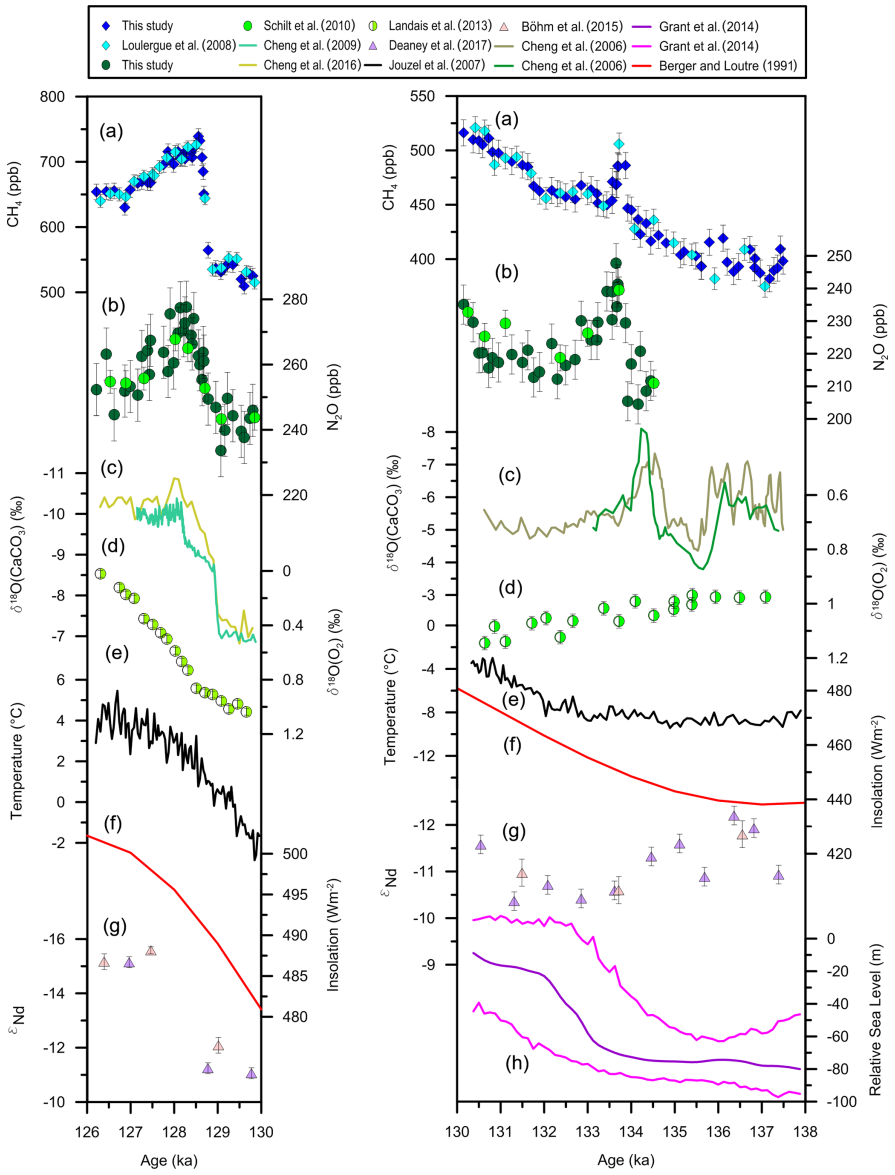

Figure 3. Details of the 129 (left panel) and 134 ka events (right panel). **(a)** Composite CH_4 record. **(b)** Composite N_2O record. **(c)** Speleothem $\delta^{18}O$ ($CaCO_3$) records: Sanbao SB25 (light green) (Cheng et al., 2009), Hulu Cave MSX (khaki) (Cheng et al., 2006), Hulu cave MSP (dark green) (Cheng et al., 2006), and Sanbao–Dongge composite (pale yellow). **(d)** $\delta^{18}O$ (O_2) from EDC on the AICC2012 timescale (Landais et al., 2013). **(e)** Antarctic surface temperature (relative to the last millennium) from EDC on the AICC2012 timescale (Jouzel et al., 2007). **(f)** Mean summer (June to August) insolation at 40° N (Berger and Loutre, 1991). **(g)** Composite ε_{Nd} from the sediment core ODP Site 1063 (Deaney et al., 2017), including data points from Böhm et al. (2015) (purple) and new measurements from Deaney et al. (2017) (pale pink), on the timescale of Deaney et al. (2017). **(h)** Relative sea level stand from the Red Sea synchronized on a radiometric timescale, including the maximum probability curve (purple) and its 95 % confidence interval (magenta) (Grant et al., 2014).

4.4 The 134 ka event

Turning to the 134 ka event, its occurrence within HS11 and the properties of the CH_4 increase (duration and amplitude) are reminiscent of the HS-type pattern of variability evidenced by Rhodes et al. (2015). HS-type fluctuations resolved in the WAIS Divide (WD) ice core fully developed within 90–190 years (Rhodes et al., 2015). The broader GAD of the EDC ice core implies that any such features would appear strongly dampened in our data. This is supported by continuous CH_4 measurements in the Vostok ice core, demonstrating the absence of the characteristic overshoot resolved in the WD ice core during HS4 (Fourteau et al., 2020; Rhodes et al., 2015). Therefore, the sharpness and amplitude of the 134 ka event is not consistent with the picture of a substantially smoothed version of an HS-type fluctuation. The $\sim$ 70 ppb rise observed in the EDC record would translate into a WD signal exceeding by far the amplitude range of the HS1, HS2, HS4, and HS5 fluctuations (32–53 ppb) (Rhodes et al., 2015). Secondly, HS-type CH_4 variability is also characterized by abrupt CO_2 jumps, millennial-scale increases in $\delta^{18}O$ (O_2), enrichment in speleothem $\delta^{18}O$ ($CaCO_3$), and the absence of concomitant N_2O variability (Bauska et al., 2016, 2018, 2021; Marcott et al., 2014; Fischer et al., 2019; Schilt et al., 2013, 2010a; Guillevic et al., 2014). The simultaneous occurrence of the CH_4 and N_2O pulses at $\sim$ 134 ka, the depletion in speleothem $\delta^{18}O$ ($CaCO_3$), and the lack of any fluctuation in the $\delta^{18}O$ (O_2) record (Landais et al., 2013) contradict these observations (Fig. 3). The 134 ka event is therefore likely to have resulted from different mechanisms and does not constitute an instance of an HS-type CH_4 fluctuation during TII. On the other hand, simultaneous rises of atmospheric CH_4 and N_2O concentrations are observed during DO-type fluctuations. During the last glacial cycle, the amplitude of DO-type CH_4 increases ranges from $\sim$ 50 to 220 ppb in Greenland ice cores and elevated concentrations lasted for centuries to millennia (Baumgartner et al., 2014; Flückiger et al., 2004). Accordingly, the magnitude of the 134 ka event fits well within the amplitude range observed for the well-resolved DO-type fluctuations in the EDC record of Loulergue et al. (2008) ($\sim$ 50–185 ppb). Going further, results from Greenland ice cores have shown that the amplitude of DO-type CH_4 rises tracks the variations in low- to mid-latitude NH summer insolation, where the most substantial changes in concentration are associated with higher insolation. This indicates that the amount or seasonal distribution of solar radiation has modulated the response of CH_4 sources during interstadials (Brook et al., 1996; Flückiger et al., 2004). The 134 ka event occurs during a time period of low NH summer insolation (Fig. 2), comparable to this at DO2. Yet, the magnitude of the 134 ka event appears larger ($\sim$ 70 ppb compared to $\sim$ 50 ppb for DO2 in the EDC record).

Associating our event with a DO-type pattern of variability requires evidence for a northward shift of the ITCZ and reinvigoration of the AMOC. Synchronous with the 134 ka event, within dating uncertainty, we observe a short-lived negative excursion in speleothem $\delta^{18}O$ ($CaCO_3$) records (Cheng et al., 2006) (Fig. 3) as well as fluctuations in proxies reflecting salinity and runoff intensity in the Bay of Bengal (Nilsson-Kerr et al., 2019). These data indicate a transient strengthening of the NH tropical monsoon systems consistent with a northward shift of the ITCZ. Concerning the behaviour of the AMOC, we are not aware of studies reporting on a potential reinvigoration at this time. Nevertheless, oceanic tracers exhibit a small and short-lived fluctuation in the time interval 133–132 ka (on the timescale of Böhm et al., 2015) before reaching their maximum HS11 values (Böhm et al., 2015). On the updated chronology of the sediment core ODP Site 1063 (Deaney et al., 2017), the negative excursion in the ε_{Nd} record of Böhm et al. (2015) coincides with a comparably small value in the data of Deaney et al. (2017) (Fig. 2). However, the revised chronology places the excursion in ε_{Nd} and $^{231}Pa/^{230}Th$ substantially earlier than the 134 ka event (Fig. 3). The onset of this excursion is at $\sim$ 137.4 ka, corresponding to a shift by $\sim$ 4900 years with respect to the timescale of Böhm et al. (2015). Since the timescale of the sediment core is tuned to the Antarctic Ice Core Chronology (AICC2012) (Bazin et al., 2013; Veres et al., 2013) within an estimated uncertainty of 400 years, the fluctuations resolved in the ice and marine cores should, in principle, not be regarded as synchronous. However, the alignment with the AICC2012 is performed using only one tie point between CH_4 and the isotopic composition of planktonic foraminifera (at $\sim$ 128.7 ka, corresponding to the abrupt CH_4 increase into the LIG) (Deaney et al., 2017). Therefore, it may be possible that the two timescales are less tightly aligned away from this tie point. If this would be the case, it could be hypothesized that the excursions in oceanic proxies are synchronous with the fluctuations of $\delta^{18}O$ ($CaCO_3$), CH_4, and N_2O.

DO-type variability is typically also imprinted in the temperature record from Antarctic ice cores as well as in the $\delta^{18}O$ (O_2) record. However, the responses of these proxies are generally attenuated or occur on longer timescales compared to those of CH_4 and $\delta^{18}O$ ($CaCO_3$). Accordingly, a short and small-amplitude interstadial at $\sim$ 134 ka might not have left discernible imprints in the respective records of Landais et al. (2013) and Jouzel et al. (2007) (Figs. 2 and 3).

Taking the proxy evidences together, we speculate that a brief and small-scale resumption of the AMOC might have occurred within HS11, accounting for the northward ITCZ shift and the rise in atmospheric CH_4 and N_2O concentrations. We acknowledge that our interpretation is limited by the relatively coarse resolution of ε_{Nd} and $^{231}Pa/^{230}Th$ as well as by the uncertainty arising from cross-dating sediment and ice core records. Concerning N_2O, we finally note that the duration of the rise and the simultaneity with the excursion in CH_4 suggest that terrestrial N_2O emissions con-

tributed by far the most to the 134 ka event (Fischer et al., 2019).

Should our interpretation hold, the 134 ka event can be regarded as a short DO-type fluctuation. We speculate that the hypothesized AMOC reinvigoration might have been perturbed by Meltwater Pulse 2B (MWP-2B). MWP-2B represents $\sim 70\,\%$ of the deglacial sea level change and coincides with the 134 ka event within dating uncertainty (Fig. 2) (Marino et al., 2015). The disruption of the oceanic circulation by freshwater forcing might have been enabled by the high susceptibility of the AMOC to perturbations at a time when the high-latitude SH was particularly cold (Buizert and Schmittner, 2015), as was the case during HS11 (Fig. 2). This situation favours the occurrence of relatively short, centennial, interstadials such as those appearing near the Last Glacial Maximum in Greenland ice cores.

5 Conclusions

In the present study, we increased the resolution of the deglacial CH_4 and N_2O records, allowing us to derive composite datasets covering TII (140–128 ka) at average resolutions of ~ 100 years. Our results display pronounced fluctuations standing out of the overall transition of CH_4 and N_2O concentrations to interglacial conditions. The most prominent one is placed at ~ 129 ka and delineates the transition into the LIG. We assume that terrestrial and marine sources contributed to the N_2O increase at this time. Additionally, we unequivocally identify a 134 and 130 ka event. We link the latter to the pattern of late HS-type N_2O increase, where changes in marine emissions are likely to be the only contributor. The former is regarded as a short DO-type fluctuation, whose timescale indicates that only terrestrial N_2O sources likely contributed to the increase. We note that these fluctuations in CH_4 and N_2O concentrations during the penultimate deglaciation are all instances of recurrent modes of variability, also evidenced during the last deglaciation as well as during the last glacial period.

Appendix A: New measurement system for CH_4 and N_2O

Although gas chromatography (GC) has been used extensively to measure CH_4 and N_2O at the University of Bern (e.g. Flückiger et al., 1999, 2002, 2004; Baumgartner et al., 2012, 2014; Loulergue et al., 2008; Schilt et al., 2010a, b, 2013; Spahni et al., 2005), the totally revised extraction and GC setup presented here has not been described before. The device is composed of different functional units, enabling the different actions of the system (standard injection, extraction, separation, and detection) (coloured boxes in Fig. A1). The measurements are carried out using three distinct lines. The ice line (IL, under vacuum, red path in Fig. A1) is used to extract air from ice core samples. The continuous-flow line (CFL, flushed with He, green path in Fig. A1) is used to measure standards to calibrate ice core measurements. Standards and samples are introduced differently into the separation unit to gain time during daily operation. Therefore, following the identical treatment principle, we also employ the standard over ice line (SOIL, blue line in Fig. A1) to periodically inject standards for comparison with similar measurements performed with the CFL in order to account for contamination stemming from the IL. The mean offset between the lines is used to correct IL data.

To extract gas from ice core samples, we use continuous extraction under vacuum. Air is released from the ice during the melting (immersing the bottom of the vessel in a $\sim 20\,^{\circ}C$ water bath) and is simultaneously adsorbed on an activated charcoal trap held at $-196\,^{\circ}C$ using liquid nitrogen (T2 in Fig. A1). Water vapour is condensed beforehand using another cold trap held at $-80\,^{\circ}C$ (T1 in Fig. A1). The progression of the extraction is monitored with a pressure gauge (P5 in Fig. A1). The completion of the extraction is indicated by a P5 pressure value $\leqslant 0.25$ mbar. When this value is reached, T2 is isolated from the vessel and heated to facilitate CH_4 and N_2O desorption from the charcoal bed. The duration and final temperature of the heating (5 min, 130 °C) ensure full recovery of the adsorbed gas. At the end of this phase, He flushes the content of T2 into the separation unit. Overall, the advantage of our procedure is the permanently low CH_4 and N_2O partial pressure, as well as total air pressure, prevailing in the vessel during the extraction. Accordingly, equilibrium conditions with respect to solubility are never reached, precluding the need of a solubility correction. This type of correction was required in traditional analyses using a melt–refreeze method, where the air sample is enclosed in the vessel head space during the extraction.

CH_4 and N_2O are separated from the bulk air in the separation unit before reaching the detection unit equipped with a thermal conductivity detector (TCD), a flame-ionization detector (FID), and an electron-capture detector (ECD) to quantify the amount of air, CH_4, and N_2O, respectively. The separation unit is composed of a succession of GC columns. CH_4 and N_2O are separated from the bulk air in the precolumn and analytical column (Fig. A1). After detection of the air peak by the TCD, V8 allows us to route CH_4 towards the FID (via T5 and T7) and N_2O towards the ECD (via T4 and T6) (Fig. A1). T5 and T4 are used to separate CH_4 and N_2O, respectively, from species having almost similar retention times. T7 and T6 are used to focus the gas to obtain sharp peaks in the chromatograph.

The amount of air, CH_4, and N_2O is quantified by integrating the area below the corresponding GC peaks. For each species, calibration curves are established between areas and the number of moles calculated using the volume, temperature, and pressure of the sample loop as well as the known CH_4 and N_2O mole fractions of the standard gases. We use a set of primary standards provided by the National Oceanic and Atmospheric Administration and referenced to the World Meteorological Organisation mole fraction scales: the WMOX2004A scale (CH_4) and NOAA-2006A (N_2O) (Dlugokencky et al., 2005; Hall et al., 2007). This set of standards brackets the glacial–interglacial range of CH_4 (358.88 ± 0.16 ppb, 838.59 ± 0.28 ppb, and 1729.30 ± 0.34 ppb) and N_2O concentrations (187.10 ± 0.12 ppb, 194.13 ± 0.12 ppb, and 300.20 ± 0.12 ppb). CH_4 and N_2O mole fractions are calculated by dividing the number of CH_4 and N_2O moles by the number moles of air. In addition, total air content can also be quantified using the TCD area as well as the volume, temperature, and pressure of the sample loop.

After calibration, the results are corrected for the line offset between CFL and SOIL. This offset accounts for the blank introduced in the IL and is averaged over, at least, a measurement campaign. The CH_4 and N_2O line offsets appear to be linearly dependent on the concentration enabling the use of linear interpolations to correct ice core results.

The uncertainty of the CH_4 and N_2O data derived with our instrument amounts to 7 and 6 ppb, respectively. It is calculated as the sum of the individual uncertainty, associated with the overall analytical procedure (1σ standard deviation of SOIL measurements) and with the line offset correction, in quadrature.

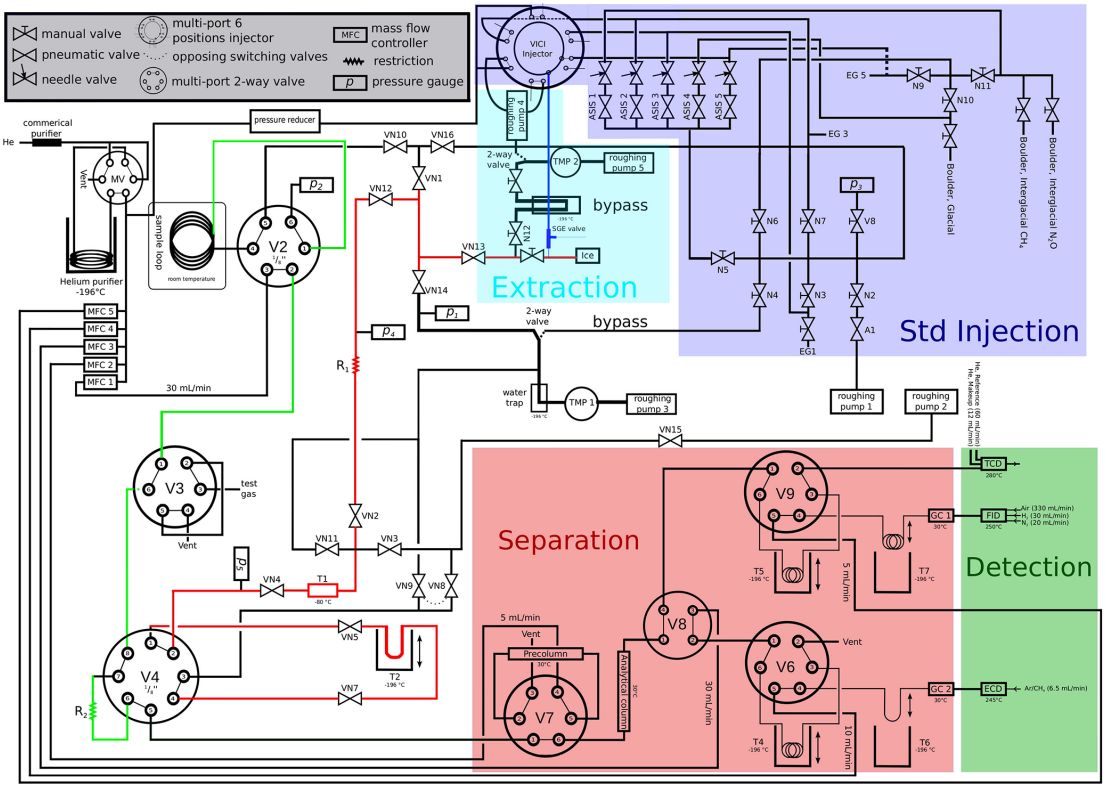

Figure A1. Flow scheme of the CH_4 and N_2O measurement system. The red, green, and blue paths highlight the ice line (IL), continuous-flow line (CFL), and standard over ice line (SOIL), respectively. Coloured boxes display the different functional units of the system discussed in Appendix A.

Appendix B: Construction of composite CH_4 and N_2O records

The construction of the composite records presented in this study is complicated by offsets between the datasets, where our results appear on average 18 ± 10 ppb (CH_4) and 21 ± 3 ppb (N_2O) higher than previous data, although all datasets show the same relative changes (Fig. B1). The offsets are calculated as the mean of the residuals between splines with cut-off periods of 10 000 years fitted through the datasets. We computed splines according to Enting (1987), using the same routine as Beck et al. (2018), where each spline is the average of 1000 iterations with data points varied within a normal distribution inside their uncertainty range.

It seems likely that the offsets are linked to the different extraction techniques employed. In fact, the published EDC data were measured at the University of Bern and Grenoble with instruments using melt–refreeze extraction (Loulergue et al., 2008; Schilt et al., 2010a). Melt–refreeze extraction is prone to underestimate CH_4 and N_2O concentrations if the refreezing is not perfectly efficient, while in our method air is quantitatively extracted from the ice samples. We note that also the values presented in previous publications had to be aligned for interlaboratory offsets on the order of 10 ppb for CH_4 (Loulergue et al., 2008), which may also reflect differences in the extraction efficiency of previously used melt–refreeze methods in different labs. Because melt–refreeze extraction has been the standard procedure for decades, the EDC records have been measured exclusively using this technique. We therefore think that additional overlapping measurements with an independent extraction technique (e.g. sublimation) are needed to resolve the dispute. Without further evidence, we prefer striving for consistency by correcting our data to the EDC benchmark records of Loulergue et al. (2008) and Schilt et al. (2010a). To achieve this, we subtract the mean offsets of 18 (CH_4) and 21 ppb (N_2O) from our results. This approach is facilitated by the high degree of co-variation between the datasets (Fig. B1).

The merging procedure described above adds an additional source of uncertainty to our results. Accounting for the uncertainty of the mean offset, taken as the standard deviation (1σ) of the residuals between the splines, increases the total uncertainty of the new data included in the composite records to 12 (CH_4) and 8 ppb (N_2O). For the published EDC values and the isotopic measurements, the uncertainties amount to 10 ppb (CH_4), 4 ppb (N_2O), 0.22 ‰ ($\delta^{15}N$ (N_2O)), and 0.34 ‰ ($\delta^{18}O$ (N_2O)), as reported in Loulergue et al. (2008), Schilt et al. (2010a), and Schmitt et al. (2014).

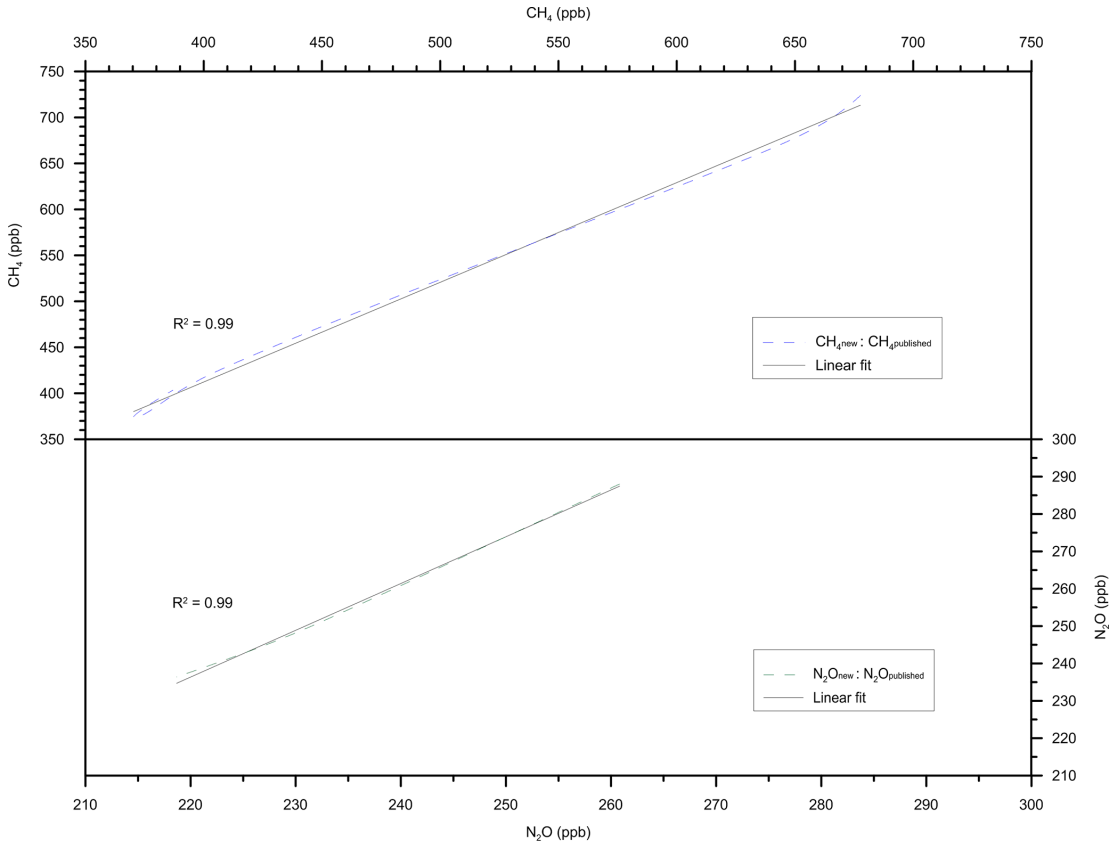

Figure B1. Offsets between new and published CH_4 and N_2O EDC records. Dashed lines show the new measurements plotted against the published ones (data are from the spline approximations introduced in Appendix B). Solid lines are linear fits through these data.

Data availability. The new CH_4 and N_2O data are available at the World Data Center for Paleoclimatology under the following link: https://www.ncdc.noaa.gov/paleo/study/33673 (Schmidely et al., 2020).

Author contributions. The present study was designed by TFS, HF, and LoS. LoS and JH performed the methane and nitrous oxide measurements. JoS provided the isotopic data. LoS wrote the text with inputs from CNA, JoS, JH, LuS, JiS, FJ, JC, HF, and TFS.

Competing interests. The authors declare that they have no conflict of interest.

Disclaimer. Publisher's note: Copernicus Publications remains neutral with regard to jurisdictional claims in published maps and institutional affiliations.

Acknowledgements. The authors would like to thank Barbara Seth for the measurements of the isotopic composition of N_2O, Gregory Teste for assistance in cutting ice samples, and Michael Bock and Jan Strähl for the construction of the new CH_4 and N_2O measurement system. We thank the reviewers and the editor for detailed and constructive comments that improved this paper. We acknowledge financial support by the Swiss National Science Foundation (SNF project numbers 200020_172745, 200020_200492, 200020_172506, 200020_200511, and 200020_159563). This work is a contribution to the European Project for Ice Coring in Antarctica (EPICA), a joint European Science Foundation/European Commission scientific programme, funded by the European Union and by national contributions from Belgium, Denmark, France, Germany, Italy, The Netherlands, Norway, Sweden, Switzerland, and the United Kingdom. The main logistic support was provided by IPEV and PNRA (at Dome C) and AWI (at Dronning Maud Land). This is EPICA publication no. 319. This project is TiPES (Tipping Points in the Earth System) contribution no. 125. This project has received funding from the European Union's Horizon 2020 research and innovation programme under grant 820970.

Financial support. This research has been supported by the Swiss National Science Foundation (SNF project numbers 200020_172745, 200020_172506, 200020_159563, 200020_200492 and 200020_200511) and by the European Union's Horizon 2020 research and innovation programme (grant no. 820970).

Review statement. This paper was edited by Luke Skinner and reviewed by two anonymous referees.

References

Alley, R. B.: Wally was right: Predictive ability of the North Atlantic "conveyor belt" hypothesis for abrupt climate change, Annu. Rev. Earth Pl. Sc., 35, 241–272, https://doi.org/10.1146/annurev.earth.35.081006.131524, 2007.

Baumgartner, M., Schilt, A., Eicher, O., Schmitt, J., Schwander, J., Spahni, R., Fischer, H., and Stocker, T. F.: High-resolution interpolar difference of atmospheric methane around the Last Glacial Maximum, Biogeosciences, 9, 3961–3977, https://doi.org/10.5194/bg-9-3961-2012, 2012.

Baumgartner, M., Kindler, P., Eicher, O., Floch, G., Schilt, A., Schwander, J., Spahni, R., Capron, E., Chappellaz, J., Leuenberger, M., Fischer, H., and Stocker, T. F.: NGRIP CH_4 concentration from 120 to 10 kyr before present and its relation to a $\delta^{15}N$ temperature reconstruction from the same ice core, Clim. Past, 10, 903–920, https://doi.org/10.5194/cp-10-903-2014, 2014.

Bauska, T. K., Baggenstos, D., Brook, E. J., Mix, A. C., Marcott, S. A., Petrenko, V. V., Schaefer, H., Severinghaus, J. P., and Lee, J. E.: Carbon isotopes characterize rapid changes in atmospheric carbon dioxide during the last deglaciation, P. Natl. Acad. Sci. USA, 113, 3465–3470, https://doi.org/10.1073/pnas.1513868113, 2016.

Bauska, T. K., Brook, E. J., Marcott, S. A., Baggenstos, D., Shackleton, S., Severinghaus, J. P., and Petrenko, V. V.: Controls on millennial–scale atmospheric CO_2 variability during the last glacial period, Geophys. Res. Lett., 45, 7731–7740, https://doi.org/10.1029/2018GL077881, 2018.

Bauska, T. K., Marcott, S. A., and Brook, E. J.: Abrupt changes in the global carbon cycle during the last glacial period, Nat. Geosci., 14, 91–96, 2021.

Bazin, L., Landais, A., Lemieux-Dudon, B., Toyé Mahamadou Kele, H., Veres, D., Parrenin, F., Martinerie, P., Ritz, C., Capron, E., Lipenkov, V., Loutre, M.-F., Raynaud, D., Vinther, B., Svensson, A., Rasmussen, S. O., Severi, M., Blunier, T., Leuenberger, M., Fischer, H., Masson-Delmotte, V., Chappellaz, J., and Wolff, E.: An optimized multi-proxy, multi-site Antarctic ice and gas orbital chronology (AICC2012): 120–800 ka, Clim. Past, 9, 1715–1731, https://doi.org/10.5194/cp-9-1715-2013, 2013.

Beck, J., Bock, M., Schmitt, J., Seth, B., Blunier, T., and Fischer, H.: Bipolar carbon and hydrogen isotope constraints on the Holocene methane budget, Biogeosciences, 15, 7155–7175, https://doi.org/10.5194/bg-15-7155-2018, 2018.

Berger, A. and Loutre, M.-F.: Insolation values for the climate of the last 10 million years, Quaternary Sci. Rev., 10, 297–317, 1991.

Bloom, A. A., Palmer, I. P., Fraser, A., Reay, D. S., and Frankenberg, C.: Large–scale controls of methanogenesis inferred from methane and gravity spaceborne data, Science, 327, 322–325, https://doi.org/10.1126/science.1175176, 2010.

Bock, M., Schmitt, J., Möller, L., Spahni, R., Blunier, T., and Fischer, H.: Hydrogen isotopes preclude marine hydrate CH_4 emissions at the onset of Dansgaard–Oeschger events, Science, 328, 1686–1689, https://doi.org/10.1126/science.1187651, 2010.

Bock, M., Schmitt, J., Beck, J., Seth, B., Chappellaz, J., and Fischer, H.: Glacial/interglacial wetland, biomass burning, and geologic methane emissions constrained by dual stable isotopic CH_4 ice core records, P. Natl. Acad. Sci. USA, 114, E5778–E5786, https://doi.org/10.1073/pnas.1613883114, 2017.

Böhm, E., Lippold, J., Gutjahr, M., Frank, M., Blaser, P., Antz, B., Fohlmeister, J., Frank, N., Andersen, M. B., and Deininger, M.: Strong and deep Atlantic meridional overturning circulation during the last glacial cycle, Nature, 517, 73–76, https://doi.org/10.1038/nature14059, 2015.

Broccoli, A. J., Dahl, K. A., and Stouffer, R. J.: Response of the ICTZ to Northern Hemisphere cooling, Geophys. Res. Lett., 33, L01702, https://doi.org/10.1029/2005GL024546, 2006.

Brook, E. J., Sowers, T., and Orchardo, J.: Rapid variations in atmospheric methane concentration during the past 110,000 years, Science, 273, 1087–1091, 1996.

Buizert, C. and Schmittner, A.: Southern Ocean control of glacial AMOC stability and Dansgaard-Oeschger interstadial duration, Paleoceanography, 30, 1595–1612, 2015.

Cheng, H., Edwards, R. L., Wang, Y., Kong, X., Ming, Y., Kelly, M. J., Wang, X., Gallup, C. D., and Liu, W.: A penultimate glacial monsoon record from Hulu Cave and two-phase glacial terminations, Geology, 34, 217–220, https://doi.org/10.1130/G22289.1, 2006.

Cheng, H., Edwards, R. L., Broecker, W. S., Denton, G. H., Kong, X., Wang, Y., Zhang, R., and Wang, X.: Ice age terminations, Science, 326, 248–252, https://doi.org/10.1126/science.1177840, 2009.

Cheng, H., Edwards, R. L., Sinha, A., Spötl, C., Yi, L., Chen, S., Kelly, M., Kathayat, G., Wang, X., Li, X., Kong, X., Wang, Y., Ning, Y., and Zhang, H.: The Asian monsoon over the past 640,000 years and ice age terminations, Nature, 534, 640–646, https://doi.org/10.1038/nature18591, 2016.

Deaney, E. L., Barker, S., and Van de Flierdt, T.: Timing and nature of AMOC recovery across Termination II and magnitude of deglacial CO_2 change, Nat. Commun., 8, 14595, https://doi.org/10.1038/ncomms14595, 2017.

Dlugokencky, E. J., Myers, R. C., Lang, P. M., Masarie, K. A., Crotwell, A. M., Thoning, K. W., Hall, B. D., Elkins, J. W., and Steele, L. P.: Conversion of NOAA atmospheric dry air CH_4 mole fractions to a gravimetrically prepared standard scale, J. Geophys. Res.-Atmos., 110, D18306, https://doi.org/10.1029/2005JD006035, 2005.

Dyonisius, M. N., Petrenko, V. V., Smith, A. M., Hua, Q., Yang, B., Schmitt, J., Beck, J., Seth, B., Bock, M., Hmiel, B., Vimont, I., Menking, J. A., Shackleton, S. A., Baggenstos, D., Bauska, T. K., Rhodes, R. H., Sperlich, P., Beaudette, R., Harth, C., Kalk, M., Brook, E. J., Fischer, H., Severinghaus, J. P., and Weiss, R. F.: Old carbon reservoirs were not important in the deglacial methane budget, Science, 367, 907–910, https://doi.org/10.1126/science.aax0504, 2020.

Enting, I.: On the use of smoothing splines to filter CO_2 data, J. Geophys. Res.-Atmos., 92, 10977–10984, https://doi.org/10.1029/JD092iD09p10977, 1987.

Epifanio, J. A., Brook, E. J., Buizert, C., Edwards, J. S., Sowers, T. A., Kahle, E. C., Severinghaus, J. P., Steig, E. J., Winski, D. A., Osterberg, E. C., Fudge, T. J., Aydin, M., Hood, E., Kalk, M., Kreutz, K. J., Ferris, D. G., and Kennedy, J. A.: The SP19 chronology for the South Pole Ice Core – Part 2: gas chronology, Δage, and smoothing of atmospheric records, Clim. Past, 16, 2431–2444, https://doi.org/10.5194/cp-16-2431-2020, 2020.

Fischer, H., Meissner, K. J., Mix, A. C., Abram, N. J., Austermann, J., Brovkin, V., Capron, E., Colombaroli, D., Daniau, A.-L., Dyez, K. A., Felis, T., Finkelstein, S. A., Jaccard, S. L., McClymont, E. L., Rovere, A., Sutter, J., Wolff, E. W., Affolter, S., Bakker, P., Ballesteros-Ctánovas, J. A., Barbante, C., Caley, T., Carlson, A. E., Churakova (Sidorova), O., Cortese, G., Cumming, B. F., Davis, B. A. S., de Vernal, A., Emile-Geay, J., Fritz, S. C., Gierz, P., Gottschalk, J., Holloway, M. D., Joos, F., Kucera, M., Loutre, M.-F., Lunt, D. J., Marcisz, K., Marlon, J. R., Martinez, P., Masson-Delmotte, V., Nehrbass-Ahles, C., Otto-Bliesner, B. L., Raible, C. C., Risebrobakken, B., Sánchez Goñi, M. F., Saleem Arrigo, J., Sarnthein, M., Sjolte, J., Stocker, T. F., Velasquez Alvárez, P. A., Tinner, W., Valdes, P. J., Vogel, H., Wanner, H., Yan, Q., Yu, Z., Ziegler, M., and Zhou, L.: Palaeoclimate constraints on the impact of 2 °C anthropogenic warming and beyond, Nat. Geosci., 11, 474–485, https://doi.org/10.1038/s41561-018-0146-0, 2018.

Fischer, H., Schmitt, J., Bock, M., Seth, B., Joos, F., Spahni, R., Lienert, S., Battaglia, G., Stocker, B. D., Schilt, A., and Brook, E. J.: N_2O changes from the Last Glacial Maximum to the preindustrial – Part 1: Quantitative reconstruction of terrestrial and marine emissions using N_2O stable isotopes in ice cores, Biogeosciences, 16, 3997–4021, https://doi.org/10.5194/bg-16-3997-2019, 2019.

Flückiger, J., Dällenbach, A., Blunier, T., Stauffer, B., Stocker, T. F., Raynaud, D., and Barnola, J.-M.: Variations in atmospheric N_2O concentration during abrupt climatic changes, Science, 285, 227–230, https://doi.org/10.1126/science.285.5425.227, 1999.

Flückiger, J., Monnin, E., Stauffer, B., Schwander, J., Stocker, T. F., Chappellaz, J., Raynaud, D., and Barnola, J.-M.: High–resolution Holocene N_2O ice core record and its relationship with CH_4 and CO_2, Global Biogeochem. Cy., 16, 10-1–10-8, https://doi.org/10.1029/2001GB001417, 2002.

Flückiger, J., Blunier, T., Stauffer, B., Chappellaz, J., Spahni, R., Kawamura, K., Schwander, J., Stocker, T. F., and Dahl-Jensen, D.: N_2O and CH_4 variations during the last glacial epoch: Insight into global processes, Global Biogeochem. Cy., 18, GB1020, https://doi.org/10.1029/2003GB002122, 2004.

Fourteau, K., Faïn, X., Martinerie, P., Landais, A., Ekaykin, A. A., Lipenkov, V. Ya., and Chappellaz, J.: Analytical constraints on layered gas trapping and smoothing of atmospheric variability in ice under low-accumulation conditions, Clim. Past, 13, 1815–1830, https://doi.org/10.5194/cp-13-1815-2017, 2017.

Fourteau, K., Martinerie, P., Faïn, X., Ekaykin, A. A., Chappellaz, J., and Lipenkov, V.: Estimation of gas record alteration in very low-accumulation ice cores, Clim. Past, 16, 503–522, https://doi.org/10.5194/cp-16-503-2020, 2020.

Grant, K. M., Rohling, E. J., Ramsey, B. C., Cheng, H., Edwards, R. L., Florindo, F., Heslop, D., Marra, F., Roberts, A. P., Tamisiea, M. E., and Williams, F.: Sea–level variability over five glacial cycles, Nat. Commun., 5, 6076, https://doi.org/10.1038/ncomms6076, 2014.

Guillevic, M., Bazin, L., Landais, A., Stowasser, C., Masson-Delmotte, V., Blunier, T., Eynaud, F., Falourd, S., Michel, E., Minster, B., Popp, T., Prié, F., and Vinther, B. M.: Evidence for a three-phase sequence during Heinrich Stadial 4 using a multi-proxy approach based on Greenland ice core records, Clim. Past, 10, 2115–2133, https://doi.org/10.5194/cp-10-2115-2014, 2014.

Hall, B. D., Dutton, G. S., and Elkins, J. W.: The NOAA nitrous oxide standard scale for atmospheric observations, J. Geophys. Res.-Atmos., 112, D09305, https://doi.org/10.1029/2006JD007954, 2007.

Hemming, S. R.: Heinrich events: Massive late Pleistocene detritus layers of the North Atlantic and their global climate imprint, Rev. Geophys., 42, RG1005, https://doi.org/10.1029/2003RG000128, 2004.

Hopcroft, P. O., Valdes, P. J., O'Connor, F. M., Kaplan, J. O., and Beerling, D. J.: Understanding the glacial methane cycle, Nat. Commun., 8, 14383, https://doi.org/10.1038/ncomms14383, 2017.

Joos, F., Battaglia, G., Fischer, H., Jeltsch-Thömmes, A., and Schmitt, J.: Marine N_2O emissions during a Younger Dryas-like event: the role of meridional overturning, tropical thermocline ventilation, and biological productivity, Environ. Res. Lett., 14, 075007, https://doi.org/10.1088/1748-9326/ab2353, 2019.

Joos, F., Spahni, R., Stocker, B. D., Lienert, S., Müller, J., Fischer, H., Schmitt, J., Prentice, I. C., Otto-Bliesner, B., and Liu, Z.: N_2O changes from the Last Glacial Maximum to the preindustrial – Part 2: terrestrial N_2O emissions and carbon–nitrogen cycle interactions, Biogeosciences, 17, 3511–3543, https://doi.org/10.5194/bg-17-3511-2020, 2020.

Jouzel, J., Masson-Delmotte, V., Cattani, O., Dreyfus, G., Falourd, S., Hoffmann, G., Minster, B., Nouet, J., Barnola, J.-M., Chappellaz, J., Fischer, H., Gallet, J. C., Johnsen, S., Leuenberger, M., Loulergue, L., Luethi, D., Oerter, H., Parrenin, F., Raisbeck, G., Raynaud, D., Schilt, A., Schwander, J., Selmo, E., Souchez, R., Spahni, R., Stauffer, B., Steffensen, J. P., Stenni, B., Stocker, T. F., Tison, J. L., Werner, M., and Wolff, E. W.: Orbital and millennial Antarctic climate variability over the past 800,000 years, Science, 317, 793–796, 2007.

Landais, A., Dreyfus, G., Capron, E., Jouzel, J., Masson-Delmotte, V., Roche, D. M., Prié, F., Caillon, N., Chappellaz, J., Leuenberger, M., Lourantou, A., Parrenin, F., Raynaud, D., and Teste, G.: Two-phase change in CO_2, Antarctic temperature and global climate during Termination II, Nat. Geosci., 6, 1062–1065, https://doi.org/10.1038/ngeo1985, 2013.

Levine, J. G., Wolff, E. W., Hopcroft, P. O., and Valdes, P. J.: Controls on the tropospheric oxidizing capacity during an idealized Dansgaard–Oeschger event, and their implications for the rapid rises in atmospheric methane during the last glacial period, Geophys. Res. Lett., 39, L12805, https://doi.org/10.1029/2012GL051866, 2012.

Loulergue, L., Schilt, A., Spahni, R., Masson-Delmotte, V., Blunier, T., Lemieux-Dudon, B., Barnola, J.-M., Raynaud, D., Stocker, T. F., and Chappellaz, J.: Orbital and millennial-scale features of atmospheric CH_4 over the past 800,000 years, Nature, 453, 383–386, https://doi.org/10.1038/nature06950, 2008.

Marcott, S. A., Bauska, T. K., Buizert, C., Steig, E. J., Rosen, J. L., Cuffey, K. M., Fudge, T. J., Severinghaus, J. P., Ahn, J., Kalk, M. L., McConnell, J. R., Sowers, T., Taylor, K. C., White, J. W. C., and Brook, E. J.: Centennial–scale changes in the global carbon cycle during the last deglaciation, Nature, 514, 616–619, https://doi.org/10.1038/nature13799, 2014.

Marino, G., Rohling, E. J., Rodríguez-Sanz, L., Grant, K. M., Heslop, D., Roberts, A. P., Stanford, J. D., and Yu, J.: Bipolar seesaw control on last interglacial sea level, Nature, 522, 197–201, https://doi.org/10.1038/nature14499, 2015.

Melton, J. R., Wania, R., Hodson, E. L., Poulter, B., Ringeval, B., Spahni, R., Bohn, T., Avis, C. A., Beerling, D. J., Chen, G., Eliseev, A. V., Denisov, S. N., Hopcroft, P. O., Lettenmaier, D. P., Riley, W. J., Singarayer, J. S., Subin, Z. M., Tian, H., Zürcher, S., Brovkin, V., van Bodegom, P. M., Kleinen, T., Yu, Z. C., and Kaplan, J. O.: Present state of global wetland extent and wetland methane modelling: conclusions from a model intercomparison project (WETCHIMP), Biogeosciences, 10, 753–788, https://doi.org/10.5194/bg-10-753-2013, 2013.

Myhre, G., Shindell, D., Bréon, F.-M., Collins, W., Fuglestvedt, J., Huang, J., Koch, D., Lamarque, J.-F., Lee, D., Mendoza, B., Nakajima, T., Robock, A., Stephens, G., Takemura, T., and Zhang, H.: Anthropogenic and Natural Radiative Forcing, in: Climate Change 2013: The Physical Science Basis. Contribution of Working Group I to the Fifth Assessment Report of the Intergovernmental Panel on Climate Change, edited by: Stocker, T. F., Qin, D., Plattner, G.-K., Tignor, M., Allen, S. K., Boschung, J., Nauels, A., Xia, Y., Bex, V., and Midgley, P. M., Cambridge University Press, Cambridge, United Kingdom and New York, NY, USA, 2013.

Nehrbass-Ahles, C., Shin, J., Schmitt, J., Bereiter, B., Joos, F., Schilt, A., Schmidely, L., Silva, L., Teste, G., Grilli, R., Chappellaz, J., Hodell, D., Fischer, H., and Stocker, T. F.: Abrupt CO_2 release to the atmosphere under glacial and early interglacial climate conditions, Science, 369, 1000–1005, https://doi.org/10.1126/science.aay8178, 2020.

Nilsson-Kerr, K., Anand, P., Sexton, P. F., Leng, M. J., Misra, S., Clemens, S. C., and Hammond, S. J.: Role of Asian summer monsoon subsystems in the inter-hemispheric progression of deglaciation, Nat. Geosci., 12, 290–295, https://doi.org/10.1038/s41561-019-0319-5, 2019.

Oyabu, I., Kawamura, K., Kitamura, K., Dallmayr, R., Kitamura, A., Sawada, C., Severinghaus, J. P., Beaudette, R., Orsi, A., Sugawara, S., Ishidoya, S., Dahl-Jensen, D., Goto-Azuma, K., Aoki, S., and Nakazawa, T.: New technique for high-precision, simultaneous measurements of CH_4, N_2O and CO_2 concentrations; isotopic and elemental ratios of N_2, O_2 and Ar; and total air content in ice cores by wet extraction, Atmos. Meas. Tech., 13, 6703–6731, https://doi.org/10.5194/amt-13-6703-2020, 2020.

Prather, M. J., Hsu, J., DeLuca, N. M., Jackman, C. H., Oman, L. D., Douglass, A. R., Fleming, E. L., Strahan, S. E., Steenrod, S. D., Søvde, O. A., Isaksen, I. S. A., Froidevaux, P., and Funke, B.: Measuring and modeling the lifetime of nitrous oxide including its variability, J. Geophys. Res.-Atmos., 120, 5693–5705, https://doi.org/10.1002/2015JD023267, 2015.

Rhodes, R. H., Brook, E. J., Chiang, J. C. H., Blunier, T., Maselli, O. J., McConnell, J. R., Romanini, D., and Severinghaus, J. P.: Enhanced tropical methane production in response to iceberg discharge in the North Atlantic, Science, 348, 1016–1019, https://doi.org/10.1126/science.1262005, 2015.

Rhodes, R. H., Faïn, X., Brook, E. J., McConnell, J. R., Maselli, O. J., Sigl, M., Edwards, J., Buizert, C., Blunier, T., Chappellaz, J., and Freitag, J.: Local artifacts in ice core methane records caused by layered bubble trapping and in situ production: a multi-site investigation, Clim. Past, 12, 1061–1077, https://doi.org/10.5194/cp-12-1061-2016, 2016.

Rosen, J. L., Brook, E. J., Severinghaus, J. P., Blunier, T., Mitchell, L. E., Lee, J. E., Edwards, J. S., and Gkinis, V.: An ice core record of near-synchronous global climate changes at the Bølling transition, Nat. Geosci., 7, 459–463, https://doi.org/10.1038/ngeo2147, 2014.

Schilt, A., Baumgartner, M., Blunier, T., Schwander, J., Spahni, R., Fischer, H., and Stocker, T. F.: Glacial–interglacial and

millennial-scale variations in the atmospheric nitrous oxide concentration during the last 800,000 years, Quaternary Sci. Rev., 29, 182–192, https://doi.org/10.1016/j.quascirev.2009.03.011, 2010a.

Schilt, A., Baumgartner, M., Schwander, J., Buiron, D., Capron, E., Chappellaz, J., Loulergue, L., Schüpbach, S., Spahni, R., Fischer, H., and Stocker, T. F.: Atmospheric nitrous oxide during the last 140,000 years, Earth Planet. Sc. Lett., 300, 33–43, https://doi.org/10.1016/j.epsl.2010.09.027, 2010b.

Schilt, A., Baumgartner, M., Eicher, O., Chappellaz, J., Schwander, J., Fischer, H., and Stocker, T. F.: The response of atmospheric nitrous oxide to climate variations during the last glacial period, Geophys. Res. Lett., 40, 1888–1893, https://doi.org/10.1002/grl.50380, 2013.

Schilt, A., Brook, E. J., Bauska, T. K., Baggenstos, D., Fischer, H., Joos, F., Petrenko, V. V., Schaefer, H., Schmitt, J., Severinghaus, J. P., Spahni, R., and Stocker, T. F.: Isotopic constraints on marine and terrestrial N_2O emissions during the last deglaciation, Nature, 516, 234–237, https://doi.org/10.1038/nature13971, 2014.

Schmidely, L., Nehrbass-Ahles, C., Schmitt, J., Han, J., Silva, L., Shin, J., Joos, F., Chappellaz, J., Fischer, H., and Stocker, T. F.: CH4 and N2O fluctuations during the penultimate deglaciation, Climate of the Past Discussions, NOAA [data set], available at: https://www.ncdc.noaa.gov/paleo/study/33673 (last access: 29 July 2021), 2020.

Schmitt, J., Seth, B., Bock, M., and Fischer, H.: Online technique for isotope and mixing ratios of CH_4, N_2O, Xe and mixing ratios of organic trace gases on a single ice core sample, Atmos. Meas. Tech., 7, 2645–2665, https://doi.org/10.5194/amt-7-2645-2014, 2014.

Schmittner, A. and Galbraith, E. D.: Glacial greenhouse-gas fluctuations controlled by ocean circulation changes, Nature, 456, 373–376, https://doi.org/10.1038/nature07531, 2008.

Skinner, L. C. and Shackleton, N. J.: Deconstructing Terminations I and II: revisiting the glacioeustatic paradigm based on deep-water temperature estimates, Quaternary Sci. Rev., 25, 3312–3321, https://doi.org/10.1016/j.quascirev.2006.07.005, 2006.

Sowers, T.: N_2O record spanning the penultimate deglaciation from the Vostok ice core, J. Geophys. Res.-Atmos., 106, 31903–31914, https://doi.org/10.1126/science.1121235, 2001.

Spahni, R., Chappellaz, J., Stocker, T. F., Loulergue, L., Hausammann, G., Kawamura, K., Flückiger, J., Schwander, J., Raynaud, D., and Masson-Delmotte, V.: Atmospheric methane and nitrous oxide of the late Pleistocene from Antarctic ice cores, Science, 310, 1317–1321, https://doi.org/10.1126/science.1120132, 2005.

Van Groenigen, K. J., Osenberg, C. W., and Hungate, B. A.: Increased soil emissions of potent greenhouse gases under increased atmospheric CO_2, Nature, 475, 214–216, https://doi.org/10.1038/nature10176, 2011.

Veres, D., Bazin, L., Landais, A., Toyé Mahamadou Kele, H., Lemieux-Dudon, B., Parrenin, F., Martinerie, P., Blayo, E., Blunier, T., Capron, E., Chappellaz, J., Rasmussen, S. O., Severi, M., Svensson, A., Vinther, B., and Wolff, E. W.: The Antarctic ice core chronology (AICC2012): an optimized multi-parameter and multi-site dating approach for the last 120 thousand years, Clim. Past, 9, 1733–1748, https://doi.org/10.5194/cp-9-1733-2013, 2013.

Chapter 6

Outlook

6.1 Improving the CIM

Given the impending development of a novel extraction head, it would perhaps be unwise to implement hardware/software changes to the CIM and instead adopt novel ideas when building the new system. Nevertheless, there is still scope to improve some auxiliary procedures or investigate ways to make the CIM more reliable throughout long measurement days. These could lead to higher reproducibility through less variability of measurement conditions such as temperature, vacuum quality, loading times, among many other parameters. The following list contains suggestions for improvement ranked by priority.

Medium prority:

- Evaluate knife performance after sharpening with whetstones of higher grit (3000 and 8000)
- Find optimal cooling settings for the LAUDA in order to avoid temperature overshoot during the first measurements
- Enforce a final weight range on gas-free ice samples and use a more precise scale
- Evaluate if bigger or better designed cold traps could lead to less ice build-up inside the CIM
- Investigate if raising the purge gas pressure from 2 to 3 (or 4) bar could lead to less ice build-up inside the CIM and what is the impact on vacuum conditions before extraction
- Find an optimal disposition of the LN spitters for a homogeneous cooling of the CIM box

Low priority:

- Standardize the set of cleaning brushes for ice removal
- Evaluate if bigger or better designed cold traps could lead to less ice build-up inside the CIM
- Evaluate if the CIM insulating XPS pannel disposition can be improved for better temperature control
- Investigate optimal sequence of measurements between ice core sample and gas-free ice samples in order to account for variable conditions throughout a day

6.2 Future measurement campaigns

6.2.1 EDC MIS 7/8

The CO_2 ice core record in the time interval 329–190 ka, approximately corresponding to MIS 7–9, is currently composed solely by Vostok measurements (see also Section 1.3.1). The relative low accuracy and low resolution of the Vostok dataset (compared to current standards) may be hiding important features (Shin et al., 2020; Nehrbass-Ahles et al., 2020). In this sense, colleagues at the University of Grenoble are carrying out CO_2 measurements with EDC ice in the period 260–190 ka, i.e. MIS 7–8. Similarly, the University of Bern has an ongoing campaign for the period 329–250 ka, i.e. MIS 8–9, with roughly 10% of the samples already measured (Fig. 6.1). It is naturally too early to interpret the new record, but there is already the indication of a novel peak at around 285 ka that could be replicating a feature in the deuterium record.

6.2.2 EDML MIS 4/5

The study by Bereiter et al. (2012) brought another CO_2 record for the time period 115–38 ka. In terms of available ice core derived CO_2 records, it remains the only alternative reconstruction to the Vostok ice core between 105–88 ka. It would be interesting to extend our EDC MIS 5 dataset until 88 ka as well, in order to have a third available reconstruction. The motivation would not be to increase resolution, since the EDML record is already highly resolved. Furthermore, the EDML record seems to evidence that the main mode of CO_2 variability is on the millennial-scales, rendering the effort to capture submillennial resolution perhaps unnecessary. However, regarding possible offsets between different ice cores, it could be useful to extend the EDC record and compare the two after glacial inception. This is motivated by an offset between EDML and EDC during the MIS 5e plateau of ca. 5 ppm (Nehrbass-Ahles (2017); Bereiter (2012); unpublished data).

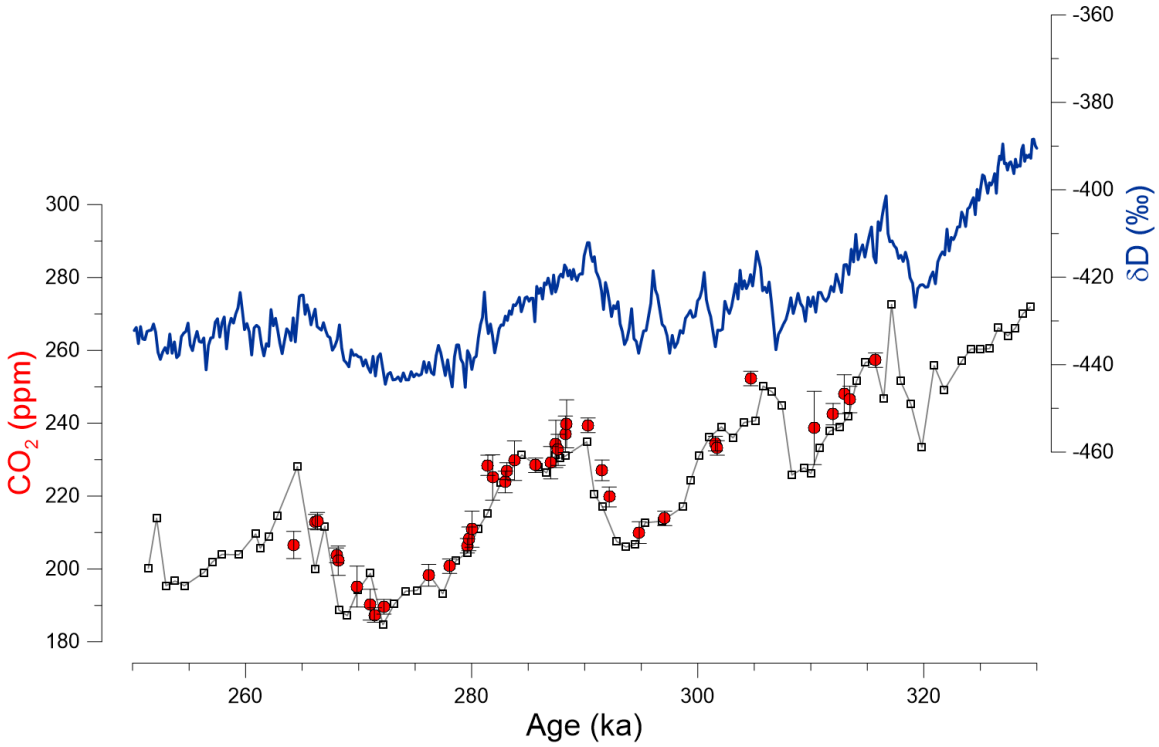

Figure 6.1: Ongoing measurements of EDC CO_2 for MIS 8. Blue: EDC deuterium (Jouzel et al., 2007); red: EDC CO_2 (this study); grey: Vostok CO_2 (Petit et al., 1999). All records on the AICC12 age scale.

A big impediment to this measurement campaign is EDC ice quality. It is estimated that the brittle ice zone of the EDC ice core ends at depths around 1200 (81 ka; AICC12) (EPICA Community Members, 2004), which is also coincident with the end of the bubble to clathrate transition zone (BCTZ). Therefore, issues such as contamination via cracks, fractionation due to layering effects (Lüthi et al. (2010); Section 3.3.2) and extraction efficiency issues between bubbles and clathrates could all play a big role in the final success of the reconstruction. These should all be weighed out carefully before proceeding.

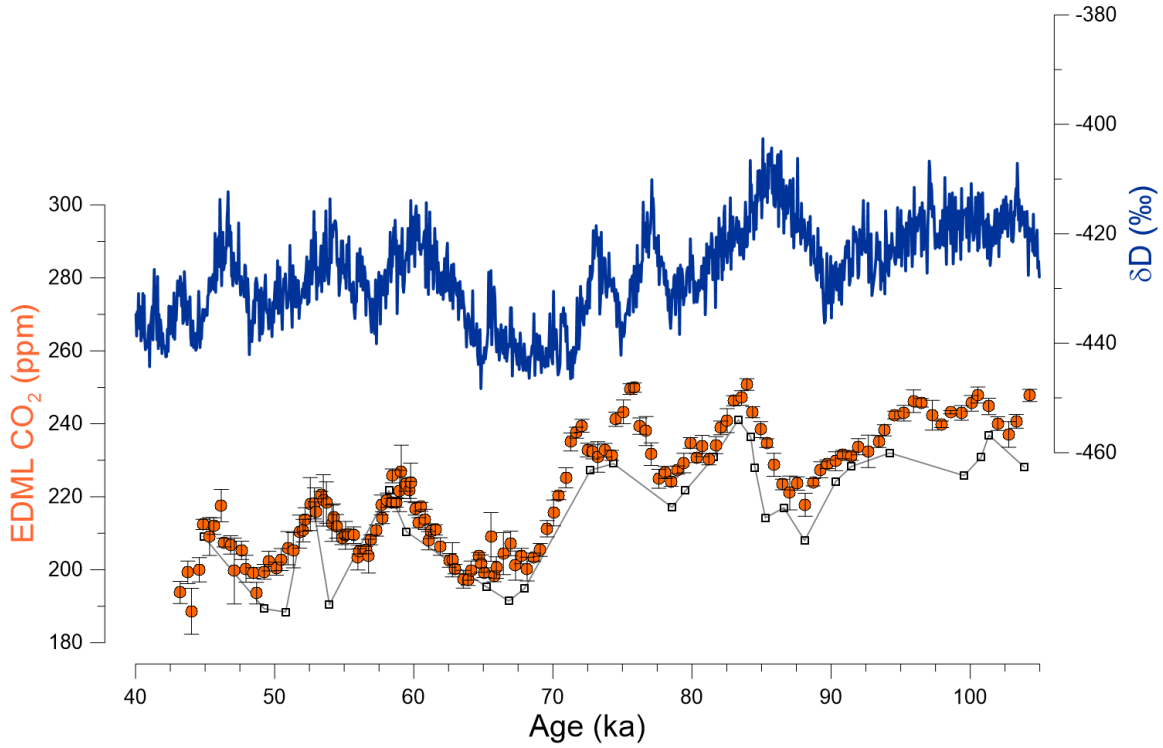

Figure 6.2: CO_2 and Antarctic temperature evolution for the MIS3–5 period. Blue: EDC deuterium (Jouzel et al., 2007); orange: EDML CO_2 (Bereiter et al., 2012); grey: Vostok CO_2 (Petit et al., 1999). All records on the AICC12 age scale.

Appendix

A.1 Long-term perspectives on anthropogenic climate change

Lucas Silva and Thomas F. Stocker

The work presented in this chapter integrates the Working Group I contribution to the Sixth Assessment Report (AR6) of the Intergovernmental Panel on Climate Change (IPCC). We were invited as Contributing Authors to write a paleo climate perspective on ongoing climate change to be included in "Section 1.2.1.2: Long-term perspectives on anthropogenic climate change" as part of "Chapter 1: Framing, context, methods". As the layout of AR6 did not include a dedicated chapter on paleoclimate, as it happened in AR5 and other previous Assessment Reports, the amount of information we could include was limited to approximately two pages of text (T. F. Stocker) and one figure (L. Silva; see Fig. A.1). As a framing chapter, Chapter 1 also had to refrain from assessment statements and exclusively refer to assessments in other chapters. These constraints made it difficult to construct a coherent and concise narrative, since much of our discussion was dependent on the discussion present in other chapters, who were being developed simultaneously.

The revision process of AR6 implied three instances of review. For transparency purposes, each Expert review is made public and every comment needs to be addressed:

- **First Order Draft** Expert review (135 comments)
- **Second Order Draft** Expert review (224 comments)
- **Final Governmental Draft** Governmental review (35 comments)

During the preparation of each draft, the paleo figure went on average through 15 different versions and internal revision each time prior to submission for expert/governmental review. Work on the first draft started in February of 2019, while the last draft was ready by March of 2021. These numbers illustrate the thorough peer-review process that is required during the preparation of an Assessment Report, even if just considering a two-page subsection of an introductory chapter.

Figure 1.5

Figure A.1 is the equivalent of Figure 1.5 in Chapter 1 of AR6. The purpose of the figure was to compare the anthropogenic impact on major climate parameters such as

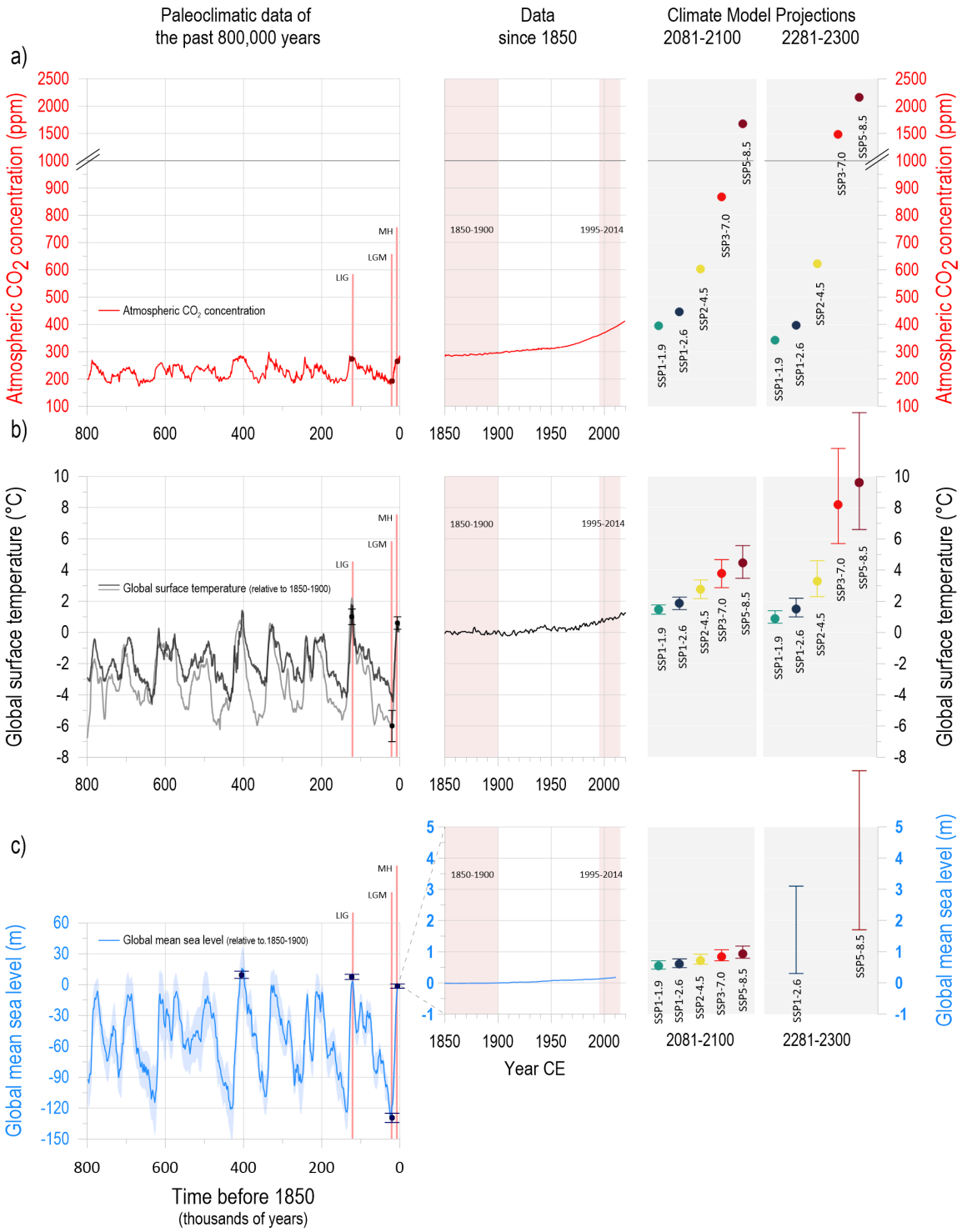

Figure A.1: (Caption next page.)

Figure A.1: (Previous page.) **Long-term context of anthropogenic climate change** based on selected paleoclimatic reconstructions over the past 800,000 years for three key indicators: atmospheric CO_2 concentrations, Global Mean Surface Temperature (GMST), and Global Mean Sea Level (GMSL). a) Measurements of CO_2 in air enclosed in Antarctic ice cores (Lüthi et al., 2008; Bereiter et al., 2015 [a compilation]; uncertainty ±1.3ppm; see Chapter 2, Section 2.2.3 and Chapter 5, Section 5.1.2 for an assessment) and direct air measurements (Tans and Keeling, 2020; uncertainty ±0.12 ppm). Projected CO_2 concentrations for five Shared Socioeconomic Pathways (SSP) scenarios are indicated by dots on the right-hand side panels of the figure (grey background) (Meinshausen et al., 2020; SSPs are described in Section 1.6). b) Reconstruction of GMST from marine paleoclimate proxies (light grey: Snyder (2016); dark grey: Hansen et al. (2013); see Chapter 2, Section 2.3.1 for an assessment). Observed and reconstructed temperature changes since 1850 are the AR6 assessed mean (referenced to 1850–1900; Box TS.3; 2.3.1.1); dots/whiskers on the right-hand side panels of the figure (grey background) indicate the projected mean and ranges of warming derived from Coupled Model Intercomparison Project Phase 6 (CMIP6) SSP-based (2081–2100) and Model for the Assessment of Greenhouse Gas Induced Climate Change (MAGICC7) (2300) simulations (Chapter 4, Tables 4.5 and 4.9). c) Sea level changes reconstructed from a stack of oxygen isotope measurements on seven ocean sediment cores (Spratt and Lisiecki, 2016; see Chapter 2, Section 2.3.3.3 and Chapter 9, Section 9.6.2 for an assessment). The sea level record from 1850 to 1900 is from Kopp et al. (2016), while the 20th century record is an updated ensemble estimate of GMSL change (Palmer et al., 2021; see also Chapter 2, Section 2.3.3.3 and Chapter 9, Section 9.6.1.1). Dots/whiskers on the right-hand side panels of the figure (grey background) indicate the projected median and ranges derived from SSP-based simulations (2081–2100: Chapter 9, Table 9.9; 2300: Chapter 9, Section 9.6.3.5). Best estimates (dots) and uncertainties (whiskers) as assessed by Chapter 2 are included in the left and middle panels for each of the three indicators and selected paleo48 reference periods used in this report (CO_2: Chapter 2, Table 2.1; GMST: Chapter 2, Section 2.3.1.1 and Cross-Chapter Box 2.3, Table 1 in Chapter 2; GMSL: Chapter 2, Section 2.3.3.3 and Chapter 9, Section 9.6.2. See also Cross-Chapter Box 2.1 in Chapter 2). Selected paleo-reference periods: LIG – Last Interglacial; LGM – Last Glacial Maximum; MH – mid-Holocene (Cross-Chapter Box 2.1, Table 1 in Chapter 2). The non-labelled best estimate in panel c) corresponds to the sea level high-stand during Marine Isotope Stage 11, about 410,000 years ago (see Chapter 9, Section 9.6.2). Further details on data sources and processing are available in the chapter data table (Table 1.SM.1)

CO_2, global temperature and mean sea level with paleo reconstructions and climate model projections. For CO_2, it is clear that we are currently outside the range of any other CO_2 level of past interglacials. This is graphically obvious even if the reader does not pay too much attention to the changes in the age scales. For temperature and sea level, however, it is much more graphically challenging to evidence the unusualness of the anthropogenic impact. This is because it is the rates of change that are particularly alarming, rather than absolute values. The concept of rate of change is nevertheless harder to grasp for the public and should be avoided. The case of global mean sea level is even more difficult because ongoing rise rates on the order of a few centimetres per year seem both intrinsically harmless and also minute when compared to a few past interglacials when mean sea level were several meters higher than today.

Figure TS.1

For the drafting of the Technical Summary we were asked to produce a figure presenting CO_2 and global temperature for the past 60 million years and projections until 2300 (Fig. A.2). The logic behind this figure was now to compare future Shared Socioeconomic Pathways (SSPs) scenarios with climates encountered in the deep geological past. The challenges again involved multiple axis with different scales, with the added difficulty of also having to link the different maps to the plots and manage space constrains. For the CO_2 plot, a big concession was the usage of a logarithmic scale for the y-axis in order to keep the figure dimensions acceptable. Logarithmic

scales can easily be misinterpreted or altogether missed and taken to be linear scales instead. However, it is worth keeping in mind that the IPCC Assessment Reports are not intended as textbook material but rather to serve as the basis for the implementation of climate policies and for international climate change negotiations. Other hurdles in presenting reconstruction that cover such an extended period are the lack of universal proxies, growing uncertainty for the oldest sections of the records, and inevitable gaps in resolution. We adopted compilations for both CO_2 and temperature in the period 60–0.8 Ma and in the case of CO_2 the scarcity of records led us to also plot individual data points. The poor resolution, however, may wrongly induce a distracted reader that the period 10–0.8 Ma experienced a smooth progression of atmospheric CO_2 concentrations.

Perhaps due to the added importance of being the first figure of the Technical Summary, Figure TS.1 shape-shifted a significant amount of times during its development. For the sake of highlighting the unavoidable back and forth progression of developing such a plot, Figure A.3 depicts a selection of several versions of Figure TS.1 prior to its final state.

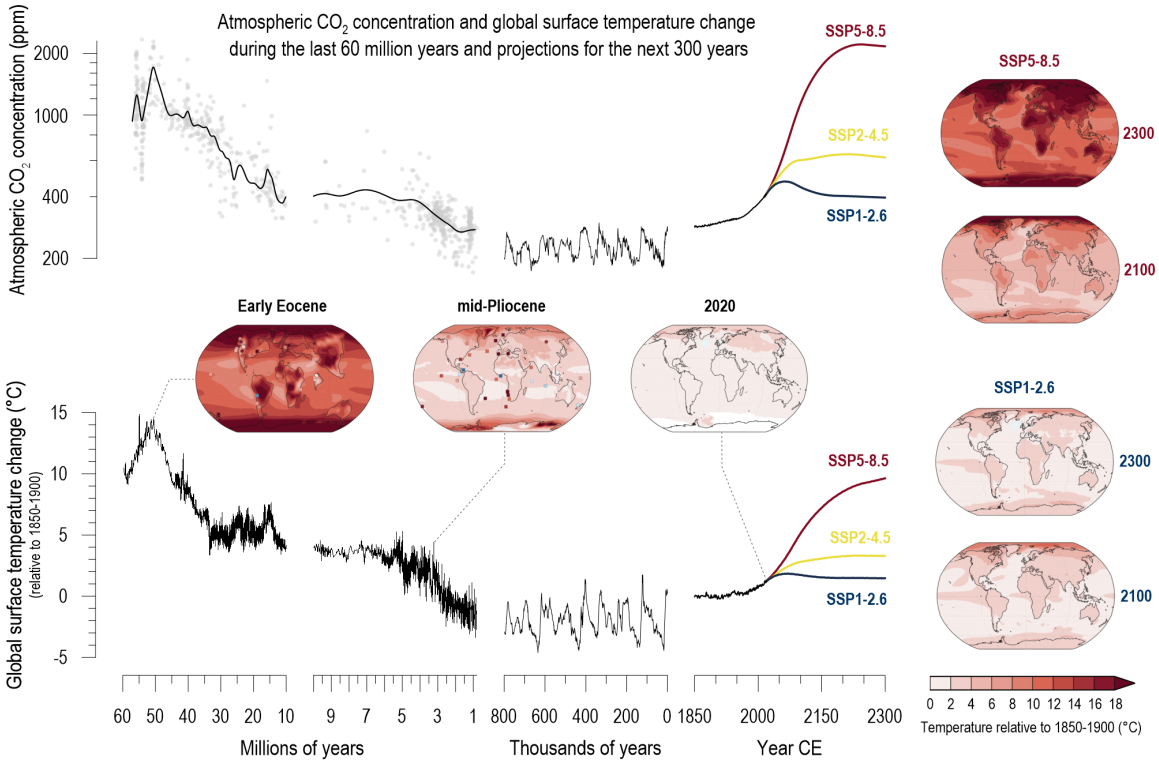

Figure A.2: **Changes in atmospheric CO2 and global surface temperature (relative to 1850-1900) from the deep past to the next 300 years.** *The intent is to show that CO2 and temperature covary, both in the past and into the future, and that projected CO2 and temperatures are similar to those only from many millions of years ago.* CO2 concentrations from millions of years ago are reconstructed from multiple proxy records (grey dots are data from 2.2.3.1, Figure 2.3 shown with cubic-spline fit). CO2 levels for the last 800,000 years through the mid-20th century are from air trapped in polar ice; recent values are from direct air measurements (Figure TS.9). 1.2.1.2, 2.2.3, Figures 1.5, 2.4, 2.5 Global surface temperature prior to 1850 is estimated from marine oxygen isotopes, one of multiple sources of evidence used to assess paleo temperatures in this report. 2.3.1.1.1, Cross-Chapter Box 2.1, Figure 1 Temperature of the past 170 years is the AR6 assessed mean (Cross-Section Box TS.1). 2.3.1.1 CO2 levels and global surface temperature change for the future are shown for three SSP scenarios (TS.1.3) through 2300 CE, using Earth System Model emulators calibrated to the assessed global surface temperatures. 4.7.1, Cross-Chapter Box 7.1 Their smooth trajectories do not account for inter8 annual to inter-decadal variability, including transient response to potential volcanic eruptions. Cross-Chapter Box 4.1 Global maps for two paleo reference periods are based on CMIP6 and pre10 CMIP6 multi-model means, with site-level proxy data for comparison (squares and circles are marine and terrestrial, respectively) (Box TS.2). Cross-Chapter Box 2.1, Figure 7.13 The map for 2020 is an estimate of the total observed warming since 1850-1900. Figure 1.14 Global maps at right show two SSP scenarios at 2100 (2081-2100) 4.5.1 and at 2300 (2281-2300; map from CMIP6 models; temperature assessed in 4.7.1). A brief account of the major climate forcings associated with past global temperature changes is in Cross-Chapter Box 2.1.

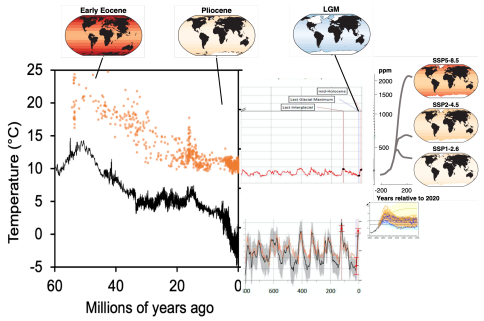

a) Early draft

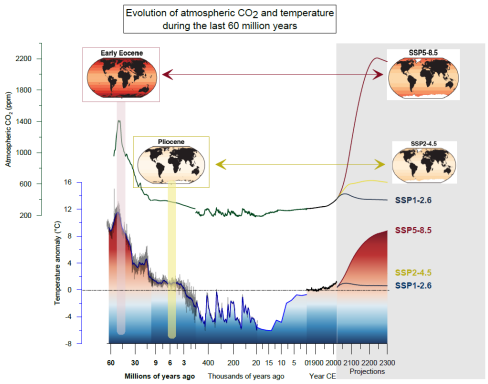

b) Version 2

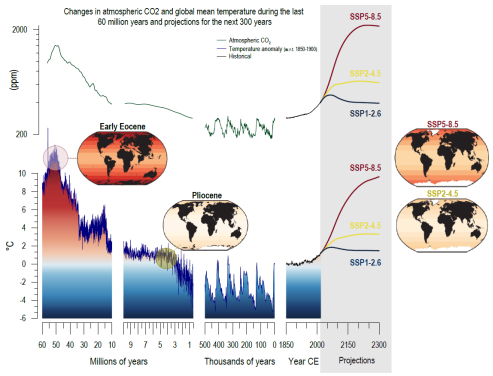

c) Version 4

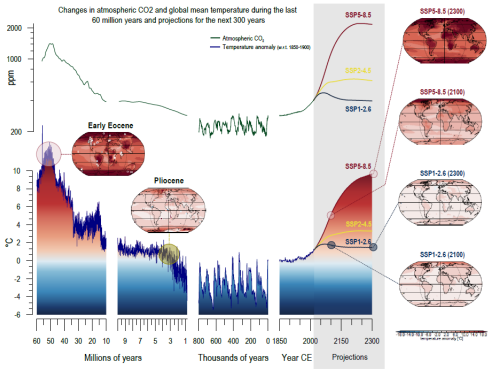

d) Version 8

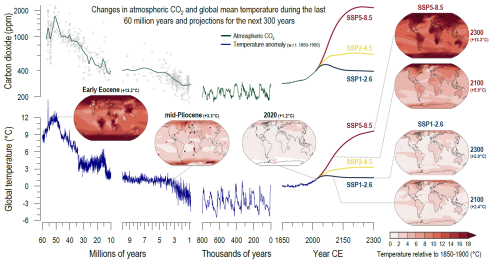

e) Version 14

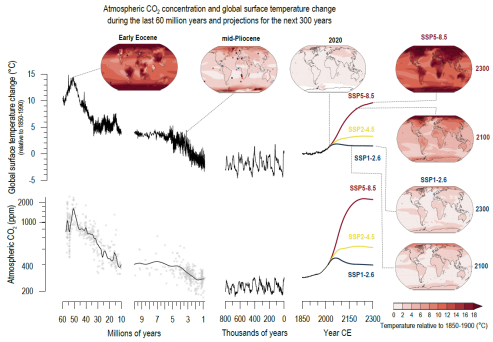

f) Version 18

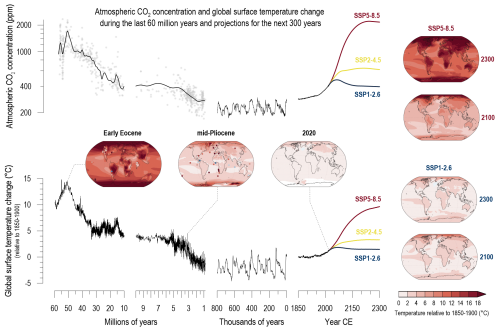

g) Version 22 (final)

Figure A.3: Evolution of Figure TS.1 through multiple versions.

A.2 Measurement protocols

The following section is an update on the measurement protocols introduced in Nehrbass-Ahles (2017).

A.2.1 Preparing a measurement campaign

A measurement campaign is an extended period of time where the full focus is on measuring as much ice as possible in an efficient way. This reduces variability among the samples as the conditions are kept mostly the same, apart from a few inevitable maintenance procedures. Plan ahead and **be realistic instead of optimistic** when it comes to how many days you will need. Consider assigning extra time to remeasurements.

1. Collect in an ice core box all the samples to be measured. Store it in an easy-to-access location on the A47 walk-in freezer.

2. Decide how many samples will be measured per day:

   (a) 16 samples: 09h-17h job. No big stress, no knocking sounds and enough time for the CIM to recover overnight.

   (b) 20 samples: Will work smoothly if it's the first or second day of measurements. Otherwise expect ice build up and poor vacuum conditions towards the end of the day.

   (c) 24 samples: start as early as possible in the day. Expect difficult working conditions from mid to end of the day, degrading vacuum and difficult cleaning procedures. There are increased chances of lost samples due to human mistakes. There won't be much time for the CIM to remove the ice build-up overnight, so this will have implications on the following measurement day. Avoid such long days unless you are in PhD panic mode (CNA, pers. comm.).

3. Pick the chosen amount of samples per day and bag them in separate plastic bags, labeled "Day 1", "Day 2", etc.. This will save a lot of time.

4. Decide how many days per week will be measurement days:

   (a) 3 days: Ideally measuring Tue-Thu; on Monday the CIM is cooled down, on Friday the CIM is thawed. It dries over the weekend.

(b) 4 days: Mon-Thu. Set the LAUDA chiller to start cooling down the CIM on Sunday. Will work smoothly if it's the first or second day of measurements. Otherwise expect ice build up and poor vacuum conditions towards the end of the day.

(c) 5 days: Measuring Mon-Fri, requires coming to the lab on Saturday for shutdown. While this could be done for a single week, it is not sustainable for several weeks in a row.

5. **Two weeks before the measurements:**

(a) Turn on the LI-COR and load its configuration file, together with the Peltier and its fan.

(b) Ensure that there are 4 full bottles of N_2 available inside the gas cabinet.

(c) Ensure enough CF copper gaskets available (30 per day) (see Section 2.3.1.7).

(d) Ensure enough VCR gaskets available (3-4 per day) (see Section 2.3.1.7).

(e) Ensure enough VCR plugs (1-2 per week).

6. **Two days before the measurements:**

(a) Consider resharpening the knife (see Section A.3.3).

(b) Consider refilling the standards gas tanks (see Section A.3.1).

(c) Consider leaking the CIM thoroughly.

(d) Consider retightening the gold gaskets on the upper and lower CF flanges with 8 N.m of torque.

(e) Set the portable freezer to $-22\,^{\circ}\mathrm{C}$ two days before, filled with eutectics.

(f) Consider refilling the 150 liter LN tank.

(g) Consider refilling the LAUDA with ethanol (95% ethanol and 5% isopropanol).

7. **One day before the measurements:**

(a) Switch on the PC.

(b) Program the LAUDA chiller for tomorrow's measurements. Let it reach -34°C at around 03:00 AM. By 08:00 AM the CIM will be roughly at $-22\,^{\circ}\mathrm{C}$.

(c) Check the ethanol by-pass valves beneath the rack on the right-hand side for leaks; set to 'CIM'.

(d) Put all necessary dewars in place.

(e) Close the CIM box carefully.

(f) Switch on the CIM cooling fan, **otherwise the CIM will not cool down**.

(g) Set the portable freezer to −22 °C two days before, filled with eutectics.

(h) Consider refilling the 150 liter LN tank.

(i) Consider refilling the LAUDA with ethanol (95% ethanol, 5% isopropanol).

(j) Make sure the cordless screwdriver battery is fully charged.

A.2.2 Daily start up

The daily start up is a 15 minute procedure before preparing the samples. The most important part is to start cooling down the cold traps, which takes a considerable amount time (0.5–1 hour). If timed correctly, it is possible to use this time to prepare the samples. When the cold trap K2 is at −85 °C, the CIM is ready to perform measurements.

1. Check temperature of CIM box (it should be between −22 °C and −24 °C; if not, check the LAUDA and the CIM fans)
2. Switch on:
   - ACP
   - Bellow
   - Magnetic bearings
   - CIM box cooling (banana plugs for the LN spitters)
   - Speakers
3. Fill all dewars with LN except the one on top of the CIM. Ensure that the K2 setpoint is set to −85 °C
4. Set N_2 regulator to 2 bar overpressure
5. Start up and run 'Steuerung2.vi' and 'Manual Valve Control.vi'
6. Check and adjust LabVIEW settings as appropriate:
   - Set prevacuum pressure threshold to 0.3 mbar
   - Check speed settings (default: 1400 rpm for 15 s; 1700 rpm for 70 s)
   - Check standard gas selection and concentrations values
   - Increase 'Starting Meas. No.' by 1
   - Verify that standard settings are in place and change valve control to computer mode (backside of the value control box)

- From now on using the Manual Valve Control.vi, open V10 and V14
- Initialize 5–8 'Auto Standardgas Measurements', dubbed SIO-measurements
- Load cooler (LittlePlaymate) with eutectics and take sample plastic cups

7. Prepare ice samples in the A54 cold room (see Section A.2.6 below)
8. Store samples including the eutectics in the portable freezer at −22 °C
9. Refill/fill all dewars, except the dewar inside the CIM box
10. After SIO-measurements are completed and K2 reaches −85 °C, let's enter the measurement loop:
    (a) Manually fill CIM with a standard gas:
        i. Close V4, V3, V2, V10, V14, V15, V13
        ii. Open V8 for 3 s; close again
        iii. Open V4, V12, V14 – wait for 10 s – close V14
        iv. Set V22 to 'blue'
        v. Open V13, V10 – wait until pressure dropped – switch V22 to 'red'
        vi. Wait for approximately 5 min (evacuation of supply tubing)
        vii. Close V12
        viii. Open V2
    (b) Enter weight of the sample (0 g)
    (c) Select 'Einkristall' in the drop down menu
    (d) Fix the pressure to e.g. 7 mbar
    (e) Select 'Standardgas II' (i.e. STD2) as the sample gas and enter calibrated mole fraction
    (f) Note in the lab book the type and number of standard gas measurements and chosen settings for the upcoming ice measurements
    (g) Calculate exact depth levels of all polar ice samples
11. Start 'Ice measurement' and prepare to load the CIM with the first ice sample
12. Approximately 30 s later, the acoustical alarm goes off. Click on the 'STOP Sound' button. A pop-up will appear, but don't click on it.
13. Let the rotor turn (temperature equilibration) for approximately 30 s; do not open the lower VCR outlet during this time
14. Press 'Enter' once. A second pop-up will appear, but don't click on it.

15. Loading the first EK sample:
    (a) Remove upper XPS lid
    (b) Use cordless screwdriver (drill mode) to unscrew the bolts of the upper CF flange
    (c) Hold the stainless flange down to prevent it from moving up and down (N_2 is pushing from below)
    (d) Screw in the flange removal tool and quickly put the flange in the metal dewar (CO_2-free and cold intermediate storage)
    (e) Remove old copper gasket
    (f) Load one of the EK samples (drop it gently)
    (g) Take a new copper gasket and place it on the knife edge of the flange
    (h) Quickly put the upper part of the flange back into the recess taking care not to damage the knife edge
    (i) Remove the flange removal tool and support the flange with one finger
    (j) Screw in the bolts halfway with the cordless screwdriver (screw mode; set to lowest possible torque) to center the flange
    (k) Finger-tighten the bolts with the cordless screwdriver (screw mode; set to lowest possible torque)
    (l) Use the torque wrench (set to 6 N.m) to systematically cross-tighten the bolts
    (m) Mount upper XPS lid
    (n) Confirm the proper mounting of the upper flange (press 'Enter')
    (o) Enter weight of the sample
    (p) Select 'Einkristall' in the drop down menu
    (q) Fix pressure to 5 – 9 mbar (should be similar to the expected pressure of the polar ice samples)
    (r) Select 'Standardgas I' (i.e. STD1) as new sample gas and enter calibrated mole fraction
    (s) Double-check whether the calibration gas settings are correct (default: 'Standardgas I', calibrated mole fraction, 'Different Pressure' set to 'false')
    (t) Note the measurement number, type of measurement, and comments for these two measurements in lab book
    (u) Refill all dewars, including the one inside the CIM box (use the plastic funnel for this); the big glass dewar just before the prevacuum pump need to be filled only twice a day

(v) Set Jumo iTRON16 controller (taped to the wooden box) to $-27\,^{\circ}\mathrm{C}$

A.2.3 Ice measurement routine

1. Loading a new sample:

   (a) Click on the 'STOP Sound' button when the acoustical alarm goes off

   (b) Put the metal dewar on the lower shelf space

   (c) Remove lower XPS cover

   (d) Open the VCR outlet using the two big wrenches; do not apply any torque to the main body of the extraction unit

   (e) Give the VCR plug a quick swipe with the plastic brush and store it inside the metal dewar with LN

   (f) Clean ice powder out of the stainless funnel with the plastic brushes, taking care not to scratch the sealing lip

   (g) Holding the VCR plug (replace if necessary8), give it a quick knock with the backside of the brush to remove remaining ice powder and reseal (first finger-tight, then another 1/8 of a turn with the wrenches; do not transmit any torque on to the main body)

   (h) Mount lower XPS lid

   (i) Confirm the removal of the old sample (press 'Enter'). For a well-trained operator, the LabVIEW timer should now read between 13'20" and 13'20"

   (j) Put the dewar on top of the CIM box

   (k) Remove upper XPS lid

   (l) Use cordless screwdriver (drill mode) to unscrew the upper CF flange

   (m) Prevent the stainless flange from oscillating vertically (N_2 is pushing from below)

   (n) Screw in the flange removal tool and quickly put the flange in the metal dewar

   (o) Use the vacuum cleaner to remove ice powder inside the rotor sample holder and the used copper gasket

   (p) Load new sample. Drop it gently

   (q) Take a new copper gasket and place it on the knife edge of the flange

   (r) Quickly put the upper part of the flange back into the recess, taking care not to damage the knife edge

   (s) Remove the flange removal tool and support the flange with one finger

(t) Screw in the bolts halfway with the cordless screwdriver (screw mode set to lowestpossible torque) to center the flange

(u) Finger-tighten the bolts with the cordless screwdriver (screw mode set to lowest possible torque)

(v) Use the torque wrench (set to 6 N.m) to systematically cross-tighten the bolts

(w) Mount upper XPS lid

(x) Confirm the proper mounting of the upper flange (press 'Enter'). For a well-trained operator, the LabVIEW timer should now read between 12'00" and 11'45"

2. Select the type of ice in the drop down menu
3. Enter weight, depth, bin and bag number into the 'Steuerung2.vi' interface
4. In case of an EK sample: fix pressure to the to be expected mean polar ice sample pressure, i.e. 5–9 mbar
5. In case of polar ice: set pressure to 'max'
6. Note measurement number, type of measurement, orientation, time of closure and comments in lab book
7. Refill all dewars
8. Check 'Turbopressure before hobeln' (this should be $<1 \times 10^{-6}$ mbar; otherwise, there is (or was) a leak)
9. If necessary: clean the used VCR® plug and replace the nickel gasket; put on the protective cap and store in lab freezer
10. Listen carefully to the sound of the rotor during extraction and note anything out of the ordinary (e.g. knocking noises due to a dynamic unbalance)
11. Continue measuring? Start over at 1a
12. Last sample loaded? Walk through the above steps again (starting at 1a), but skip steps 1p, 3, and 7, and continue with section A.2.4

A.2.4 Daily shutdown

The daily shutdown takes about 45 minutes to 1 hour. Ideally, it could take longer, to really allow the water inside the cold traps to first be transferred to the big cold trap above the ACP and away from the CIM, before opening the CIM to evacuation. In practice, there is no time to do that.

1. Deactivate the following modules in the ‘Steuerung2.vi’ interface (do not terminate the vi!):
   (a) ‘Hobeln?’
   (b) ‘Manual Refill?’
   (c) ‘Run’
2. Select a random ice core (anything but ‘Einkristall’)
3. Set Jumo iTRON16 controller (affixed onto the wooden box) to >40°C
4. Wait until ‘Now doing? +H’ indicates the ‘Standy-by’ mode
5. Print the ‘Results window’ (File + Print Window) and glue it into lab book
6. Stop ‘Steuerung2.vi’ by clicking on the ‘STOP’ button and close both open VIs
7. Refill dewar inside CIM box
8. Initialize the predefined ‘Programm 3’ using the command unit of the Lauda thermostat (heat from -27 to -10℃over at least 5 h; hold temperature at -10℃for 0.5–1.5 h; cool down again to -34℃over at least 6 h. Pumping level should be set to 3-4)
9. Change valve control to ‘Manual’ mode (note that manual operation requires experience)
10. Close V10 and V14; set V22 to ‘red’
11. Remove dewar under K2 cold trap
12. Set Jumo iTRON16 (the one with casing) to 3 – 9°C and thaw K2 cold trap
13. After the K2 cold trap has thawed, re-set the temperature to -85°C
14. Set V22 to ‘blue’
15. Remove the dewar under the K3 cold trap and let it thaw as well
16. After the K3 cold trap has thawed, re-open V10 and V14
17. Switch off:
   (a) Bellow power supply unit
   (b) Magnetic bearings power supply unit
   (c) CIM box cooling (liquid nitrogen pump; banana plugs)

18. Read out the measurement data of the day (using 'ReadData.vi'), save the data in 'Übertragungsfile.xls' (in German, 'transfer file'), and backup raw measurement data on CO2 Rohdaten CIM folder
19. Refill big glass dewar just before the prevacuum pump to the very top
20. Remove metallic insulator from K2 and allow to dry overnight
21. If necessary: quickly open the frontmost XPS board and defrost the fans with compressed air; do not open the box longer than a few seconds
22. Was today the last of several days of measurements?
    (a) If so, switch off fans inside the CIM box (banana plug) and the LAUDA chiller and continue with section A.2.5 on the next day.
    (b) If not, start over with A.2.2 on the next day

A.2.5 Weekly shutdown

After the CIM has thawed (1 night after the last day of measurements):

1. Switch V22 to 'red'. Make sure it doesn't go above $3 \times 10^{0.6}$ mbar. If it does, switch back to 'blue' quickly
2. Switch off the ACP 15 pump
3. Remove big glass dewar and cold trap (corrugated hose)
4. Remove glass dewar inside CIM box
5. Remove XPS boards (when temperature of CIM >18°C) and let the CIM dry

A.2.6 Sample preparation in the cold room

Set aside 1–1.5 hours to prepare all samples on a typical measurement day. With the right polar equipment (see Section A.5.2) you will need only one 5 minute break.

1. Grab the previously prepared bag of samples for that particular day from the A47 freezer
2. Quickly transport the gathered bags, including the EK stick inside an insulated bag to the A54 freezer
3. Prepare a sheet of paper to take notes
4. Assemble protective plastic covers at saw

5. Set saw to desired sample dimension (edge length; default: 21mm)
6. Put on single-use plastic gloves over insulating gloves
7. Prepare EK samples (default: one full 21mm-thick disk results in seven samples)
   (a) Always remove some ice from all surfaces that have been in contact with ambient air during storage with the saw or the straight razor
   (b) **Check for signs of contamination**
   (c) Cut off a disk (full cross-section)
   (d) Dice disk into 7 cubes. Keep the 1–2 largest leftovers as starting EK and dummies.
   (e) Use the straight razor to remove ice at the vertices; shave all faces of the cubic sample until the desired weight is reached; try to produce equally sized sample
   (f) Clean samples from remaining sawdust using the plastic brush
   (g) Put all EK samples in a non-numbered plastic cup
   (h) Note down individual EK weights
8. Prepare up to 24 polar ice samples
   (a) Open bag at bottom; note bag number (and all further relevant information); note sample orientation
   (b) Check for signs of contamination, particularly for cracks in the ice
   (c) Make a quick sketch of the ice and outline any special features
   (d) Consider how much ice needs to be removed from the outer surface (2 – 10mm depending on storage history and potential level of contamination; typically 5mm). **Generously remove ice close to cracks and breaks**
   (e) Remove some ice on the outermost cross-sectional surface. Note that the saw produces 1.5mm-thick cuts
   (f) Cut off a cross-sectional slice and repack the remaining ice and properly close the bag using staples (do not use the sealer)
   (g) Remove the outermost lateral surface ice of the freshly cut piece that was in contact with ambient air during storage
   (h) Using the “cheese" sample holder, split the piece in three “cheese" samples of 6–8 grams each.
   (i) Use the straight razor to remove some ice at the vertices if necessary. Focus on the outer round part.

(j) Clean samples from remaining sawdust with the plastic brush

(k) Put each sample separately in a numbered plastic cups, close it with the respectively numbered cap, and note the exact weight

(l) Ensure that any direct contact/touching (i.e. heating) as well as any contamination of ice is minimized

9. Store all prepared samples in the cooler and buffer the temperature with eutectic elements

10. Clean the saw and workbench thoroughly

11. Remove the protective plastic cover from the saw to allow for sublimation of the residue saw dust

12. Return remaining ice bags and the EK ice in an insulated bag to your storage box in the A47 freezer; do not leave this ice in the sample preparation freezer

13. Quickly transport the prepared samples to the CO_2 lab

A.3 Maintenance procedures

A.3.1 Refilling the standard gas tanks

The following section is an update on the maintenance procedures introduced in Nehrbass-Ahles (2017).

Always refill the standard gas tanks when the system is **dry** and with **cold traps at room temperature**.

1. Expand one standard volume of gas into the region around pressure sensor 'P1' with the bellow in the reference position
   (a) Start with valves in standby position
   (b) Turn on the ACP
   (c) Close V3, V4 and V1
   (d) Set V21 to 'blue'
   (e) Open V7 (or V8) for 3 s. Close again
   (f) Open V3 (or V4)
   (g) Note down the pressure (P1)
   (h) Open V1 and pump for 5 min
   (i) Set V21 to 'red'
   (j) Wait until pressure is low; reset standard valve settings
2. Connect the standard reference gas cylinder (STD) to M3
3. Evacuate the standard gas container STD1 (or STD2) including supply tubing
   (a) Start with valves in standby position
   (b) Close all valves except V20 – V22, including manual valves (M5)
   (c) Switch V22 to 'blue'
   (d) Open V7 (or V8), V3 (or V4), V12, and V13. Pump for 5 min
   (e) Close V3 (or V4)
   (f) Open M4 and M3. Pump for 5 min
   (g) Open M1 (or M2) and V3 (or V4). Pump for 15 min
   (h) Close V12
   (i) Open V2, V1, V6 and M5

(j) Set V22 to ‘red’. Pump for 2 min

(k) Open V10, V13, V14, and V15

(l) Pump for approximately 20 h; use a stopwatch and note the time on the next day

4. Check pressure level at TMP LI-COR (it should be $<4 \times 10^{-8}$ mbar)

5. Purge and condition the STD1 container (or STD2) with standard gas

(a) Close all valves except V20 – V22, including manual valves (M5)

(b) Open the references gas cylinder at main valve and set outlet pressure of Tescom pressure regulator to 1.0-–1.1 bar (atmospheric! Not overpressure!)

(c) Set V22 to ‘blue’

(d) Open V13, V12, V3 (or V4) and M3

(e) Open M4 for approximately 2 s. Close again

(f) Double-check pressure setting at pressure regulator again (tap the gauge twice)

(g) Now read the following block before acting:

i. Open M1 (or M2) and V7 (or V8). Start timer and flush the container for exactly 25 s

ii. Close V7 (or V8)

iii. Close M1 (or M2) exactly 30 s after V7 (or V8)

(h) Close M3 and the main standard gas cylinder valve

(i) Restore standby valve settings, but keep V4 (or V3) closed

6. Let the gas equlibrate for 2 h

7. Fill the STD1 container (or STD2) with standard gas

(a) Close all valves except V20 – V22

(b) Open the references gas cylinder at main valve

(c) Set V22 to ‘blue’

(d) Open V13, V12, V3 (or V4) and M3

(e) Open M4 for approximately 2 s; close again

(f) Triple-check pressure setting at pressure regulator (tap the gauge twice)

(g) Open M1 (or M2) and V7 (or V8); start timer and flush the container for exactly 30 s

(h) Close V7 (or V8)

(i) Close M1 (or M2) exactly 30 s after V7 (or V8)

(j) Close M3 and the main standard gas cylinder valve; set the outlet pressure of the pressure regulator to the minimum (turn counterclockwise)

(k) Open M4 and pump for 15 min

(l) Switch V22 to 'red' and pump for 30 min

(m) Close M4

(n) Restore standby valve settings

8. Note the calibrated CO2 mole fraction, cylinder ID, pressure inside the standard gas container (low pressure gauge of pressure regulator) and cylinder pressure (high pressure gauge of pressure regulator) in the lab book and on the standard gas container. Repeat step 1 the following day.

A.3.2 Refilling the LN tank

Refilling the LN tank is a procedure that carries some risk, especially if treated lightly after it becomes routine.

1. Bring the 150 liter LN tank to the workshop.
2. Position it in order to ease the access to the exhaust tube and lock the wheels.
3. Connect the exhaust system and tie it with the available cord.
4. Disconnect the hose and connect the supply hose. **Make sure not to overtighten the supply hose, because it will get very cold and very hard to open it afterwards. Use two wrenches if necessary. DO NOT use a single wrench, otherwise the applied torque will damage the tank.**
5. Open the exhaust valve on top of the tank. Leftover LN will purge out.
6. Open the input valve on top of the tank.
7. Open the main valve in the station to allow refilling.
8. Check that the red light is continuously on.
9. Double-check steps 6–8.
10. Press start. You will hear the tank being filled. Check for leaks at the inlet. If there is one, stop the process and reconnect the supply hose.
11. Wait for about 15–30 minutes.
12. Check that the red light is continuously on. If it's blinking, than it has not yet finished filling the tank.
13. Close input and exhaust valves at the top of the tank.
14. Disconnect the supply hose and connect your own. Use wrenches if necessary.
15. Close main valve at the station.
16. Note down on the paper outside (No.17 for KUP) the amount used.
17. Leave everything as it was before.
18. Be very careful maneuvering the tank back into the lab. It will be very heavy and difficult to control.

A.3.3 Resharpening the knife

Initial preparations:

- Set aside at least two hours for this procedure. Set aside a whole afternoon if you are new to this.
- Dip all whetstones in a water tin and let them bubble out for 15 minutes.
- Prepare a clean workspace with available aluminium foil, chemwipes and plenty of paper towel.

Removing the knife:

- Unscrew the funnel while the N_2 purge is on.
- Feel and support the knife holder with your middle and ring finger.
- In between the two fingers, slip through the long allen wrench.
- Carefully unscrew the knife holder. Be careful not to let it fall.
- Unscrew the razor from the holder
- Dip the holder in isopropanol while you resharpen the knife

Resharpening the knife:

- Through a looking glass, assess the status of the razor's edge. Deep dents will require starting with the 400 grit stone. Otherwise, start with the 1000 grit stone.
- Assemble the knife in the new knife sharpener. Mind the two different angles, and the two different supports needed for each.
- Insert the whetstone. Maintain it wet by regularly adding water to the surface.
- Gently touch down the razor on the whetstone. Push it towards you, without pressing down, making it slide along the wetstone. You'll hear a gentle scratching noise. See recorded video for clarity.
- Lift the razor and push it back to the start.
- Perform 30–50 laps before changing to the other side and repeat.
- Switch to a stone of higher grit and repeat.

A.3.4 Exchanging a bottle of N_2

The replacement of N_2 bottles poses perhaps the highest risk for an accident in the lab. While the exact step-by-step procedure to exchange a bottle of N_2 can be found inside the gas cabinet, a few other precautions should be kept in mind.

- Order the necessary N_2 at least 2–3 days in advance from the workshop.
- The standard N_2 used for CO_2 measurements is Alphagaz I (N_2>99.999%), 50 liters, 200 bar.
- When picking up a new bottle from the workshop, always use a heavy-duty bottle carts. Never attempt to carry one on your own.
- Be especially mindful when transporting bottles while using the lift due to the risk of suffocation.
- When moving across very short distances (<2 m), gently spin the bottle through the floor, holding it with both hands. Never attempt to lift it. **Never tilt it more than the minimum necessary.**
- Keep in mind the weight difference between used and freshly filled bottles.
- Prior to exchanging the gas bottle, clean the outlet thoroughly with chemwipes and isopropanol. Let the outlet dry before connecting it.
- Never leave a bottle unchained. If there are no chains available, then that is not the right place to leave a bottle.

A.4 Delicate procedures

A.4.1 Dealing with unforeseen circumstances

No amount of procedures in this appendix can cover all the tricky issues that are part of an experimental PhD. Unforeseen circumstances are unfortunately a reality of lab work and it is up to the scientist to weave his way out of them while employing good practices of damage control. In the case of our lab there are a few pointers worth mentioning.

If something bad happens during measurements and the CIM is in immediate danger:

- Close all valves immediately. Either act on the board if you can (via the Steuerung2.Vi interface), or act more drastically on the main air supply behind the LI-COR. This will cause all valves to be off except the manual ones.
- Switch V20/21/V22 to blue (ACP).
- Safeguard the bellow by closing M5.
- Proceed carefully. Recall that Steuerung2.vi might still be controlling the valve settings.

If there is no immediate danger, think before you act, especially when it comes to the valve board. Problems tend to multiply in these situations. One trick is to close all valves on the main board regardless of their lighting situation and then switch control to manual. In this way, Steuerung2.vi no longer can cause any damage. Then, section by section, evacuate whatever air is left inside the system and get back to standard settings.

A.4.2 Bringing the bellow to atmospheric pressure

Bringing the bellow to atmospheric pressure from vacuum (or vice-versa) is a painstaking procedure that can easily go wrong. Pick the right day to do this and make sure you will not be disturbed.

1. Start from standard valve settings.
2. Take a picture of the pressure display. It will help you understand later if you managed to bring the system back to the same conditions
3. Turn off the pressure sensors of both turbo pumps (CH1/CH4) in the display. The filaments inside need to cool down and they take an estimated 15 min to do so. Physically remove CH3 from the display and label it. This is a sensitive sensor.
4. Now it's time to connect the pressure gauge that will allow inflating the bellow in a controlled way. The goal is to slowly inflate both sides of the bellow step by step and bring it to atmosphere without sudden bursts of pressure that could damage it.
5. Close every single valve in the board. Only V20/21/22 will be lighting up in turbo mode.
6. Borrow a pressure gauge from the workshop.
7. Attach the pressure sensor to the inlet near V11 while flushing with N_2. Carefully tighten it using two wrenches.
8. Connect the display and see if it makes sense (it should be above 1000 mbar or hPa).
9. Close the manual valve at the right of V11 and check the display. It pressure is dropping, you have a leak.
10. Set the N_2 regulator to it its minimum (closed).
11. Turn on the ACP and set V22 to blue. Evacuate the line by opening the manual valve, V11 and V13.
12. Close the manual valve, and then close V13. Set the N_2 regulator to 0 (room pressure).
13. Recheck that the manual valve was closed during the last step.

14. Open V16 and V9. Now the pathway between the bellow and the N_2 bottle is open. Make sure that M5 is also open.

15. Close the manual valve next to the inlet of the bellow. The pressure gauge should be at its minimum, indicating -1 bar.

16. Check that the bellow is off.

17. Now it's time to disconnect the magnetic coupled oil pump. Start by disconnecting the safety valve by unplugging the electrical cord

18. The goal now is to let air in without having a reflux of oil going into the inlet tube. To do so, be prepared to vent it and the same time turn off the pump.

19. Open the lowermost clamp (the uppermost is also possible, but remember that the valve is made of aluminium and is therefore easily scratchable) on the INLET side.

20. Tilt the whole thing so as to let air in. As soon as you hear it, turn off the pump while keeping it tilted and with the air flowing.

21. Cover the pump's inlet with aluminium foil.

22. Connect again the power supply to the safety valve. This is important because we need a source of air in order to inflate the bellow.

23. Due to friction, the bellow will not inflate by rotating the main axle, but instead it will simply apply tension to the connector. This stretch is visible and needs to be monitored. The goal is therefore to do this in a quasi-static process so that we're always close to equilibrium and no harm is done to the connector.

24. Start with the N_2 side by increasing very slowly the pressure by 50 mbar. **The manual valve is extremely sensitive, so be very gentle when opening it**. By now the connector should look more compressed.

25. Raise 50 mbar on the other side, by opening the inlet valve of the bellow and checking the pressure gauge. Note that this pressure gauge is very ad-hoc. What matters is seeing that the connector is not stretching too much to either side.

26. Keep raising 50 mbar on each side in alternate turns until both manual valves are fully opened, meaning atmospheric pressure on both sides of the bellow has been reached.

27. Close M5. Now the bellow is safe.

A.4.3 Replacing the connector inside the bellow

During my PhD I have had to replace the connector three times usually due to power outages and related issues. It is a minute and time consuming procedure that you don't want to do while being under stress.

1. Start by bringing the bellow to atmospheric pressure according to Section A.4.2.
2. Make sure the bellow is off.
3. Open the Plexiglas cover carefully with an Allen wrench.
4. Provide a pathway for air to inflate the bellow from the inside. Using N_2 is too risky, so unfortunately the system has to be flushed with room atmosphere. However, keep V10 and V14 closed so that at least the CIM doesn't get contaminated. Open the blind flange next to V11 to let air in.
5. Loosen the screws of the connector.
6. Push the bellow to the side or turn the main axle motor in order to remove the old connector.
7. Take note of the two different diameters of the holes on both ends of the new connector.
8. Notice the already flattened end of the main axle. You will want to position the new connector in the same place. Make a mark in the main axle with a pen.
9. Insert the connector in the motor end, by inserting the big diameter end about half-way in. Screw it when you think it's in the right position.
10. Screw the other side by physically bringing together the main axles and the connector. You may need a second set of hands to help out.
11. Use the program FaltenbagManualMove.vi to manually test it. Don't forget to run Steuerung2.vi and turn on the bellow first.
12. You may have to fool Steuerung2.vi by pressing the sensors yourself in the minimum and then in the reference, while the connector is not yet screwed in (the motor will then just turn by itself).
13. Close the bellow with Plexiglas cover. Do not screw in the screws sequentially as this will lead to poor air tightening. Instead, cross-screw oposing screws little by little. Note that they do not need to be individually very tight.

A.4.4 Shutting down the system

Shutting down the CIM entirely might be adequate if you're going on vacations for a prolonged time, for deep cleaning of the CIM's interior or if for some reason the CIM won't need to be operated for many months. Do keep in mind that bringing it to fully operational mode needs at least two weeks, because that is the time the LI-COR needs to fully stabilize.

1. Start by bringing the bellow to atmospheric pressure according to Section A.4.2.
2. It's a smart idea to keep the system filled with N_2 while in shutdown mode, either at room pressure or slightly overpressure.
3. Physically disconnect the air supply of V20/V21/22 by replacing these by blind tubes directly in the main FESTO controllers. Be careful that the metal part stays facing the outside. If you by accident press it the wrong way, you will likely destroy the controller.
4. **Do not be fooled by the electronic board**. V20/21/22 are OR valves, but when you disconnect the air supply none of the air ways is allowed. The electronic valve board will nevertheless always light the choice according to the switch, indicating that it is open.
5. Close V11.
6. Set the N_2 regulator to 0.5 bar overpressure.
7. Since the manual valve next to V11 should by now be open, it is safe to disconnect the pressure gauge and the display. N_2 will be flushing out during the process. Seal it with a blind flange.
8. Since the pumps are safe (V20/21/22 are disconnected), open the valves in this sequence: V10 / V14 / V16 / V15 / V13 / V9 / V1 / V5 / V6 / V2 / V12.
9. Keep V3, V4, V7 and V8 closed. This maintains the standard gases isolated. Leave M4 closed as well.
10. Obviously, leave M5 closed. The bellow is at room pressure!
11. Switch off V11 and set the N_2 regulator to the minimum.
12. Click the power button once in the display of both TMPs. They will slowly descend from 1500 Hz to 0.
13. Switch off the pumps completely using the main switch in the back.

14. Switch of the LI-COR by switching off the UPS. As of today, only the LI-COR is connected to the UPS. This may not always be the case!
15. Switch off the PC and turn the speakers off.
16. In the back of the PC, unplug CIM fans, spitters, LI-COR peltier and LI-COR fan.
17. Remove CH2 and label it. Switch off the Pfeiffer sensor display.
18. Disconnect the cold trap controller (-85°C). Unplug the green/yellow/red/black cables and disconnect the power supply.
19. Close all N_2 bottles in the gas cabinet.
20. Make sure the LAUDA is off.
21. Turn off the ACP and vent it.
22. Turn off cooling fans above the ACP.
23. Recheck that the standard gas bottle main valve is closed.
24. Turn off the portable freezer, open the lower ballast and keep the lid open.
25. Enjoy your holidays :)

A.5 Safety in the lab

A.5.1 Dealing with liquid nitrogen

Liquid nitrogen should not be underestimated. Throughout my PhD I had several minor incidents which luckily did not go beyond scares and light burns. Apart from inflicting severe burns, it can lead to suffocation in case of a major leak.

- **Spillage** Spills are likely the number one incident you will face. It is very important not to be wearing anything metallic, namely rings or bracelets. **These will get very cold very fast and lead to a burn.** Through the Leidenfrost effect, liquid nitrogen will trickle when in touch with your skin, but it will be absorbed by most fabrics. Soaked gloves or sweaters were my most frequent issues.

- **Drinking hazard** It might seem silly, but I did reach out a couple of times to drink from a dewar when I was distracted while in measurement mode. To avoid this, always place the dewars in the same predefined locations and always keep your water bottle away from them. There have been cases of accidental ingestion of liquid nitrogen, and the results range from a permanently destroyed esophagus to death.

- **Suffocation** Liquid nitrogen has an expansion ration of about 600 when transitioning from liquid to gas phase. This can reduce the available concentration of O_2 drastically and eventually lead to suffocation as a worst case scenario. In the lab, throughout a measurement day, with frequent door opening, I have seen the O_2 detector swing between 20.5% and 21%. Only values below 19% should really start to worry you in terms of long exposures, but the effect is nevertheless there. In closed spaces, such as an elevator or storage room, spillage of N_2 could play a much bigger role.

A.5.2 Working under cold conditions

Preparing samples in the cold room can often take more than one hour. Usually, putting on an extra polar jacket and gloves is enough to endure the $-20\,^{\circ}\mathrm{C}$, but it can be uncomfortable. Uncomfortable conditions lead to a hurried attitude and to experimental mistakes, from dropping samples to uneven shaving, or overall less careful treatment of the samples.

I have found that for long cutting sessions it is very worth to take the time to wear polar boots, double deck two down-feathered jackets and an extra winter hat, below the jacket's hoodie. All the extra volume may be a bit of a nuisance but it

keeps you warm longer and it reduces the amount of needed breaks to usually just one. Wearing polar pants, on the other hand, doesn't seem to be worth the trouble.

Regarding gloves, it is worthwhile to wear inner gloves from merino wool. However, keep in mind that warming hands means warming ice samples. It is inevitable that your hands will be cold after a cutting session. The cold itself is unlikely to inflict any frostbite. Very cold fingers, nose and ears are frequent guest, but nothing that an afterwards trip to the coffee break won't solve.

As a rule of thumb, contacting with cold surfaces is what will make you cold the faster, so avoid touching anything as much as possible, and keep a small distance between your waist and the working bench. Faster and hassle-free cutting sessions were achieved for me when I was warm, had arrived early and had a good night sleep. A busy mind will often lead to mistakes, and wandering from thought to thought while working in the cold room will lead to losing the thread of what you are doing. Stay focused!

A.5.3 Hazardous substances

The hazardous substances in the CO_2 lab are mainly ethanol (95%, with 5% isopropanol) and acetone. Keep in mind to keep them away from heat sources, especially the oil pump. Any specific questions, such as disposal, should be directed to Thomas Wagner, the responsible for safety regarding chemicals.

During the moving of the lab, small beads of mercury were found amidst the cracks of the old flooring. The collected mercury was safely disposed. Subsequently, an external company has hired to sweep the room with a mercury detector and found no abnormal levels of mercury.

A.5.4 Alarms

The CO_2 lab is equipped with an oxygen meter. While the sensor is inside the lab, the display is outside. Normal oxygen concentrations are around 20.9%.

In general, if the alarm goes off you should consider evacuating immediately. However, once every year or so the oxygen meter alarm will go off because the chemicals inside the sensor need to be replaced. You can safely disable the alarm after making sure that there is no danger. The responsible company will take care of the necessary maintenance.

Data

This chapter contains all ice core measurements performed during this PhD. The tables should be read as follows:

- **Bag No.** The specific bag number from that ice core project. In case of EDC, they are all from EDC99.
- **Meas. No.** The unique measurement number assigned by the CIM. For internal use only.
- **Depth (m)** The depth of that particular sample, taken as the midpoint of usually a 2.5 cm-thick sample.
- **CO_2 (ppm)** Atmospheric CO_2 concentrations after corrections. In case of MIS 5 samples, these include gravitational correction.
- **Depth mean (m)** Average depth of all available replicates. In some cases, neighboring vertical depth levels have also been measured, leading to a maximum of 6 replicates.
- **CO_2 mean (ppm)** Average CO_2 concentration of all available replicates.
- **sigma (ppm)** Sample standard deviation of the CO_2 concentration of all available replicates, calculated as $\sigma = \sqrt{\frac{\sum (x_i - \mu)^2}{N-1}}$
- **TAC (ml kg^{-1})** Total air content, calculated as $\mathrm{TAC}_{MIS\,5} = p \cdot m \cdot K$, where p is the pressure in the bellow at maximum volume, m is the weight of the sample and $K = 1121$ is a constant determined using calibrated TAC measurements (see Section 3.1).

EDC

MIS 5

Table A.1: Measurements performed for the LIG dataset with the EDC ice core (Chapter 4).

Bag No.	Meas. Date	Meas. No.	Depth (m)	CO_2 (ppm)	Depth mean (m)	CO_2 mean (ppm)	sigma (ppm)	TAC (ml kg^{-1})
2641	11/03/18	23383	1452.46	230.3	1452.5	231.4	1.5	93.7
	11/03/18	23409	1452.46	232.5				
2643	28/12/18	25377	1453.64	234.4	1453.6	233.7	1.0	93.3
	28/12/18	25401	1453.64	233.0				
2646	25/01/18	22775	1455.29	246.5	1455.3	245.9	0.8	91.8
	25/01/18	22803	1455.29	245.3				
2648	08/01/19	25527	1455.86	242.3	1455.9	243.5	2.0	92.0
	08/01/19	25545	1455.86	241.3				
	25/08/20	27392	1455.90	244.8				
	25/08/20	27416	1455.90	245.5				
2650	07/12/18	25327	1456.96	240.1	1457.0	241.3	1.7	89.4
	07/12/18	25347	1456.96	242.5				
2651	19/07/18	24815	1457.61	238.0	1457.6	238.3	2.5	91.7
	19/07/18	24829	1457.61	240.3				
	19/07/18	24845	1457.61	242.3				
	26/01/18	22851	1457.64	236.6				
	26/01/18	22873	1457.64	236.8				
	26/01/18	22899	1457.64	235.8				
2653	06/12/18	25268	1458.61	246.1	1458.6	245.1	1.5	95.1
	06/12/18	25284	1458.61	244.0				
2654	28/01/19	25951	1459.69	240.3	1459.7	241.3	1.5	91.5
	28/01/19	25969	1459.69	242.3				
2656	31/01/18	22993	1460.40	241.7	1460.4	243.5	2.5	95.3
	31/01/18	23021	1460.40	245.3				
2657	29/12/18	25462	1461.34	240.2	1461.3	239.9	0.4	90.0
	29/12/18	25486	1461.34	239.6				
2659	10/01/19	25629	1462.44	247.7	1462.4	248.4	1.0	92.1
	10/01/19	25647	1462.44	249.1				
2661	11/03/18	23391	1463.49	247.5	1463.5	247.6	0.1	90.9
	11/03/18	23413	1463.49	247.7				

Bag No.	Meas. Date	Meas. No.	Depth (m)	CO_2 (ppm)	Depth mean (m)	CO_2 mean (ppm)	sigma (ppm)	TAC (ml kg^{-1})
2663	28/12/18	25375	1464.11	244.6	1464.1	242.2	1.9	90.6
	20/08/20	27313	1464.15	240.8				
	20/08/20	27321	1464.15	242.9				
	20/08/20	27331	1464.15	240.5				
2664	28/12/18	25385	1465.19	246.4	1465.2	244.7	2.4	89.2
	28/12/18	25407	1465.19	243.0				
2666	23/03/18	23756	1466.16	242.6	1466.2	241.5	1.5	89.7
	23/03/18	23778	1466.16	240.5				
2668	11/02/19	26226	1466.89	246.6	1466.9	248.2	4.0	90.9
	11/02/19	26268	1466.89	245.3				
	11/02/19	26248	1466.89	252.7				
2668	05/02/19	26172	1467.25	252.8	1467.3	251.5	1.8	88.2
	05/02/19	26186	1467.25	250.2				
2670	28/12/18	25379	1467.99	246.4	1468.0	246.4	1.2	88.3
	28/12/18	25397	1467.99	247.6				
	28/12/18	25419	1467.99	245.2				
2670	14/02/19	26413	1468.35	248.4	1468.4	248.8	1.3	90.4
	14/02/19	26427	1468.35	247.8				
	14/02/19	26443	1468.35	250.3				
2671	27/02/18	23169	1469.04	250.3	1469.0	250.3		92.8
2673	09/01/19	25570	1469.61	255.0	1469.6	254.6	0.5	90.0
	09/01/19	25590	1469.61	254.3				
2673	06/12/18	25282	1470.13	256.4	1470.1	257.1	1.0	86.6
	06/12/18	25300	1470.13	257.8				
2674	12/02/19	26305	1470.69	260.4	1470.7	261.0	0.8	89.1
	12/02/19	26325	1470.69	261.6				
2676	25/01/18	22773	1471.84	261.5	1471.8	262.7	1.7	95.6
	25/01/18	22801	1471.84	263.9				
2678	14/01/19	25696	1472.36	247.8	1472.4	247.6	0.2	89.6
	14/01/19	25714	1472.36	247.5				
2678	29/12/18	25442	1472.91	252.0	1472.9	251.7	0.5	88.9
	29/12/18	25466	1472.91	251.4				
2680	13/02/19	26362	1473.46	252.7	1473.5	251.9	1.2	87.7
	13/02/19	26364	1473.46	251.0				
2680	05/12/18	25225	1473.99	245.4	1474.0	244.8	0.8	90.7
	05/12/18	25241	1473.99	244.2				
2681	18/03/18	23521	1474.47	244.1	1474.5	244.5	0.6	91.8
	18/03/18	23541	1474.47	245.0				
2683	09/01/19	25584	1475.15	242.6	1475.2	242.7	0.2	91.3
	09/01/19	25604	1475.15	242.9				
2684	26/08/21	29209	1476.16	236.0	1476.2	243.9	8.3	89.0
	02/09/21	29273	1476.16	237.9				
	24/01/19	25892	1476.17	252.9				
	24/01/19	25910	1476.17	248.9				

Bag No.	Meas. Date	Meas. No.	Depth (m)	CO_2 (ppm)	Depth mean (m)	CO_2 mean (ppm)	sigma (ppm)	TAC (ml kg^{-1})
2686	09/03/18	23318	1477.19	244.7	1477.2	243.7	1.4	95.1
	09/03/18	23342	1477.19	242.7				
2690	06/12/18	25280	1478.96	242.4	1479.0	242.8	0.6	89.9
	06/12/18	25298	1478.96	243.2				
2691	23/04/18	24061	1479.99	242.4	1480.0	241.9	0.7	93.6
	23/04/18	24081	1479.99	241.4				
2693	29/01/19	26003	1480.61	242.1	1480.6	241.9	1.3	93.9
	29/01/19	26021	1480.61	240.5				
	25/08/20	27384	1480.65	241.3				
	25/08/20	27402	1480.65	243.6				
2694	28/01/19	25953	1481.69	237.5	1481.7	237.4	0.2	89.0
	28/01/19	25971	1481.69	237.3				
2696	26/01/18	22865	1482.52	236.5	1482.5	236.9	0.6	91.6
	26/01/18	22891	1482.52	237.4				
2701	25/04/18	24193	1485.06	237.3	1485.1	237.1	0.5	90.9
	25/04/18	24219	1485.06	237.3				
	25/04/18	24245	1485.06	236.5				
2703	14/01/19	25688	1486.11	234.2	1486.1	235.2	1.4	91.1
	14/01/19	25706	1486.11	236.1				
2706	31/01/18	22999	1487.94	237.7	1487.9	237.1	0.9	96.2
	31/01/18	23029	1487.94	236.4				
2708	28/01/19	25943	1489.39	234.0	1489.4	234.5	0.7	93.0
	28/01/19	25961	1489.39	235.0				
2711	31/05/18	24554	1491.01	235.6	1491.0	236.5	1.7	92.0
	31/05/18	24570	1491.01	236.7				
	01/05/18	24365	1491.03	238.8				
	01/05/18	24389	1491.03	235.0				
2713	12/02/19	26295	1492.10	235.4	1492.1	236.5	1.1	91.4
	12/02/19	26315	1492.10	237.5				
	25/08/20	27386	1492.11	236.6				
2716	25/01/18	22777	1493.79	240.2	1493.8	240.4	0.3	95.0
	25/01/18	22805	1493.79	240.6				
2718	26/08/21	29207	1494.86	244.0	1494.9	242.0	2.9	86.8
	26/08/21	29223	1494.86	240.0				
2721	31/05/18	24564	1496.43	241.7	1496.4	241.5	2.1	92.9
	23/04/18	24059	1496.46	243.4				
	23/04/18	24079	1496.46	239.3				
2723	11/02/19	26228	1497.64	246.8	1497.6	246.4	0.6	91.5
	11/02/19	26250	1497.64	245.9				
2726	25/01/18	22793	1499.24	244.4	1499.2	245.4	1.4	92.3
	25/01/18	22821	1499.24	246.4				
2728	16/01/19	25757	1499.86	249.3	1499.9	250.2	1.2	88.0
	16/01/19	25777	1499.86	251.0				
2730	11/02/19	26242	1500.96	248.9	1501.0	247.9	1.3	92.2
	11/02/19	26262	1500.96	247.0				

Bag No.	Meas. Date	Meas. No.	Depth (m)	CO_2 (ppm)	Depth mean (m)	CO_2 mean (ppm)	sigma (ppm)	TAC (ml kg^{-1})
2731	16/03/18	23462	1502.04	251.7	1502.0	250.5	1.7	91.2
	16/03/18	23482	1502.04	249.3				
2733	04/02/19	26113	1503.14	252.1	1503.1	251.7	0.5	89.5
	04/02/19	26131	1503.14	251.4				
2736	02/06/18	24590	1504.76	250.9	1504.8	252.4	2.2	93.1
	02/06/18	24600	1504.76	250.9				
2736	16/01/18	22550	1504.79	255.5	1504.8	252.4	2.2	93.1
	16/01/18	22560	1504.79	252.2				
2739	28/01/19	25945	1505.91	253.6	1505.9	253.0	0.9	88.3
	28/01/19	25963	1505.91	252.4				
2740	07/12/18	25329	1506.99	250.0	1507.0	250.0	0.0	88.1
	07/12/18	25349	1506.99	250.0				
2741	02/06/18	24594	1507.51	253.4	1507.5	253.0	0.5	94.0
	02/06/18	24606	1507.51	252.6				
2743	06/12/18	25276	1508.64	253.8	1508.6	254.8	1.4	90.2
	06/12/18	25296	1508.64	255.8				
2746	26/01/18	22855	1509.91	250.7	1509.9	250.7		86.8
2748	29/01/19	26009	1510.86	254.4	1510.9	255.0	0.9	90.2
	29/01/19	26027	1510.86	255.6				
2750	10/01/19	25631	1511.96	253.3	1512.0	252.9	0.5	92.8
	10/01/19	25651	1511.96	252.6				
2751	01/05/18	24357	1512.60	254.0	1512.6	252.9	1.5	91.8
	01/05/18	24383	1512.60	251.9				
2753	10/08/20	27268	1514.14	255.1	1514.1	253.5	1.2	88.2
	10/08/20	27286	1514.14	253.8				
	10/08/20	27292	1514.14	252.5				
	07/12/18	25323	1514.14	252.8				
2756	30/01/18	22932	1515.79	249.7	1515.8	249.8	0.1	94.0
	30/01/18	22950	1515.79	249.9				
2759	16/01/19	25749	1517.44	252.9	1517.4	253.7	1.2	88.7
	16/01/19	25771	1517.44	254.5				
2761	16/03/18	23458	1518.53	251.6	1518.5	251.3	0.5	93.5
	16/03/18	23478	1518.53	250.9				
2763	14/01/19	25698	1519.11	255.3	1519.1	256.2	1.3	89.5
	14/01/19	25718	1519.11	257.2				
2764	11/02/19	26230	1520.19	255.0	1520.2	255.7	1.0	90.4
	11/02/19	26252	1520.19	256.4				
2766	27/02/18	23147	1521.10	259.4	1521.1	258.4	1.4	94.0
	27/02/18	23171	1521.10	257.4				
2769	14/02/19	26429	1522.91	258.8	1522.9	258.3	0.7	88.2
	14/02/19	26445	1522.91	257.8				
2771	22/03/18	23676	1523.96	257.3	1524.0	257.0	0.4	94.0
	22/03/18	23702	1523.96	256.7				
2773	17/01/19	25800	1525.14	262.4	1525.1	262.3	0.1	90.2
	17/01/19	25820	1525.14	262.2				

Bag No.	Meas. Date	Meas. No.	Depth (m)	CO_2 (ppm)	Depth mean (m)	CO_2 mean (ppm)	sigma (ppm)	TAC (ml kg^{-1})
2776	30/01/18	22922	1526.43	259.1	1526.4	260.6	2.1	93.1
	30/01/18	22940	1526.43	262.0				
2778	14/01/19	25700	1527.36	257.7	1527.4	259.5	2.6	89.9
	14/01/19	25720	1527.36	261.4				
2780	09/01/19	25580	1528.50	259.7	1528.5	260.4	0.9	89.7
	09/01/19	25600	1528.50	261.0				
2781	09/03/18	23298	1529.44	269.0	1529.4	267.1	2.7	93.9
	09/03/18	23326	1529.44	265.2				
2786	31/01/18	22997	1531.99	270.6	1532.0	269.2	1.8	92.9
	31/05/18	24548	1532.02	269.8				
	31/05/18	24566	1532.02	267.2				
2790	24/01/19	25894	1533.96	265.4	1534.0	265.0	0.6	88.8
	24/01/19	25914	1533.96	264.5				
2793	31/01/19	26058	1535.61	269.0	1535.6	268.5	0.6	89.3
	31/01/19	26076	1535.61	268.1				
2796	30/01/18	22930	1537.74	267.9	1537.7	268.1	0.3	91.2
	30/01/18	22946	1537.74	268.3				
2798	12/02/19	26303	1538.89	274.4	1538.9	273.5	1.3	87.5
	12/02/19	26323	1538.89	272.6				
2801	19/07/18	24819	1540.15	270.5	1540.2	271.7	2.2	92.8
	19/07/18	24835	1540.15	274.2				
	19/07/18	24847	1540.15	271.5				
	01/05/18	24349	1540.18	273.4				
	01/05/18	24375	1540.18	268.8				
2806	25/01/18	22771	1543.29	271.9	1543.3	272.6	1.0	94.7
	25/01/18	22797	1543.29	273.3				
2811	24/04/18	24128	1546.04	272.6	1546.0	272.5	0.1	90.1
	24/04/18	24154	1546.04	272.5				
2816	23/01/18	22674	1548.79	271.1	1548.8	270.7	0.6	93.4
	23/01/18	22702	1548.79	270.3				
2821	31/05/18	24556	1551.43	277.2	1551.4	276.1	1.6	90.7
	31/05/18	24574	1551.43	276.8				
	16/03/18	23452	1551.46	274.2				
2823	11/02/19	26240	1552.11	269.4	1552.1	273.9	4.4	90.4
	11/02/19	26260	1552.11	270.8				
	26/08/21	29221	1552.15	277.8				
	02/09/21	29257	1552.15	277.4				
2824	20/08/20	27329	1553.16	271.7	1553.2	274.2	2.0	88.5
	20/08/20	27335	1553.16	276.8				
	20/08/20	27337	1553.16	273.5				
	24/01/19	25882	1553.19	273.4				
	24/01/19	25900	1553.19	275.6				
2826	09/03/18	23308	1554.29	278.7	1554.3	278.5	0.3	92.3
	09/03/18	23332	1554.29	278.3				

Bag No.	Meas. Date	Meas. No.	Depth (m)	CO_2 (ppm)	Depth mean (m)	CO_2 mean (ppm)	sigma (ppm)	TAC (ml kg^{-1})
2831	02/06/18	24598	1557.01	272.0	1557.0	273.5	2.5	92.2
	02/06/18	24608	1557.01	271.5				
	21/03/18	23596	1557.04	273.5				
	21/03/18	23622	1557.04	277.0				
2833	29/01/19	26013	1558.14	276.4	1558.1	277.1	1.1	88.2
	29/01/19	26031	1558.14	277.9				
2836	25/01/18	22795	1559.79	275.5	1559.8	275.8	0.4	91.4
	25/01/18	22823	1559.79	276.0				
2837	16/01/19	25745	1560.34	275.3	1560.3	275.4	0.1	92.4
	16/01/19	25765	1560.34	275.5				
2840	28/12/18	25381	1561.46	274.4	1561.5	275.1	0.9	90.4
	28/12/18	25405	1561.46	275.7				
2841	23/03/18	23766	1562.54	270.6	1562.5	270.6	0.1	90.7
	23/03/18	23790	1562.54	270.7				
2843	08/01/19	25517	1563.11	272.0	1563.1	271.1	0.8	87.4
	02/09/21	29239	1563.15	270.9				
	02/09/21	29269	1563.15	270.5				
2845	31/01/19	26056	1564.21	275.0	1564.2	271.8	5.8	85.9
	31/01/19	26074	1564.21	278.4				
	02/09/21	29247	1564.25	266.9				
	02/09/21	29249	1564.25	266.9				
2846	18/07/18	24770	1565.26	272.7	1565.3	274.9	2.5	93.3
	30/01/18	22924	1565.29	274.3				
	30/01/18	22942	1565.29	277.6				
2848	17/01/19	25806	1566.39	273.8	1566.4	275.1	1.8	90.4
	17/01/19	25828	1566.39	276.3				
2851	25/04/18	24217	1567.56	277.8	1567.6	274.0	2.6	90.2
	31/05/18	24558	1567.59	273.0				
	31/05/18	24578	1567.59	271.8				
	31/05/18	24568	1567.60	273.2				
2854	13/02/19	26370	1569.16	277.2	1569.2	277.7	0.8	89.7
	13/02/19	26382	1569.16	278.3				
2855	17/01/19	25810	1570.24	277.2	1570.2	276.5	1.1	88.1
	17/01/19	25830	1570.24	275.7				
2858	10/01/19	25635	1571.36	267.8	1571.4	270.4	2.3	83.9
	10/01/19	25657	1571.36	269.1				
	26/08/21	29205	1571.40	272.3				
	02/09/21	29233	1571.40	272.4				
2860	08/01/19	25525	1572.46	276.4	1572.5	275.6	1.0	89.9
	08/01/19	25541	1572.46	274.9				
2861	18/03/18	23527	1573.41	269.3	1573.4	270.4	1.6	94.1
	18/03/18	23547	1573.41	271.5				
2863	07/12/18	25359	1574.11	273.1	1574.1	273.1		90.3
2864	29/01/19	26005	1575.19	279.4	1575.2	279.8	0.6	87.5
	29/01/19	26023	1575.19	280.2				

Bag No.	Meas. Date	Meas. No.	Depth (m)	CO_2 (ppm)	Depth mean (m)	CO_2 mean (ppm)	sigma (ppm)	TAC (ml kg^{-1})
2866	18/07/18	24764	1576.26	272.2	1576.3	273.5	2.5	91.5
	18/07/18	24782	1576.26	271.5				
	26/01/18	22869	1576.29	273.1				
	26/01/18	22893	1576.29	277.2				
2871	27/02/18	23167	1578.90	276.5	1578.9	276.5		93.9
2873	25/08/20	27388	1580.11	272.8	1580.1	275.7	2.5	87.2
	25/08/20	27396	1580.11	276.4				
	25/08/20	27420	1580.11	273.9				
	06/12/18	25274	1580.14	276.5				
	06/12/18	25292	1580.14	279.1				
2876	23/01/18	22672	1581.79	274.4	1581.8	274.2	0.3	94.5
	23/01/18	22700	1581.79	274.0				
2881	16/01/18	22552	1584.48	274.4	1584.5	275.1	1.0	89.8
	16/01/18	22562	1584.48	275.8				
2886	30/01/18	22926	1587.24	274.6	1587.2	275.4	1.1	94.9
	30/01/18	22944	1587.24	276.1				
2891	02/06/18	24592	1589.93	275.4	1589.9	274.0	2.1	91.4
	02/06/18	24602	1589.93	271.5				
	22/03/18	23670	1589.96	276.1				
	22/03/18	23694	1589.96	273.1				
2893	07/12/18	25325	1590.71	275.7	1590.7	275.0	1.0	86.6
	07/12/18	25333	1590.71	274.3				
2893	14/01/19	25690	1591.14	272.4	1591.1	273.8	2.0	90.3
	14/01/19	25708	1591.14	275.3				
2895	10/01/19	25639	1591.71	271.1	1591.7	272.1	1.2	85.9
	10/01/19	25649	1591.71	271.6				
	26/08/21	29213	1591.75	273.8				
	02/09/21	29275	1591.75	272.1				
2895	10/08/20	27262	1592.24	273.6	1592.2	273.3	0.3	90.6
	10/08/20	27270	1592.24	272.9				
	10/08/20	27288	1592.24	273.3				
	17/01/19	25804	1592.24	273.3				
	17/01/19	25826	1592.24	273.4				
2896	18/07/18	24766	1592.76	276.0	1592.8	272.1	4.4	85.6
	18/07/18	24784	1592.76	275.3				
	23/01/18	22662	1592.79	266.8				
	23/01/18	22690	1592.79	270.3				
2898	12/02/19	26291	1593.50	275.3	1593.5	275.7	0.6	89.5
	12/02/19	26311	1593.50	275.4				
	12/02/19	26331	1593.50	276.4				
2900	09/01/19	25572	1594.46	277.2	1594.5	276.7	0.7	90.0
	09/01/19	25592	1594.46	276.2				
2901	01/05/18	24345	1595.14	274.1	1595.1	274.6	0.5	92.1
	01/05/18	24369	1595.14	274.5				
	01/05/18	24395	1595.14	275.2				

Bag No.	Meas. Date	Meas. No.	Depth (m)	CO_2 (ppm)	Depth mean (m)	CO_2 mean (ppm)	sigma (ppm)	TAC (ml kg^{-1})
2903	26/08/21	29217	1596.61	274.6	1596.6	273.2	2.0	82.2
	02/09/21	29243	1596.61	271.7				
2906	31/05/18	24560	1598.26	274.5	1598.3	273.1	2.0	88.7
	31/05/18	24576	1598.26	272.6				
	21/03/18	23604	1598.29	270.5				
	21/03/18	23624	1598.29	274.7				
2911	11/03/18	23373	1600.96	273.0	1601.0	273.7	1.1	92.0
	11/03/18	23401	1600.96	274.5				
2914	16/01/19	25753	1602.69	276.1	1602.7	277.0	1.2	86.4
	16/01/19	25773	1602.69	277.9				
2916	23/01/18	22650	1603.79	274.1	1603.8	273.2	1.2	94.5
	23/01/18	22682	1603.79	272.3				
2918	20/08/20	27315	1604.86	273.1	1604.9	273.2	1.1	86.5
	20/08/20	27323	1604.86	271.3				
	20/08/20	27353	1604.86	274.0				
	08/01/19	25515	1604.89	274.0				
	08/01/19	25531	1604.89	273.6				
2921	18/03/18	23531	1606.09	274.6	1606.1	273.8	1.1	93.6
	18/03/18	23551	1606.09	273.0				
2923	28/12/18	25389	1607.64	275.0	1607.6	273.7	1.9	86.1
	28/12/18	25411	1607.64	272.3				
2926	25/01/18	22783	1609.29	273.4	1609.3	273.9	0.8	89.8
	25/01/18	22811	1609.29	274.5				
2928	14/02/19	26417	1610.36	277.0	1610.4	277.1	1.8	89.6
	14/02/19	26431	1610.36	278.9				
	13/02/19	26360	1610.39	275.4				
2931	31/01/18	22987	1612.04	277.2	1612.0	278.3	1.5	86.3
	31/01/18	23017	1612.04	279.3				
2934	17/01/19	25802	1613.69	276.4	1613.7	276.3	0.2	87.3
	17/01/19	25822	1613.69	276.1				
2937	08/01/19	25521	1615.34	272.6	1615.3	272.6		84.5
2941	09/03/18	23316	1617.08	273.6	1617.1	274.3	1.0	93.3
	09/03/18	23340	1617.08	275.0				
2946	23/01/18	22678	1620.24	273.9	1620.2	274.2	0.5	93.7
	23/01/18	22704	1620.24	274.6				
2948	04/02/19	26121	1621.39	276.9	1621.4	276.8	0.1	88.1
	04/02/19	26139	1621.39	276.8				
2950	31/01/19	26060	1621.96	277.0	1622.0	278.2	1.7	87.4
	31/01/19	26078	1621.96	279.4				
2951	26/04/18	24276	1622.64	278.6	1622.6	278.1	0.7	94.1
	26/04/18	24296	1622.64	277.3				
	26/04/18	24320	1622.64	278.3				
2953	09/01/19	25582	1623.61	272.8	1623.6	273.1	0.4	89.7
	09/01/19	25602	1623.61	273.4				

Bag No.	Meas. Date	Meas. No.	Depth (m)	CO_2 (ppm)	Depth mean (m)	CO_2 mean (ppm)	sigma (ppm)	TAC (ml kg^{-1})
2954	09/01/19	25576	1624.69	274.4	1624.7	274.3	0.2	91.8
	09/01/19	25596	1624.69	274.1				
2956	18/07/18	24762	1625.76	272.6	1625.8	272.7	1.3	92.4
	18/07/18	24780	1625.76	273.3				
	27/02/18	23149	1625.79	273.9				
	27/02/18	23173	1625.79	270.9				
2959	24/01/19	25884	1627.44	277.1	1627.4	276.7	0.5	88.8
	24/01/19	25902	1627.44	276.4				
2961	11/03/18	23389	1628.45	274.0	1628.5	273.6	0.6	93.4
	11/03/18	23411	1628.45	273.2				
2963	28/01/19	25939	1629.11	271.9	1629.1	272.1	0.3	88.7
	28/01/19	25957	1629.11	272.4				
2964	14/01/19	25692	1630.19	273.0	1630.2	274.3	1.9	85.7
	14/01/19	25712	1630.19	275.6				
2966	31/01/18	23009	1631.24	280.1	1631.2	280.9	1.0	92.5
	31/01/18	23039	1631.24	281.6				
2973	05/02/19	26168	1634.61	278.9	1634.6	277.2	2.5	86.7
	05/02/19	26188	1634.61	275.4				
2976	23/01/18	22664	1636.79	277.6	1636.8	278.4	1.1	93.4
	23/01/18	22692	1636.79	279.2				
2979	05/12/18	25219	1637.95	275.0	1637.9	274.3	1.0	89.7
	05/12/18	25237	1637.95	273.6				
2983	06/12/18	25290	1640.11	278.8	1640.1	276.1	2.5	87.0
	10/08/20	27260	1640.15	275.5				
	10/08/20	27264	1640.15	273.9				
2986	27/02/18	23151	1641.85	275.8	1641.9	274.9	1.2	91.8
	27/02/18	23177	1641.85	274.0				
2991	09/03/18	23310	1644.62	278.1	1644.6	276.9	1.6	92.8
	09/03/18	23336	1644.62	275.8				
2993	05/12/18	25215	1645.61	275.4	1645.6	275.2	0.3	90.1
	05/12/18	25231	1645.61	275.0				
2994	07/12/18	25335	1646.69	275.9	1646.7	276.3	0.6	87.3
	07/12/18	25353	1646.69	276.8				
2996	23/01/18	22652	1647.79	273.9	1647.8	273.7	0.3	90.4
	23/01/18	22654	1647.79	273.5				
3001	01/05/18	24343	1650.17	271.4	1650.2	272.2	1.4	90.3
	01/05/18	24367	1650.17	271.4				
	01/05/18	24393	1650.17	273.7				
3003	02/09/21	29235	1651.61	271.9	1651.6	274.6	4.6	84.4
	02/09/21	29265	1651.61	272.0				
	28/12/18	25417	1651.64	279.9				
3006	26/01/18	22871	1653.11	276.0	1653.1	275.4	0.8	92.5
	26/01/18	22895	1653.11	274.9				

Bag No.	Meas. Date	Meas. No.	Depth (m)	CO_2 (ppm)	Depth mean (m)	CO_2 mean (ppm)	sigma (ppm)	TAC (ml kg^{-1})
3008	25/08/20	27382	1654.36	282.7	1654.4	280.0	2.5	88.1
	25/08/20	27412	1654.36	282.6				
	25/08/20	27414	1654.36	278.4				
	05/12/18	25229	1654.39	278.8				
	05/12/18	25247	1654.39	277.3				
3011	31/01/18	22985	1656.01	278.6	1656.0	279.5	1.3	91.8
	31/01/18	23015	1656.01	280.4				
3016	26/01/18	22849	1658.79	277.7	1658.8	277.6	0.1	92.7
	26/01/18	22875	1658.79	277.6				
3021	27/02/18	23159	1661.40	275.8	1661.4	275.1	1.1	88.8
	27/02/18	23183	1661.40	274.3				
3026	24/04/18	24124	1663.94	276.7	1663.9	276.1	0.8	93.0
	24/04/18	24152	1663.94	275.5				
3031	11/03/18	23375	1667.01	271.9	1667.0	272.9	1.4	90.8
	11/03/18	23403	1667.01	273.9				
3036	26/01/18	22863	1669.65	272.7	1669.6	274.4	2.3	91.4
	26/01/18	22889	1669.65	276.0				
3037	12/02/19	26301	1670.34	279.1	1670.3	277.7	2.0	91.3
	12/02/19	26321	1670.34	276.3				
3039	11/03/18	23379	1671.44	277.2	1671.4	278.1	1.3	91.5
	11/03/18	23405	1671.44	279.0				
3040	05/12/18	25227	1671.99	278.8	1672.0	277.9	1.3	89.1
	05/12/18	25245	1671.99	277.0				
3041	16/01/18	22548	1672.42	276.9	1672.4	276.8	0.2	92.5
	16/01/18	22558	1672.42	276.6				
3045	28/12/18	25391	1674.74	277.6	1674.7	277.6	0.1	88.8
	28/12/18	25415	1674.74	277.7				
3050	18/03/18	23525	1676.99	275.1	1677.0	273.9	1.7	90.9
	18/03/18	23545	1676.99	272.7				
3050	23/01/18	22670	1677.49	277.5	1677.5	276.4	1.6	94.7
	23/01/18	22698	1677.49	275.3				
3054	26/04/18	24286	1679.69	275.8	1679.7	276.1	0.4	96.2
	26/04/18	24310	1679.69	276.4				
3055	29/12/18	25456	1680.24	276.2	1680.2	276.4	0.2	91.1
	29/12/18	25482	1680.24	276.5				
3056	22/03/18	23674	1680.66	271.2	1680.7	271.1	0.1	95.0
	22/03/18	23700	1680.66	271.0				
3060	26/04/18	24270	1682.46	274.6	1682.5	274.7	0.1	97.3
	26/04/18	24300	1682.46	274.8				
3060	15/01/18	22503	1682.99	274.9	1683.0	274.9	0.1	94.2
	15/01/18	22517	1682.99	275.0				

Bag No.	Meas. Date	Meas. No.	Depth (m)	CO_2 (ppm)	Depth mean (m)	CO_2 mean (ppm)	sigma (ppm)	TAC (ml kg^{-1})
3066	26/01/18	22859	1685.76	275.1	1685.8	275.3	0.2	91.1
	26/01/18	22883	1685.76	275.4				
3066	20/08/20	27319	1686.22	270.4	1686.2	272.3	1.4	93.4
	20/08/20	27355	1686.22	272.0				
	15/01/18	22495	1686.25	273.6				
	15/01/18	22509	1686.25	273.2				
3071	23/03/18	23750	1688.57	272.8	1688.6	272.5	0.4	93.3
	23/03/18	23772	1688.57	272.2				
3073	29/12/18	25452	1689.71	273.8	1689.7	274.5	1.0	91.3
	29/12/18	25476	1689.71	275.2				
3076	15/01/18	22497	1691.40	270.5	1691.4	270.8	0.4	92.3
	15/01/18	22511	1691.40	271.1				
3076	01/05/18	24355	1691.65	270.3	1691.6	270.1	0.4	90.6
	01/05/18	24379	1691.65	269.8				
3080	25/04/18	24199	1693.46	274.2	1693.5	274.7	0.7	92.3
	25/04/18	24227	1693.46	275.2				
3081	26/01/18	22853	1694.44	273.4	1694.4	273.8	0.6	90.1
	26/01/18	22879	1694.44	274.2				
3086	19/07/18	24817	1697.12	272.3	1697.1	272.7	2.4	90.3
	19/07/18	24831	1697.12	270.5				
	01/05/18	24363	1697.15	271.8				
	01/05/18	24387	1697.15	276.0				
3090	23/04/18	24055	1698.96	271.5	1699.0	272.6	1.6	91.1
	23/04/18	24075	1698.96	273.7				
3091	25/01/18	22791	1699.62	274.3	1699.6	274.1	0.4	90.6
	25/01/18	22817	1699.62	273.8				
3093	05/12/18	25221	1700.61	280.7	1700.6	279.3	2.0	87.0
	05/12/18	25239	1700.61	277.9				
3094	29/12/18	25446	1701.16	277.7	1701.2	277.3	0.6	87.0
	29/12/18	25472	1701.16	276.9				
3094	05/12/18	25217	1701.69	281.1	1701.7	280.5	0.9	86.0
	05/12/18	25235	1701.69	279.9				
3096	31/01/18	22995	1702.41	281.2	1702.4	281.5	0.5	83.8
	31/01/18	23025	1702.41	281.9				
3101	20/07/18	24870	1705.11	276.1	1705.1	276.9	1.0	88.0
	20/07/18	24886	1705.11	277.1				
	11/03/18	23385	1705.11	276.2				
	11/03/18	23419	1705.11	278.3				
3104	10/01/19	25633	1706.66	276.2	1706.7	276.4	0.3	87.1
	10/01/19	25655	1706.66	276.6				
3107	29/12/18	25454	1708.80	274.8	1708.8	275.8	1.3	87.2
	29/12/18	25478	1708.80	276.7				
3109	23/01/18	22648	1709.94	280.1	1709.9	279.1	1.4	87.8
	23/01/18	22680	1709.94	278.2				

Bag No.	Meas. Date	Meas. No.	Depth (m)	CO_2 (ppm)	Depth mean (m)	CO_2 mean (ppm)	sigma (ppm)	TAC (ml kg^{-1})
3111	16/03/18	23454	1710.82	278.3	1710.8	278.5	0.3	88.3
	16/03/18	23476	1710.82	278.7				
3113	08/01/19	25519	1711.61	279.9	1711.6	280.0	0.3	88.4
	08/01/19	25537	1711.61	280.2				
3114	29/01/19	25999	1712.64	281.8	1712.6	282.8	1.3	83.7
	29/01/19	26017	1712.64	283.7				
3116	25/04/18	24215	1713.36	282.0	1713.4	280.9	1.6	89.0
	25/04/18	24243	1713.36	279.8				
3116	20/07/18	24880	1713.57	277.7	1713.6	279.6	1.7	87.5
	20/07/18	24896	1713.57	280.3				
	21/03/18	23618	1713.60	280.7				
3117	13/02/19	26358	1714.34	284.2	1714.3	284.6	0.5	85.2
	13/02/19	26374	1714.34	284.9				
3118	29/12/18	25444	1714.89	283.0	1714.9	282.7	0.4	85.9
	29/12/18	25468	1714.89	282.4				
3119	10/01/19	25641	1715.40	282.0	1715.4	282.2	0.4	85.9
	10/01/19	25659	1715.40	282.5				
3121	18/03/18	23535	1716.12	285.3	1716.1	284.4	1.3	88.3
	18/03/18	23555	1716.12	283.5				
3123	31/01/19	26082	1717.11	287.1	1717.1	289.7	2.5	86.4
	14/02/19	26425	1717.14	292.1				
	14/02/19	26441	1717.14	289.8				
3123	29/01/19	26001	1717.64	282.7	1717.6	283.8	1.5	82.6
	29/01/19	26019	1717.64	284.8				
3124	29/12/18	25448	1718.14	285.2	1718.1	285.6	0.5	85.3
	29/12/18	25474	1718.14	285.9				
3126	15/01/18	22499	1718.95	283.6	1718.9	284.7	1.6	88.0
	15/01/18	22515	1718.95	285.8				
3127	05/02/19	26174	1719.31	286.8	1719.3	287.0	0.3	84.8
	05/02/19	26192	1719.31	287.1				
3127	14/02/19	26419	1719.81	285.7	1719.8	285.7	1.6	85.4
	14/02/19	26435	1719.81	285.9				
	31/01/19	26068	1719.84	287.5				
	31/01/19	26086	1719.84	283.6				
3129	05/02/19	26182	1720.44	284.3	1720.4	284.2	0.2	88.0
	05/02/19	26198	1720.44	284.0				
3129	12/02/19	26289	1720.80	280.6	1720.8	283.1	2.6	86.6
	12/02/19	26309	1720.80	285.8				
	12/02/19	26329	1720.80	282.7				
3130	16/01/19	25747	1721.06	281.0	1721.1	281.0	0.0	85.6
	16/01/19	25767	1721.06	281.0				
3131	16/01/18	22546	1721.62	277.2	1721.6	277.9	0.9	85.9
	16/01/18	22556	1721.62	278.5				

Bag No.	Meas. Date	Meas. No.	Depth (m)	CO_2 (ppm)	Depth mean (m)	CO_2 mean (ppm)	sigma (ppm)	TAC (ml kg^{-1})
3133	28/01/19	25949	1722.61	274.6	1722.6	275.6	1.4	85.1
	28/01/19	25967	1722.61	276.6				
3133	20/07/18	24884	1723.11	272.4	1723.1	273.2	2.1	85.0
	20/07/18	24902	1723.11	275.7				
	23/04/18	24063	1723.14	270.9				
	23/04/18	24083	1723.14	273.8				
3136	20/08/20	27343	1724.51	269.5	1724.5	271.5	1.6	87.3
	20/08/20	27347	1724.51	271.0				
	24/04/18	24120	1724.52	272.8				
	24/04/18	24150	1724.52	272.7				
3140	16/01/19	25743	1726.99	269.3	1727.0	269.6	0.5	83.2
	16/01/19	25763	1726.99	270.0				
3141	31/01/18	23007	1727.37	276.0	1727.4	275.7	0.4	87.2
	31/01/18	23037	1727.37	275.5				
3143	09/01/19	25586	1728.11	269.4	1728.1	267.2	2.1	81.3
	09/01/19	25606	1728.11	265.0				
	02/09/21	29241	1728.15	265.8				
	02/09/21	29263	1728.15	268.4				
3144	26/04/18	24284	1729.19	270.2	1729.2	269.8	0.5	90.1
	26/04/18	24306	1729.19	269.5				
3146	25/01/18	22813	1729.81	267.7	1729.8	267.7	0.5	83.2
	20/07/18	24876	1729.84	268.2				
	20/07/18	24894	1729.84	267.2				
3146	15/01/18	22505	1730.15	265.7	1730.1	265.6	0.2	89.7
	15/01/18	22519	1730.15	265.4				
3148	28/01/19	25941	1731.39	267.4	1731.4	267.1	0.5	85.6
	28/01/19	25959	1731.39	266.7				
3151	25/04/18	24207	1732.59	268.0	1732.6	264.9	2.1	89.3
	25/04/18	24235	1732.59	263.4				
	20/07/18	24874	1732.59	263.7				
	20/07/18	24892	1732.59	264.6				
3153	29/12/18	25458	1733.61	262.7	1733.6	262.6	0.1	85.3
	29/12/18	25484	1733.61	262.6				
3154	17/01/19	25812	1734.64	263.2	1734.6	263.5	0.4	88.3
	17/01/19	25834	1734.64	263.7				
3156	11/03/18	23371	1735.51	262.0	1735.5	262.8	1.2	90.0
	11/03/18	23395	1735.51	263.6				
3158	06/12/18	25270	1736.37	261.9	1736.4	263.5	2.2	84.4
	06/12/18	25288	1736.37	265.1				
3159	11/02/19	26232	1737.44	262.5	1737.4	262.8	0.3	84.7
	11/02/19	26254	1737.44	263.0				
3161	02/09/21	29231	1738.43	259.7	1738.4	265.0	5.2	86.5
	02/09/21	29255	1738.43	261.5				
	31/01/18	22989	1738.45	268.2				
	31/01/18	23019	1738.45	270.5				

Bag No.	Meas. Date	Meas. No.	Depth (m)	CO_2 (ppm)	Depth mean (m)	CO_2 mean (ppm)	sigma (ppm)	TAC (ml kg^{-1})
3163	11/02/19	26238	1739.17	261.5	1739.2	261.8	0.5	86.5
	11/02/19	26258	1739.17	262.1				
3163	24/01/19	25890	1739.64	261.4	1739.6	262.2	1.2	82.8
	24/01/19	25908	1739.64	263.0				
3164	23/01/18	22658	1740.19	263.1	1740.2	262.7	0.6	90.7
	23/01/18	22684	1740.19	262.2				
3166	26/01/18	22861	1741.10	259.1	1741.1	258.5	0.9	86.8
	26/01/18	22885	1741.10	257.9				
3171	09/03/18	23312	1743.80	257.2	1743.8	257.6	0.6	86.5
	09/03/18	23338	1743.80	258.1				
3173	31/01/19	26066	1744.82	256.0	1744.8	256.8	0.7	81.9
	20/08/20	27311	1744.86	257.7				
	20/08/20	27327	1744.86	256.5				
	20/08/20	27351	1744.86	257.0				
3174	24/01/19	25886	1745.69	260.9	1745.7	260.7	0.3	85.1
	24/01/19	25904	1745.69	260.5				
3176	26/08/21	29215	1746.39	252.9	1746.4	250.4	2.6	85.0
	02/09/21	29251	1746.39	249.3				
	27/02/18	23157	1746.41	247.3				
	27/02/18	23181	1746.41	252.1				
3176	19/07/18	24827	1746.76	252.4	1746.8	254.7	1.6	86.2
	19/07/18	24841	1746.76	255.0				
	23/03/18	23758	1746.79	255.4				
	23/03/18	23782	1746.79	256.0				
3178	04/02/19	26117	1747.39	253.1	1747.4	252.3	1.1	83.7
	04/02/19	26135	1747.39	251.5				
3179	04/02/19	26123	1748.44	254.0	1748.4	253.5	0.8	89.7
	04/02/19	26141	1748.44	252.9				
3181	21/03/18	23588	1749.11	255.5	1749.1	254.7	3.3	83.7
	21/03/18	23614	1749.11	252.2				
	20/07/18	24882	1749.11	259.0				
	20/07/18	24900	1749.11	252.0				
3183	17/01/19	25818	1750.15	253.3	1750.1	253.0	0.4	85.6
	17/01/19	25838	1750.15	252.7				
3184	14/01/19	25686	1751.19	250.4	1751.2	249.9	0.6	85.8
	14/01/19	25704	1751.19	249.5				
3186	09/03/18	23306	1752.29	249.9	1752.3	250.7	1.1	84.9
	09/03/18	23330	1752.29	251.5				
3187	05/02/19	26178	1752.84	249.8	1752.8	248.7	1.7	85.8
	05/02/19	26190	1752.84	247.5				
3190	13/02/19	26368	1754.06	250.6	1754.1	252.5	2.8	86.4
	13/02/19	26380	1754.06	254.5				
3191	25/01/18	22781	1754.58	253.4	1754.6	252.6	1.1	88.2
	25/01/18	22807	1754.58	251.8				

Bag No.	Meas. Date	Meas. No.	Depth (m)	CO_2 (ppm)	Depth mean (m)	CO_2 mean (ppm)	sigma (ppm)	TAC (ml kg^{-1})
3193	13/02/19	26372	1755.65	254.5	1755.6	252.0	3.5	83.5
	13/02/19	26384	1755.65	249.5				
3194	23/04/18	24051	1756.16	244.9	1756.2	245.2	0.5	90.0
	23/04/18	24071	1756.16	245.6				
3194	07/12/18	25337	1756.69	245.9	1756.7	246.3	0.5	84.7
	07/12/18	25357	1756.69	246.6				
3196	23/01/18	22668	1757.55	245.2	1757.5	244.8	0.6	89.5
	23/01/18	22694	1757.55	244.4				
3198	16/01/19	25759	1758.36	244.4	1758.4	243.7	1.1	85.6
	16/01/19	25779	1758.36	242.9				
3199	29/01/19	26011	1759.44	242.3	1759.4	242.3	0.1	87.3
	29/01/19	26029	1759.44	242.4				
3201	25/04/18	24197	1760.54	238.5	1760.5	239.0	0.7	88.0
	25/04/18	24225	1760.54	239.5				
3203	31/01/19	26054	1761.64	235.9	1761.6	236.6	1.0	84.4
	31/01/19	26072	1761.64	237.3				
3206	24/04/18	24108	1763.06	235.0	1763.1	236.1	1.9	88.4
	24/04/18	24144	1763.06	236.3				
	25/08/20	27394	1763.10	238.6				
	25/08/20	27404	1763.10	234.4				
3207	12/02/19	26299	1763.84	240.0	1763.8	238.6	1.9	85.3
	12/02/19	26319	1763.84	237.3				
3210	05/02/19	26180	1764.96	234.3	1765.0	233.9	0.5	86.2
	05/02/19	26196	1764.96	233.6				
3211	25/01/18	22787	1765.61	235.6	1765.6	234.5	1.5	87.1
	25/01/18	22815	1765.61	233.5				
3213	07/12/18	25339	1766.61	235.3	1766.6	233.9	1.9	88.8
	07/12/18	25355	1766.61	232.5				
3214	12/02/19	26293	1767.69	239.2	1767.7	237.5	2.4	85.6
	12/02/19	26313	1767.69	235.7				
3216	27/02/18	23153	1768.79	229.6	1768.8	230.1	0.8	91.9
	27/02/18	23179	1768.79	230.7				
3221	24/04/18	24160	1771.02	229.6	1771.0	230.6	2.3	89.6
	24/04/18	24134	1771.04	229.0				
	24/04/18	24112	1771.06	233.2				
3223	29/12/18	25464	1772.64	226.8	1772.6	225.8	1.4	86.0
	29/12/18	25488	1772.64	224.8				
3224	01/05/18	24373	1772.67	226.0	1772.7	226.0		85.3
3224	01/05/18	24347	1772.69	223.0	1772.7	224.8	2.6	88.4
	01/05/18	24397	1772.71	226.7				
3227	17/01/19	25814	1774.31	223.5	1774.3	224.4	1.3	85.0
	17/01/19	25836	1774.31	225.3				
3228	15/01/18	22493	1775.39	226.2	1775.4	225.4	1.1	86.7
	15/01/18	22507	1775.39	224.7				

Bag No.	Meas. Date	Meas. No.	Depth (m)	CO_2 (ppm)	Depth mean (m)	CO_2 mean (ppm)	sigma (ppm)	TAC (ml kg^{-1})
3230	24/01/19	25896	1776.08	222.5	1776.1	223.7	1.7	86.4
	24/01/19	25916	1776.08	224.9				
3230	11/02/19	26244	1776.38	222.2	1776.4	222.5	0.4	84.9
	11/02/19	26264	1776.38	222.8				
3231	25/04/18	24213	1776.78	221.0	1776.8	221.2	0.2	90.4
	25/04/18	24239	1776.78	221.3				
3233	04/02/19	26115	1777.61	218.7	1777.6	219.1	0.5	86.1
	04/02/19	26133	1777.61	219.4				
3233	25/08/20	27408	1778.11	218.4	1778.1	217.5	0.6	93.0
	25/08/20	27422	1778.11	217.2				
	09/01/19	25574	1778.14	216.9				
	09/01/19	25594	1778.14	217.6				
3234	23/01/18	22660	1778.69	220.6	1778.7	219.6	1.5	86.9
	23/01/18	22688	1778.69	218.6				
3237	04/02/19	26111	1779.81	215.8	1779.8	216.3	0.7	87.2
	04/02/19	26129	1779.81	216.8				
3237	08/01/19	25529	1780.34	216.8	1780.3	216.5	0.4	87.7
	08/01/19	25547	1780.34	216.2				
3239	26/04/18	24272	1780.92	213.7	1780.9	215.2	1.8	90.0
	26/04/18	24314	1780.94	217.3				
	26/04/18	24292	1780.96	214.8				
3240	04/02/19	26143	1781.56	216.8	1781.6	219.2	2.1	88.4
	14/02/19	26423	1781.59	219.9				
	14/02/19	26437	1781.59	220.8				
3241	09/03/18	23328	1782.09	210.6	1782.1	210.3	0.5	87.9
	20/07/18	24872	1782.09	209.7				
3241	20/07/18	24890	1782.09	210.6	1782.1	210.3	0.5	87.9
3243	25/08/21	29153	1783.65	206.5	1783.7	206.5		82.5
3249	23/08/21	29059	1786.40	212.0	1786.4	213.6	2.2	
	23/08/21	29121	1786.40	215.1				
3258	25/08/21	29133	1791.35	199.2	1791.4	197.9	1.8	
	26/08/21	29199	1791.35	196.7				
3259	23/08/21	29120	1791.90	209.6	1791.9	209.6		
3264	23/08/21	29073	1795.20	205.7	1795.2	205.7		
3271	25/08/21	29137	1799.05	199.8	1799.1	199.4	0.5	
	25/08/21	29169	1799.05	199.0				
3274	23/08/21	29063	1800.15	211.7	1800.2	209.1	3.7	
	23/08/21	29089	1800.15	206.5				
3277	25/08/21	29145	1801.80	199.7	1801.8	199.9	0.3	
	25/08/21	29167	1801.80	200.1				
3280	25/08/21	29151	1803.45	198.0	1803.5	197.0	1.4	
	25/08/21	29187	1803.45	196.0				
3283	23/08/21	29057	1805.10	200.6	1805.1	200.6		
3289	25/08/21	29157	1808.95	187.3	1809.0	188.0	1.0	
	25/08/21	29173	1808.95	188.7				

Bag No.	Meas. Date	Meas. No.	Depth (m)	CO_2 (ppm)	Depth mean (m)	CO_2 mean (ppm)	sigma (ppm)	TAC (ml kg^{-1})
3293	26/08/21	29197	1810.60	191.1	1810.6	190.1	1.4	
	26/08/21	29201	1810.60	189.1				
3294	23/08/21	29116	1811.15	197.6	1811.2	197.6		
3303	25/08/21	29129	1816.60	190.6	1816.6	192.8	3.2	
	25/08/21	29181	1816.60	195.0				
3304	25/08/21	29135	1816.70	192.2	1816.7	189.0	4.5	
	25/08/21	29177	1816.70	185.8				
3307	23/08/21	29081	1818.30	196.7	1818.3	196.7		
3310	25/08/21	29143	1819.95	193.7	1820.0	194.5	1.1	
	25/08/21	29175	1819.95	195.2				
3317	25/08/21	29161	1823.80	195.2	1823.8	194.8	0.6	
	25/08/21	29165	1823.80	194.3				
3320	25/08/21	29141	1825.45	191.4	1825.5	193.9	3.5	
	25/08/21	29147	1825.45	196.4				
3323	23/08/21	29097	1827.10	206.0	1827.1	205.8	0.2	
	23/08/21	29109	1827.10	205.6				
3327	23/08/21	29107	1829.30	204.3	1829.3	204.3		
3329	23/08/21	29079	1830.40	203.6	1830.4	201.5	3.0	
	23/08/21	29087	1830.40	199.4				
3332	23/08/21	29083	1832.05	199.9	1832.1	196.7	4.6	
	23/08/21	29099	1832.05	193.4				

Full bag experiments

Table A.2: Measurements performed for the full bag experiments with the EDC ice core (Section 3.3.2).

Bag No.	Meas. Date	Meas. No.	Depth (m)	CO_2 (ppm)	Depth mean (m)	CO_2 mean (ppm)	sigma (ppm)	TAC (ml kg^{-1})
2884	03/12/20	27767	1585.67	278.6	1585.67	275.0	3.1	83.1
	03/12/20	27769	1585.67	273.7				
	03/12/20	27775	1585.67	272.7				
	03/12/20	27771	1585.69	276.9	1585.69	277.5	0.8	85.8
	03/12/20	27777	1585.69	278.5				
	03/12/20	27783	1585.69	277.2				
	03/12/20	27781	1585.71	276.8	1585.71	276.8		85.4
	03/12/20	27761	1585.73	273.3	1585.73	274.1	1.1	82.4
	03/12/20	27763	1585.73	274.9				
	04/12/20	27818	1585.75	276.4	1585.75	276.4	1.4	89.0
	04/12/20	27832	1585.75	277.8				
	04/12/20	27848	1585.75	274.9				
	07/10/20	27591	1585.81	276.0	1585.81	273.2	3.9	70.5
	03/12/20	27755	1585.81	270.5				
	07/10/20	27595	1585.83	275.6	1585.83	275.6		88.2
	03/12/20	27753	1585.86	274.2	1585.86	274.1	0.0	74.8
	03/12/20	27759	1585.86	274.1				
	09/09/20	27532	1585.91	273.6	1585.91	273.9	0.5	89.9
	09/09/20	27534	1585.91	274.5				
	09/09/20	27566	1585.91	273.7				
	09/09/20	27542	1585.93	268.8	1585.93	270.9	2.9	87.6
	09/09/20	27558	1585.93	274.2				
	09/09/20	27564	1585.93	269.5				
	09/09/20	27526	1585.96	283.1	1585.96	281.9	1.9	90.5
	09/09/20	27538	1585.96	279.8				
	09/09/20	27556	1585.96	283.0				
	09/09/20	27540	1585.98	290.4	1585.98	287.4	2.7	89.7
	09/09/20	27550	1585.98	285.1				
	09/09/20	27554	1585.98	286.7				
	09/09/20	27524	1586.01	280.1	1586.01	278.7	1.5	91.6
	09/09/20	27530	1586.01	278.9				
	09/09/20	27562	1586.01	277.2				

Bag No.	Meas. Date	Meas. No.	Depth (m)	CO_2 (ppm)	Depth mean (m)	CO_2 mean (ppm)	sigma (ppm)	TAC (ml kg^{-1})
2884	09/09/20	27522	1586.03	265.5	1586.03	270.7	4.5	87.0
	09/09/20	27546	1586.03	273.9				
	09/09/20	27548	1586.03	272.6				
	08/09/20	27465	1586.06	278.7	1586.06	275.7	2.6	90.8
	08/09/20	27473	1586.06	274.5				
	08/09/20	27501	1586.06	274.0				
	08/09/20	27475	1586.08	276.4	1586.08	276.1	1.0	86.5
	08/09/20	27483	1586.08	276.8				
	08/09/20	27493	1586.08	275.0				
	08/09/20	27467	1586.11	275.1	1586.11	275.2	0.1	88.4
	08/09/20	27487	1586.11	275.4				
	08/09/20	27491	1586.11	275.2				
	08/09/20	27457	1586.13	274.0	1586.13	273.7	0.4	93.9
	08/09/20	27461	1586.13	273.3				
	08/09/20	27477	1586.13	273.9				
	08/09/20	27459	1586.16	276.8	1586.16	275.7	0.9	90.2
	08/09/20	27497	1586.16	275.4				
	08/09/20	27499	1586.16	275.0				
	08/09/20	27469	1586.18	275.7	1586.18	277.6	1.9	87.7
	08/09/20	27481	1586.18	277.8				
	08/09/20	27485	1586.18	279.4				
3081	15/01/20	26993	1694.10	273.5	1694.10	275.2	2.5	89.6
	15/01/20	27013	1694.10	277.0				
	15/01/20	27005	1694.12	277.9	1694.12	278.1	0.3	89.8
	15/01/20	27027	1694.12	278.4				
	15/01/20	26997	1694.14	273.8	1694.14	274.5	1.0	89.7
	15/01/20	27019	1694.14	275.2				
	09/10/19	26905	1694.18	279.0	1694.18	279.1	0.2	89.0
	09/10/19	26925	1694.18	279.2				
	09/10/19	26901	1694.21	275.6	1694.21	274.8	1.2	88.9
	09/10/19	26919	1694.21	274.0				
	09/10/19	26909	1694.23	274.8	1694.23	274.6	0.2	92.1
	09/10/19	26927	1694.23	274.5				
	09/10/19	26917	1694.25	278.7	1694.25	277.1	2.3	90.9
	09/10/19	26935	1694.25	275.5				
	09/10/19	26911	1694.27	279.0	1694.27	276.9	3.0	90.0
	09/10/19	26929	1694.27	274.8				
	04/10/19	26852	1694.29	279.1	1694.29	278.9	0.3	95.2
	04/10/19	26866	1694.29	278.8				
	04/10/19	26858	1694.32	279.5	1694.32	278.1	2.0	93.4
	04/10/19	26872	1694.32	276.7				
	04/10/19	26864	1694.34	281.0	1694.34	279.0	2.8	97.3
	04/10/19	26878	1694.34	277.0				
	04/10/19	26854	1694.36	277.8	1694.36	277.3	0.7	87.9
	04/10/19	26870	1694.36	276.9				

Bag No.	Meas. Date	Meas. No.	Depth (m)	CO_2 (ppm)	Depth mean (m)	CO_2 mean (ppm)	sigma (ppm)	TAC (ml kg^{-1})
4824	23/02/21	28382	2652.66	204.7	2652.66	204.8	0.8	87.6
	23/02/21	28395	2652.66	204.0				
	23/02/21	28405	2652.66	205.6				
	23/02/21	28371	2652.69	200.6	2652.69	201.0	1.8	86.5
	23/02/21	28375	2652.69	203.0				
	23/02/21	28399	2652.69	199.4				
	23/02/21	28391	2652.71	200.2	2652.71	198.9	1.1	90.4
	23/02/21	28397	2652.71	198.1				
	23/02/21	28403	2652.71	198.6				
	23/02/21	28381	2652.73	200.1	2652.73	200.0	0.2	91.8
	23/02/21	28389	2652.73	199.9				
	23/02/21	28370	2652.75	199.2	2652.75	200.1	1.5	92.7
	23/02/21	28387	2652.75	201.8				
	23/02/21	28407	2652.75	199.2				
	22/02/21	28327	2652.78	197.6	2652.78	198.7	1.5	88.4
	22/02/21	28347	2652.78	199.8				
	22/02/21	28329	2652.80	199.4	2652.80	199.3	0.9	89.6
	22/02/21	28335	2652.80	200.1				
	22/02/21	28345	2652.80	198.4				
	22/02/21	28337	2652.82	198.9	2652.82	199.3	0.4	89.8
	22/02/21	28349	2652.82	199.6				
	22/02/21	28355	2652.82	199.4				
	22/02/21	28331	2652.85	198.3	2652.85	199.4	1.2	91.2
	22/02/21	28353	2652.85	199.2				
	22/02/21	28357	2652.85	200.7				
	19/02/21	28307	2652.88	197.6	2652.88	198.5	1.3	84.1
	19/02/21	28311	2652.88	199.5				
	19/02/21	28303	2652.90	199.9	2652.90	199.1	1.1	89.9
	19/02/21	28313	2652.90	198.3				
	19/02/21	28293	2652.92	200.2	2652.92	199.4	1.1	88.3
	19/02/21	28295	2652.92	198.6				
	19/02/21	28287	2652.95	198.8	2652.95	199.2	2.0	90.1
	19/02/21	28289	2652.95	197.5				
	19/02/21	28315	2652.95	201.4				
	19/02/21	28277	2652.97	197.4	2652.97	197.5	0.2	92.5
	19/02/21	28285	2652.97	197.3				
	19/02/21	28317	2652.97	197.7				
	18/02/21	28226	2653.00	201.5	2653.00	200.1	2.0	95.3
	18/02/21	28248	2653.00	198.8				
	18/02/21	28240	2653.02	198.0	2653.02	198.7	0.8	89.1
	18/02/21	28244	2653.02	199.6				
	18/02/21	28254	2653.02	198.4				
	18/02/21	28230	2653.07	203.1	2653.07	203.6	0.9	88.6
	18/02/21	28238	2653.07	203.1				
	18/02/21	28252	2653.07	204.7				

Bag No.	Meas. Date	Meas. No.	Depth (m)	CO_2 (ppm)	Depth mean (m)	CO_2 mean (ppm)	sigma (ppm)	TAC (ml kg^{-1})
4824	18/02/21	28232	2653.09	199.0	2653.09	199.5	2.3	91.9
	18/02/21	28236	2653.09	197.6				
	18/02/21	28246	2653.09	202.0				
	17/02/21	28204	2653.11	197.7	2653.11	198.6	0.8	88.4
	17/02/21	28208	2653.11	198.6				
	17/02/21	28212	2653.11	199.4				
	17/02/21	28184	2653.14	197.2	2653.14	198.0	0.9	91.0
	17/02/21	28194	2653.14	198.9				
	17/02/21	28210	2653.14	197.9				
	17/02/21	28192	2653.16	199.3	2653.16	198.3	0.8	92.5
	17/02/21	28200	2653.16	197.8				
	17/02/21	28202	2653.16	197.8				
	17/02/21	28186	2653.18	198.4	2653.18	199.0	0.5	89.2
	17/02/21	28188	2653.18	199.0				
	17/02/21	28196	2653.18	199.5				
4974	29/12/20	28011	2735.17	285.6	2735.17	284.7	1.3	92.2
	29/12/20	28031	2735.17	283.8				
	29/12/20	28019	2735.19	282.9	2735.19	281.8	1.1	86.9
	29/12/20	28043	2735.19	280.8				
	18/02/21	28260	2735.19	281.7				
	29/12/20	28009	2735.22	281.2	2735.22	278.9	2.2	89.5
	29/12/20	28035	2735.22	278.6				
	29/12/20	28037	2735.22	276.9				
	29/12/20	28029	2735.24	282.4	2735.24	282.3	0.2	90.7
	29/12/20	28045	2735.24	282.1				
	29/12/20	28047	2735.24	282.3				
	29/12/20	28021	2735.26	280.7	2735.26	280.8	0.1	89.5
	29/12/20	28027	2735.26	280.9				
	29/12/20	28023	2735.28	280.9	2735.28	280.1	1.2	87.0
	29/12/20	28051	2735.28	278.8				
	18/02/21	28258	2735.28	280.6				
	29/12/20	28013	2735.30	279.7	2735.30	279.9	1.2	72.0
	29/12/20	28039	2735.30	281.2				
	29/12/20	28057	2735.30	278.8				
	11/12/20	27943	2735.33	282.2	2735.33	281.5	1.4	87.5
	11/12/20	27951	2735.33	282.5				
	11/12/20	27959	2735.33	279.9				
	11/12/20	27927	2735.35	280.8	2735.35	281.2	0.5	90.2
	11/12/20	27963	2735.35	281.7				
	11/12/20	27965	2735.35	281.3				
	11/12/20	27925	2735.38	280.0	2735.38	281.4	1.8	87.1
	11/12/20	27949	2735.38	280.8				
	11/12/20	27955	2735.38	283.5				

Bag No.	Meas. Date	Meas. No.	Depth (m)	CO_2 (ppm)	Depth mean (m)	CO_2 mean (ppm)	sigma (ppm)	TAC (ml kg^{-1})
4974	11/12/20	27941	2735.40	280.6	2735.40	281.4	1.1	87.7
	11/12/20	27957	2735.40	282.2				
	11/12/20	27947	2735.42	280.9	2735.42	280.9		90.7
	09/12/20	27889	2735.45	285.0	2735.45	284.0	1.3	62.5
	09/12/20	27893	2735.45	283.1				
	09/12/20	27885	2735.47	280.4	2735.47	281.1	1.3	91.0
	09/12/20	27901	2735.47	282.5				
	09/12/20	27917	2735.47	280.3				
	09/12/20	27897	2735.49	281.3	2735.49	280.9	0.6	87.2
	09/12/20	27913	2735.49	280.5				
	09/12/20	27877	2735.51	275.7	2735.51	278.8	4.3	91.4
	09/12/20	27899	2735.51	281.8				
	09/12/20	27875	2735.54	281.4	2735.54	281.4	1.0	89.4
	09/12/20	27907	2735.54	282.3				
	09/12/20	27909	2735.54	280.4				
	09/12/20	27873	2735.56	278.7	2735.56	280.5	1.9	92.2
	09/12/20	27881	2735.56	282.6				
	09/12/20	27905	2735.56	280.1				
	04/12/20	27826	2735.60	281.8	2735.60	281.1	0.9	90.8
	04/12/20	27840	2735.60	280.1				
	04/12/20	27850	2735.60	281.5				
	04/12/20	27814	2735.62	285.3	2735.62	283.6	1.6	90.9
	04/12/20	27816	2735.62	282.2				
	04/12/20	27834	2735.62	283.3				
	04/12/20	27806	2735.64	284.0	2735.64	283.0	1.0	88.9
	04/12/20	27822	2735.64	281.9				
	04/12/20	27842	2735.64	283.0				
	04/12/20	27810	2735.66	281.5	2735.66	281.7	1.4	88.1
	04/12/20	27824	2735.66	280.4				
	04/12/20	27830	2735.66	283.2				
	04/12/20	27808	2735.68	282.3	2735.68	282.1	0.3	90.0
	04/12/20	27838	2735.68	282.3				
	04/12/20	27846	2735.68	281.7				

MIS 6

Table A.3: Measurements performed for the MIS 6 dataset with the EDC ice core (Section 5.2).

Bag No.	Meas. Date	Meas. No.	Depth (m)	CO_2 (ppm)	Depth mean (m)	CO_2 mean (ppm)	sigma (ppm)	TAC (ml kg^{-1})
3246	03/09/19	26688	1785.23	208.9	1785.23	209.0	0.2	89.3
	03/09/19	26710	1785.23	209.2				
3253	02/09/19	26613	1788.67	206.2	1788.67	206.1	0.1	89.1
	02/09/19	26635	1788.67	206.0				
3263	03/09/19	26686	1794.58	201.8	1794.58	201.2	0.5	89.1
	03/09/19	26708	1794.58	200.7				
3269	03/09/19	26678	1797.73	200.9	1797.73	200.6	0.3	89.7
	03/09/19	26700	1797.73	200.3				
3286	02/09/19	26611	1807.23	196.3	1807.23	195.8	0.5	91.8
	02/09/19	26633	1807.23	195.3				
3299	27/08/19	26564	1814.04	191.8	1814.04	193.0	1.0	90.5
	27/08/19	26586	1814.04	192.8				
	27/08/19	26590	1814.04	194.3				
3313	02/09/19	26631	1821.67	204.0	1821.68	201.1	2.1	92.3
	02/09/19	26653	1821.67	199.1				
	04/09/19	26745	1821.69	201.9				
	04/09/19	26763	1821.69	199.2				
3369	27/08/19	26550	1852.54	200.7	1852.54	199.9	0.6	91.7
	27/08/19	26570	1852.54	199.8				
	27/08/19	26588	1852.54	199.3				
3396	04/09/19	26757	1867.73	204.1	1867.73	202.4	1.7	93.6
	04/09/19	26775	1867.73	200.6				
3434	02/09/19	26617	1888.22	188.5	1888.23	190.2	1.0	90.9
	02/09/19	26641	1888.22	191.2				
	04/09/19	26753	1888.24	190.3				
	04/09/19	26771	1888.24	190.6				
3439	27/08/19	26552	1890.97	185.5	1890.97	186.0	0.5	86.5
	27/08/19	26572	1890.97	186.5				
3463	27/08/19	26554	1904.58	198.7	1904.58	199.1	0.4	85.4
	27/08/19	26574	1904.58	199.6				
3469	03/09/19	26680	1907.54	204.2	1907.54	203.7	0.5	89.0
	03/09/19	26702	1907.54	203.2				

Bag No.	Meas. Date	Meas. No.	Depth (m)	CO_2 (ppm)	Depth mean (m)	CO_2 mean (ppm)	sigma (ppm)	TAC (ml kg^{-1})
3501	27/08/19	26560	1925.48	199.9	1925.47	202.4	1.5	90.5
	27/08/19	26580	1925.48	203.6				
	04/09/19	26749	1925.46	203.3				
	04/09/19	26767	1925.46	202.8				
3508	02/09/19	26615	1929.33	196.8	1929.33	197.0	0.2	87.6
	02/09/19	26639	1929.33	197.2				
3526	02/09/19	26655	1939.23	190.0	1939.22	189.5	0.7	91.6
	04/09/19	26755	1939.21	190.1				
	04/09/19	26773	1939.21	188.6				
3533	03/09/19	26694	1943.14	191.7	1943.14	191.3	0.5	88.7
	03/09/19	26716	1943.14	190.8				
3539	03/09/19	26692	1945.97	199.0	1945.97	198.3	0.8	88.2
	03/09/19	26712	1945.97	197.5				
3546	27/08/19	26562	1950.23	202.2	1950.23	201.3	0.9	87.7
	27/08/19	26582	1950.23	200.3				
3566	02/09/19	26625	1961.23	195.2	1961.23	195.3	0.2	89.2
	02/09/19	26649	1961.23	195.5				
3578	27/08/19	26548	1967.83	201.4	1967.83	201.2	0.2	91.5
	27/08/19	26568	1967.83	201.1				
3596	03/09/19	26676	1977.65	195.2	1977.64	194.1	1.2	89.8
	03/09/19	26696	1977.65	193.0				
	04/09/19	26747	1977.63	195.5				
	04/09/19	26765	1977.63	192.7				
3601	04/09/19	26743	1980.48	190.2	1980.48	191.0	0.8	91.3
	04/09/19	26759	1980.48	191.8				
3633	27/08/19	26558	1998.08	211.7	1998.08	211.6	0.2	85.5
	27/08/19	26578	1998.08	211.4				
3639	02/09/19	26621	2000.97	216.7	2000.97	217.6	1.0	88.3
	02/09/19	26643	2000.97	218.6				
3666	02/09/19	26623	2016.23	200.8	2016.23	200.2	0.6	89.4
	02/09/19	26647	2016.23	199.6				
3699	03/09/19	26684	2033.97	225.5	2033.97	224.2	1.4	91.1
	03/09/19	26704	2033.97	222.8				

Byrd

Table A.4: Measurements performed for the QCLAS.

Bag No.	Meas. Date	Meas. No.	Depth (m)	CO_2 (ppm)	Depth mean (m)	CO_2 mean (ppm)	sigma (ppm)
53	03/08/20	27171	1797.72	217.8	1797.72	218.9	9.0
	03/08/20	27181	1797.72	212.5			
	03/08/20	27185	1797.72	213.2			
	03/08/20	27187	1797.72	236.1			
	03/08/20	27191	1797.72	213.0			
	03/08/20	27197	1797.72	220.7			

Acknowledgements

The support of my family and peers carried me in the personal voyage of manbirthing this document. I would like to warmly thank

... **Thomas Stocker** for supervising with unwaivering support and guidance; for your understanding and flexibility that allowed my best self to pursue this PhD. Your unassailable trust in my work reassured me when I was not able to trust myself.

... **Hubertus Fischer** for scientific prowess and constructive criticism in all discussions. Your diligent and expeditious work were a beacon of professionalism for me.

... **Ed Brook** for examining this thesis.

... **Jochen Schmitt** for the openness to wild ideas, ease of approach and patience to listen.

... **Christoph Nehrbass-Ahles** for mentoring me on how to dance with the CIM, and how to patiently endure her diva tantrums. Without your teachings I would not have produced a single data point.

... **Bernhard Bereiter** for ingeniously putting the CIM together.

... **Loïc Schmidely** for experimental companionship and mutual support during our meetings.

... **Juhyeong Han** for sharing, for listening and for caring.

... **Chantal Zeppenfeld, Florian Krauss and Tito Arosio** for that uplifting beer when I needed it the most.

... **Stéphanie Musy, Jean-Elie Fontaine, Angélique Hameau and Vasileios Mandrakis** for the personal exchanges, the sharing of the struggle and the compassionate support.

... **Jeemijn Scheen and Zhijun Liu** for pulling me out of the office when I needed a break.

... **Lars Mächler, Camilla Jensen, Imogen Gabriel, Daniel Baggenstos, Marcel Häberli, Markus Grimmer, Bärbel Seth, Jonas Beck, Michaela Mühl and Sarah Eggleston** for joining me in the non-sense during the coffee breaks and taking it in stride.

... **Christian Wirths** for putting up with an office mate in constant depressing mood since he started.

... **Remo Walther, Samuel Marending and Kurt Grossenbacher** for lending a hand and their expertise whenever the CIM was in need of a hands-on approach.

... **Peter Nyfeler** for taking the time and patience to assist me with anything cylinder-related.

... **Gunnar Jansen** for insurmountable patience when helping me deal with IT headaches. Nicest guy at KUP. There, I said it.

... **Doris Rätz, Bettina Schüpbach, Claudia Maschke and Sue Nydegger** for always promptly helping me with a smile, whatever the subject I came to annoy them with.

... **all ICYS members** for volunteering their time and energy for the benefit of the community. A word of thanks to **Amy King** with whom I pleasantly steered the ship for a long while.

... **all EastGRIP members** with whom I shared a lively routine for 2 months on the ice sheet.

And last but not least...

... **Catarina Dias, Roman Krupa and Tiago Costa** for blindly believing that I could push through while not really knowing what I have been doing for the past four years. And no, with this PhD I cannot give you the weather forecast for the weekend.

... **my family in Portugal** who endure my absence with the same *Saudade* as I endure theirs.

... **Inês, Raul and Artur** for shining light on what really matters and giving me my happiest moments. Without your love, laughter and support I'd still be writing the introduction.

Publications

Silva, L., Nehrbass-Ahles, C., Schmidely, L., Schmitt, J., Fischer, H. and Stocker, T. F. Assessing atmospheric CO_2 variability during Marine Isotope Stage 5 based on the EDC ice core, *in preparation*.

2021: Technical Summary. In Climate Change 2021: The Physical Science Basis. Contribution of Working Group I to the Sixth Assessment Report of the Intergovernmental Panel on Climate Change [Masson-Delmotte, V., P. Zhai, A. Pirani, S.L. Connors, C. Péan, S. Berger, N. Caud, Y. Chen, L. Goldfarb, M.I. Gomis, M. Huang, K. Leitzell, E. Lonnoy, J.B.R. Matthews, T.K. Maycock, T. Waterfield, O. Yelekçi, R. Yu, and B. Zhou (eds.)]. **Contributing Author**. Cambridge University Press. In Press.

2021: Framing, Context, and Methods. In Climate Change 2021: The Physical Science Basis. Contribution of Working Group I to the Sixth Assessment Report of the Intergovernmental Panel on Climate Change [Masson-Delmotte, V., P. Zhai, A. Pirani, S.L. Connors, C. Péan, S. Berger, N. Caud, Y. Chen, L. Goldfarb, M.I. Gomis, M. Huang, K. Leitzell, E. Lonnoy, J.B.R. Matthews, T.K. Maycock, T. Waterfield, O. Yelekçi, R. Yu, and B. Zhou (eds.)]. **Contributing Author**. Cambridge University Press. In Press.

Schmidely, L., Nehrbass-Ahles, C., Schmitt, J., Han, J., **Silva, L.**, Shin, J., Joos, F., Chappellaz, J., Fischer, H. and Stocker, T. F. (2021). CH_4 and N_2O fluctuations during the penultimate deglaciation. *Climate of the Past*, 17(4):1627-1643

Shin, J., Nehrbass-Ahles, C., Grilli, R., Chowdhry Beeman, J., Parrenin, F., Teste, G., Landais, A., Schmidely, L., **Silva, L.**, Schmitt, J., Stocker, T. F., Fischer, H., and Chappellaz, J. (2020). Millennial-scale atmospheric CO_2 variations during the Marine Isotope Stage 6 period (190–135 ka). *Climate of the Past*, 16(6):2203–2219

Nehrbass-Ahles, C., Shin, J., Schmitt, J., Bereiter, B., Joos, F., Schilt, A., Schmidely, L., **Silva, L.**, Teste, G., Grilli, R., Chappellaz, J., Hodell, D., Fischer, H., and Stocker, T. F. (2020). Abrupt CO_2 release to the atmosphere under glacial and early interglacial climate conditions. *Science*, 369(6506):1000–1005

Silva, L. (2014). Optical sensors for acoustic detection. Master thesis. University of Porto

Declaration of consent

on the basis of Article 18 of the PromR Phil.-nat. 19

Name/First Name: Borges da Silva, Lucas

Registration Number: 17-128-943

Study program: PhD Physics

Bachelor ☐ Master ☐ Dissertation ☑

Title of the thesis: High-resolution reconstruction of atmospheric CO2 concentrations during the last interglacial with the EDC ice core

Supervisor: Thomas Stocker

I declare herewith that this thesis is my own work and that I have not used any sources other than those stated. I have indicated the adoption of quotations as well as thoughts taken from other authors as such in the thesis. I am aware that the Senate pursuant to Article 36 paragraph 1 litera r of the University Act of September 5th, 1996 and Article 69 of the University Statute of June 7th, 2011 is authorized to revoke the doctoral degree awarded on the basis of this thesis.
For the purposes of evaluation and verification of compliance with the declaration of originality and the regulations governing plagiarism, I hereby grant the University of Bern the right to process my personal data and to perform the acts of use this requires, in particular, to reproduce the written thesis and to store it permanently in a database, and to use said database, or to make said database available, to enable comparison with theses submitted by others.

Bern, 11.03.2022

Place/Date

Lucas Silva Digitally signed by Lucas Silva Date: 2022.03.11 11:22:11 +01'00'

Signature